

AD-A112 271

BATTELLE COLUMBUS LABS OH
RESEARCH TO DEVELOP PROCESS MODELS FOR PRODUCING A DUAL PROPERTY—ETC(U)
OCT 81 6 D LAMOTI, Y ALTAN

F/8 11/8

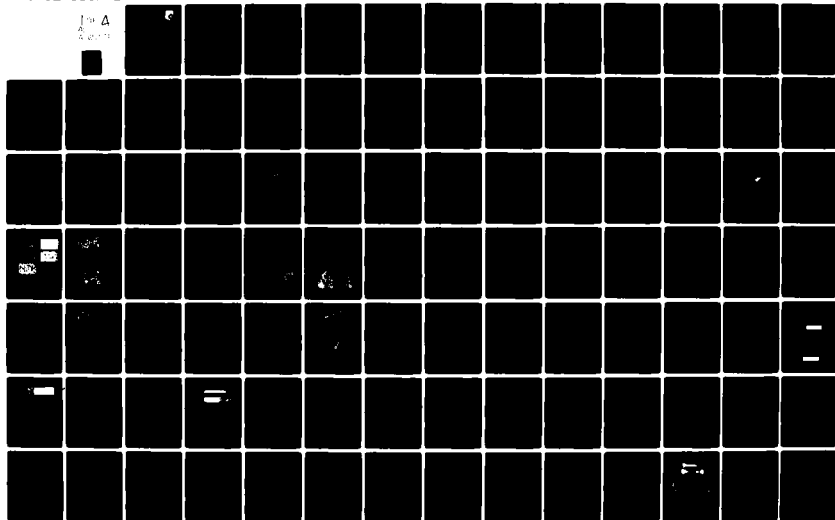
F33615-78-C-5025

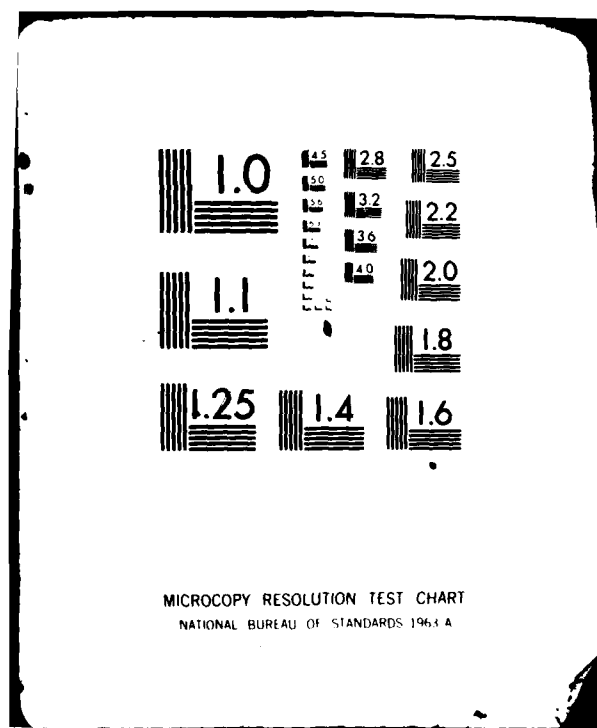
UNCLASSIFIED

AFMIL-TR-81-8130

ML

1 to Δ
A. 10. 10. 10.

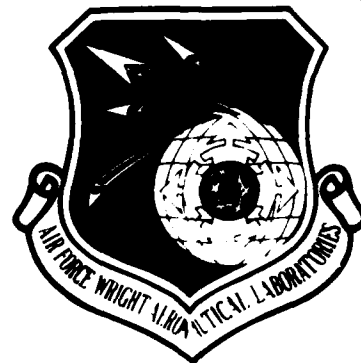




ADA 112271

DTIC FILE COPY

AFWAL-TR-81-4130



12

**RESEARCH TO DEVELOP PROCESS MODELS FOR PRODUCING
A DUAL PROPERTY TITANIUM ALLOY COMPRESSOR DISK**

G. D. Lahoti
T. Altan

Battelle's Columbus Laboratories
Columbus, Ohio 43201

October 1981

Interim Report for Period 1 August 1980 - 31 July 1981

Approved for public release; distribution unlimited.

**MATERIALS LABORATORY
AIR FORCE WRIGHT AERONAUTICAL LABORATORIES
AIR FORCE SYSTEMS COMMAND
WRIGHT-PATTERSON AIR FORCE BASE, OHIO 45433**

**DTIC
ELECTE
MAR 22 1982**

E

82

08

02

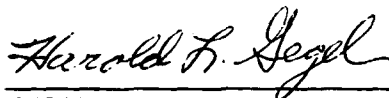
126

NOTICE

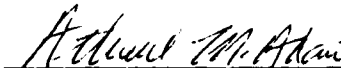
When Government drawings, specifications, or other data are used for any purpose other than in connection with a definitely related Government procurement operation, the United States Government thereby incurs no responsibility nor any obligation whatsoever; and the fact that the government may have formulated, furnished, or in any way supplied the said drawings, specifications, or other data, is not to be regarded by implication or otherwise as in any manner licensing the holder or any other person or corporation, or conveying any rights or permission to manufacture use, or sell any patented invention that may in any way be related thereto.

This report has been reviewed by the Office of Public Affairs (ASD/PA) and is releasable to the National Technical Information Service (NTIS). At NTIS, it will be available to the general public, including foreign nations.

This technical report has been reviewed and is approved for publication.



HAROLD L. GEGEL
Project Engineer



ATTWELL M. ADAIR
Technical Area Manager
Processing & High Temperature
Materials Branch
Metals & Ceramics Division

FOR THE COMMANDER



HENRY L. GRAHAM, Chief
Processing & High Temperature
Materials Branch
Metals & Ceramics Division

"If your address has changed, if you wish to be removed from our mailing list, or if the addressee is no longer employed by your organization please notify AFWAL/MLLM, W-PAFB, OH 45433 to help us maintain a current mailing list".

Copies of this report should not be returned unless return is required by security considerations, contractual obligations, or notice on a specific document.

Unclassified

SECURITY CLASSIFICATION OF THIS PAGE (When Data Entered)

REPORT DOCUMENTATION PAGE		READ INSTRUCTIONS BEFORE COMPLETING FORM												
1. REPORT NUMBER AFWAL-TR-81-4130	2. GOVT ACCESSION NO. AD A112271	3. RECIPIENT'S CATALOG NUMBER												
4. TITLE (and Subtitle) RESEARCH TO DEVELOP PROCESS MODELS FOR PRODUCING A DUAL PROPERTY TITANIUM ALLOY COMPRESSOR DISK		5. TYPE OF REPORT & PERIOD COVERED INTERIM ANNUAL TECHNICAL REPORT, 8/1/80 to 7/31/81												
7. AUTHOR(s) G. D. Lahoti and T. Altan		6. PERFORMING ORG. REPORT NUMBER												
9. PERFORMING ORGANIZATION NAME AND ADDRESS Battelle's Columbus Laboratories 505 King Avenue Columbus, OH 43201		8. CONTRACT OR GRANT NUMBER(s) F33615-78-C-5025												
11. CONTROLLING OFFICE NAME AND ADDRESS AF Wright Aeronautical Laboratories (AFWAL/MLLM) Wright-Patterson Air Force Base, OH 45433		10. PROGRAM ELEMENT, PROJECT, TASK AREA & WORK UNIT NUMBERS P.E. 61102 F 2306 P7 03												
14. MONITORING AGENCY NAME & ADDRESS (if different from Controlling Office) DCASMA, Dayton Defense Electronics Supply Center Dayton, OH 45444		12. REPORT DATE October 1981												
		13. NUMBER OF PAGES 372												
		15. SECURITY CLASS. (of this report) Unclassified												
		15a. DECLASSIFICATION/DOWNGRADING SCHEDULE												
16. DISTRIBUTION STATEMENT (of this Report) Approved for Public release; distribution unlimited.														
17. DISTRIBUTION STATEMENT (of the abstract entered in Block 20, if different from Report)														
18. SUPPLEMENTARY NOTES														
19. KEY WORDS (Continue on reverse side if necessary and identify by block number) <table border="0"> <tr> <td>Process Modeling</td> <td>Interface Effects</td> <td>Dual-Property Disk</td> </tr> <tr> <td>Constitutive Equation</td> <td>Integrated System</td> <td>Disk Forging</td> </tr> <tr> <td>Formability</td> <td>Computer Modeling</td> <td>Ti-6242 Alloy</td> </tr> <tr> <td>Workability</td> <td>Processing Conditions</td> <td>Microstructure/Properties</td> </tr> </table>			Process Modeling	Interface Effects	Dual-Property Disk	Constitutive Equation	Integrated System	Disk Forging	Formability	Computer Modeling	Ti-6242 Alloy	Workability	Processing Conditions	Microstructure/Properties
Process Modeling	Interface Effects	Dual-Property Disk												
Constitutive Equation	Integrated System	Disk Forging												
Formability	Computer Modeling	Ti-6242 Alloy												
Workability	Processing Conditions	Microstructure/Properties												
20. ABSTRACT (Continue on reverse side if necessary and identify by block number) <p>This program is aimed at developing a science-based methodology for analyzing, optimizing, and designing metal-deformation processes to control microstructure and properties in a finished part. The validity and application of this approach will be demonstrated by developing forging process for a compressor disk from Ti-6242 alloy, as an example.</p>														

DD FORM 1 JAN 73 1473 EDITION OF 1 NOV 65 IS OBSOLETE

Unclassified
SECURITY CLASSIFICATION OF THIS PAGE (When Data Entered)

Unclassified

SECURITY CLASSIFICATION OF THIS PAGE(When Data Entered)

> Material behavior under processing conditions is being characterized by developing constitutive equations, formability and workability indices, and processing condition-microstructure-property maps. Computerized process models for axisymmetric deformation from rate-sensitive materials were developed. A test procedure for determining interface heat-transfer and friction coefficients was developed. The material, process, and interface models are being integrated in a system of computer programs for designing and optimizing the forging process for a compressor disk. Finally, the validity of these models will be evaluated by forging a sub-scale compressor disk from Ti-6242.

Accession For	
DTIC GRA&I	<input checked="checked" type="checkbox"/>
DTIC T'B	<input type="checkbox"/>
Unannounced	<input type="checkbox"/>
Justification	
By	
Distribution/	
Availability Codes	
Dist	Avail and/or Special
A	



Unclassified

SECURITY CLASSIFICATION OF THIS PAGE(When Data Entered)

FOREWORD

This Third Annual Technical Report covers the work performed under Contract No. F33615-78-C-5025, from August 1, 1980 to July 31, 1981. It is published for technical information only and does not necessarily represent the recommendations, conclusions, or approval of the Air Force. This contract with Battelle's Columbus Laboratories, Columbus, Ohio was initiated under the project "Research to Develop Process Models for Producing a Dual-Property Titanium Alloy Compressor Disk". It is being conducted under the direction of Dr. Harold L. Gegel/MLLM, Air Force Wright Aeronautical Laboratories (AFSC), Wright-Patterson Air Force Base, Ohio. Battelle's Columbus Laboratories is the prime contractor on this program with Wright State University, University of California, McGill University and Los Alamos National Laboratory as subcontractors. At Battelle, Dr. T. Altan, Senior Research Leader, and Dr. G. D. Lahoti, Senior Research Scientist are the program manager and principal investigator, respectively.

This report represents the work done by a team of organizations and individuals given below:

- o Battelle's Columbus Laboratories, Columbus, Ohio
Dr. T. Altan (Program Manager)
Dr. G. D. Lahoti (Principal Investigator)
Drs. S. L. Semiatin, S. I. Oh and E. W. Collings
- o Wright State University, Dayton, Ohio
Drs. J. F. Thomas, Jr. and P. Dadras
- o McGill University, Montreal, Canada
Dr. J. J. Jonas
- o University of California, Berkeley, California
Dr. S. Kobayashi
- o Los Alamos National Laboratory, New Mexico
Drs. G. K. Lewis and J. E. Hockett
- o Dr. V. Tipnis, Tipnis Associates, Inc., Consultant
- o Dr. R. Raj, T. M. Shaw and S. Baik, Cornell University,
Ithaca, New York
- o Dr. C. C. Chen, Chen-Tech Industries, Inc., Tustin, California

TABLE OF CONTENTS

Section	Page
I INTRODUCTION	1
II PROGRAM PURPOSE AND OBJECTIVES	3
III PROGRAM HIGHLIGHTS	4
Phase I. Material Behavior Under Processing Conditions	4
Phase II. Process Modeling for Disk Type Forging	5
Phase III. Interface Effects	5
Phase IV. Integration of Material and Process Models	6
Phase V. Property/Microstructure Relationships in the Forged Disks	6
IV PROGRAM PROGRESS	9
V MATERIAL BEHAVIOR UNDER PROCESSING CONDITIONS	11
Material Characterization and Development of Constitutive Equations (Task 1.1.)	11
High Strain Rate Plastometer Tests and Development of Constitutive Equations	16
Characterization of Dynamic Metallurgical Behavior Under Processing Conditions (Processing- Microstructure Relationships) (Task 1.2.)	23
VI PROCESS MODELING FOR DISK TYPE FORGING	52
Process Modeling With Matrix Method (Task 2.1)	52
Process Modeling with Finite-Element Methods (Task 2.2.)	59
Development of an Interactive System to Predict Metal Flow and Temperatures (Task 2.3.)	66
Development of Process Model and Integration With Fracture/Failure Model (Task 2.4.)	72

TABLE OF CONTENTS (CONT'D)

Section	Page
VII INTERFACE EFFECTS	73
Selection of Lubricants for Disk Forging Task (3.1.)	73
Determination of Heat Transfer Coefficients and Interface Effects (Task 3.2.)	74
Analysis of Metal Flow and Temperatures in Ring and Flange Type Configurations (Task 3.3.)	77
VIII INTEGRATION OF MATERIAL AND PROCESS MODELS	78
Process Optimization and Forging of Subscale Disk (Tasks 4.1, 4.2, and 4.3)	78
Development of an Economic Model for Processing Alternatives (Task 4.4.)	79
IX PROPERTY/MICROSTRUCTURE RELATIONSHIPS IN THE FORGED DISK	86
X FUTURE WORK	87
Material Behavior Under Processing Conditions	87
Process Modeling for Disk Type Forging	87
Interface Effects	87
Integration of Material and Process Models	87
Property/Microstructure Relationships in the Forged Disk	88
APPENDIX A: DETERMINATION OF HIGH-STRAIN-RATE-FLOW-STRESS DATA FOR Ti-6242 + Si BY USING A PLASTOMETER	89
APPENDIX B: EFFECT OF PROCESSING VARIABLES ON MICROSTRUCTURE OF Ti-6242	105
APPENDIX C: EVALUATION OF PROCESSING-MICROSTRUCTURE-PROPERTY RELATIONSHIPS FOR Ti-6242 Si	137

TABLE OF CONTENTS (CONT'D)

Section	Page
APPENDIX D: MODELING OF FLOW INSTABILITY IN Ti-6242	193
APPENDIX E: DEVELOPMENT OF A PROCESSING MAP USING ALUMINUM AS A MODEL MATERIAL	217
APPENDIX F: THERMOVISCOPLASTIC ANALYSIS OF TITANIUM ALLOY FORGING	243
APPENDIX G: PROCESS MODELING WITH THE FINITE-ELEMENT METHOD OF ANALYSIS (PROGRAM ALPID)	267
APPENDIX H: ECONOMIC MODELS FOR PROCESSING ALTERNATIVES	325

LIST OF ILLUSTRATIONS

Figure		Page
1	Program Approach for the Project on Progress Modeling to Produce a Dual Property Titanium Alloy Compressor Disk	7
2	Outline of the Dual-Property Compressor Disk Program . . .	8
3	$\Delta\sigma/\sigma$ and Its Dependence on Temperature and Strain Rate . .	13
4	Stress Drop $\Delta\sigma$ vs. Log Aging Time	13
5	Diagram of the Compression End of the Los Alamos CAM Plastometer, Die Stack and Heating Assembly	17
6	True Stress-Strain Curves at a Strain Rate of 1 s^{-1}	19
7	True Stress-Strain Curves at a Strain Rate of 10 s^{-1}	20
8	True Stress-Strain Curves at a Strain Rate of 100 s^{-1} . . .	21
9	Yield Surface for $\alpha+\beta$	24
10	Yield Surface for β Ti-6242 Alloy at 900C	25
11	Microstructures in As-Deformed Compression Samples of $\alpha+\beta$ Preform Microstructure Forged at a Strain Rate of 10 Sec.^{-1} and at Temperatures of (a) 899C (1650F), (b) 927C (1700F), (c) 954C (1750F), (d) 982C (1800F) and (e) 1010C (1850F)	27
12	Microstructures Formed in $\alpha+\beta$ Preform Microstructure Material after a Heat Treatment of 954C (1750F)/2 hrs. Which Follows Compression at a Strain Rate of 10 Sec.^{-1} at Temperatures of (a) 899C (1650F), (b) 954C (1750F), and (c) 1010C (1850F)	28
13	Microstructures in As-Deformed Compression Samples of a β Preform Microstructure Forged at a Strain Rate of 10 Sec.^{-1} and at Temperatures of (a) 899C (1650F), (b) 927C (1700F), (c) 954C (1750F), and (d) 982C (1800F). .	30
14	Microstructures Formed in β Preform Microstructure Material After a Heat Treatment at 913C (1675F) for Either (a,c) 15 Minutes or (b,d) 2 Hours, Following Deformation at (a,b) 899C (1650F), 10 Sec.^{-1} or (c,d) 954C (1750F), 10 Sec.^{-1} . .	31

LIST OF ILLUSTRATIONS (CONT'D)

Figure		Page
15	Microstructures Formed in β Preform Microstructure Material After a Heat Treatment at 954C (1750F) for Either (a,c) 15 Minutes or (b,d) 2 Hours, Following Deformation at (a,b) 899C (1650F), 10 Sec. ⁻¹ or (c,d) 954C (1750F), 10 Sec. ⁻¹	32
16	Fatigue Crack Growth Data for Microstructures that can be Characterized as being Bimodal (Serial Number 1C), Coarse Lamellar (Serial Number 4B), Elongated Alpha (Serial Numbers 6C and 6D), or Colony (Serial Numbers 1B and 2B)	37
17	Torque-Shear Strain Curve and Photographs of Torsion Samples Showing Localization of Deformation for 304 Stainless Steel Deformed at a Surface Shear Strain Rate of 0.5 sec. ⁻¹	42
18	Stress-Strain Plots for Ti-6242 Determined in Torsion at T = 913C (1675F) and a Surface Effective Strain Rate of 0.01 sec. ⁻¹	44
19	A Schematic of the Types of Damage Seen in Large Deformation of Ti-6242, with a β -Preform Structure	46
20	A Processing Map for Ti-6242	49
21(a)	Grid Distortion in Hot-Die Forging of ($\alpha+\beta$)-Preform and Comparison with Experimental Macrostructure.	54
21(b)	Theoretical Grid Distortion and Comparison with Macrostructures in Hot-Die Forging of (β)-Preform.	54
22	Local Strain, Strain-Rate, and Temperature Variations During (β)-Phase Hot-Die Compression and Corresponding Microstructures After Compression.	55
23	(a) Preform Geometry and Grid Distortions in ($\alpha+\beta$)/ β Composite Forging at (b) 30 Percent and (c) 60 Percent Reduction in Height	57
24	Local Strain, Strain-Rate, and Temperature Variations During ($\alpha+\beta$)/ β Composite Forging and Corresponding Microstructures After Forging.	58

LIST OF ILLUSTRATIONS (CONT'D)

Figure		Page
25	Description of Arbitrarily Shaped Dies and the Die Surface Coordinate Orientation	62
26	Structures and Interactions of ALPID and FEMGRA	63
27	Calculated FEM Grid Distortions at Die Displacements of (a) 0.0Ho, (b) 0.2Ho, (c) 0.4Ho and (d) 0.58Ho.	65
28	Predicted Grid Distortion for Disk Forging	67
29	Grid Distortion Predicted for Trapped Die Forging	68
30	Computed Forging Load for Trapped Die	69
31	Effective Strain Distribution in Disk Forging	70
32	Effective Strain Distribution in Disk Forging	71
33	Fixture for Interface Heat Transfer Studies	75
34	Temperature Distribution in Upper and Lower Dies and an Interface Layer Demonstrating the Assumption of a Fixed Intermediate Temperature, T_m	76
35	Structural Features and Resultant Properties of the Disk Produced by Selected Forging and Heat Treating Combinations.	80
36	Percent Processing Time Savings and Lead Time Dis-Savings for Alternatives to Conventional Press Forging of Ti-6242 Compressor Disk.	83
37	Percent Cost Savings and Dis-Savings for Alternatives to Conventional Press Forging of Ti-6242 Compressor Disk	84

LIST OF TABLES

Table		Page
1	Program Schedule and Progress Under Various Phases	10
2	Thermomechanical Processing of Ti-6242	35
3	LCF Results for Six Optimal Forge-Heat Treat Cycles	36
4	A Listing of the Values for the Parameters in Equation (5)	50

SUMMARY

This interim annual report describes the work performed during the third year of this program by Battelle's Columbus Laboratories (prime contractor) and its subcontractors, namely, Wright State University, McGill University, Cornell University, University of California, Los Alamos National Laboratory, and Dr. V. Tipnis, Tipnis Associates, Inc., Consultant. In order to develop a science-based methodology for analyzing, optimizing and designing metal-deformation processes to control microstructure and properties in a finished part, detailed mathematical models of the work-piece material, the forming process, and the tool-workpiece interface are being developed. The applicability and validity of these models will be illustrated by developing a forging process for a Ti-6242 compressor disk with dual properties.

Uniform compression tests were conducted to develop constitutive equations for Ti-6242 under normal forging conditions. For this purpose, low strain rate tests were conducted at Wright State University, and high strain rate tests were conducted in a plastometer at Los Alamos National Laboratory. In addition, use of a mechanical press to obtain high strain rate data was demonstrated at Battelle. Similarly, use of an MTS machine to obtain high strain rate data was investigated at the University of Pittsburgh.

The microstructure of the uniformly compressed specimens was characterized to develop processing conditions/microstructure maps. In addition, a series of pancake forging tests were conducted at Wyman-Gordon to determine the forgeability and optimum heat treat conditions, and to characterize microstructure/property relationships for the alloy under investigation.

Models for the prediction of flow instability in hot forging of Ti-6242 are being developed. To this end, an analysis of the torsion test was developed and actual torsion tests are being conducted to validate the models. Further, a task was undertaken to identify and develop criteria for the microscopic fracture/failure models likely to be found in hot working of Ti-6242. Two types of defects, namely the shear bands and grain boundary cracking are being investigated in detail and processing maps are being developed to identify potential regions of defect formation.

In order to establish process models, mathematical and computer models were developed to simulate metal flow that occurs during forging of axisymmetric components, such as a compressor disk. For this purpose, the matrix method with temperature calculation fractures was used at the University of California, and the finite-element method was used at Battelle. These process models are being implemented in an interactive system of computer programs with graphics capabilities.

The tool-workpiece interface conditions are being characterized by determining friction factors and interface heat transfer coefficients for selected lubrication systems and forging conditions. At Battelle, a test procedure and fixture was developed to determine the interface heat transfer coefficient during forging.

The material, process, and interface models, described above, are being integrated in a system to design and optimize the forging process for a subscale compressor disk. A subscale disk will be forged and its properties/microstructures will be evaluated to illustrate the application and validity of this processing science program. Finally, an economic model was developed to evaluate the dual property disk approach with respect to various other alternatives.

SECTION I

INTRODUCTION

A large number of aerospace components are manufactured by means of one or more material deformation processes followed by heat treatment and machining. This is the case especially for highly stressed critical engine and airframe parts such as disks, blades, vanes, and structural rib-web type components. The manufacturing cost of these components, used in Air Force systems, continues to rise. Therefore, innovations are sought to reduce the processing and life cycle costs of such products while improving material utilization and properties. Such innovations can be achieved by the combined application of materials science, mechanics, and mechanical engineering disciplines to develop advanced metal processing techniques, more productive and less costly than the state-of-the-art methods.

Recognizing the need for innovative techniques in deformation processing, the Air Force has initiated a new effort on processing research and development. This effort includes an appropriate combination of basic and applied research, a coordinated application of materials data, process analysis, computer-aided simulation of metal flow, and equipment behavior. This new approach is expected to encourage innovative approaches for the future application and development of metal forming technology.

In order to implement the computer-aided design and manufacturing (CAD/CAM) approach, detailed mathematical models of the workpiece material, the forming process, and the workpiece-tool interface conditions are required. However, these models do not now exist in a sufficiently complete form. Hence, the overall objective of this program is to develop and verify the required models and integrate them to form an interactive computer program for process design. The process models are to be developed to a level of sophistication sufficient to allow the control of microstructure and properties in addition to the shape of the finished part. Although the methodology to be developed will be generally applicable to a range of deformation processes, the validation and application will be restricted to the forging process for a Ti-6Al-2Sn-4Zr-2Mo (designated as Ti-6242 hereafter) turbine compressor disk. Since

the optimal properties of a compressor disk vary from the bore to the rim, a gradient in microstructure and properties ("dual property") is desired for the final disk. The program goal is to produce a subscale Ti-6242 compressor disk with high tensile and high low-cycle fatigue properties at the bore region, and good creep and high stress rupture properties at the rim region.

SECTION II

PROGRAM PURPOSE AND OBJECTIVES

The overall purpose of this program is to develop an innovative scientific approach for the analysis and practical application of metal-deformation processes. This new approach must consider a deformation process as a system which includes the metallurgy, mechanics, interface effects, finished shape and microstructure. The program will (a) illustrate how to bring metallurgy and mechanics together, (b) establish the interaction and control of microstructure-property relationships in the finished product, and (c) demonstrate the feasibility for applying a scientific methodology to solve relevant industrial deformation processing problems.

The specific objective of the program is to develop a science-based methodology for analyzing, optimizing and designing metal-deformation processes to control microstructure and properties in a finished shape. The methodology to be developed in this program will be generally applicable to all deformation processes. The validity and application of the scientific methodology, being developed in this program, will be illustrated using the forging process for an engine disk from Ti-6242 alloy, as an example.

Thus, the specific objectives of this program will be achieved by performing the following five tasks:

- (1) Generate data on material behavior under processing conditions
- (2) Develop a computerized model for simulating and optimizing disk-type forging processes
- (3) Develop quantitative data and analysis to characterize material-die interface effects
- (4) Integrate material and process models and apply the computerized model to a disk forging
- (5) Evaluate the properties and microstructure of the forged disks and illustrate the application of the computerized approach developed in this program.

SECTION III

PROGRAM HIGHLIGHTS

Battelle's Columbus Laboratories is the prime contractor on this program with, Wright State University, McGill University, University of California, and Los Alamos National Laboratory acting as subcontractors. In addition, several consultants are involved under various tasks of the program. This program is being conducted in the following five phases:

Phase I - Material Behavior Under Processing Conditions

Phase II - Process Modeling for Disk Type Forging

Phase III - Interface Effects

Phase IV - Integration of Material and Process Models

Phase V - Property/Microstructure Relationships in the Forged Disks

The Scope of Work defined in the RFP No. F33615-78-R-5025 serves as the basis for detailed approach in this study. The various tasks and subtasks in each phase are given in the following.

Phase I. Material Behavior Under Processing Conditions

Task 1.1. Material Characterization and Development of Constitutive Equations

Subtask 1.1.1. Low Strain-Rate Tests and Development of Constitutive Equations

Subtask 1.1.2. High Strain-Rate Plastometer Tests and Development of Constitutive Equations

Subtask 1.1.3. Use of a Mechanical Press in Obtaining High Strain-Rate Compression Data

Subtask 1.1.4. Use of an MTS Machine in Obtaining High Strain-Rate Compression Data

Subtask 1.1.5. Accuracy, Reliability and Manageability of Constitutive Equations

Subtask 1.1.6. Determination of Yield Locus, Flow Rule, and Constitutive Equations Along Various Loading Paths

Task 1.2. Characterization of Dynamic Metallurgical Behavior Under Processing Conditions (Processing-Microstructure Relationships)

Subtask 1.2.1. Structural and Microstructural Evaluation of Uniformly Compressed Samples under Task 1.1.

Subtask 1.2.2. Pancake Forging Tests for Microstructure-Property Evaluation

Subtask 1.2.3. Development of Flow Instability Models

Task 1.3. Theoretical and Experimental Forming Limit Representation (Workability)

Subtask 1.3.1. Theoretical Formability for Sheet Metal and Bulk Forming Processes

Subtask 1.3.2. Experimental and Theoretical Investigation of Forming Limit Criteria in Disk Forging

Subtask 1.3.3. Development of Microscopic Fracture/Failure Models

Subtask 1.3.4. Validation of Microscopic Fracture/Failure Models

Phase II. Process Modeling for Disk Type Forging

Task 2.1. Process Modeling with Matrix Method

Task 2.2. Process Modeling with Upper Bound and Finite-Difference Methods

Task 2.3. Development of an Interactive System to Predict Metal Flow and Temperatures

Task 2.4. Development of Process Model and Interaction with Material Models

Phase III. Interface Effects

Task 3.1. Selection of Lubricants for Disk Forging

Task 3.2. Determination of Heat Transfer Coefficients and Interface Effects

Task 3.3. Analysis of Metal Flow and Temperatures in Ring and Flange (Spike) Type Configurations

Phase IV. Integration of Material and Process Models

- Task 4.1. Establishment of Forging Process Conditions,
Speed, Temperatures, Contact Times
- Task 4.2. Computer-Aided Design of the Preform Shape
- Task 4.4. Improvement of the Interactive Process
Design System and Development of an Economic Model

Phase V. Property/Microstructure Relationships in the Forged Disks

- Task 5.1. Evaluation of Microstructures and
Comparison with Predictions
- Task 5.2. Evaluation of Mechanical Properties and
Comparison with Predictions
- Task 5.3. Titanium Alloy Selection

The program approach is illustrated in Figure 1. The overall plan for conducting this program is summarized in a block diagram given in Figure 2.

PROCESSING SCIENCE PROGRAM

PROGRAM APPROACH

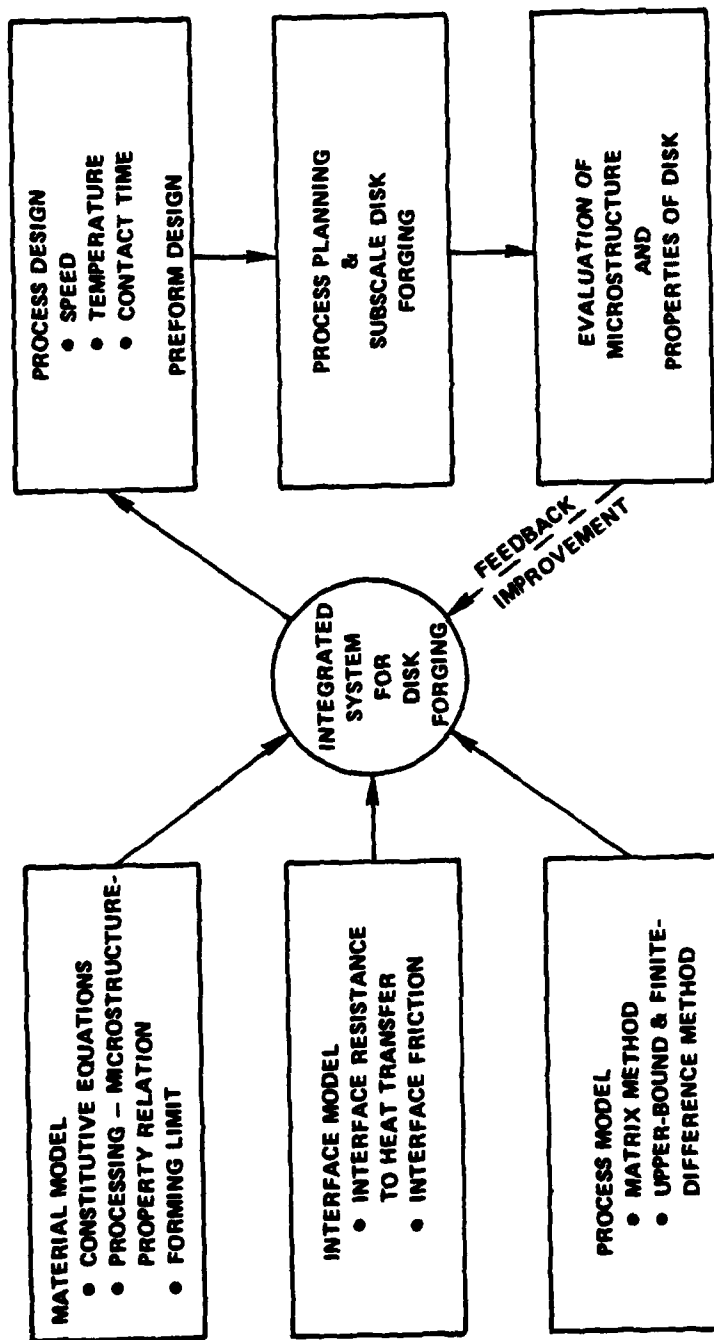


Figure 1. Program Approach for the Project on Progress Modeling to Produce a Dual Property Titanium Alloy Compressor Disk

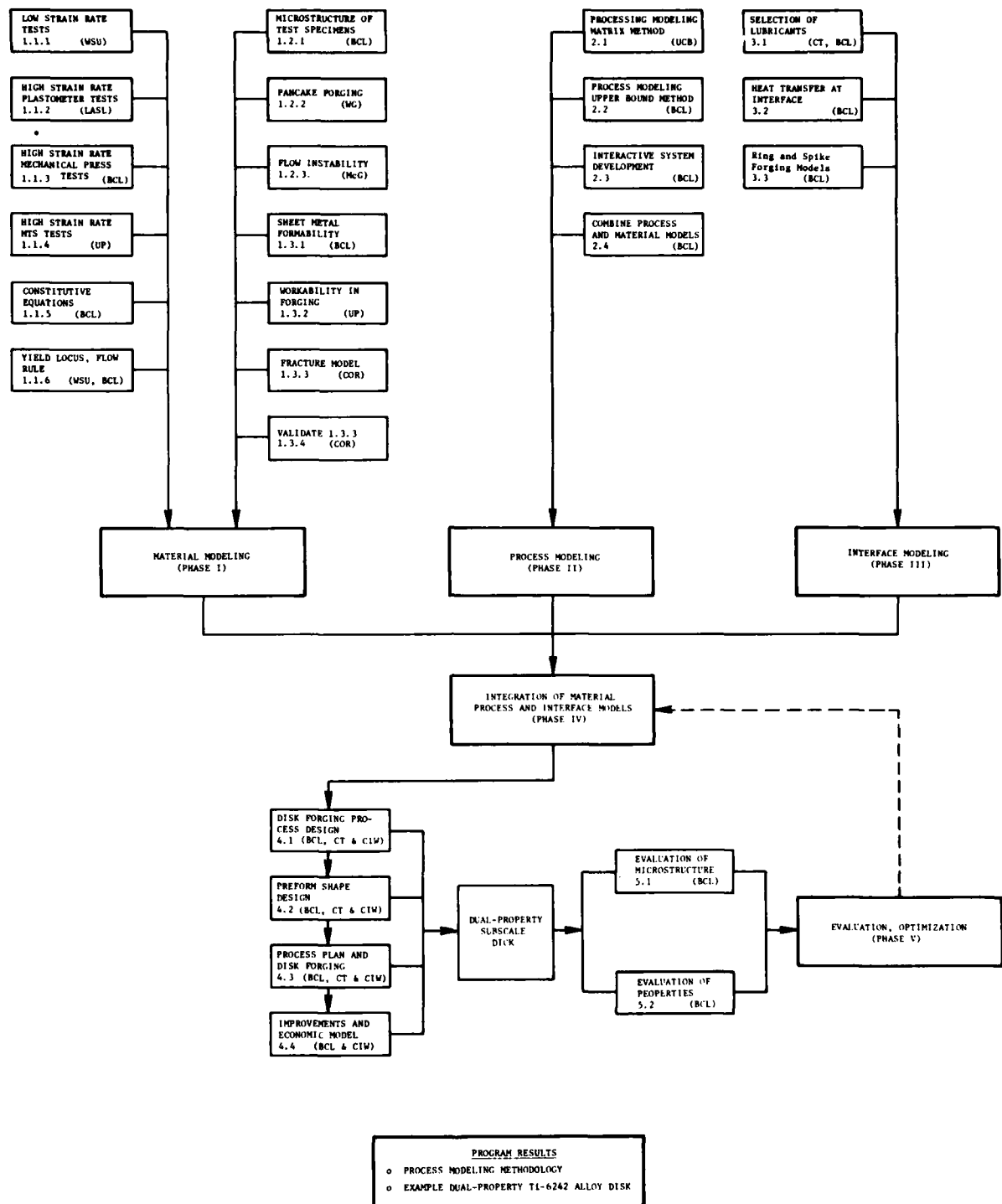


Figure 2. Outline of the Dual-Property Compressor Disk Program (BCL - Battelle-Columbus WG = Wyman Gordon, UCB = University of California, Berkeley, UP = University of Pittsburgh, LASL = Los Alamos Scientific Laboratory, McG = McGill University COR = Cornell University, CT = Chen-Tech Industries, CIW = Cameron Iron Works) Numbers Indicate Various Tasks and Subtasks.

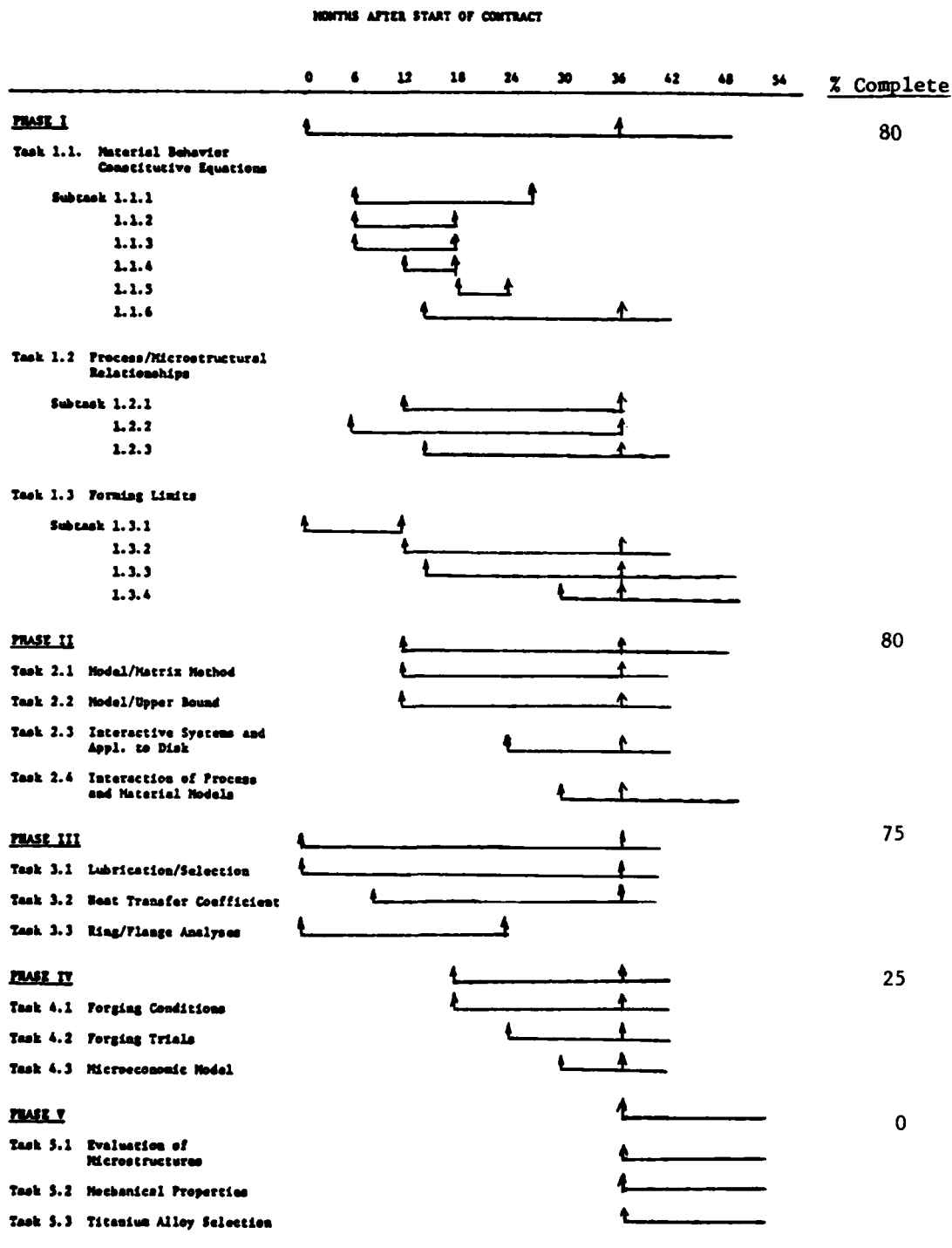
SECTION IV

PROGRAM PROGRESS

The program schedule and progress under the various phases of the program are given in Table 1. As per schedule, the work on Phase I, II, III, and IV continued during the second year of the program. No work was scheduled and conducted on Phase V during the first three years of the program. In Table 1, the progress under each phase is assessed by estimated percent of completed work. Detailed description of the progress under each phase and each task of the program are given in the following sections.

TABLE 1

PROGRAM SCHEDULE AND PROGRESS UNDER VARIOUS PHASES



SECTION V

MATERIAL BEHAVIOR UNDER PROCESSING CONDITIONS

In order to develop usable predictive models for a deformation process, it is necessary to determine quantitative relationships which describe the behavior of an engineering alloy under deformation processing conditions. Under the present program, Ti-6242 was selected as a candidate alloy to produce a dual-property compressor disk. Thus, the work under this phase of the program is focused on the development of material models for the titanium alloy Ti-6242.

The material required for the test specimens under this phase was supplied to Battelle by Wyman-Gordon in two different initial (preform) microstructures ($\alpha+\beta$ and β). The details of the processing conditions to obtain the two preform microstructures were given in the First Annual Report⁽¹⁾.

Material Characterization and Development of Constitutive Equations (Task 1.1.)

A process simulation model, which takes into account the influence of material properties on the stress and strain distribution, during deformation, requires the flow stress data on the material as input. The basic information needed is a plastic flow law, or a constitutive equation, expressing the dependence of the flow stress on strain, strain rate, temperature and one or more explicitly history-dependent state variables. These constitutive equations describing the plastic deformation of a material enter the forming analysis in two distinct ways. In the first place, they are required for the forming process model in order to determine the required loads and predict the strain-strain rate-temperature path for each element of the deformation zone. The design process requires that this be done as a function of process variables such as a temperature, ram rate, and preform shape. The strain-strain rate-temperature path will determine the microstructure and properties of each element of the

(1) Lahoti, G. D. and Altan T., "Research to Develop Process Models for Producing a Dual Property Titanium Alloy Compressor Disk", Interim Annual Report, AFML-TR-79-4156, December 1979.

finished part. In the second place, the constitutive equation is used to determine workability indices, such as strain rate sensitivity, which can be used in workability models which predict the maximum strains that the workpiece can undergo without failure.

Under this task, the constitutive equations for Ti-6242 were developed, primarily by conducting uniform compression tests at various forging temperatures and strain rates, by various members of the team. In addition, a limited number of tension tests were conducted by Wright State University. The details of the test conditions were included in the First Annual Report⁽¹⁾.

Low Strain Rate Tests and Development of Constitutive Equations

Work under this subtask is being conducted at Wright State University. In the previous reporting periods, work had concentrated on (a) characterization of the compressive flow properties of Ti-6242 in both $\alpha+\beta$ and β preform conditions, (b) characterization of the tensile flow properties of β preform material, (c) development of constitutive equations, and (d) application of flow parameters to characterize the initiation and growth of plastic instabilities. The results of these studies were summarized earlier^(1,2).

During the current reporting period, additional compression tests were conducted on β preform microstructure samples in order to determine the effects of level of deformation and heat treatment on final microstructure. The results of this investigation are summarized later under the section on "Structural and Microstructural Evaluation of Uniform Compression Samples".

A second area of investigation concerned observations of strain aging in the Ti-6242 alloy. In the low strain rate compression testing of $\alpha+\beta$ material an abrupt load drop phenomenon was observed⁽³⁾. This is shown schematically and plotted as a normalized stress drop $\Delta\sigma/\sigma$ vs. temperature and strain rate in Figure 3. It is seen that $\Delta\sigma/\sigma$ is

-
- (2) Lahoti, G. D., and Altan, T., "Research to Develop Process Models for Producing a Dual Property Titanium Alloy Compressor Disk", Interim Annual Report, AFML-TR-80-4162, October 1980.
- (3) Dadras, P., and Thomas, J. F., Jr., "Characterization and Modeling for Forging Deformation of Ti-6Al-2Sn-4Zr-2Mo-0.1Si", Metallurgical Transaction A, in press.

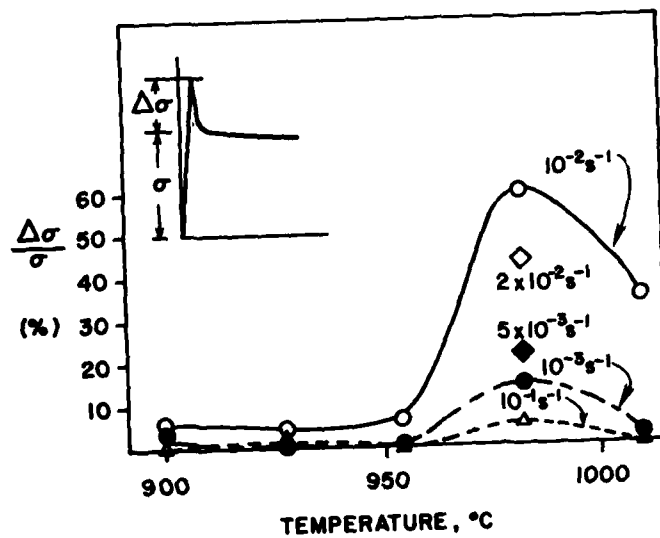


Figure 3. $\Delta\sigma/\sigma$ and its dependence on temperature and strain rate

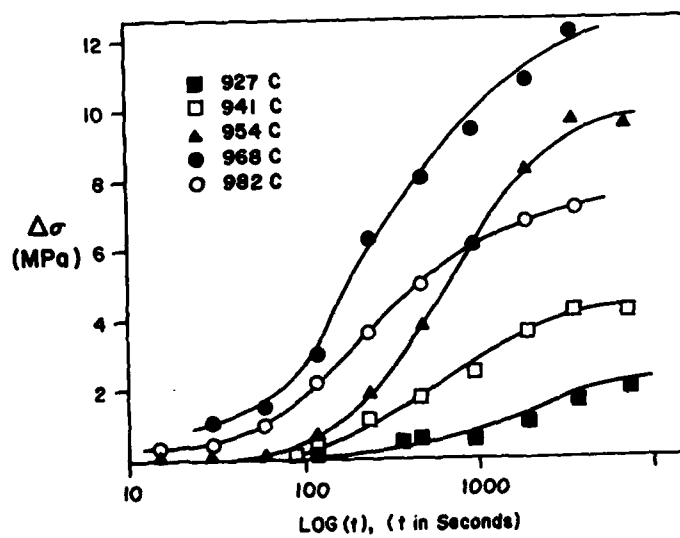


Figure 4. Stress drop $\Delta\sigma$ vs. log aging time.

consistently largest at a strain rate at 10^{-2} s^{-1} and, independent of strain rate, is always larger at 982C (1800F) than any other temperature investigated in this test sequence. In the earlier analysis of flow stress behavior of $\alpha+\beta$ material for constitutive relation development,⁽²⁾ the load drop phenomenon was ignored, and the nearly perfectly plastic behavior of the flow stress after the peak was emphasized. However, the likelihood that the load drop phenomenon is due to a static strain aging process which could be related to solid solution strengthening and creep resistance indicated that a further investigation would be of interest. A reasonable hypothesis is that the phenomenon is related to the silicon addition to the alloy.

In order to study the static strain aging hypothesis, interrupted compression tests have been conducted at five temperatures ranging from 927C (1700F) to 982C (1800F) and for aging times between 15 and 7200 seconds. For each test, after the initial yield drop and a total strain $\epsilon=0.03$, the specimen was unloaded and aging occurred in situ followed by reloading to another strain increment $\epsilon=0.03$. A starting strain rate of 10^{-2} s^{-1} was maintained for the initial as well as subsequent loadings. Since the flow stress of $\alpha+\beta$ Ti-6242 beyond the peak is independent of strain, it was possible to investigate a complete series of aging times at a given temperature by repeated tests on a single specimen.

A summary of the results plotted as $\Delta\sigma=\sigma_U-\sigma_f$ vs. $\log t_a$ where σ_U is the upper yield stress, σ_f is the flow stress beyond the peak, and t_a is the aging time is shown in Figure 4. It is noticed that substantial stress drops occur for most of the aging treatments, with the maximum effect produced by aging at 968C (1775F). At each temperature, approach to a saturation level for $\Delta\sigma$ is evident.

One characteristic feature of the flow and aging behavior is that the sole strengthening effect of the aging process is a transient increase in the flow stress which rapidly disappears with the stress drop. The subsequent flow stress is unaffected. This lack of residual strengthening may be considered as an indication that aging is not associated with irreversible structural changes such as precipitation of silicides. Hence, diffusion of silicon, silicon-interstitial pairs, or some other species in solution is thought to account for the aging phenomenon through dislocation pinning.

For Ti-6242, mechanisms of high temperature plastic deformation have not been explicitly identified. However, for the $\alpha+\beta$ structure, it is expected that sliding and migration of primary α grain boundaries in the β matrix will be the dominant mechanism. This would be consistent with the constant flow stress behavior and the fact that the α grains remain equiaxed after extensive plastic deformation. Therefore, it is hypothesized that aging involves interaction between a mobile species and dislocations near the boundaries. Such an event can impede the start of grain boundary sliding, thus requiring higher stresses for the initiation of deformation.

In order to analyze the kinetics of the aging process, it is postulated that the diffusion of the mobile species follows the model for atmosphere formation around dislocations proposed by Cottrell and Bilby⁽⁴⁾. This predicts that the linear density of solute segregated to dislocations is proportional to $(Dt_a/T)^{2/3}$ where D is the relevant diffusion coefficient and T is the absolute temperature. The degree of completion of atmosphere formation is measured in terms of a normalized stress drop ξ such that

$$\xi = \frac{\Delta\sigma - \Delta\sigma_o}{\Delta\sigma - \Delta\sigma_o} = C \left(\frac{Dt_a}{T} \right)^{2/3} \quad (1)$$

The analysis results in an apparent activation energy of 675 kJ/mole (160 kcal/mole). Although it is expected that silicon is associated with the aging process, an independently measured activation energy for direct comparison with this result is not known. In creep tests on a group of Si-bearing commercial titanium alloys, a range of apparent activation energies for silicon precipitation on mobile dislocations was determined as 430 to 560 kJ/mole⁽⁵⁾. Both this result and the activation energy determined here are anomalously large though they differ by approximately 30%. Thus, the identification of silicon as the responsible species is not definite.

To further investigate the hypothesis that migration of silicon is responsible for the strain aging phenomenon, two $\alpha+\beta$ Ti-6242 bars with low silicon (0.02 wt. %) and high silicon (0.20 wt. %) compared to the composition (0.08 wt.%) investigated here have been obtained. Specimens for interrupted compression tests are currently being prepared.

(4) Cottrell, A. H. and Bilby, B. A., "Dislocation Theory of Yielding and Strain Aging of Iron", Proc. Phys. Soc., 1949, Vol. A62, pp. 49-62.

(5) Patton, N. E. and Mahoney, M. W., "Creep of Titanium-Silicon Alloys", Met. Trans. A., 1976, Vol. 7A, pp. 1685-1694.

In conclusion, it has been demonstrated that the stress drops observed during deformation of $\alpha+\beta$ Ti-6242 at temperatures between 927C and 982C are related to a static strain aging phenomenon which follows classical aging kinetics. Silicon atoms or silicon-interstitial pairs are suggested as the responsible diffusing species. In any case, maximum strengthening due to strain aging occurs at the same temperature, 968C (1775F) as is generally used for solution treatment of $\alpha+\beta$ Ti-6242.

High Strain Rate Plastometer Tests and Development of Constitutive Equations

This part of the program was conducted at the Los Alamos National Laboratory. Details of the investigation are given in Appendix A. The purpose of this study was to conduct constant strain rate compression tests (a) to determine the dependence of flow stress on strain rate and temperature, (b) to investigate strain hardening and flow softening behavior, and (c) to characterize the structures produced by hot-working both $\alpha+\beta$ and β preform microstructures as a function of strain, strain rate and temperature.

High temperature compression tests at true strain rates of 1, 10 and 100 s⁻¹ were run on Ti-6242Si material supplied by Battelle Columbus Laboratories. The specimens were 1.27 cm (0.500 in.) diam. by 1.98 cm (0.780 in.) thick and were compressed in both the $\alpha+\beta$ and β microstructure to a total true strain of 0.7.

The tests were conducted on the Los Alamos cam plastometer. A schematic diagram of the compression end of the machine and die stack is shown in Figure 5. The cam lobe is designed so that the vertical motion of the die stack corresponds to a constant true strain rate when the cam rotates at constant angular velocity.

The specimen is compressed upon insertion of the cam follower into the loading stack while the cam rotates at the desired testing speed. The cam follower insertion, compression of the specimen, and cam follower extraction all occur within one rotation of the cam. Load and position versus time data are used to calculate true stress and strain.

The test specimen and compression platens were lubricated prior to each test. Lubricants used to minimize barreling of the specimen were Acheson Colloids Co. Deltaglaze 347 for temperatures of 1010C (1850F) and greater and Deltaglaze 349 for temperatures below 1010C (1850F).

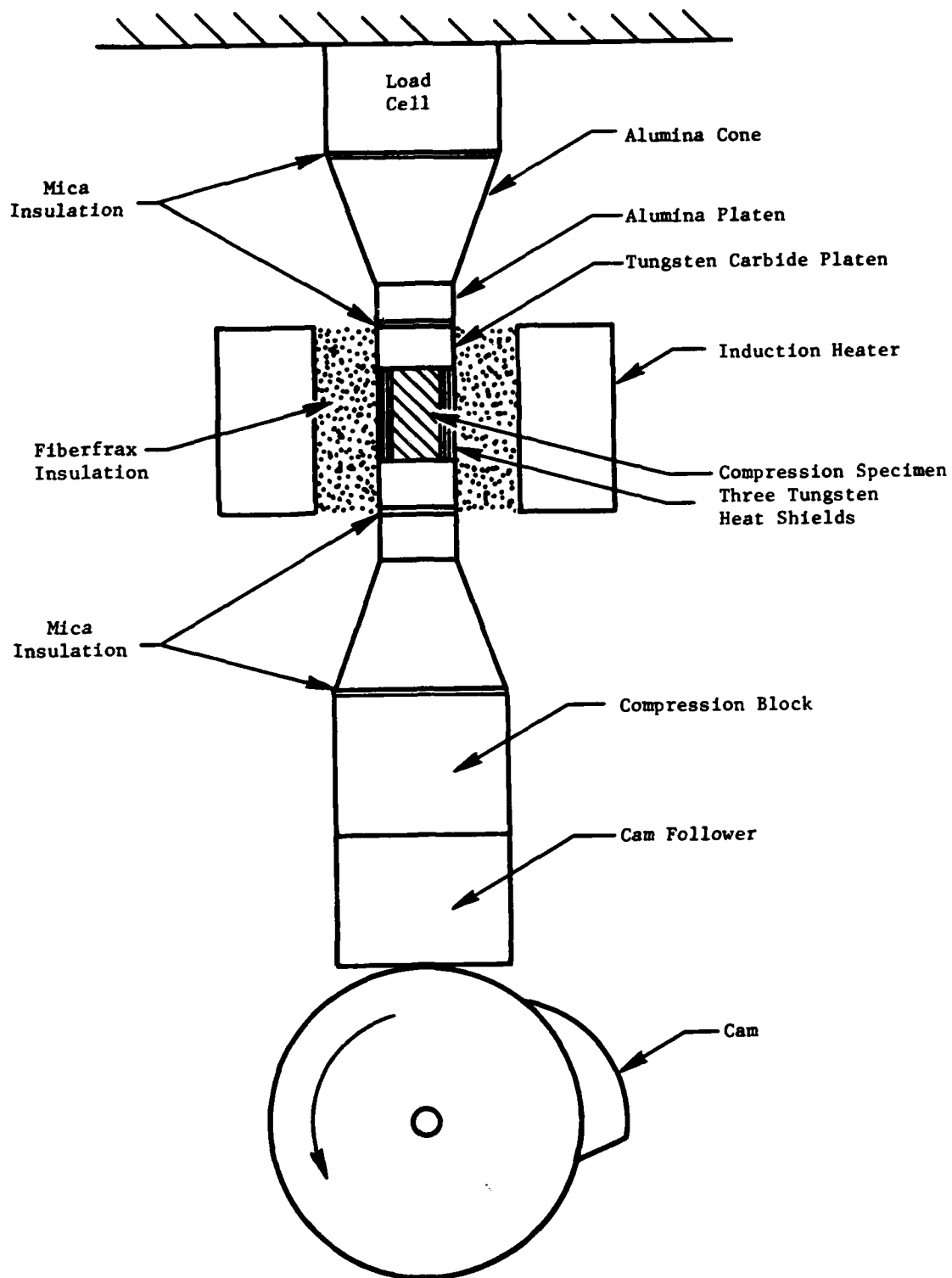


Figure 5. Diagram of the compression end of the Los Alamos CAM Plastometer, die stack and heating assembly.

The specimens were heated with an induction coil and held at temperature for a minimum of six minutes prior to compression testing.

Temperatures were monitored in the center of the specimen and on the outside surface near each end. Two seconds prior to testing, the power to the induction coil was turned off to prevent induction currents from affecting data acquisition systems. The temperature drop at the center of the specimen was negligible during this time. Temperature drops up to 5C were common for the surface thermocouples.

The true stress-true strain data from these tests are shown in Figures 6-8 for strain rates of 1, 10, and 100 s⁻¹. These curves represent averaged data from at least three tests for each condition.

The data shown the expected increase in flow stress with increasing strain rate and decrease in flow stress with increasing temperature except for the 1038C (1900F) strain rate of 10 s⁻¹ test condition. This flow curve was at higher flow stresses than the 1010C (1850F) strain rate of 10 s⁻¹ condition for the $\alpha+\beta$ material. The data at a strain rate of 1 s⁻¹ at 1010C (1850F) and 1038C (1900F) show almost equivalent flow stress at these two temperatures. At a strain rate of 100 s⁻¹ the flow stress at 1010C (1850F) is higher than at 1038C (1900F) as expected.

Comparison of these data with those from an MTS machine and a mechanical press show excellent agreement at equal temperatures and strain rates. Thus, it is obvious that it is not necessary to use a cam plastometer to obtain high strain rate flow stress data for process modeling purposes.

Use of a Mechanical Press in Obtaining High Strain Rate Compression Data

This part of the program is now complete, and the results were included in the First Annual Interim Report.

To summarize, uniform compression tests were conducted on Battelle's 4.45 MN (500 ton) mechanical press. The specimens with grooved ends were coated with glass lubricants, and were heated together with a fixture with titanium carbide anvils. Data were obtained at various test temperatures and strain rates for specimens with both $\alpha+\beta$ and β microstructures. The flow behavior of the two microstructures differed markedly. $\alpha+\beta$ microstructures deformed stably, and the flow softening in this material could be attributed to adiabatic heating. The compressive deformation of β specimens gave rise

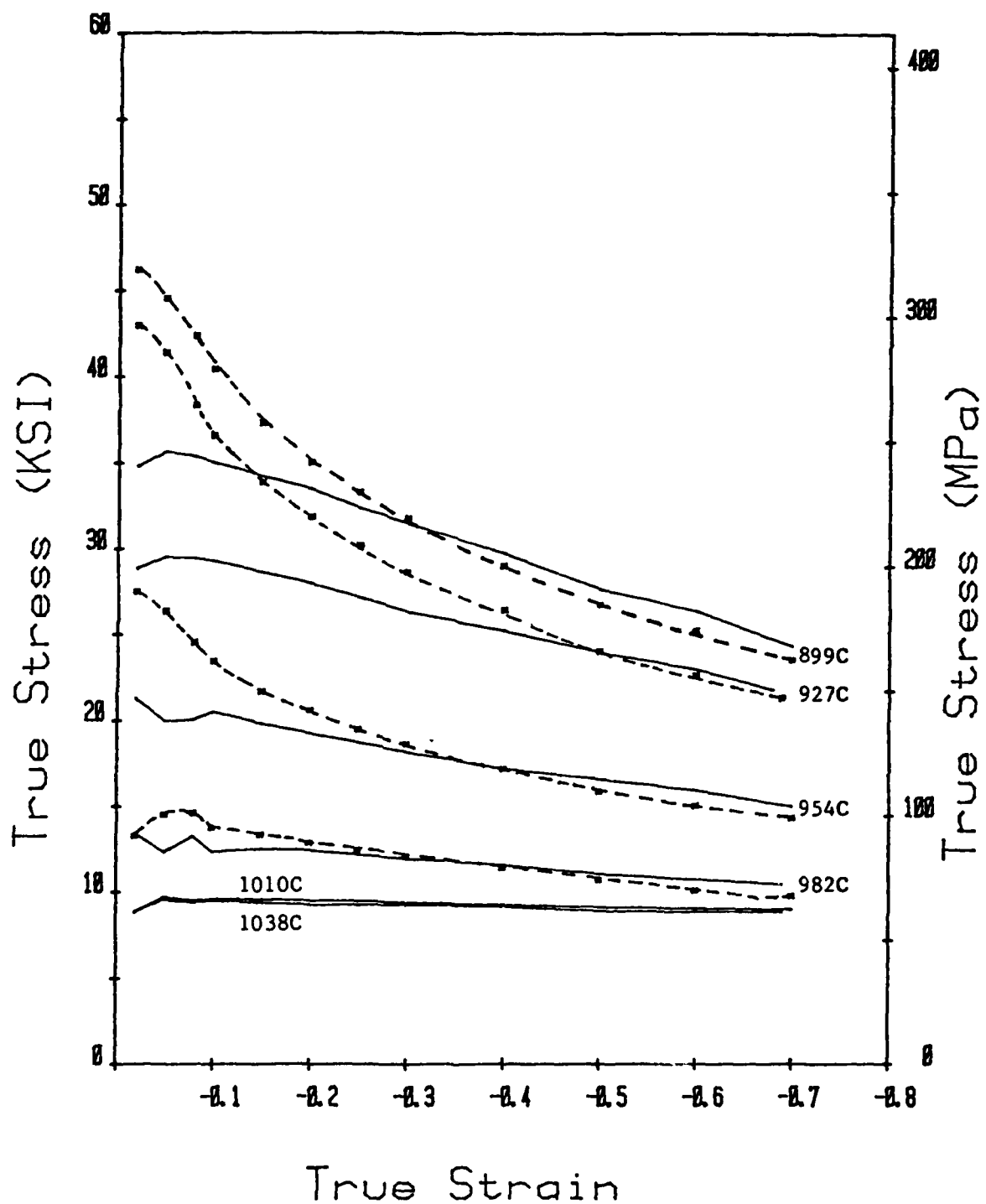


Figure 6. True Stress-Strain Curves at a Strain Rate of 1 s^{-1} . Solid Lines Are $\alpha+\beta$. Dashed Lines are β .

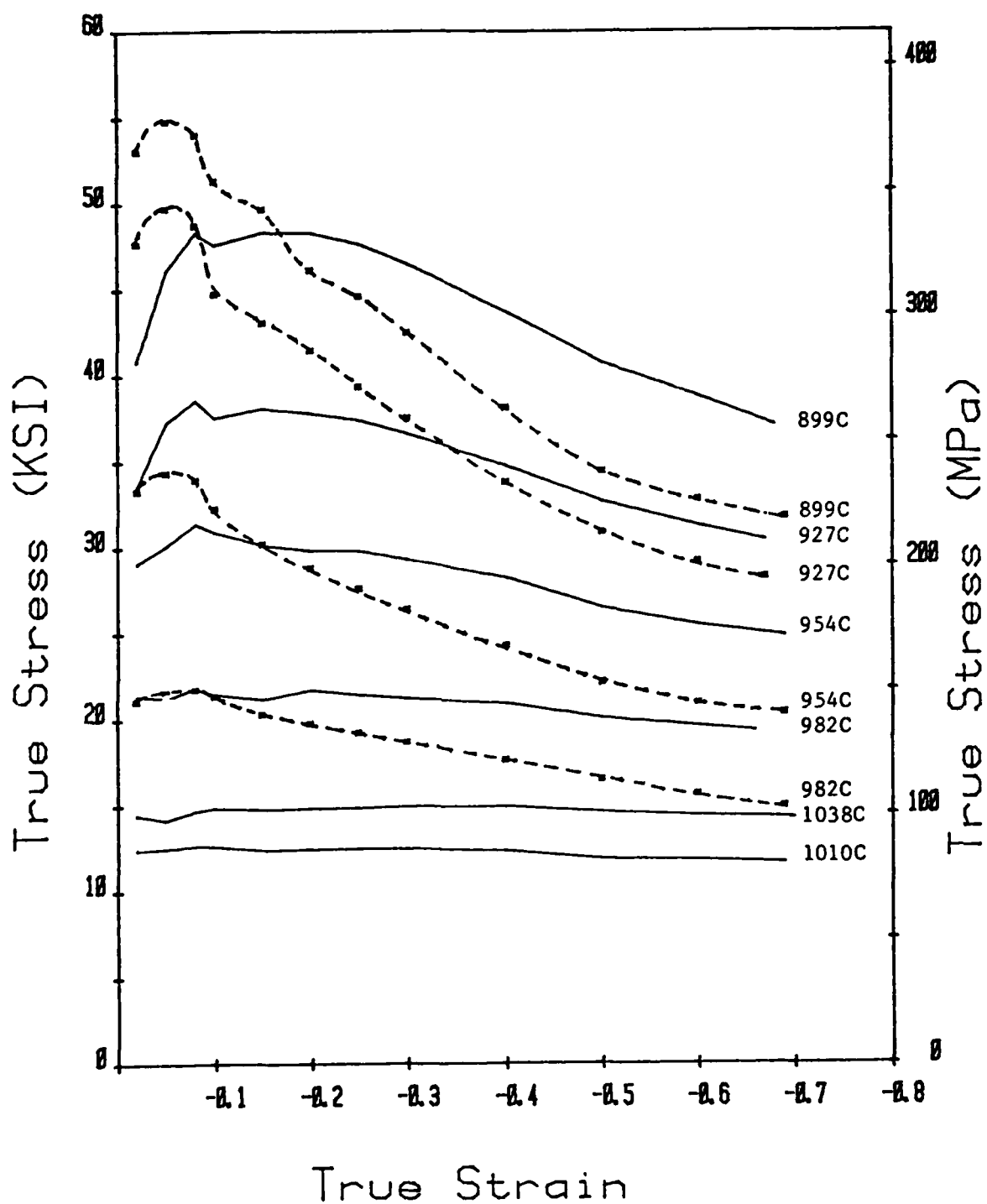


Figure 7. True Stress-Strain Curves at a Strain Rate of 10 s^{-1} .
Solid Lines are $\alpha+\beta$. Dashed Lines are β .

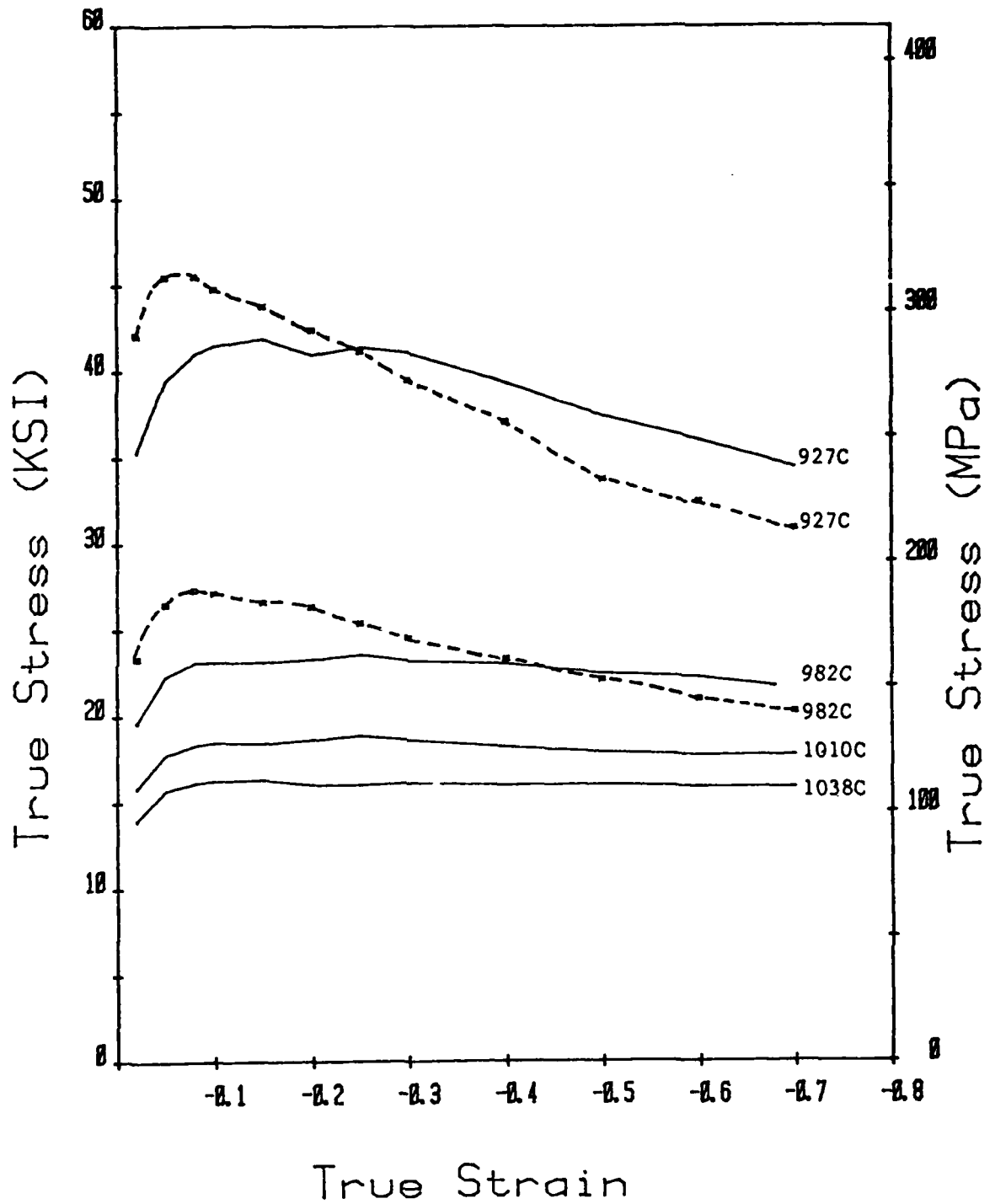


Figure 8. True Stress-Strain Curves at a Strain Rate of 100 s^{-1} . Solid Lines are $\alpha+\beta$. Dashed Lines are β .

to nonuniform, unstable flow. The stress-strain curves for this microstructure showed an additional amount of flow softening in excess of that could be attributed to adiabatic heating.

Use of an MTS Machine in Obtaining High Strain Rate Compression Data

This part of the program was conducted by the University of Pittsburgh. It has been completed and results have been summarized in Appendix C of the Second Annual Interim Report.

In this phase of the research, the deformation behavior of Ti-6242 was examined by means of isothermal compression tests using an MTS machine. Tests were performed on $\alpha+\beta$ preform material at constant strain rates up to 10 sec.^{-1} and at temperatures above and below the transus temperature. Results of these tests (flow curves, microstructures, etc.) are very similar to those obtained on the cam plastometer and in the mechanical press.

Accuracy, Reliability and Manageability of Constitutive Equations

The aim of this part of the program is to develop constitutive equations which are accurate, reliable, and manageable for use in a computerized process model of disk forging. For this purpose, the uniform compression test data developed by various team members have been analyzed. Various types of constitutive equations have been investigated. One such equation under study was the one due to Hart⁽⁶⁾.

Other investigations in this area have concentrated on fitting low strain rate data to various analytical forms. This work has been very important because of the selection of (low rate) isothermal forging conditions for the disk forging and its associated process simulation. This work was carried out at the Wright State University and was described in Appendix A1 of the Second Annual Interim Report. Described in closed-form algebraic expressions, the WSU equations are very manageable and replicate the measured flow stress data to a high degree of precision.

(6) Hart, E. W., "A Phenomenological Theory for Plastic Deformation of Polycrystalline Metals", Acta Metallurgical, Vol. 18, p. 599 (1970).

Determination of Yield Locus, Flow Rule, and Constitutive Equations Along Various Loading Paths

Comparison of torsion data published in the literature to flow stress data obtained under the various subtasks show Ti-6242 may have a fairly isotropic (von Mises) yield locus at modest strain levels ($\epsilon \approx 0.2$) at hot working temperatures. Other literature sources are also being examined to verify this finding.

The yield surface for $\alpha+\beta$ Ti-6242 is a smooth surface, and it is nearly independent of strain at hot working temperatures, as shown in Figure 9. On the other hand, the yield surface for β Ti-6242 is dependent on the strain, strain rate and temperature, and show large peaks at low values of strain, as shown in Figure 10. However, at large strain ($\bar{\epsilon} = 0.7$ to 1.0), the yield surfaces for both $\alpha+\beta$ and β material tend to converge.

Characterization of Dynamic Metallurgical Behavior Under Processing Conditions (Processing-Microstructure Relationships)
(Task 1.2)

The microstructures in titanium alloys can be quite varied and result in a wide range of properties. In addition, morphology and volume fractions of the different phases, among other things, depend strongly on processing and heat treatment history. Because of this, it is important that the relationships between microstructure, processing, and properties be thoroughly understood. The work under this task has served to delineate such relationships for the Ti-6242 alloy and will be described next.

Structural and Microstructural Evaluation of Uniform Compression Samples

Work under this part of the program was conducted at Battelle and Wright State University, using samples from compression tests performed at Wright State University and Los Alamos National Laboratory.

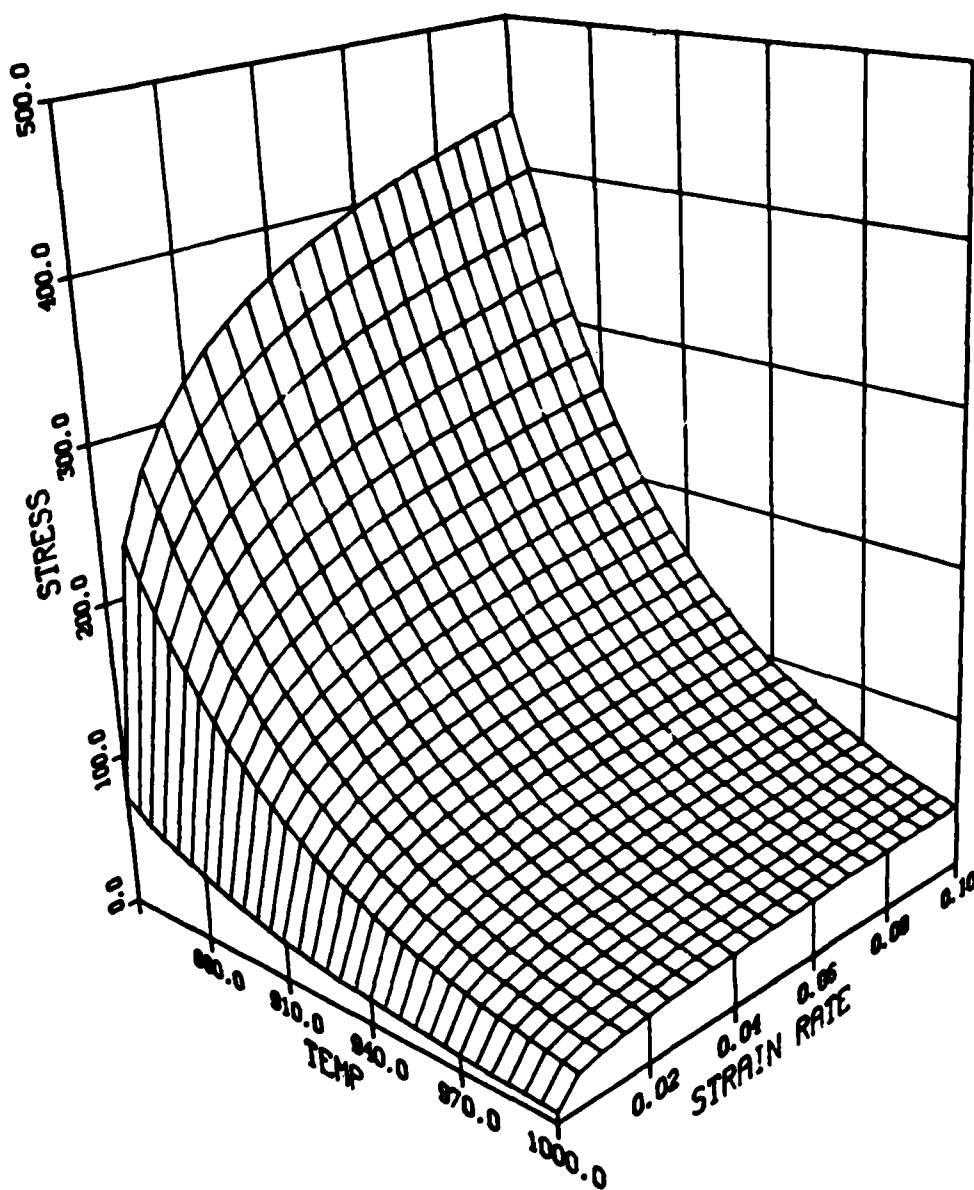


Figure 9. Yield Surface for $\alpha+\beta$ Ti-6242 Alloy.

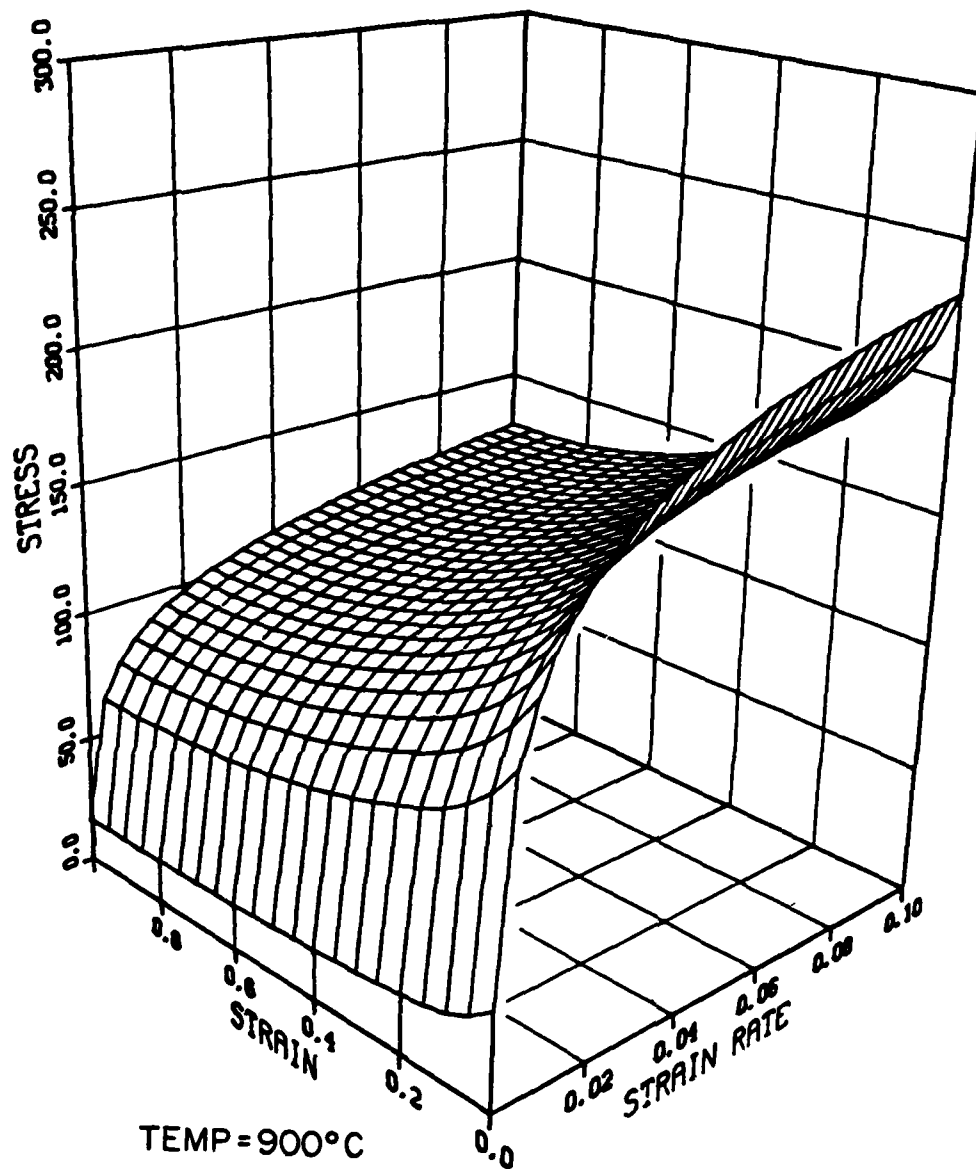


Figure 10. Yield Surface for β Ti-6242 Alloy at 900C.

The objective of the microstructural evaluation was to document the effects of strain, strain rate, and temperature on the microstructures developed in the forging of Ti-6242. To this end, $\alpha+\beta$ preform samples deformed at temperatures of 899, 927, 954, 982, 1010 and 1038C (1650, 1700, 1750, 1800, 1850, and 1900F) and strain rates of 10^{-3} , 10^{-2} , 10^{-1} , 1, 10 and 100 sec.^{-1} were examined metallographically. Similarly, analysis was done on β preform samples deformed at the same strain rates but only the first five of the seven temperatures (because the β microstructure reverts to the single phase bcc Ti above the transus temperature of approximately 990C (1815F) as does the $\alpha+\beta$ microstructure). All initial metallography was done on samples compressed to 50 percent reduction in height. Further observations on selected β microstructure samples compressed to various degrees ($\epsilon=0.2$ to 1.0) at 899C (1650F) and strain rate of $2 \times 10^{-3} \text{ sec.}^{-1}$ are in progress. These last investigations are being conducted in view of the tentative selection of this microstructure and these processing conditions for the actual disk forgings to be done in Phases IV and V of the program. In addition, the effect of post deformation heat treatment on microstructural response was documented for all test conditions.

Metallography on low-strain-rate samples (10^{-3} to $10^{-1} \text{ sec.}^{-1}$) compressed to 50 reduction in height was described in Appendix D of the Second Interim Annual Technical Report⁽²⁾. Hence, metallography on only high-strain-rate samples (1 to 100 sec.^{-1}) compressed to 50 percent reduction at Los Alamos are briefly given in the following. Further details of this investigation are included in Appendix B. A brief summary of observations for the β microstructure samples compressed to various degrees is also given below and in Appendix B.

Metallographic Results for $\alpha+\beta$ Microstructure Compression Samples.

Previously⁽²⁾ it was found that heat treatment of $\alpha+\beta$ material below the transus temperature leads to minimal changes in alpha grain size except at temperatures near the transus (i.e., at $T \geq 954\text{C}$ (1750F)). It has now been found that subtransus deformation or subtransus deformation plus subtransus heat treatment acts as a driving force in producing amounts of primary alpha which depend on deformation temperature (Figure 11) or post-deformation heat-treatment temperature (Figure 12) in a manner suggested by a pseudo binary equilibrium phase diagram for the Ti-Mo system. This finding is similar to that for previously examined low-strain-rate compression samples and emphasizes the improvement in transformation kinetics

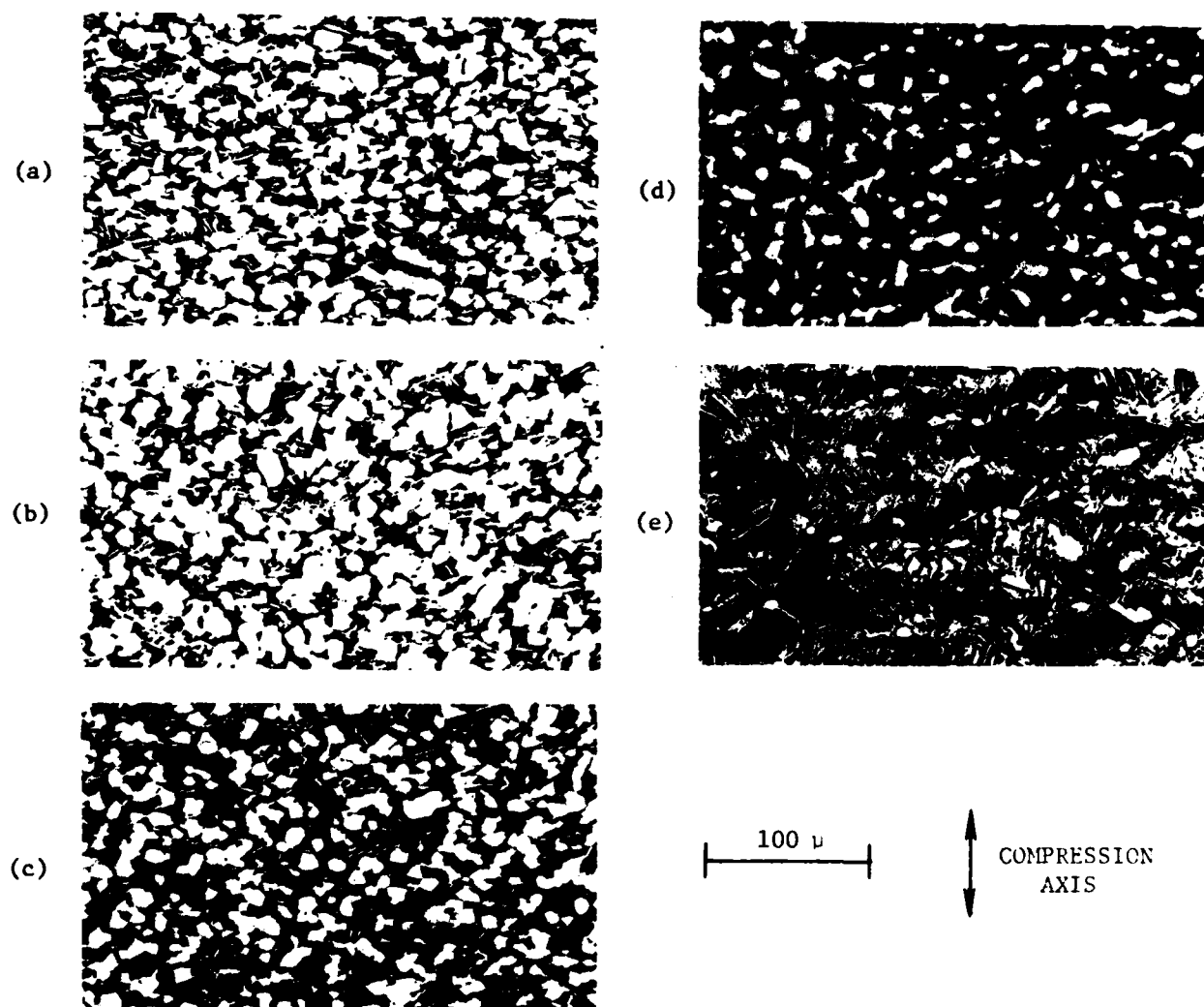


Figure 11. Microstructures in As-Deformed Compression Samples of $\alpha+\beta$ Preform Microstructure Forged at a Strain Rate of 10 Sec.^{-1} and at Temperatures of (a) 899 C (1650 F), (b) 927 C (1700 F), (c) 954 C (1750 F), (d) 982 C (1800 F), and (e) 1010 C (1850 F).

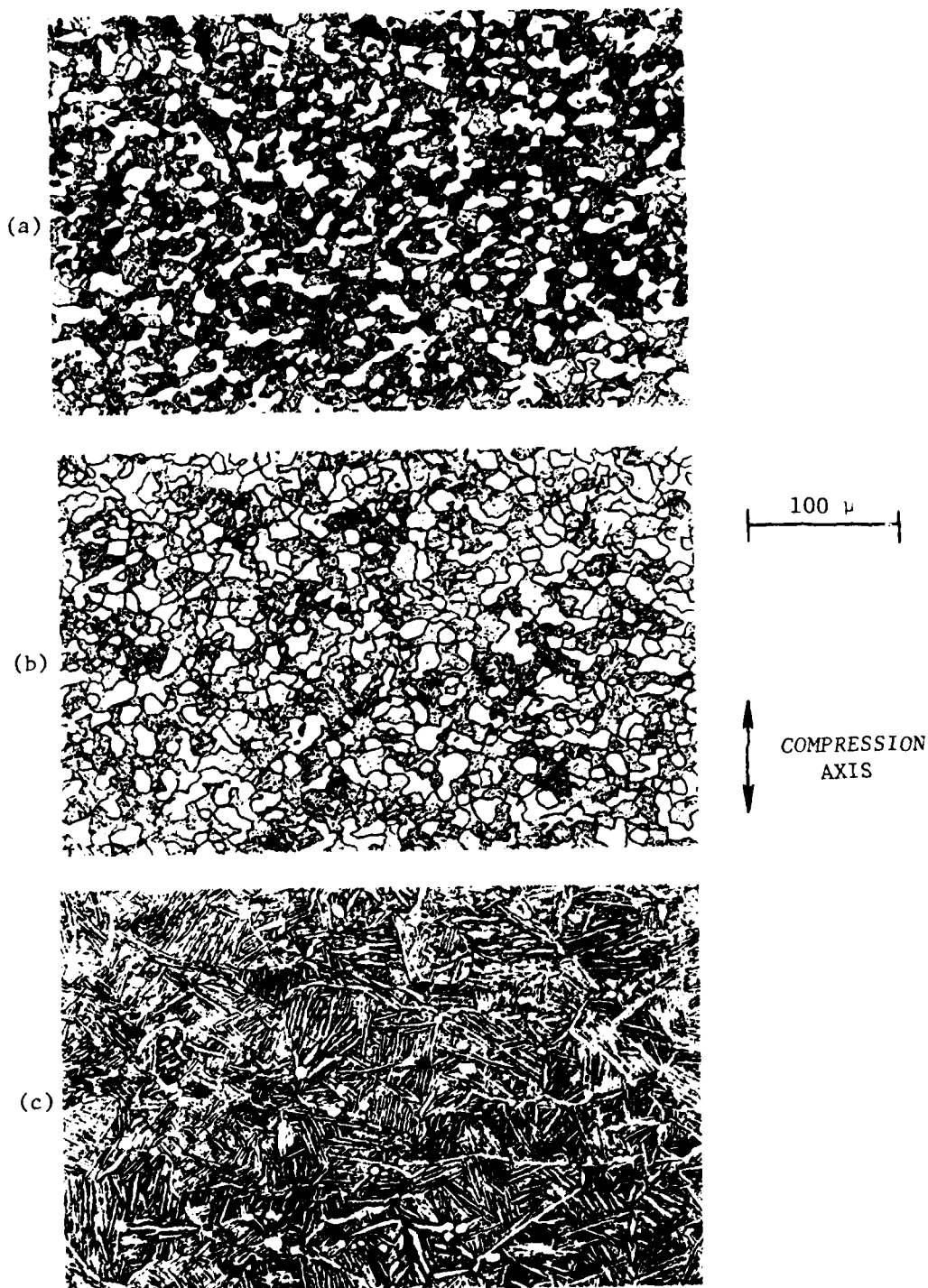


Figure 12. Microstructures Formed in $\alpha+\beta$ Preform Microstructure Material after a Heat Treatment of 954 C (1750 F)/2 Hrs. Which Follows Compression at a Strain Rate of 10 Sec.^{-1} at Temperatures of (a) 899 C (1650 F), (b) 954 C (1750 F), and (c) 1010 C (1850 F).

brought about by hot work or residual hot work. Development of a hot-worked substructure also appears to be effective in speeding up the kinetics of the transformation of the beta matrix phase when $\alpha+\beta$ compression samples are cooled after hot deformation.

High-rate deformation, like low-rate-deformation, above the transus temperature or heat treatment alone above the transus temperature bring about the development of transformed beta microstructures of Widmanstatten alpha (slow cooling rate) or martensitic alpha (fast cooling rate) in $\alpha+\beta$ preform material, (e.g., Figure 11). This observation to be expected from analysis of the phase diagram and transformation kinetics.

Metallographic Results for β Microstructure Compression Samples.

As for low-strain-rate compression, subtransus-high-strain rate compression of the β microstructure to 50 percent reduction leads to grossly nonuniform flow, and, at temperatures approaching the beta transus, phenomena similar to dynamic recrystallization to form primary alpha (Figure 13). The temperatures at which the latter phenomena occur in high-rate deformation are slightly greater than those for low-rate deformation. This trend is analogous to that typically observed in single-phase materials. From these observations, one may conclude that sufficiently high deformations at suitably high subtransus forging temperatures can result in the development of equilibrium $\alpha+\beta$ microstructure in starting material of β microstructure.

Sub-transus-heat treatment of high-strain-rate- β -microstructure-compression samples after deformation leads to initial recrystallization in the areas of highest deformation followed by general recrystallization at long times, provided the heat treatment temperature is high enough (Figures 14 and 15). Gegel⁽²⁾ suggests that the lowest practical temperature for heat treatment of the Ti-6242 alloy with the β microstructure is 916C (1680F). Present observations support this conclusion. As with $\alpha+\beta$ microstructure samples, heat treatment of deformed β microstructure samples above the transus temperature again leads to development of transformed beta microstructures upon cooling.

Metallographic Results for Heat Treated β Microstructure Samples Compressed Various Degrees. Metallographic observations of β preform compression samples deformed to various strains between 0.2 and 1.0 offer a basis for rationalizing previous documentation of the tendency of β microstructure flow curves to approach $\alpha+\beta$ flow curves at large strains ($\epsilon \approx 0.5$ to 1.0). Furthermore, observations on deformed and heat-treated

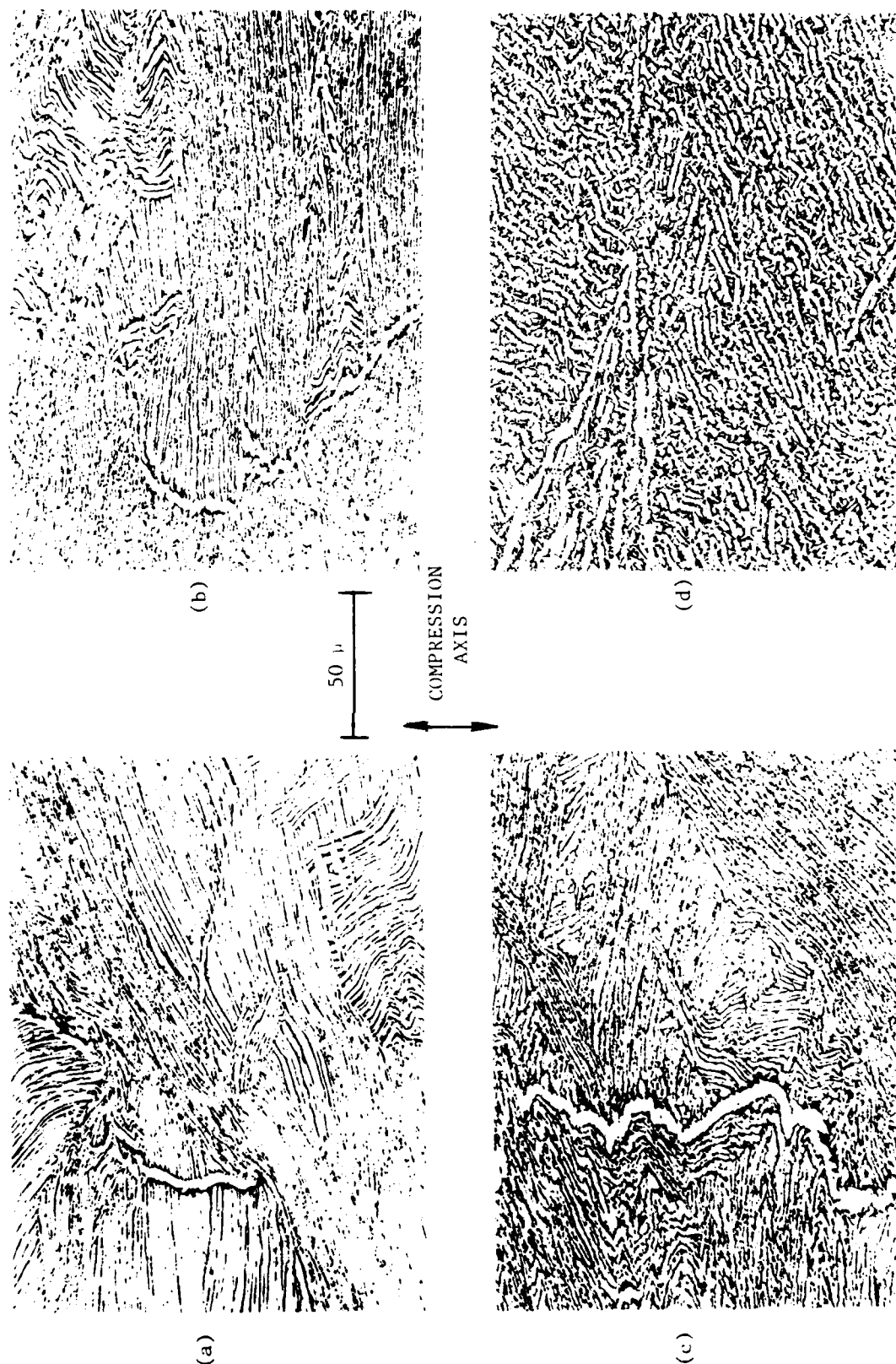


Figure 13. Microstructures in As-deformed Compression Samples of Preterm Microstructure Forged at a Strain Rate of 10 Sec.⁻¹ and at Temperatures of (a) 899°C (1650°F), (b) 927°C (1700°F), (c) 954°C (1750°F), and (d) 982°C (1800°F).

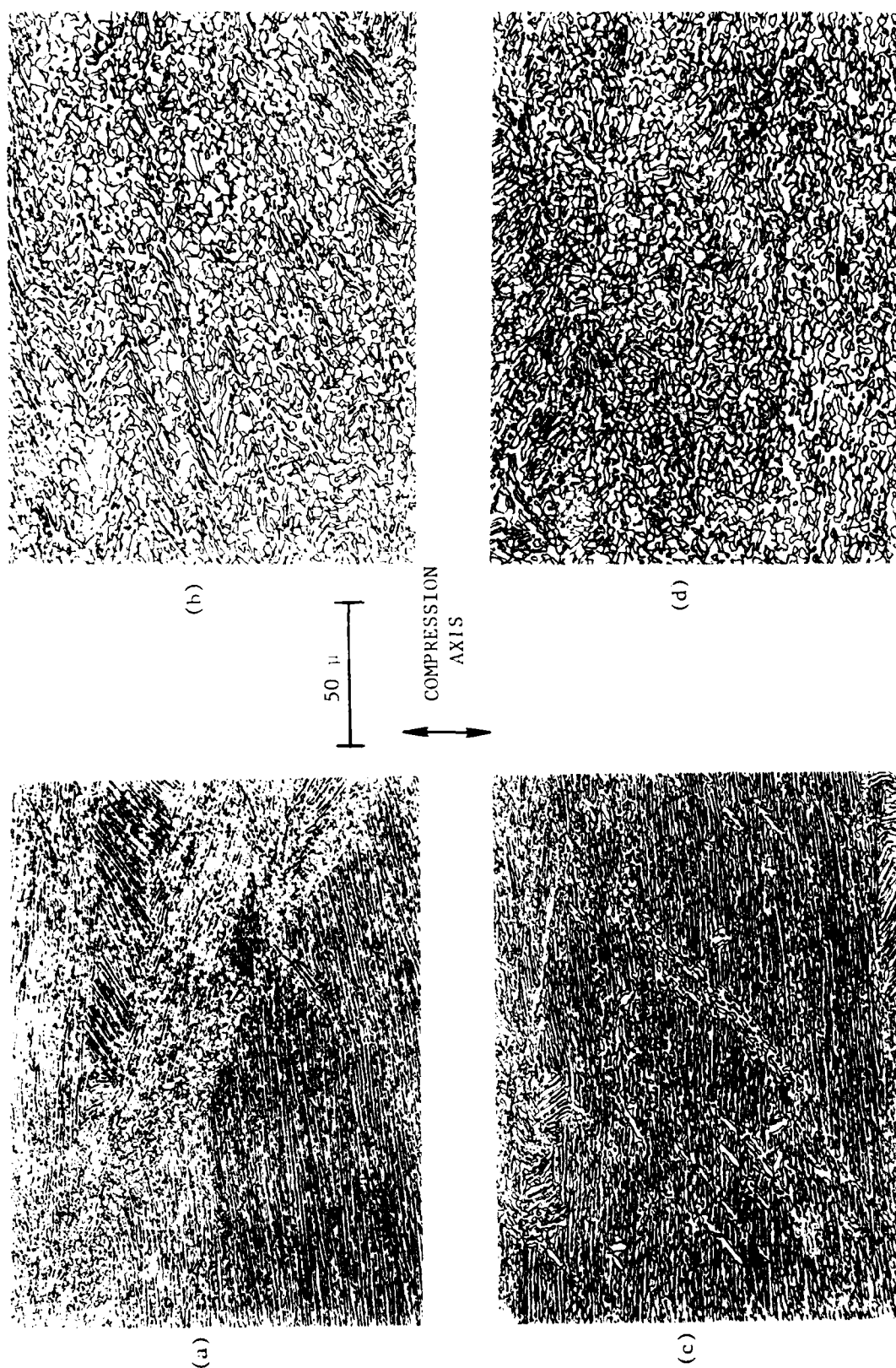


Figure 14. Microstructures Formed in ϵ Preform Microstructure Material After a Heat Treatment at 913 C (1675 F) for Either (a,c) 15 Minutes or (b,d) 2 Hours, Following Deformation at (a,b) 899 C (1650 F), 10 Sec.⁻¹ or (c,d) 954 C (1750 F), 10 Sec.⁻¹.

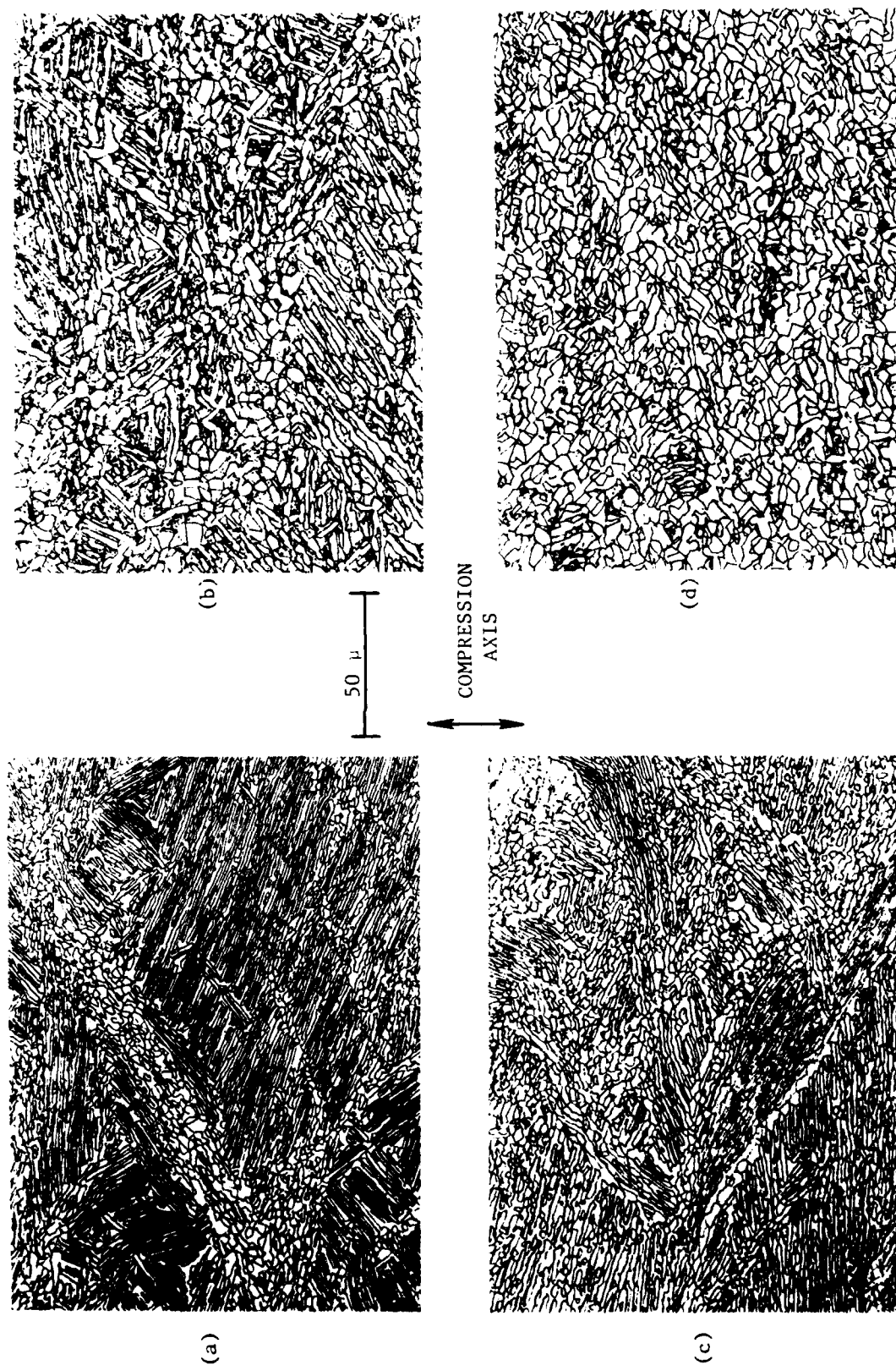


Figure 15. Microstructures Formed in ϵ Preform Microstructure Material After a Heat Treatment at 954 C (1750 F) for Either (a,c) 15 Minutes or (b,d) 2 Hours, Following Deformation at (a,b) 899 C (1650 F), 10 Sec.⁻¹ or (c,d) 954 C (1750 F), 10 Sec.⁻¹.

β microstructure samples have produced data which might be helpful in refining the processing conditions for producing the dual-microstructure, dual-property disk.

Observations of the strain dependence of the deformed microstructural features can be summarized as follows:

1. At $\epsilon < 0.2$, the as-forged microstructures show no distinct transformations. The transformed β structure is retained.
2. At $\epsilon = 0.2$ to 0.4 , regions of intense localized shear develop, and these affect the post-deformation heat treatment response, causing coarsening and breakup of the Widmanstätten platelets.
3. At $\epsilon > 0.4$, regions of dynamic recrystallization, which evolve to the $\alpha + \beta$ structure during heat treatment at 951°C (1745°F), are first observed and increase in size with increasing strain.
4. Strains $\epsilon > 1.0$ are required for the equiaxed $\alpha + \beta$ structure to predominate.

Thus, critical strains for designing the dies and β preform shape for direct forging of a Ti-6242 dual property disk have been suggested. Since complete transformation to the $\alpha + \beta$ structure has not been observed even at $\epsilon = 1.0$, it may be that further optimization of the forging temperature in the range $900 - 930^\circ\text{C}$ ($1652 - 1706^\circ\text{F}$) and heat treatment in the range $950 - 970^\circ\text{C}$ ($1742 - 1778^\circ\text{F}$) should be considered.

Pancake Forging Test for Microstructure/Property Evaluation

This part of the program was conducted by Wyman-Gordon with assistance from Battelle, Carnegie-Mellon University, and Metcut Research Associates, Inc. The objective of this research was to determine the interrelation between processing, microstructure, and service properties. To this end an extended series of pancake forgings were made by Wyman-Gordon. After giving these forgings various heat treatments, the macrostructures, microstructures, and room temperature tensile and elevated temperature tensile and creep properties were determined. From these tests, six forging-heat treatment cycles which appeared to have the most attractive properties were selected for further characterization of structure/property relations (Table 2). The material from these cycles can be differentiated by descriptions

of their microstructures as being bimodal (i.e., equiaxed alpha in transformed beta matrix), coarse lamellar, elongated alpha, or colony. The characterization included room temperature and elevated temperature tensile properties, creep properties, and fatigue properties. The tensile and creep properties have been reported previously⁽²⁾. During the current reporting period, the low-cycle fatigue (LCF) and fatigue-crack-growth (FCG) behavior of the six treatments have been documented. Details of this work can be found in Appendix C.

Low-cycle fatigue tests were run under strain control (using a triangular waveform of 0.33 Hz frequency) on specimens with smooth, round gage sections. The tests were done in air at 510C (950F) using total strain amplitudes of 0.8 pct. and 1.6 pct. A few tests were run at other strains, but the fatigue-life data from these tests were extrapolated to these two strain levels to allow direct comparison of the data for all six forging-heat-treatment conditions. The data from these tests showed that a fine "bimodal" microstructure of equiaxed alpha in a transformed beta matrix (such as that of serial number 1C) yields the best LCF performance (Table 3). On the other hand, colony microstructure (such as serial numbers 1B) tended to have poor LCF performance. These results can be rationalized from the fact that LCF behavior is controlled by crack initiation, which is difficult in microstructures with short slip lengths (e.g., bimodal microstructures) and easy in those with long slip lengths (e.g., colony microstructures).

Fatigue-crack-growth tests were performed also in air at 510C (950F) using compact-tension specimens conforming to ASTM specification E399. The cyclic frequency was 30 Hz, and an R-ratio (ratio of minimum to maximum load) of 0.1 was employed. Crack growth at 510C (950F) was characterized by crack arrest at growth rates below about 1×10^{-8} m/cycle and has been termed apparent threshold stress intensity, ΔK_{TH}^{APP} . The dependence of crack growth rate on microstructure contrasted sharply with the dependence of LCF behavior on microstructure. Colony microstructures and elongated α microstructures gave similar data, exhibiting the lowest fatigue crack growth rates and the highest ΔK_{TH}^{APP} (Figure 16). The bimodal microstructure produced by $\alpha+\beta$ processing gave the highest growth rates and the lowest ΔK_{TH}^{APP} . Extensive scanning electron fractography was conducted, the results of which are in agreement with the above data trends. The microstructural effects on fatigue crack growth rates were observed to be consistent with roughness-induced closure models.

TABLE 2. Thermomechanical Processing of Ti-6242.

<u>Serial Number</u>	<u>Preform</u>	<u>Forging*</u>	<u>Solution** Treatment</u>	<u>Microstructure</u>
1B	$\alpha+\beta$	$\alpha+\beta$ (β_T-40F)	β/AC ($\beta_T+30F/1h$)	Colony
2B	$\alpha+\beta$	$\alpha+\beta$ (β_T-115F)	β/AC ($\beta_T+20F/1h$)	Colony
4B	$\alpha+\beta$	β (β_T+60F)	$\alpha+\beta/AC$ ($\beta_T-20F/1h$)	Coarse Lamellar
1C	$\alpha+\beta$	$\alpha+\beta$ (β_T-40F)	$\alpha+\beta/AC$ ($\beta_T-20F/1h$)	Bimodal
6C	β	$\alpha+\beta$ (β_T-40F)	$\alpha+\beta/AC$ ($\beta-20F/1h$)	Elongated α (high vol %)
6D	β	$\alpha+\beta$ (β_T-40F)	$\alpha+\beta/WQ$ ($\beta_T-20F/1h$)	Elongated α (low vol %)

* $\beta_T = 1815F$, AC from forging

** followed by aging at $1100F/8h/AC$

Table 3. LCF Results for Six Optimal Forge-Heat Treat Cycles

Serial Number	Cycles to Failure ($\epsilon_{\text{total}} = 0.8\%$)	Cycles to Failure ($\epsilon_{\text{total}} = 1.6\%$)
1B	7,243	900***
2B	>68,000**	1,537
4B	8,735	1,500
1C	>90,034	1,975
6C	5,365	1,068
6D	>89,270	1,480

* Followed by aging at 1100F/8 hours/AC

** Interpolation from data at $\epsilon = 0.65\%$ and $\epsilon = 1.6\%$

*** Interpolation from data at $\epsilon = 0.8\%$ and $\epsilon = 2.0\%$

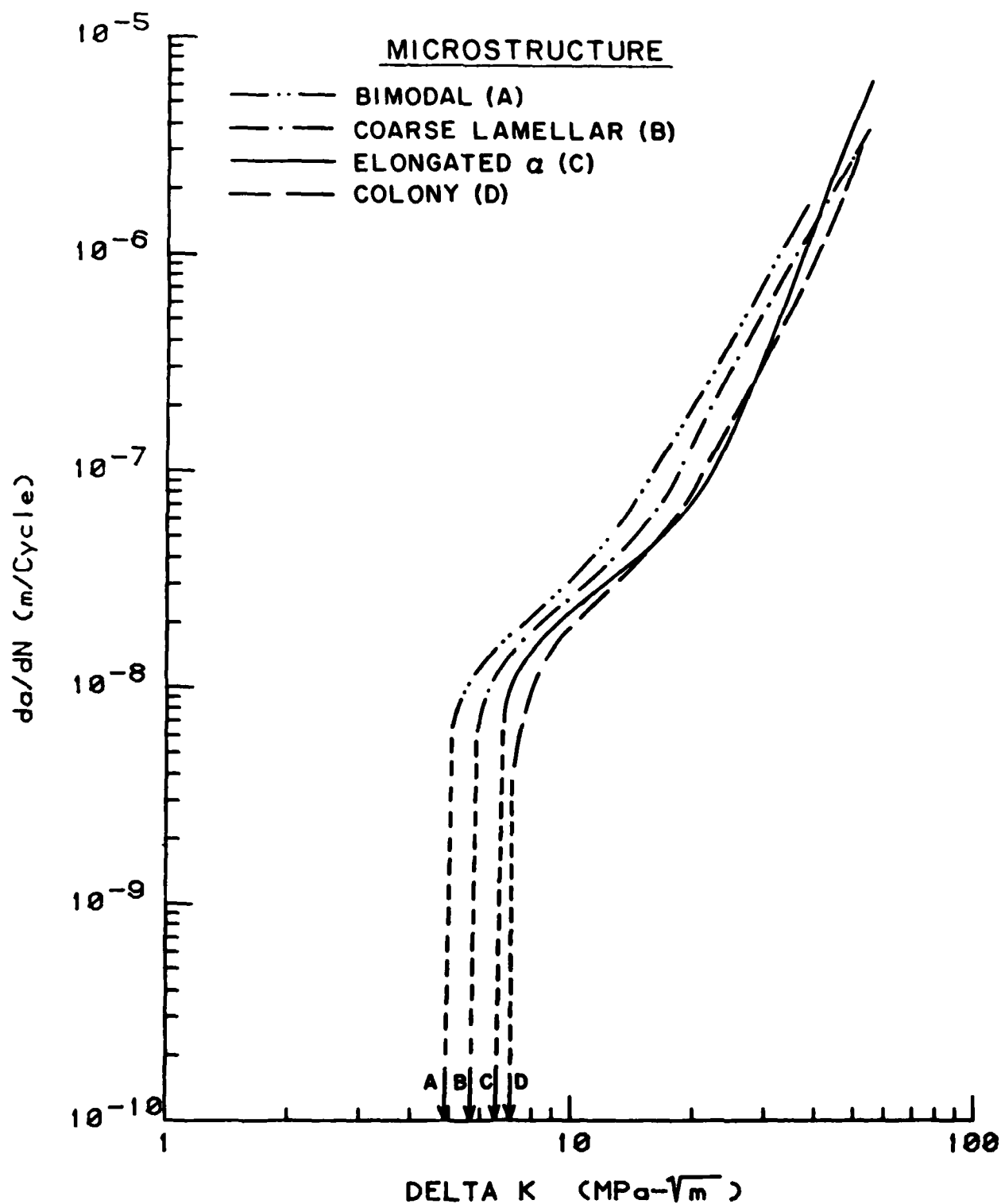


Figure 16. Fatigue Crack growth data for Microstructures that can be characterized as being bimodal (serial number 1C), coarse lamellar (serial number 4B), elongated alpha (serial numbers 6C and 6D), or colony (serial numbers 1B and 2B).

Development of Flow Instability Models

The objective of this subtask is to develop models for the prediction of flow instability in hot working of Ti-6242. To this end, an analysis was performed for the torsion test and actual torsion tests were begun to validate the model which was developed. Details of this investigation are reported in Appendix D.

The analysis is based on previous work employing strain and strain-rate gradients which was concerned with the cases of uniaxial tension and compression. The present treatment is expressed in terms of twist and twist rate gradients and applied to torsion bars containing geometric (machining) and strength defects (deformation defects were not considered). The analysis differs from the previous treatments in two important respects:

- (i) Unlike the cases of tension and compression, there is no change in the area of cross-section during an experiment;
- (ii) Account is taken of the heat generated by the deformation, as well as of the heat lost by conduction along the bar and by convection from the surface of the bar.

It should be pointed out that the current method employs the twist and twist rate as 'state variables'. Although these simplifying assumptions are very useful, the employment of the twist in this way is not rigorously valid, as it is equivalent to using the accumulated strain to quantify the state of work hardening of the material. (This limitation does not apply to the twist rate). As a result, research is continuing with the aim of replacing the twist by the current value of the torque or couple, or by some other, more appropriate, quantity. For the moment, no account is taken of radiation losses from the sample; the addition of a suitable term for this effect does not, however, present any problems, and the analysis will be extended in this direction at a later date.

The usefulness of an analysis in torsion is that it concerns deformation by shear. Thus torsion testing can be applied to the study of shear and deformation band development under forging conditions. In this way, the effects reported by Semiatin and Lahoti of Battelle's Columbus Laboratory and by Dadras and Thomas of Wright State University can be investigated in more detail.

The research carried out to date has shown the great importance of heating effects in promoting unstable flow. It thus confirms the trends noted by the above workers. It also permits predictions to be made regarding process modifications which can lessen the tendency for the flow to localize. In brief, appreciable localization cannot occur, even under flow softening conditions, unless significant temperature gradients are developed within the material. The magnitude of the temperature gradients, in turn, depends on the balance between the rate of heat generation by deformation heating and the rate of heat loss by radiation, convection and conduction. In flow softening materials such as Ti-6242 in the transformed beta condition, which are prone to flow localization because of the instability of their microstructures, plastic instability can be eliminated principally in two ways:

- (i) A low strain rate can be used (e.g., isothermal forging) which permits the near equalization of temperature by means of conduction during strain (this possibility has been treated by numerous workers);
- (ii) A high strain rate can be used, as in normal forging, but the increments of deformation must be separated by 'rest periods' of about one to two minutes on average, to permit temperature equalization to occur between straining intervals. This method appears to be very effective in reducing flow localization; however, it does require additional heating capacity and lowers the rate of production.

Experiments were conducted on two material (304 stainless steel and Ti-6242) to assess the accuracy of the predictions made by the theory. These experiments showed that severe flow localization can be produced, even in the absence of flow softening, (i.e., under normal work hardening conditions), as long as appreciable temperature gradients are permitted to develop within the material. By contrast, when the temperature gradients are reduced or eliminated, by either of methods (i) and (ii) above, macroscopic flow localization is prevented, or reduced to acceptable levels. The critical strain rates and holding periods required to avoid localization determined in the experiments were in reasonable agreement with the predictions of the theory, which takes into account the thermal and mechanical properties of the material.

The Method of Analysis. The aim of the calculation is to predict the twist gradient along the torsion bar as a function of time or of the overall amount of twist. Localization corresponds to a twist gradient which is much higher in one location than elsewhere. The second variable of importance is the temperature gradient, which is also calculated as a function of time or of overall twist. During flow localization, there is also a localization of the heating effect. The calculation is carried out using an iterative technique in which the following three simultaneous equations are solved.

$$m\lambda' + \Gamma\lambda + \phi\mu + 3\frac{d\ln R}{dx} = 0 \quad (2)$$

$$T = \frac{\eta\dot{\theta}C}{\pi R^2 \rho c} + \frac{k}{\rho c} \frac{d^2 T}{dx^2} + \frac{2h}{R\rho c} (T_{\text{ext}} - T) \quad (3)$$

$$\int_L \dot{\theta} dx = \text{constant} \quad (4)$$

Equation (2) is the torsion equivalent of the well-known relation pertaining to tension and compression. It contains a new term $\phi\mu$ to represent the balance between heat generation and heat loss and the final term is the 'area gradient term' which applies in the case of torsion. Here m is the rate sensitivity of the torque $\partial \ln C / \partial \ln \dot{\theta}$, λ' is the twist rate gradient $\partial \ln \dot{\theta} / \partial x$, Γ is the work hardening coefficient of the torque $\partial \ln C / \partial \theta$, λ is the twist gradient $\partial \theta / \partial x$, ϕ is the temperature sensitivity of the torque $\partial \ln C / \partial T$, μ is the temperature gradient $\partial T / \partial x$, and $d \ln R / dx$ is the radius gradient. Relation (2) is only valid when the torque C is a unique function of θ , $\dot{\theta}$, R and T .

Equation (3) is employed to calculate the balance between the rates of heat generation and dissipation. Here η is conversion efficiency of mechanical work into heat, $\dot{\theta}C$ is the mechanical work term, where $\dot{\theta}$ is the twist rate and C is the couple or torque, R is the radius of the bar, ρ is the density of the material, c is the heat capacity, k is the thermal conductivity, h is the corrective heat transfer coefficient, and T_{ext} , T and t are the temperature of the surroundings, that of the relevant slice of the sample, and the time, respectively. To prevent the analysis from becoming unduly complicated, radial temperature gradients were neglected in the calculations, i.e., the temperature was taken as being uniform within a particular slice of the specimen.

Equation (4) is required to ensure that the sum of the twist increments in the individual slices is equal to the overall or macroscopic twist.

In the first step of any simulation, the twist rate gradient for each slice is calculated from equation (2). As the temperature is initially uniform, it depends only on the radius gradient $d\ln R/dx$. The actual twist rates (as opposed to the differences between slice rates) can only be found by iteration using equation (4). Once the local twist rates are known, the heating rates dT/dt are readily obtained from equation (3), as there are no temperature gradients at the beginning of each experiment, and so the heat transfer terms can be neglected. A time interval dt is then selected, from which the amounts of twist and of temperature increase can be determined for each element of the bar. From these quantities, the coefficients Γ_1 and ϕ_1 are evaluated, as these depend on θ_1 , and the temperature gradient terms are also computed.

The subsequent calculations are similar in broad outline, but somewhat more involved. In this case, the twist rate gradient computation takes into account, not only the radius gradient, but also the work hardening - twist gradient and temperature sensitivity - temperature gradient terms. As before, the actual twist rates in each element are found by iteration. For the heating rate calculation, allowance is now made for the effect of conduction (the influence of convection and radiation have been neglected to date). The application of a time increment dt then leads to the determination of θ_1 from $\dot{\theta}_1$, and T_1 from \dot{T} . Finally, Γ_1 , θ_1 and d^2T/dx^2 are made available for the step that follows.

Comparison of Theory and Experiment. The change in appearance of a sample of 304 stainless steel during the course of a torsion experiment is shown in Figure 17. The torque-strain curve is also displayed, which shows that the sample, which was deformed at room temperature, work hardened in the conventional way. Because of the relatively high twist rate (equivalent to a shear strain rate of the surface of 0.5 s^{-1}), coupled with the comparatively low thermal conductivity, the flow began to localize at an average shear strain of 0.1. The evolution of the localization can be clearly seen from Figure 17, and it is evident that the deformation is highly localized by the time a strain of 0.75 is attained. Samples tested at lower strain

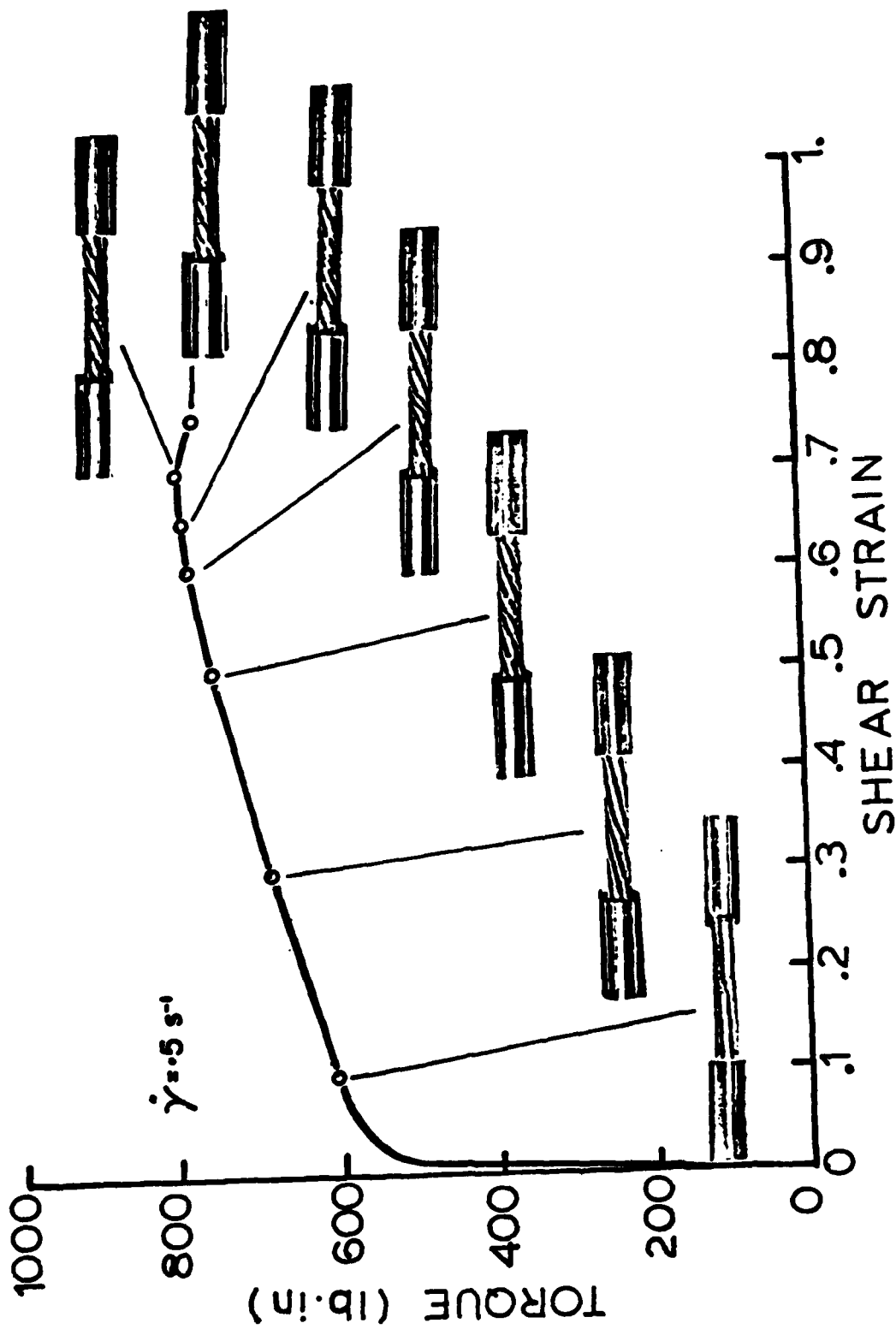


Figure 17. Torque-Shear Strain Curve and Photographs of Torsion Samples Showing Localization of Deformation for 304 Stainless Steel Deformed at a Surface Shear Strain Rate of 0.5 sec.^{-1} .

rates were able to be deformed uniformly to much larger strains. Although failure again occurred by localization, in these cases, the instability was judged to be associated with a process of cavity formation, rather than of the local concentration of heat.

Qualitatively similar results were obtained on Ti-6242 samples which were given a prior β heat treatment. In $\alpha+\beta$ samples, no localization occurred. A comparison is made in Figure 18 of the flow curves determined in two torsion bars, heat treated according to these two procedures. It can be seen that there is only a small amount of flow softening in the ($\alpha+\beta$) material. By contrast, the β material displays marked flow softening at the test temperature of 913C (1675F). The reason why flow softening is required at elevated temperatures (and not at room temperatures) is because of the stabilizing effect of the higher values of rate sensitivity pertaining to high temperature deformation. (This point is developed at greater length in the Appendix D together with a detailed comparison of the experimental and theoretical results expressed in terms of the strains and temperatures in the 'bulk' and localized regions of the sample.)

Theoretical Formability for Sheet Metal and Bulk Forming Processes

The work under this task was completed earlier. A computer program for predicting limit strains in biaxial stretching of sheet, using Marciniak's approach was developed. The details of this study are included in Appendix F of the Second Annual Interim Report.

Experimental and Theoretical Investigation of Forming Limit Criteria in Disk Forging

Emphasis in this part of the program is on the mechanism of fracture during metalworking processes at elevated temperatures. Work with a single phase alloy (Co-Ni-Cr-Mo) was conducted at the University of Pittsburgh. The details of this study are included in Appendix G of the Second Annual Interim Report.

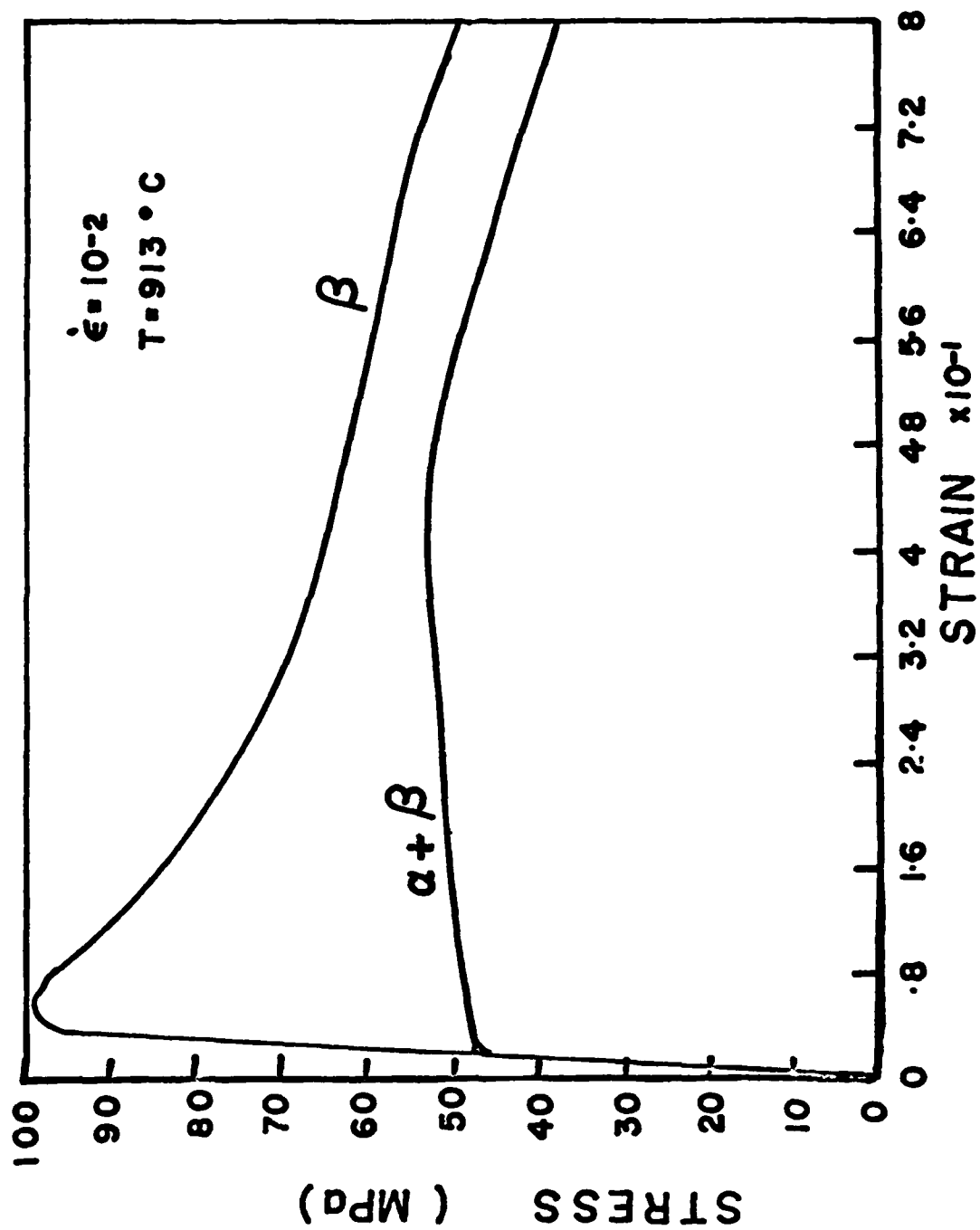


Figure 18. Stress-Strain Plots for Ti-6242 Determined in Torsion at $T = 913^{\circ}\text{C}$ (1675°F) and a Surface Effective Strain Rate of 0.01 sec.^{-1} .

Development of Microscopic Fracture/Failure Criteria

The objective of this task is to identify and develop criteria for the microscopic fracture/failure modes likely to be found in hot working of Ti-6242. This work is being conducted by Cornell and is reported in detail in Appendix E.

The observations based upon the previous work conducted under this program indicate that the type of defects shown in Figure 19 are the only relevant defects in forging of Ti-6242, especially with β preform microstructure. Under compressive state of stress, shear bands (regions of localized deformation) are common, and under tensile state of stress, small cracks or voids, typically $10\mu\text{m}$ to $100\mu\text{m}$ in size, can appear at the prior β -grain boundaries. The difference in the scale of the two types of flaws is significant. Shear bands form on a scale much larger than the grain size while grain-boundary cracks are smaller than the grain size.

Much work is yet needed to quantify the two types of flaws. For a first attempt, however, a simple workability map has been developed using an intuitive understanding of why these defects do and do not form. For the grain boundary cracks it is thought that the strain-rate sensitivity of cracking is coupled to the relaxation of stresses at interfaces by $\alpha \rightleftharpoons \beta$ phase transformation. At the lower strain-rates, the local stress concentration produced by boundary sliding or intra-colony slip is quickly relaxed and fracture is precluded; while at the higher strain-rates, the kinetics of phase change are not fast enough and the stress-concentrations produce fracture^(7,8,9). Thus, a transition strain-rate will separate the fracture region from the safe region should be expected.

-
- (7) Nadiv, S., Gegel, H. L., and Morgan, J., Interim Annual Report, 1978-79, this program, p. 105.
 - (8) Gegel, H. L., Nadiv, S., Malas, J. C., and Morgan, J. T., Interim Annual Report, 1979-80, this program, p. 403.
 - (9) Gegel, H. L., Nadiv, S., and Raj, R., Scripta Metall., 1980, vol. 14, p. 241.

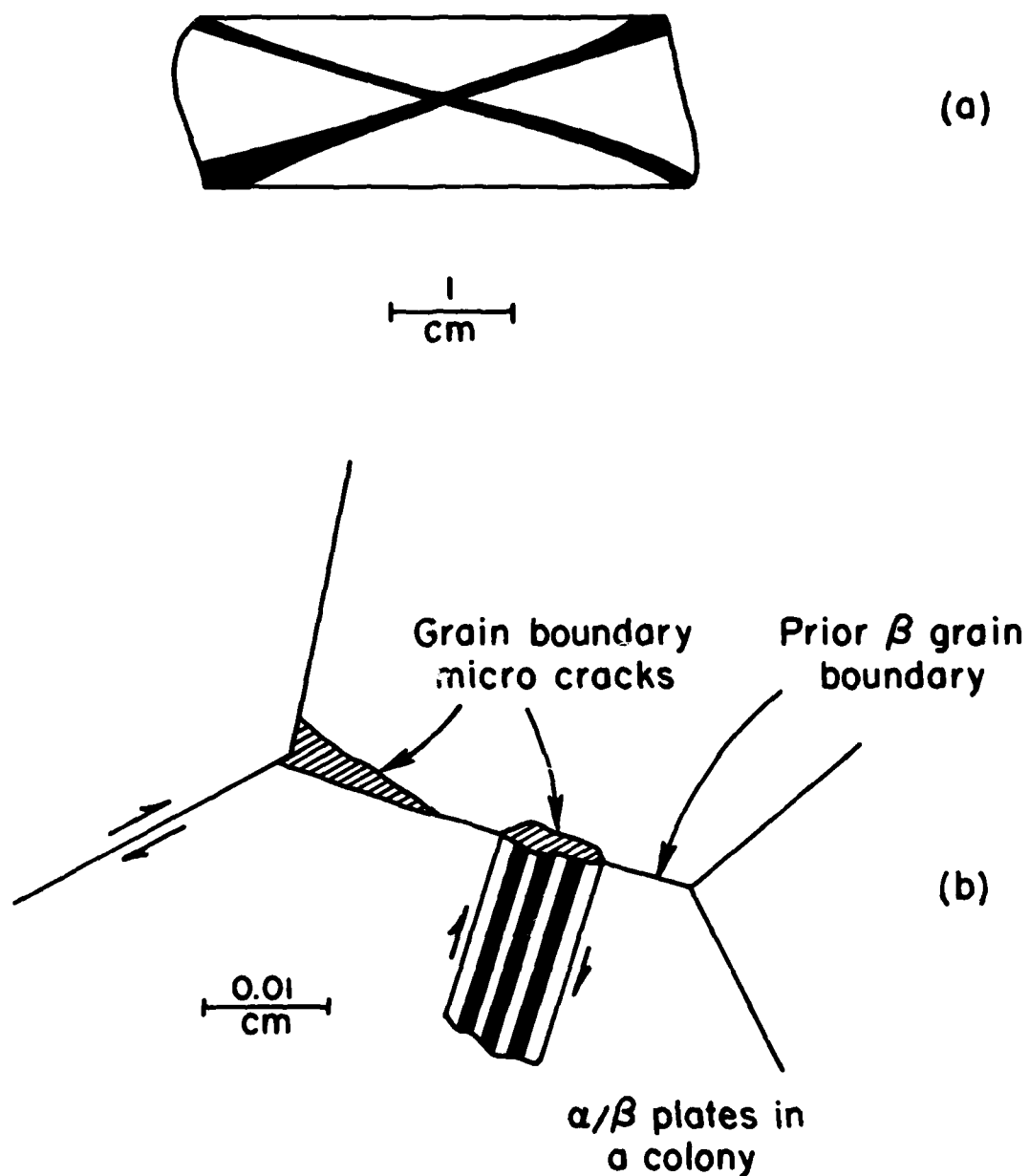


Figure 19. A schematic of the types of damage seen in large deformation of Ti-6242, with a β -preform structure. (a) shear localization of flow in compression, and (b) grain boundary cracking in simple tension experiments. The scales are approximate; they are meant to emphasize the difference in the size of the two defects.

Shear localization occurs on a scale larger than the grain size. A criterion for localization has been formulated by extending the work of Hill⁽¹⁰⁾ on the growth of time-independent localized necking in thin sheets, to include rate and temperature sensitive parameters such as the strain rate sensitivity and the change in flow stress with temperature. Rigorous work on this topic has been done by Semiatin and Lahoti and Jonas. Semiatin and Lahoti have reported systematic shift from severe localization, to mild localization, to no localization as the strain-rate and temperature are changed⁽¹¹⁾. Extension of Hill's work has led to the following criterion for the growth of localization:

$$\Gamma + m \left(\frac{\partial \ln \dot{\epsilon}_p}{\partial \epsilon_p} \right)_T + \frac{1}{\rho C_p} \left(\frac{\partial Y}{\partial T} \right)_{\epsilon_p, \dot{\epsilon}_p} \leq K \quad (5)$$

where Γ is the strain hardening coefficient defined as

$$\Gamma = \left(\frac{\partial \ln Y}{\partial \epsilon_p} \right)_{\dot{\epsilon}_p, T}$$

Y is the flow stress. ϵ_p and $\dot{\epsilon}_p$ are the effective or plastic strain and strain-rates, and m , the strain-rate sensitivity is defined as usual as:

$$m = \left(\frac{\partial \ln Y}{\partial \ln \dot{\epsilon}_p} \right)_{\epsilon_p, T} \quad (6)$$

$(\partial Y / \partial T)$ is the temperature dependence of the flow stress; ρ and C_p are the density ($4.5 \times 10^3 \text{ kg/m}^3$ for Ti) and constant-pressure specific heat ($525 \text{ JK}^{-1}\text{kg}^{-1}$). For convenience, a quantity α is defined as $\alpha = (\partial \ln \dot{\epsilon}_p / \partial \epsilon_p)_T$. It is not a material property but rather a measure of the extent of localization. The greater α is, the more severe is the localization. We assume here that $\alpha = 8$ represents the approximate degree of localization seen in experiments of Semiatin and Lahoti. The number K in Equation (5) is left as a floating parameter. In simple deformation states, e.g., thin sheet deformed in

(10) Hill, R., J. Mech. Phys. Solids, 1952, vol. 1, pp. 19-30.

(11) Semiatin, S. L., and Lahoti, G. D., "The Occurrence of Shear Bands in Isothermal, Hot Forging," to be published, Battelle Columbus Laboratories, Columbus, Ohio.

uniaxial tension⁽¹⁰⁾, its value can be specified exactly but in complex situations it can be left simply as a constant equal to zero. The farther the left hand side deviates from zero the more severe is the localization; that is the implication of Equation (5).

The left hand side in Equation (5) has been calculated using the data generated by Thomas and Dadras⁽¹²⁾ and the results are tabulated in Table 4. The approximations in these results, listed as footnotes, should be noted.

A workability map for Ti-6242 is given in Figure 20. The curve which contains a minimum is drawn by applying Equation 5 to the data in Table 4. The shear localization data of Semiatin and Lahoti (for compression tests) are shown as solid and open circles. The open circles imply no localization and the increasing diameter of the solid circles means increasing localization. For this data $\alpha = 8$ appears to provide good fit between experiment and Equation (5). Interestingly a minimum appears where data is lacking. Experiments in this region would be a good test for the analysis.

The results for grain boundary fracture from tensile tests by Thomas and Dadras are shown as solid (fracture) and open (no-fracture) triangles. As expected the transition strain-rate increases with temperature (the kinetics of stress-relaxation by phase change would increase with temperature). There is no model to predict its position quantitatively at the present time, however. Note that shear localization appears less likely in tension than in compression. This is interesting because it implies that shear-localization may be sensitive to the stress-state. Our tentative explanation is that because of the geometry of deformation α must reach larger values in tension tests, than in compression tests where flow is quite constrained, before localization would become activated.

In the first attempt, therefore, the safe region for Ti-6242, β -preform, forging is likely to lie in the shaded area in Figure 20. If one desires to operate at the highest possible strain-rate then we must forge close to the β -transus temperature in the region marked A in Figure 20.

(12) Dadras, P. and Thomas, J. F., Jr., Interim Annual Report, this program, 1979-80, p. 94.

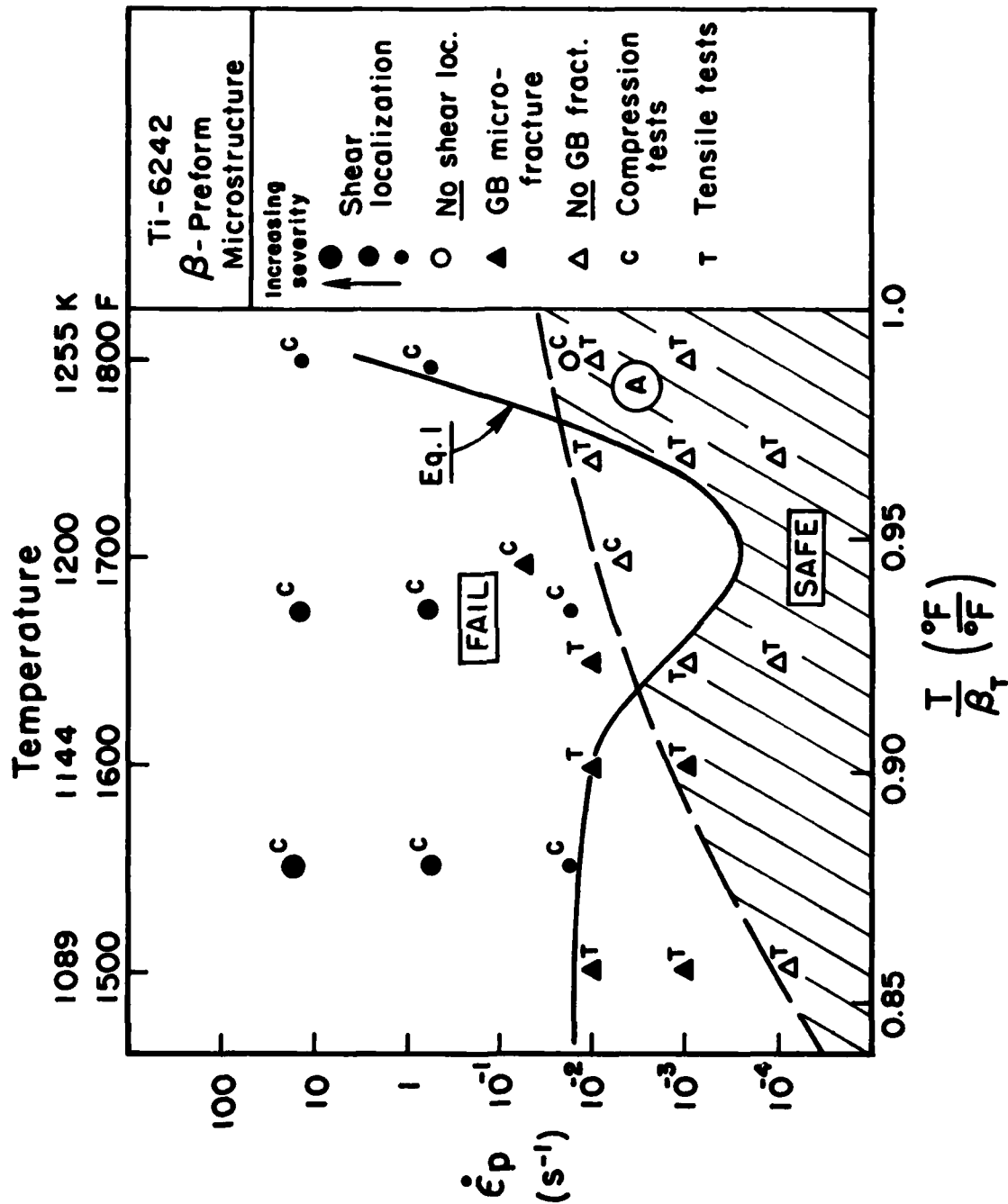


Figure 20. A processing map for Ti-6242. The solid line separates the fail and safe regions for shear localization, the dashed line those for grain boundary fracture. The optimum conditions for forming (high strain-rates yet no defects) will be near A in the SAFE region.

TABLE 4

A Listing of the Values for the Parameters in Equation (5)
(Derived from Reference 12). The Last Column is the Value
for the Left Hand-Side in Equation (5).

T (°F)	$\dot{\epsilon}_p$ (s^{-1})	γ'	$\gamma^{(1)}$	$m^{(1)}$	$(\partial Y / \partial T)^{(1)}_{\epsilon_p, \dot{\epsilon}_p}$ (MPa/K)	Eq. 1 (LHS) ($\alpha=8$)
1800	10^{-1}	-0.85*	-0.34	0.245	-2.4	0.6
	10^{-2}	-0.85*	-0.68	0.265	-1.55	0.78
	10^{-3}	-1.02*	-1.02	0.295	-0.8	1.0
1750	10^{-1}	-1.49	-1.06	0.22	-2.05	-0.17
	10^{-2}	-1.61	-1.47	0.25	-1.3	-0.02
	10^{-3}	-2.2	-2.2	0.32	-0.7	0.06
1700	10^{-1}	-1.84	-1.43	0.19	-1.9	-0.71
	10^{-2}	-1.90	-1.77	0.24	-1.25	-0.38
	10^{-3}	-2.37	-2.37	0.31	-0.68	-0.18
1650	10^{-1}	-1.61	-1.26	0.185	-1.65	-0.48
	10^{-2}	-1.79	-1.67	0.235	-1.1	-0.26
	10^{-3}	-2.14	-2.14	0.305	-0.6	0.05
1600**	10^{-2}	-1.55	-1.44	0.23	-1.0	-0.02
1550**	10^{-2}	-1.49	-1.40	0.22	-0.85	0.0
1500**	10^{-2}	-1.37	-1.30	0.21	-0.7	0.07

* Assumed that γ' follows Equation (5) at $T = 1800^\circ F$

** m and $(\partial Y / \partial T)$ are extrapolated from the data at higher temperature.

(1) γ , m and $(\partial Y / \partial T)$ represent the temperature corrected values using the procedure in Ref. 12. γ' are the values from the raw tensile data.

Validation of Microscopic Fracture/
Failure Models

The objective of this task is to validate fracture/failure models through experimental measurements. Beta-annealed Ti-6242 material has been processed for this purpose. Uniaxial tension and plane strain tension specimens have been machined from this material. In addition, gridding techniques were developed during the current reporting period in order to allow precise measurement of strains at or near fracture.

SECTION VI

PROCESS MODELING FOR DISK TYPE FORGING

Under this phase of the program, mathematical and computer models of axisymmetric compression are being developed to simulate metal flow that occurs during forging of axisymmetric components, such as a compressor or a turbine disk, while taking into consideration the problem of non-steady-state heat transfer in a moving incompressible medium with heat sources. These models also take into consideration the dependence of material behavior on strain, strain rate, and temperature, and it is expected that analyses will provide information on these parameters so that the properties of the deformed materials may be predicted. This effort is being carried out by using an "exact" method (finite-element method) at the University of California and Battelle in parallel. Further, these developments are being implemented in an interactive system of computer programs for design and optimization of the forging process.

Process Modeling With Matrix Method (Task 2.1)

Work under this part of the program is being conducted at the University of California, Berkeley. The details are given in Appendix F.

Theoretical considerations pertaining to several disciplines are needed to perform a coupled analysis of viscoplastic deformation and heat transfer. The finite element method applied to the analysis of metal forming processes for rigid plastic materials is extended to rigid viscoplastic materials. For thermo-viscoplastic analyses a thermodynamic theory of deformation utilizing the concept of internal parameters developed by Perzyna is adapted to a rigid viscoplastic material, considering plastic strain and the dislocation density as the only internal parameters. A scheme of numerical integration of heat-balance equations leads to the coupled analysis of deformation and heat transfer, and the algorithm is implemented in the finite element program. The finite-element formulations are then applied to titanium alloy forgings.

Compression of ($\alpha+\beta$) Preforms

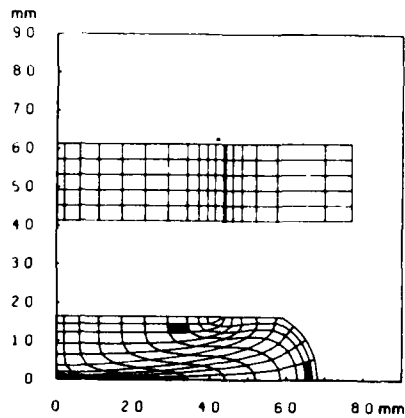
The preform, which measured 81.25 mm (3.25 inch) in diameter and 81.25 mm (3.25 inch) thick, was heated to 1227K (1775F), and the dies to 624K (700F). A computer-controlled hydraulic press compressed the preform with an average strain rate of 3.0/min. Although a glass-type material was used as a lubricant, the temperature difference between the dies and the workpiece prevents effective lubrication. In simulation, therefore, sticking friction was imposed as the interface boundary condition.

Figure 21(a) shows the grid distortion at the 60 percent reduction in height. A rigid zone beneath the die due to die chilling is evident and, consequently, the shear band formation is distinctively traceable. Because of this nonuniform deformation, the amount of barreling and folding is pronounced. The flow lines obtained by Chen under the same forging conditions in Figure 21(a) demonstrate striking similarity with the computed results.

Compression of (β) Preforms

Simulation of hot compression of (β) preforms was performed under the same conditions as those for compression of ($\alpha+\beta$) preforms in specimen dimensions, initial die and workpiece temperatures, and the strain-rate. The grid distortion at the 62 percent reduction in height, along with the experimental flow lines, is shown in Figure 21(b). Comparing the results in Figure 21(b) with the results for ($\alpha+\beta$) preform compression given in Figure 21(a), the experimental flow lines clearly indicate that strain concentration is more pronounced for the (β) phase alloy, while the computed grid distortions show little difference between the two materials. The tendency for more strain concentration in the (β) phase alloy is seen in the computed results.

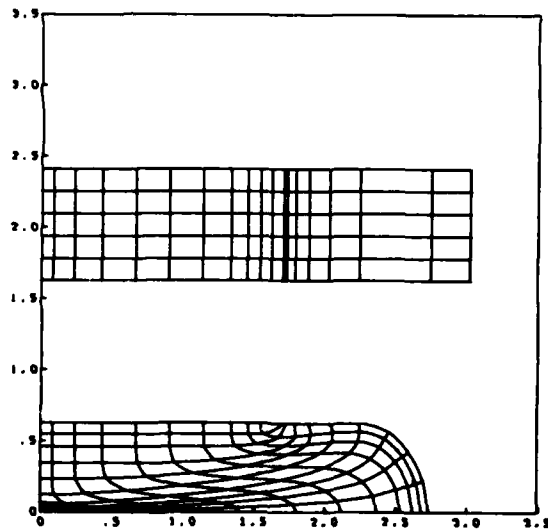
Figure 22 shows the microstructure at three locations and computed local strain, strain-rate, and temperature variations during deformation at these locations. Around point B (element 17) the microstructures should not be very different from the original ones, because a very small amount of deformation has occurred. However, it appears that transformation into the ($\alpha+\beta$) phase has begun at certain spots. This is probably caused by the workpiece being heated for some time to a temperature just below the transus temperature. Around point A (element 99) the transformation into ($\alpha+\beta$) phase



P3: 1775F/700F
3.0 min. $^{-1}/\alpha+\beta$



Figure 21(a). Grid distortion in hot-die forging of $(\alpha + \beta)$ -preform and comparison with experimental macrostructure. (Macrostructure, courtesy of C. C. Chen, Chen-Tech Industries, Inc)



2.54 cm
1 inch

P8: 1775F/700F
3.0 min. $^{-1}/\beta$

Figure 21(b). Theoretical grid distortion and comparison with macrostructures in hot-die forging of (β) -preform. (Microstructures, courtesy of C. C. Chen, Chen-Tech Industries, Inc.

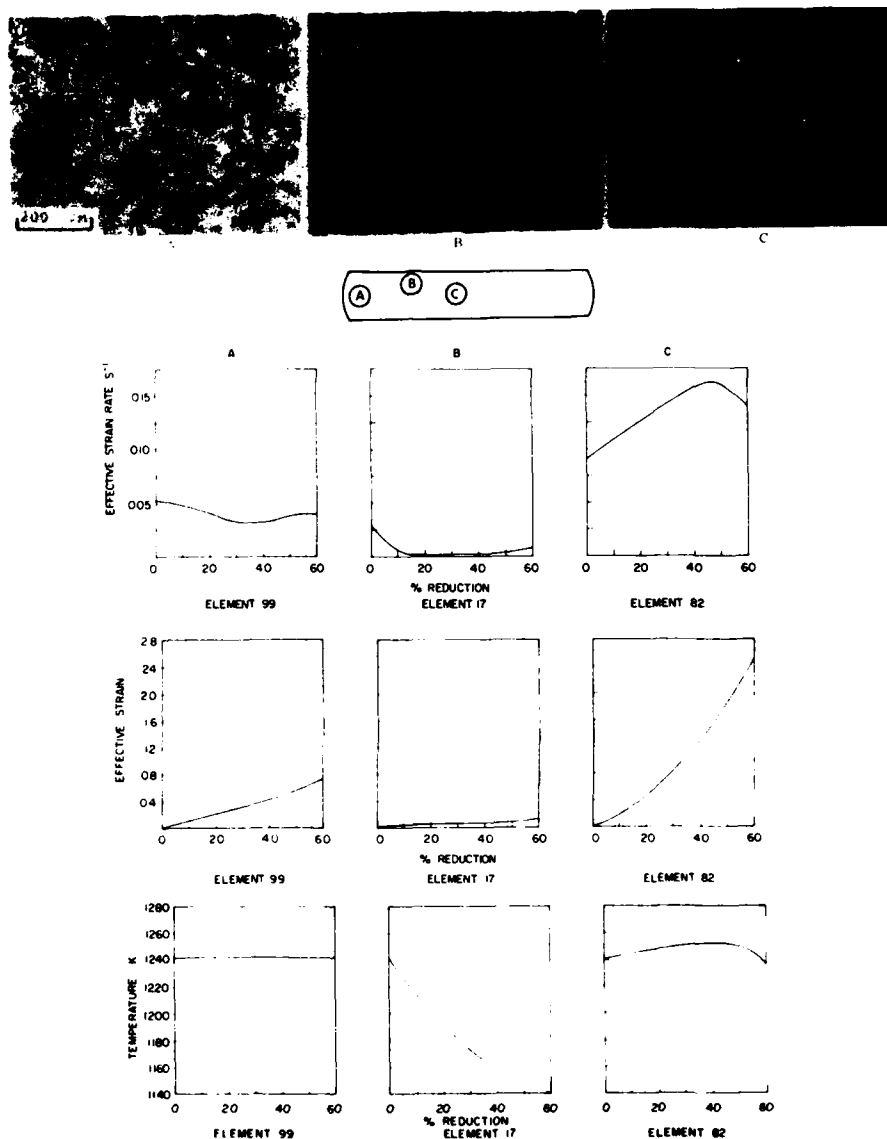


Figure 22. Local strain, strain-rate, and temperature variations during (B)-phase hot-die compression and corresponding microstructures after compression. (Microstructures, courtesy of C. C. Chen, Chen-Tech Industries, Inc.)

is in a more advanced stage. This can be due to a tensile hydrostatic stress and considerable amount of deformation. In the central region C (element 82), the deformation is very large and the reduction in grain size is drastic. A combination of high pressure and temperature in this region makes feasible a full transformation into the (β) phase, and upon cooling, a new refined grain structure of the (β) transformed phase is obtained.

Isothermal Forging at ($\alpha+\beta$)/(β) Composite

A preform is a cylindrical composite material consisting of a central core of ($\alpha+\beta$) phase and an outer ring of (β) transformed phase, both diffusion-bonded together.

The diameter of the preform, shown in Figure 23(a), is 140.63 mm (5.625 inch) and its height is 50 mm (2.00 inch). The diameter of the ($\alpha+\beta$) phase at the center is 76.2 mm (3.00 inch) and the taper angle is 20°. Isothermal forging (dies and workpiece at the same initial temperature) at 955C (1750F) at constant ram speed of 5.08 mm/min. (0.2 in./min) was applied. Total reduction in height was 60 percent. At these high temperatures, the glass-type lubricant is very effective and a friction factor of 0.2 was used along the boundary in computer simulations.

Grid distortions at 30 percent and 60 percent reduction in height with 5.08 mm/min (0.2 in./min) ram speed are shown in Figures 23(b) and (c), respectively. It took 28 percent reduction for the taper to be absorbed and for deformation to proceed as in a cylinder compression. It is evident from Figure 23 that the deformation is more or less uniform.

The resulting microstructures at various locations after forging are shown in Figure 24. The strain, strain-rate and temperature variations during forging were found to be almost the same at all locations, and typical variations for 5.08 mm/min (0.2 in./min) ram speed are also shown.

The temperature histories indicate that no appreciable changes took place. Therefore, any microstructural modifications must be due to maintaining the workpiece at an elevated temperature for some time (total deformation time is 6 min) under pressure and to the amount of deformation imposed.

On the $\alpha+\beta$ side (points D and E), although the average stresses are negative, the microstructure should be stable. No outstanding amounts of deformation (final strain ≈ 1.0) or temperature rises are locally imposed.

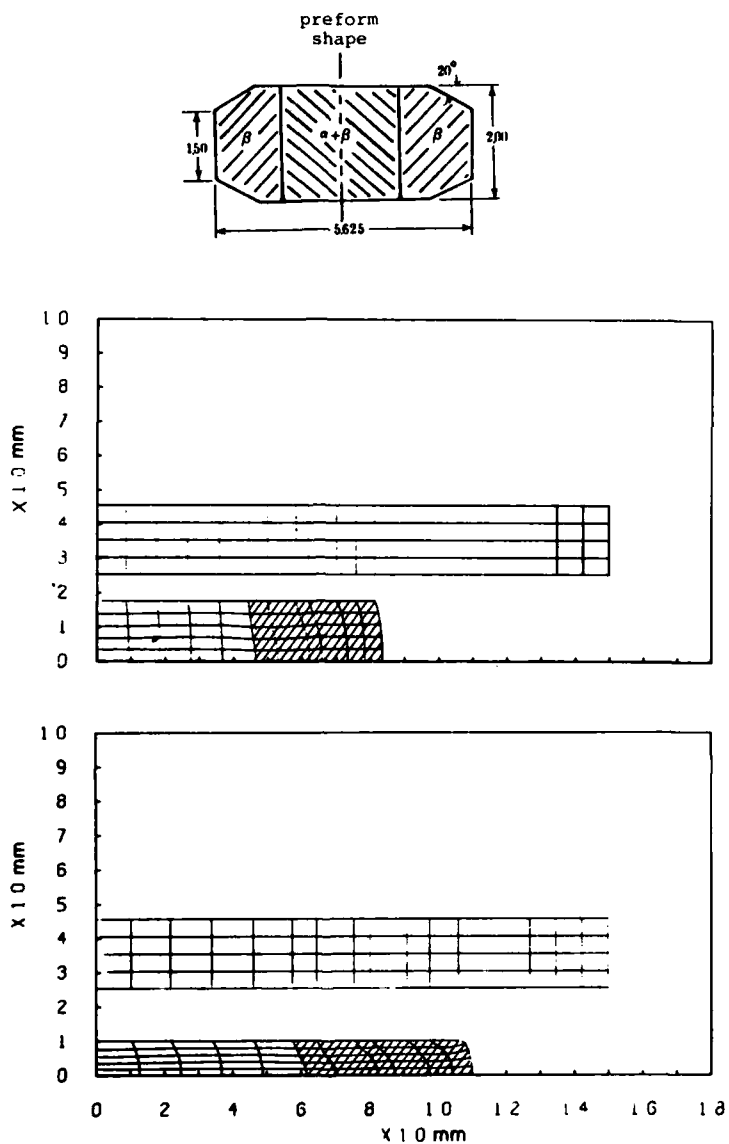


Figure 23. (a) Preform geometry and grid distortions in $(\alpha + \beta)/\beta$ composite forging at (b) 30 percent and (c) 60 percent reduction in height.

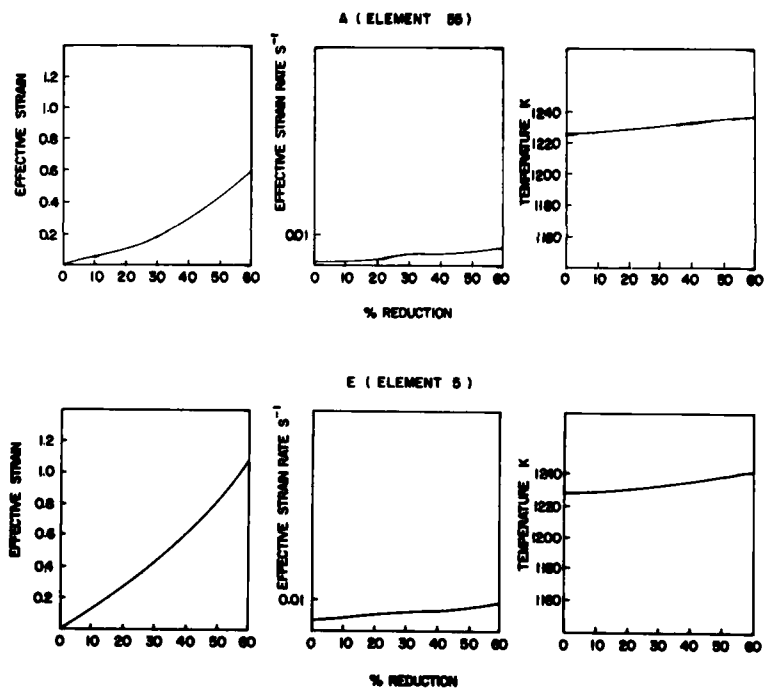
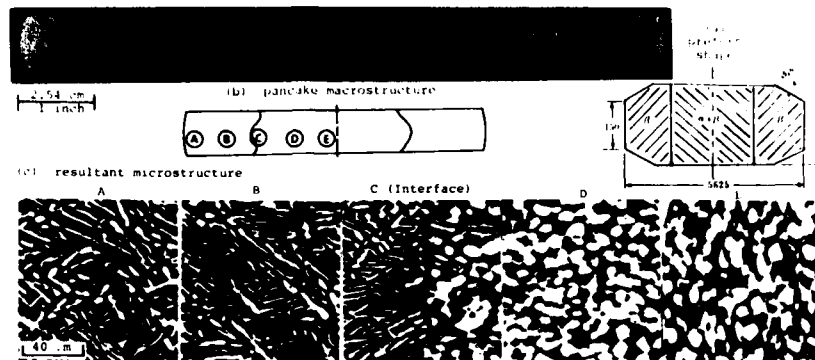


Figure 24. Local strain, strain-rate, and temperature variations during $(\alpha + \beta)/\beta$ composite forging and corresponding microstructures after forging. (Microstructures, courtesy of C. C. Chen, Chen-Tech Industries, Inc.)

Deformation occurs in both phases, and being so slow, the dislocations created by deformation have time to annihilate without needing to recrystallize. Moreover, grain growth would be dampened by the alternating type of structure from grain to grain. Therefore, an unchanged microstructure during deformation should be expected. On the (β) transformed side (points A and B), there is a drive for change into the more stable $\alpha+\beta$ structure, as none of the temperature, time, and deformation that provides energy to nucleate new grain surfaces for diffusion, etc. However, the micrograph of point A when compared to the one of point B show that at A the transformation occurs more rapidly, even with small strain. This can be attributed to stress distributions: in the periphery the stresses are much less compressive than inside, even starting with positive average stress; accordingly, the relative transus temperature is higher, increasing the potential for transformation.

Process Modeling with Finite-Element Methods (Task 2.2)

The work under this part of the program is being conducted at Battelle. Under this task, a general-purpose finite-element program, named ALPID, which is capable of treating deformation processes with arbitrarily-shaped dies, has been developed. This program is based on the rigid-plastic and rigid-viscoplastic finite-element methods developed by Kobayashi and his co-workers. The important features of the program ALPID include:

- (1) use of higher order elements such as linear, quadratic and cubic elements of serendipity and Lagrangian families.
- (2) general description of die and automation of die boundary condition which enable the user to use any number of arbitrarily shaped dies with different friction types and coefficients, and
- (3) automatic initial guess generation by which input data requirements are reduced to the level of those for simple elastic analysis and the solution efficiencies are improved remarkably.

Through these improvements, it has become possible to apply the finite-element method (FEM) more efficiently to a wide class of metalforming problems of practical importance. Some of the details of the program ALPID and its application to several axisymmetric problems were described in the previous interim report⁽²⁾. During the current reporting period, the program ALPID was further refined and applied to spike forging and disk forging processes. The details of this investigation are included in Appendix G.

Rigid-Viscoplastic Finite-Element Method

The FEM program ALPID is based on the isothermal rigid-viscoplastic formulation. The variational principal functional for rigid-viscoplastic material can be written as

$$\phi = \int_V E(\dot{\epsilon}^*) dV - \int_{S_F} \tilde{F} \cdot \tilde{v}^* ds + \int_V \frac{1}{2} K(\dot{\epsilon}_{kk})^2 dV \quad (7)$$

Here the work function $E(\dot{\epsilon})$ can be expressed as

$$E(\dot{\epsilon}) = \int_0^{\dot{\epsilon}} \bar{\sigma} d\dot{\epsilon} \quad (8)$$

and K is a large positive constant which penalizes the dilational strain rate component. It can be readily shown that the mean stress is $\sigma_m = K\epsilon_{kk}$. In this formulation, the flow stress $\bar{\sigma}$ is a function of effective strain $\bar{\epsilon}$ and the effective strain rate $\dot{\bar{\epsilon}}$, and can be expressed as

$$\bar{\sigma} = \bar{\sigma}(\bar{\epsilon}, \dot{\bar{\epsilon}}) \quad (9)$$

The above functional ϕ reduces to that for a rigid-plastic material when $\bar{\sigma}$ is a function of $\bar{\epsilon}$ only. The details of the discretization procedure and the solution process for the functional are given in Appendix G.

The implementation of the die boundary conditions are based on arbitrary die shapes. The formulation allows the unified treatments of die boundary conditions without the die shape restrictions. The die shape

is described by the coordinates of corner points and the associated corner radii in sequential order, as shown in Figure 25. This scheme seems to provide the simplest way of data preparation without loss of generality in describing arbitrarily shaped dies. The program ALPID can handle as many dies as needed with different frictions and movements in single process. At each stage of deformation, the die definition curves along the die-workpiece contact zones are discretized by using the distribution functions and node positions of the workpiece. The frictional boundary conditions can be implemented based on the discretized die description.

Because of the nonlinearity in the constitutive equations, the solution process of rigid-plastic or rigid-viscoplastic FEM requires an adequate initial guess velocity field. In past FEM solutions, the searching for the proper initial guess was not only time consuming but has also limited the applicability of the method to relatively simple problems. An algorithm for automated initial guess generation has been implemented in ALPID. It was shown that the solution efficiency has been improved through the initial guess generation and that the data preparation requirements have been reduced to those of linear elastic FEM solutions.

The graphic display of FEM input data and of the results is an important part of analysis by ALPID since the analysis involves relatively large amounts of information. The interactive user-oriented program FEMGRA provides a means of complete graphic display for ALPID. The structures and the interactions of the two programs are shown in Figure 26. FEMGRA is capable of displaying the load-displacement relation, the FEM grid distortion, the relative position of the dies, the velocity vector fields, and the contour plots of stress, strain, and strain rates including their effective quantities at any stage of deformation. The place obtained by FEMGRA can be displayed either on CRT terminal for quick viewing or on CALCOMP plotter as hard copies.

Modeling of the Spike Forging Process

In order to validate the present formulation, solutions of the spike forging process were obtained. In spike forging, a cylindrical billet is forged in an impression die containing a central cavity. The deformation

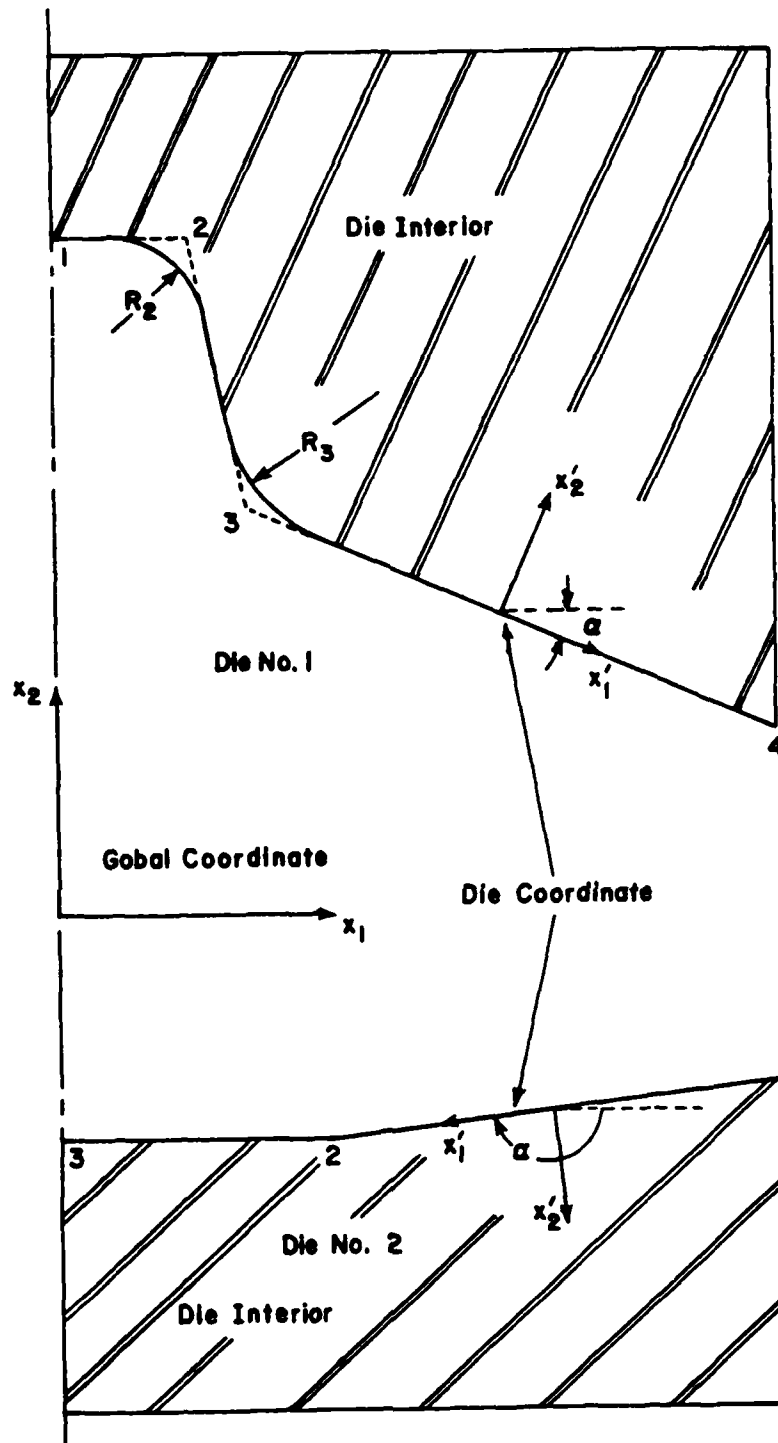


Figure 25. Description of Arbitrarily Shaped Dies and the Die Surface Coordinate Orientation.

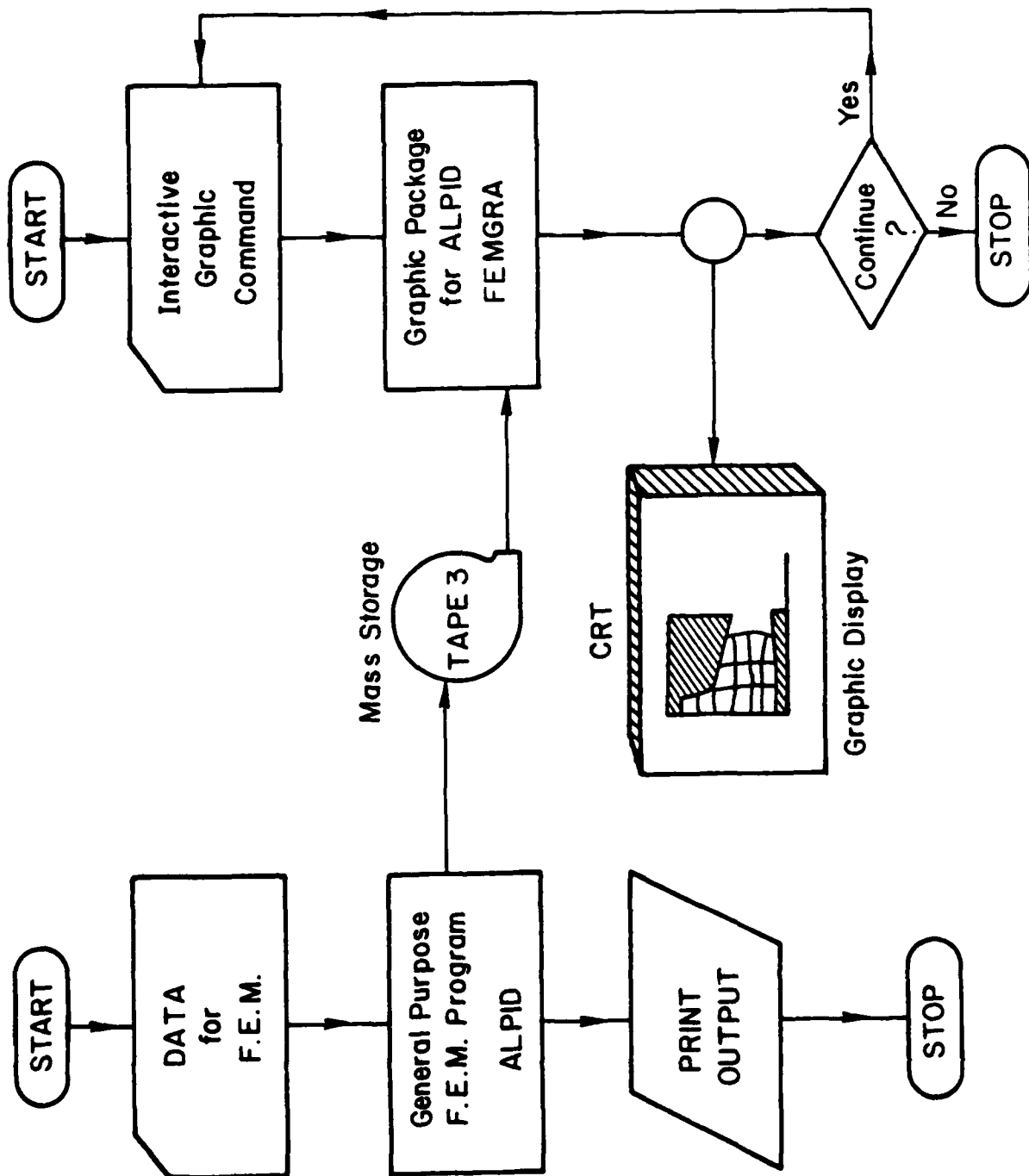


Figure 26. Structures and Interactions of ALPID and FEMGRA.

characteristics of the spike forging process are such that the portion of the material near the outside diameter flows radially outward while the center of the top surface is extruded, forming a spike.

In the present study, two different conditions for interface friction ($m = 0.3$ and 0.6) were selected in order to evaluate the effect of friction on the deformation pattern in the spike forging process. The simulations were performed, using the program ALPID, for isothermal forging of Ti-6242 with ($\alpha+\beta$) preform microstructure at 954C (1750F). The nominal strain rate at the early stages of deformation was selected to be 0.4 sec^{-1} . The predicted grid distortions for the two friction conditions are shown in Figure 27. It can be seen that the spike height is not affected during earlier stages of deformation, and that the effect of friction becomes significant only during later stages of deformation. This behavior conforms to the experimental observations made by various investigators. Further details of the deformation mechanics in terms of velocity strain and strain rate are given in Appendix G.

Modeling of the Disk Forging Process

It was demonstrated earlier that a dual microstructure/property compressor disk can be forged by a direct forging approach⁽²⁾. This required defining the processing variables and preform shape such that the controlled flow localization in the central region of a β microstructure preform occurred for recrystallization to take place in that region. The major variables to be selected for the process optimization were the preform shape and microstructure, forge temperature, die temperature, strain, strain rate and solution treat temperature. This approach is especially attractive because of its simplicity and it can provide a practical and economical method of manufacturing

The forging was done isothermally at 900C (1650F) with the average nominal strain rate of approximately 0.175 min^{-1} . The slow strain rate was necessary to prevent the temperature rise due to deformation heating and also to prevent the unstable strain localization. Even though the β microstructure preforms were used for the actual forging the ($\alpha+\beta$) and β microstructures were used in the simulation for the analysis in order to examine the influence of microstructure on the deformation pattern. The effects of friction were also examined by using two different friction shear factors.

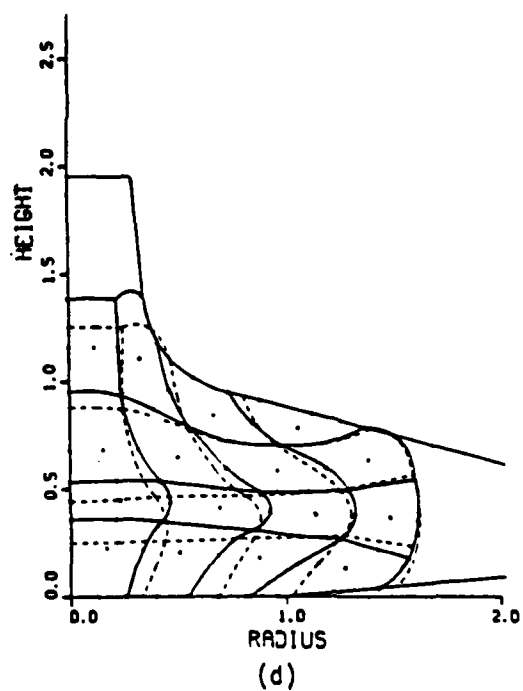
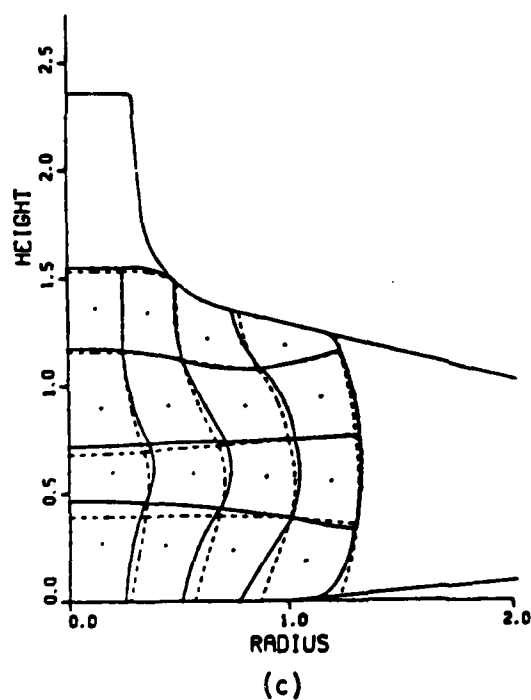
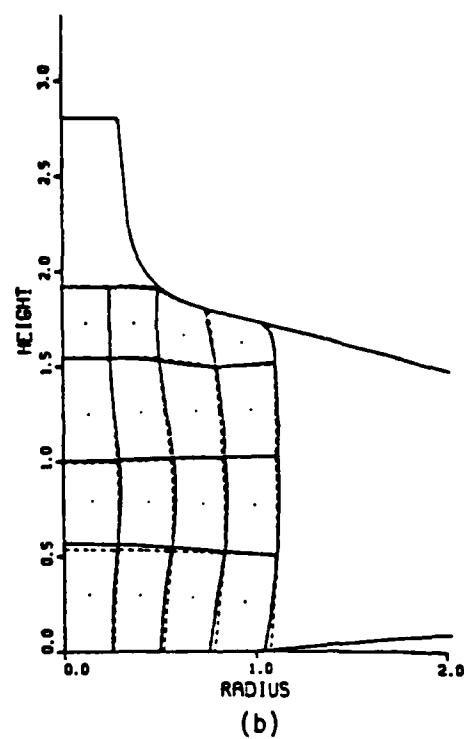
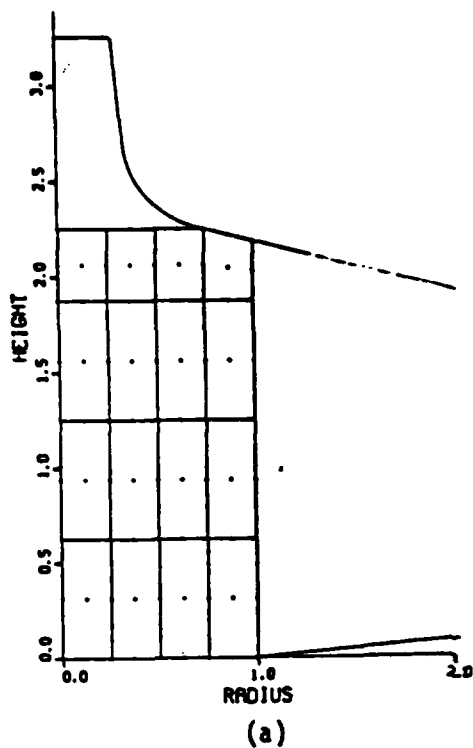


Figure 27. Calculated FEM Grid Distortions at Die Displacements of (a) $0.0H_0$, (b) $0.2H_0$, (c) $0.4H_0$ and (d) $0.58H_0$, Solid Lines for $m = 0.6$ and Dotted Lines for $m = 0.3$. Units are Multiples of the Undeformed Radius.

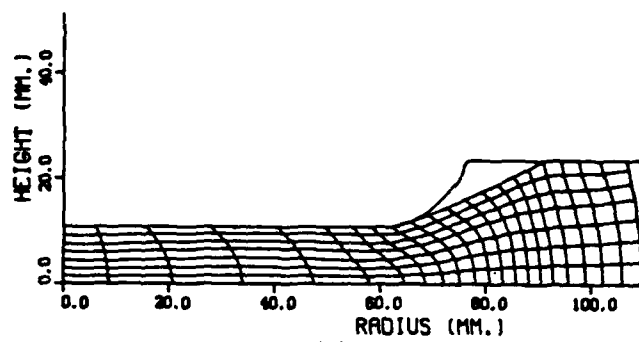
Figure 28 shows the distorted grid pattern in the quarter section of the disk at various reductions in height. It is worth noting that once the metal in the rim region of the disk touches the die surface, the gap between the die corner and the workpiece grows. This behavior in metal flow did not change significantly with increasing friction. Further, the metal flow was nearly the same for both $\alpha+\beta$ and β preform microstructures. Thus, in order to obtain corner fill, the simulation was continued with trapped-dies, as shown in Figure 29. The corner fill is obtained within a few extra percent of reduction. However, as seen in Figure 30, the load required increases rather rapidly and as compared to open die forging, almost four times more force is required to nearly fill die corner. These observations related to metal flow and forces were also made during the experiments.

In order to use the modeling of disk forging to control microstructure and thereby obtain desired properties, one must know the distribution of deformation parameters quantitatively. Therefore, the effective strain and effective strain rate distributions were plotted in Figures 31 and 32, respectively. It is seen that the maximum strain and strain rate occur in the central region where deformation-induced recrystallization is desired. Thus variables gradually diminish towards the rim region and are minimum near the outer edges, where no phase transformation is desired. Thus, the program ALPID is capable of providing information required for control of microstructure/properties through processing.

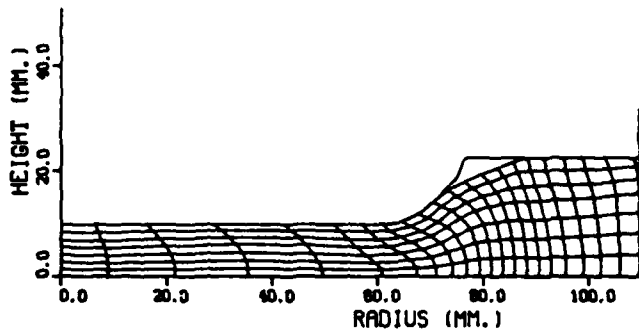
Development of an Interactive System to Predict Metal Flow and Temperatures (Task 2.3)

This part of the program is being conducted at Battelle. The objective of this task is to develop a versatile computerized system for the design and analysis of axisymmetrical forging components. The interactive computer program will utilize both the finite-element method and the matrix method for analyzing the mechanics of deformation.

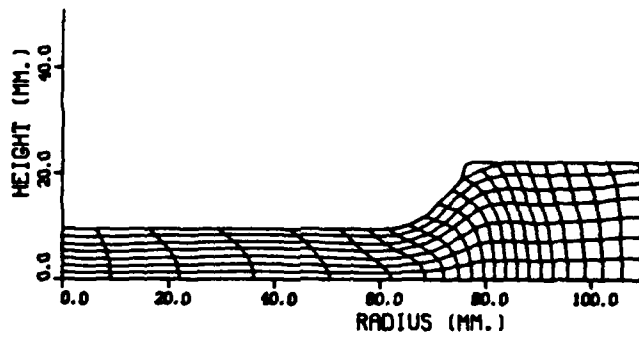
The computerized system for design and analysis were developed in two separate subsystems. The first subsystem utilizes the graphical display capabilities provided by TCS package. The FEM program ALPID is used in batch mode to analyze a problem, for example, the spike forging process. The output is stored on a random access file called TAPE3. An independent interactive graphics program FEMGRA, based on the TCS package, uses the



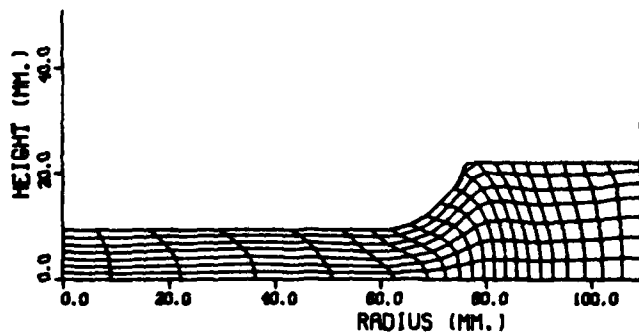
(a)



(b)



(c)



(d)

Figure 28. Predicted Grid Distortion for Disk Forging (Ti-6242-0.1Si, β -Microstructure, $m = 0.3$, $T = 900^\circ\text{C}$) (a) 10% Reduction in Height, (b) 30%, (c) 50%, (d) 70%.

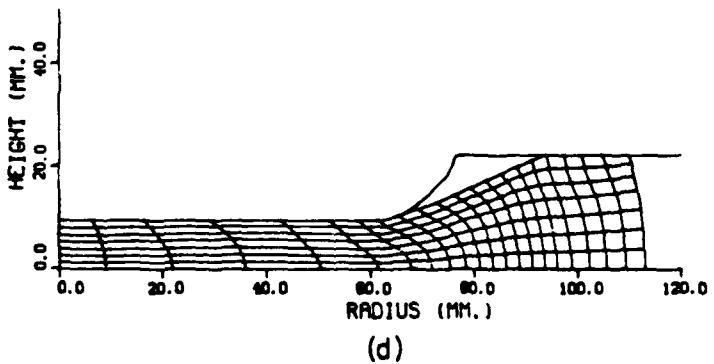
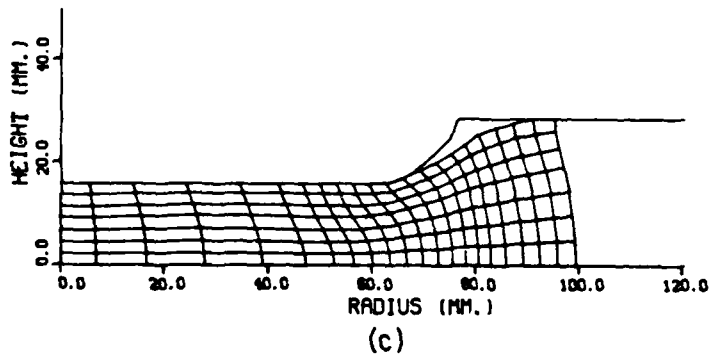
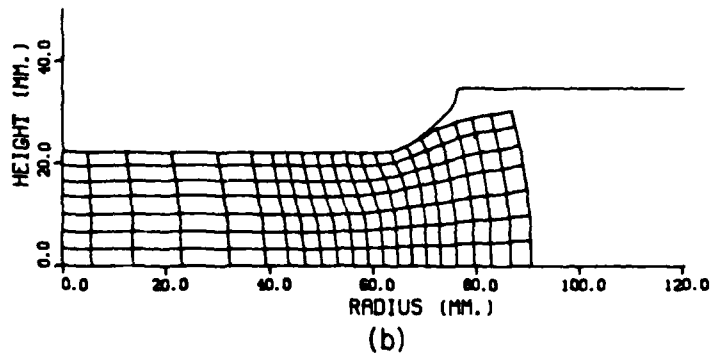
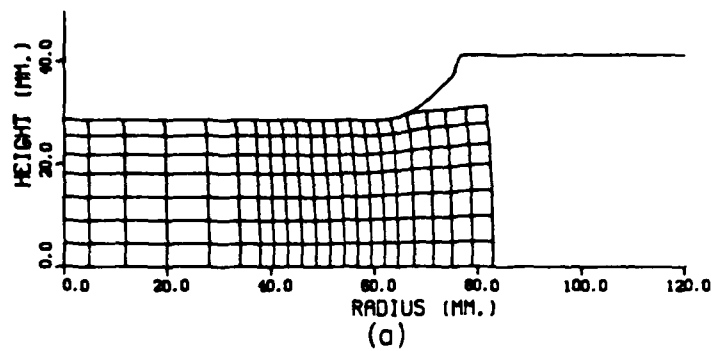


Figure 29. Grid Distortion Predicted for Trapped Die Forging (Ti-6242-0.1Si, β -Microstructure, $m = 0.3$, 900C) Reduction: (a) 66%, (b) 69%, (c) 70%, (d) 70.25%.

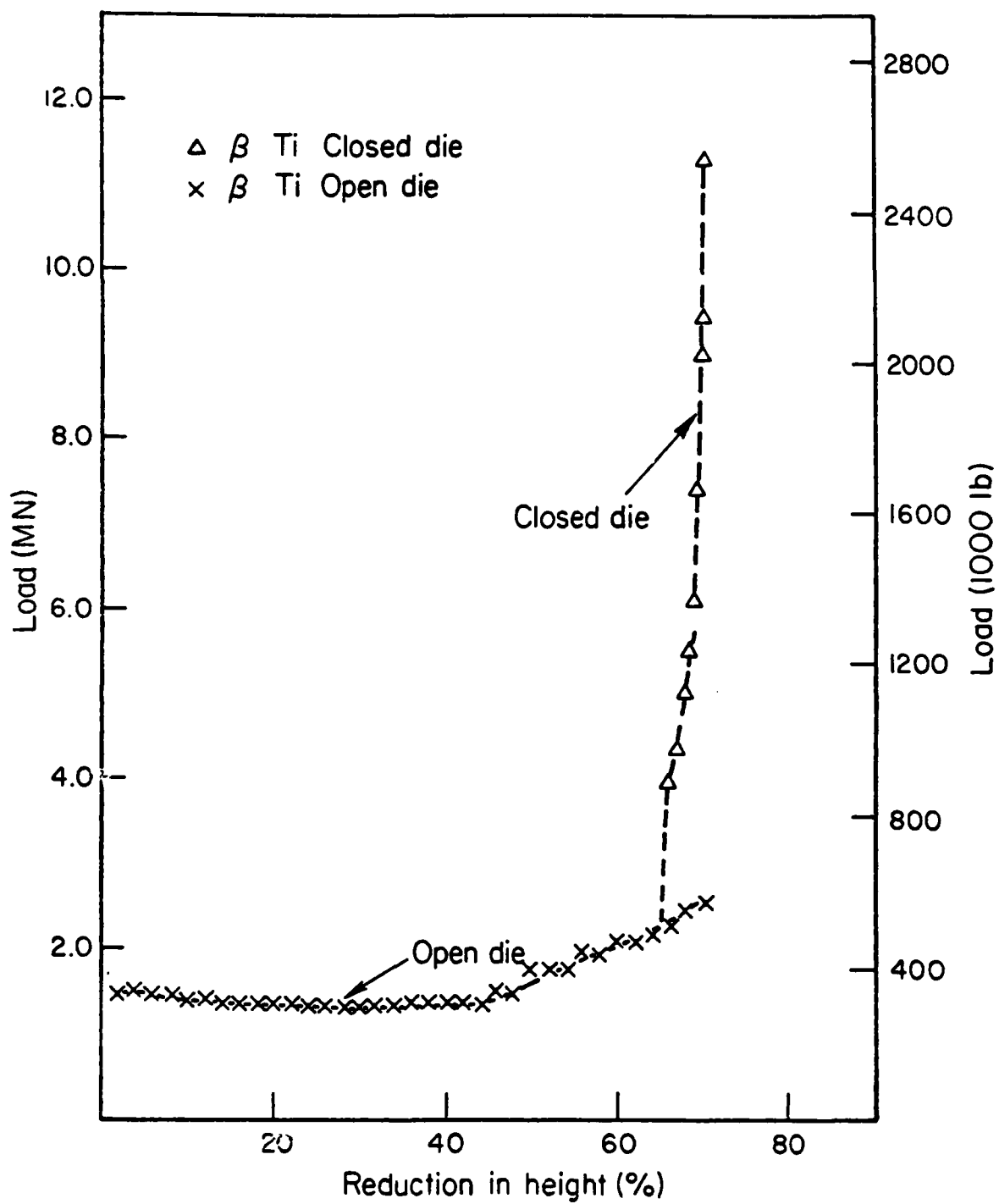


Figure 30. Computed Forging Load for Trapped Die (Ti-6242-0.1Si, $m = 0.3$, $T = 900^\circ\text{C}$).

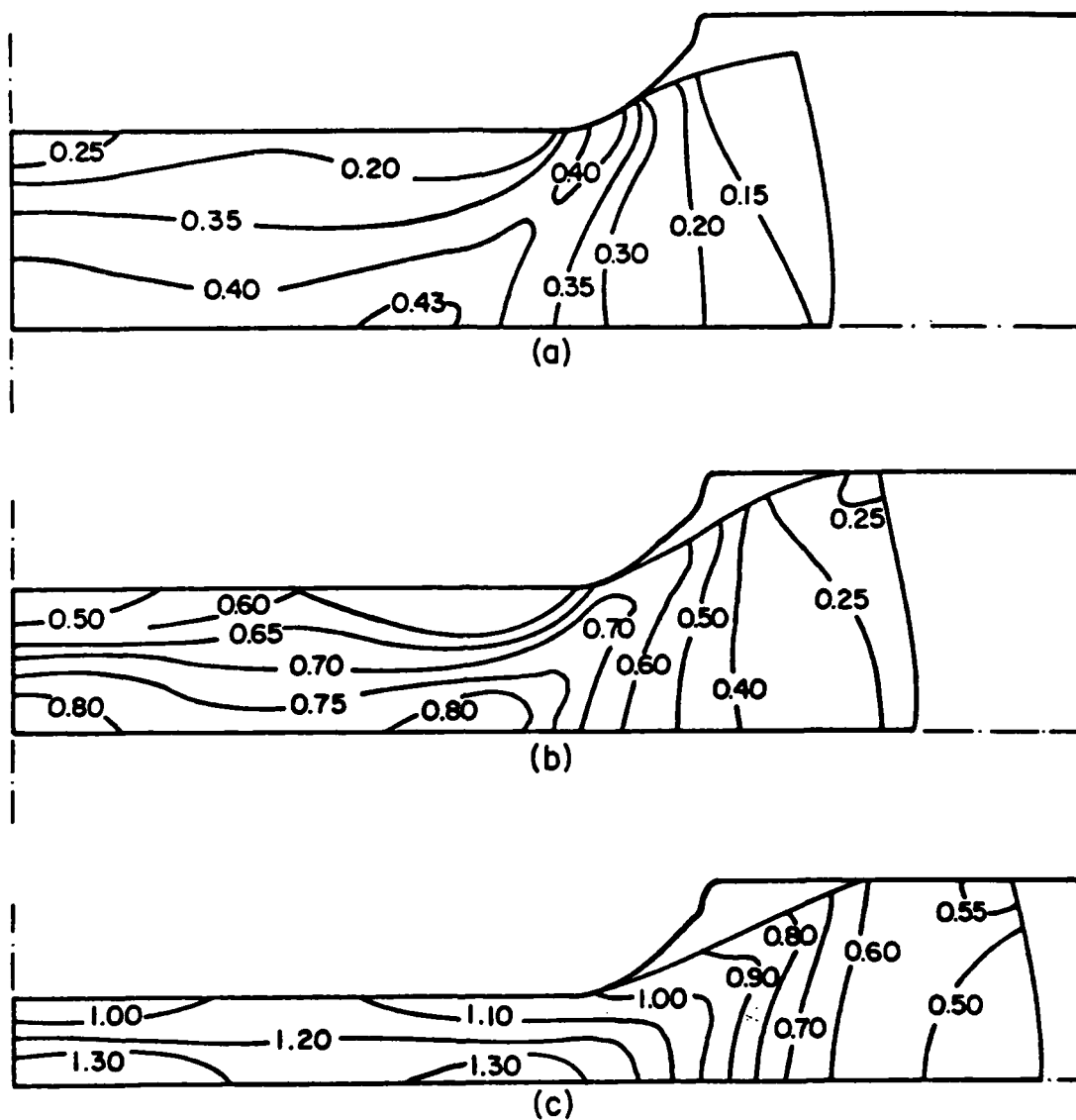


Figure 31. Effective Strain Distribution in Disk Forging (Ti-6242-0.1Si, β -Microstructure, 900C, $m = 0.30$) (a) 30% Reduction in Height at Center, (b) 50%, (c) 70%.

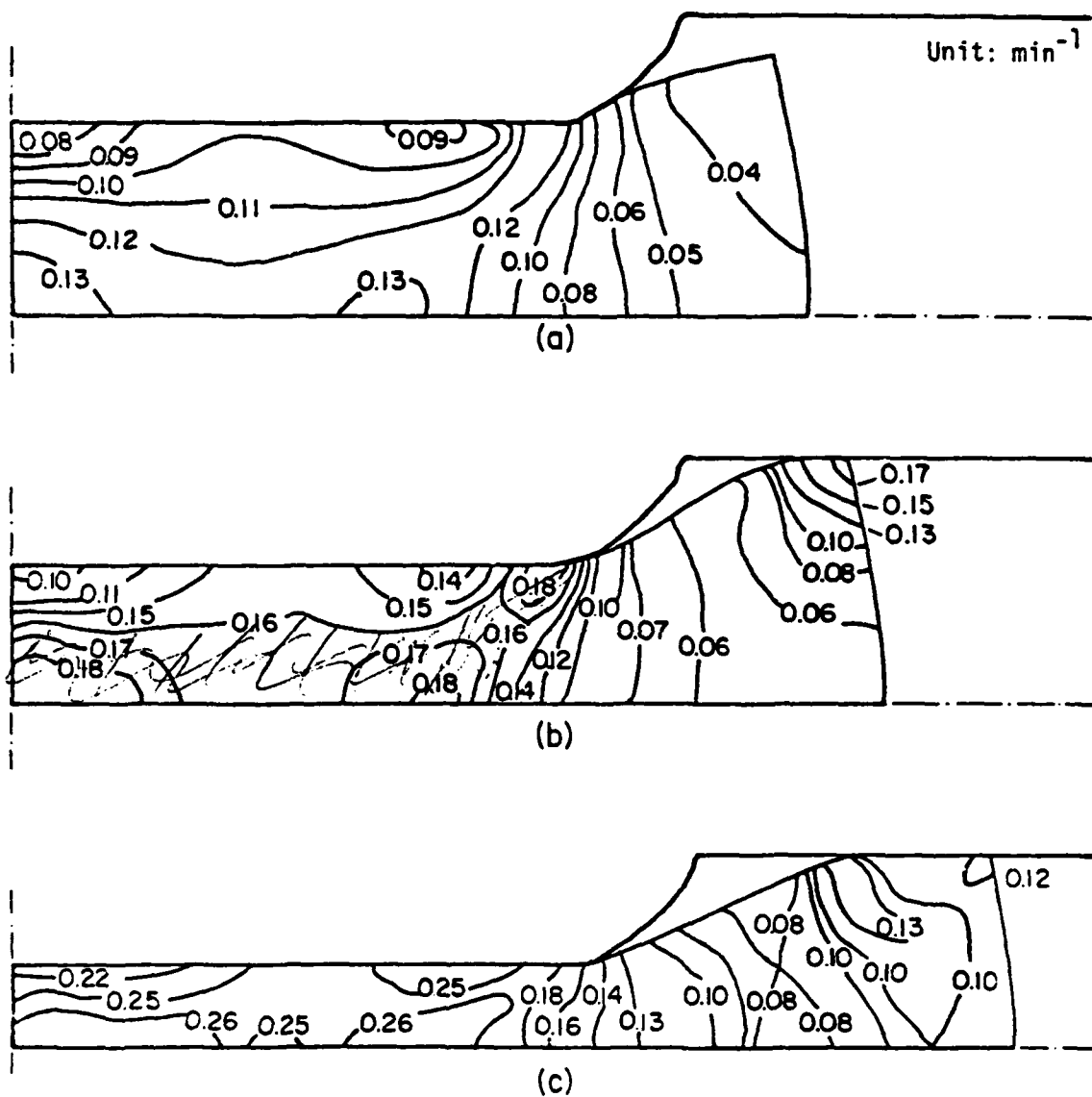


Figure 32. Effective Strain Rate Distribution in Disk Forging (Ti-6242-0.1Si, β -Microstructure, 900C, $m = 0.30$) (a) 30% Reduction in Height at Center, (b) 50%, (c) 70%.

information from TAPE3 and displays the grid distortion patterns on a CRT terminal, as shown in Figure 27, at the desired stages of deformation. In addition, it can plot the load-displacement diagrams and the die pressure distributions. Thus, the computations by FEM are made in a batch mode and the results are displayed graphically in an interactive mode.

The second system is based on the graphical display package named DISPLA. The output from ALPID, stored in TAPE3, is used to obtain contour graphs, as shown in Figure 31 and 32 for the disk forging process. Such contours can be plotted for strain, strain rate, temperature, stress, or any other quantity stored in TAPE3. In this case, the CRT terminal is used for preview only and, if acceptable, the information is transferred to CALCOMP plotter for report quality graphs.

Development of Process Model and Integration With Fracture/Failure Model (Task 2.4)

The work under this part of the program is under progress at Battelle. The computer program ALPID was implemented with the constitutive equations developed under Phase I of the program. Once the fracture/failure models are developed, they will be incorporated in ALPID.

SECTION VII

INTERFACE EFFECTS

In metal-deformation processing, and in particular in forging, the lubricant at the material-die interface plays several important roles: (a) it controls the heat transfer from the workpiece into the dies and the temperature gradients within the deforming metal, and (b) it influences the friction conditions at the interface. The net effect is to change the velocity fields, or metal flow, within the deformation zone and to strongly influence the limiting strain to failure. In addition, lubricants directly influence such factors as part surface quality, metal flow, grain structure, mechanical properties, dimensional consistency, and load and energy requirements. Further, lubricants which provide effective separation and thermal insulation between the sliding metal and the die promote long die life.

During forging, heat is lost from the billet by conduction and radiation through the lubricant. Laboratory insulation tests can be performed to measure the thermal conductivity of lubricant/interface layer. In these tests, a lubricant film is squeezed between two flat punches, simulating the forging dies (same material, surface finish and temperature as the forging die). The pressure and temperature conditions created at the interface layer are similar to those present in the actual forging. During the test, the surface temperature and temperatures at various depths from the interface are measured. These data, analyzed together with pressure, interface layer temperature, and lubricant thickness give quantitative information on thermal conductivity of the lubricant under various conditions.

The objective of this phase of program is to characterize the interface effects in axisymmetric compression of disk-type forgings. This includes characterization of heat transfer coefficients and the friction conditions at the tool-workpiece interface.

Selection of Lubricants for Disk Forging Task (3.1)

This task is being conducted at Battelle, with assistance from Dr. C. C. Chen of Chen-Tech Industries, Inc. Based on the previous studies on evaluation of lubricants for isothermal forging several lubricants

were selected for evaluation prior to use in subscale disk forging. These include DELTAGLAZE 149 and DELTAGLAZE 69 from Acheson Colloids Company, and GFBN-8, OPT-112, TRW-111 and Boron Nitride from the TRW, Inc. These lubricants are being tested for their lubricity and the heat transfer characteristics. Based on the results of these tests, one or two lubricants will be selected for use in subscale disk forging.

Determination of Heat Transfer Coefficients and Interface Effects (Task 3.2)

The part of the program is being conducted at Battelle. The objective of this task is to develop a procedure for calculation of an effective heat transfer coefficient for the lubricated tool/material interface, and to determine the values of these coefficients for the particular combinations of lubricant and die materials to be used under this program.

In order to measure the interface heat transfer coefficient, a test fixture as shown in Figure 33 was designed and constructed. It consists of a pair of IN100 dies, screwed to a pair of superalloy supports. The supports rest on alumina blocks which act as insulators. The lower and upper end of the fixture are water-cooled. The thermocouples are imbedded in the dies in such a way that they lie underneath the alloy sample which is being deformed. The dimensions of the dies are so selected that a standard ring specimen can be used. The entire length of the fixture between the lower and upper supports can be enclosed in a clam-shell furnace to heat the dies and the specimen to desired temperatures. The details of the construction and testing of the fixture were described earlier⁽²⁾.

Based on Klafs' analysis,⁽¹³⁾ a theory for determining a heat transfer coefficient for heat flow across an interface layer was given in the previous report⁽²⁾. This theory was based on an assumption of a fixed intermediate temperature T_m (Figure 34). This assumption resulted in error when the material of the upper and lower dies were different. Therefore, a more rigorous analysis was undertaken, making no prior assumptions about the time dependence of the interface temperature, but by solving the equations of heat flow simultaneously in both regions allowing the boundary layer to float. Based on this analysis, it was shown that the temperature at some point within the skin layer turns out to be constant throughout the experiment,

(13) Klafs, U., Doctoral Dissertation, Technical University of Hannover, Germany (1969).

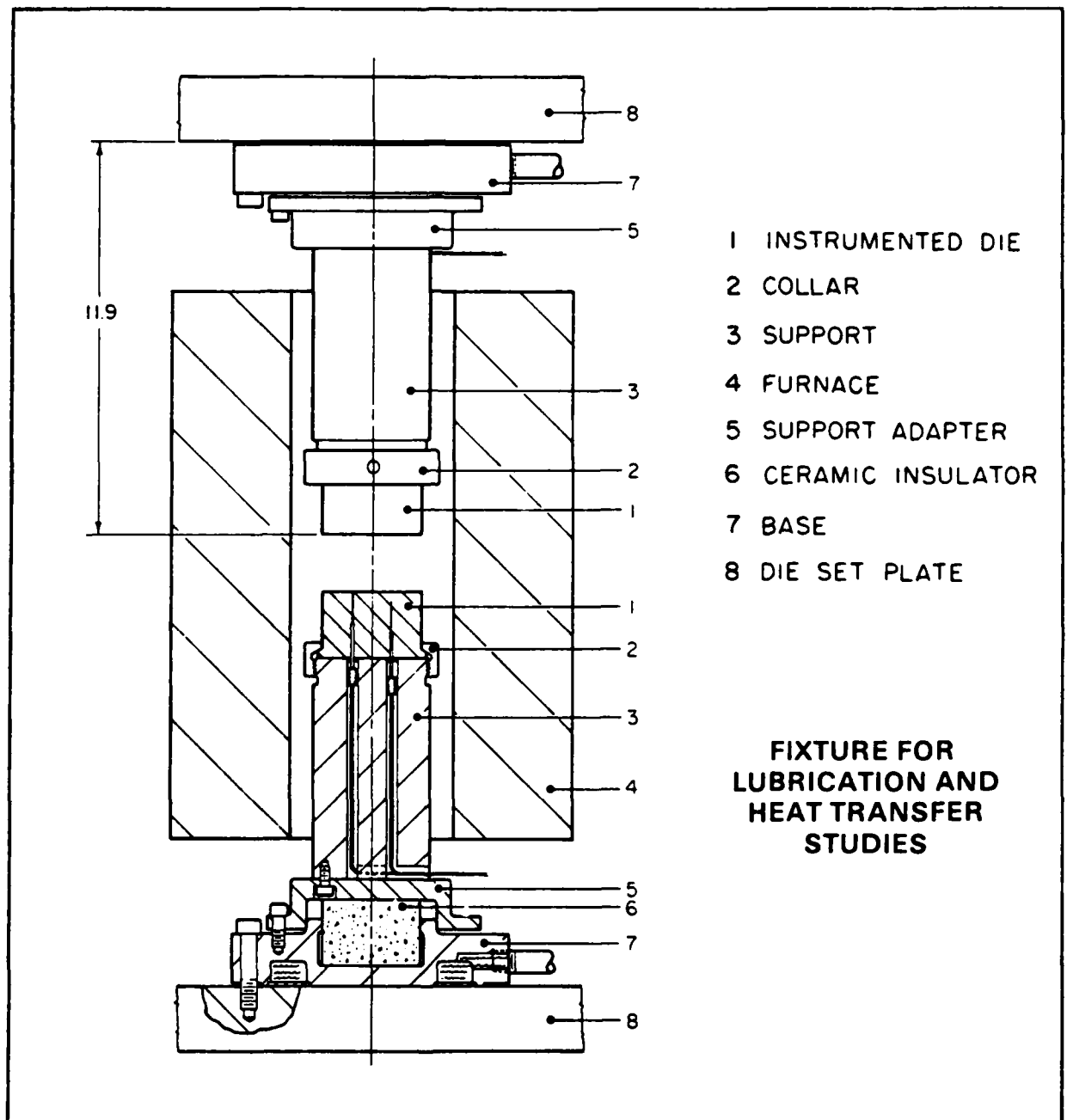


Figure 33. Fixture for Interface Heat Transfer Studies

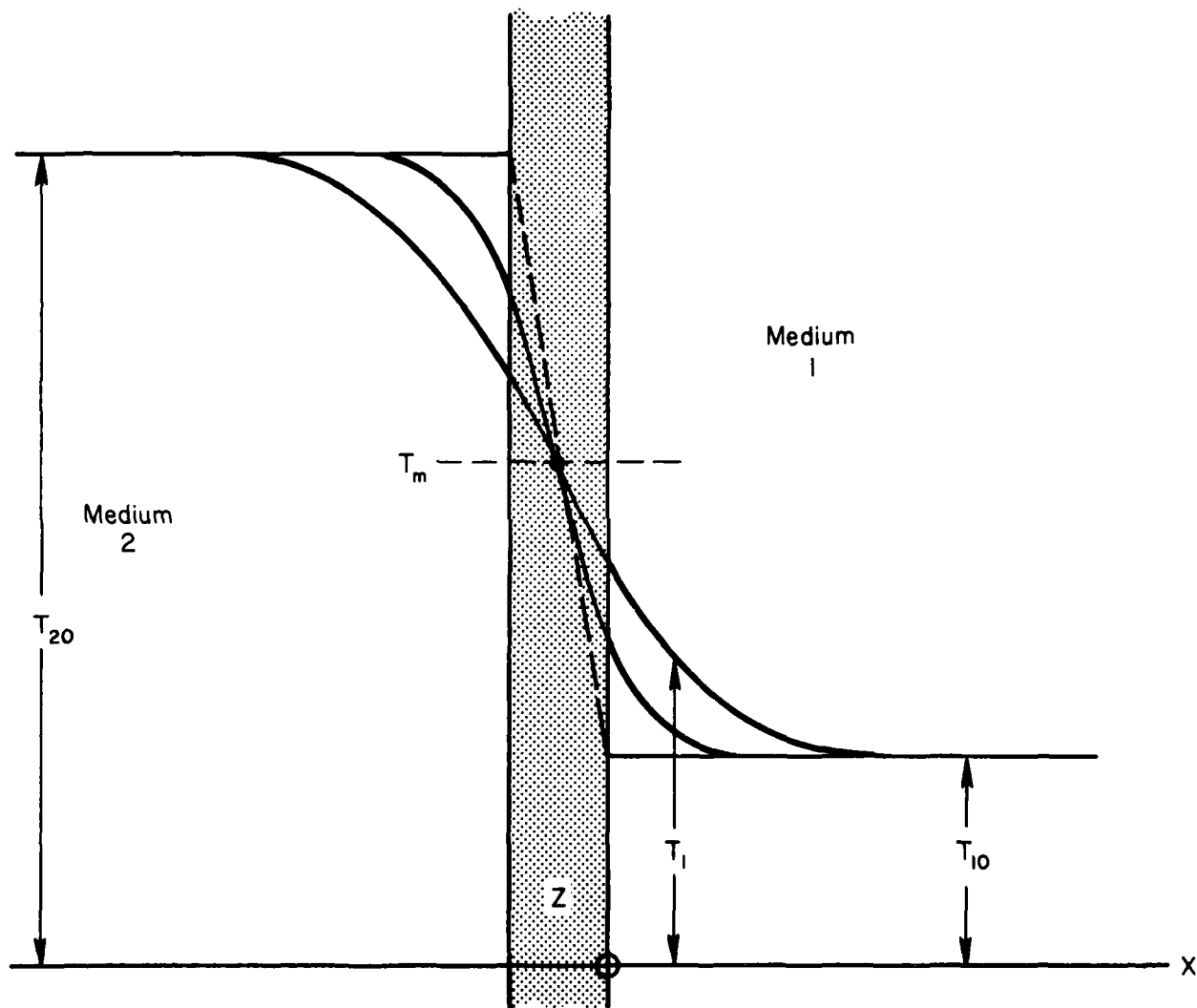


Figure 34. Temperature Distribution in Upper and Lower Dies and an Interface Layer Demonstrating the Assumption of a Fixed Intermediate Temperature, T_m .

but this is physically different from its being held fixed. As a consequence, either two thermocouples are needed to measure T_{20} as well as T_{10} and T_1 , or thermal-physical properties of the material of both dies are known, if one thermocouple is used. The details of this analysis will be presented with the experimental results for various lubricants selected in this program.

Analysis of Metal Flow and Temperatures in Ring
and Flange Type Configurations (Task 3.3)

This part of the program is being conducted at Battelle. Forging of a ring geometry and a flange type configuration have been used for characterizing friction conditions in metal processing and for evaluating lubricants. The variation in internal diameter of a ring during compression or the height of spike in compression of flange type configuration is a good indication of the frictional conditions at the tool/material interface. These tests are very easy to conduct since the technique requires either measuring the internal diameter of a ring or the height of the spike after forging.

At the University of California, Berkeley, the matrix method of analysis was developed and applied to predict metal flow and temperature distribution during ring compression. This analysis will be used (a) in evaluating the lubricants under Task 3.1, and (b) to determine heat transfer coefficients under Task 3.2.

Similarly, the spike forging process is being analyzed at Battelle by the general finite-element method (see Figure 27). The problem of plastic deformation has been solved completely and the results appear excellent. Further, the effect of heat generation and heat transfer during forging were included in the analysis. Currently, the temperature capabilities of the program are being tested. Once complete, it will be used to analyze hot forging of Ti-6242.

SECTION VIII

INTEGRATION OF MATERIAL AND PROCESS MODELS

The objective of this phase of the program is to develop an interactive computer program which will integrate the material behavior models with the process model to investigate the interaction of the basic components of this analytical processing system. This system will be used to design forging preform, dies, calculate loads, temperature distributions, metal flow patterns, and to predict microstructural changes.

Process Optimization and Forging of Subscale Disk (Tasks 4.1, 4.2, and 4.3)

Work under these tasks is under progress at Battelle. The material constitutive equations developed under Phase I of the program has been implemented in the mechanics model (the computer program ALPID). Further, it has been demonstrated that the predictions from ALPID are sensitive to the starting microstructure of the workpiece material and the detailed deformation characteristics calculated by this model can be correlated to microstructural response of the material due to deformation processing (see Section VI). Thus, with the knowledge of processing conditions-microstructure property relationship (Phase I) and predictive capabilities of ALPID, it is now possible to establish the forging process conditions, such as speed, temperature, contact time. In addition, the computer program ALPID can be used in designing the optimum preform configuration. Work is under progress currently to optimize the processing conditions for the subscale forging of dual microstructure/property compressor disk.

An investigation has already been conducted to broadly define the processing variables and preform shape requirements for producing the dual microstructure/property forgings by direct forge processings. This attempt was designed to provide an economic and practical method for manufacturing applications. The basic concept is to produce dual property forgings by controlling flow localization for recrystallization to take place in the central regions. Major variables selected for the process were preform microstructure, forge temperature, die temperature, strain (strain rate), and solution-treat temperature.

Billet mulds were converted and machined to the required sizes. They were isothermally forged at various forging conditions and both forged and machined preforms were used. After forging operations, the disks were cut into half-disks and heat-treated at various solution-treat temperatures. As a result, both optimum forging (1650F (899C)/1650F (899C)/0.2"/min. 0.5cm/min.) (60%) and Heat-treating (1745F (951C)/4 hours/AC + 1100F (593C)/8 hours/AC) conditions were selected for uses in producing experimental disk forgings. The preform requirement was also selected provide adequate localized flow.

Figure 35 illustrates an example of the structural features and property results from the experimental disks produced. Note that experimental disks with excellent dual microstructural features and mechanical properties were consistently produced by direct forging approach. Thus, this portion of the program has defined appropriate forging variables, heat-treat conditions and preform shape requirements for a practical process model of disk type forgings.

The results demonstrated clearly that hot-die forging provided an excellent control of processing variables for achieving the dual property goal required for the program. The process requires the preforms with transformed- β microstructures, and the *forge/die temperatures* have to be closely controlled for maintaining microstructural stability. Preform shape design is necessary in order to provide adequate flow-localization and amount of strain by forging deformation must be sufficient for local recrystallization to take place. Solution temperature should be adequately controlled to give microstructural stability.

Development of an Economic Model for Processing Alternatives (Task 4.4)

This part of the program was conducted by Dr. Vijay A. Tipnis, Tipnis Associates, Inc., Cincinnati, Ohio, under a consulting contract from the Battelle Columbus Laboratory. The following is a summary of the report included in the Appendix I.

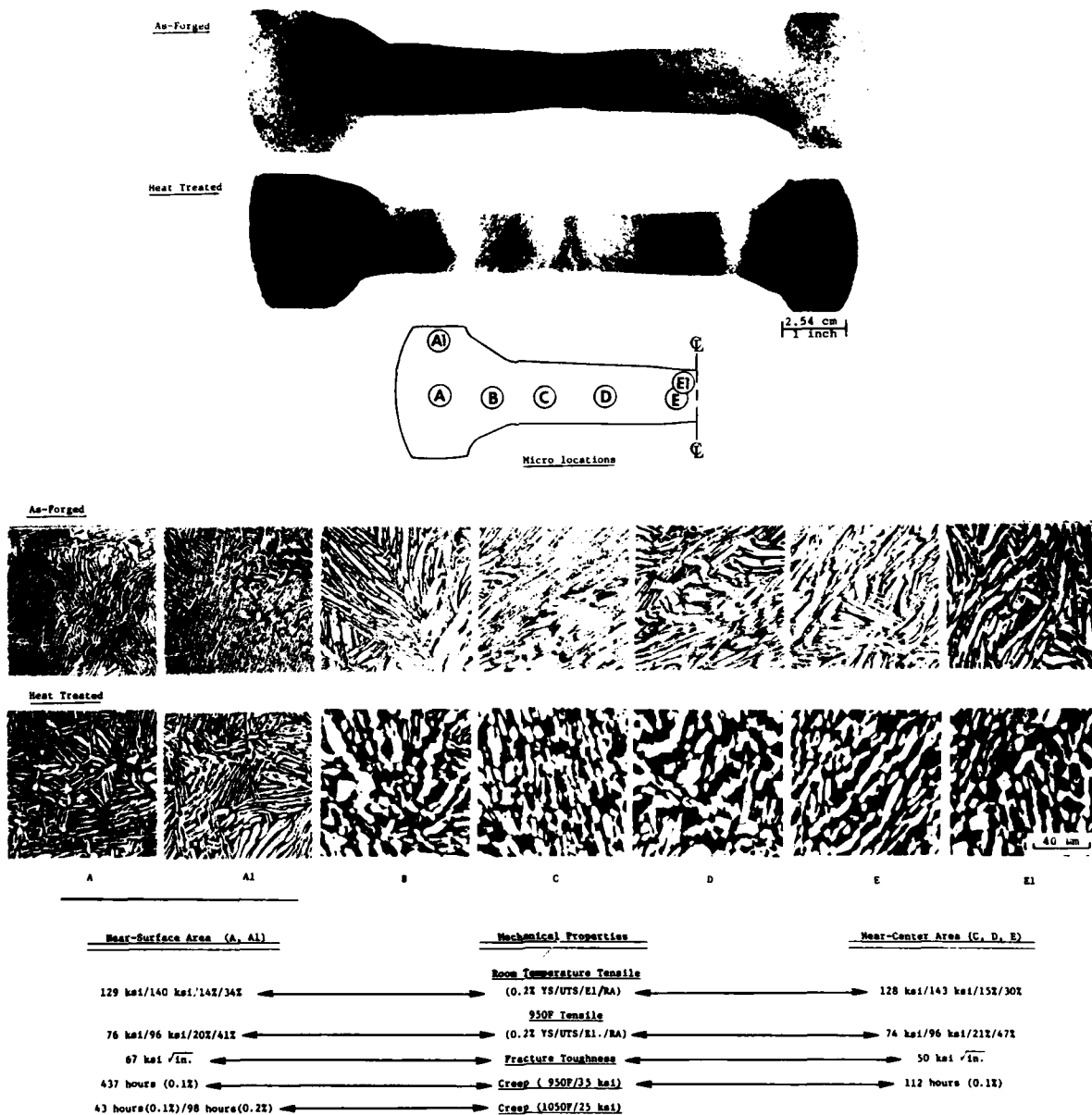


Figure 35. Structural Features and Resultant Properties of the Disk Produced by Selected Forging and Heat Treating Combinations

The objective of this task was to develop economic models for the evaluation of various alternative process plans which can be potentially used for manufacturing of compressor disk forgings from Ti-6242 alloy. The alternatives investigated were: conventional press forging + machining (baseline), isothermal forging and hot die forging + machining, hot isostatic pressing (HIP) + forging + machining, and dual property disk forging + machining.

Under other tasks of this program sub-scale dual property compressor disks for the Ti-6242 alloy have been successfully forged. The dual property forging technique is essentially a hot die forging with controlled strain rate to obtain the defined microstructure and property control and to improve life-limiting properties such as low cycle fatigue (at the hub) and creep (at the circumference). The improvement in the life-limiting properties can have a significant favorable impact on the life cycle costs such as fuel costs and operation and support costs. Thus, the viable processing alternatives should be evaluated by taking into account the life cycle costs as well, particularly if there is a possibility of a significant reduction in weight and/or improvement in the engine performance due to the life-limiting properties; this is especially important for dual property disk and BLISK processes.

The traditional approach to the process economics and investment decisions is to wait until all the experimentation on conceptual and technological feasibility of the process has been completed. This often leads to substantial research and development expenditures, only to find that the process was not economically feasible in the first place. Recently, a significant improvement over the traditional approach is made by establishing the necessary and sufficiency conditions for economic feasibility and by introducing the economic sensitivity analysis methods. These techniques allow identification of the 'opportunity windows' and 'targets' where technological development should be directed for a process to be economically feasible.

Under this task, the recent approach was extended to forging and HIP processes and applied to the evaluation of the NNS forging alternatives mentioned above. This involved the establishment of macroeconomic (at processing sequence level) models for blank processing and part manufacturing phases. Also, these models were integrated into the life cycle models for fuel and operation and support cost elements that are sensitive to the life-limiting properties of the dual property disk. Another important

extension was indicated by linking the microeconomic models to the process and phenomenological models such as material, interface, and fracture/wear constraints.

To illustrate the application of the above economic models, time and cost data were obtained or assumed for blank fabrication and part manufacturing sequence for the four viable alternatives for the compressor disk of Ti-6242. The data used is merely indicative of the type of data necessary; it is not intended to reflect the actual cost of goods sold. For evaluation of the alternatives, the time and cost savings as compared to the baseline process, rather than the actual times and costs, are relevant. For a detailed discussion, refer to the Appendix I. Below are a few pertinent results:

Referring to Figure 36, as compared to the conventional press forging + machining, HIP + forging + machining shows 18 percent processing time savings; and isothermal forging + machining and dual property forging + machining show 16 percent each. However, HIP + forging requires approximately 20 percent more lead time and isothermal forging and dual property forging 100 percent more lead time than conventional forging due to HIP canning development and die design, and die manufacturing, respectively. The processing time savings can be converted into cost savings whenever there is an opportunity to do additional work in-house on farmed-out jobs where the farm-out cost rate is higher than the in-house rate.

Referring to Figure 37, as compared to conventional press forging + machining, although blank fabrication, manufacturing, and consumable cost savings are positive (16 percent), the raw material (PM) and tooling cost dis-savings of HIP + forging + machining result in net dis-savings. Thus, HIP + forging + machining is a viable alternative only if there is a significant opportunity cost to the accrued time savings. The discounted payback period for different investments in HIP technology when HIP material cost is twice that of billets have been determined in the Appendix I.

The net cost savings for isothermal and dual property alternatives are about the same (15 percent); raw material, blank fabrication, manufacturing, and consumable lead to positive cost savings, however, tooling (dies & tools, etc.) lead to dis-savings.

AD-A112 271

BATTELLE COLUMBUS LABS OH
RESEARCH TO DEVELOP PROCESS MODELS FOR PRODUCING A DUAL PROPERTY--ETC(U)
OCT 81 @ D LAHOTI, T ALTAN

F/S 11/6

F33615-78-C-5025

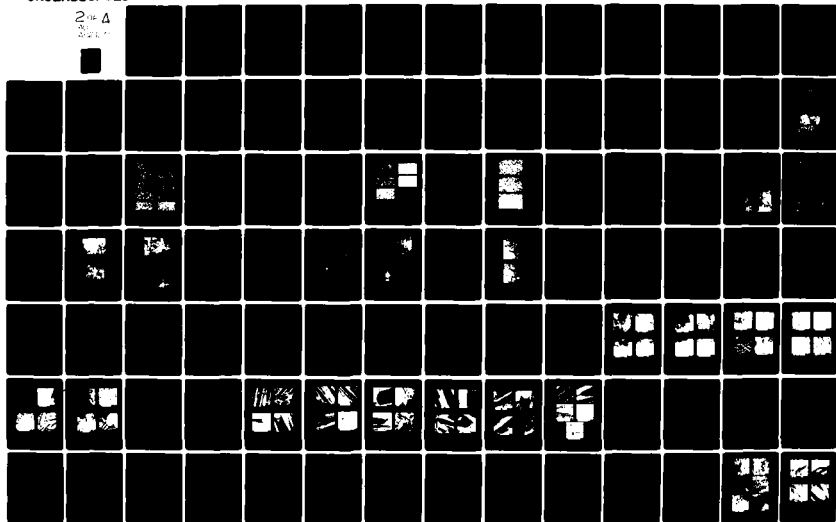
UNCLASSIFIED

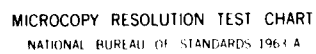
AFWAL-TR-81-4130

NL

2 of 4

2001





MICROCOPY RESOLUTION TEST CHART
NATIONAL BUREAU OF STANDARDS 1963 A

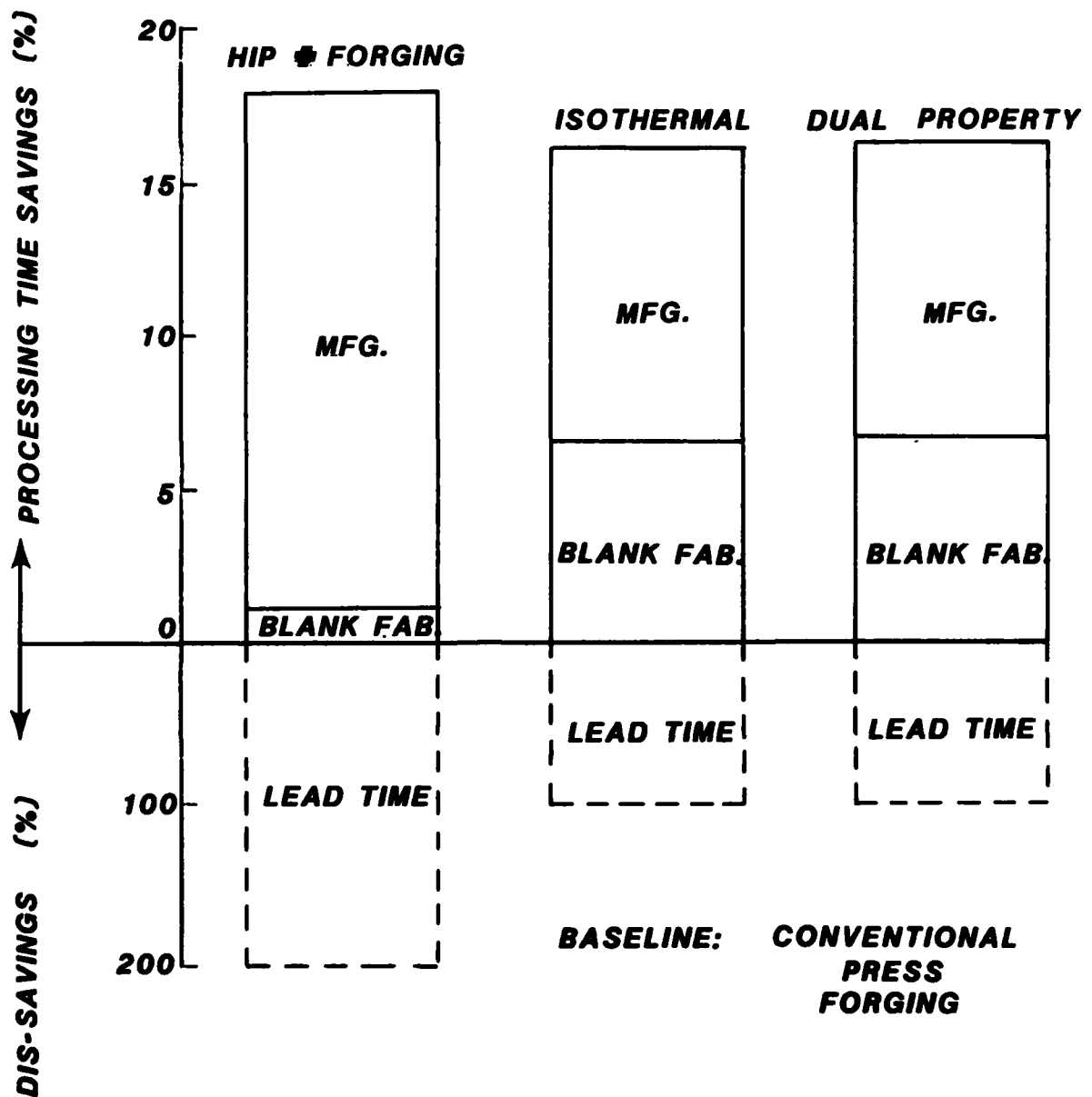


Figure 36. Percent Processing Time Savings and Lead Time Dis-savings for Alternatives to Conventional Press Forging of Ti-6242 Compressor Disk

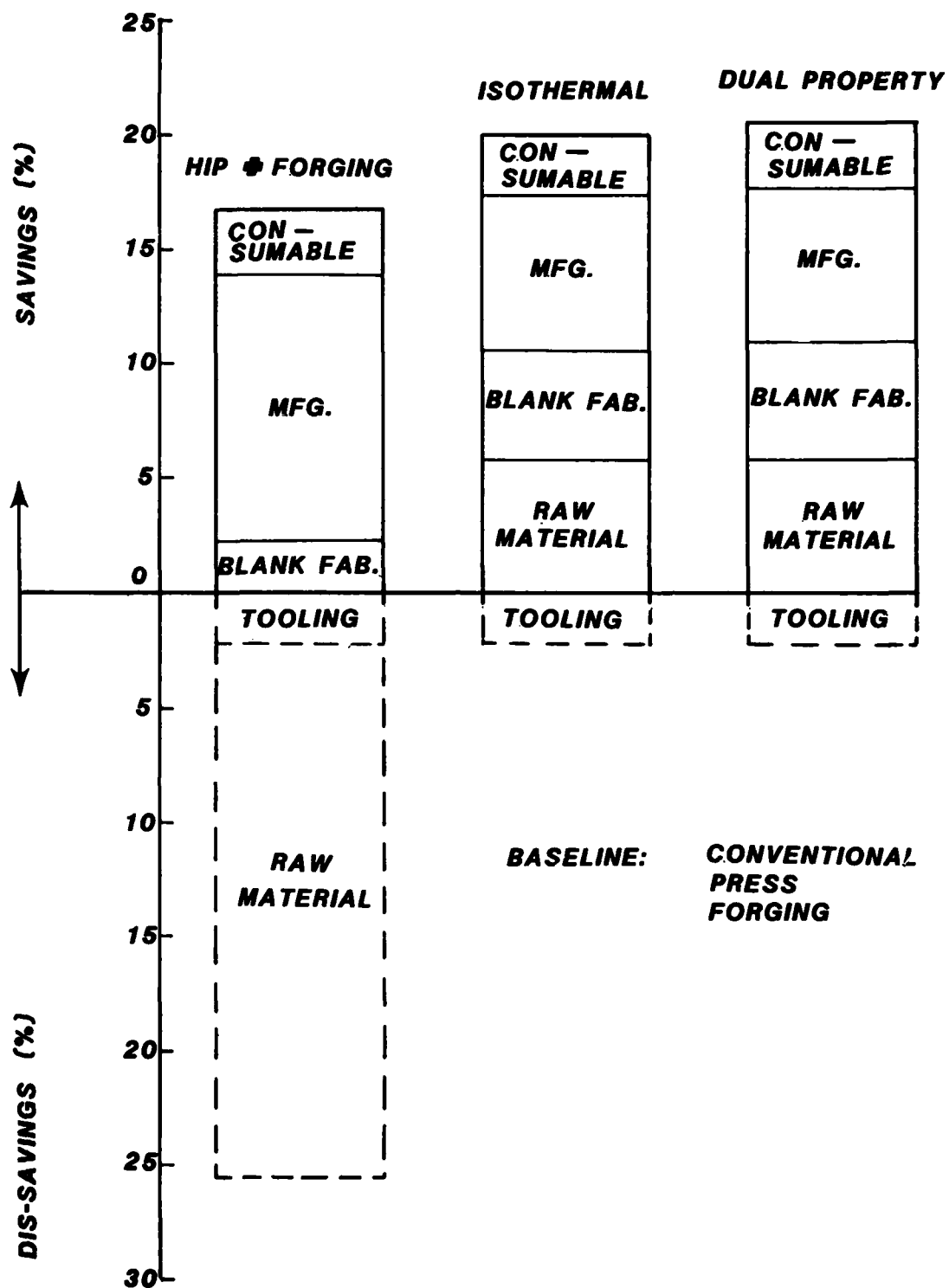


Figure 37. Percent Cost Savings and Dis-savings for Alternatives to Conventional Press Forging of Ti-6242 Compressor Disk

The application of the methodology illustrates the usefulness of conducting ongoing economic feasibility analysis during NNS process R&D, development, and implementation phases.

Further work needs to be conducted to establish microeconomics of P/M, HIP, and forging processes and of the die design/manufacturing stages. For improving the forging equipment utilization and reducing the long lead times and blank fabrication times, economics of computer integrated flexible forging systems must be established.

SECTION IX

PROPERTY/MICROSTRUCTURE RELATIONSHIPS IN THE FORGED DISK

The objective of this phase of the program is to investigate metallurgically the forgings designed and produced under this program to determine whether the microstructure and the mechanical properties pertinent to design requirements for the dual property disk correspond to the predictions. This will involve detailed metallographic examination of the forged disk, and determination of mechanical properties (tensile, creep, LCF, fracture toughness) of the forged material. During this reporting period, no work was scheduled under this phase of the program. Consequently, no work was conducted under this phase of the program.

SECTION X

FUTURE WORK

During the next twelve months, the following work is planned to be conducted under this program:

Material Behavior Under Processing Conditions

- (a) A study to investigate defect formation during hot forging of Ti-6242 and to predict process parameters for achieving stable metal flow will continue.

Process Modeling for Disk Type Forging

- (a) The work on development of the comprehensive system of computer programs for design and optimization of the process will continue.

Interface Effects

- (a) The fixture for the heat transfer study will be used to conduct tests to measure the friction factor and the heat transfer coefficient at the interface.

Integration of Material and Process Models

- (a) Based on the pancake tests, process modeling studies, and interface effects studies, conditions for forging of a subscale disk will be defined.
- (b) The disk forging tests will be designed and conducted.

Property/Microstructure Relationships in the
Forged Disk

- (a) The work on evaluation of the microstructure of forged disk will be started.
- (b) Mechanical properties of the forged disk will be evaluated.

Finally, a plan will be undertaken to summarize the results of this program in a series of monographs.

APPENDIX A

DETERMINATION OF HIGH-STRAIN-RATE-FLOW-STRESS
DATA FOR Ti-6242 + Si BY USING A PLASTOMETER

Gary K. Lewis
Los Alamos National Laboratory
Los Alamos, NM 87545

APPENDIX A

DETERMINATION OF HIGH-STRAIN-RATE-FLOW-STRESS DATA FOR Ti-6242 + Si BY USING A PLASTOMETER

Introduction

Cam plastometers are used to compress materials at constant true strain rates that are comparable to deformation rates used in many metal-forming operations. The Los Alamos cam plastometer is modelled after the first such machine conceived by Orowan.⁽¹⁾ Some of the past high strain rate studies and descriptions of the machine are in references 2-5.

The Los Alamos cam plastometer is capable of testing compression specimens at strain rates of -0.1 to -250 s^{-1} . In this study, constant true strain rate tests at -1 , -10 and -100 s^{-1} were used to obtain true stress-true strain compression curves for Ti-6242 + Si in the β and $\alpha + \beta$ conditions.

Testing Procedure

Right circular cylinder uniaxial compression specimens of Ti-6242 + Si in the α and the $\alpha + \beta$ conditions were supplied by Battelle Columbus Laboratories. Specimen dimensions were 0.27 cm (0.500 in.) diam. by 0.98 cm (0.780 in.) thick. Each specimen had circular grooves on the ends to retain lubricant during compression.

A schematic diagram of the pressing end of the cam plastometer is shown in Figure A-1. The cam lobe is designed to compress the specimen at a constant true strain rate by displacing the die stack vertically while turning at constant angular velocity. A specimen is compressed by

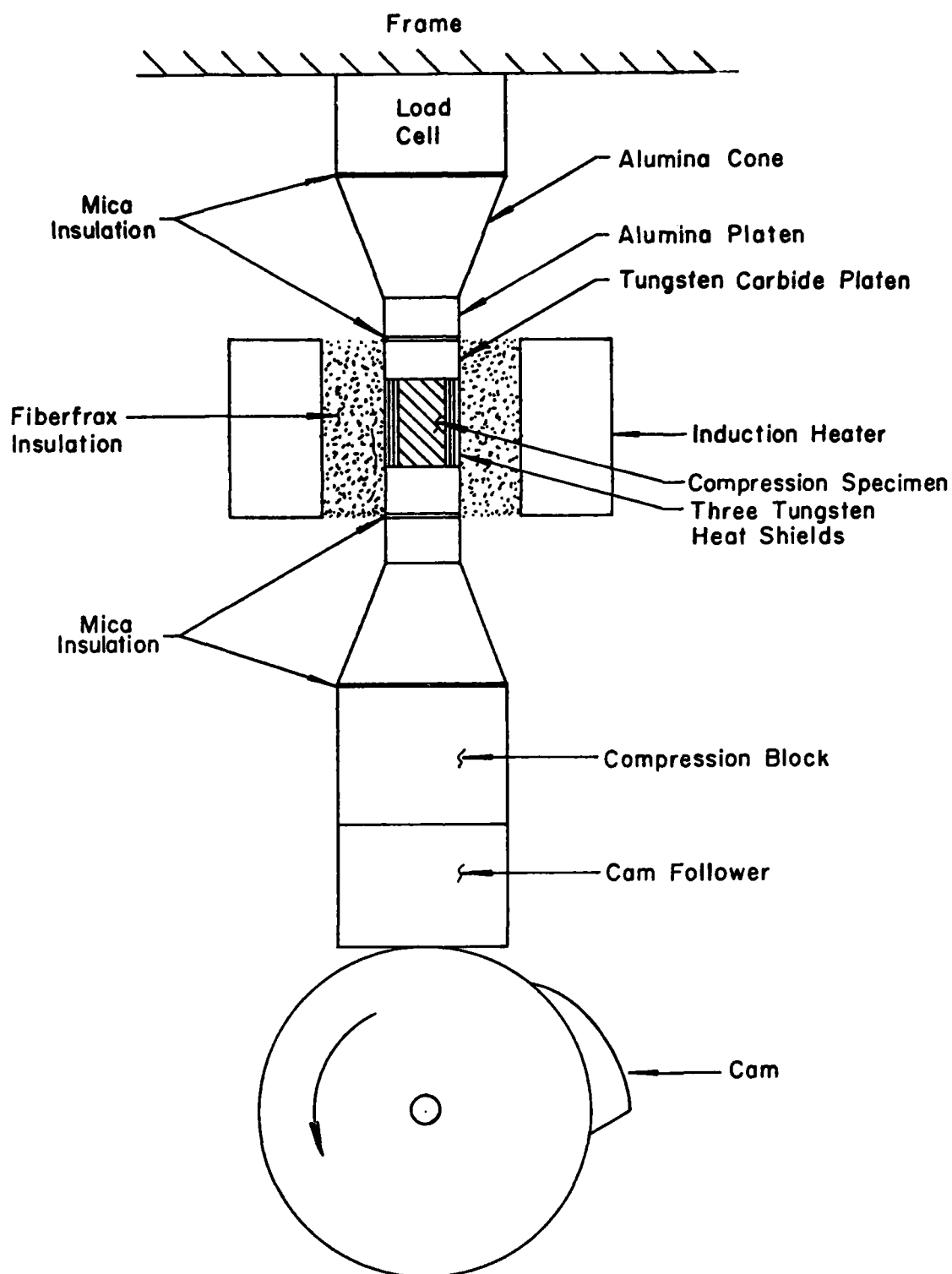


FIGURE A-1. DIAGRAM OF THE COMPRESSION END OF THE LOS ALAMOS CAM PLASTOMETER, DIE STACK AND HEATING ASSEMBLY

inserting the cam follower, compressing with the cam lobe, and retracting the follower within one revolution of the cam. Slits in a drum that rotate with the cam allow light sensing units to time the cam insertion and retraction.

All specimens were induction heated by a water-cooled copper coil that surrounds the pressing platens and specimen. Heat losses are minimized by tungsten heat shields and fiberfrax insulation within the coil and by mica insulation in the die stack. The tungsten carbide platens at each end of the specimen are heated to the specimen testing temperature.

The specimen temperature was monitored by three thermocouples. Two of the thermocouples were welded into conical recesses that were 0.15-cm (0.060 in.)-deep and centered at 0.32 cm (0.125 in.) from the top and bottom of the cylinder on a line parallel with the specimen axis. These two thermocouples were welded, 0.02-cm (0.010 in.)-diam, chromel-alumel wires and extended from the specimen through the coil inside of two-hole-alumina insulators. The third thermocouple was a 0.05-cm (0.020 in.)-o.d., sheathed, chromel-alumel thermocouple that was placed in a hole midway along the length of the specimen extending into the center. This thermocouple also extended through the coil inside of a single-hole tubular insulator.

Temperature control was accomplished by moving the coil up and down the vertical axis of the specimen until the surface thermocouples equilibrated. The power into the coil was adjusted until the center thermocouple read the desired test temperature.

The temperature difference between surface and center thermocouples was usually 50-70°C. However, this difference was attributed to surface radiation loss and coil effects on the surface thermocouples. To prove that the bulk of the specimen was at the correct test temperature, holes were drilled into a test specimen from the outside diameter to within 0.15 cm (0.060 in.) of the opposite side of the specimen and sheathed thermocouples were inserted for comparison with the center thermocouple. Heating of this specimen showed a 10°C maximum gradient from the center to the outside position. A similar experiment to measure

the gradient from top to bottom of the specimen showed less than 10°C variation when the coil was adjusted to equilibrate the surface thermocouples.

Lubricant was applied to the specimen and to the platen and baked at about 65°C . Acheson Chemical Co., Deltaglaze 347 was used in tests at 1010°C and above and Deltaglaze 349 was used in tests below 1010°C . The tungsten carbide platens were polished to a 6 micron finish and freshly polished platens were used for each test.

Testing was accomplished by heating the specimen to the desired test temperature and holding for at least six minutes with the center thermocouple at temperature. The power to the induction coil was turned off and the specimen compressed after a two second hold to allow transient signals from the coil to diminish and not affect data acquisition.

Load cell output and position data for each test were recorded on separate channels by a Nicolet storage oscilloscope and stored on a floppy disk. Each channel stored 2048 data points. Power to the 89 kN (20 kip) load cell is supplied through a B & F Input signal conditioner and the load cell signal is amplified through an Ectron differential-DC amplifier for input to the Nicolet. Position data were recorded as a series of pulses from an infrared diode and sensor. The drum on the cam has 360 slits and pins that transmit and break the light path for each degree of rotation. These pulses were recorded directly on the Nicolet as a function of time. Temperatures for the thermocouple and one outside thermocouple were recorded on a Hewlett Packard two-channel chart recorder. The three thermocouples were monitored on Doric and Newport digital readouts.

Data Reduction and Analysis

Data were taken in two different manners over the course of the test program. Initially only load versus time data were taken and in later tests load and position versus time data were taken.

Load Data Only. When only load data were taken, the true strain, ϵ_t , was calculated by Equation A-1. This equation assumes that

the true strain rate, ϵ_t , is constant and therefore no slowing of the cam occurs when the specimen is loaded.

$$\epsilon_t = \dot{\epsilon}_t t \quad (t = \text{elapsed time}) \quad (\text{Equation A-1})$$

The average true strain rate was calculated by dividing the measured total true plastic strain, ϵ_t , by the elapsed time between maximum load, t_f , and the start time, t_1 , taken as the time when the load curve first started to deviate from linearity. These times are shown graphically in Figure A-2.

$$\dot{\epsilon}_t = \frac{\epsilon_t}{t_f - t_1} \quad (\text{Equation A-2})$$

By using equations A-3 and A-8, the true stress was calculated from the true strain.

$$\ln(1 + e) = \epsilon_t \quad (\text{Equation A-3})$$

Load and Position Data. Figure A-2 shows typical load and position versus time plots obtained for a compression test. The position curve shows a series of square wave pulses with each cycle representing one degree of cam rotation. Although the curves are drawn solid in Figure A-2 the pulses and load curve as recorded on the Nicolet oscilloscope were actually a series of points with an exact time associated with each point. For any time, load-position points were known. Zero time, t_0 , was taken as the point where loading first started. The difference in height between the load curves prior to t_0 and after the test was completed was used to calculate the preload applied to the specimen because of thermal expansion and hold-down pressure applied through the compression frame. The preload was added to the loads calculated from the zero time reference point to get the instantaneous load.

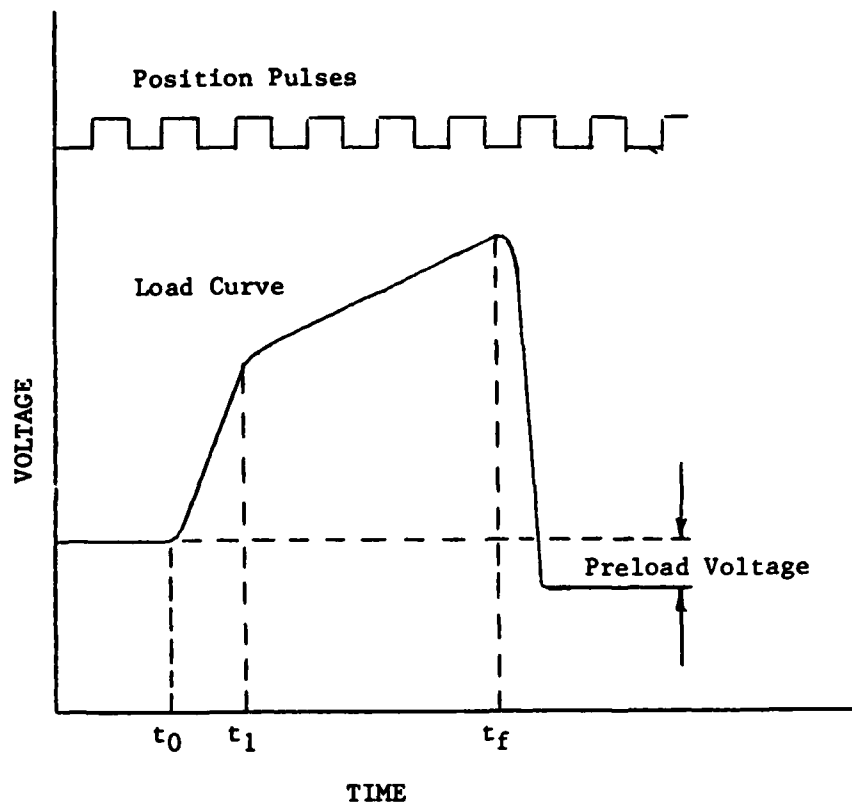


FIGURE A-2. SCHEMATIC DIAGRAM OF TYPICAL LOAD-POSITION TEST DATA. FOR REAL DATA THERE ARE 45 CYCLES (DEGREES) FROM THE START TIME, t_0 , TO MAXIMUM LOAD TIME, t_f .

Specimen Deflection Calculation. The upward vertical displacement of the compression block was measured for each degree of cam rotation and a polynomial equation (Equation A-4) was fit to this data. The die stack deflection between compression block and the top of the load cell was measured as a function of load and a polynomial equation (Equation A-5) was fit to these data. The instantaneous specimen deflection (Equation A-6) was calculated by subtracting the die stack deflection from the calculated compression block deflection at the corresponding load and cam position.

Compression Block Vertical Displacement Polynomial Equation:

y = vertical displacement

x = cam position (0-45°)

$$y = -0.672 + 12.498x - 0.095x^2 + .003x^3 - (2.2 \times 10^{-4})x^4 + (6.92 \times 10^{-6})x^5 - (6.97 \times 10^{-8})x^6 \quad (\text{Equation A-4})$$

Diestack Deflection Polynomial Equation:

S = deflection

P = load

$$S = 0.781 + 2.075 P - 0.180 P^2 + (5.41 \times 10^{-3})P^3 + (7.32 \times 10^{-6})P^4 \quad (\text{Equation A-5})$$

Instantaneous Deflection Equation:

Δl = Total specimen deflection at any instant

$$\Delta l = y - s \quad (\text{Equation A-6})$$

True Stress-True Strain Calculations. The true strain, ϵ , at any time was calculated by equation A-7.⁽⁶⁾ The original specimen length is l_0 and the instantaneous deflection, Δl .

$$\epsilon = \ln \frac{(l_0 - \Delta l)}{l_0} \quad (\text{Equation A-7})$$

Equation A-8 was used to calculate the corresponding true stress, σ , where P is the instantaneous load, A_0 the initial specimen area and $e (= \frac{\Delta l}{l_0})$ the engineering strain.

$$\sigma = \frac{P}{A_0} (1 + e) \quad (\text{Equation A-8})$$

Comparison of the Two Methods of Calculation. Figure A-3 shows a comparison of data calculated from a test by using the load data only and data calculated from the same test using the load and position data. Figure A-3a was for an $\alpha + \beta$ specimen at 899°C, $\dot{\epsilon} = 10 \text{ s}^{-1}$ and Figure A-3b was for a β specimen at 982°C, $\dot{\epsilon} = 10 \text{ s}^{-1}$. There is little variation in flow stress in comparing the curves for each set of data.

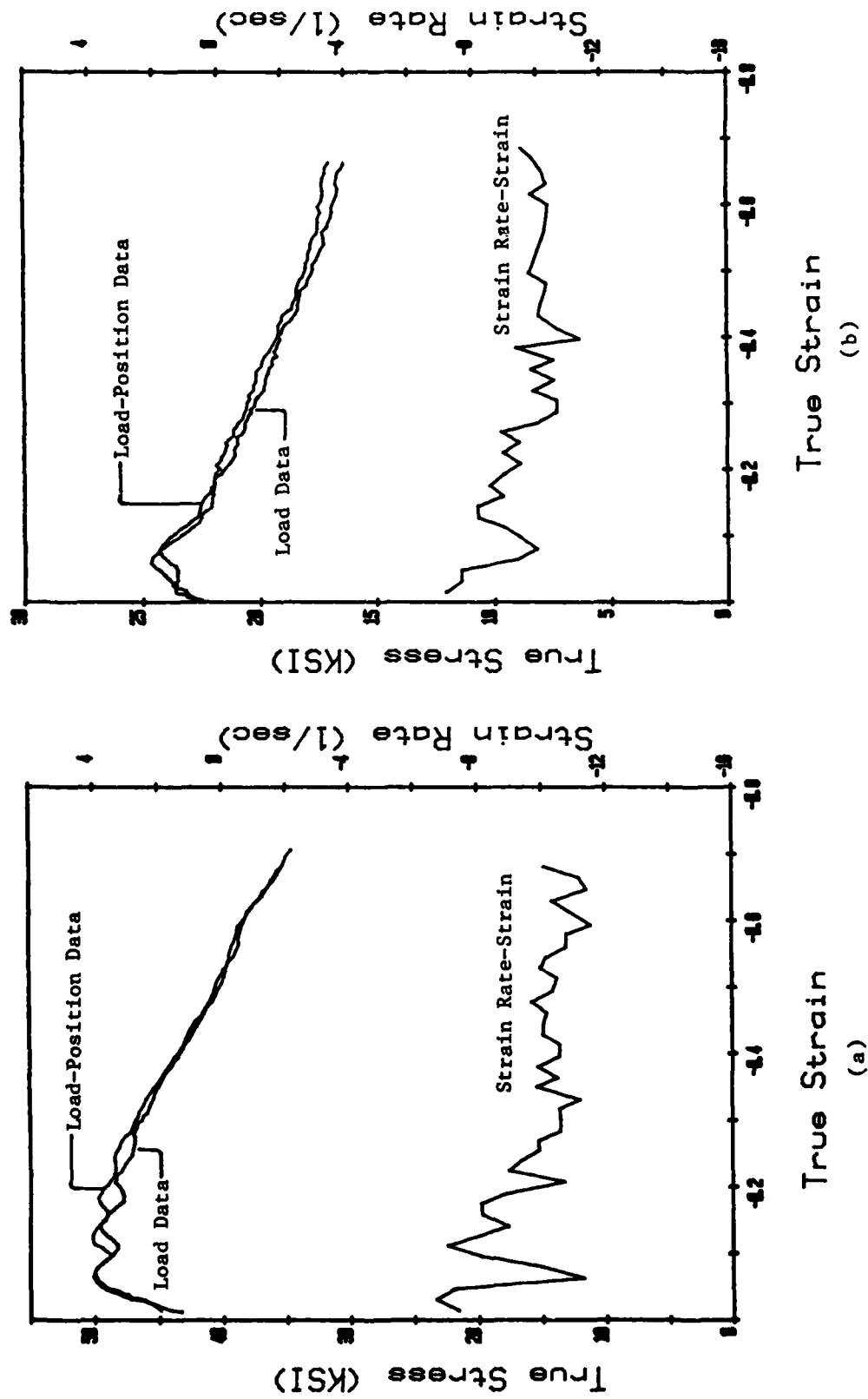


FIGURE A-3. TYPICAL TRUE STRESS-STRAIN AND STRAIN RATE-STRAIN CURVES AT A STRAIN RATE OF -10 s^{-1} . THE TWO FLOW STRESS CURVES REPRESENT CALCULATIONS FROM THE SAME TEST. ONE CURVE IS CALCULATED FROM LOAD-TIME DATA ONLY AND THE OTHER FROM THE SAME LOAD-TIME DATA PLUS CAM POSITION DATA. TEST CONDITIONS WERE (a) $\alpha+\beta$, 899C and (b) β , 982C.

The advantage of using the load and position data for the calculations is that the position curve provides a means of calculating the true strain independent of the cam velocity.

Strain Rate Versus Strain. Strain rate versus strain curves are also shown in Figure A-3 for the two tests. The strain rate was calculated for each degree by dividing the incremental strain between two degrees by the corresponding incremental time.

The largest variations in strain rate are at the start of loading, as shown in Figure A-3. These velocity oscillations raise and lower the true stress according to the increase and decrease in strain rate, respectively. The rises in the flow stress curve calculated from position data align with the troughs in the strain rate data (higher strain rate). Fewer flow stress and strain rate oscillations are found for the higher temperature test (982°C) in Figure A-3b.

The strain rate starts to stabilize around 10 s^{-1} at a true strain of 0.27 for both tests. At this point the strain rate oscillates close to a strain rate of 10 s^{-1} . The sawtooth type curve occurs because of small deviations in the size of the degree slits and in the position of the pins between slits on the timing drum attached to the cam. If one pin is slightly bent, the slit on one side of that pin is wider and on the other side the slit is narrower than required for one degree of cam rotation. A longer elapsed time would be recorded for the wide slit and a shorter time for the narrow slit producing a low followed by a high calculated strain rate.

Results and Conclusions

The results of the testing at strain rates of -1, -10, and -100 s^{-1} are shown in Figures A-4, -5 and -6, respectively. These curves represent the average values for tests run at each condition for the $\alpha + \beta$ (solid lines) and β (dashed lines) Ti-6242 + Si material. Tests at a strain rate of -0.1 s^{-1} were attempted but the cam was slowed to an extent that prevented stabilization of the speed, so tests at this strain rate were stopped.

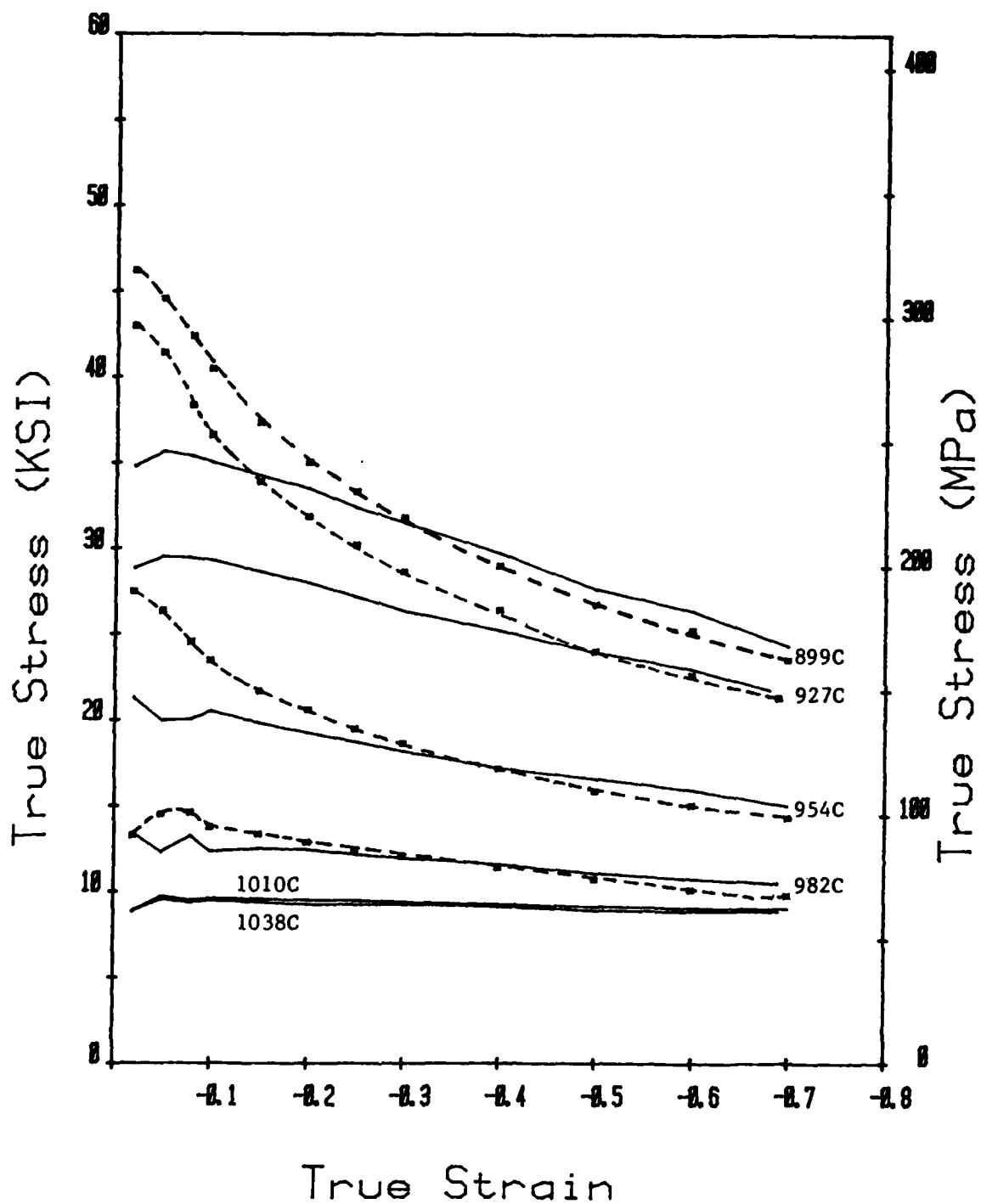


FIGURE A- 4. TRUE STRESS-STRAIN CURVES AT A STRAIN RATE OF -1 s^{-1} .
SOLID LINES ARE $\alpha+\beta$. DASHED LINES ARE β .

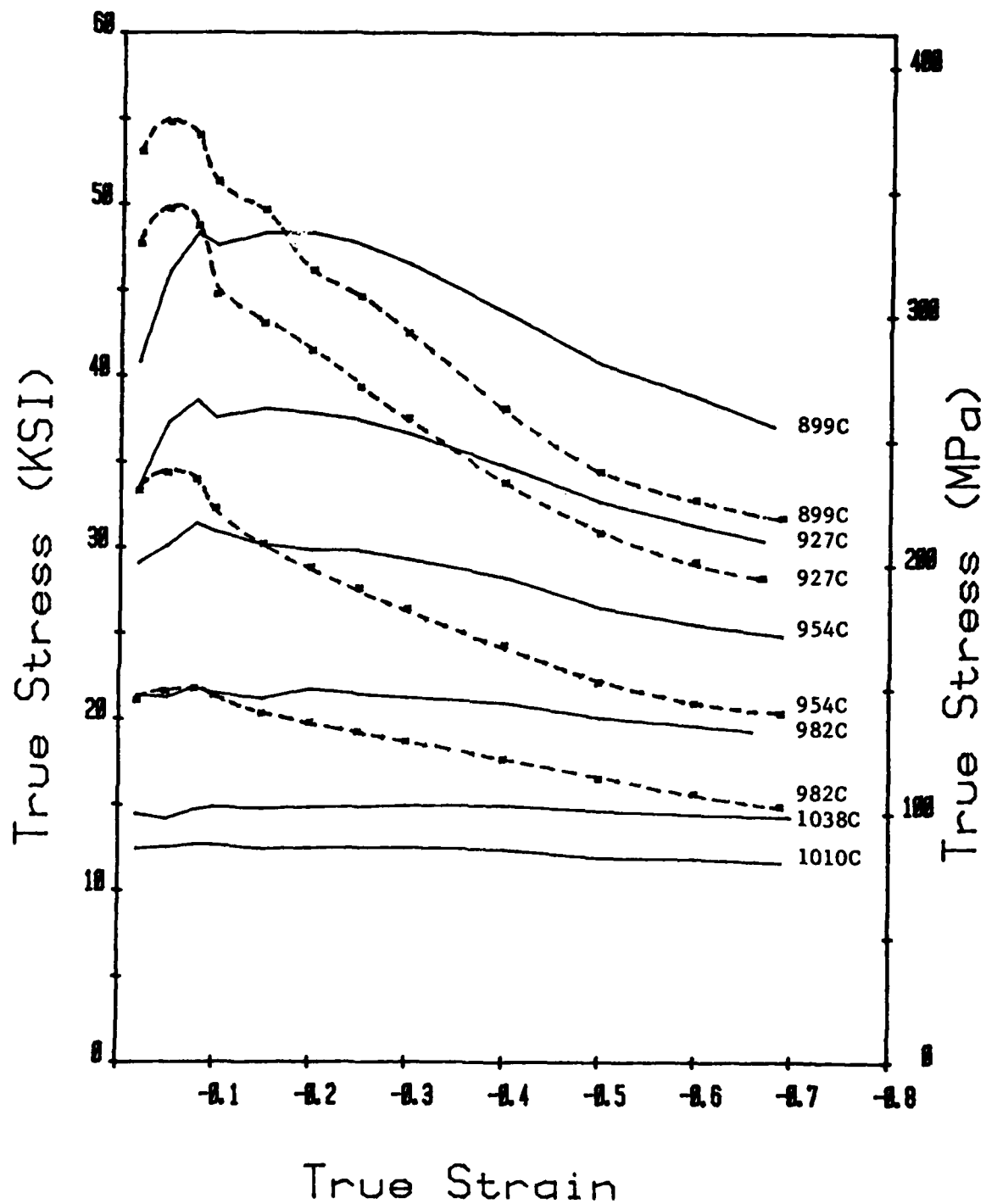


FIGURE A-5. TRUE STRESS-STRAIN CURVES AT A STRAIN RATE OF -10 s^{-1} .
SOLID LINES ARE $\alpha+\beta$. DASHED LINES ARE β .

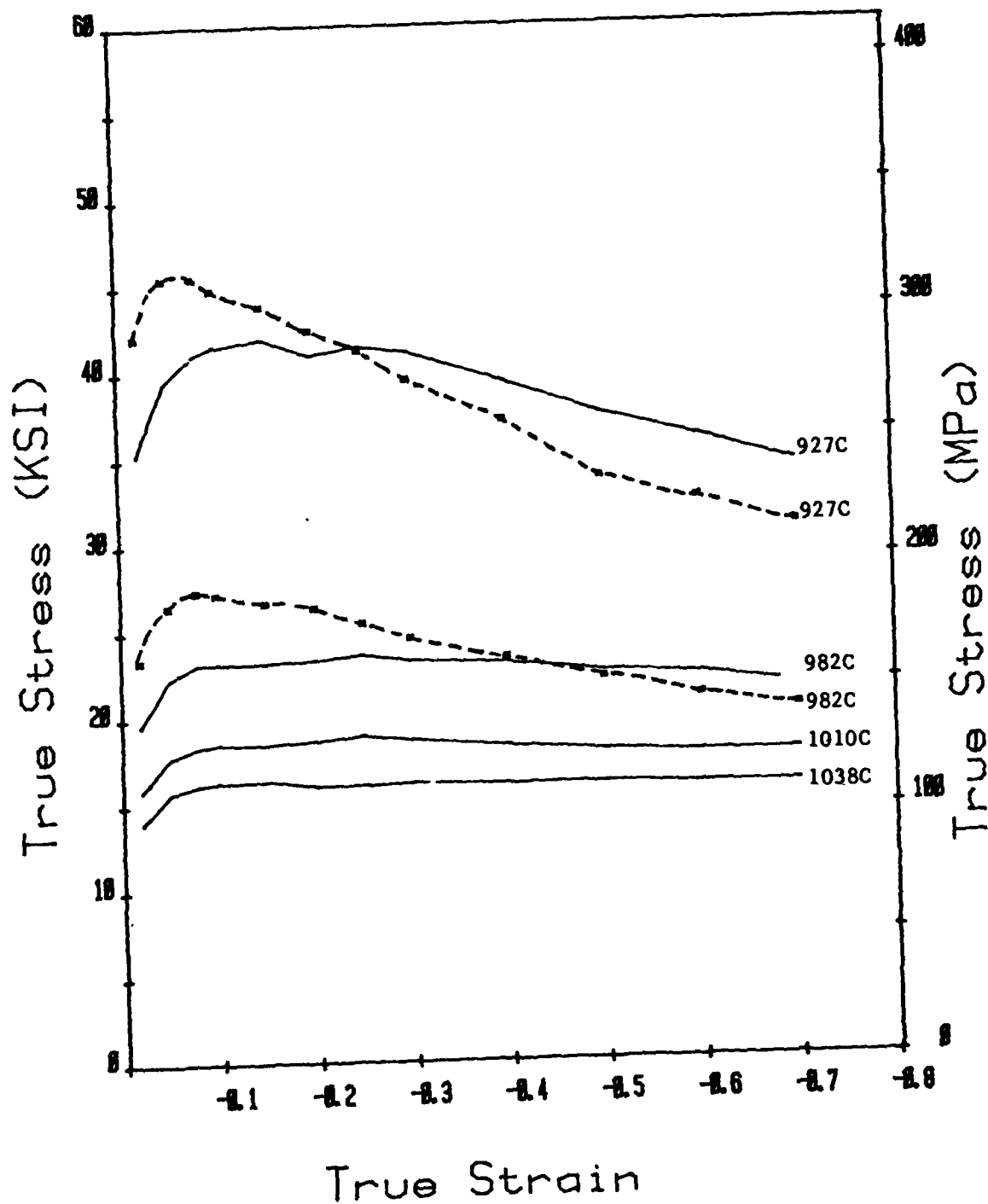


FIGURE A-6. TRUE STRESS-STRAIN CURVES AT A STRAIN RATE OF -100 s^{-1} .
SOLID LINES ARE $\alpha+\beta$. DASHED LINES ARE β .

The flow stresses increase with decreasing temperature and increasing strain rate as expected with the exception of tests at 1038°C and a strain rate of -10 s^{-1} . The flow stress at 1038°C was higher than at 1010°C and a strain rate of -10 s^{-1} . The data at a strain rate of -1 s^{-1} at 1010°C and 1038°C show almost equivalent flow stress at these temperatures. At a strain rate of -100 s^{-1} the flow stress at 1010°C is higher than at 1038°C as expected.

Standard deviations from the mean true stresses were calculated for each set of tests. The maximum standard deviation and the corresponding true strain are shown in Table A-1. The highest maximum for the $\alpha + \beta$ material is 20.0 MPa (2.9 ksi) and for the β material is 38.6 MPa (5.6 ksi). Most of the maximums for both types of material occur at strains of less than 0.08.

TABLE A-1

MAXIMUM STANDARD DEVIATIONS (σ_{\max})

		$\alpha + \beta$		β	
Test Temp °C	Strain Rate s ⁻¹	σ_{\max} MPa (ksi)	ϵ	σ_{\max} MPa (ksi)	ϵ
899	1	9.0 (1.3)	0.08	17.9 (2.6)	0.05
	10	20.0 (2.9)	0.02	24.1 (3.5)	0.40
927	1	15.2 (2.2)	0.02	35.9 (5.2)	0.02
	10	13.8 (2.0)	0.08	38.6 (5.6)	0.05
	100	13.8 (2.0)	0.05	9.7 (1.4)	0.40
954	1	6.2 (0.9)	0.02	22.1 (3.2)	0.05
	10	15.9 (2.3)	0.20	25.5 (3.7)	0.05
982	1	6.2 (0.9)	0.02	9.7 (1.4)	0.05
	10	11.7 (1.7)	0.02	17.2 (2.5)	0.05
	100	6.9 (1.0)	0.08	7.6 (1.1)	0.02
1010	1	2.8 (0.4)	0.08		
	10	1.4 (0.2)	0.02		
	100	3.4 (0.5)	0.02		
1038	1	8.3 (1.2)	0.02		
	10	16.6 (2.4)	0.30		
	100	4.1 (0.6)	0.20		

References

- (1) Orowan, E., "The Cam Plastometer", Report MW/F/22/50 of the Forging Committee in the Mechanical Working Division, British Iron and Steel Research Association, March, 1950.
- (2) Hockett, J. E., "The Rolling Pressures of Uranium Sheet and Plate", Report LA-2233, Los Alamos Scientific Laboratory, Los Alamos, New Mexico, January, 1959.
- (3) Hockett, J. E., "Compression Testing at Constant True-Strain Rates", in Proceedings, American Society for Testing Materials, v. 59, p. 1309-1317, 1959.
- (4) Hockett, J. E., "On Relating the Flow Stress of Aluminum to Strain, Strain Rate, and Temperature", Report LA-3544, Los Alamos Scientific Laboratory, Los Alamos, New Mexico, December, 1966.
- (5) Hockett, J. E., "Compression Tests at High True-Strain Rates", in Metal Progress, Dec., 1966.
- (6) Dieter, G. E., Mechanical Metallurgy, McGraw-Hill, Inc., 1976, p. 76-79.

APPENDIX B

EFFECT OF PROCESSING VARIABLES ON
MICROSTRUCTURE OF Ti-6242

S. L. Semiatin
Battelle's Columbus Laboratories
Columbus, Ohio 43201,

P. Dadras and J. F. Thomas, Jr.
Wright State University
Dayton, Ohio 45435

J. C. Malas
Materials Laboratory
Air Force Wright Aeronautical Laboratories
Wright-Patterson Air Force Base, Ohio 43433

APPENDIX B

EFFECT OF PROCESSING VARIABLES ON MICROSTRUCTURE OF Ti-6242

Introduction

As with ferrous alloys, titanium alloy systems are known to possess a rich variety of possible microstructures and properties. This is especially true in two-phase-alloy systems such as the α/β ones of titanium and the $\alpha/\text{Fe}_3\text{C}$ ones of iron. Because of this flexibility in microstructure and properties, these alloys find applications in widely differing service environments. These uses and capabilities are limited only by the ingenuity with which materials and mechanical engineers can devise thermal-mechanical processing sequences to enhance desired critical properties while maintaining other less important properties at certain minimal levels. As an example, much work has been done (and continues to be done) on ways to enhance the fracture toughness of structural alloys without losing strength. That this is possible can be seen in the development of alloys such as Ti-10V-2Fe-3Al (a near-beta alloy)⁽¹⁾ and the maraging steels⁽²⁾.

The emergence of processing science and process modelling has filled a void in the traditional study of microstructure-property relationships by metallurgists. From this discipline, the realization that deformation and deformation history as well as final heat treatment can have a profound effect on final microstructure has been made. One of the major research efforts in this area is the Dual Property Disk program reported herein. Its specific objective has been to develop a science-based methodology for analyzing, optimizing, and designing deformation processing sequences in order to control the microstructure and properties in a finished forging, which in this case is a titanium alloy compressor disk. As part of this program, uniaxial compression tests were performed on the program alloy, Ti-6Al-2Sn-4Zr-2Mo-0.1Si, to obtain flow stress data. Using the compression samples, the effect of preform

microstructure and processing parameters on final microstructure has been determined. To do this, optical microscopy was performed on compression samples which had been (1) heat treated alone, (2) hot forged, or (3) hot forged and given a post-forging heat treatment. Many different microstructures were observed in these studies, and attempts were made to rationalize their development.

Materials and Procedures

Materials

The Ti-6242 alloy used in the program was melted and broken down by RMI Company of Niles, Ohio, and had a composition of 6.1% Al, 2.1% Sn, 3.9% Zr, 2.1% Mo, 0.084% Si, balance titanium. Wyman-Gordon Company finish forged the material to 12.07 cm (4.75 in.) diameter bar. Finish forging was done at either 954 C (1750 F) followed by annealing at 968 C (1775 F) (2 hours + air cool) or 1038 C (1900 F) followed by annealing at 1024 C (1875 F) (2 hours + air cool). From the former forge-heat treatment cycle a microstructure of globular alpha phase (α -grain size = 10 μ) in a matrix of transformed beta phase was produced (Figure B-1a).^(3,4) This microstructure is referred to as the α + β -perform microstructure or simply α + β -microstructure, and it possesses good high temperature fatigue properties. The second forge-heat treatment cycle was above the $\beta \rightarrow \alpha$ + β -transus temperature (990 C [1815 F]) and produced a transformed beta microstructure (Widmanstätten or basketweave microstructure) of prior β -grain size \approx 400 μ (Figure B-1b).^(3,4) This microstructure is referred to as the β -preform microstructure or simply β -microstructure. It is known to have good high temperature creep properties.

Procedures

The Ti-6242 samples were examined after heat treatment alone, after preheating and uniaxial compression, or after preheating, uniaxial compression, and post-deformation heat treatment. Heat treatment for most

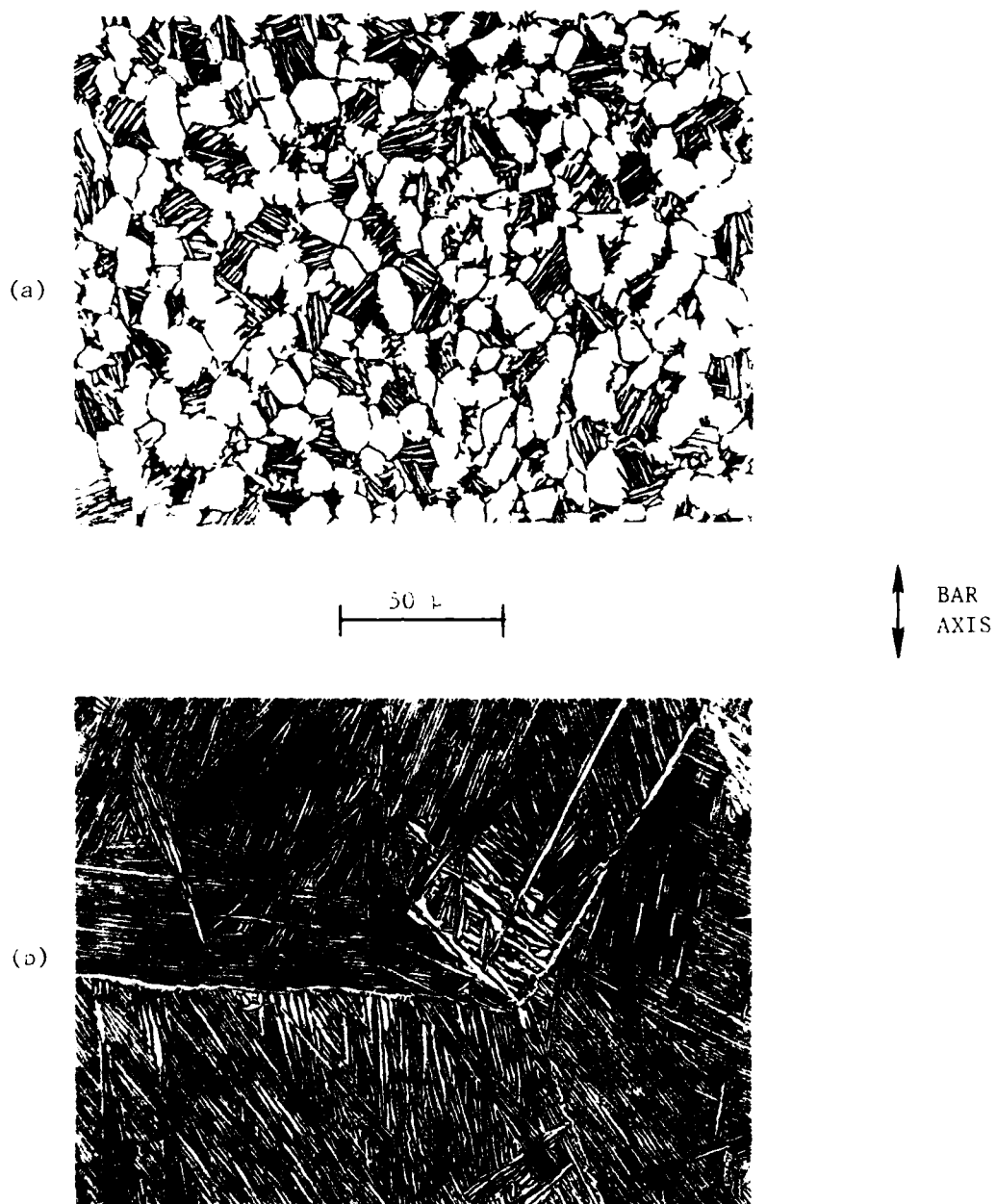


Figure B-1. As-Received Microstructures of
(a) $\alpha+\beta$ Preform Material and
(b) β Preform Material.

of the samples was performed by wrapping them in tantalum foil, encapsulating them in quartz tubes (evacuated and back filled with a one-third to one-half atmosphere of argon), heating in tube furnaces which were controlled to ± 3 C (± 5 F) of the desired temperature, and water quenching the capsules after specified times. A few samples were heated unencapsulated in the furnaces with an argon atmosphere (argon flow rate ≈ 0.84 cu m/hr [30 cu ft/hr]) and air cooled after heat treatment. Since preheating for forging and solution treatment after forging are done typically in the range of 899-1010 C (1650-1850 F) in commercial operations, these heat-treating temperatures were chosen for the present study.

Uniaxial compression samples for the investigation were obtained from tests⁽⁵⁾ conducted by Wright State University and Los Alamos Scientific Laboratory. In these tests, $\alpha+\beta$ -microstructure samples were deformed at temperatures of 899, 927, 954, 982, 1010, and 1038 C (1650, 1700, 1750, 1800, 1850, and 1900 F) and strain rates of 10^{-3} , 10^{-2} , 10^{-1} , 1, 10, and 100 sec^{-1} and then examined metallographically. Similarly, analysis was done on β -microstructure samples deformed at the same strain rates but only the first four of the six temperatures (since the β -microstructure reverts to the single phase bcc Ti above the transus temperature as done at the $\alpha+\beta$ -microstructure). Low strain rate tests (10^{-3} to 10^{-1} sec^{-1}) were performed by Wright State. Prior to testing, the samples were heated in a furnace for 30 minutes (15 minutes to heat to test temperature and 15 minutes to soak at temperature), and they were air cooled after testing. High strain rate ($1-100 \text{ sec}^{-1}$) were performed on a cam plastometer at Los Alamos. These samples were induction heated to test temperature in several minutes and held at temperature for 5 to 6 minutes before compression, after which they were air cooled.

Most of the metallography was done with samples which had been compressed to 50 percent reduction in height ($\epsilon \approx 0.7$). In addition, a brief metallographic investigation of the microstructures developed in β -preform material compressed to various strains (0.2 to 1.0) at $T = 899$ C (1650 F), $\dot{\epsilon} = 2 \times 10^{-3} \text{ sec}^{-1}$ was performed. These latter samples were examined in both the as-deformed condition as well as after heat treatment at $T = 951$ C (1745 F). In this case, the sample capsules were air cooled

after heat treatment. The special forging and heat treating parameters for these samples were chosen on the basis of projected processing parameters to be used in forging of subscale compressor disks of β -perform material, which are to be conducted later in the Dual Property Disk Program. These parameters have been found to yield the desired dual microstructure/dual property disk by direct forging of β -perform material, followed by heat treatment.

Metallography was performed on the Ti-6242 samples using standard procedures. The samples were sectioned along the bar axis (as-received material) or compression axis, mounted, and hand ground on (wet) SiC papers, moving progressively from 120 to 240 to 400 to 600 grits. For rough polishing, a suspension of Linde A ($0.3 \mu \text{Al}_2\text{O}_3$), manufactured by Buehler, Ltd., in a solution of 10% oxalic acid in water was used on a fast wheel with a Lintless cloth (Century Glove Co.). Finish polishing was accomplished with a suspension of Linde B ($0.05 \mu \text{Al}_2\text{O}_3$), manufactured by Buehler, Ltd., in the 10% oxalic solution on a slow wheel with a Microcloth (Buehler, Ltd.). To reveal the microstructure, dipping (~ 5 -10 sec) in an etchant of 3.5 volume percent HNO_3 , 1.5 volume percent HF, 95 volume percent H_2O was found to be highly effective.

Results and Discussion

$\alpha+\beta$ -Preform Microstructure

Microstructure After Heat Treatment. Metallographic results demonstrated that preheat temperature, deformation, and post-heat-treatment temperature and time all influence the microstructure developed in $\alpha+\beta$ -preform material. The effect of preheating at temperatures from 899 C (1650 F) to 982 C (1800 F) was described in Appendix D of the previous Interim Annual Technical Report.⁽⁵⁾ Briefly, the effect of increasing preheat temperature is to decrease the percent of globular alpha phase and increase the fineness of the Widmanstatten alpha in the transformed beta matrix (Figure B-2). This qualitative behavior does not appear to be affected much by the time at temperature (15 minutes versus 2 hours) for any of the microstructures.

As was discussed in the previous Interim Annual Report, the observed effects of preheating can be expected from classical metallurgical

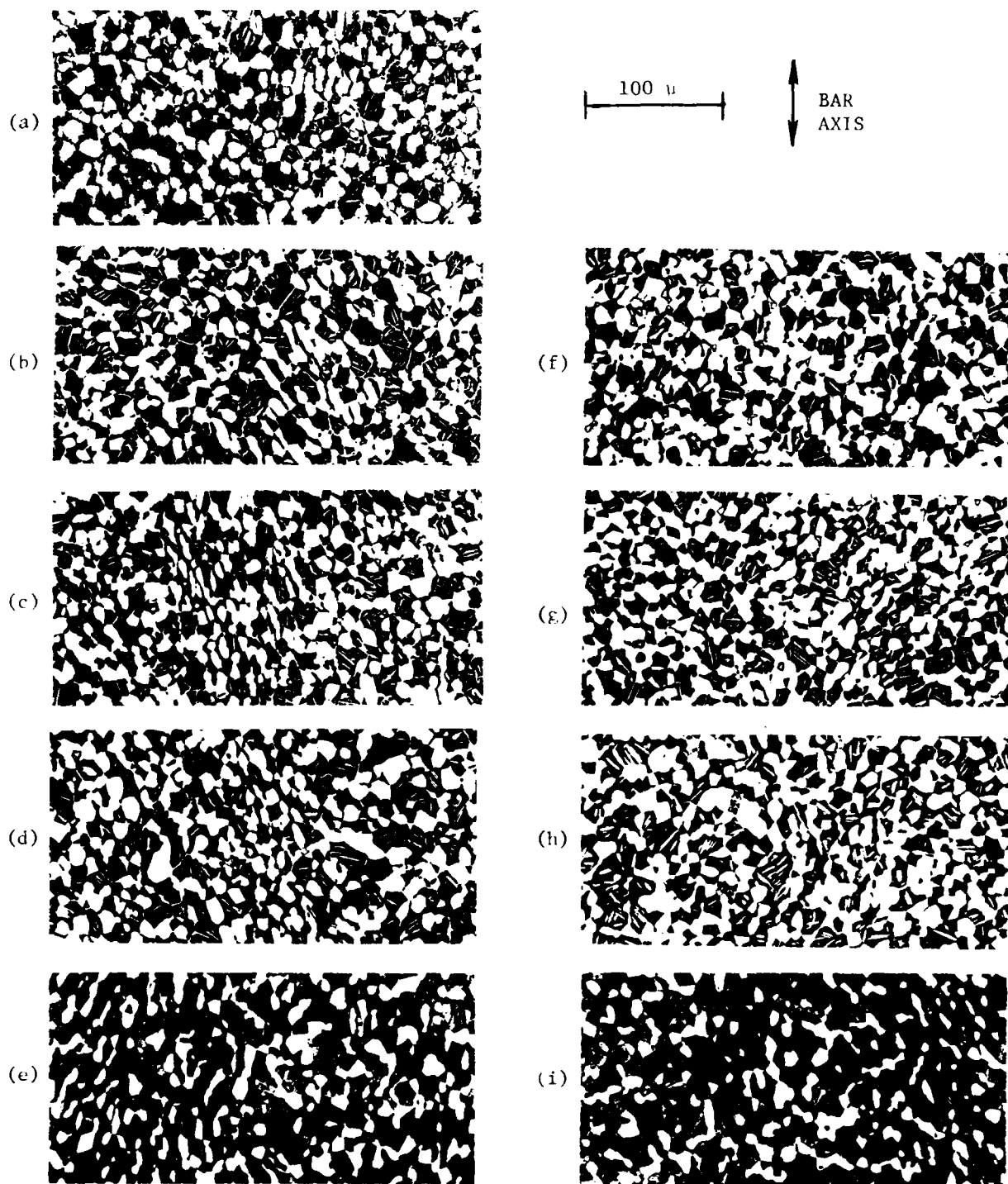


Figure B-2. Microstructures in $\alpha+\beta$ Preform Microstructure Material (a) As-Received and After Heat Treatment for 15 Mins. (+ AC) at (b) 899 C (1650 F), (c) 927 C (1700 F), (d) 954 C (1750 F), (e) 982 C (1800 F), and for 2 Hrs. (+ AC) at (f) 899 C (1650 F), (g) 927 C (1700 F), (h) 954 C (1750 F), and (i) 982 C (1800 F).

concepts for the most part. With the aid of the pseudo-binary phase diagram for titanium-molybdenum alloys containing 6 weight percent aluminum, 2 weight percent tin, and 4 weight percent zirconium (Figure B-3), it can be deduced using the inverse lever rule that the percent of globular alpha phase in the microstructure should decrease rapidly as the temperature is increased up to the transus temperature. This is as observed. Furthermore, the phase diagram suggests that the matrix phase rapidly becomes more and more dilute as the preheat temperature is increased. Because of this, one might expect the kinetics of the Widmanstatten reaction to become faster as the beta phase becomes leaner with increasing temperature.⁽⁶⁾ Thus, the matrix phase ought to be somewhat coarse Widmanstatten at the higher preheat temperatures and finer or even martensitic at the lower preheat temperatures. Surprisingly, this is the opposite of what is actually observed (Figure B-2). Part of this paradox may be resolved if one assumes that the M_s temperature is below room temperature for the concentrated beta phase produced by lower temperature preheating.⁽⁷⁾ Hence, the matrix would have to be either a Widmanstatten microstructure or metastable, retained beta phase. Alternatively, one might suspect that the low temperature preheating is insufficient to cause reversion of the beta matrix phase. This is in qualitative agreement with Gegel's finding⁽⁵⁾ that reversion begins at 916 C (1680 F). If this were the case, the matrix microstructure would be similar to that in the as-received material (which was annealed at 968 C (1775 F)). This is what is observed.

The development of a martensitic matrix phase for high temperature preheating must result from a high cooling rate (because of a small sample size) and a relatively high M_s temperature. These conclusions are somewhat tentative and warrant further investigation for their verification.

Microstructures After Preheating and Deformation. The as-compressed $\alpha+\beta$ -microstructures, although dependent on temperature, were shown previously to be insensitive to strain rates in the range of 10^{-3} sec^{-1} to 10^{-1} sec^{-1} .⁽⁵⁾ Metallography on samples compressed at strain rates between 1 and 100 sec^{-1} , examined during the current reporting period, also showed a general insensitivity to strain rate for a

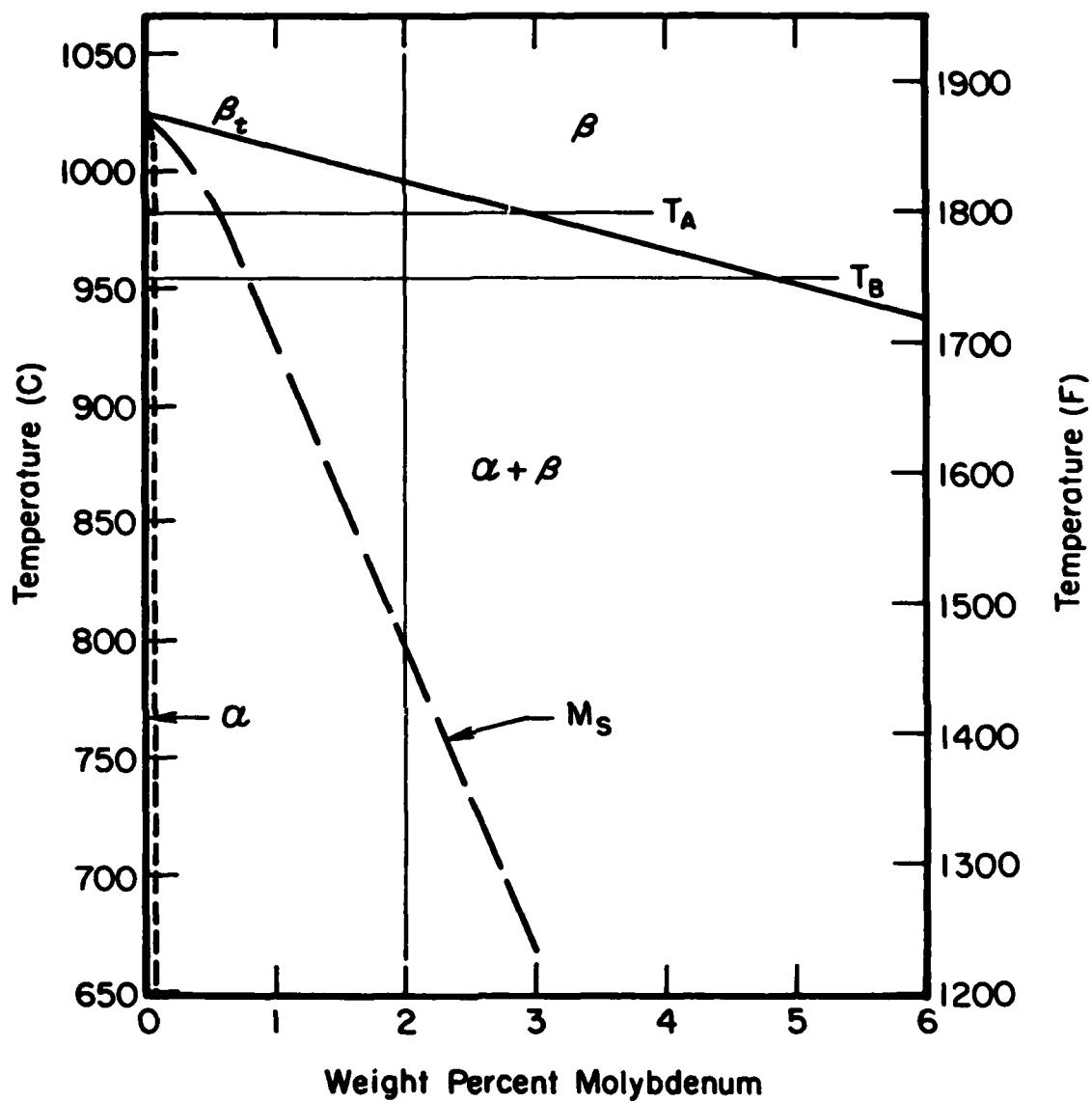


Figure B-3. Approximate Pseudo-Binary Equilibrium Phase Diagram for Titanium Alloys Containing 6 Wt. Percent Al, 2 Wt. Percent Sn, and 4 Wt. Percent Zr.

given test temperature. In fact, these observed microstructures are very similar to the low-strain-rate ones. Typical $\alpha+\beta$ -microstructures after deformation at 10 sec^{-1} and various temperatures are shown in Figure B-4.

Similar to the low-strain-rate tests, the combined, simultaneous effects of high temperature and deformation bring about a variation of percent alpha with temperature (in the temperature regime of 899 C [1650 F] to 982 C [1800 F]) which is more marked (Figure B-4) than in the microstructures of samples given high-temperature exposure alone (Figure B-2). For instance, compare the microstructures in samples preheated at 899 C (1650 F) and preheated and compressed at 899 C (1650 F) [Figures B-2b and B-4a]. Obviously, deformation has given rise to a far larger amount of primary alpha phase, one which is probably closer to the equilibrium amount. However, the flow curves from the compression tests are not suggestive of dynamic recrystallization, the most obvious mechanism for equilibrating the amount of primary alpha at different temperatures. An alternate explanation might involve interphase boundary migration. This explanation might also support the observation that the alpha grains retain their nearly equiaxed shape after the large 50 percent reduction.⁽⁸⁾

Another observation for the $\alpha+\beta$ -microstructures deformed subtransus involves the morphology of the matrix phase. In contrast to the microstructures in samples preheated alone, this morphology is a Widmanstätten one in all high-strain-rate compression tests. This behavior can be rationalized in terms of the work of Weiss and Jonas.⁽⁹⁾ They showed that precipitation kinetics can be considerably enhanced by concurrent hot deformation as well as by previous hot work in which a dislocation substructure is retained. For the hot worked Ti-6242 being examined here, it is plausible that the subtransus deformation developed a sufficiently hot-worked substructure to enhance the nucleation-and-growth-Widmanstätten reaction (a precipitation-type reaction). Thus, the matrix phase in all cases is a Widmanstätten morphology. This contrasts to the low-strain-rate compression microstructures⁽⁵⁾, which develop less of a hot-worked substructure and whose matrix phase is sometimes martensitic.

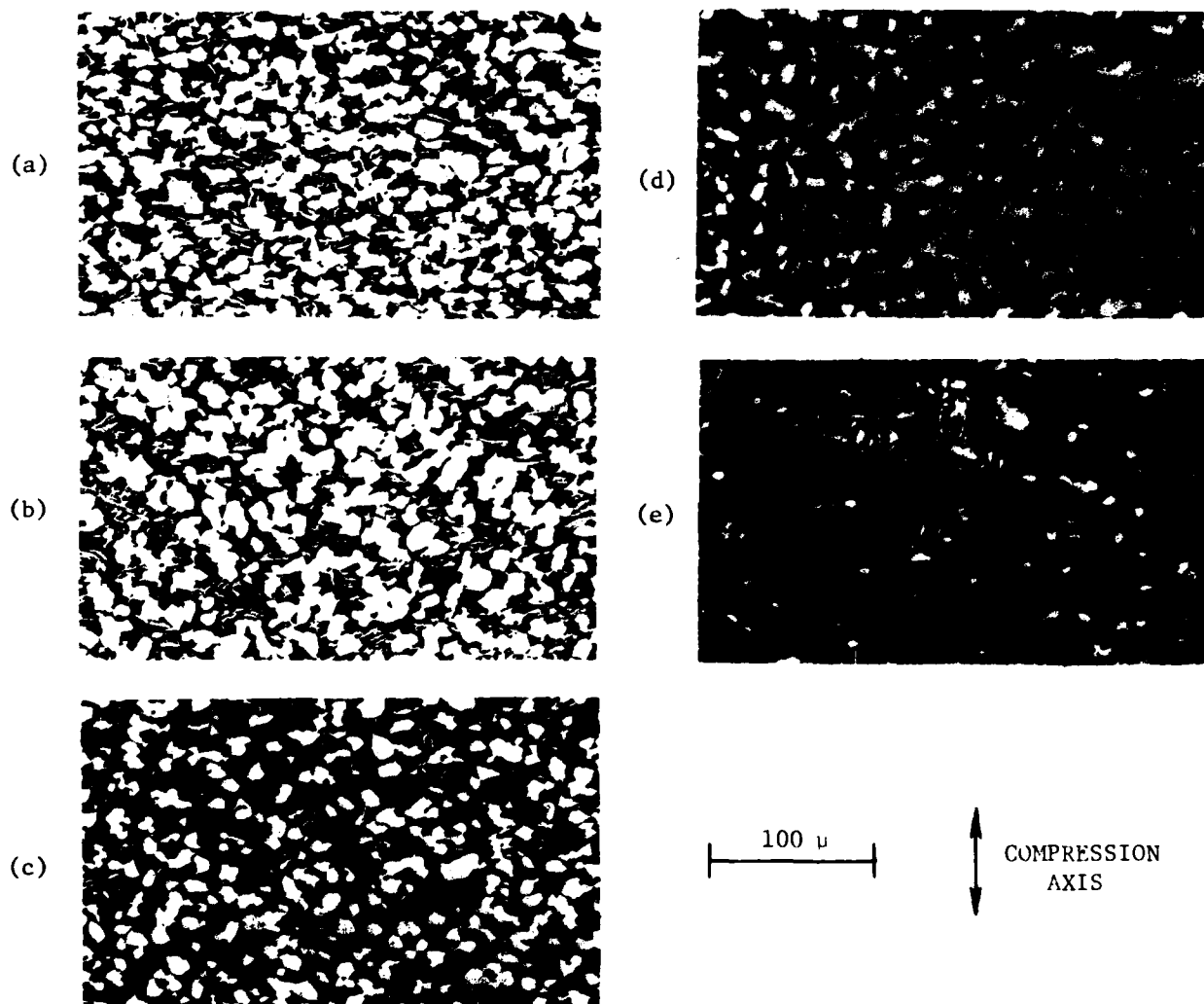


Figure B-4. Microstructures in As-Deformed Compression Samples of $\alpha+\beta$ Preform Microstructure Forged at a Strain Rate of 10 Sec.^{-1} and at Temperatures of (a) 899 C (1650 F), (b) 927 C (1700 F), (c) 954 C (1750 F), (d) 982 C (1800 F), and (e) 1010 C (1850 F).

In summary, the result of the subtransus, high-strain-rate hot working is an $\alpha+\beta$ -microstructure of globular alpha in a transformed beta matrix which is probably close to the equilibrium configuration for each pre-heat/compression temperature.

When the $\alpha+\beta$ -microstructure is deformed above the transus temperature, the microstructure during working is totally beta phase, and microstructures which are either totally Widmanstätten or martensitic are obtained after cooling to room temperature (Figure B-4e). Note in this final figure that a small amount of primary alpha is still evident, indicating insufficient preheating time.

Microstructures After Deformation and Heat Treatment. When forging is done below the transus temperature, post forging heat treatment benefits from the residual hot working substructure in the attainment of microstructures close to the equilibrium ones for the heat treatment temperatures employed. The effect was demonstrated during the previous reporting period for samples compressed at low strain rates and subsequently heat treated.⁽⁵⁾ A similar trend has now been found for samples compressed at high strain rates. For example, the microstructures of samples compressed at 899 C (1650 F), 10 sec⁻¹ or 954 C (1750 F), 10 sec⁻¹ and then given a heat treatment of 954 C (1750 F) for 2 hours are nearly identical (Figure B-5). On the other hand, high-strain-rate beta working like low-strain-rate beta working, both of which produce a transformed beta microstructure on cooling below the transus temperature (Figure B-4e), develops microstructures which are relatively resistant to heat treatment below the transus temperature (Figure B-5c). When heat treatment is done above the transus temperature, identical microstructures are obtained for all samples--namely, a transformed beta microstructure of Widmanstätten or martensitic alpha.

β -Perform Microstructure

Microstructures After Preheating and Deformation. During the previous reporting period, microstructures in β -perform material were surmised to be insensitive to subtransus preheating.⁽⁵⁾ Dilatation

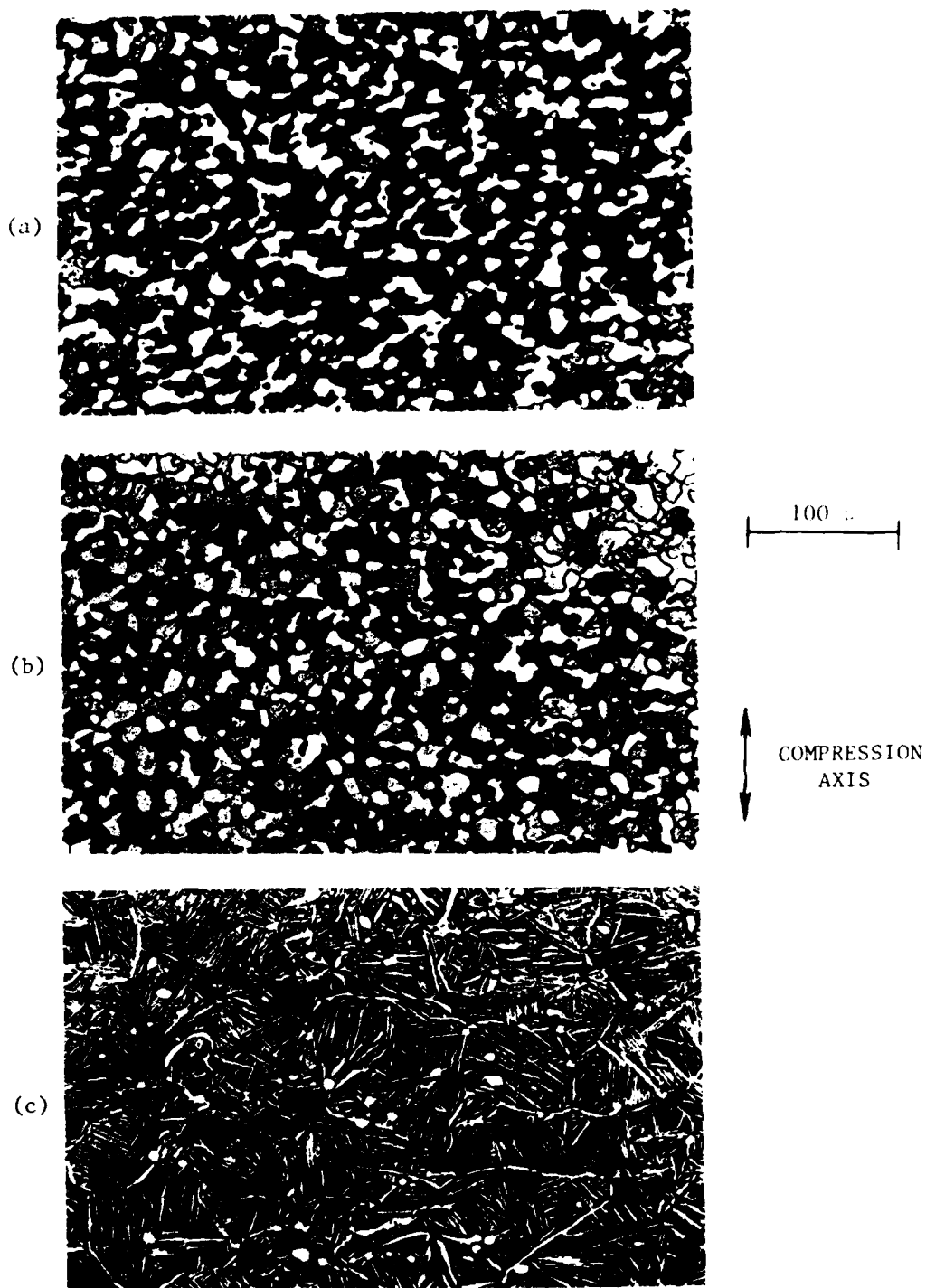


Figure B-5. Microstructures Formed in $\alpha+\beta$ Preform Microstructure Material after a Heat Treatment of 954 C (1750 F)/2 Hrs. Which Follows Compression at a Strain Rate of 10 Sec.^{-1} at Temperatures of (a) 899 C (1650 F), (b) 954 C (1750 F), and (c) 1010 C (1850 F).

studies done by Gegel, *et al.*, which also appeared in the previous Interim Annual Technical Report, implied, however, that there is indeed an alpha platelet reversion during subtransus heat treatment above 916 C (1680 F). This reversion is masked by a reverse reaction during cooling to room temperature, thus preventing direct observation of high temperature microstructures. It is not unreasonable to assume though that the basic acicular morphology of the β -microstructure is changed little by preheating below the transus temperature.

As was shown by the microstructures for low-strain-rate-compression tests⁽⁵⁾, the morphology of the β -preform microstructure is greatly affected by subtransus forging at high strain rates following preheating. The microstructure exhibits very non-uniform deformation after fifty percent reduction at temperatures of 899, 927, and 954 C (1650, 1700, and 1750 F) (Figure B-6). This is true of all three of the so-called high strain rates of 1, 10, and 100 sec⁻¹. This non-uniform deformation is manifested primarily by bending of the alpha and beta platelets and "kinking" of the alpha phase situated at the prior beta grain boundaries. Other studies have shown that this mode of deformation is connected with large degrees of flow softening observed in the uniaxial deformation of this microstructure. (5,10,11)

Deformation at 982 C (1800 F) and strain rates of 1 to 100 sec⁻¹ leads to much more uniform two-phase β -microstructures (Figure B-6). This observation is analogous to observations of the β -microstructure deformed at 954 C (1750 F), 10⁻³ sec⁻¹ and at 982 C (1800 F), 10⁻³ to 10⁻¹ sec⁻¹.⁽⁵⁾ All of these deformation conditions appear to allow sufficient time at the given temperature to enable dynamic changes in the morphology of the alpha phase to one which is either lenticular or a combination of lenticular and globular. The flow curves corresponding to the temperatures and strain rates at which the alpha morphology exhibits these changes also show large degrees of flow softening, similar to the curves measured at the lower test temperatures. In these cases, it is postulated that the large changes in dislocation substructure, which bring about the flow softening⁽¹²⁾, supply enough energy to break up the alpha platelets

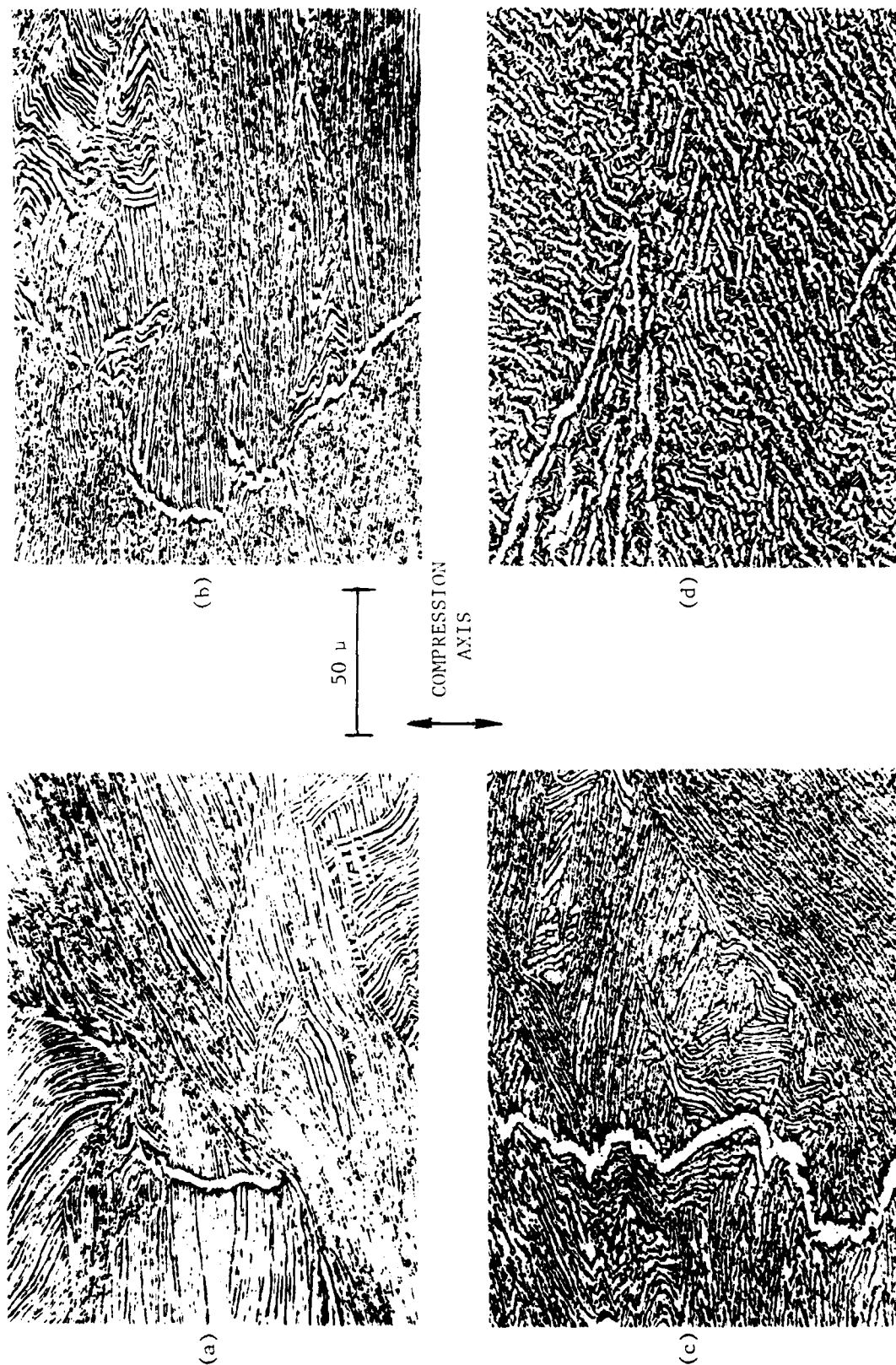


Figure B-6. Microstructures in As-Deformed Compression Samples of ϵ Preform Microstructure Forged at a Strain Rate of 10 Sec.^{-1} and at Temperatures of (a) 899°C (1650°F), (b) 927°C (1700°F), (c) 954°C (1750°F), and (d) 982°C (1800°F).

and allow them to modify their morphology. This point will be examined in more detail when the microstructures in β -microstructure samples compressed various amounts at 899 C (1650 F) are discussed.

Microstructures After Deformation and Heat Treatment. The microstructures after fifty percent deformation at high strain rates and heat treatment, which were documented during the current reporting period, are similar to those for low-strain-rate deformation followed by heat treatment, which were reported previously.⁽⁵⁾ As for the low-strain-rate samples, subtransus heat treatment of high-strain-rate β -preform microstructure samples deformed at subtransus temperatures induces static recrystallization whose extent depends on heat treatment time and temperature. When the heat treatment is done at relatively low temperatures such as 913 C (1675 F), very fine alpha grains are the result of recrystallization after short times (15 minutes) (Figure B-7). Longer heating times (e.g., 2 hours) at this temperature result in an almost totally recrystallized structure of alpha grains. These long-time microstructures, when compared to those for the low-strain-rate samples⁽⁵⁾, show more recrystallization probably because of the larger degrees of hot work which are normally introduced in higher strain-rate deformations.

At somewhat higher heat treatment temperatures such as 954 C (1750 F), the recrystallization process is enhanced relative to low-temperature heat treatment, and there is even some alpha grain growth with increasing heat treating time (Figure B-8). Long-time heating at 954 C (1750 F) promotes microstructural transformations involving formation of large amounts of lenticular and equiaxed alpha. The higher temperature recrystallization of these high-strain-rate samples also appears to be greater than that for the low-strain-rate samples.⁽⁵⁾ In fact, for the 10 sec^{-1} sample compressed and heat treated (for 2 hours) at 954 C (1750 F), there appears to be almost no vestige of the starting β -preform microstructure. Short-time heat treating of high-strain-rate-compression samples at 954 C (1750 F), on the other hand, leaves large indications yet of the starting microstructure, as do the short-time, lower temperature heat treatments (Figure B-7) and all of the short-time subtransus heat treatments of low-strain-rate samples.⁽⁵⁾ Although the

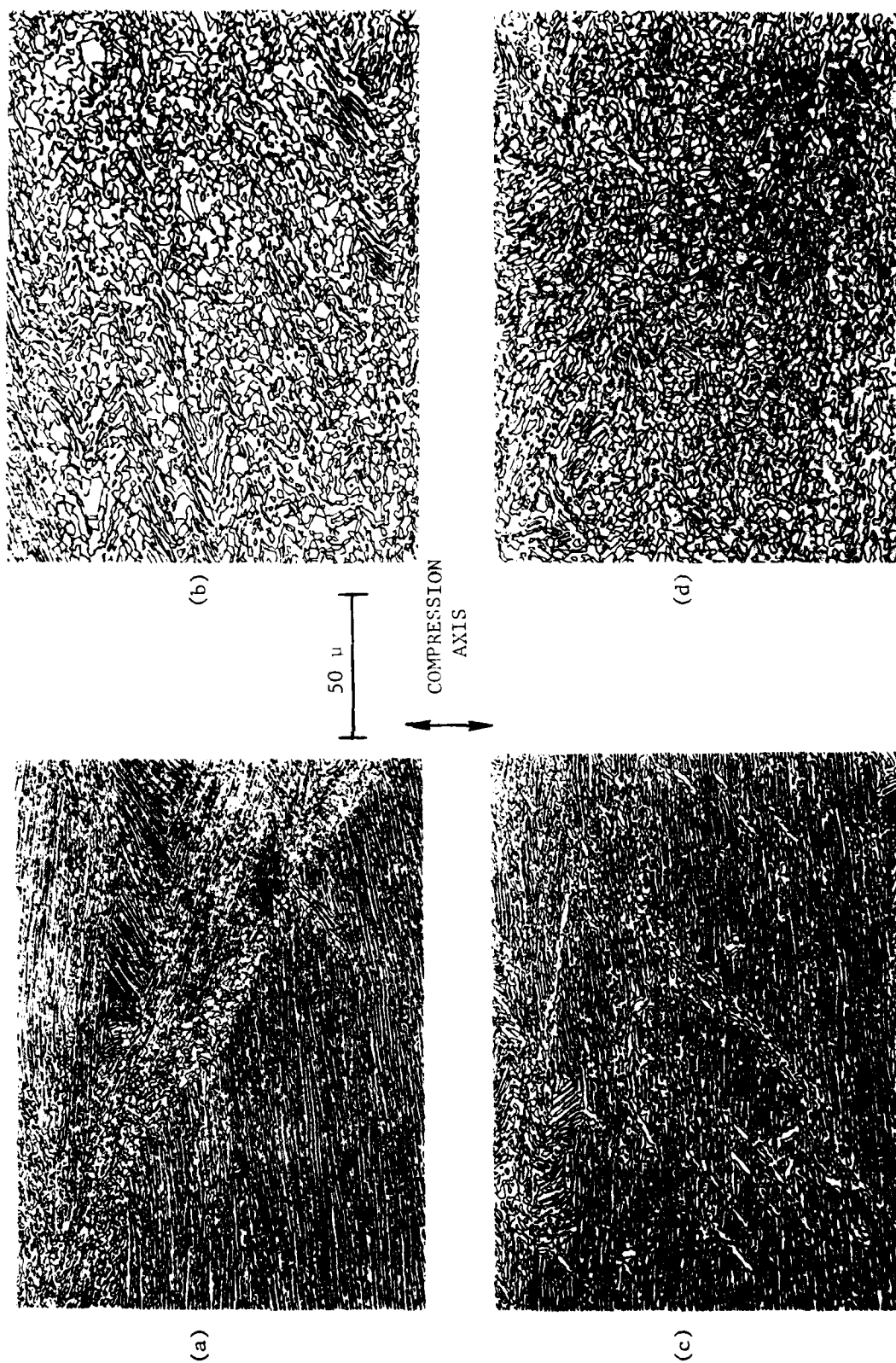


Figure B-7. Microstructures Formed in a Preform Microstructure Material After a Heat Treatment at 913 C (1675 F) for Either (a,c) 15 Minutes or (b,d) 2 Hours, Following Deformation at (a,b) 899 C (1650 F), 10 Sec.⁻¹ or (c,d) 954 C (1750 F), 10 Sec.⁻¹.

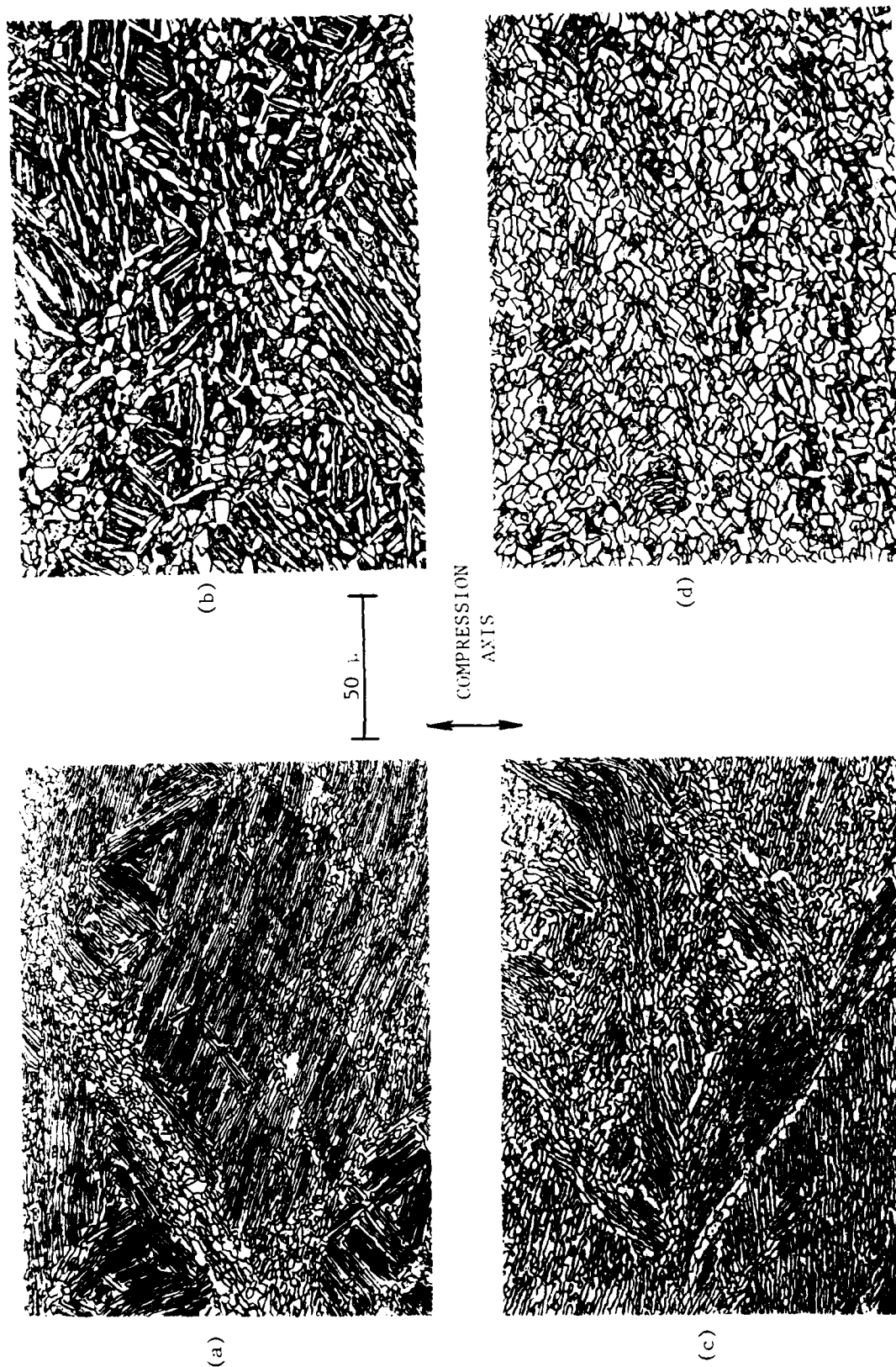


Figure B-8. Microstructures Formed in ϵ Preform Microstructure Material After a Heat Treatment at 954 C (1750 F) for Either (a,c) 15 Minutes or (b,d) 2 hours, Following Deformation at (a,b) 899 C (1650 F), 10 Sec.⁻¹ or (c,d) 954 C (1750 F), 10 Sec.⁻¹.

microstructural changes are minimal for these short-time heat treatments, an insight into the mode of flow localization produced during deformation is obtained. All of the short-time heat treatments of deformed β -microstructure samples exhibit bands of recrystallized alpha grains which form along lines at angles of approximately 60 degrees to the compression axis. These observations follow if it is hypothesized that the bands of grains occur along lines of very high deformation or flow localization which coincide with the maximum shear strain directions. These regions probably result from flow softening, whose onset is early in the deformation, and rotate away from the compression axis during ensuing deformation.

When heat treatment of β -microstructure samples is conducted above the beta transus temperature, microstructures identical to those for α -microstructure compression specimens given similar heat treatments are obtained. That is to say, heating at these temperatures leads to a single-phase bcc titanium microstructure of equiaxed grains (whose size depends on heat treatment temperature and time) which reverts to a transformed beta microstructure upon cooling to room temperature (Figure B-9).

Microstructures After Varying Levels of Deformation and Heat Treatment. Investigation of the effects of level of deformation at 899 C (1650 F) and post forging heat treatment at 951 C (1745 F) gave a much clearer idea of the deformation mode during hot forging of the β -preform microstructure and subsequent recrystallization during heat treatment.

Forging deformation at 899 C (1650 F) is inherently non-uniform. In order to characterize the as-forged microstructures, two distinct features must be recognized. These are illustrated in Figure B-10. At the lowest strains, $\epsilon = 0.2$ to 0.3 , the first observable effect of deformation (Figure B-10a) is the occurrence of regions of intense localized shear which results in sharp curvature of the α - and β -platelets in the Widmanstätten microstructure. The number of these regions increases with

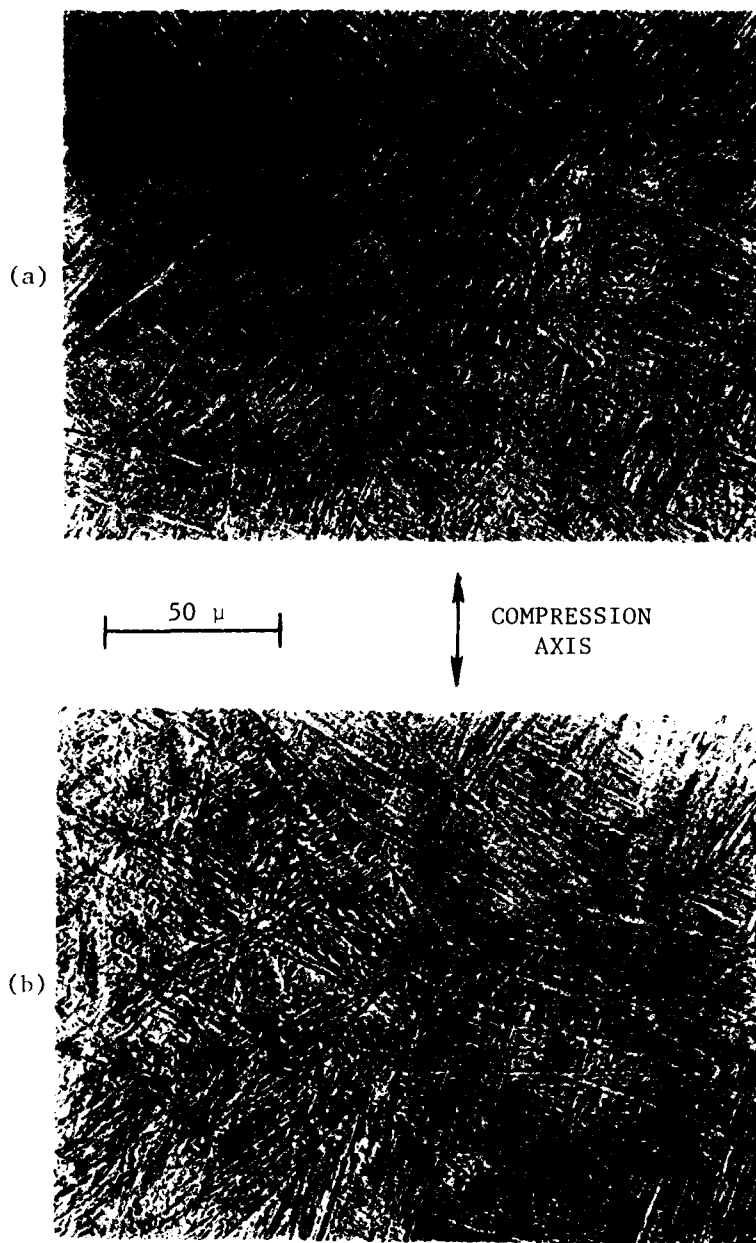


Figure B-9. Microstructures Formed in β Preform Microstructure Material Deformed at 954 C (1750 F) and at Strain Rates of (a) 1 Sec.⁻¹ and (b) 10 Sec.⁻¹ and Subsequently Heat Treated at 1010 C (1850 F) for (a) 15 Minutes and (b) 2 Hours.



Figure B-10a. Region of Intense Localized Shear in α Ti-6242 As-Forged at 899 C (1650 F), $\epsilon = 0.3$.

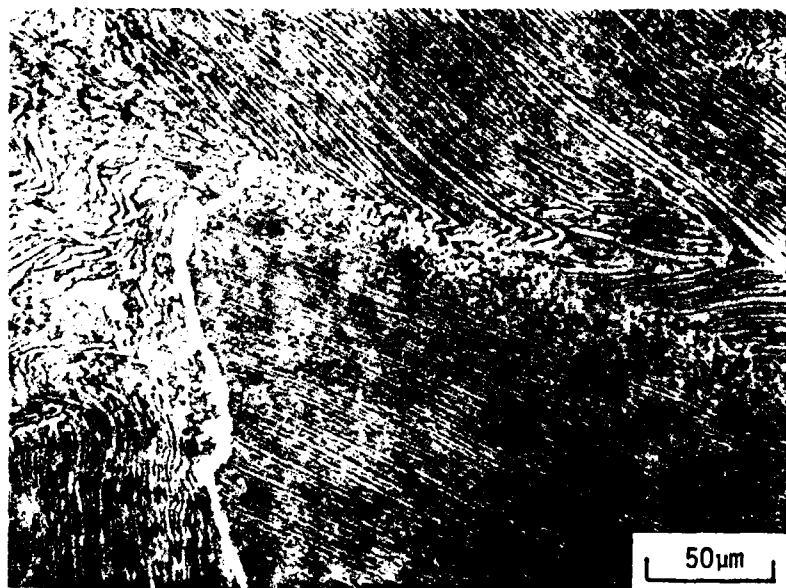


Figure B-10b. Dynamically Recrystallized Boundary in β Ti-6242 As-Forged at 899 C (1650 F), $\epsilon = 0.4$.

strain, although they never occupy more than a small fraction of the specimen volume. It may be that only Widmanstatten colonies of certain orientations with respect to the applied stress are subject to sharp curvature by localized shear.

The second feature (Figure B-10b), which first appears at a strain of approximately $\epsilon = 0.4$, is a breakup of the Widmanstatten microstructure occurring first in narrow regions near the colony boundaries. Since the transformed β -perform microstructure does not revert to an equiaxed microstructure at temperature prior to deformation (note the sheared colonies with curved platelets), this breakup of the Widmanstatten microstructure must be occurring during straining. Hence, it is appropriate to refer to this feature as a dynamic recrystallization.

With further straining the volume fraction of the dynamically recrystallized regions increases. The regions become thicker and occur more frequently. In addition, the highly sheared colonies also occur more frequently particularly near the recrystallized regions. These structures are illustrated at a magnification of 400X in Figure B-11 for strains $\epsilon = 0.7$ and $\epsilon = 1.0$. In Figure B-12, the interaction between sheared and recrystallized regions is shown in two views at a higher magnification, 1000X.

During post deformation heat treatment at 951 C (1745 F), the as-forged microstructures coarsen noticeably. This is observed for all Widmanstatten colonies, not just those with significant recrystallized or sheared regions. The highly sheared regions coarsen to a greater extent, and the curved platelets break up into short, straight sections which remain tangent to the curved directions. This is shown in Figure B-13a. It is the dynamically recrystallized regions which evolve to the equiaxed α - and equiaxed transformed β -grain structure referred to in this work as equilibrium $\alpha+\beta$. This is shown for a small strain case ($\epsilon = 0.4$) in Figure B-13b.

This description remains relevant for the higher strain specimens, with the $\alpha+\beta$ -microstructure which evolves from the dynamically recrystallized regions occupying a proportionately larger fraction of the specimen volume. To illustrate this, heat treated structures

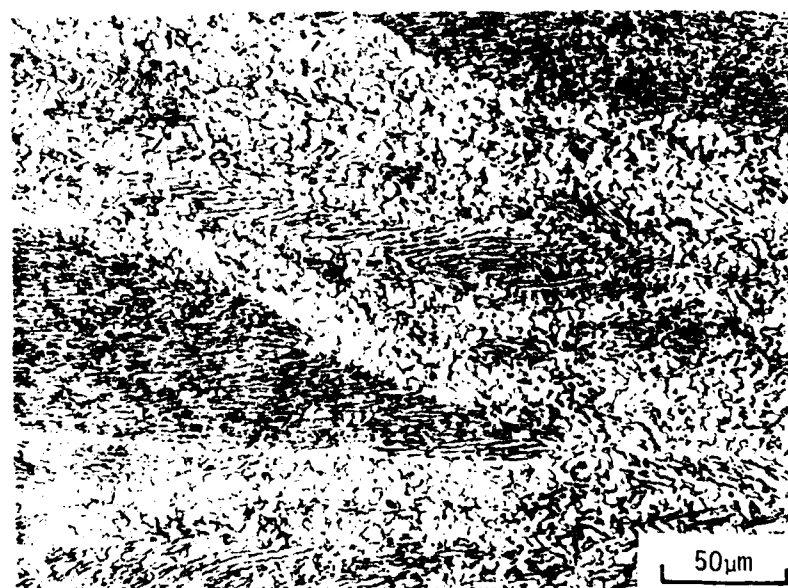


Figure B-11. Recrystallized and Sheared Regions in β Ti-6242 As-Forged at 899 C (1650 F), $\epsilon = 0.7$ (top) and $\epsilon = 1.0$ (bottom).

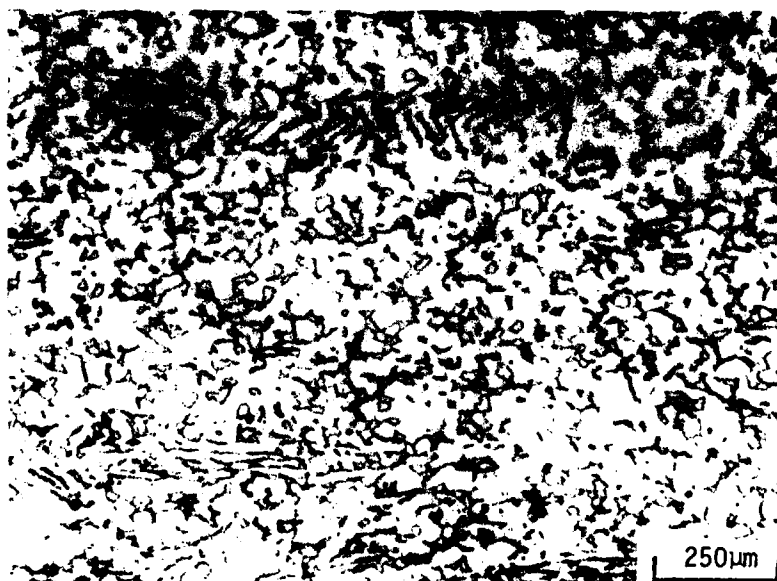
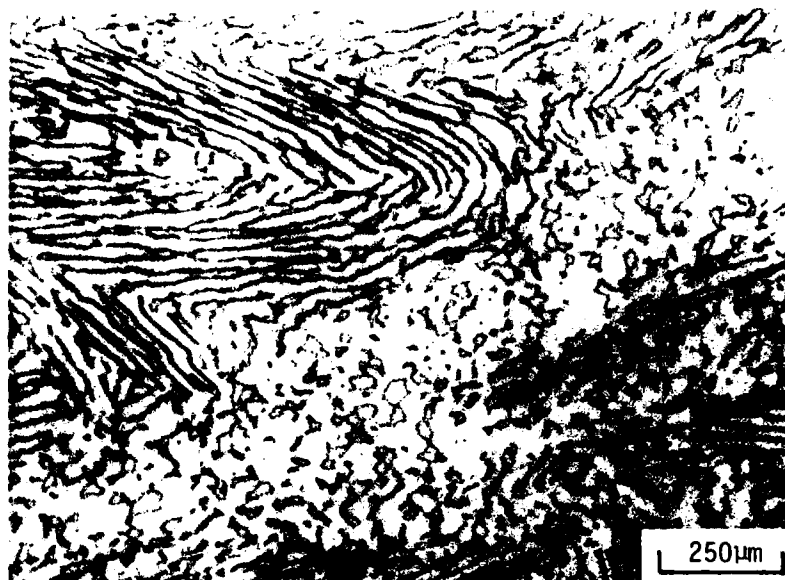


Figure B-12. Interaction of Recrystallized and Sheared Regions in β Ti-6242 As-Forged at 899 C (1650 F), $\epsilon = 1.0$.

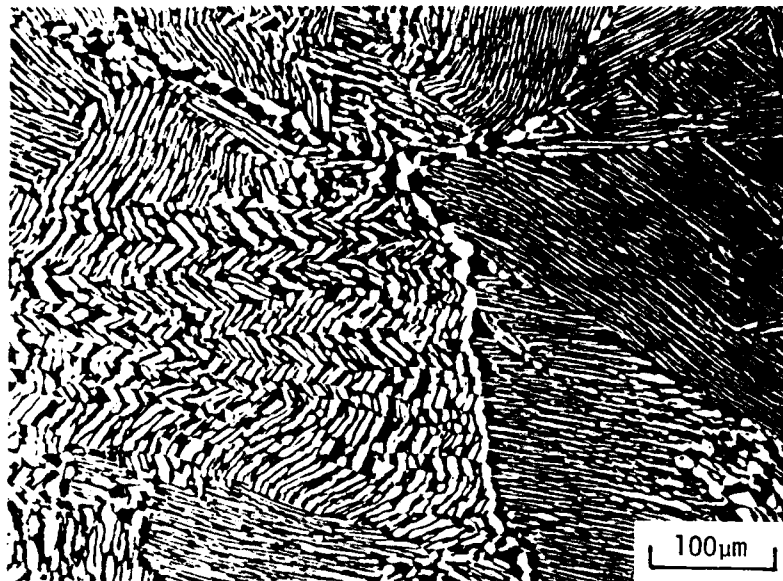


Figure B-13a. Coarsening and Breakup of Sheared Regions in β Ti-6242 Forged at 899 C (1650 F) + 951 C (1745 F)/4 Hr/AC, $\epsilon = 0.3$.

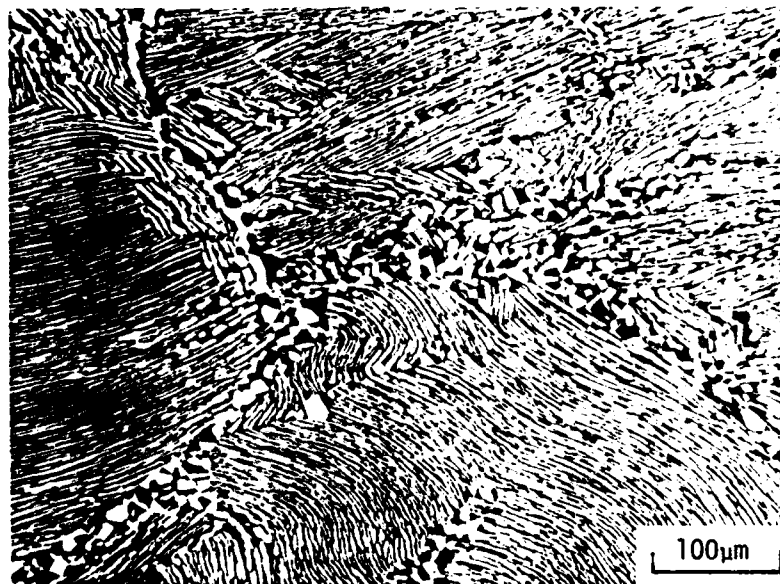


Figure B-13b. Initiation of Equiaxed $\alpha+\beta$ -Structure in β Ti-6242 Forged at 899 C (1650 F) + 951 C (1745 F)/4 Hr/AC, $\epsilon = 0.4$.

at strains of $\epsilon = 0.7$ and $\epsilon = 1.0$ are shown in Figure B-14. It should be noted that, in both Figures B-13 and B-14, the magnification is 200X, a factor of two less than that used in Figures B-10 and B-11 for the as-forged microstructures, illustrating the overall coarsening which takes place during heat treatment outside of the localized regions.

Summary and Conclusions

The effects of heat treatment alone, hot deformation, and the combination of hot deformation and subsequent heat treatment on the microstructures developed in $\alpha+\beta$ - and β -preform samples of Ti-6Al-2Sn-4Zr-2Mo-0.1Si were documented. The following conclusions were drawn:

- Heat treatment of as-received $\alpha+\beta$ -microstructure material below the transus temperature leads to minimal changes in the alpha grain size except at temperatures near the transus ($T \geq 954$ C). However, the morphology of the transformed beta matrix of this microstructure is a function of heat treatment temperature over the observed range of 899 to 982 C (1650 to 1800 F), higher temperatures leading to a refined matrix phase.
- Subtransus heat treatment of as-received β -microstructure material appears to lead to negligible changes in microstructure. It is believed that although there may be alpha platelet reversion during heat treatment, the basic acicular morphology remains the same during heat treatment, and thus during cooling back to room temperature after heat treatment.
- For the $\alpha+\beta$ -microstructure, subtransus deformation or subtransus deformation plus subtransus heat treatment leads to a greater variation of alpha grain size than observed in the heat

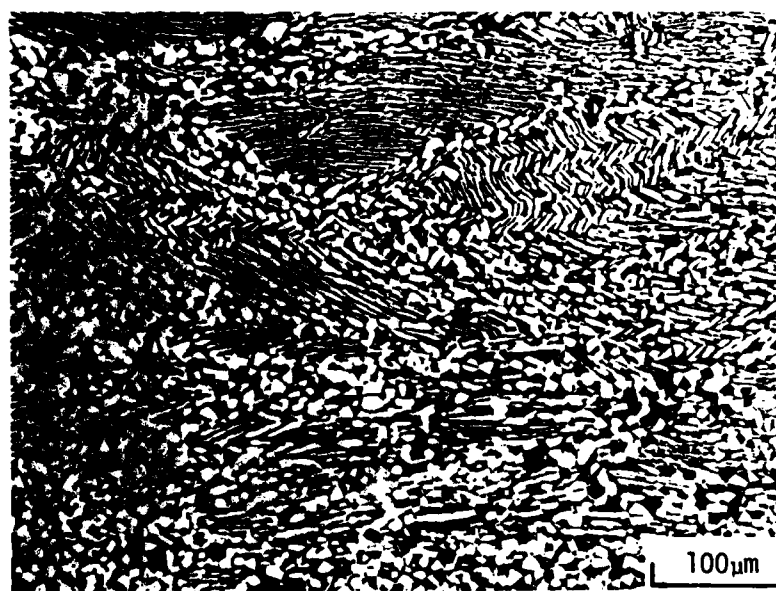
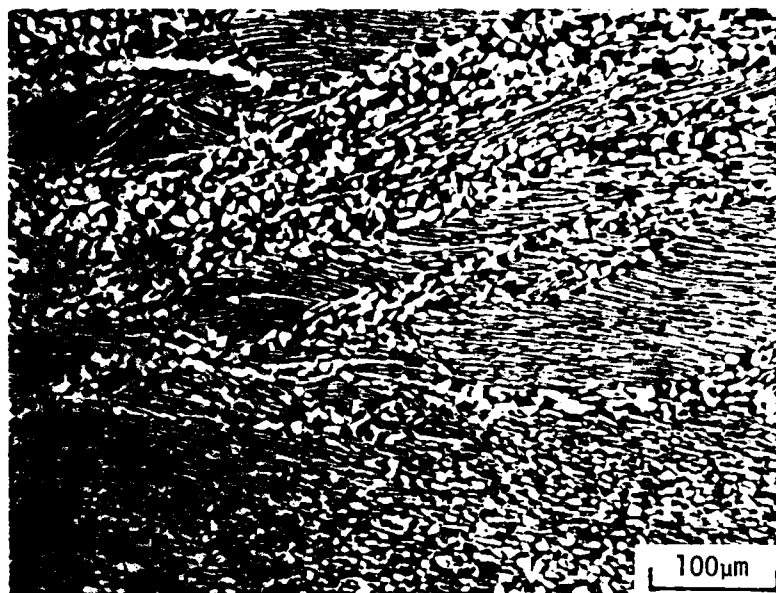


Figure B-14. Development of Equilibrium $\alpha+\beta$ -Structure in β Ti-6242 Forged at 899 C (1650 F) + 951 C (1745 F)/4 Hr/AC, $\epsilon = 0.7$ (top) and $\epsilon = 1.0$ (bottom).

treatment studies. It was concluded that structures containing percentages of globular alpha close to the equilibrium amounts had been developed. This finding is similar to that for previously examined low-strain-rate compression samples and emphasizes the improvement in transformation kinetics brought about by hot work or residual hot work. This hot work also appears to be effective in speeding up the kinetics of the transformation of the beta matrix phase when $\alpha+\beta$ -compression samples are cooled after hot deformation.

- As for low-strain-rate compression, subtransus-high-strain-rate compression of the β -microstructure leads to grossly non-uniform flow, and, at temperatures approaching the beta transus, a phenomenon similar to dynamic recrystallization forms primary alpha. The temperatures at which this latter phenomenon occurs in high-rate deformation are slightly greater than those for low-rate deformation. This trend is analogous to that typically observed in single-phase materials. Heat treatment of high-strain-rate- β -microstructure compression samples after deformation leads to initial recrystallization in the areas of highest deformation followed by general recrystallization at long times, provided the heat treatment temperature is high enough. Gegel⁽⁵⁾ suggests that the lowest practical temperature for heat treatment of the Ti-6242 alloy with the β microstructure is 916 C (1680 F). Present observations support this conclusion.
- The critical strains for die and preform design to make a dual microstructure/dual property disk

using β preform material have been suggested by a series of low-strain-rate β -microstructure compression tests at 899 C (1650 F), followed by heat treatment at 951 C (1745 F). The conclusions from these studies are as follows:

1. At $\epsilon < 0.2$, the as-forged microstructures show no distinct transformations. The transformed β -structure is retained.
2. At $\epsilon = 0.2$ to 0.4 , regions of intense localized shear develop, and these affect the post-deformation heat treatment response.
3. At $\epsilon > 0.4$, regions of dynamic recrystallization, which evolve to the $\alpha+\beta$ -structure during heat treatment, are first observed and increase in size with increasing strain.
4. Strains $\epsilon > 1.0$ are required for the equiaxed $\alpha+\beta$ -structure to predominate after heat treatment.

Since complete transformation to the $\alpha+\beta$ -microstructure does not occur even at $\epsilon = 1.0$, it may be that further investigation of disk processing at forging temperatures in the range 900 to 930 C (1652 to 1706 F) and heat treatment at temperatures in the range 950 to 970 C (1742 to 1778 F) would be worthwhile.

- Deformation or heat treatment of the $\alpha+\beta$ - and β -microstructures above the transus temperature leads to development of transformed beta microstructures of Widmanstätten alpha (slow cooling rate) or martensitic alpha (fast cooling rate).

Acknowledgments

The care and patience taken by Mr. C. R. Thompson, who performed the metallography, and Mr. Ralph Smith, who performed the heat

treatments, are gratefully acknowledged. In addition, thanks are due to Mr. Gary Lewis, Los Alamos Scientific Laboratory, who conducted the high-strain-rate compression tests and supplied the deformed samples to Battelle for metallography.

References

1. Chen, C. C. and Boyer, R. R., "Practical Considerations for Manufacturing High Strength Ti-10V-2Fe-3Al Alloy Forgings", *Journal of Metals*, Vol 31, No. 7, 1979, pp. 33-39.
2. Cox, T. B. and Low, J. R., "An Investigation of the Plastic Fracture of AISI 4340 and 18 Nickel-200 Grade Maraging Steels", *Met. Trans.*, Vol 5, 1974, pp. 1457-1470.
3. Chen, C. C., "Metallurgical Fundamentals to Ti-6Al-2Sn-4Zr-2Mo-0.1Si Alloy Forgings. I. Influence of Processing Variables on the Deformation Characteristics and Structural Features of Ti-6242 Si Alloy Forgings", Report RD-77-110, Wyman-Gordon Company, North Grafton, Massachusetts, October, 1977.
4. Hammond, C. and Nutting, J., "The Physical Metallurgy of Superalloys and Titanium Alloys", in *Forging and Properties of Aerospace Materials*, The Metals Society, London, 1978, p.75.
5. Lahoti, G. D. and Altan, T., "Research to Develop Process Models for Producing a Dual Property Titanium Alloy Compressor Disk", Technical Report AFWAL-TR-80-4162, Battelle's Columbus Laboratories, Columbus, Ohio, October, 1980.
6. Reed-Hill, R. E., *Physical Metallurgy Principles*, Second Edition, Van Nostrand Company, New York, Chapter 18, 1973.
7. Williams, J. C., Carnegie Mellon University, Pittsburgh, Pennsylvania, Private Communication, 1981.
8. Jonas, J. J., McGill University, Montreal, Quebec, Private Communication, 1981.
9. Weiss, I. and Jonas, J. J., "Interaction Between Recrystallization and Precipitation During High Temperature Deformation of HSLA Steels", paper presented at AIME Symposium on "Recrystallization and Grain Growth in Materials", Chicago, Illinois, October, 1977.
10. Semiatin, S. L., Lahoti, G. D., and Altan, T. A., "Determination and Analysis of Flow Stress Data for Ti-6242 at Hot Working Temperatures", *Process Modelling: Fundamentals and Applications to Metals*, T. Altan, H. Burte, H. Gegel, and A. Male, eds., American Society for Metals, Metals Park, Ohio, 1980, pp. 387-408.

11. Dadras, P. and Thomas, J., "Compressive Plastic Instability and Flow Localization in Ti-6242", *Res Mechanica Letters*, Vol 1, No. 3, 1981, pp. 97-103.
12. Abson, D. J. and Jonas, J. J., "Hot Compression Behavior of Thermo-mechanically Processed Alpha Zirconium", *Metals Technology*, Vol 4, 1977, pp. 462-468.

APPENDIX C

EVALUATION OF PROCESSING-MICROSTRUCTURE-
PROPERTY RELATIONSHIPS FOR Ti-6242 Si

J. E. Allison and J. C. Williams
Carnegie-Mellon University
Pittsburgh, Pennsylvania 15213

and

S. L. Semiatin
Battelle's Columbus Laboratories
Columbus, Ohio 43201

APPENDIX C

EVALUATION OF PROCESSING-MICROSTRUCTURE- PROPERTY RELATIONSHIPS FOR Ti-6242 Si

Introduction

A central question in the design and fabrication of a dual property compressor disk is the selection of microstructures which optimize the performance of the component at the different locations. Such selection is predicated on a detailed understanding of the dependence of second tier properties such as creep and fatigue on microstructure. In general, such an understanding does not exist and further work is required to establish such information. The work reported here was done with this in mind.

The effect of microstructure on creep properties (as well as tensile properties) has been documented previously in the ongoing project (Appendix E of the Second Annual Interim Technical Report). The objective of the present effort has been to obtain a detailed understanding of the low-cycle fatigue (LCF) behavior as well as fatigue-crack-growth (FCG) response of various microstructures which can be produced in the program alloy, Ti-6Al-2Sn-4Zr-2Mo-0.1Si (Ti-6242). To this end, fatigue tests were conducted in air at 510 C (950 F), the aim operating temperature of the dual property compressor disk. These tests were done by Carnegie-Mellon University (FCG) and Metcut Research Associates, Inc. (LCF). In addition, a more detailed look into Ti-6242 microstructures was pursued via transmission- and scanning-electron microscopy (as well as optical metallography). This work was also performed by Carnegie-Mellon University. Before reviewing this work, however, a review of some of the important concepts of processing-microstructure-property relationships will serve to put the present work into a proper perspective.

Background

This section contains a brief summary of the relevant aspects of titanium alloy physical metallurgy. It is not intended to be an exhaustive

review, but rather to summarize the conventional wisdom regarding trends in microstructure/property relations. Readers interested in a more detailed treatment are referred to other reviews.(1-5)

Alloying Behavior

The microstructure and equilibrium constitution of titanium alloys is strongly influenced by the alloying additions which are present. Alloying elements in Ti can be classified into three groups according to their effect on the α/β -allotropic transformation temperature. Those which suppress it stabilize the high temperature β -phase and are known as β -stabilizers; conversely, those which increase the transformation temperature stabilize the low temperature α -phase and are known as α -stabilizers. There is a third group of elements which have essentially no effect on the allotropic transformation temperature and these are known as neutral elements. Prominent examples of β -stabilizers include Mo, V, Fe, Cr, and Mn, while the most important α -stabilizers are aluminum and oxygen. Neutral elements include Sn and Zr, although in the presence of other β -stabilizers both of these elements tend to also act as moderately weak β -stabilizers.

As an extension of the above, it is often useful to characterize or classify titanium alloys according to their equilibrium constitution. Those alloys which are essentially 100 percent α -phase and which contain no β -stabilizing elements as deliberate alloying additions are known as α -alloys. Those which contain a mixture of the α - and β -phases are known as α/β -alloys and those alloys in which the β -phase can be retained (albeit metastable) by quenching from the β -phase field to room temperature are known as β -alloys. It is worth commenting in the latter context that these alloys should be called metastable β -alloys and, therefore, the common terminology (β -phase alloy) represents something of a misnomer. The balance of this review will deal with α/β -alloys because it is this type of alloy (Ti-6242) which is dealt with.

Heat Treatment

The effect of heat treatment on the microstructure of a given α/β -alloy is determined by the temperature at which the alloy is heated and the

rate at which it is subsequently cooled. After cooling there are often additional aging treatments which are applied either to stabilize the microstructure or to produce additional decomposition of the transformation products. These aging treatments will be described later.

The most common heat treatments for alloys such as Ti-6242, which have very moderate β -stabilizer content, are annealing treatments which affect the volume fractions of the equilibrium or primary α and the α/β -mixture which forms as a transformation product on cooling. For example, a heat treatment in which the alloy is reheated into the β -phase field and air cooled is known as β -annealing because the resulting microstructure is fully transformed to a Widmanstätten structure with no remnant primary α . Other treatments which involve heating into the two-phase $\alpha+\beta$ -region are known as duplex annealing because they lead to a duplex microstructure consisting of coarse primary α and a finer α/β -mixture which results from decomposition of the β -phase during cooling. As will be briefly described in the property section below, the morphology of the constituents and their volume fractions affect second tier properties such as tensile ductility, fracture toughness, and fatigue performance to a significant extent. Thus, although alloys like Ti-6242 are ostensibly not considered to be heat treatable because the strength cannot be varied over a significant range, the effects of heat treatment on second tier properties are still very important and worthy of detailed consideration when selecting a processing or subsequent heat treatment scheme.

The other variable mentioned above, which has not been discussed, is cooling rate. On very rapid cooling (e.g., water quenching) the β -phase can transform to a martensitic product which has a fine, acicular morphology. This product is supersaturated with respect to β -stabilizing elements (Mo in the case of Ti-6242). The subsequent aging of this martensitic product results in equilibration by precipitation of β -phase as will be described in somewhat more detail below. In alloys which contain more β -stabilizing elements, especially Mo and Nb, an orthorhombic martensite (α'') can be formed. If α'' forms in Ti-6242, it does so under very particular circumstances and in limited volume fractions. Thus, it will not be discussed further here.

Since the Widmanstätten structure forms by nucleation and growth, it competes with the heterogeneous nucleation and growth of α at prior β -grain

boundaries. The kinetics of the latter process are very fast and thus β -annealing followed by air cooling typically leads to an essentially continuous layer of grain boundary α . Examples of this are seen in the colony microstructures described in the results and discussion section below.

The aging reactions that are relevant to the heat treatment and/or subsequent elevated temperature use of Ti-6242 are threefold: decomposition of α to form α_2 , decomposition of martensitic α' to form $\beta + \alpha$, and decomposition of metastable β to form $\alpha + \beta$.

The α_2 phase forms as an ordered, coherent precipitate which has a composition based on Ti_3Al and has a DO_{19} structure. In alloys which contain Sn, this alloying element also contributes to α_2 formation. This is because Ti_3Sn also has a DO_{19} structure. Thus, in alloys which contain both Al and Sn, the α_2 forms with a composition $\text{Ti}_3(\text{Al}, \text{Sn})$. The maximum temperature for α_2 formation in Ti-6242 depends on oxygen content and exact alloy composition, but is generally $\sim 550^\circ\text{C}$ (1022°F). Thus it is not surprising that no α_2 was seen in the heat treated samples examined in this study, but α_2 may still form during long time exposure to $\sim 500^\circ\text{C}$ (932°F) in service.

The tempering or aging of α' proceeds by the nucleation and growth of bcc β -phase precipitates which are rich in β -stabilizing elements (mainly Mo in this case). Because the α' has a dense substructure, the β -precipitates are largely heterogeneously nucleated at martensite plate boundaries and at dislocations. These precipitates tend to stabilize the structure from further changes during elevated temperature exposure, but are too widely spaced and too inhomogeneously distributed to contribute significantly to the strength.

The β -phase which is present in the transformed regions of the matrix can be lean in Mo compared to the equilibrium composition at $\sim 595^\circ\text{C}$ (1100°F). Thus, during aging this β -phase can further decompose by nucleation and growth to produce fine particles of Mo lean α in a β -matrix which is consequently enriched in Mo. This reaction tends to strengthen the β -phase, but because of its low volume fraction, this has little effect on the overall properties. It does, however, stabilize the microstructure against further changes during elevated temperature service.

Thermomechanical Processing

In addition to heat treatment effects, the microstructure of α/β -Ti alloys can be altered by combined thermal and mechanical treatment. This is frequently called thermomechanical processing (TMP). The principal effect of TMP in α/β -alloys is to alter the morphology of the α -phase. This is typically accomplished by mechanically working the alloy at a temperature in the $\alpha+\beta$ -phase field. For Ti-6242 this temperature range is typically 815-970 C (1500-1775 F). Such working deforms the Widmanstätten α -plates which are present after cooling from the β -phase field. These plates then undergo a recrystallization reaction and assume a globular or at least lower aspect ratio morphology. This α -phase morphology can be seen in the micrographs of the bimodal microstructure* shown later in this report. The globular α -phase has less interfacial area per unit volume, and this characteristic affects the mechanical properties as will be discussed below.

Microstructure/Property Relations

As stated earlier, the principal effect of microstructure on the properties of Ti-6242 is reflected in the second tier (fracture-related) properties. This is because Ti-6242 is not considered to be heat treatable, and, thus, the strength does not vary over a significant range as a function of heat treatment. The microstructural variations which can be achieved in this alloy have been described above and are illustrated in the microstructure section of the results and discussion. The principal fracture-related properties of interest are tensile ductility, fracture toughness, creep and fatigue resistance (both crack initiation and crack propagation). In this section the general role of microstructure in affecting these properties will be described briefly.

The principal factor which affects tensile ductility of α/β -alloys is the morphology of the α -phase. In alloys which have been $\alpha+\beta$ -processed to produce equiaxed microstructures, the ductility is substantially higher compared

*In other sections of this Interim Report, this is referred to as the $\alpha+\beta$ -microstructure.

to the Widmanstätten or colony α/β -microstructures in β -annealed or β -processed material. The primary reason for this is the difference in the area of α/β -interface per unit volume in these two microstructural conditions. In the Widmanstätten or colony microstructures the α/β -interface density is much higher. These interfaces act as sites for void nucleation and, therefore, lead to a large number of void nuclei at relatively low strains. Since titanium alloys exhibit relatively little work hardening, the strain to produce coalescence of these voids is relatively constant. As a result, the ductility depends critically on the propensity for nucleation of voids which in turn scales with the α/β -interface density. Thus, the equiaxed α -microstructures have the best tensile ductility in alloys such as Ti-6242.

The fracture toughness of α/β alloys, especially lower strength ($\sigma_y < 1050\text{MPa}$) alloys, is typically much higher in the β -processed condition. The reasons for this seem to be the much more irregular crack path in the colony or Widmanstätten microstructure. The frequent redirection of the crack front apparently increases the rate of energy dissipation per unit crack extension compared to the equiaxed or $\alpha+\beta$ -processed condition. It is interesting to note that $\alpha+\beta$ -processed microstructures which have a high volume fraction of Widmanstätten α -structure show little if any improvement in toughness compared to equiaxed α -structures. This is apparently due to the finer microstructural scale which does not promote an irregular crack path. Once the alloy is heated above the β -transus, however, the β -grain size grows rapidly. It is this grain size increase which leads to a coarser microstructure and a more irregular crack path. Thus, in alloys such as Ti-6242 the fracture toughness is highest in the β -processed or β -annealed microstructure.

Creep strength of alloys such as Ti-6242 is substantially increased by the addition of Si. It appears that the optimum amount is ~ 0.08 weight percent although up to 0.25 Si is used in other, similar alloys. The role of Si seems to be that of forming atmospheres (or even small precipitates) along the mobile dislocations and retarding their motion by a solute drag mechanism.⁽⁶⁾ Microstructure also affects creep, but the reasons are not so well understood. For example, the elongated α -morphology microstructures generally have better creep resistance than equiaxed α -microstructures, while colony microstructures seem to be the most creep resistant. These results suggest that α/β -boundary sliding

is also important in creep of these alloys but the details of this and its importance relative to thermally activated dislocation glide are not clear at present. Nevertheless, the best creep strength is obtained in Ti-6242 with a colony microstructure.

The fatigue performance of α/β -Ti alloys is very sensitive to microstructure, but different measures of fatigue performance such as fatigue life and fatigue crack growth rate do not vary in the same way with microstructure. The unifying concepts appear to be slip length and slip reversibility.⁽⁷⁾ Microstructures which have long slip lengths tend to promote early crack initiation, but tend to also exhibit good slip reversibility. In the presence of a crack, the extent of slip reversibility at the crack tip controls the amount of permanent damage which accumulates in each cycle. Thus, microstructures which have long slip lengths and good slip reversibility tend to exhibit slower crack growth rates. In the cases of Ti-6242 equiaxed α/β -microstructures exhibit the best fatigue life, whereas colony microstructures have the best fatigue crack propagation resistance. This dilemma places an additional burden on the component designer who must decide whether to design to crack initiation or to crack growth.

Materials and Experimental Procedures

Material for microstructural characterization and fatigue testing was obtained from pancake forgings made by Wyman-Gordon Company. Six material conditions were examined; the histories of these are summarized in Table C-1. These six conditions were selected after an extended examination of more than thirty forging/heat treatment cycles and were surmised (through tensile and creep tests) to include the range of properties desired in a dual property compressor disk. From Table C-1 it can be seen that the six conditions differ both in forging history and in subsequent heat treatment practice, although all six were given the same final aging treatment (1100 F/8 hr/air cool). The effect of these variations in processing and thermal history was to alter the morphology and volume fractions of the various microstructural constituents as has been described above in the background section. Each of these conditions were sectioned and prepared for metallographic examination by electropolishing in a solution

Table C-1. Thermomechanical Processing Of Ti-6242

Serial Number	Preform	Forging*	Solution** Treatment	Microstructure
1B	$\alpha + \beta$	$\alpha + \beta$ (β_T -40F)	β /AC (β_T +130F/1h)	Colony
2B	$\alpha + \beta$	$\alpha + \beta$ (β_T -115F)	β /AC (β_T +130F/1h)	Colony
4B	$\alpha + \beta$	β (β_T +60F)	$\alpha + \beta$ /AC (β_T -20F/1h)	Coarse Lamellar
1C	$\alpha + \beta$	$\alpha + \beta$ (β_T -40F)	$\alpha + \beta$ /AC (β_T -20F/1h)	Bimodal
6C	β	$\alpha + \beta$ (β_T -40F)	$\alpha + \beta$ /AC (β_T -20F/1h)	Elongated α (high vol. %)
6D	β	$\alpha + \beta$ (β_T -40F)	$\alpha + \beta$ /WQ (β_T -20F/1h)	Elongated α (low vol %)

* β_T = 1815 F, AC from forging.

**Followed by aging at 1100 F/8h/AC.

consisting of 93-3/4 percent methanol, 5 percent H_2SO_4 , 1-1/4 percent HF and polished in a Buehler recirculating pump cell at approximately 23 volts open circuit. The samples were etched in Kroll's etch (95 percent H_2O , 2 percent HF, 3 percent HNO_3) for optical metallographic examination. Subsequent to metallographic examination, they were re-etched to produce greater surface relief for examination in the SEM. Thin foils for TEM were prepared using the dual jet technique. To do this, thin sections were prepared with a diamond saw, mechanically ground to about 6 mils (150 μm), and then 3-mm-diameter disks were mechanically punched. These disks were electro-thinned in the dual jet apparatus at about -50 C (-58 F) using an electrolyte consisting of 60 parts methanol, 34 parts butanol, and 6 parts perchloric acid, at a voltage of about 20 volts open circuit. The thin foils were examined in a JEOL JEM120CX. The SEM metallography and the fractographic results (on fatigue-crack-growth specimens) were obtained by examining the specimens in a JEOL JSM35U. Fractographic examination was performed on regions of the specimen which corresponded to three crack growth rates.

Low-cycle-fatigue tests were run under strain control using a triangular waveform of 0.33 Hz. The specimens had smooth, round gage sections measuring 6.45-mm (0.25-in.) diameter by 19.35-mm (0.75-in.) long. The tests were done in air at 510 C (950 F) using strain amplitudes of 0.8 percent and 1.6 percent. A few tests were run at other strains, but the fatigue-life data from these tests were interpolated to these two strain levels to allow direct comparison of the data for all six forging/heat treatment conditions.

Fatigue crack growth experiments were conducted using an 89 KN (20,000 lb) servohydraulic test system. The compact specimen geometry was used with $H/W = 0.6$, $W = 63.5$ mm, and thickness, B , of 9.5 mm. The test system was equipped with a resistance furnace for radiation heating of the specimen. All tests were performed in laboratory air at a test temperature of 510 C (950 F), at a cyclic frequency of 30 Hz and an R-ratio (P_{min}/P_{max}) of 0.1. Compact specimens were machined from the pancake forgings such that the FCG direction was in a radial direction.

Crack lengths were measured using a hybrid electric potential-optical technique. The crack length was periodically measured using a 30X travelling microscope. These optical measurements were made at temperature during cycling using stroboscopic illumination through quartz windows in the furnace. An electric potential technique⁽⁸⁾ was used to interpolate between these periodic optical measurements using a constant 15 ampere current level. Care was taken to reduce thermal emf gradients and fluctuations by proper furnace design and the use of titanium wires and mechanical couplings for monitoring the electric potential change.

Low crack growth rates were achieved using load-shedding, ΔK decreasing, procedures which conformed to ASTM E-647-78T.⁽⁹⁾ An attempt was made to achieve growth rates as low as 1×10^{-9} m/cycle. However, in general, this was unsuccessful as will be described in the results section. Upon reaching the low growth rate regime the tests were continued under constant load, ΔK increasing, conditions. Crack growth rates were determined using the direct secant method.⁽⁹⁾ Data smoothing was not performed, except that inherent to the electric potential technique.

Results

Microstructures

The microstructures of the six conditions are presented in Figures C-1 through C-6. The condition number shown in the captions of these figures correspond to those in Table C-1 from which the forging and heat treatment history can be obtained. From Figures C-1 to C-6, it can be seen that the six conditions can be subdivided into four groups so that the conditions in each group have some microstructural similarity. Both conditions shown in Figures C-1 and C-2, for example, are β -solution treated and exhibit grain boundary α at prior β -boundaries and a colony microstructure. This type of microstructure has been discussed in general in the earlier section. Here it is worth noting that the colonies represent groups or packets of plates of α , all of which have the same orientation with respect to the parent β -phase. As a result, the effective

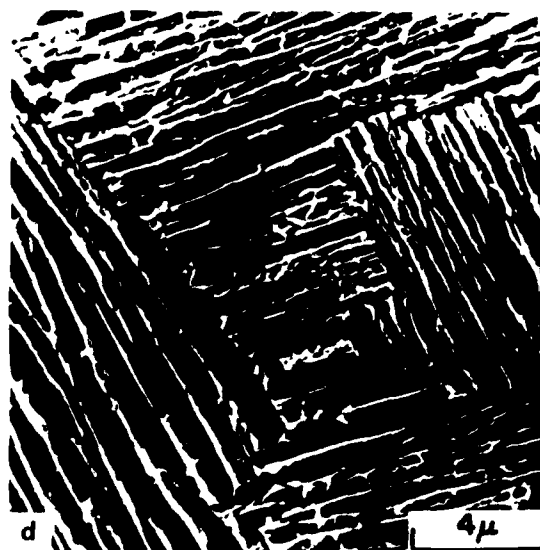
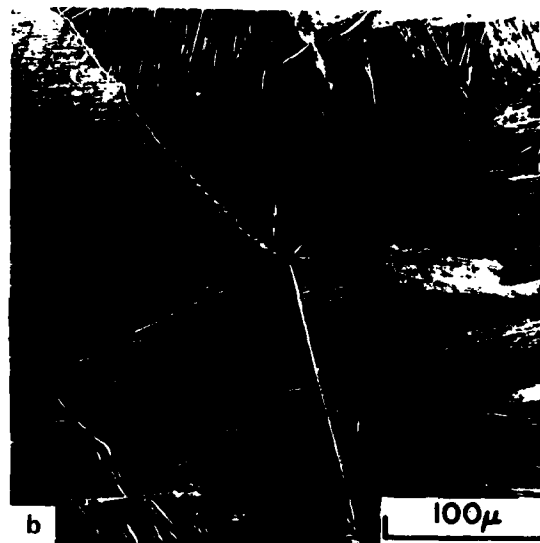


Figure C-1. Microstructure of Condition 1B; Light Microscopy (a,b) and Scanning Electron Microscopy (c,d)

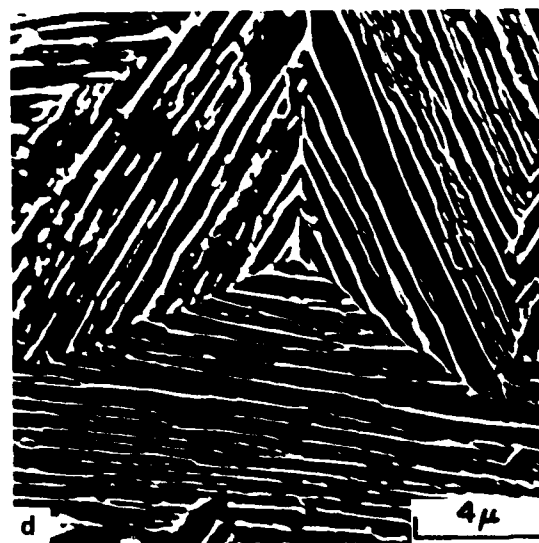
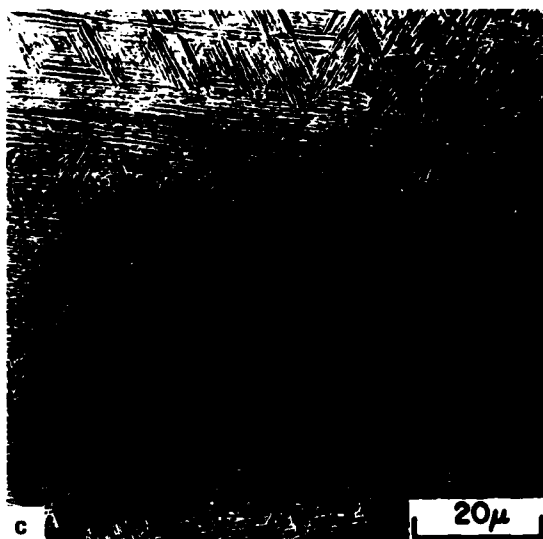
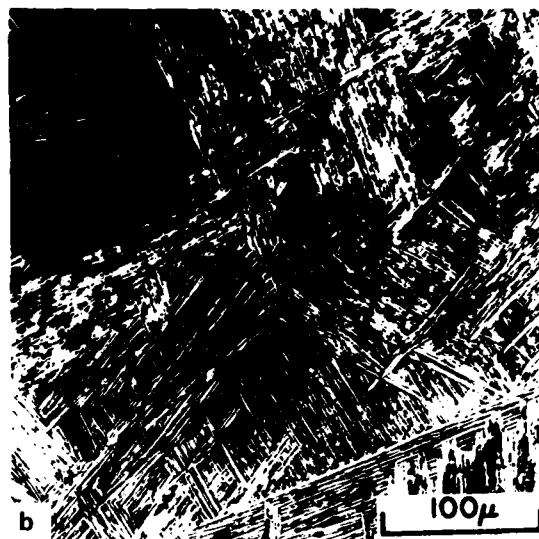
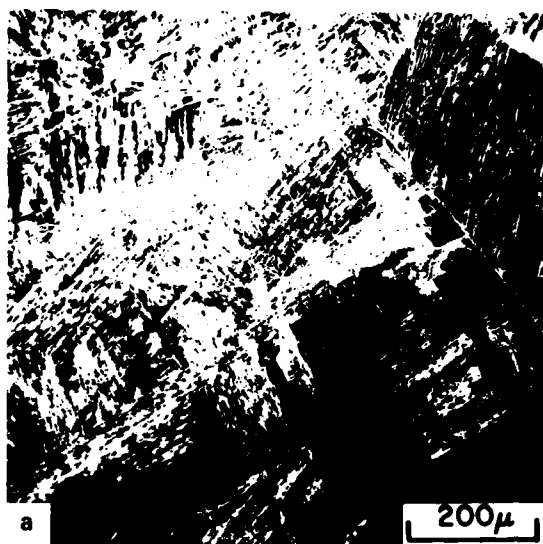


Figure C-2. Microstructure of Condition 2B; Light Microscopy (a,b) and Scanning Electron Microscopy (c,d)

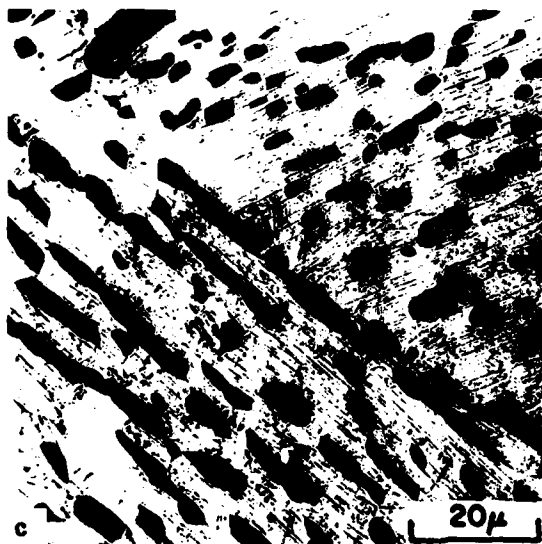
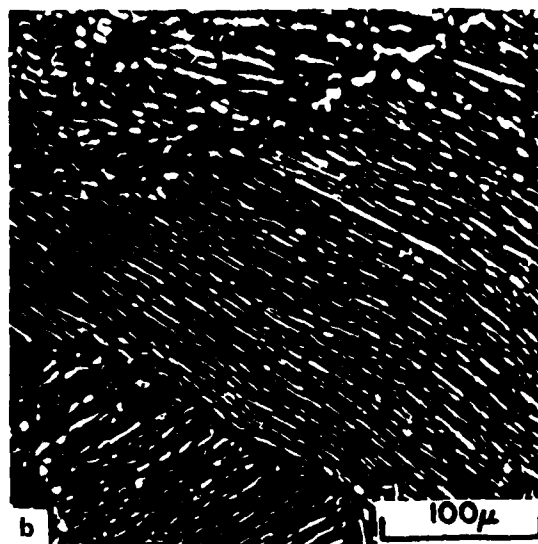
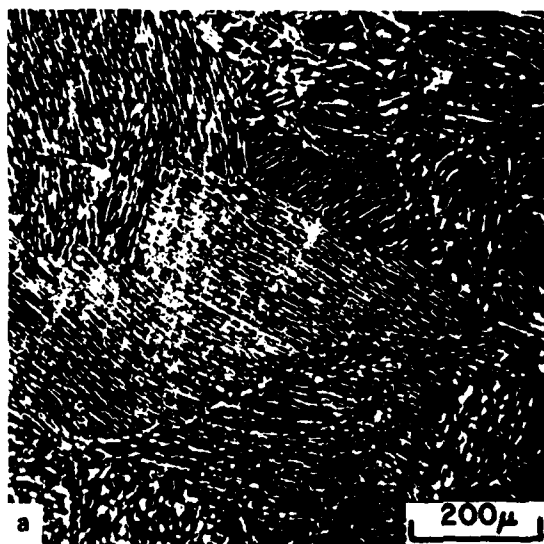


Figure C-3. Microstructure of Condition 6D; Light Microscopy (a,b) and Scanning Electron Microscopy (c,d)

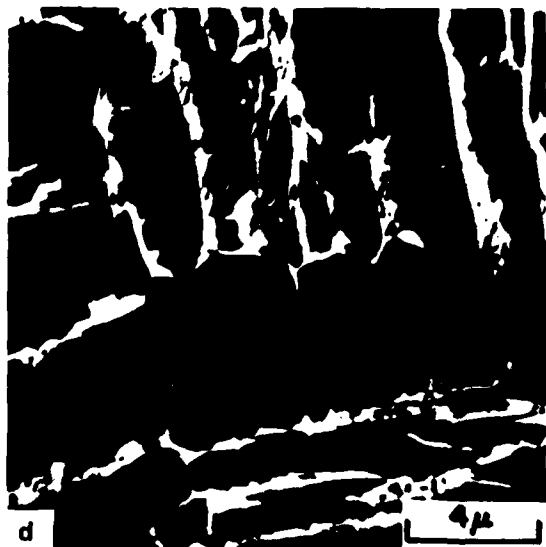
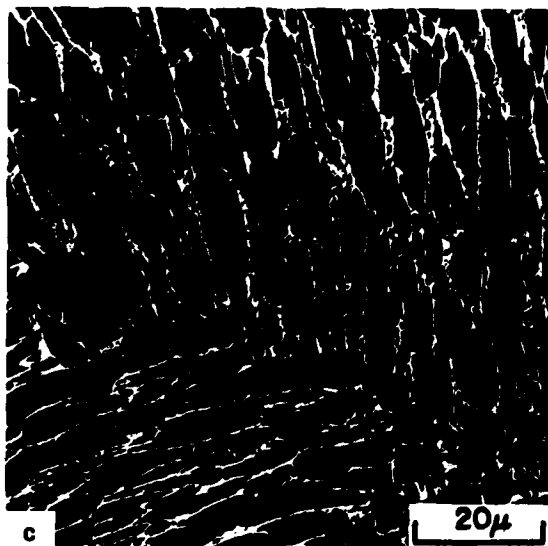
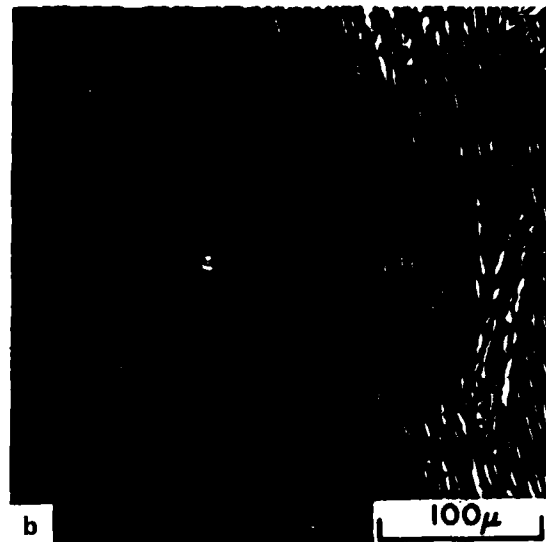
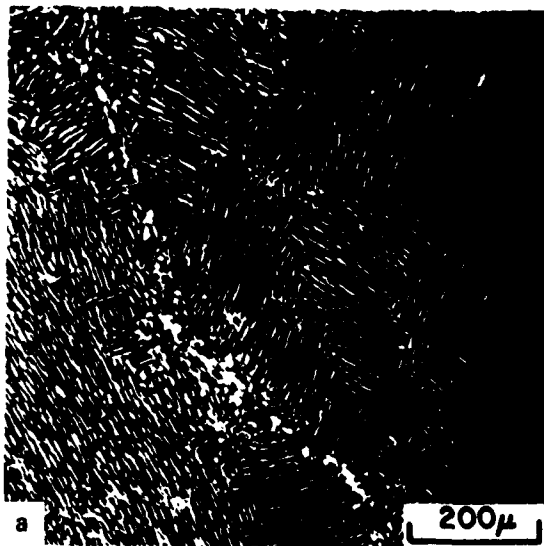


Figure C-4. Microstructure of Condition 6C; Light Microscopy (a,b) and Scanning Electron Microscopy (c,d)

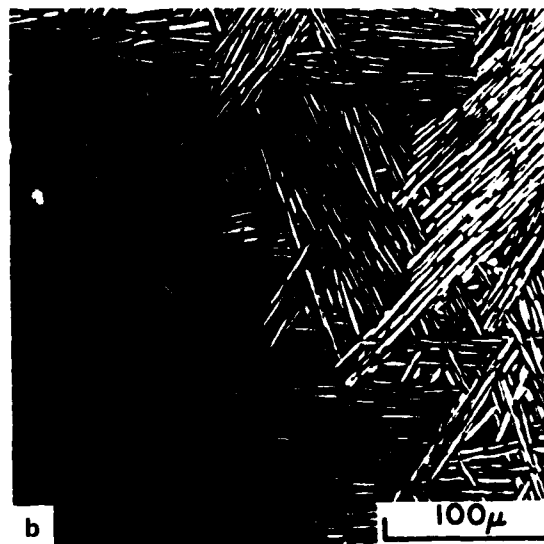
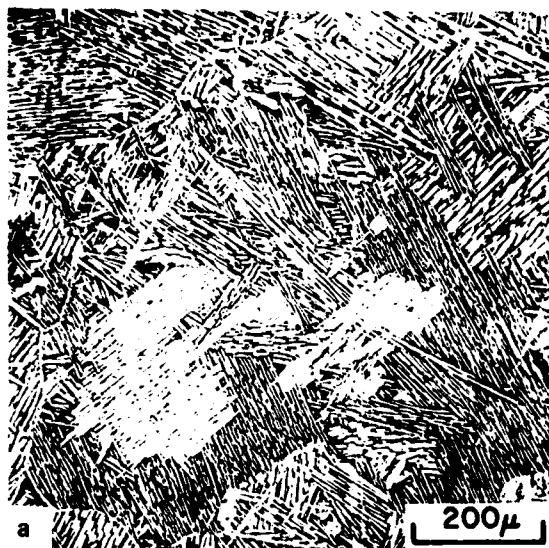


Figure C-5. Microstructure of Condition 4B; Light Microscopy (a,b) and Scanning Electron Microscopy (c,d)

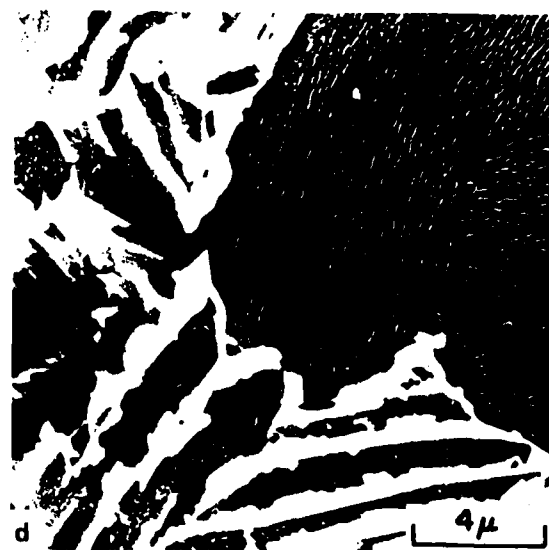
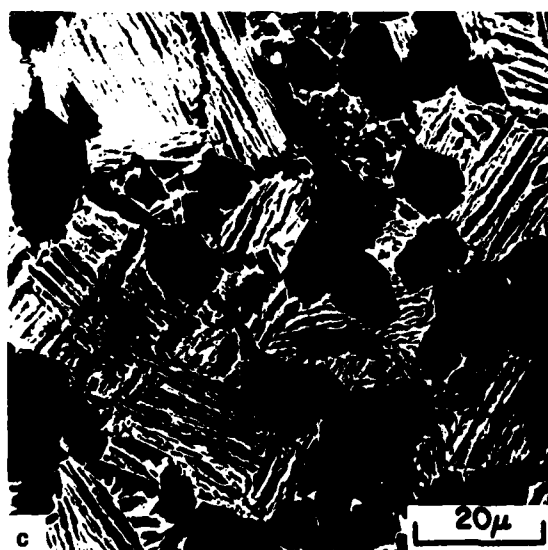
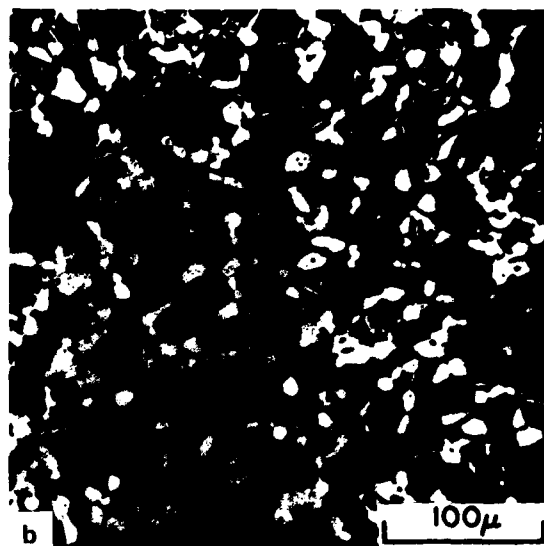
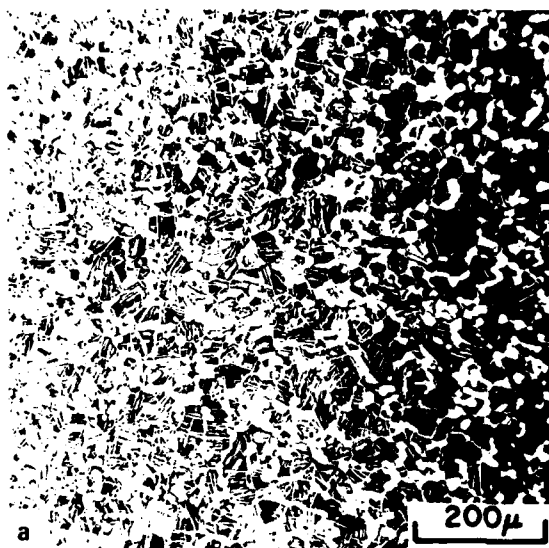


Figure C-6. Microstructure of Condition 1C; Light Microscopy (a,b) and Scanning Electron Microscopy (c,d)

slip length in this microstructure is the colony size rather than the individual platelet size or the prior β grain size. As was discussed in the background section, the relationship between slip length and slip reversibility is important, and thus this point should be borne in mind. The SEM metallography of these microstructures, which also is shown in Figures C-1 and C-2, is helpful for visualizing the microstructure at higher magnifications. In these micrographs the thin ribs which have a bright contrast are the β -phase, whereas the grey, broader regions are α . This contrast is basically reversed from that seen in the light micrographs where the thin β -regions essentially lie within the dark etching boundaries and are not resolvable.

The next two conditions are shown in Figures C-3 and C-4 and can be generally described as elongated primary α -microstructures in which the volume fraction of elongated primary α has been altered by varying the cooling rate from the solution treatment temperature. In each of these microstructures, the primary α is still very much elongated, although each condition has received some α/β -work. The principal difference lies in the cooling rate from the solution treatment temperature which is 11 C (20 F) beneath the β -transus. Condition 6D, Figure C-3, was quenched from the solution treatment temperature and, as a result, the β -matrix transformed martensitically during quenching. This matrix etches as a generally nondescript grey in the light micrographs, but can be seen to consist of a fine lamellar structure in the SEM micrographs. The average slip length of this microstructure is somewhat smaller than the primary α -grain size, to account for the very short slip length when the crack tip is within the tempered martensite regions. On the other hand, condition 6C was air cooled from the solution treatment temperature and the elongated primary α grew epitaxially during this air cooling operation. As a result, the volume fraction of elongated α is substantially higher in this condition, and the matrix tends to be relatively thin regions of β -phase as can be better seen in the SEM micrograph. The principal difference between condition 6C (Figure C-4) and conditions 1B or 2B is the aspect ratio of the elongated α . The aspect ratio of the elongated α in condition 6C is less than it is in the β -treated conditions which reflects the effect of α/β -working on primary α -morphology. At first glance, the slip length of this microstructure appears to be the colony size, which is comparable to, although slightly smaller than, that of condition 1B. However, as will be seen in transmission electron microscopy, the thin β -regions

have decomposed to a random α/β -mixture during the aging treatment. Thus, the individual plate dimensions may be a more appropriate measure of the slip length.

The final two conditions are not particularly similar and, therefore, will be individually discussed. The first of these is condition 4B (Figure C-5) which has been β -forged and $\alpha+\beta$ -solution treated, leaving an elongated α morphology in a β -phase matrix which is essentially interconnected. The amount of β -phase and the morphology of the α can be seen to be intermediate to the β -treated material and the $\alpha+\beta$ treated conditions described earlier. Much like condition 6C, the slip length of this microstructure appears to be the colony size, which is slightly smaller than that of conditions 1B and 6C. However, as will be seen in transmission electron microscopy the thin β -regions have actually decomposed to a random α/β -mixture during the aging treatment. Thus the individual plate dimension may be a more appropriate measure of the slip length.

The last condition (condition 1C) is an $\alpha+\beta$ -forged, $\alpha+\beta$ -solution treated condition which consists of equiaxed primary α in a lamellar α/β -matrix. This is shown in Figure C-6. From the SEM micrographs contained in this figure, the details of the lamellar α/β -regions can be seen more clearly. These micrographs show that the matrix in this condition is similar to that seen in condition 1B or 2B, except that it occurs on a finer scale reflecting the smaller dimensions of the prior β regions. Some continuous α at sub-boundaries in the β -matrix can also be seen, particularly in the light micrographs of Figure C-6. The slip length in this microstructure is nominally the average between the equiaxed α -grain size and the transformed β -colony size.

These six conditions have also been examined by TEM, and the results of this examination are summarized in Figures C-7 through C-12. The TEM microstructure of condition 1B is shown in Figure C-7 from which the long lamellar α and the narrow β -regions can be clearly seen. In addition, in Figure C-7b a region of grain boundary α can be seen. It is interesting to note in this case that the lamellar α on one side of the boundary has grown epitaxially from the grain boundary α whereas there is a continuous film of β along the boundary on the other side. The other microstructural feature of interest is the irregular

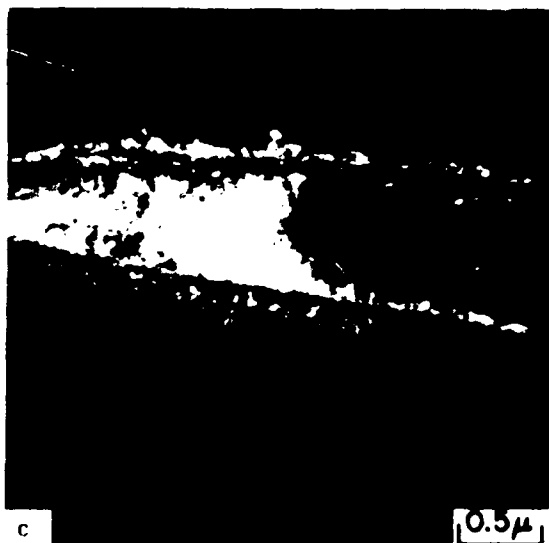
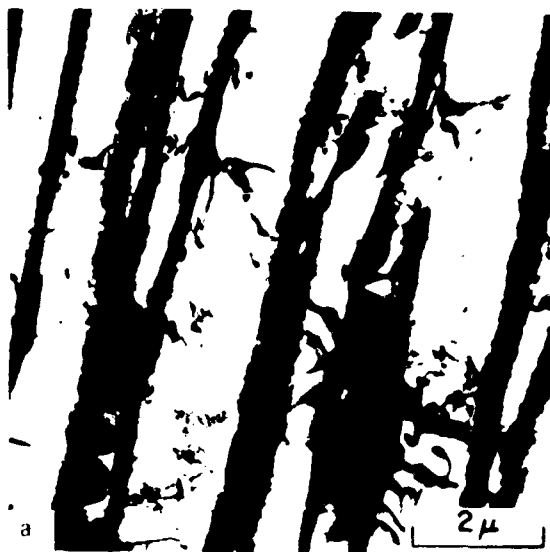


Figure C-7. Transmission Electron Micrographs of Condition 1B

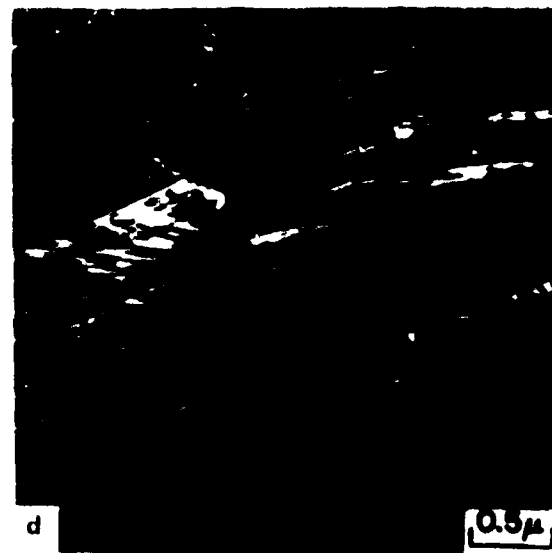
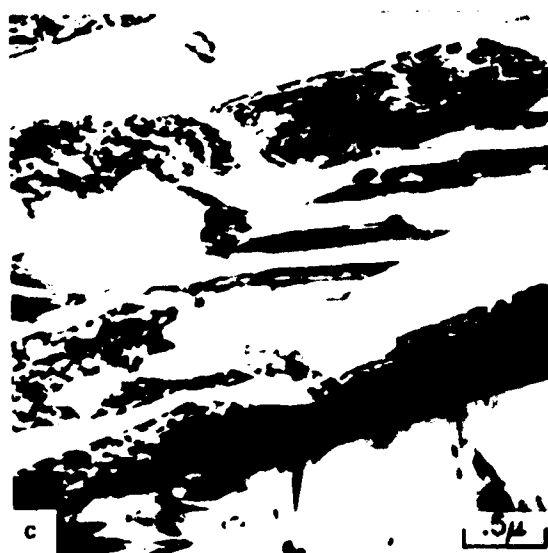


Figure C-8. Transmission Electron Micrographs of Condition 2B

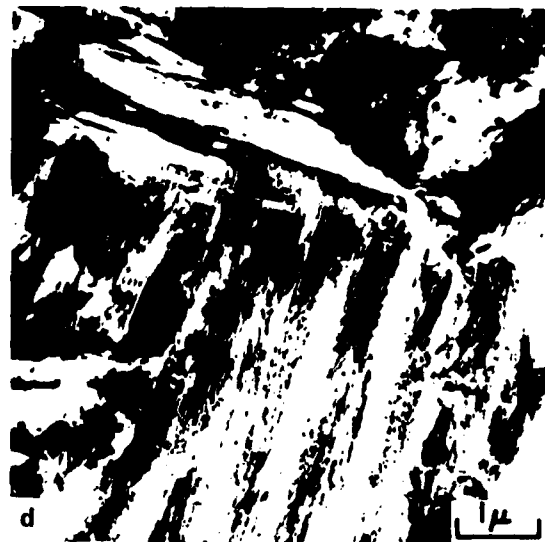
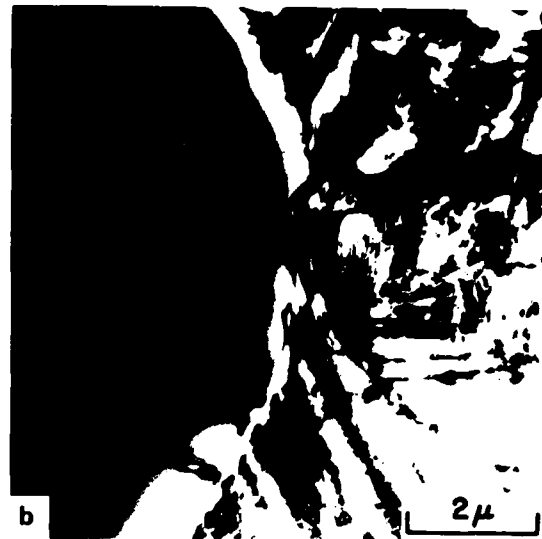
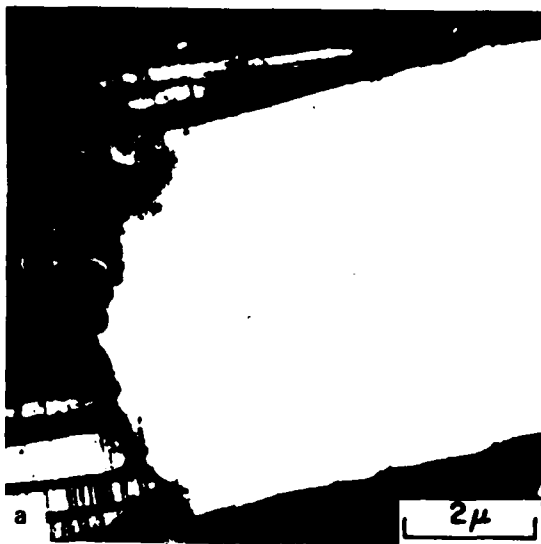


Figure C-9. Transmission Electron Micrographs of Condition 6D

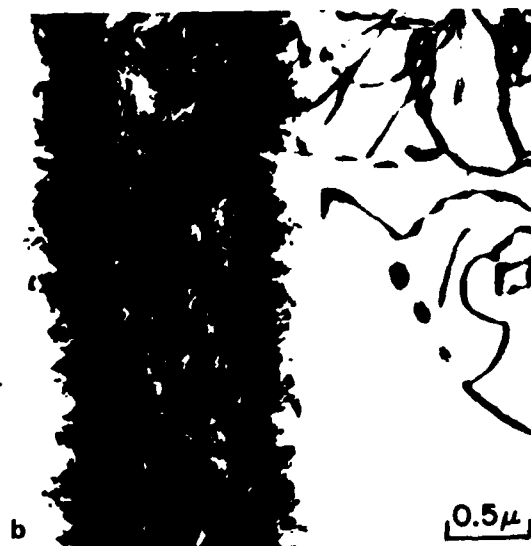
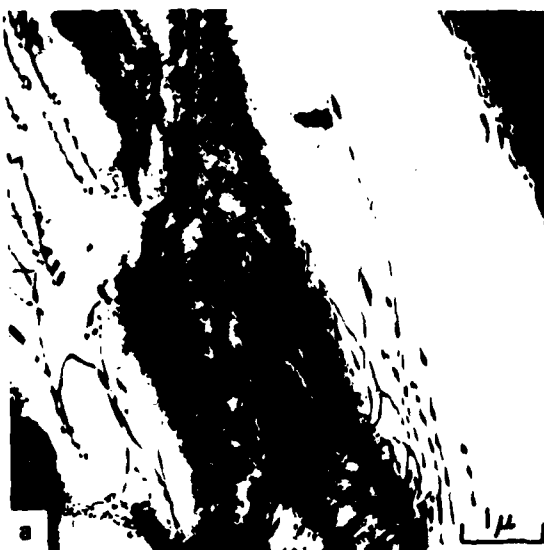


Figure C-10. Transmission Electron Micrographs of Condition 6C

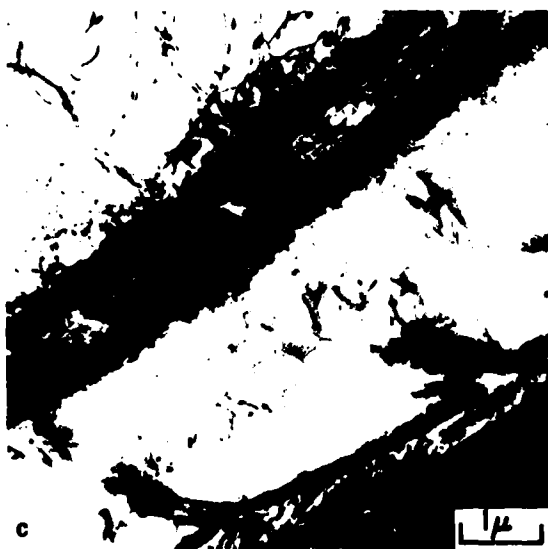
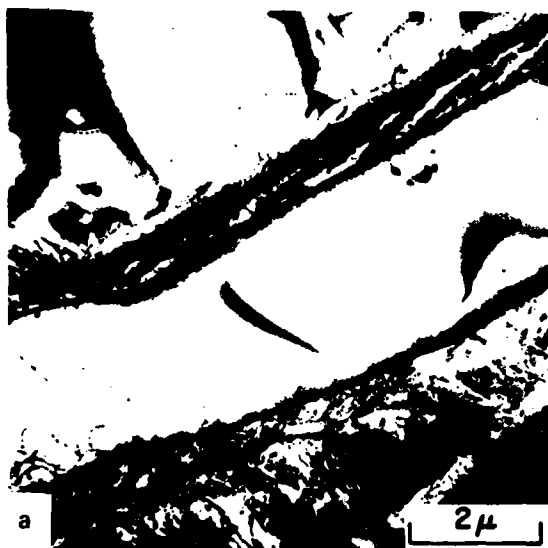


Figure C-11. Transmission Electron Micrographs of Condition 4B

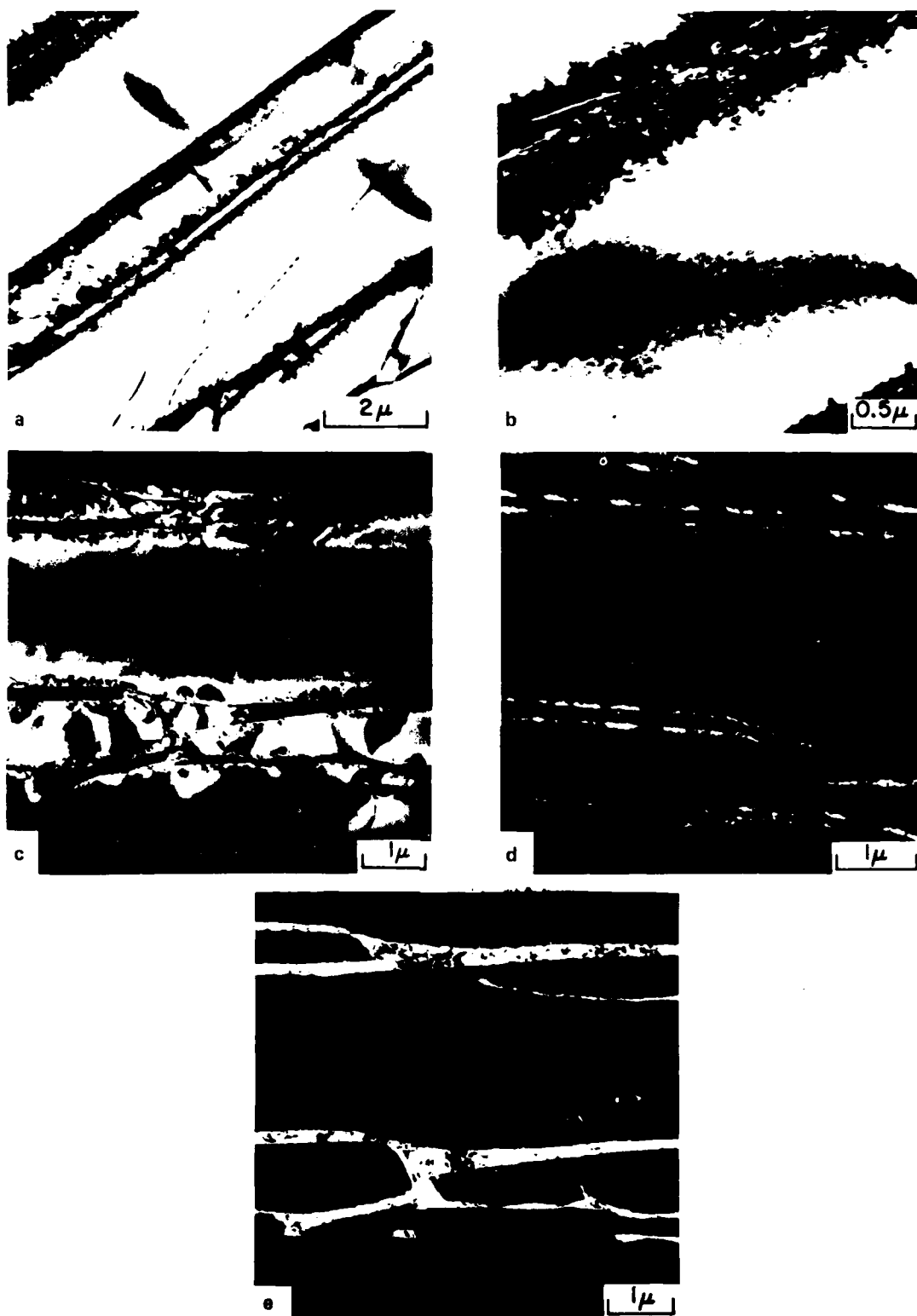


Figure C-12. Transmission Electron Micrographs of Condition 1C

nature of the α/β -interfaces. These other interfaces have this appearance because a third microstructural constituent known as interface phase is present along them. Figure C-7c is a dark field micrograph which shows this phase. Some of the other α/β -interfaces appear not to contain interface phase and instead are simple dislocation boundaries. Examples of these are shown in Figure C-7d.

The TEM microstructure of condition 2B is shown in Figure C-8. From these micrographs the similarity to condition 1B (Figure C-7) can be seen. These micrographs are selected to further illustrate the general features contained in both of these microstructures. Figure C-8a shows the general lamellar structures with the irregular or ragged α/β -interfaces due to the presence of interface phase. Figure C-8b shows the interface phase more clearly and at a higher magnification. The white regions separating the parallel interface phase regions is the β -phase. This is surrounded on each side by the wide α -phase lath. If the α/β -interfaces lie through the foil at a relatively shallow angle, the detailed nature of the β -phase can be seen. This is shown in Figures C-8c and C-8d which are a bright field, dark field pair. It should be emphasized that the width of the β -regions in these micrographs is exaggerated because of the orientation that they have with respect to the surfaces of the thin foil. That is to say their projected width is much greater than their true width.

The TEM microstructure of condition 6D is summarized in Figure C-9. From this figure the microstructure can be seen to consist of blocky primary α particles as shown in parts a, b, and c and fine, lenticular α' martensite as shown in all four parts of this figure. Figure C-9c shows the dislocations which are sometimes punched out in the primary α due to the stresses induced by the martensitic transformation. Figure C-9d shows the fine nature of the martensitic α' . For reference this can be compared to the much coarser lamellar or colony α which was shown in Figures C-7 and C-8.

The TEM microstructure of condition 6C is shown in Figure C-10. The microstructure of this condition is very similar to 6D because it has the same forging history and is solution treated at the same temperature except that it is air cooled rather than water-quenched following solution treatment. The result of this difference is to lead to nucleation and growth of lamellar α between

the larger elongated primary α -particles. Moreover, these primary α -particles tend to "grow back" into the β -phase during their cooling from the solution treatment temperature. This can be readily seen in the light metallography by comparing Figures C-3 and C-4. The other interesting feature that can be seen in the TEM micrographs is the propensity for the α/β -interfaces to act as dislocation sources for subsequent yielding. This is particularly clear in Figures C-10c and C-10d, although the high dislocation density in the vicinity of the α/β -interfaces is also obvious in Figures C-10a and C-10b. The source of this high dislocation density is thought to be the differences in thermal expansion coefficient between the two phases which leads to the generation of dislocations during cooling from the solution treatment temperature. The presence of such dislocations may have important implications on second tier properties such as Bauschinger effect.

The TEM microstructure of condition 4B is shown in Figures C-11a-d. This structure consists of a relatively high volume fraction of elongated α platelets which are characteristic of β -forged material. The subsequent subtransus solution treatment enriches the β -phase in Mo thereby retarding the decomposition kinetics. This leads to a somewhat larger volume fraction of β -phase than is normally seen in β -worked material. This β -phase can be seen in the TEM micrographs, especially Figures C-11a and C-11b, to have partially decomposed to an α/β -mixture during the final aging treatment. In this condition, as in condition 6C, Figure C-10 the high density of dislocations along the α/β -interfaces is very noticeable. The principal difference between conditions 4B and 6C is the size and morphology of the primary α -plates. In this condition, because it is β -forged, the plates are larger and have a higher aspect ratio. This can be more readily seen in the light metallography by comparing Figure C-5 to Figures C-3 and C-4.

The TEM microstructure of condition 1C is shown in Figures C-12a-e. This condition consists of a modest volume fraction of equiaxed primary α -particles in a lamellar α/β -matrix. Figures C-12a and C-12b show the general features of the lamellar α/β -structure. Several things can be seen in these photos. First, the interface phase present along the α/β -interfaces is relatively

obvious. Second, the wider regions of β -phase have decomposed during the final aging operation as can best be seen in Figure C-12b. Figures C-12c, d, and e show the bright field microstructure, the interface phase in dark field, and the β -phase in dark field, respectively.

Low-Cycle Fatigue

Data from low-cycle-fatigue tests at 510 C (950 F) showed that a bimodal microstructure (such as that of condition 1C) exhibits the best low-cycle-fatigue performance (Table C-2). On the other hand, colony microstructures (such as condition 1B) tend to have poor LCF performance. These trends are rather sketchy because of data scatter, but can be rationalized from the fact the LCF is controlled by crack initiation. In microstructures with short slip lengths (e.g., bimodal microstructures), initiation is difficult. In contrast, it is easy in microstructures with long slip lengths (e.g., colony microstructures).

Fatigue Crack Growth

FCG testing as described in the section on experimental procedures was also conducted for all six microstructural conditions. The results of these tests are presented in Figures C-13 through C-18. Duplicate specimens of each microstructural condition were also tested and yielded identical results. Four general groupings of the fatigue crack growth rate (FCGR) data were observed for the six microstructural conditions tested. The FCG response of conditions 1B and 2B were similar, and thus these conditions are grouped together. Likewise, conditions 6C and 6D were grouped together. Condition 1C and condition 4B, whose FCG responses were distinct, were not grouped together.

The following load-shedding technique was used to achieve low growth rates. Starting at a nominal ΔK of 20-25 MPa \sqrt{m} the specimens were precracked at room temperature ($R = 0.1$, frequency = 30 Hz) using rapid load shedding to a growth rate of $\sim 1 \times 10^{-8}$ m/cycle. The specimens were then surrounded by the resistance furnace, heated and held at 510 C (950 F) for at least two hours. Load shedding was again performed to achieve low growth rates, with growth increments of 0.3-0.5mm or more and load drops of 2.5 percent. As the growth rates approached 1×10^{-8} m/cycle premature crack growth arrest occurred. Upon

Table C-2. LCF Results

Serial Number	Cycles to Failure ($\epsilon_{\text{total}} = 0.8\%$)	Cycles to Failure ($\epsilon_{\text{total}} = 1.6\%$)
1B	7,243	900**
2B	>68,000*	1,537
4B	8,735	1,500
1C	>90,034	1,975
6C	5,365	1,068
6D	>89,270	1,480

**Interpolation from data at $\epsilon = 0.65\%$ and $\epsilon = 1.6\%$.

***Interpolation from data at $\epsilon = 0.8\%$ and $\epsilon = 2.0\%$.

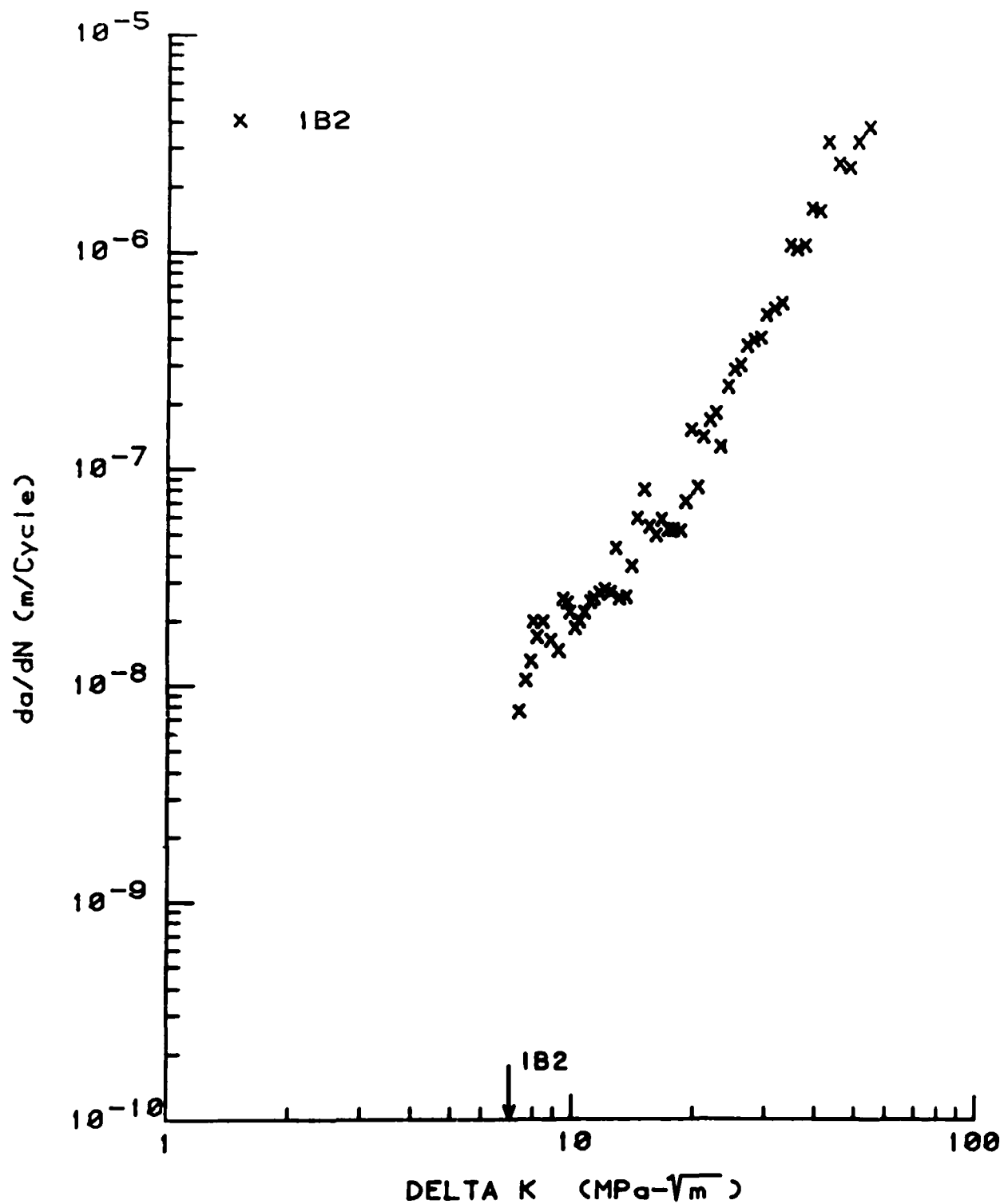


Figure C-13. Fatigue Crack Growth Behavior of Condition 1B at 510 C (950 F) in Laboratory Air

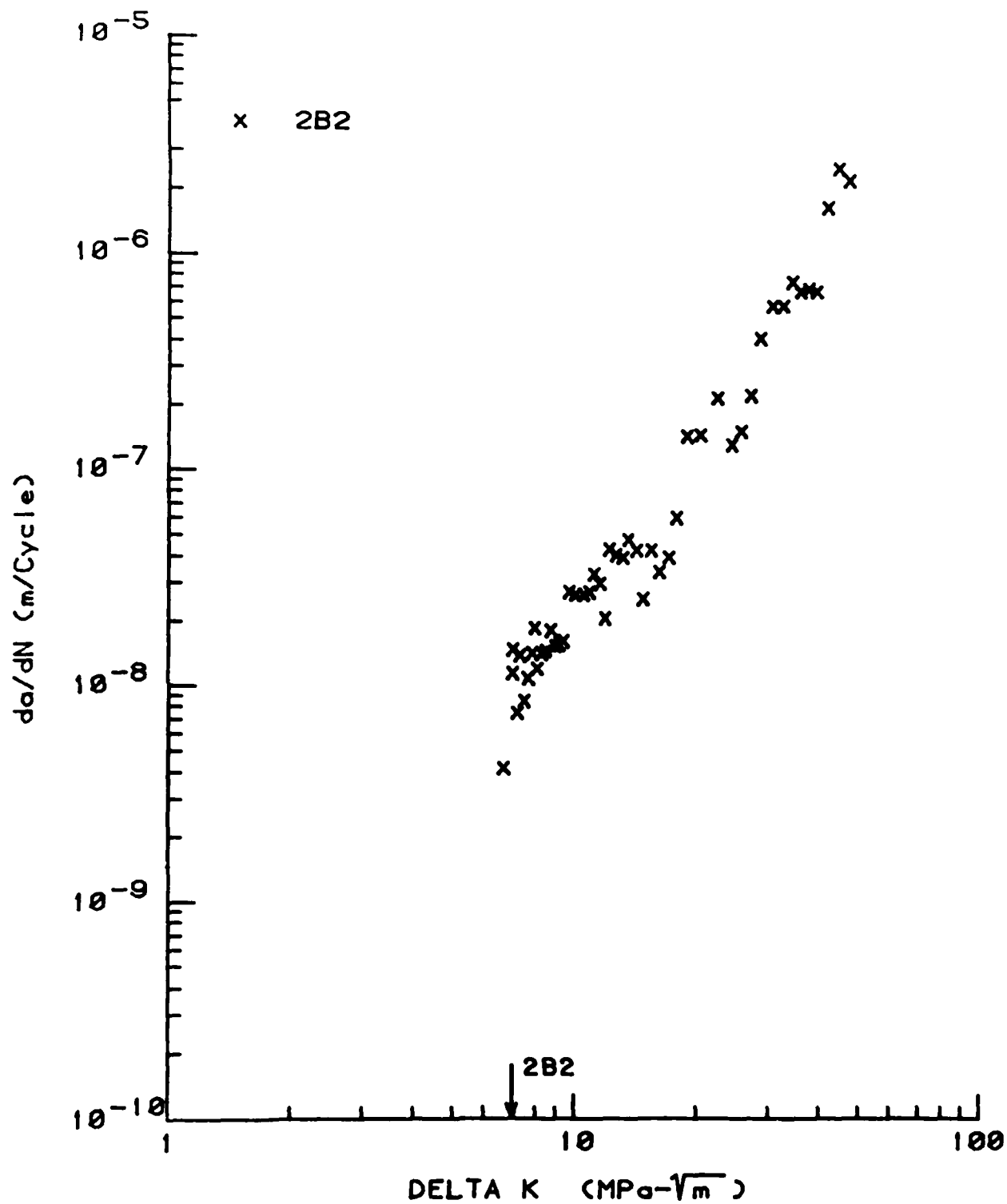


Figure C-14. Fatigue Crack Growth Behavior of Condition 2B at 510 C (950 F) in Laboratory Air

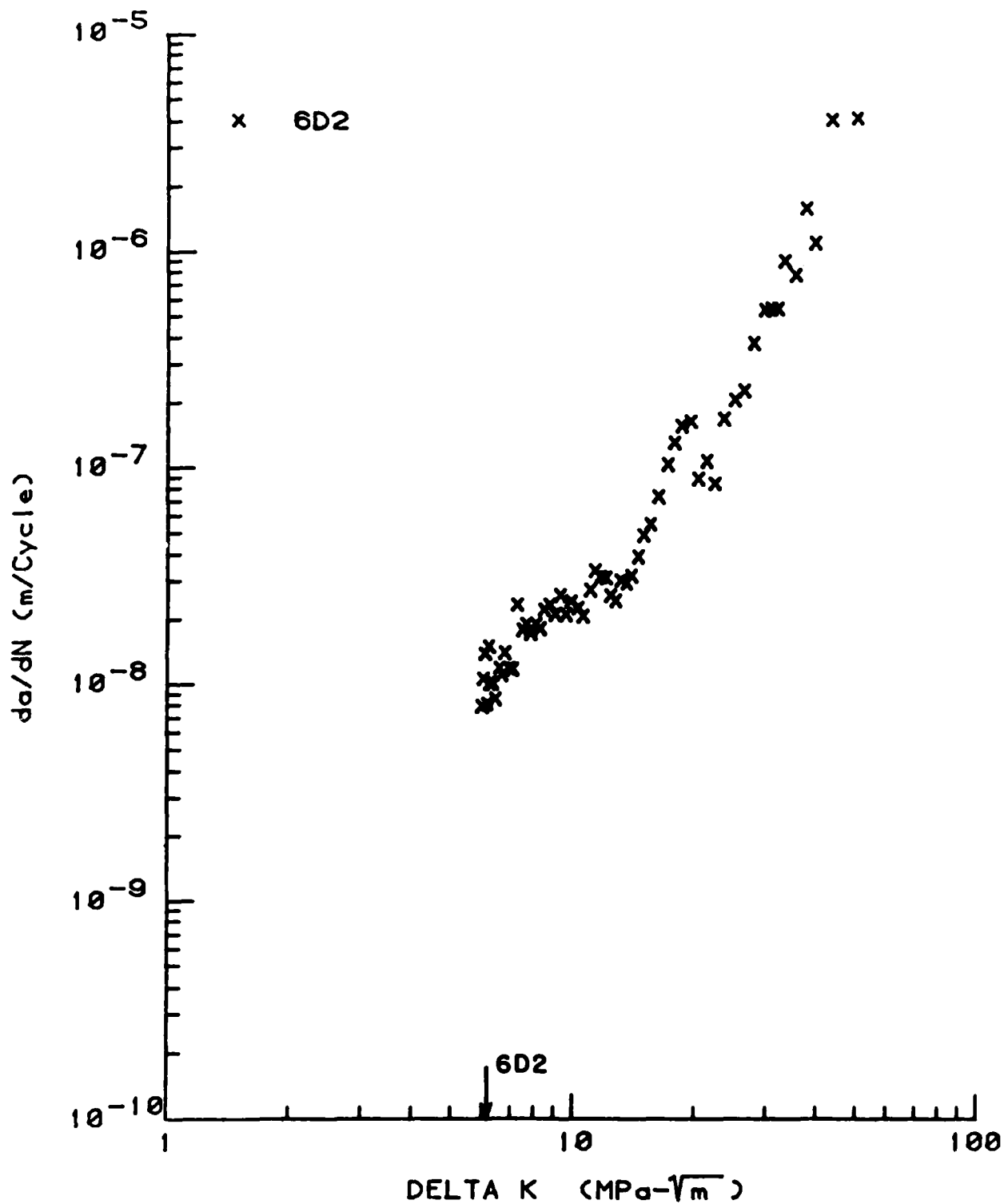


Figure C-15. Fatigue Crack Growth Behavior of Condition 6D at 510 C (950 F) in Laboratory Air

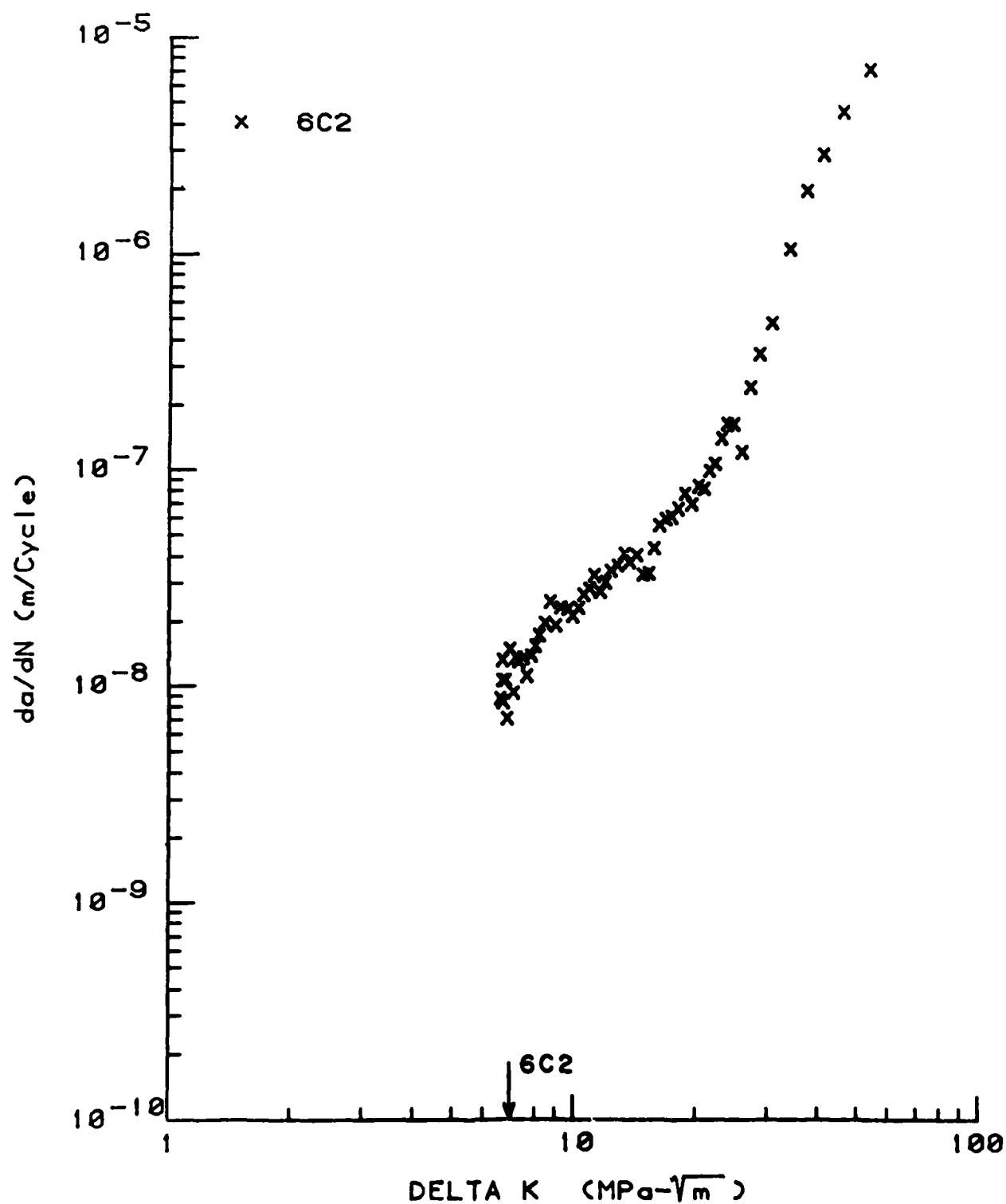


Figure C-16. Fatigue Crack Growth Behavior of Condition 6C at 510 C (950 F) in Laboratory Air

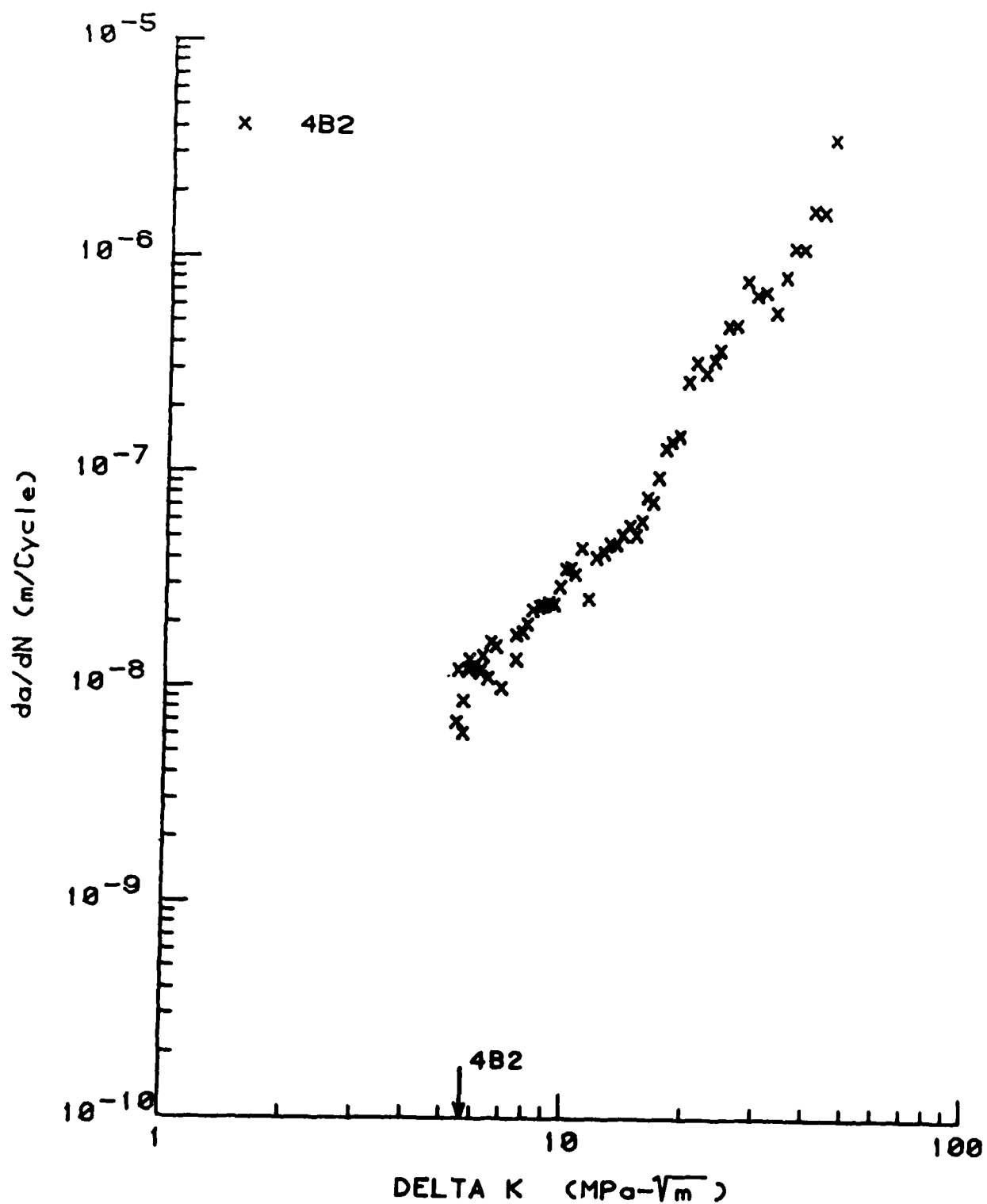


Figure C-17. Fatigue Crack Growth Behavior of Condition 4B at 510 C (950 F) in Laboratory Air

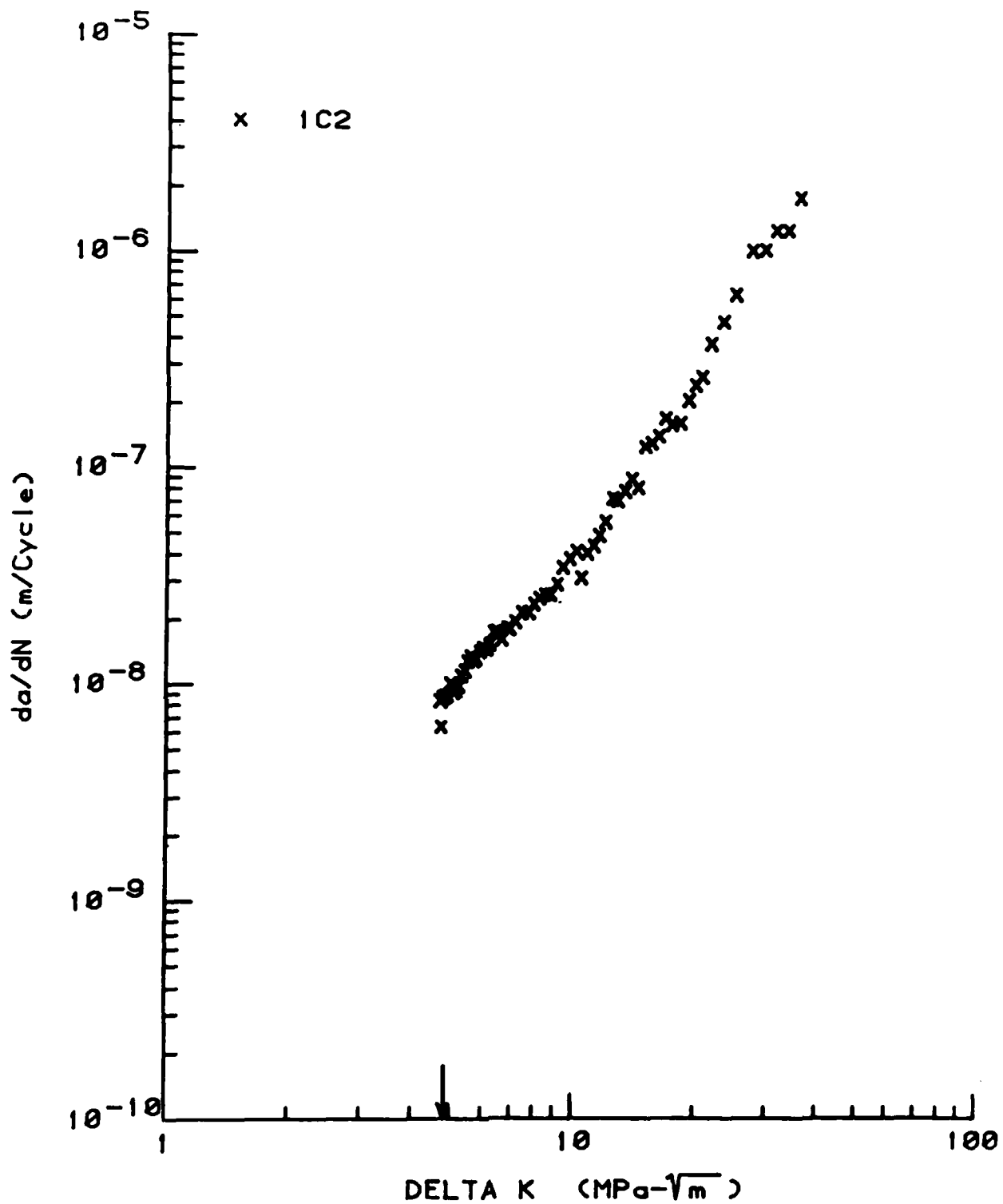


Figure C-18. Fatigue Crack Growth Behavior of Condition 1C at 510 C (950 F) in Laboratory Air

crack arrest load increases of up to 20 percent were required to reinitiate fatigue crack growth. Upon reinitiation, loading shedding was continued using load decrements of 1 to 3 percent. This laborious procedure was iterated until the crack length (as measured from the notch tip) was ~ 15 mm. The lowest stress intensity at which crack growth arrest occurred was then taken as an operational definition of the threshold ΔK or an apparent threshold, ΔK_{TH}^{APP} . These values appear in Table C-3 and as arrows on the respective FCGR plots.

The FCGR data for the $\alpha+\beta$ -forged condition 1C, shown in Figure C-18, was unique in that it smoothly increased with ΔK . This is not surprising considering the straight, nonbranching nature of the crack path and the flatness of the fracture surface. All other conditions showed some scatter due primarily to crack branching. The most pronounced scatter was for the β -annealed conditions 1B and 2B, an example of which is plotted in Figure C-19 with the $\alpha+\beta$ -forged condition for comparison.

Although the influence of titanium microstructure on FCG has been thoroughly examined at room temperature (see for example References 4 and 10), there is generally a lack of information on elevated temperature fatigue crack growth and virtually no information on the influence of microstructure at elevated temperature. In the present study, growth rates at 510 C (950 F) were altered a factor of two to four via microstructural manipulation. As shown in Figure C-19, the colony microstructure of condition 1B exhibited two to four times lower growth rates than the bimodal microstructure of condition 1C. In a recent investigation⁽¹¹⁾, Ruppen and McEvily concluded that the processing of Ti-6242 to produce differing microstructures had a negligible influence on FCG at 538 C (1000 F). The range of microstructures in that study was, however, somewhat limited. Ruppen and McEvily's microstructures were quite similar to the colony microstructures investigated in this study and, in fact, their data are in general agreement with the FCGR data for condition 1B and 2B. FCGR data on $\alpha+\beta$ -processed Ti-6242 was generated by Pratt & Whitney Aircraft Company (PWA)⁽¹²⁾ at 538 C (1000 F), and it is in general agreement with FCGR data from condition 1C. The results of these independent studies agree quite well with the results of this investigation, although at the higher temperature of these investigations the influence of microstructure on FCG is somewhat diminished. It should be

Table C-3. Apparent Threshold Stress Intensity, ΔK_{TH}^{APP} (MPa \sqrt{m})

Microstructure/ Sample	1C	4B	6D	6C	2B	1B
1	5.1	5.1	5.9	7.1	--	7.7
2	4.9	5.7	6.2	7.0	6.9	7.0
Average (Rounded)	5.0	5.4	6.1	7.1	6.9	7.4

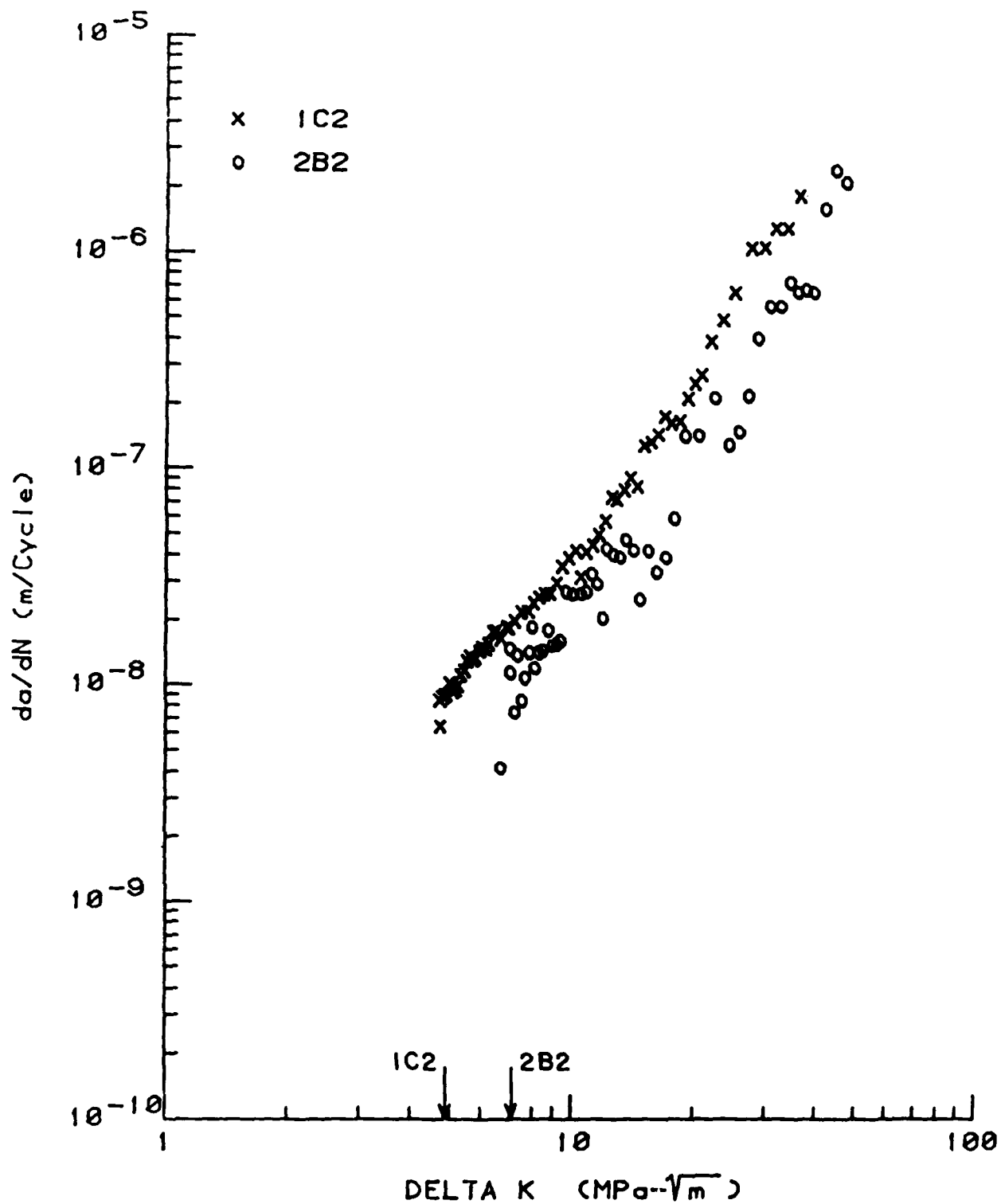


Figure C-19. Comparison of Elevated Temperature Fatigue Crack Growth Behavior for $\alpha+\beta$ -Forged Material (Sample 1C2) and β -Treated Material (Sample 2B2)

noted that these investigations report no data below 1×10^{-8} m/cycle, and one investigator reported⁽¹³⁾ difficulties in obtaining growth rates below this value, similar to this investigation.

Figure C-20 is a composite of the FCGR data generated in this investigation, using trend lines for the different groupings. The colony (1B, 2B) and elongated α (6C, 6D) microstructures gave quite similar data, exhibiting the lowest growth rates and the highest ΔK_{TH}^{APP} . The bimodal microstructure (1C) produced by $\alpha+\beta$ -processing gave the highest FCG rates and lowest ΔK_{TH}^{APP} .

The ranking observed in this investigation agrees in general with the concept that slip length is a critical parameter, controlling fracture related properties as described in the background section. That is, the bimodal microstructure of condition 1C, which has a very fine grain size and thus a short slip length, exhibits the highest FCG rates and lowest ΔK_{TH}^{APP} . This is in contrast to the low growth rates observed in the colony microstructures (1B, 2B) in which the slip length is the colony size and thus significantly longer. The intermediate conditions 4B, 6D, and 6C are not readily explainable in terms of slip length. Conditions 4B and 6C appear to have roughly the same slip length; however, condition 4B exhibits higher growth rates and a lower ΔK_{TH}^{APP} . Moreover the microstructure for condition 6D is a matrix of randomly oriented martensite with the elongated primary α presumably representing the maximum possible slip length. Since these primary α -grains are similar in size to the bimodal grain size (1C), similar growth rates would be expected. Figure C-20 shows that this is not the case and that the data for condition 6D fall quite close to the data for the colony microstructure.

An alternative rationale for the ranking shown in Figure C-20 is based on roughness-induced closure. Recent investigations at C-MU⁽¹⁴⁾ and elsewhere^(15,16) indicate that the fracture surfaces with high surface roughness lead to early crack closure due to asperity contact. That is, as the load is increased during a cycle the crack remains closed until an opening K , K_{op} is reached. The crack growth is controlled then by an effective ΔK , ΔK_{eff} , which equals $K_{max} - K_{op}$ rather than $K_{max} - K_{min}$. The growth rate for a given ΔK decreases as K_{op} increases.

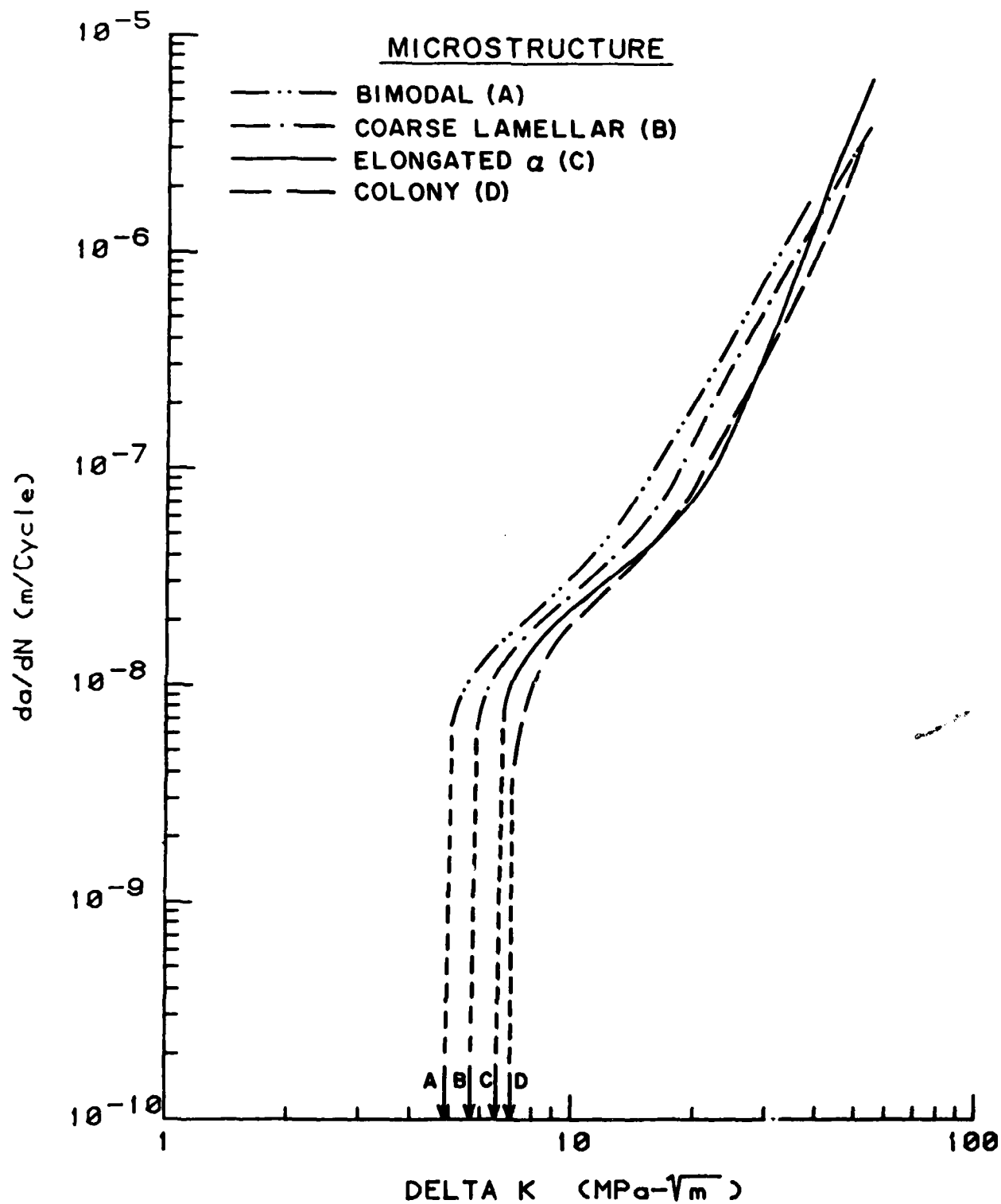


Figure C-20. Trend Lines Showing the Influence of Microstructure on Fatigue Crack Growth Behavior of Ti-6242 at 510 C (950 F) in Laboratory Air

It is thought that K_{op} increases as fracture surface roughness increases, leading to lower ΔK_{eff} and hence to lower growth rates.

The SEM fractographs shown in Figure C-21, show that the macroscopic roughness of the fracture surfaces rank in the same manner as do the growth rates. That is, the low growth rate conditions, 6C, 6D and, especially 1B and 2B, have very rough fracture surfaces, while the faster growth rate condition 1C has an extremely flat fracture surface. Condition 4B has a macroscopic roughness in between these two extremes. In a qualitative sense, the FCG behavior observed in this study is consistent with concepts of roughness-induced closure.

Fractography

In this section, results of fractographic investigation will be presented for each of the six conditions for three comparable crack growth rates. This methodology was described in an earlier section. In Figures C-21 to C-27, the direction of crack propagation is from top to bottom.

Condition 1B is the colony or β -treated microstructure and has relatively large regions of constant crystallographic orientation. The presence of such regions is reflected in the fracture surfaces, especially at low ΔK 's by the presence of fairly large facets such as shown in Figure C-22a. These facets often are joined by secondary cracks as can be seen in Figure C-22b. At higher growth rates, the flatness and smoothness of these facets tends to diminish, possibly reflecting the increase in reversed plastic zone size. This can be seen in Figures C-22c and C-22d. At still higher growth rates, the crack propagation occurs by formation of striations as seen in Figures C-22e and C-22f. The striations often have periodic secondary cracks associated with them as can be seen in Figure C-22g.

The fractography of condition 2B is shown in Figure C-23. The features to be found on the fracture surface of this condition are remarkably similar to those found in Figure C-22 (condition 1B). This is not surprising since their microstructures are both β -treated microstructures. In Figure C-23a, the facets which are characteristic of low ΔK crack growth can be seen, and the

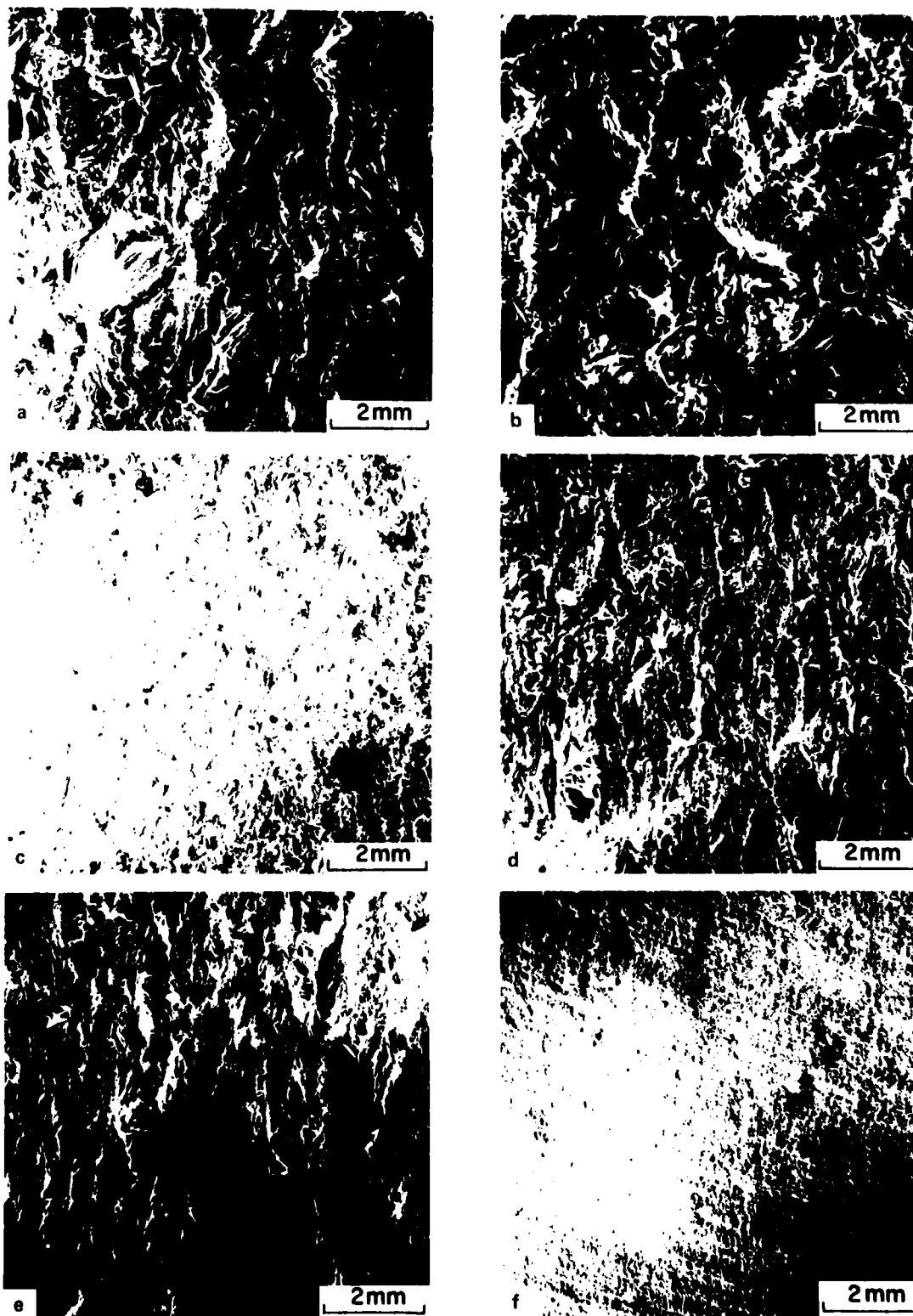


Figure C-21. Low Magnification SEM Fractographs of Fatigue Fracture Surfaces at $da/dN \approx 1 \times 10^{-7}$ m/cycle. (a) Condition 1B; (b) Condition 2B; (c) Condition 6D; (d) Condition 6C; (e) Condition 4B; (f) Condition 1C.

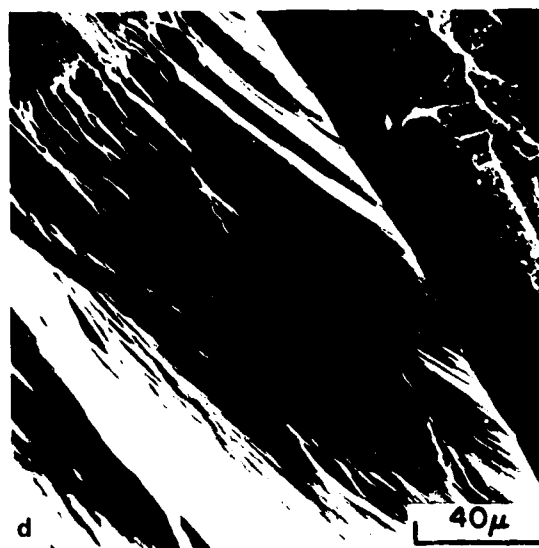
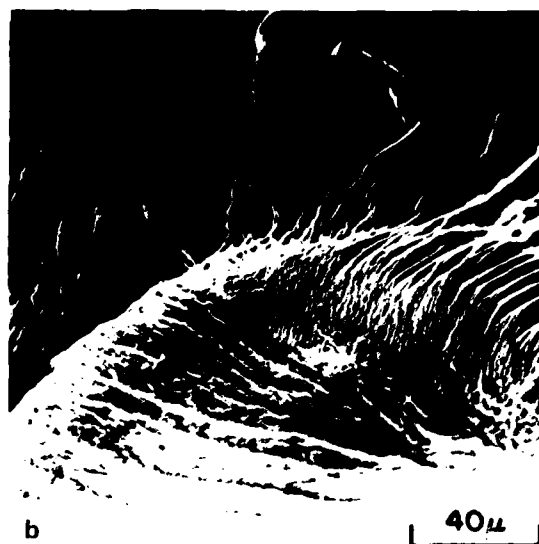
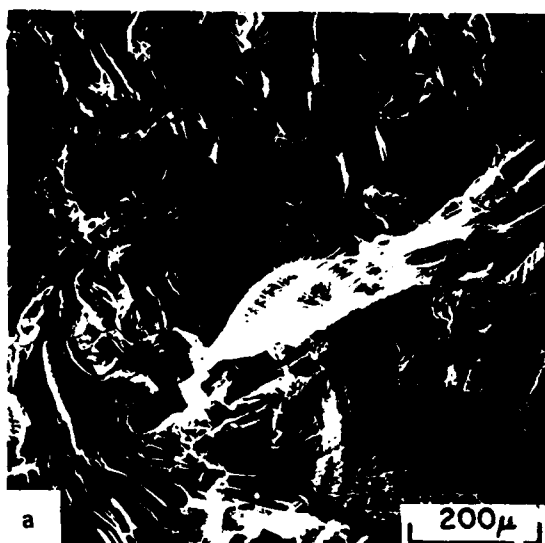


Figure C-22. SEM Fractographs of Condition 1B
 (a-b) $da/dN \sim 1 \times 10^{-8}$ m/cycle;
 (c-d) $da/dN \sim 1 \times 10^{-7}$ m/cycle;
 (e-g) $da/dN \sim 1 \times 10^{-6}$ m/cycle.

AD-A112 271

BATTELLE COLUMBUS LABS OH
RESEARCH TO DEVELOP PROCESS MODELS FOR PRODUCING A DUAL PROPERTY--ETC(U)
OCT 81 © D LAMOTI, T ALTAN

F/G 11/6

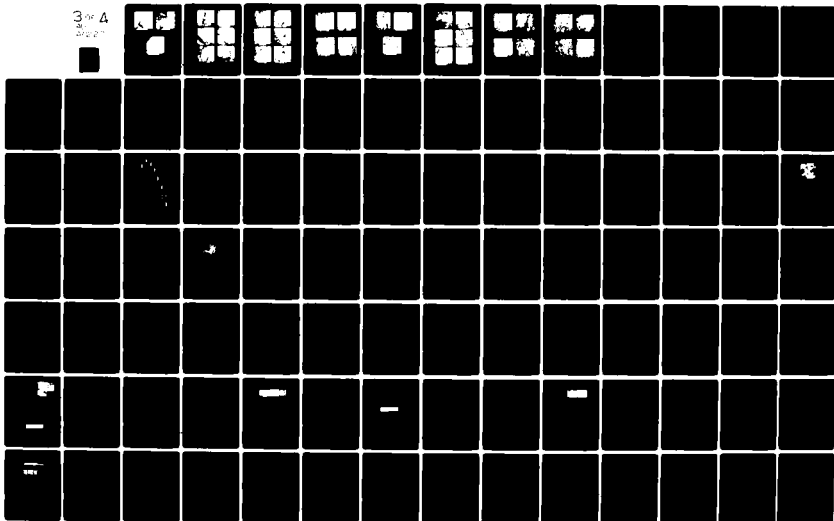
F33619-78-C-5025

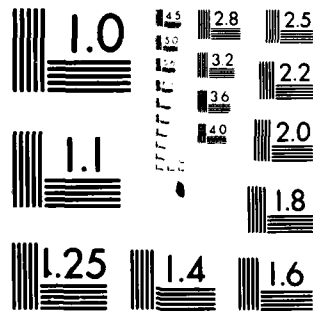
UNCLASSIFIED

AFWAL-TR-81-8130

NL

3 of 4
2/2/81





MICROCOPY RESOLUTION TEST CHART
NATIONAL BUREAU OF STANDARDS 1963-A

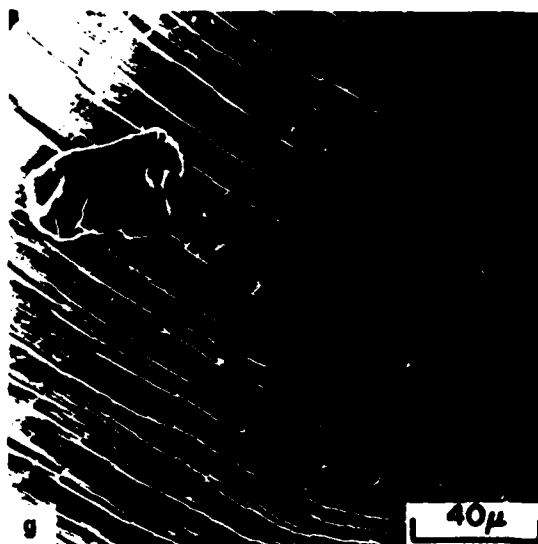
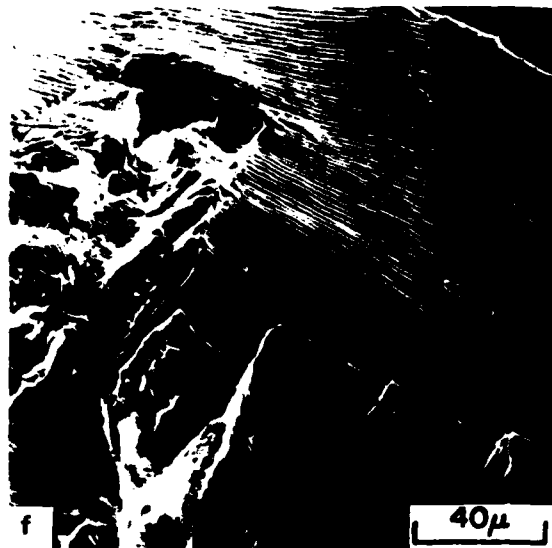


Figure C-22. (Continued)

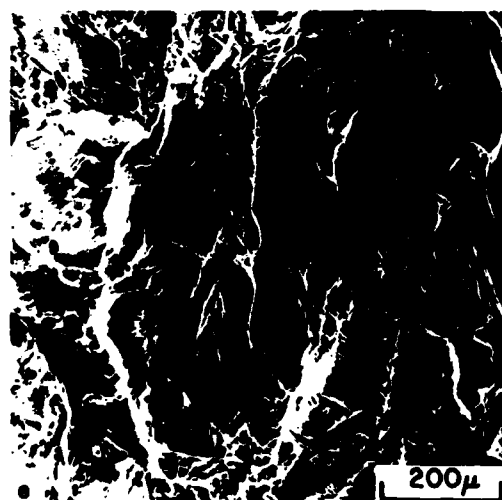
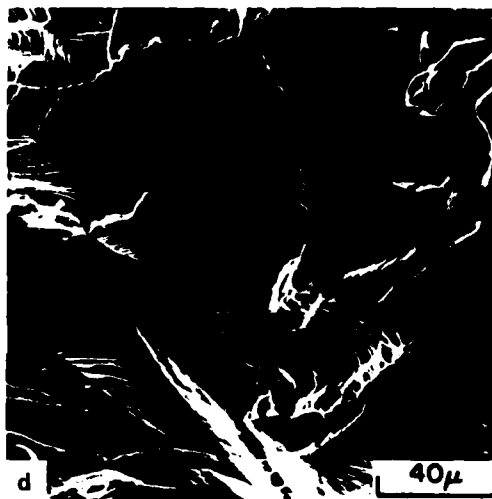
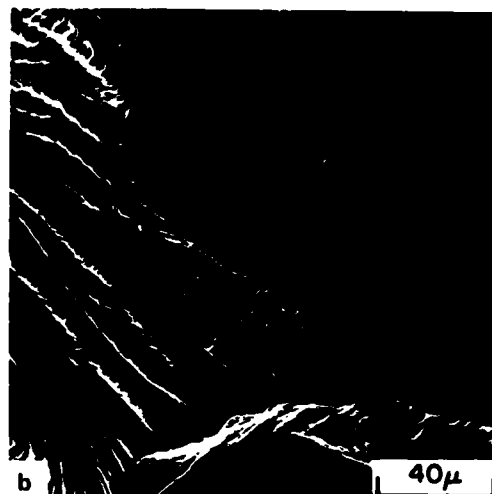


Figure C-23. SEM Fractographs of Condition 2B
 (a-b) $da/dN \sim 1 \times 10^{-8}$ m/cycle;
 (c-d) $da/dN \sim 1 \times 10^{-7}$ m/cycle;
 (e-f) $da/dN \sim 1 \times 10^{-6}$ m/cycle.

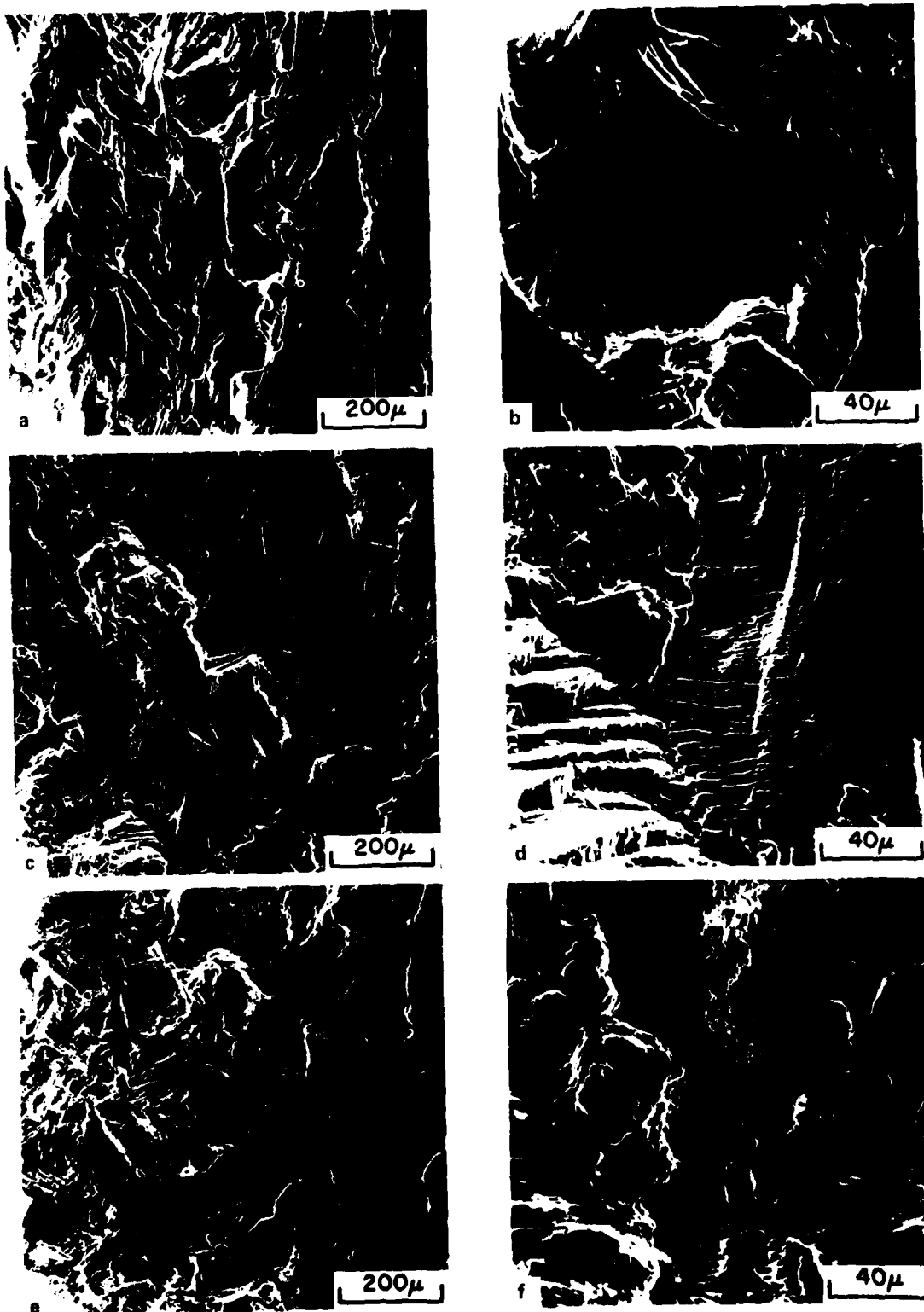


Figure C-24. SEM Fractographs of Condition 6D
 (a-b) $da/dN \sim 1 \times 10^{-8}$ m/cycle;
 (c-d) $da/dN \sim 1 \times 10^{-7}$ m/cycle;
 (e-f) $da/dN \sim 1 \times 10^{-6}$ m/cycle.

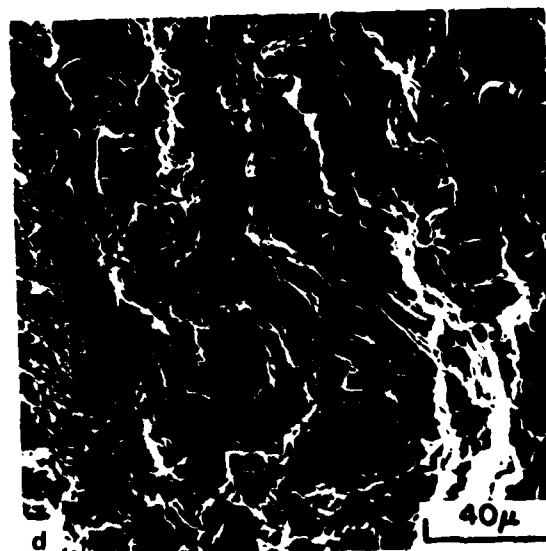
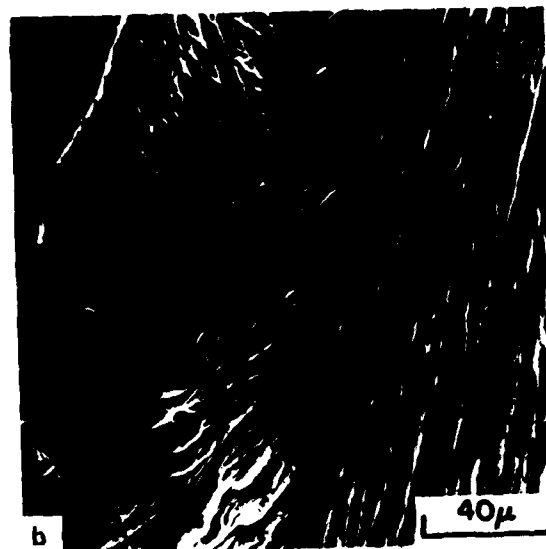


Figure C-25. SEM Fractographs of Condition 6C
 (a-b) $da/dN \sim 1 \times 10^{-8}$ m/cycle;
 (c-e) $da/dN \sim 1 \times 10^{-7}$ m/cycle;
 (f-g) $da/dN \sim 1 \times 10^{-6}$ m/cycle.

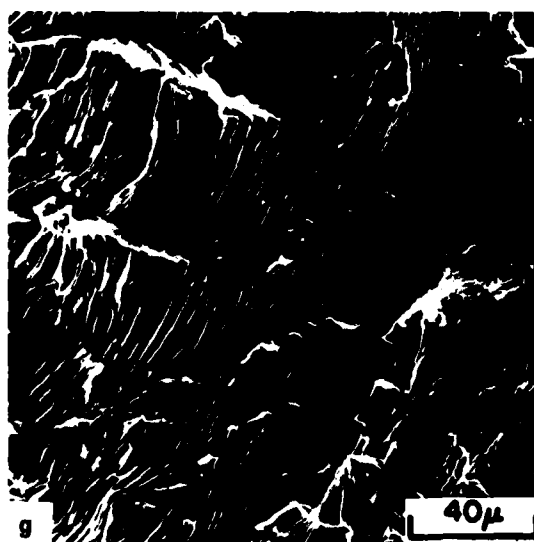
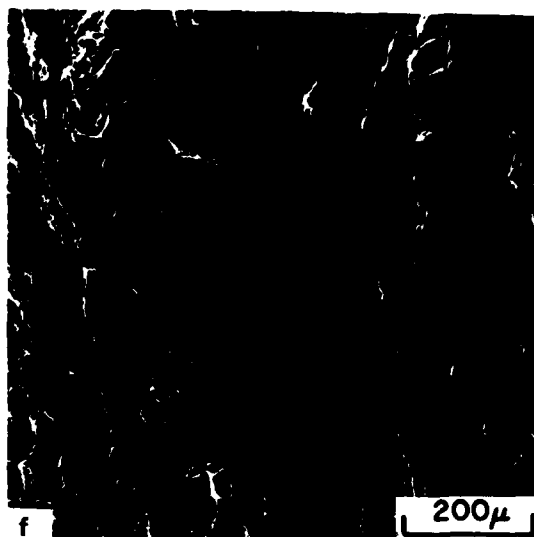
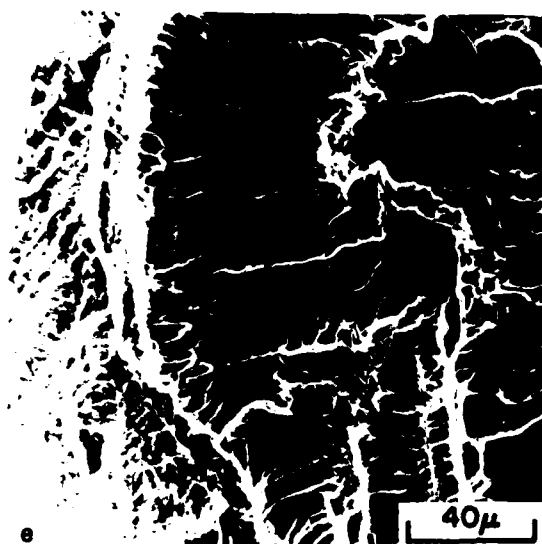


Figure C-25. (Continued)

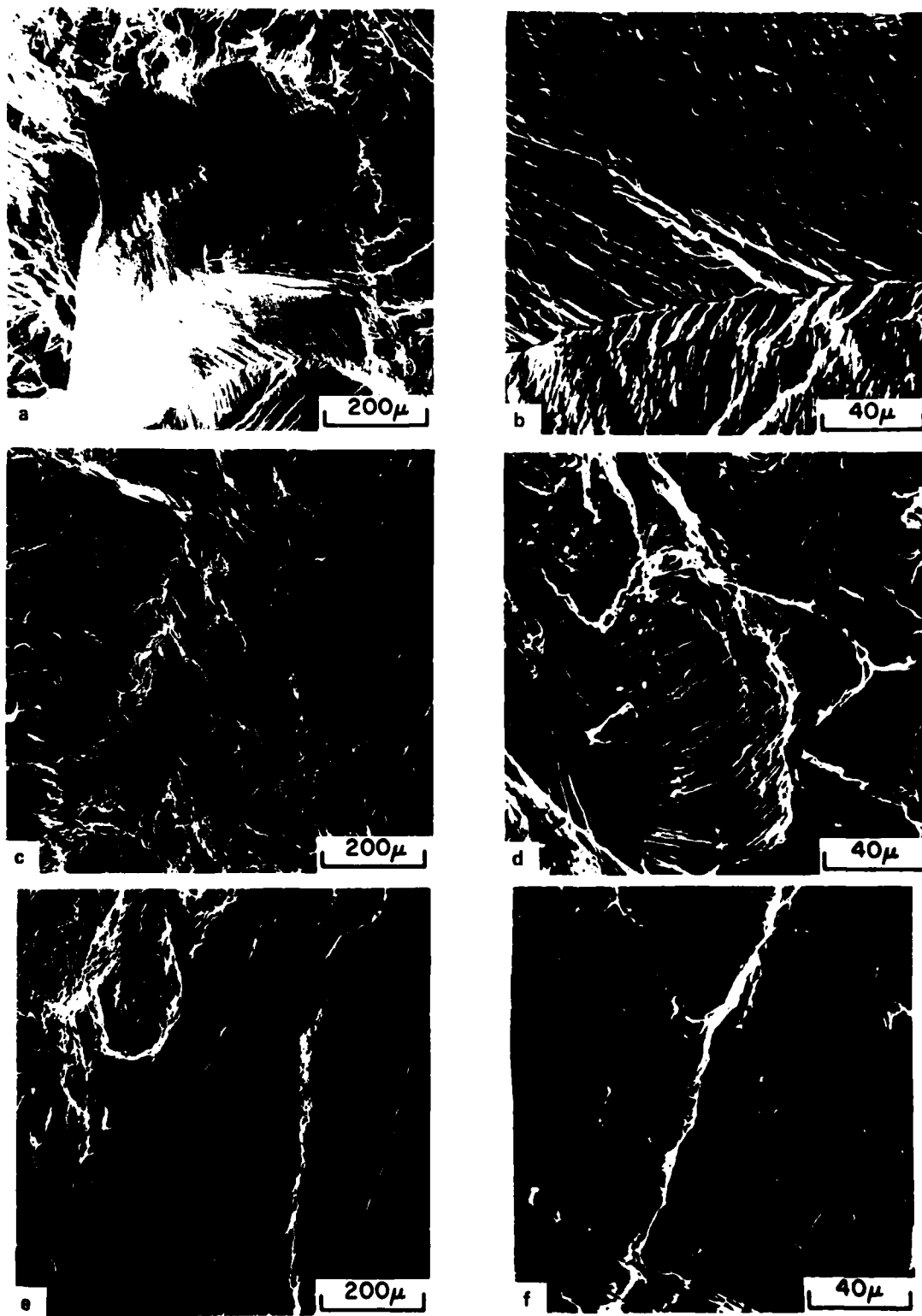


Figure C-26. SEM Fractographs of Condition 4B
 (a-b) $da/dN \sim 1 \times 10^{-8}$ m/cycle;
 (c-d) $da/dN \sim 1 \times 10^{-7}$ m/cycle;
 (e-f) $da/dN \sim 1 \times 10^{-6}$ m/cycle.

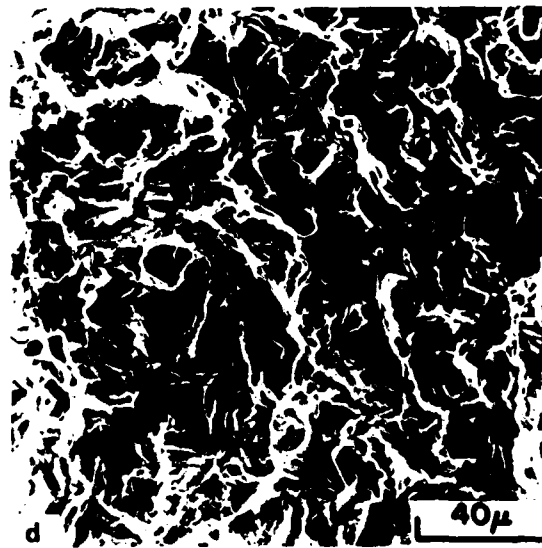
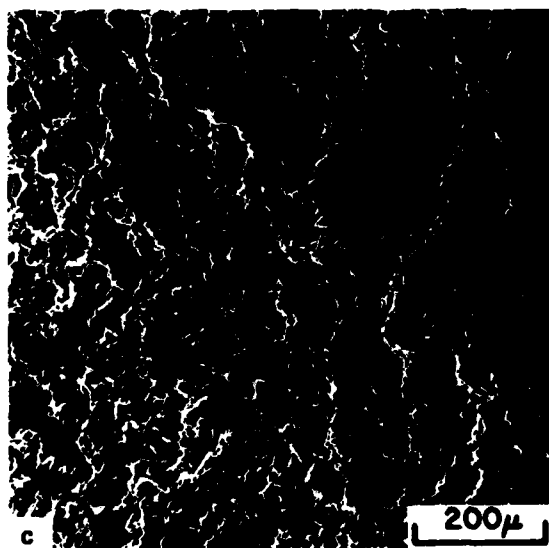
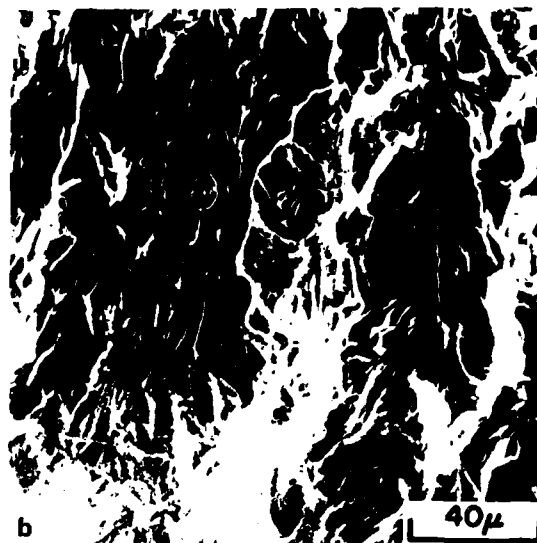
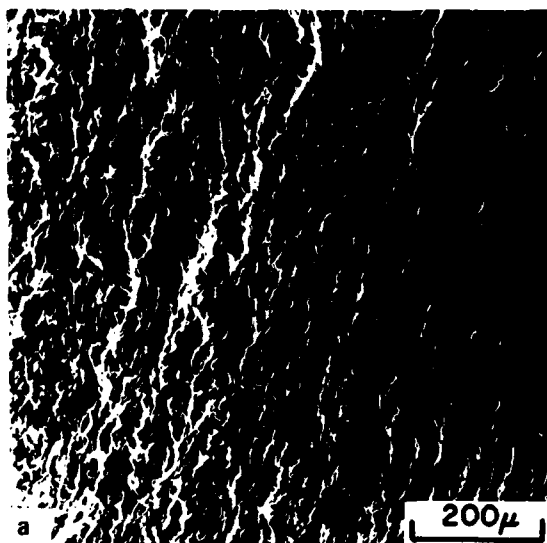


Figure C-27. SEM Fractographs of Condition 1C
 (a-b) $da/dN \sim 1 \times 10^{-8}$ m/cycle;
 (c-e) $da/dN \sim 1 \times 10^{-7}$ m/cycle;
 (f-h) $da/dN \sim 1 \times 10^{-6}$ m/cycle.

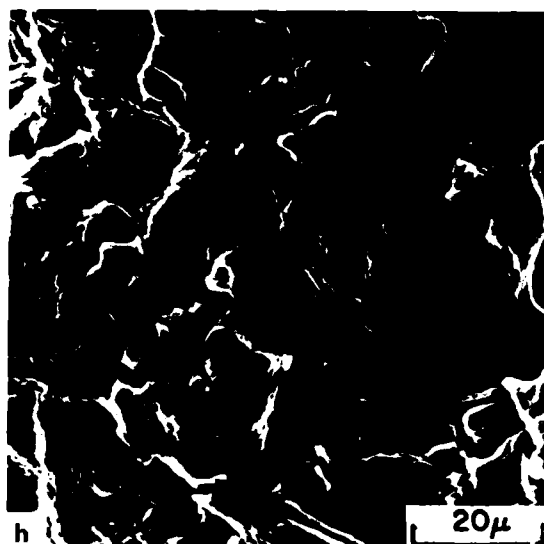
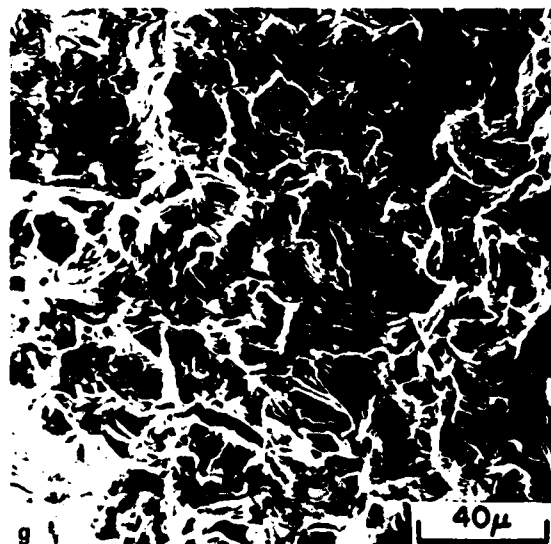
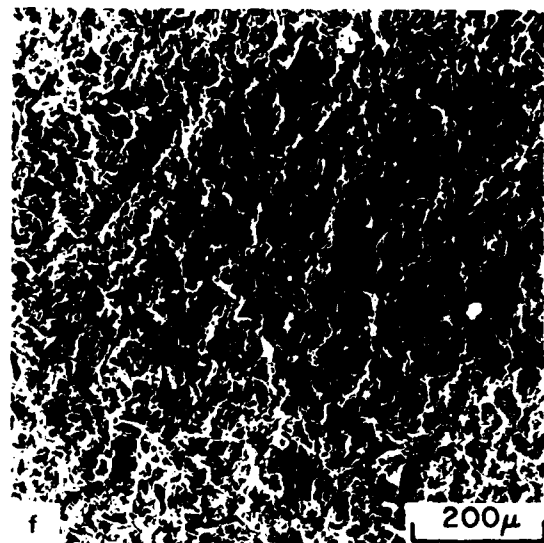
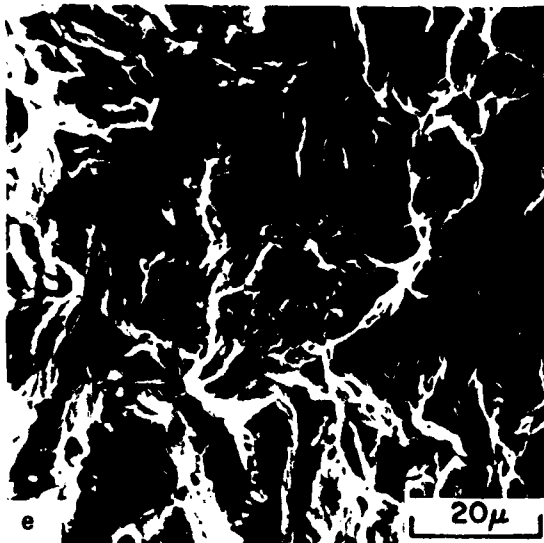


Figure C-27. (Continued)

secondary cracks which occur at the intersection of these facets are shown in Figure C-23b. As in Figure C-22, the higher ΔK crack growth rate regions show somewhat greater surface roughness (Figures C-23c and C-23d) and at the highest crack growth rates the cracks propagate by the formation of striations as seen clearly in Figures C-23e and C-23f. The striations are most clearly seen in the higher magnification fractograph of Figure C-23f.

The fracture topography of condition 6D is shown in Figure C-24. From these fractographs, the tendency toward faceted growth is still seen at low growth rates, but this seems to transition more quickly to a rougher, more irregular fracture surface as the growth rate increases. For example, Figures C-24a and C-24b show these facets with features which are reminiscent of individual α -plates. Figures C-24c and C-24d show the appearance of these facets at somewhat higher growth rates where striations and extensive secondary cracking can be seen. Figures C-24e and C-24f show the fractographic appearance at still higher growth rates where a number of striations can be seen but where there is also present a high density of tear ridges. Such an appearance is consistent with microstructures which have constituents of smaller dimensions.

The fracture topography of condition 6C is shown in Figure C-25. This microstructural condition again exhibits facets at the lowest growth rates, but the facets are microscopically rougher and tend to contain a higher density of tear ridges compared to the earlier conditions, especially 1B and 2B. At higher growth rates the facet dimensions tend to diminish rather quickly which is consistent with the smaller regions of constant crystallographic orientation in this microstructure. These facets also contain significant densities of tear ridges and poorly defined striations as seen in Figures C-25d and C-25e. It is interesting to note that Figures C-25d and C-25e are taken at the same magnification, yet the scale of the features are significantly different. It is suggested that this reflects regions of different sized scale within the microstructure of this particular condition. At the highest growth rates, fields of striations surrounded by complex tear ridges are again seen, as shown in Figures C-25f and C-25g.

The fracture topography of condition 4B is shown in Figure C-26. This condition is somewhat similar to the colony structures which have been described earlier. The principal difference in microstructure is the dimensions of the

transformed β -regions which separate the individual plates within a colony. At low growth rates the crack propagates by the formation of relatively well-defined facets as seen in Figure C-26a and again there are secondary cracks evident along the lines of intersection of the individual facets (Figure C-26b). At higher growth rates the microscopic fracture topography is somewhat rougher than that seen in conditions 1B and 2B, presumably due to the presence of transformed β -regions between the individual α -plates (see, for example, Figure C-11a). At the highest growth rates in this microstructural condition, fields of striations are formed as shown in Figures C-26e and C-26f.

The fracture topography of condition 1C is shown in Figure C-27 from which the distinct difference in facet size and geometry can be seen by comparing Figures C-27a to Figures C-22a or C-23a. Such differences are directly relatable to the different geometries of the primary α in this microstructure compared to all of the other microstructures described above. At higher magnifications it can be seen that the crack still propagates by facet formation at the low growth rates, but that the facet size is much smaller and the degree of secondary cracking at the junction between individual facets is less obvious. At somewhat higher growth rates the secondary cracking becomes more obvious as shown in Figures C-27c, d, and especially e. At the highest growth rates small fields of striations are seen and these presumably correspond to small α/β -colonies within the transformed matrix or to the individual globular primary α -particles. Examples of these striation fields are shown in Figures C-27f and C-27g. The striations are particularly obvious at even higher magnifications (possibly due to the smaller primary α -particle size), and an example of this is shown in Figure C-27h.

Summary

The microstructure for six thermomechanical processing conditions has been characterized by light, scanning-electron, and transmission-electron microscopy. Low-cycle fatigue and fatigue crack propagation testing at 510 C (950 F) was also conducted for all six microstructural conditions. Low-cycle fatigue results showed that bimodal microstructures are most resistant to crack initiation

and that colony microstructures are least resistant to crack initiation. This trend was explained on the basis of the variation of slip length with microstructure and thus the ability to open the intense surface slip bands needed for fatigue crack initiation. As for crack propagation, growth rates at 510 C (950 F) were significantly higher than growth rates at room temperature. Crack growth at 510 C (950 F) was also characterized by crack arrest at growth rates below about 1×10^{-8} m/cycle and has been termed apparent threshold stress intensity, ΔK_{TH}^{APP} . Colony microstructures and elongated α -microstructures gave similar data, exhibiting the lowest fatigue crack growth rates and the highest ΔK_{TH}^{APP} . The bimodal microstructure produced by $\alpha+\beta$ -processing gave the highest growth rates and the lowest ΔK_{TH}^{APP} . Extensive scanning electron fractography was conducted on the crack growth samples, the results of which are in agreement with the above data trends. The microstructural effects on fatigue crack growth rates were observed to be consistent with roughness-induced closure models.

References

- (1) Jaffee, R. I., *Progress in Metal Physics*, Vol. III, Pergamon Press, London, 1958, p. 65.
- (2) Williams, J. C., "Phase Transformations in Titanium Alloys: A Review", *Titanium Science and Technology*, Vol. 3, Jaffee, R. I. and Burte, H. M., eds., Plenum Press, 1973, p. 1433.
- (3) Chesnutt, J. C., Rhodes, C. G., and Williams, J. C., "The Relationship Between Mechanical Properties, Microstructure and Fracture Topography in $\alpha+\beta$ Titanium Alloys", *ASTM STP 600*, ASTM, Philadelphia, 1976, p. 99.
- (4) Chesnutt, J. C., Thompson, A. W., and Williams, J. C., "Influence of Metallurgical Factors on the FCGR in $\alpha-\beta$ Titanium Alloys", AFML-TR-78-68, Air Force Materials Laboratory, Air Force Systems Command, Wright-Patterson AFB, OH, May 1978.
- (5) Margolin, H., Chesnutt, J. C., Luetjering, G., and Williams, J. C., "Fracture, Fatigue and Wear: A Critical Review", *Titanium '80, Science and Technology*, Vol. 2, Kimura, H. and Izumi, O., eds., TSM-AIME, 1981, p. 2337.
- (6) Paton, N. E. and Mahoney, M. W., *Met. Trans. A*, Vol. 7, 1976, p. 1685.
- (7) Williams, J. C. and Luetjering, G., "The Effect of Slip Length and Slip Character on the Properties of Titanium Alloys", *Titanium '80, Science and Technology*, Vol. 1, Kimura, H. and Izumi, O., eds., TMS-AIME, 1981, p. 671.

References
(Continued)

- (8) Ritchie, R. O. and Knott, J. F., *Acta Met.*, Vol. 21, 1973, p. 639.
- (9) Hudak, J. J., Saxena, A., Bucci, R. J., and Malcolm, R. C., "Development of Standard Methods of Testing and Analyzing FCGR Data", AFML-TR-78-40, Air Force Materials Laboratory, Air Force Systems Command, Wright-Patterson AFB, OH, May 1978.
- (10) Peters, M., Gysler, A., and Luetjering, G., "Influence of Microstructure on the Fatigue Behavior of Ti-6Al-4V", *Proc. of Fourth International Conf. on Titanium, Kyoto, Japan*, TMS-AIME, May, 1980, p. 1777.
- (11) Ruppen, J. A. and McEvily, A. J., "The Effect of Elevated Temperature and Environment on the FCG Characteristics of Ti-6Al-2Sn-4Zr-2Mo-0.1Si", *Fatigue of Eng. Mat. and Struc.*, Vol. 2, 1979, p. 63.
- (12) Beyer, J. R., Sims, D. L., and Wallace, R. M., "Titanium Damage Tolerant Design Data for Propulsion Systems", AFML-TR-77-101, Air Force Materials Laboratory, Air Force Systems Command, Wright-Patterson AFB, OH, August 1977.
- (13) Ruppen, J. A., private communication.
- (14) Allison, J. E. and Williams, J. C., "The Influence of Deformation Mode on FCG in Ti-Al Alloys", presented at AIME Annual Meeting, Chicago, IL, February, 1981.
- (15) Walker, N. and Beevers, C. J., "A Fatigue Crack Closure Mechanism in Titanium", *Fatigue of Engineering Materials and Structures*, Vol. 1, 1979, p. 135.
- (16) Mayes, I. C. and Baker, T. J., "Load Transference Across Crack Faces During FCG at Positive Values of R in Low Growth Rate Regime", *Metals Science*, Vol. 15, 1981, p. 320.

APPENDIX D

MODELING OF FLOW INSTABILITY
IN Ti-6242

G.R. Canova and J.J. Jonas
McGill University
Montreal, Quebec

APPENDIX D

MODELING OF FLOW INSTABILITY IN Ti-6242

Introduction

The torsion test appears to be of great use for the investigation of industrial processes. Its importance for rolling mill simulation is evident from the abundant literature of the past decade. The present report is concerned with the simulation of flow localization in forging, which is a process that occurs in shear. This makes the torsion test particularly useful, as it also involves deformation by shear.

Another advantage of the torsion test is the absence of changes in geometry during straining, a simplification which enables the physical parameters involved in the phenomenon to be studied more directly. If the investigation were to be carried out in tension, for example, flow localization would still take place, of course, but the preponderant effect of the reduction in cross-section with strain would obscure to some extent the effect of the metallurgical and heat transfer parameters. Similar problems occur in compression, which appears to be closer to forging than torsion. Even though Jonas et al. (1) found that a modified Considère construction applies, which indicates that whenever flow softening occurs, the flow should become inhomogeneous, it is not clear from such an analysis just why severe barrelling and shear instabilities arise under some testing conditions, but not under others.

By contrast, the effects of the physical and metallurgical coefficient on the localization of flow in torsion can be readily followed. This is done by drawing lines parallel to the longitudinal axis of the sample, the slopes of which give the value of the local shear strain. Thus, as long as the slope of the line remains constant with displacement

along the axis during deformation, no localization takes place. Conversely if, at a particular cross-section, the slope increases more quickly than elsewhere, then it is clear that the flow has concentrated at that location. Since the latter kind of process occurs in forging and can be readily produced or prevented in torsion, it is possible to study the parameters involved in the onset and evolution of the instability of the plastic flow.

Theoretical Analysis

The approach to be described below is restricted to quasi static conditions of testing, under which the couple C can be assumed to be fully transmitted along the sample. The validity of the engineering flow laws will also be taken for granted, so that the stress τ will be considered to depend uniquely on the strain γ , strain rate $\dot{\gamma}$ and temperature T . Although such a simplification is not, of course, valid at elevated temperatures, a full 'state variable' approach makes the analysis much more cumbersome, and will not be described at this stage. Under 'engineering law' conditions, any local shear stress within the radial distribution can be written:

$$\begin{aligned}\tau_r &= \tau(\gamma, \dot{\gamma}, T) \text{ with} \\ \gamma &= r\theta; \dot{\gamma} = r\dot{\theta}\end{aligned}$$

where r is the local radius, θ and $\dot{\theta}$ are respectively the twist per unit length and twist rate per unit length.* The couple, which is written:

$$C = 2\pi \int_0^R \tau r^2 dr = C(R, \theta, \dot{\theta}, T) \quad (1)$$

will, therefore, be dependent on R , the outer radius, and on θ , $\dot{\theta}$ and T , as defined above.**

*For convenience, in what follows, we will call them the twist and twist rate.

**Equ. (1) can also be expressed as:

$$C = 2\pi \bar{\tau} \int_0^R r^2 dr = 2\pi \bar{\tau} R^3 / 3$$

which means that a maximum in the torque C does not correspond to a maximum in the outer shear stress, but to a maximum in the average shear stress.

The chain rule applied to the couple leads to:

$$d \ln C = \left. \frac{\partial \ln C}{\partial \theta} \right|_{\dot{\theta}, R, T} d\theta + \left. \frac{\partial \ln C}{\partial \ln \dot{\theta}} \right|_{\theta, R, T} d \ln \dot{\theta} + \left. \frac{\partial \ln C}{\partial \ln R} \right|_{\theta, \dot{\theta}, T} d \ln R + \left. \frac{\partial \ln C}{\partial T} \right|_{\theta, \dot{\theta}, R} dT \quad (2)$$

The first partial is the rate of 'work hardening' of the torque, and is a kind of average work hardening. It has been shown (2) that:

$$\left. \frac{\partial \ln C}{\partial \theta} \right|_{\dot{\theta}, R, T} = \frac{\int_0^R H(r) \tau r^3 dr}{\int_0^R \tau r^2 dr}, \text{ where } H(r) = \left. \frac{\partial \ln \tau}{\partial \gamma} \right|_{\dot{\gamma}}$$

is the local work hardening rate. In what follows it will be referred to as Γ . The second term, $\left. \frac{\partial \ln C}{\partial \ln \dot{\theta}} \right|_{\theta, R, T}$ is the twist rate (or strain rate)

sensitivity of the torque. In a similar way, it has been shown that:

$$\left. \frac{\partial \ln C}{\partial \ln \dot{\theta}} \right|_{\theta, R, T} = \frac{\int_0^R M(r) \tau r^2 dr}{\int_0^R \tau r^2 dr}$$

It also represents an average strain rate sensitivity, and will be represented by m .

$\left. \frac{\partial \ln C}{\partial T} \right|_{\theta, \dot{\theta}, R}$ is the temperature sensitivity of the torque. This negative

number, which is called ϕ below, is again an average since:

$$\phi = \frac{\int_0^R \phi(r) \tau r^2 dr}{\int_0^R \tau r^2 dr},$$

where $\phi(r)$ is the local temperature sensitivity of the stress. The term $\left. \frac{\partial \ln C}{\partial \ln R} \right|_{\theta, \dot{\theta}, T}$ changes with time. It is known to be rigorously

equal to 3 in the elastic range, and increases slightly during plastic deformation. (For example, it is equal to about 3.25 in copper at room temperature at large strains (3)). For simplicity, it will be taken as constant here, which will lead to a small error. It will be represented by Δ .

This error is diminished if very small geometric defects are taken into account. As the analysis below deals with geometric defects of the

order of 1%, $\Delta \frac{d \ln R}{dX}$ is a very small but non zero term.

The dependence of Γ , M , and ϕ on R can therefore be ignored.

Using Equ. (2) and assuming $\frac{d \ln R}{dt} = 0$, the couple is given by:

$$\frac{d \ln C}{dt} = m \frac{d \ln \dot{\theta}}{dt} + \Gamma \dot{\theta} + \phi \frac{dT}{dt} \quad (3)$$

where t is the time. Also, the gradients are given by:

$$m \frac{d \ln \dot{\theta}}{dx} + \Gamma \frac{d\theta}{dx} + \phi \frac{dT}{dx} + \Delta \frac{d \ln R}{dx} = 0 \quad (4)$$

If $\frac{d\theta}{dx}$ is called λ , then

$$\frac{d \ln \dot{\theta}}{dx} = \frac{1}{\dot{\theta}} \frac{d\dot{\theta}}{dx} = \frac{d^2 \theta}{\dot{\theta} dt dx} = \frac{d(d\theta/dx)}{d\theta} = \lambda'.$$

We call $dT/dx = \mu$, and $d \ln R/dx = \delta$.

Another relation is derived from the fact that the tests are conducted at constant speed (RPS), i.e. $RPS = \int_0^L \dot{\theta} dx$ (5), where L is the entire gauge length.

Calculation of the Heat Exchange

At any location of the sample, the temperature changes due to heat generation are given by: $\rho c \frac{dT}{dt}(r) = \eta \tau_r \dot{\gamma}_r$ (6) where ρ is the density,

c the specific heat and η the fraction of work converted into heat. Since the useful variable in one case is the torque C , we will multiply equ. (6) by $2\pi r dr$ and integrate it. The result is:

$$2\pi \rho c \int_0^R r \frac{dT}{dt}(r) = \eta \dot{\theta} 2\pi \int_0^R \tau r^2 dr. \text{ This can also be written as}$$

$$\rho c \frac{dT}{dt} \pi R^2 = \eta \dot{\theta} C \text{ or } \frac{dT}{dt} = \frac{\eta \dot{\theta} C}{\pi R^2 \rho c} \quad (7)$$

There is, of course, a radial heating rate distribution, as shown by Lahoti and Altan (4). However, at each location x along the

sample axis, the average radial heating rate (and temperature) is of more significance since we are more concerned with the longitudinal distribution. If radial gradients are not neglected and conduction is taken into account, following the same procedure as for equ. (7), we have:

$$\rho c \frac{dT}{dt} = \eta \tau \dot{\gamma} + k \left[\frac{d^2 T}{dx^2} + \frac{1}{r} \frac{d}{dr} \left(r \frac{dT}{dr} \right) \right].$$

Therefore,

$$2\pi \rho c \int_0^R r \frac{dT}{dt} = \eta \dot{\theta} C + 2\pi k \int_0^R r \frac{d^2 T}{dx^2} + 2\pi k \int_0^R \frac{d}{dr} \left(r \frac{dT}{dr} \right) dr \quad \text{or}$$

$$\frac{dT}{dt} = \frac{\eta \dot{\theta} C}{\pi R^2 \rho c} + \frac{k}{\rho c} \frac{d^2 \tilde{T}}{dx^2} + \frac{2k}{R \rho c} \frac{dT}{dR}. \quad (70)$$

The term $\frac{dT}{dR}$ is the radial temperature gradient at the surface of the specimen.

The case described in Fig. 1 (3), i.e., at high twist rates, represents a nearly adiabatic condition, and can be taken as a strict upper bound of the cases presented here. Note that the curve at $t = .057$ will be taken as the upper bound since it corresponds approximately to the conditions employed. From Fig. 1, it can be seen that the slope $\frac{dT}{dR}$ at the outer radius is rather

small, so that the third term of the RHS of equ. (7a) can be neglected. If the convective term is also introduced we have:

$$\frac{dT}{dt} = \frac{\eta \dot{\theta} C}{\pi R^2 \rho c} + \frac{k}{\rho c} \frac{d^2 \tilde{T}}{dx^2} + \frac{2h}{R \rho c} (T_o - \tilde{T}) \quad (8)$$

where T_o is the outside temperature, and h the heat transfer coefficient.

In summary the evolutionary law:

$$\frac{d \ln C}{dt} = m \frac{d \ln \dot{\theta}}{dt} + \Gamma \dot{\theta} + \phi \dot{T} \quad (3)$$

and the following equations:

$$m \lambda' + \Gamma \lambda + \phi \mu + \Delta \delta = 0 \quad (4)$$

$$RPS = \int_0^L \dot{\theta} dx \quad (5)$$

$$\dot{T} = \frac{\eta \dot{\theta} C}{\pi R^2 \rho c} + \frac{k}{\rho c} \frac{d^2 \tilde{T}}{dx^2} + \frac{2h}{R \rho c} (T_o - \tilde{T})$$

have to be solved at any instant in order to find the longitudinal distributions of twist, twist rate, temperature and heating rate, and to

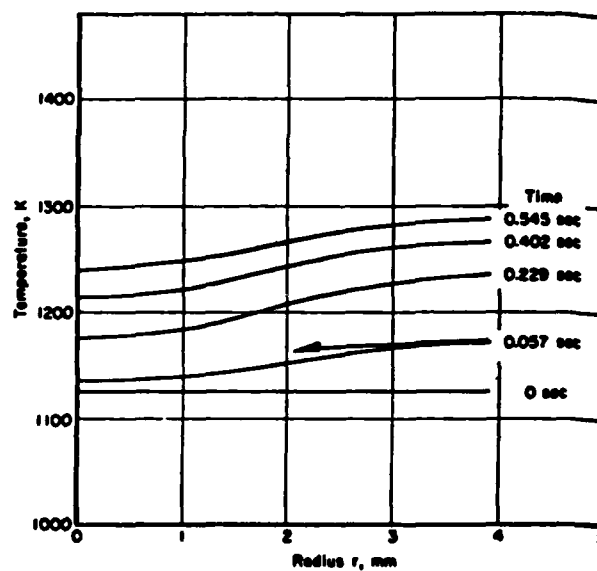


Figure D-1. Temperature distribution across a torsion test specimen
(Ti6Al-4V, dimensions: 7.62 mm ϕ \times 25.4 mm long, test rpm = 1160).

predict the actual torque C . It is implicit in the present analysis that the material parameters m , r , ϕ depend on θ , $\dot{\theta}$ and T , whereas Δ will be taken approximately to be equal to 3.

Some Theoretical Predictions

All testing conditions will lie between the following two extreme cases: (i) $\phi\mu = 0$, i.e. isothermal conditions (i.e., very high k and/or h) or (ii) when the material is temperature insensitive. Then $k = h = 0$, i.e. purely adiabatic conditions.

For these two cases equation (4) becomes:

$$(i) \quad m\lambda' + \Gamma\lambda + 3\delta \approx 0 \quad (4i)$$

$$(ii) \quad m\lambda' + \left(\Gamma + \frac{\eta C \phi}{\pi R^2 \rho c}\right)\lambda + 3\delta \approx 0 \quad (4ii)$$

The latter is derived from Equ. (7), assuming that the term dR/dx is negligible. Therefore equ. (7) reduces to:

$$\frac{dT}{dx} = \frac{\eta C}{\pi R^2 \rho c} \cdot \frac{d\theta}{dx}.$$

Substituting the latter into equ. (4) we get equ. (4ii).

Three typical flow curves are presented in Fig. 2. Case (a) corresponds to the work hardening material that is deformed at low temperatures. In Case (b), the stress saturates, a situation which occurs at around half the homologous melting temperature. In Case (c) the work hardens up to a peak stress, and then it softens, a behaviour which is often exhibited at high homologous temperatures. The examples presented above describe the behaviour of the material in isothermal conditions. The two curves (i) and (ii) shown in Fig. 3(a), (b) and (c), and which correspond to eqs. (4i) and (4ii) respectively, represent the twist rate gradient λ' , is θ (i.e. the overall applied twist) for the cases (a), (b), (c) as shown in Fig. 2. Obviously, the higher the λ' , the faster the localization will develop.

All curves start from the value $\lambda'_1 = -\frac{3}{m}\delta$, which only depends

on the geometric defect size and the rate sensitivity. It is worth noting that if the condition $\phi\mu = 0$ is fulfilled and if the sample is defect free

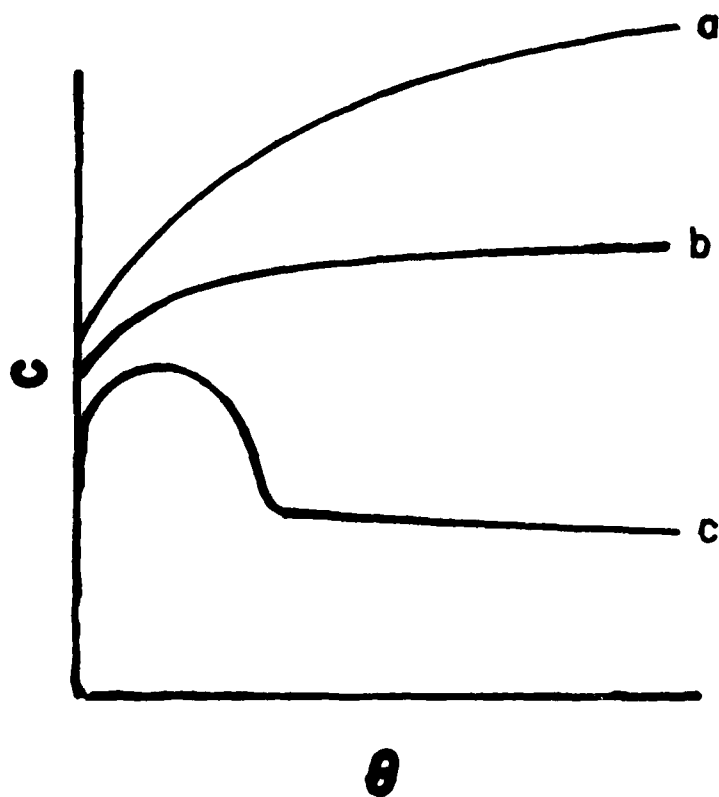


Figure D-2. Typical flow behaviours
a) work hardening
b) work hardening with saturation
c) flow softening

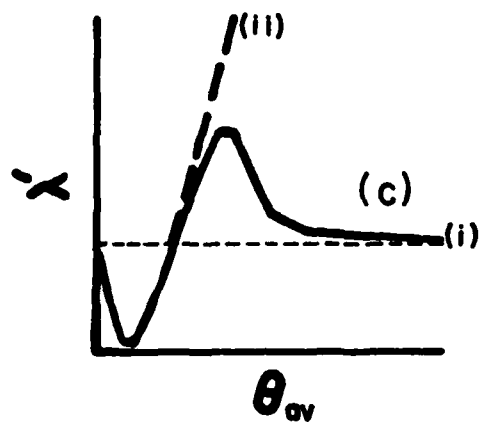
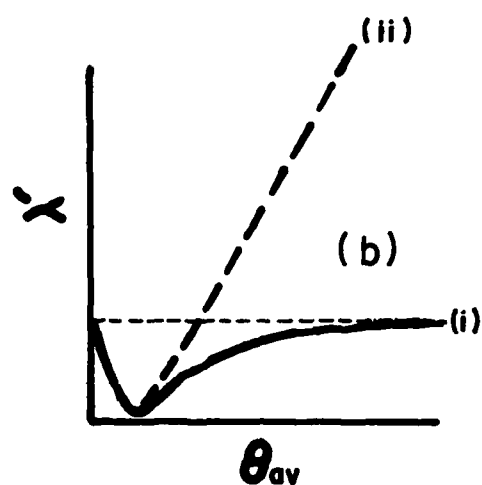
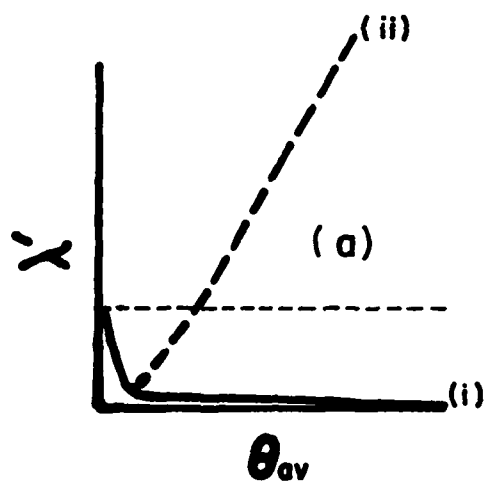


Figure D-3. Evolution of the twist-rate gradient λ' with the applied twist θ_{av} , for the three cases described in Fig. D-2, in isothermal (i) and adiabatic conditions (ii).

(i.e. $\delta = 0$), no localization will occur even when the material exhibited flow softening.

Among the three types of flow curves, only the flow softening one may lead to measurable localization which, however, never becomes unbounded and thus catastrophic shear instability is never observed. Therefore, flow softening can only initiate plastic instability, but it is not enough to lead to catastrophic concentration of flow.

However, when the test is adiabatic, i.e. there is no heat exchange with the surroundings, the flow will always become unstable; the strain at which the forming limit is reached for small values of the rate sensitivity can be considered as the one at which the 'apparent' work hardening $\Gamma + \frac{nC\theta}{\pi R^2 \rho c}$ becomes zero. Obviously, this forming limit criterion is not applicable at higher values of m . In the latter case a critical value of the slope $\frac{d\lambda'}{d\theta}$ has to be taken as the criterion for the attainment of the forming limit (4). Case (c) is the one which will lead to instability in the shortest time period.

If the test is fully adiabatic, there is no heat flow due to conduction or convection, and therefore in the absence of any defect, there will be flow softening without any flow localization. This is, of course, an extreme case, but if the thermal conductivity is not exactly zero, heat will flow outwards through the grips. Thus a temperature gradient ($\mu \neq 0$) will develop leading to flow localization even in the absence of defects.

An interesting type of test that has been performed by G. Ferron (5), is to deform the material in steps, in between of which the test is stopped and the temperature is homogenized. This procedure (Fig. 4) tends to inhibit flow localization. Another way of avoiding the development of temperature gradients is to deform the sample very slowly.

Numerical Integration - Comparison With the Experimental Observations

In this section the numerical integration of equations (3,4,5,8) is described, and the comparison between the theoretical predictions and the experimental results will also be demonstrated.

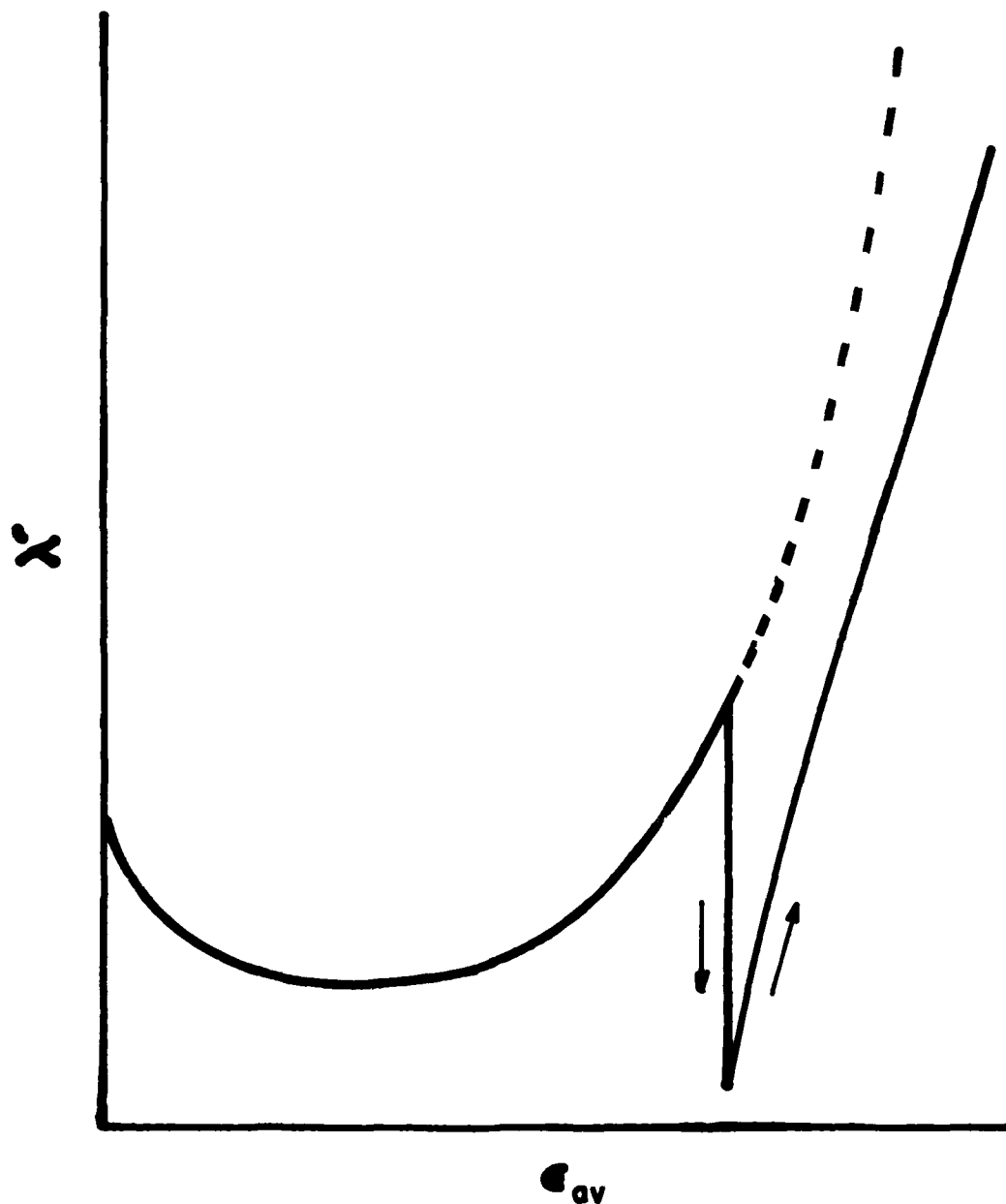


Figure D-4. Effect of the holding of the test on the flow localization due to thermal effect. Note the stabilizing effect due to the homogenization of the temperature. After reference (3).

a) Integration Procedure

The 'sample' is divided into 100 slices. Twenty of those describe a geometric defect of sinusoidal shape that has a maximum size of 3.4%. At $t = 0$, both λ and μ are zero, so that equ. (4) gives directly the local twist rate gradient because, $\ln \frac{\dot{\theta}_{i+1}}{\dot{\theta}_i} = -\frac{3}{m} \ln \frac{R_{i+1}}{R_i}$. Therefore $\dot{\theta}_i = \dot{\theta}_1 \left(\frac{R_1}{R_i}\right)^{-3/m}$

substituting the latter into equ. (5), we have $RPS = \dot{\theta}_1 \int_0^L \left[\frac{R_1}{R(x)}\right]^{-3/m} dx$

an expression which gives directly the twist rate of the first slice, and therefore the whole distribution of $\dot{\theta}$. Here i is the slice index and $i = 1$ to 100. Using equ. (8), the entire heating rate distribution can be derived. Applying a time increment that has to be adjusted in order to prevent unrealistic gradient distributions, the new temperatures and twists are calculated at time $t = dt$ and therefore the new torque can be derived through equ. (3). Once this is done t is increased by a time increment dt that may differ from the previous one.

At any time $t \neq 0$, the knowledge of the values of the twist and temperature gradients during the previous time increment are used for the deviation of the actual twist rate gradient through equ. (4). Also the use of equ. (8) is slightly modified by the introduction of the conduction and convection terms, the rest of the procedure being as was explained above.

The model has been used to predict the behaviour of 304 stainless steel at room temperature. It had been shown (6) that an overall shear strain rate $\dot{\gamma} = .5 \text{ s}^{-1}$ led to instabilities due to thermal softening. This particular material was chosen because it exhibits low thermal conductivity, as in the case of Ti-6242. Unlike Ti-6242 that has to be tested at high temperatures, the steel was deformed at room temperature in order to evaluate more accurately Γ , m and ϕ . The control of the sample is done much easier at room temperature than if the experiments were carried out at elevated temperatures. Isothermal tests were conducted in a temperature controlled silicon oil bath. The liquid was stirred in order to ensure forced convection.

b) Comparison with Experimental Results

Samples of 304 stainless steel were machined as shown in Fig. 5. Block lines were drawn parallel to the longitudinal axis of the sample so that the local strains could be calculated. The method used for this calculation is the following (shown in Fig. 6): pictures of the sample were taken at different amounts of applied strain, and then the negatives were enlarged. Reference X-Y axes were taken as shown in Fig. 6. The angle corresponding to any point M is given by:

$\theta = \cos^{-1}(\frac{y}{R_1})$, where R_1 is the apparent radius of the sample on the enlarged negative. Two points M and M^1 can define the local strain as follows: $\gamma(M, M^1) = R_1 \frac{\theta^1 - \theta}{x^1 - x}$. We can see from this formula the reason that the origin

of the angles and the x axis is not important since here only differences are of interest. The torque/strain curve shown in Fig. 7 is a typical example of the progress of flow localization.

Another set of curves of the variation of the temperature in and outside the defect region was obtained by attaching a thermocouple on the sample and monitoring its output on a HP X-Y recorder.

In the following analysis it is assumed that C can be expressed as follows:

$C = C_0 \exp(\Gamma/\theta) \theta + \phi(\theta) T \dot{\theta}^m$, and therefore Γ is temperature insensitive* as well as θ .

The curves are shown in Fig. 8. The Γ - θ relationship that is used is $\Gamma = .189127 \exp(-.434564 * \theta)$. The correlation between the data and this relationship is illustrated in Fig. 9. The temperature sensitivity of the torque is approximated by a second order polynomial. In case θ exceeded the value of 5 the polynomial acquired its maximum value. The polynomial is:

$\phi = (.019137 \theta^2 - .166493 \theta - .011303) 10^{-2}$. Note that ϕ is always negative, and its dimensions are $^{\circ}\text{C}^{-1}$. Finally the value of m was taken from the literature (5) to be .02 and constant.

*This is only an approximation, since only a small range of temperatures is considered. Thus an average Γ was taken into account.

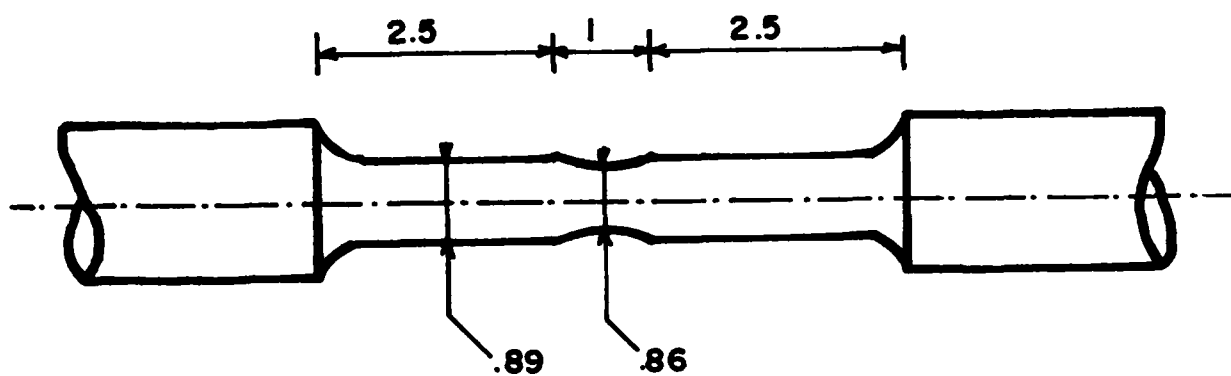


Figure D-5. Torsion samples used for the instability measurements. Those used to determine the material parameters had no defect.

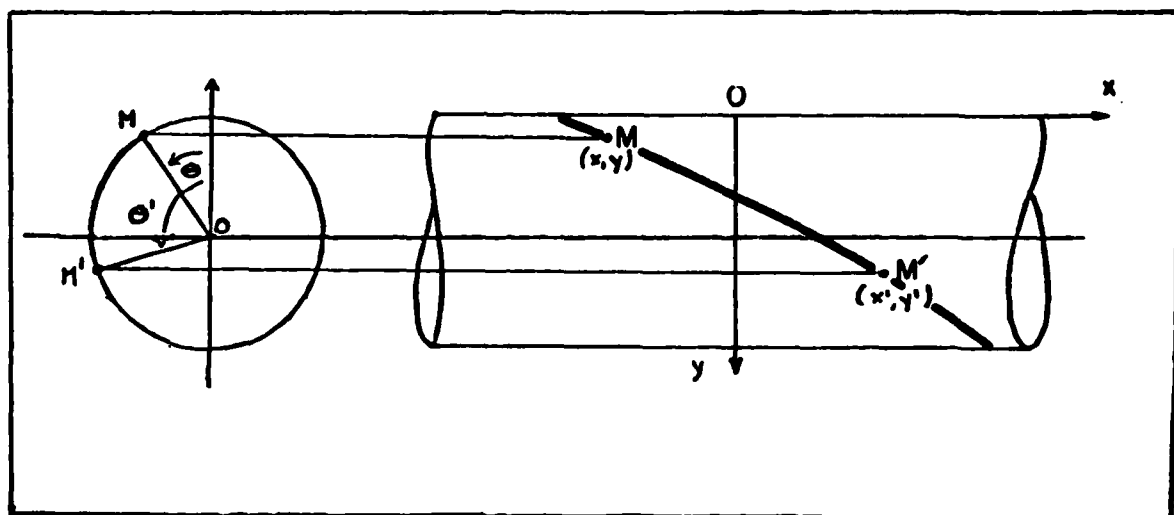


Figure D-6. Photographic method of calculating the local strains.

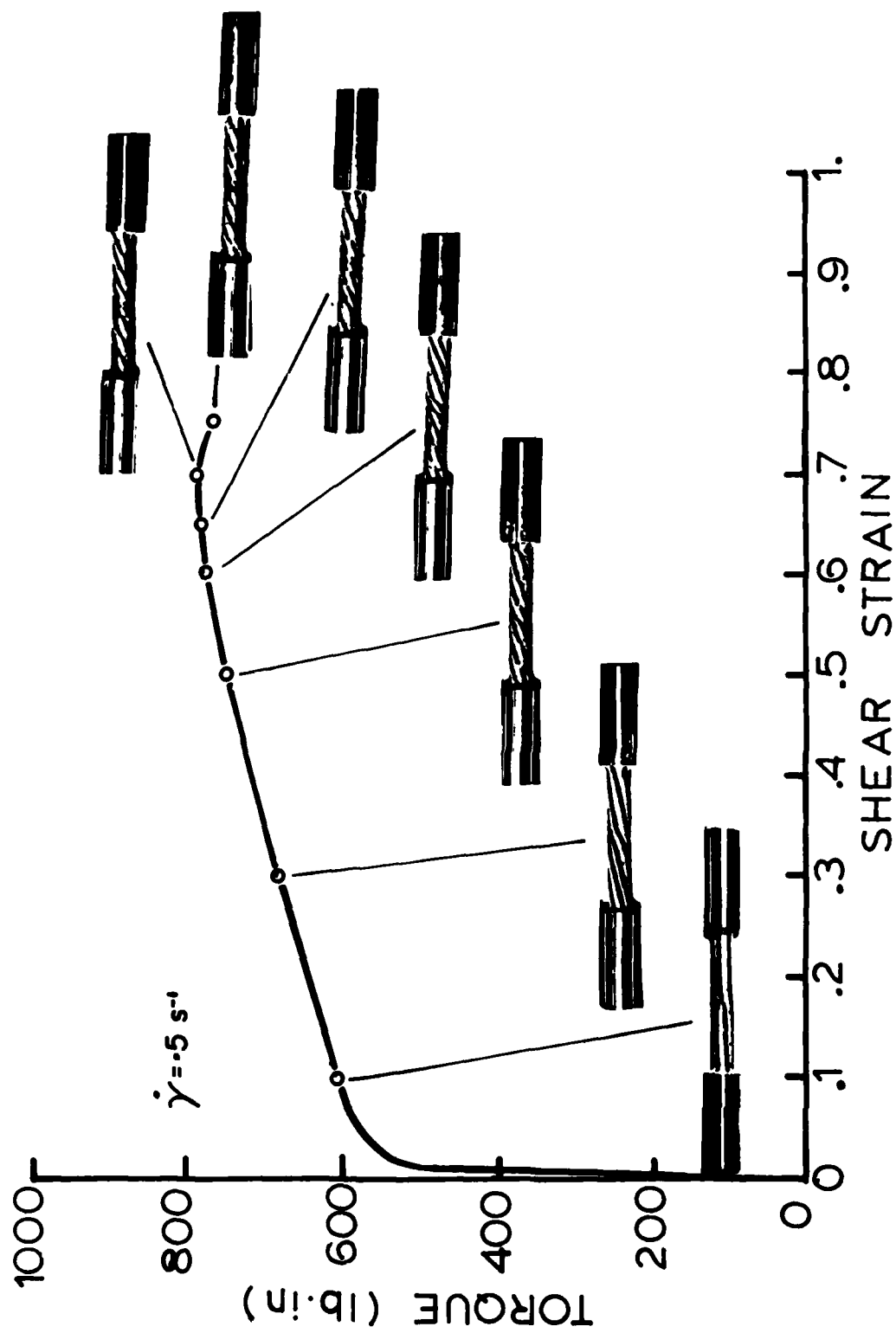


Figure D-7. Typical evolution of the flow localization in 304 stainless steel torsion bars. Note $\dot{\gamma} = .5s^{-1}$.

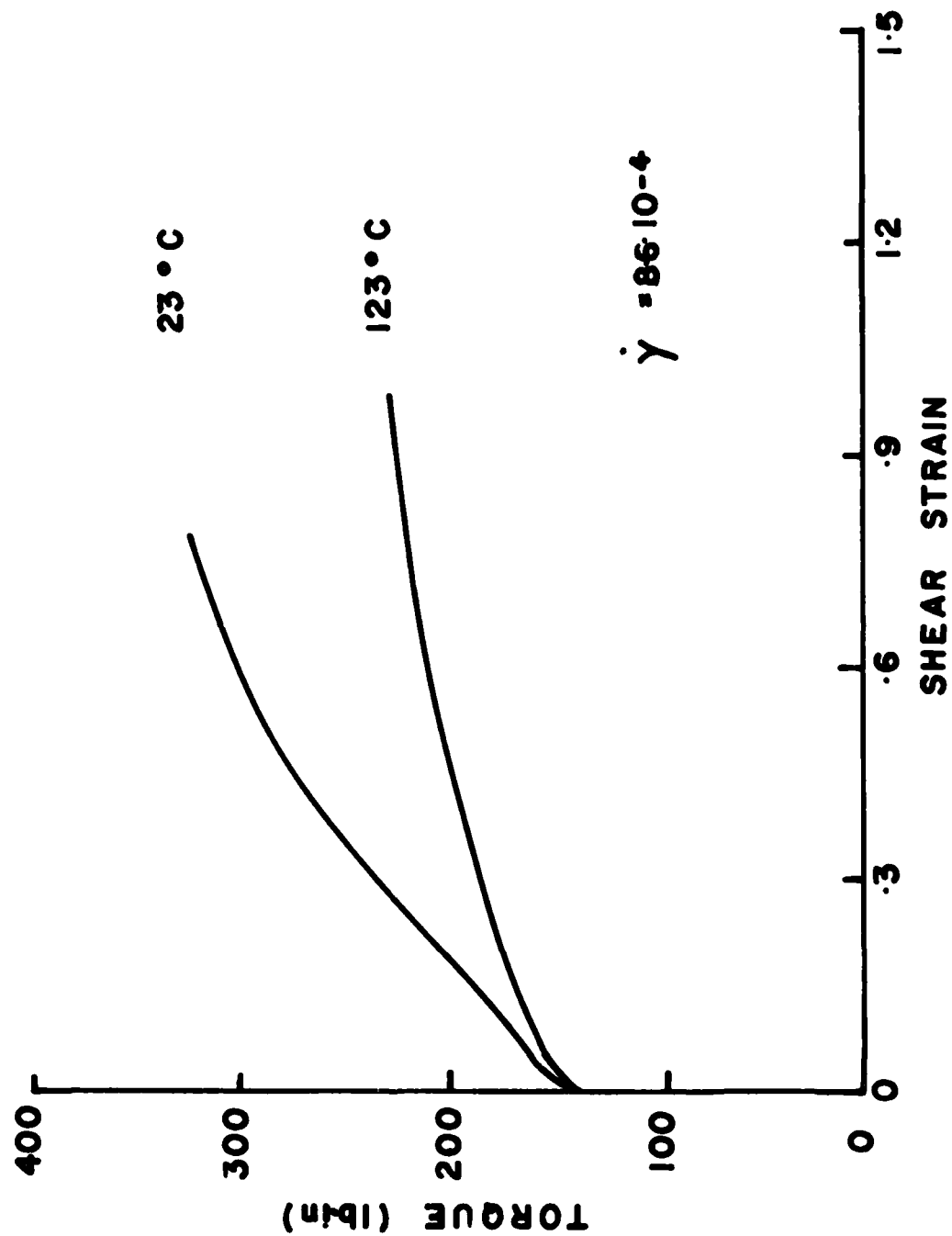


Figure D-8. Slow strain rate tests with controlled temperature.

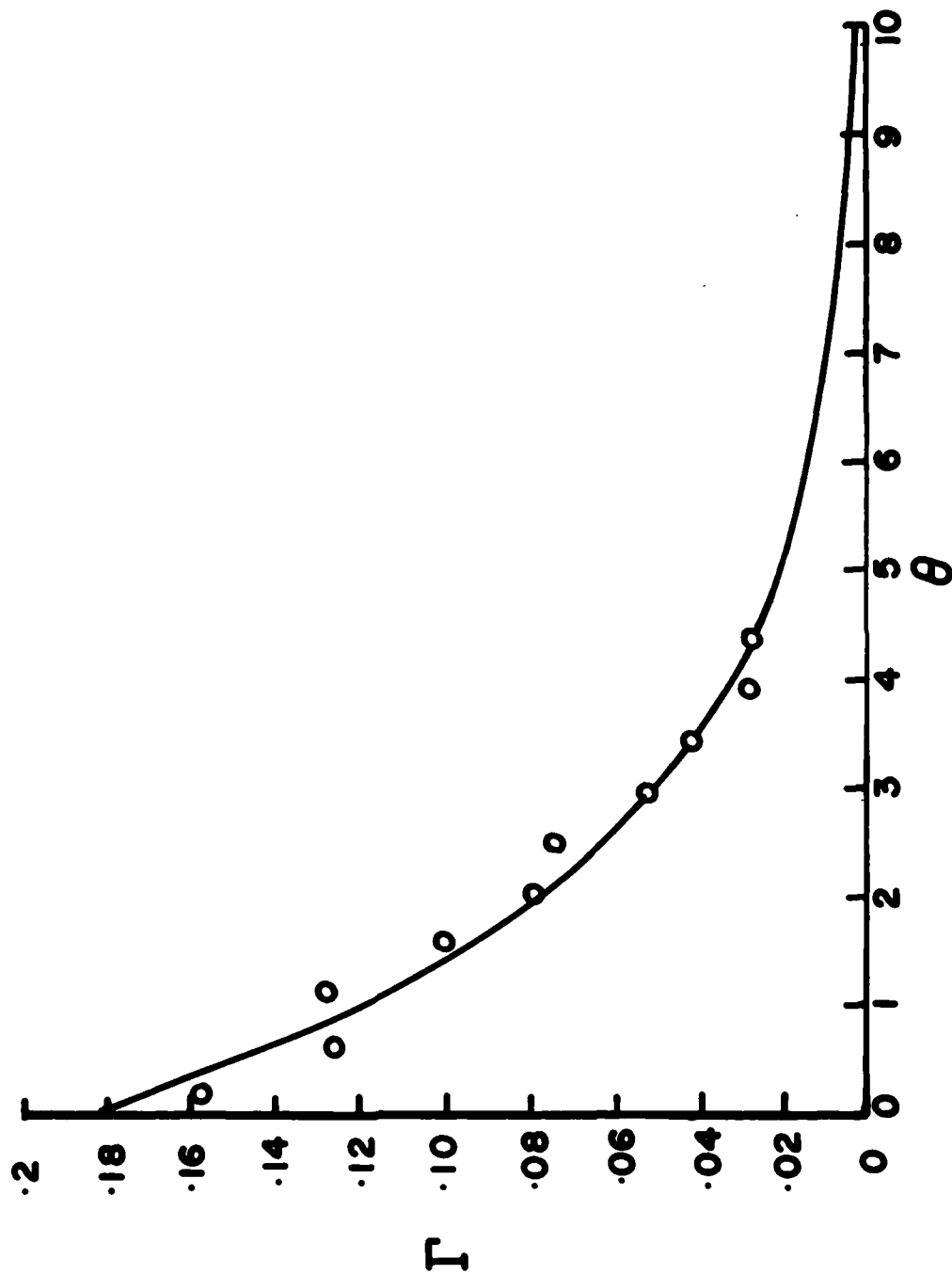


Figure D-9. Determination of Γ by the law $\Gamma = .189127 \exp(-.434564\theta)$.

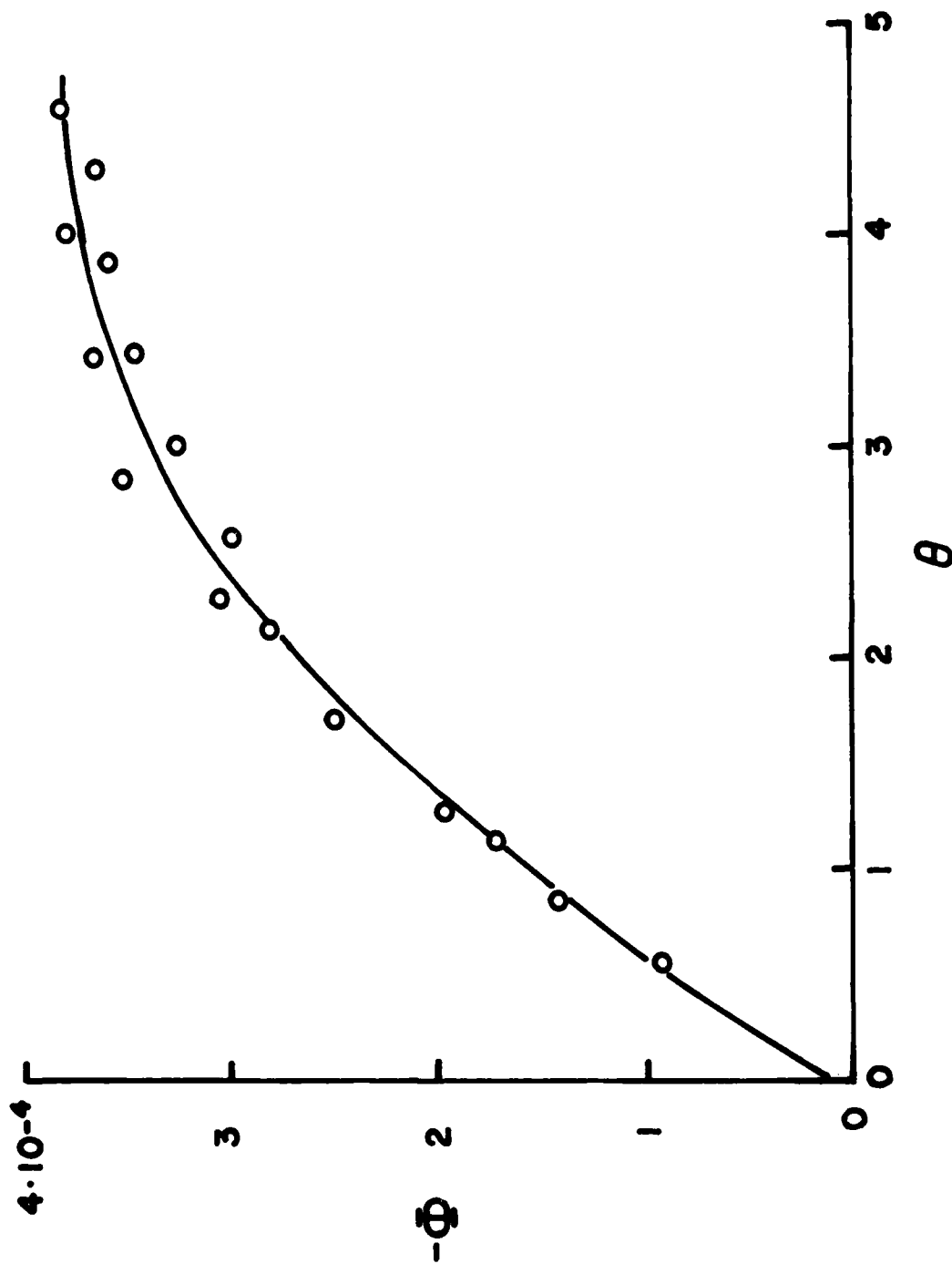


Figure D-10. Fitting of ϕ by the polynomial: $\phi = (.0191370)^2 - .1664930$
 $- .011303) \cdot 10^{-2}$.

Fig. 11 shows the experimental as well as the theoretical results. The upper curve represents the evolution of the strain inside the defect region (as an average over the entire neck length), whereas the lower one the defect free region (also as an average). The two curves are in fairly good agreement. The discrepancy can be attributed partly to the experimental error, but also to the assumption that the work hardening is temperature insensitive. If Γ is a function of T (i.e. decreasing with T), it is obvious that the localization process will accelerate and therefore the measured and predicted curves will come closer.

The temperature measurements of Fig. 12 were considerably affected by the response time and the thickness of the thermocouple. Also in this case, despite the qualitative agreement, the assumption that the work hardening is rate insensitive did delay the predicted flow concentration.

Conclusions

A model has been developed which predicts flow localization in torsion in terms of the material parameters m , Γ and Φ , and the result is given in terms of strain rate gradient (λ'), strain gradient (λ) and temperature gradient (μ).

It has been shown that, in isothermal conditions, ($\Phi\mu = 0$), only the flow softening case can eventually lead to measurable flow localization (which stabilizes), provided that there is an initial imperfection.

When $\Phi\mu$ is no longer negligible, flow localization can be promoted even in the absence of any defect, the temperature gradient being sufficient in certain cases for initiating a strain concentration. This is true irrespective of the work hardening law that the material obeys.

Plastic instability starts to be measurable when the 'apparent' work hardening reaches zero. However, a forming limit cannot be defined at the corresponding strain since the strain rate sensitivity (m) may delay the catastrophic shear localization. It should rather be defined when a critical slope of the $\lambda' - \theta$ curve is reached.

The model predicts fairly well the localization of flow, but can be improved by a better description of the material parameters, which will be done in the near future.

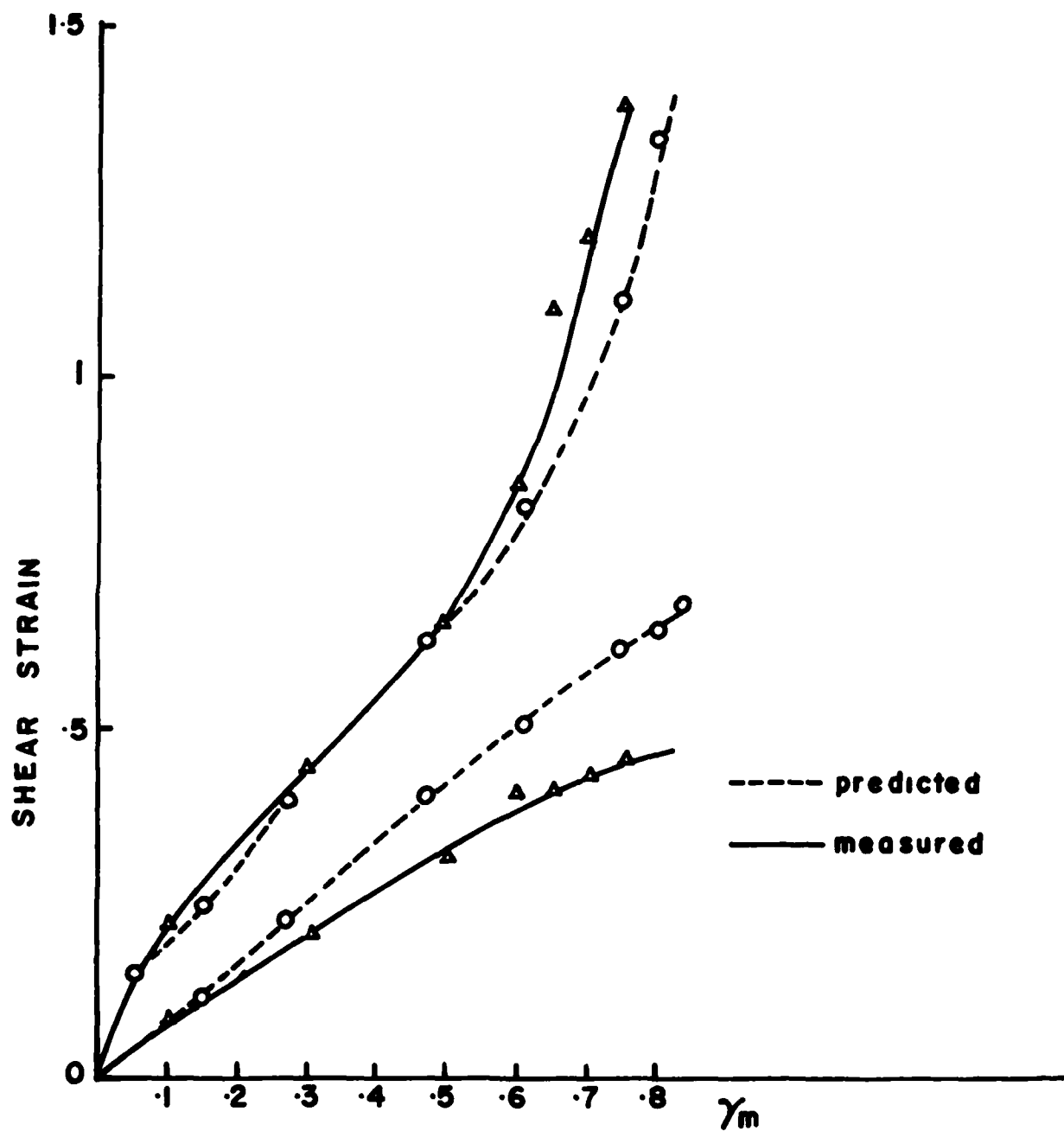


Figure D-11. Comparison of predicted with measured temperatures in the neck (upper curves) and in the bulk (lower curves).

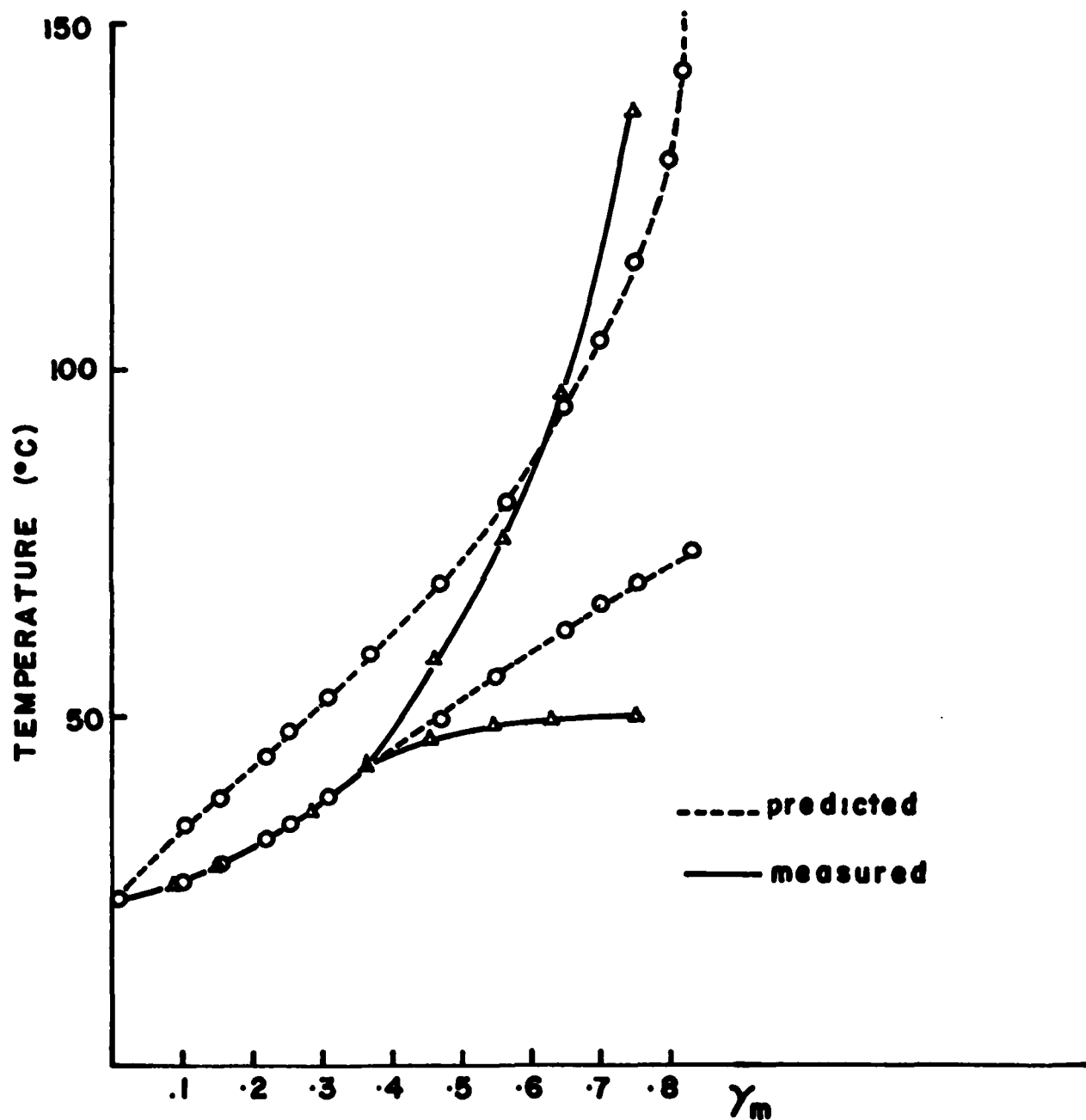


Figure D-12. Comparison of predicted with measured temperatures in the neck (upper curve) and in the bulk (lower curve).

Future Work

The model for the prediction of flow instability in torsion that has been checked on 304 stainless steel at room temperature needs to be corrected by taking into account the temperature dependence of the work hardening. β preform Ti-6242 tested at $\dot{\epsilon} = 10^{-2} \text{ s}^{-1}$ and $T = 913^\circ\text{C}$ promotes instability, whereas the $\alpha + \beta$ preform type does not. The next step is to measure Γ and ϕ as a function of θ , T and $\dot{\epsilon}$ (the latter effect cannot be neglected at that temperature) in order to predict the strain and temperature evolutions. The same photographic technique will be used to calculate local strains.

References

- (1) Jonas, J.J., Holt, R.A., and Coleman, C.E., Acta Met., 24, 911 (1976).
- (2) Canova, G.R. et al., unpublished work.
- (3) Lahoti, G.D., and Altan, T., J. Eng. Mat. Tech., Trans. ASME, 97, 113 (1975).
- (4) Christodoulou, N., Masters Thesis, McGill University (1978).
- (5) Ferron, G., Mat. Sc. Eng., in press.
- (6) Grandillo, A. et al., internal report, (1980).

APPENDIX E

DEVELOPMENT OF A PROCESSING MAP USING
ALUMINUM AS A MODEL MATERIAL

Rishi Raj

Cornell University
Ithaca, NY 14853

APPENDIX E

DEVELOPMENT OF A PROCESSING MAP USING ALUMINUM AS A MODEL MATERIAL

Introduction

The yield and the product quality in a high temperature forming process depends to a large extent on the ductility of the material. It is also true that the metal often becomes rate-sensitive during high temperature deformation; this requires forming to be carried out within a certain "window" in the strain-rate and temperature field. Metallurgical phenomena are so complex that one would always have to rely on experience to successfully operate a process, but it has now become possible to define these "windows" on a mechanistic basis, at least for simple materials such as aluminum, which can serve as a guideline for the control of process variables.*

In this Appendix[†] we build such a process map on the basis of cavity nucleation mechanisms, dynamic recrystallization and adiabatic heating effects. We limit ourselves to fairly fast processes, typically at strain rates higher than about 10^{-3} s^{-1} and a temperature field which extends from about $0.4 T_m$ to $0.8 T_m$ --equivalent to 373°F to 750°F in aluminum. The map is constructed on the basis of nucleation thresholds. As such it represents a conservative account of the fracture strain, since fracture requires nucleation, growth and linking of cavitation damage. The growth strains have not been included in the map, because doing so would have required the specification of the strain-state and the stress-state in addition to strain-rate and temperature. In certain instances, when the integrity of the forged component is important, it may in fact be more sensible to design the process in terms of initiation of microcracks rather than fracture, since microcracks may cause degradation of properties such as fatigue.

*Wray²⁴ has thought about $\dot{\epsilon}$ vs T maps to categorize failure mechanisms several years ago. The attempt in this paper is to consider the problem more quantitatively.

[†]The work presented here has been published in Metallurgical Transactions, June 1981.

Damage Mechanisms

A. Cavities at Particles of a Second Phase

The influence of hard particles on low temperature ductility of metals has been rigorously studied by Palmer and Smith⁽¹⁾ and Edelson and Baldwin⁽²⁾. Cavities initiate because particles do not deform themselves, which forces the matrix around the particles to deform more than average, which in turn produces more work hardening and, therefore, a higher stress near the particles. When the stress gets large enough, the interface may separate or the particle itself may crack, whichever occurs first. A picture from Palmer and Smith⁽¹⁾ and an accompanying schematic is shown in Fig. 1. The result is that the ductility is strongly dependent on the size and the density of the second phase particles.

If a material containing hard particles is deformed at an elevated temperature then the rate of work-hardening will be reduced by recovery. In addition, diffusion will transport matter from regions of compression around the particles to regions of tension, thus relieving the stress concentration. The relaxation time for the diffusional mechanism can be theoretically calculated. Other creep process will serve to reduce this relaxation time further, but the relaxation should occur at least as fast as calculated for the diffusional mechanism alone. This concept leads to an expression for a threshold strain rate; if the applied strain rate is slower, then cavities will not form because the stress-concentration around the particles would be relaxed more rapidly than it is produced. The critical strain rate is given by⁽³⁾

$$\dot{\epsilon}_d = \frac{118(1-\nu)(1-2\nu + \frac{2}{\pi})}{(\frac{5}{6} - \nu)^2} \frac{G\Omega}{kT} \frac{f_v \delta D_b}{p^3} . \quad (1)$$

The material then would suffer ductile fracture only if the applied strain rate,

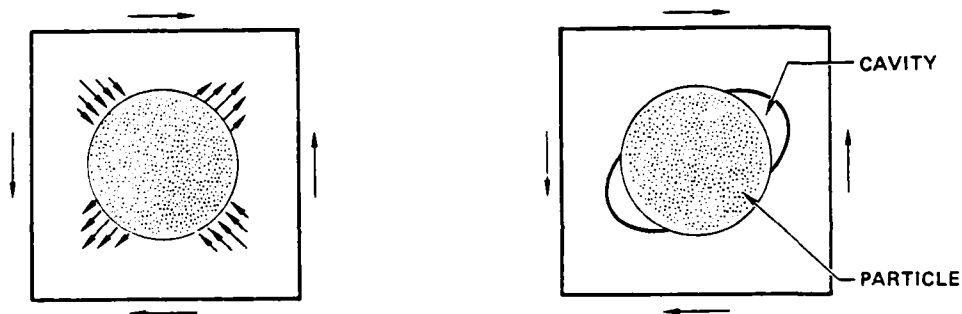
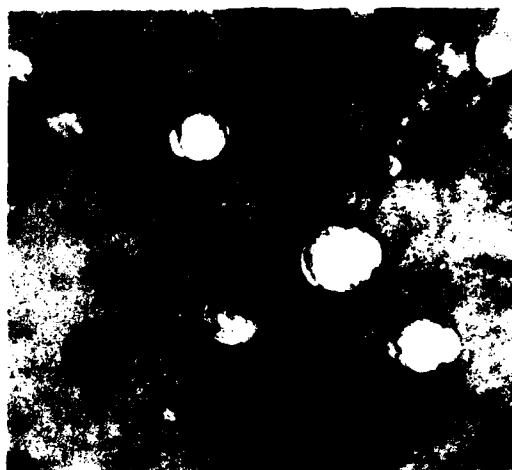


Fig. 1. In ductile fracture cavities initiate at hard particles as shown in a micrograph by Palmer and Smith.⁽¹⁾ If tensile stresses produced by inhomogeneous flow around the particle, shown in (b) had been relaxed by diffusional transport then the cavity, as shown in (c), would not have initiated. Micrograph magnification X150,000.

$$\dot{\epsilon} > \dot{\epsilon}_d .$$

(2)

Here G is the shear modulus, Ω is the atomic volume, δD_b the self diffusivity times the interface width at the particle-matrix interface, f_v and p are the volume fraction and the size of the particles.

It should be noted that Eq. (1) applies when particles are all of the same size and when they do not deform themselves to relax the stress concentration. In real materials neither of these conditions are strictly correct but one can speculate how $\dot{\epsilon}_d$ will change if the particles have a size distribution and if they can deform does not mean that cavities will not form; any mismatch between the flow properties of the matrix and the particles will give rise to stress concentration and the potential for cavity initiation at the interface. However, a malleable particle will serve to relax the local stress, which will allow a strain-rate greater than $\dot{\epsilon}_d$ to be tolerated without producing cavities. In this sense, $\dot{\epsilon}_d$ is a sort of lower bound on the strain-rate, i.e., Eq. (2) gives a limiting condition for ductile fracture. The other point is that $\dot{\epsilon}_d$ depends on f_v/p^3 , therefore, it is extremely sensitive to the particle size. Since particles are expected to have a statistical distribution, the question arises how this should be accounted for when applying Eq. (1). A distribution in p will produce a spread in $\dot{\epsilon}_d$ i.e., as the strain rate is gradually decreased, fracture would occur by cavitation at the larger particles at slower strain rates and by cavitation at the finer particles at faster strain rates. It should be kept in mind, though, that $\dot{\epsilon}_d$ depends on f_v as well as p . A more detailed analysis of the stochastic version of Eq. (1) is needed; at the moment all that can be said is that as the distribution shifts towards larger particle sizes, $\dot{\epsilon}_d$ will decrease. For a conservative estimate of $\dot{\epsilon}_d$, it would be appropriate to use the value of p in the tail of the particle size distribution, rather than the average value of p .

It is possible to calculate the strain for the nucleation of cavities at particles if a value for a limit nucleation strain, i.e.,

one when there is no relaxation of stress known, and if a power-law hardening of the matrix around the particles is assumed. The exact calculation for the parabolic and linear hardening materials is included in the publication. For parabolic hardening, the nucleation strain, ϵ_n , expressed as a ratio of the limit nucleation strain, ϵ_n^0 , is given by:

$$\frac{\epsilon_n}{\epsilon_n^0} = 2 \left(\frac{\dot{\epsilon}}{\dot{\epsilon}_d} \right)^2 \left\{ - \frac{\dot{\epsilon}_d}{\dot{\epsilon}} - \ln \left(1 - \frac{\dot{\epsilon}_d}{\dot{\epsilon}} \right) \right\} \quad (3)$$

A plot of ϵ_n/ϵ_n^0 vs $\dot{\epsilon}_d/\dot{\epsilon}$ is shown in Fig. 2. A graph for a linear hardening material is also included. The latter serves to show that the power law has little effect on the nucleation strain and that nucleation would occur within a factor of 2 of the limit nucleation strain even when the strain-rate is only 1.5 times the critical strain-rate.

B. Wedge Cracking at Grain Boundaries

Grain boundaries slide easily at temperatures above about $0.4 T_m$. The result is that significant stress concentrations are produced at the triple grain junctions. These can produce wedge type micro-cracks at the grain boundaries. Their size will be about the grain size, as shown in Fig. 3, and if a sufficient number of them form then the material would fracture.

The probability of wedge cracking will vary with the applied strain-rate. If the strain-rate is so high that the matrix deforms at a rate faster than the boundaries can slide, then sliding effects would be negligible and wedge cracking will not occur. If the strain-rate is very slow, then there will be enough time to relax the high stresses at the triple junctions. Qualitatively then, the probability of wedge cracking will peak at an intermediate strain rate.

The upper strain-rate above which wedge cracks should not form can be calculated and measured.⁽⁴⁾ It would depend on the sliding resistance, k_b , of a single boundary, such as one in a bicrystal, when

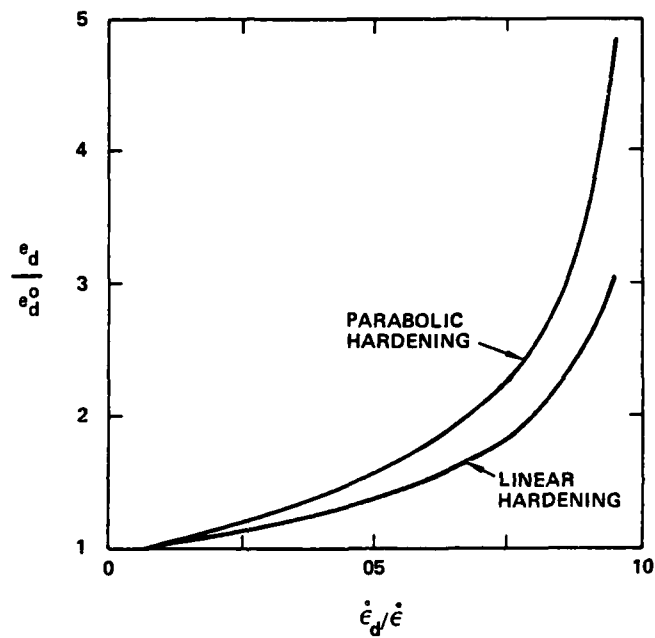


Fig. 2. The increase in the nucleation strain, ϵ_n , normalized with respect to the lowest possible value of the nucleation strain, ϵ_n^0 , as the applied strain rate, $\dot{\epsilon}$, approaches the critical strain-rate, $\dot{\epsilon}_d$, thus $\dot{\epsilon}$ is very large when $\dot{\epsilon}_d / \dot{\epsilon} = 0$, $\dot{\epsilon} = 2\dot{\epsilon}_d$ in the center and $\dot{\epsilon} = \dot{\epsilon}_d$ on the right. Note that $\epsilon_n / \epsilon_n^0$ approaches ∞ as $\dot{\epsilon} \rightarrow \dot{\epsilon}_d$.



Fig. 3. As shown by this classical picture by Yim and Grant,⁽²³⁾ sliding is a necessary condition for the initiation and propagation of wedge cracks. Permission to publish granted by ASM. Magnification not available.

a shear stress, σ_s , is applied to the boundary. Normally, the sliding rate is linear,^(5,6) so that the following equation applies:

$$\sigma_s = k_b \dot{U} \quad , \quad (3)$$

where \dot{U} is the rate of sliding.

Sliding rate of a boundary in a bicrystal is limited only by its intrinsic resistance as there is no constraint against the offsets produced at the surface of the bicrystal during sliding. In a polycrystal, however, there is an additional constraint to sliding from triple grain junctions. It can be asserted, therefore, that for a given applied stress the sliding rate in polycrystals will be slower than the sliding rate \dot{U} as given by Eq. (3). If \dot{U} is the maximum possible rate of sliding in a polycrystal, then the maximum possible strain-rate below which sliding will still be possible will be given by:

$$\dot{\epsilon}_w = \frac{\dot{U}}{d} \quad , \quad (4)$$

where d is the grain-size. In a polycrystal wedge-cracking will be possible only if the applied strain rate

$$\dot{\epsilon} < \dot{\epsilon}_w \quad . \quad (5)$$

It follows from Eqs. (3) and (4) that $\dot{\epsilon}_w$ depends on the flow stress, σ_s and on k_b . k_b can be calculated with a sufficient degree of confidence^(5,7) by using the following equation when the boundary contains particles of area fraction f_b and average size p :

$$k_b = \frac{kT}{8\Omega} \frac{f_b p^2}{\delta D_b} \quad (6)$$

where Ω is the atomic volume and δD_b is the interface width times the self diffusivity along the interface. Nevertheless, the best way to estimate k_b is through measurements of grain boundary damping by internal

friction.^(6,7) This yields a relaxation time, τ_s , for grain boundary sliding which is related to k_b through the equation:⁽⁷⁾

$$\tau_s = k_b \frac{1.14(1 - \nu^2)d}{E} \quad (7)$$

where E , ν are the Young's modulus and the Poisson's ratio. Combining Eqs. (3) through (7) yields an expression for $\dot{\epsilon}_w$:

$$\dot{\epsilon}_w = 1.14 \frac{s(1 - \nu^2)}{E \tau_s} \quad (8)$$

Further discussion on the use of the internal friction technique to estimate, $\dot{\epsilon}_w$, and on the problem of wedge cracking, is contained in Ref. 4, copies of which are available upon request.

Dynamic Recrystallization

At high temperatures, usually above $0.7 T_m$, and at high strain-rates, many metals recrystallize dynamically. This phenomena is of crucial importance in hot-working. It provides a means to grain refinement and homogenization of structure. Although this is possible in simple deformations, such as upsetting of cylinders, in which the strains and the strain-rates in different parts are essentially uniform, in more complex forming operations dynamic recrystallization may produce shear bands. Shear bands usually form when there is little constraint to deformation from the dies at angles which are approximately 45° to the direction of maximum principal stress. Dynamic recrystallization is therefore included in our map, because it must be controlled during a hot-forming process.

The phenomenon of dynamic recrystallization is exemplified by the unusual stress-strain curves it produces. A schematic and an example are included in Fig. 4.^(8,9) At high strain-rates, dynamic recrystallization starts after a peak stress is reached and occurs continuously thereafter which leads to continuous flow softening. At

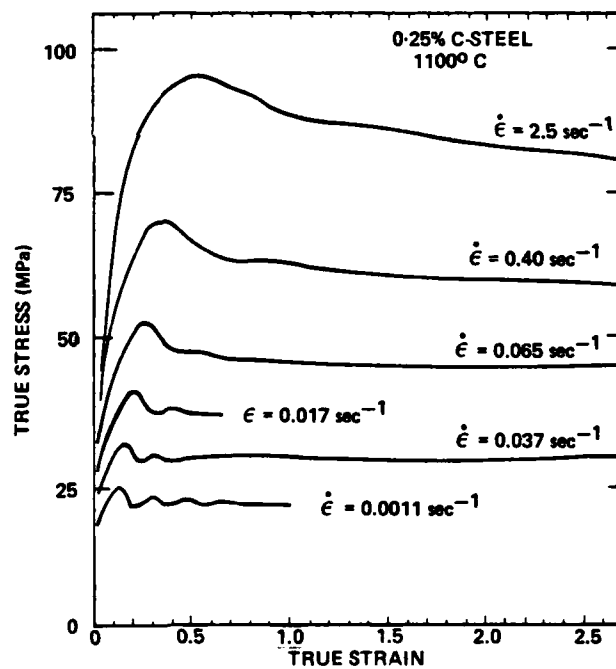
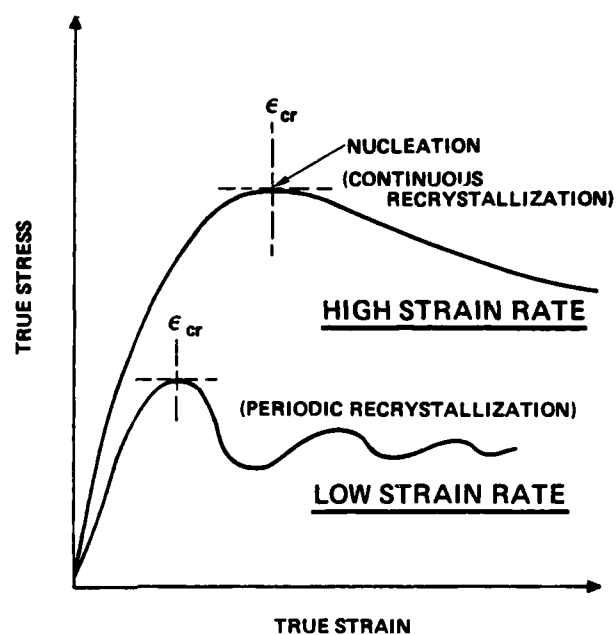


Fig. 4. A schematic of the $\sigma \sim \epsilon$ curve when there is dynamic recrystallization. An actual example due to Rosard and Blain⁽⁹⁾ is shown on the right.

lower strain rates, recrystallization begins at a lower strain, but thereafter it is periodic rather than continuous. For the map we shall consider the criterion for the start of dynamic recrystallization which is expressed in terms of strain, ϵ_{cr} , the strain rate, $\dot{\epsilon}_r$ and T, the temperature. It is then possible to express a relation between strain rate and temperature for dynamic recrystallization in the following form:

$$\dot{\epsilon}_r = Z(\epsilon_{cr}) e^{-Q/RT} \quad (9)$$

Phenomenological studies show that Z is an increasing function of ϵ_{cr} .^(10,11)

Adiabatic Heating

It is possible to calculate the strain rate at which adiabatic heating may lead to catastrophic flow localization. We assume a power law constitutive equation for flow of the following form:

$$\dot{\epsilon} = A' e^{\frac{-Q}{RT}} \bar{\sigma}^n \quad (10)$$

where

$$\bar{\sigma} = \frac{\sigma}{G}, \quad (11)$$

and where A' is a dimensionless parameter.

The rate of temperature change in a volume element will be given by

$$\frac{dT}{dt} = \frac{G}{\rho C_p} \dot{\epsilon} \bar{\sigma}, \quad (12)$$

where ρ and C_p are the density and the specific heat of the material.

Taking logarithm of both sides of Eq. (10) and differentiating and asserting that the $\dot{\epsilon}$ is controlled and held constant, and then substituting from Eq. (11) we obtain

$$\frac{-d \ln \bar{\sigma}}{d \epsilon} = \frac{QG}{nRT^2 \rho C_p} \bar{\sigma} \quad (13)$$

A reasonable condition for localization would be

$$\frac{d \ln \bar{\sigma}}{d \epsilon} < -1 \quad (14)$$

which means that localization would occur if the flow stress decreases by more than a factor of e (≈ 2.7) when the true strain increases by unity. This leads to the condition:

$$\bar{\sigma}_h = \frac{nRT^2 \rho C_p}{QG} \quad (15)$$

with the implication that localization is likely if $\bar{\sigma} > \bar{\sigma}_h$. The corresponding critical strain-rate $\dot{\epsilon}_h$ can be computed by inserting $\bar{\sigma}_h$ into Eq. (10)

The implications of Eq. (15) are interesting. A lower temperature a low value of n , and a high Q will precipitate localization at a lower $\bar{\sigma}_h$, or a lower $\dot{\epsilon}_h$. This result is consistent with observations of forging of a near α Ti alloy above and below the $(\alpha + \beta) \rightarrow \beta$ transition temperature, β_T .⁽¹³⁾ Below β_T the flow stress is highly temperature and strain-rate sensitive, i.e., n is small and Q_v is large and localization occurs easily, whereas above β_T , the flow stress is practically independent of temperature, i.e., $n \rightarrow \infty$ and localization is usually not observed.

Construction of a Processing Map for Aluminum

In this section, a processing map for aluminum is constructed on the basis of the equations generated earlier. Curves are plotted for each of the mechanisms, separately at first, and then in concert, to delineate the "safe" region where processing without the risk of damage should be possible. All diagrams are drawn in the strain-rate and temperature field. The material parameters for aluminum used in these calculations are summarized together in Appendix II.

A. Ductile Fracture: Cavity Formation at Particles

A plot of $\dot{\epsilon}_d$ vs T for various values of ρ , the particle size, and for different values of $(\epsilon_n/\epsilon_n^0)$ are shown in Fig. 5. The suitability of our model to the data of Ayres⁽¹⁵⁾ has been discussed in an earlier paper.⁽³⁾ Ayres observed an increase in ductility below a characteristic strain-rate, as the strain-rate was lowered. The characteristic strain-rate changed with temperature; the four data points included in Fig. 5 represent the characteristic strain-rate as a function of temperature as measured by Ayres. The particle size, $p = 0.5 \mu\text{m}$, and the volume fraction $f_v = 0.05$ were taken from the fractographs in reference 15. It should be noted that Ayres tested an Al-4% Mg alloy rather than pure Al and that he interpreted the ductility enhancement in terms of a change in strain rate sensitivity rather than cavity nucleation. The use of his data in the present model is, therefore, tentative.

The threshold strain-rate is quite sensitive to the particle size and, to a lesser extent, to the volume fraction of the particles. A factor of 4 increase in particle size leads to a drop in the threshold strain-rate by nearly two orders of magnitude.

B. Wedge Cracking

Here we shall use the grain boundary internal friction data on high purity aluminum, reported by Kê.⁽⁶⁾

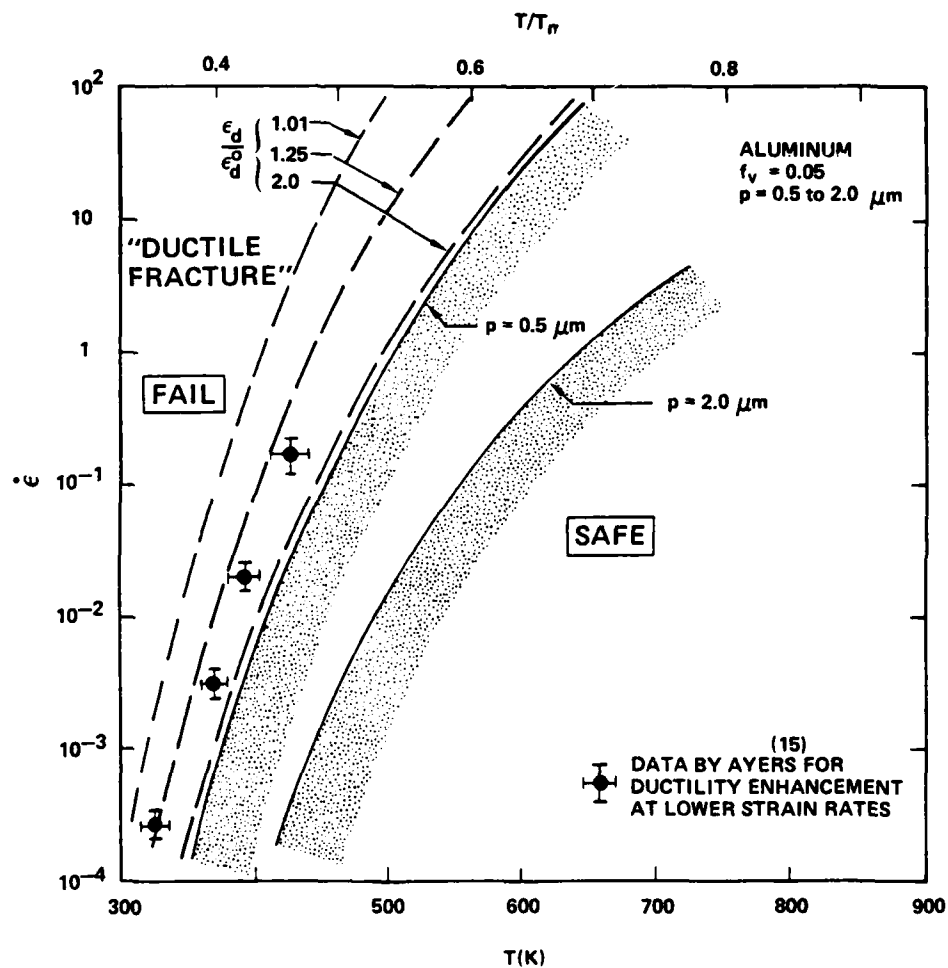


Fig. 5. A cavity initiation map for the initiation of cavities at second phase particles, as in ductile fracture.

If we assume a flow stress of about 4×10^{-2} G,
we obtain:

$$\dot{\epsilon}_w = 4.1 \times 10^5 \exp(-20.1 \text{ kcal mol}^{-1}/RT) \text{ s}^{-1} \quad (16)$$

for a grain size of $d = 200 \text{ } \mu\text{m}$. It should be noted that combining Eqs. (7) and (8) lead to results that $\dot{\epsilon}_w$ is inversely proportional to the grain size.

A plot for $\dot{\epsilon}_w$ for two different values of d is shown in Fig. 6. Some data points for the transition to wedge cracking measured by Servi and Grant⁽¹⁶⁾ on commercial aluminum are also shown. The agreement is only fair because of the difference in the alloys used in internal friction and fracture studies.

The region encompassing the $\dot{\epsilon} > \dot{\epsilon}_w$ should be safe against wedge crack failures.

C. Dynamic Recrystallization and Adiabatic Heating

Dynamic recrystallization in pure aluminum is usually not observed, but there is evidence of it in dilute alloys of aluminum.⁽¹⁷⁻¹⁹⁾ For the map, we assumed the data of Sellers and Tegart.⁽¹⁷⁾ The $(\dot{\epsilon}, T)$ curves for two different values of ϵ_{cr} , 0.5 and 2.0 are shown in Fig. 7. They cannot be relied on completely because of the scarcity of dynamic recrystallization data in Al, but they serve adequately enough to delineate the trends. If a map were to be constructed for steel, for which a considerable amount of data has been published, then the regions of dynamic recrystallization could be defined more firmly.

The type of data necessary to evaluate Eqs. (15) and (10) for adiabatic heating is not available in the literature. Qualitatively, localization of flow due to adiabatic heating will be most probable at intermediate temperatures. At low temperatures, the temperature and strain-rate sensitivity will decrease, which will cause $\bar{\sigma}_h$ (Eq. 15) to become large, while at high temperatures $\bar{\sigma}_h$ will be large because of high T . In our

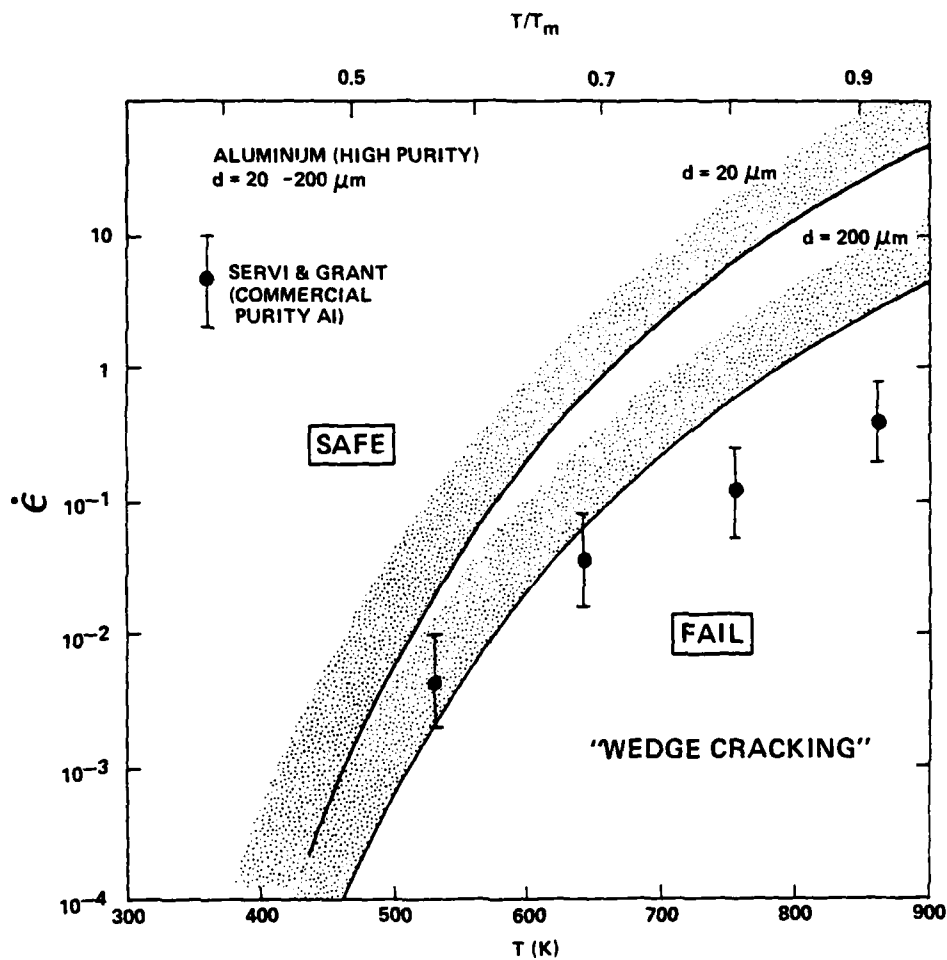


Fig. 6. A map for wedge cracking at grain boundaries. Wedge cracking is possible only if the strain-rate is less than a critical value. The critical strain-rate depends on the grain-size and on the size and spacing of any second phase particles in the grain boundaries.

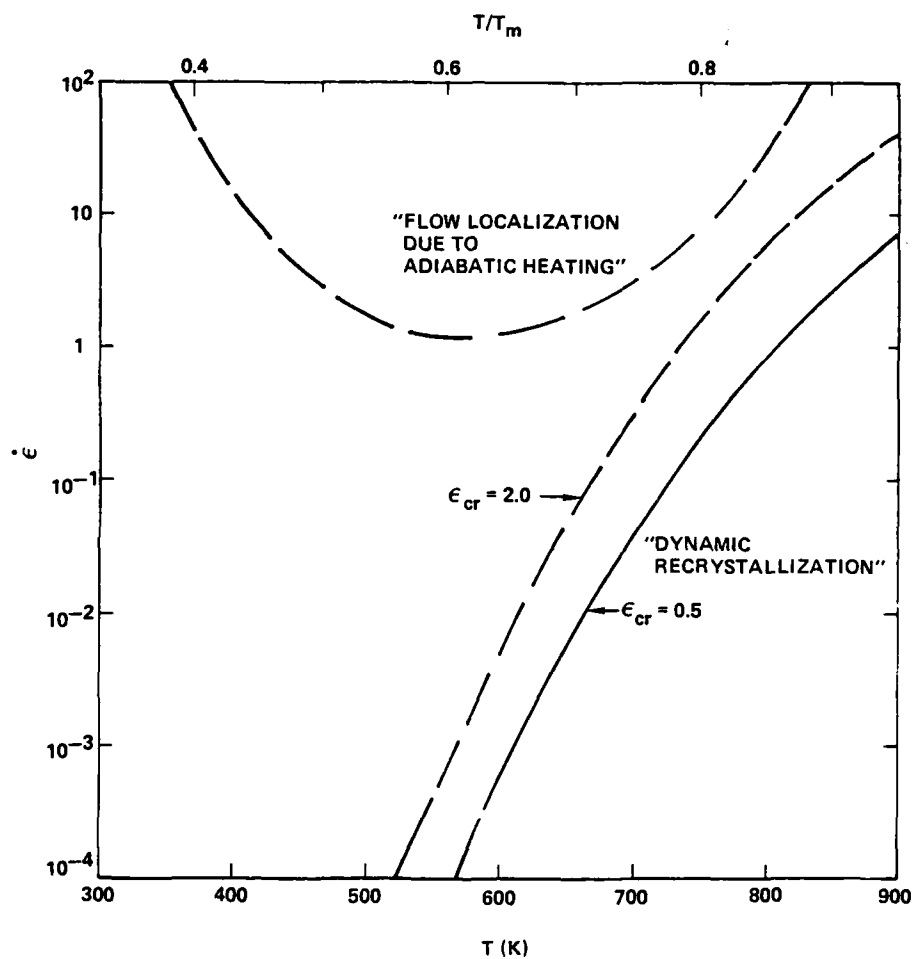


Fig. 7. Regions in which dynamic recrystallization is expected. The region of adiabatic heating is based on simple reasoning and is hypothetical.

diagram, therefore, we shall take the liberty of delineating a region where we think that localization of flow is most likely. This boundary, however, should be regarded with caution.

D. A Processing Map for Aluminum

The superimposition of the curves in Figs. 5, 6 and 7 leads to a composite shown in Fig. 8. Some interesting conclusions can be drawn from this diagram:

- 1) In the intermediate temperature and intermediate strain-rate regions, a "safe" window is predicted within which the material should be free from the risk of cavitation damage, and from flow localization due to dynamic recrystallization. The strain-rates and the temperature range in this window correspond quite well to the actual variables employed in commercial processes.
- 2) At a constant temperature, a maximum in ductility is predicted with respect to the strain-rate. For example, in the map, at 500K, the ductility should be maximum at a strain-rate of 10^{-3} to 10^{-1} s^{-1} . Below it wedge-cracking, while above it ductile fracture, would reduce ductility.
- 3) It should be remembered that apparent failure in a forming process is not always due to microstructural reasons alone, which is the basis of this map. Failure may also result from "continuum" effects which depend on the macroscopic flow properties of the material such as flow stress, work hardening rate and strain-rate sensitivity. A good example of this is found in sheet metal forming in which shear localization in the thickness direction can terminate a forming process. (20,21,22) Ultimately, both continuum and metallurgical phenomena must be combined to define the formability of the material as a function of the process variables.
- 4) The safe region shown in Fig. 8 is sensitive to the micro-structure of the metal. This is shown schematically in Fig. 9.

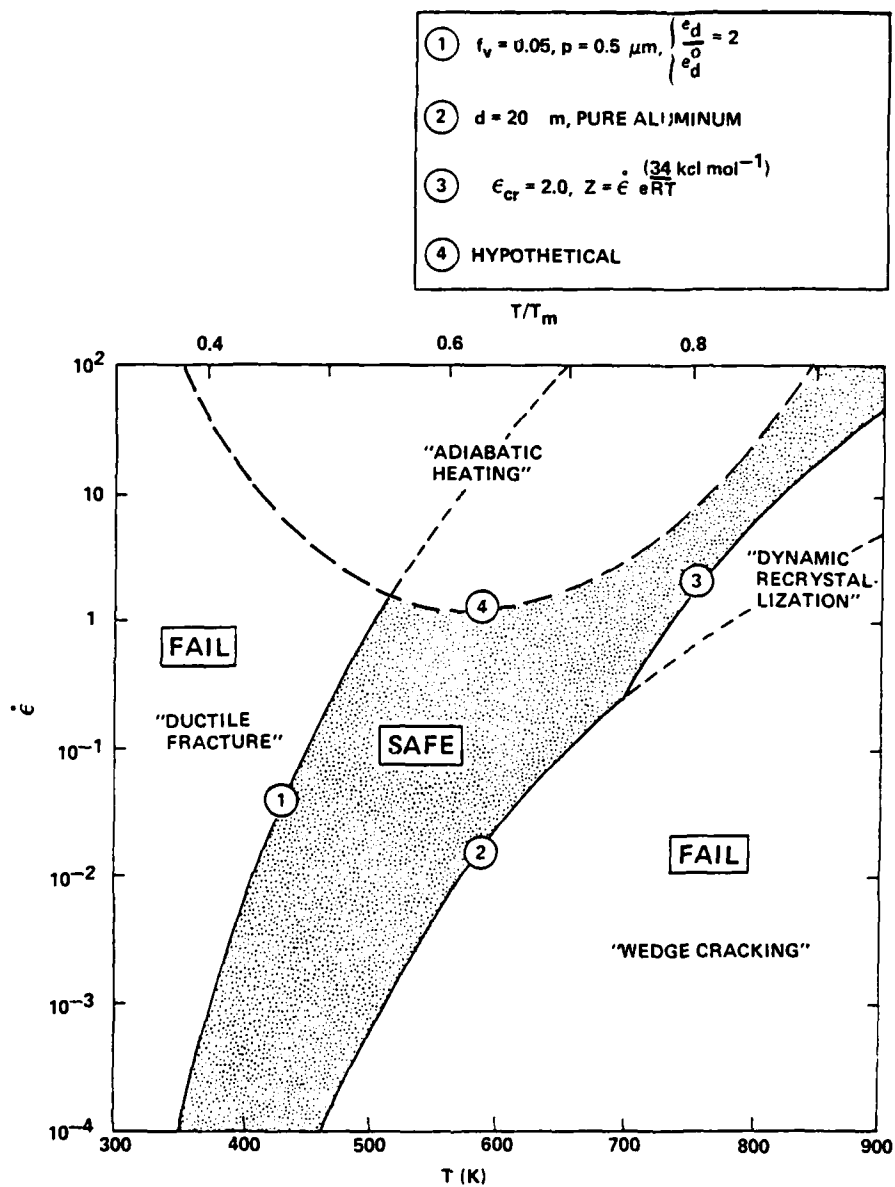


Fig. 8. A composite processing map delineating the safe region for forming. The boundaries will shift with microstructure. Instabilities due to purely continuum effects such as shear localization in sheet metal forming have not been considered.

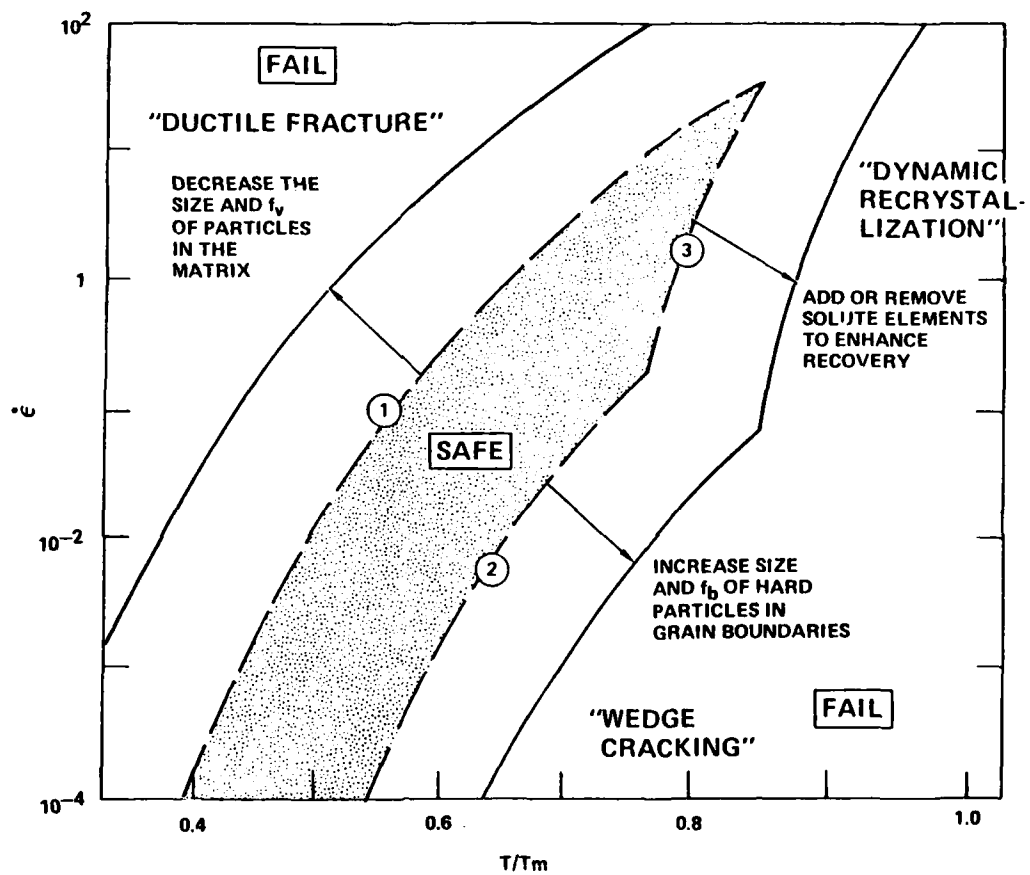


Fig. 9. A schematic of how the boundaries will shift with the micro-structure.

To decrease the probability of ductile fracture, the size and the volume fraction of the particles in the matrix should be reduced. The boundary curve 1 is very sensitive to the particle size ($\dot{\epsilon}_d \propto 1/p^3$). The incidence of wedge cracking can also be reduced by making sliding more difficult; this is achieved most directly by introducing large particles into the grain boundary. In this instance the strain rate at boundary curve 2 is $\dot{\epsilon}_w \propto 1/(f_b p^2)$, so that the size of the particles is again an important factor. Increasing the grain size should also decrease $\dot{\epsilon}_w$. Dynamic recrystallization and recovery are usually coupled inversely. The easier the recovery from work hardening, the more difficult is recrystallization. It follows that in order to move boundary curve 3 outwards, solid solution elements should be added (or removed) which enhance recovery of dislocations.

- 5) The boundary curves 1, 2, and 3 shown in the map can be experimentally determined. The position of boundary curve 1 can be measured by doing variable strain-rate tests at different temperature as described by Ayres.⁽¹⁵⁾ The position of boundary curve 2 can be ascertained through measurement of the relaxation time for grain boundary damping in internal friction as described in the example on page . Traditional methods, such as hot torsion tests, can be employed to specify the strain-rate and temperature conditions under which the material exhibits dynamic recrystallization. In fact attempts have been made in the literature to study various modes of high temperature fracture in torsion experiments.⁽²⁵⁾

Ductility in Superplastic Forming

This topic is not covered in the maps presented here. Since grain boundary sliding is intrinsic in superplastic behavior, one must operate within the wedge-cracking region in order to attain large deformations.

It should be remembered that the wedge-cracking strain-rate bound, $\dot{\epsilon}_w$, is based on a necessary condition for wedge cracking, i.e., sliding must occur in order to form wedge cracks. This, of course, is not a sufficient condition for wedge-cracking. For the latter one must calculate the time-dependent stresses near triple junctions incorporating sliding which causes the high stress, and local creep and diffusion which will seek to relieve the stress concentration. The competition between these two processes, both of which are rate dependent, will determine the extent of the actual stress concentration. Once the stresses have been estimated, one must then invoke a criterion for the nucleation and propagation of a wedge crack which would involve the local chemistry of the boundary, interface energies, and the size and the type of particles of a second phase which may be present at and near the triple grain junctions. Solutions and answers to these questions will no doubt be forthcoming in the near future from this research group.

Summary

A type of processing map is presented which considers three or four mechanisms by which damage can be introduced during warm and hot forming, and which then delineates regions in the strain-rate and temperature field in which these damage mechanisms will be avoided. In particular, initiation of cavities at hard particles which can lead to ductile transgranular fracture, wedge cracking which can lead to intergranular fracture, and dynamic recrystallization which can precipitate flow localization, have been considered. It is shown that ductile fracture should prevail at high strain-rates and low temperatures, wedge cracking at low strain-rates and high temperatures, and dynamic recrystallization at high strain-rates and high temperatures. This combination raises the possibility that there may be a region at intermediate strain-rates and intermediate temperatures which may be free from all three damage mechanisms. Equations have been developed for the three mechanisms and used to construct a map for aluminum. A safe region enclosed on all sides by these damage mechanisms does indeed emerge, as

shown in Fig. 8. Certain notes of caution and other remarks about such a map should be kept in mind, as outlined below:

- 1) These maps are conservative since they consider only the conditions under which nucleation of damage is possible. Specific criteria for nucleation are not invoked, only the conditions under which local stress-concentrations will or will not arise, have been considered. It is assumed that if stress-concentrations do not arise that nucleation should not occur.
- 2) Dynamic recrystallization can be useful or detrimental in a forming process. If it occurs uniformly in the entire forging, as it would in simple cases such as pancake forging, then it is desirable. If, however, it is localized then it may produce a microstructural discontinuity in the component.
- 3) The adiabatic heating region shown in Fig. 8 at the very high strain-rates is hypothetical. It is based on some simple reasoning but is not supported by observation.
- 4) The boundary curves that enclose the safe forming region are sensitive to the microstructure, as shown schematically in Fig. 9. This idea can be useful, at least qualitatively, in one aspect of alloy development, i.e., the formability of the alloy.
- 5) As it happens, a safe window encompassing a reasonable range of strain-rate and temperatures is predicted for aluminum for plausible values of the microstructural and process variables. It is not necessary that a window of such size will necessarily be obtained for other materials, although such an exercise would be well worth carrying out.
- 6) It should be remembered that the formability is not always limited by microdamage mechanisms. In sheet metal forming, for example, shear localization in the thickness direction, which often limits the forming process, can be modeled on

the basis of gross flow properties of the material such as flow stress, work hardening rate and strain-rate sensitivity. These instabilities are more a "continuum" rather than a metallurgical phenomena.

- 7) The ductility of superplastic materials has not been dealt with in this paper. The mechanism of superplasticity requires that boundary sliding should occur, which means that superplastic forming must be carried out within the wedge cracking region. In order to determine what would limit the ductility in superplastic deformation, one must consider in detail the criteria of wedge crack initiation and propagation.

References

1. I. G. Palmer and G. C. Smith, 2nd Bolton Landing Conf. Oxide Dispersion Strengthening, p. 252, Gordon and Breach, New York, NY, 1960.
2. B. I. Edelson and W. M. Baldwin, Jr., Trans. ASM, 1962, Vol. 55, p. 230.
3. R. C. Koeller and R. Raj, Acta Met., 1978, Vol. 26, p. 1551.
4. C. Gandhi and R. Raj, "Wedge Type Intergranular Fracture in Ni During Creep," unpublished research, 1980.
5. R. Raj and M. F. Ashby, Met. Trans., 1972, Vol. 3, p. 1937.
6. T. S. Kê, Phys. Rev., 1947, Vol. 72, p. 41.
7. D. R. Mosher and R. Raj, Acta Met., 1974, Vol. 22, p. 1469.
8. J. J. Jonas and M. J. Luton, Advances in Deformation Processing, Ed. J. J. Burke and V. Weiss, 1978, Plenum Press, New York, NY, p. 215.
9. C. Rosard and P. Blain, Rev. Metall. (Paris), 1958, Vol. 55, p. 573.
10. W. J. McG Tegart, Ductility, Amer. Soc. for Metals, Metals Park, Ohio, 1967, p. 133.

11. J. J. Jonas and H. J. McQueen, Treatise on Materials Science and Technology, Vol. 6: Plastic Deformation of Materials, Ed. R. J. Arsenault, 1975, Acad. Press, p. 394.
12. M. J. Luton and C. M. Sellars, Acta Met., 1969, Vol. 17, p. 1033.
13. H. L. Gegel, "Development of a Dual Property, Dual Microstructure Titanium Disk," AFML, Program, 1979, in progress. (Progress reports available from Dr. G. D. Lahoti, Battelle Columbus Laboratories, Columbus, OH.)
14. H. J. Frost, "Deformation Mechanism Maps," Ph.D. Thesis, Harvard University, 1974.
15. R. A. Ayres, Met. Trans., 1977, Vol. 8A, p. 487.
16. I. S. Servi and N. J. Grant, J. Metals, 1951, Vol. 3, p. 909.
17. C. M. Sellars and W. J. McG Tegart, Acta Met., 1966, Vol. 14, p. 1136.
18. K. J. Gardner and R. Grimes, Metal Sci. J., 1979, Vol. 13, p. 216.
19. D. Hardwick and W. J. McG Tegart, J. Inst. Metals, 1961-62, Vol. 90, p. 17.
20. R. Hill, J. Mech. Phys. Solids, 1952, Vol. 1, p. 19.
21. Z. Marciniak and K. Kuczynski, Inst. J. Mech. Sci., 1967, Vol. 9, p. 609.
22. A. K. Ghosh, Met. Trans., 1977, Vol. 8A, p. 1221.
23. W. M. Yim and N. J. Grant, Amer-Soc. Metals, Metals Park, OH, 1967, p. 101.
24. P. J. Wray, J. App. Phys., 1969, Vol. 40, p. 4018.
25. E. Shapiro and G. E. Dieter, Met. Trans., 1971, Vol. 2A, p. 1385.

APPENDIX F

THERMOVISCOPLASTIC ANALYSIS OF TITANIUM ALLOY FORGING

Shiro Kobayashi
Department of Mechanical Engineering
University of California
Berkeley

APPENDIX F

THERMOVISCOPLASTIC ANALYSIS OF TITANIUM ALLOY FORGING

Introduction

When deformation takes place at high temperatures, material properties can vary considerably with temperature. During a metalworking process, large nonhomogeneities in deformation and, consequently, heat generation, usually occur. Moreover, especially if the dies are at a considerably lower temperature than the workpiece, the heat losses by conduction to the dies and by radiation and convection to the environment result in severe temperature gradients within the workpiece. Thus, including temperature effects in the analysis of metal-forming problems is very important. Furthermore, at elevated temperatures, plastic deformation can induce phase transformations and alterations in grain structures which in turn can modify the flow resistance of the material as well as other mechanical properties. Including these metallurgical effects in the process analysis contributes significantly to the understanding of material behavior under plastic deformation.

The importance of temperature calculations during a metal-forming process has been recognized for a long time. Until recently, the majority of the work has been based on procedures that uncouple the problem of heat transfer from the metal deformation problem.

Several research workers have used the approach of determining the flow fields in the problem either experimentally or by calculations, and then by using these fields for the calculation of heat generation. Among these is the work of Johnson and Kudo⁽¹⁾ on extrusion, and Tay, Stevenson, and Dans⁽²⁾ on machining. Another approach⁽³⁾ uses Bishop's numerical method, in which heat generation and transportation are considered to occur instantaneously for each time step, with conduction taking place during the time step.

This approach is represented by the work of Altan and Kobayashi⁽⁴⁾ on extrusion; Lahoti and Altan⁽⁵⁾ on compression and torsion; and Nagpal, Lahoti, and Altan⁽⁶⁾ on forging. Usually the temperature calculations are done by finite differences, or by finite elements, and the upper-bound technique is the most common for determining flow patterns, if not experimental.

As far as we know, a paper by Oden, Bhandary, Yagawa, and Chung⁽⁷⁾ presents the first coupled analysis of deformation and heat transfer, although the application is to a three-dimensional rectangular bar, which was constrained in one direction and heated at one corner area of the specimen. The formulation is for elastoviscoplastic materials.

Zienkiewicz, Onate, and Heinrich⁽⁸⁾ have made a coupled thermal analysis in steady-state extrusion. Rebelo and Kobayashi^(9,10) developed the method for a coupled analysis of viscoplastic deformation and heat transfer.

In this paper a summary of the theory for developing computer simulations of transient viscoplastic metal deformation coupled with a heat transfer analysis is given. The results of calculations by applying the finite-element formulations to titanium 6242 alloy forging are shown.

The finite-element simulation analysis is performed for (1) the compression of a solid cylinder of $(\alpha + \beta)$ -phase alloy, (2) the compression of a solid cylinder of a β -phase alloy, and (3) the compression of a tapered preform of $(\alpha + \beta)/\beta$ composite.

Basic equations

The basis of finite-element metal flow modeling, using the variational approach, is to formulate proper functionals, depending upon specific constitutive relations. The solution of the original boundary value problem is obtained by the solution of the dual variational problem where the first-order variation of the functional vanishes.

Characterizing the behavior of the materials as rigid-viscoplastic, the functional becomes

$$\pi = \int_V E(\dot{\underline{\epsilon}}) dv + \int \lambda \dot{\underline{\epsilon}}_V dv - \int_{S_F} \underline{F} \cdot \underline{u} ds, \quad (1)$$

using the Lagrange multiplier approach for the incompressibility constraint. In Eq. (1) the work function $E(\dot{\underline{\epsilon}})$ is expressed by

$$E(\dot{\underline{\epsilon}}) = \int_0^{\dot{\underline{\epsilon}}} \bar{\sigma} d\dot{\underline{\epsilon}} \quad (2)$$

The analysis of viscoplastic deformation, based on Eq. (1), was given by Oh, Rebelo, and Kobayashi⁽¹¹⁾ and as far as equilibrium equations are concerned, the only modification is the temperature dependence of the flow stress. Experimental data on flow stress are fitted by the expression of the form

$$\bar{\sigma} = Y \left[1 + \left(\frac{\dot{\underline{\epsilon}}}{Y} \right)^n \right] \quad (3)$$

where Y is static yield stress; $\dot{\underline{\epsilon}}$, strain rate; γ , n , material parameters and Y , n , γ are functions of strain and temperature.

Heat balance equations are, upon finite-element discretization, reduced to the form (see, e.g., Eq. (12)):

$$\underline{C}\dot{\underline{T}} + \underline{K}\underline{T} = \underline{Q},$$

where \underline{C} is the heat capacity matrix; \underline{K} , heat conduction matrix; \underline{Q} , heat flux vector; \underline{T} , vector of nodal point temperatures; $\dot{\underline{T}}$, vector of nodal point temperature rates. The heat flux vector \underline{Q} in Eq. (4) has several components (see Eq. (9)).

The first component is the contribution of the net heat generated inside the deforming body, the second one the contribution of the heat radiated into the body, and the third, the contribution of the heat transferred by convection. The fourth term represents the contribution of the heat transferred between workpiece and die through their interface (with or without lubricant), and the last term is the contribution of the heat generated by friction between die and workpiece.

Time dimensions

In order to describe a deformation process in time, integration of rate equations must be performed with respect to time. As far as the strain equation is concerned, the assumption of no inertial effects requires that for small intervals of time, velocities (and strain rates) change by very small amounts. The strains at time $t + \Delta t$ are obtained from their values and rates at time t

$$\epsilon_{t+\Delta t} = \epsilon_t + \dot{\epsilon}_t \Delta t \quad (5)$$

Similar treatment is made with respect to updating displacements, using velocities.

The theory necessary to integrate Eq. (4) can be found in numerical analysis books^(13,14). It suffices to say that the one-step method is used. Convergence of a scheme requires consistency and stability. Consistency is satisfied by an approximation of the type

$$T_{t+\Delta t} = T_t + \Delta t * [(1 - \beta)T_t + \Delta T_{t+\Delta t}] \quad (6)$$

where β is a parameter varying between 0 and 1.

For unconditional stability, β should be greater than 0.5, and a value of 0.75 was chosen. Selection of a proper value for β is an important factor in the situation where it is desired that the time step be as large as possible, provided that the increments in strain are compatible with an infinitesimal analysis. In the standard test problem for checking numerical integration schemes, this value of β gives good accuracy in a wide range of values of Δt starting at zero.

An implementation of the algorithms above to include the coupling of the solution of stress equilibrium equations with heat balance and to update internal parameters, by considering $T_{t+\Delta t}$ as a primary dependent variable, has been described in detail elsewhere⁽⁹⁾.

Applications

Chen⁽¹⁵⁾ investigated the behavior of titanium alloys at high temperatures and attempted to find the optimum forging/heat treatment procedure for the required mechanical properties in pancake forgings of $(\alpha + \beta)$ -phase and (β) -phase preforms. In order to determine the optimum procedure, the details of deformation involved in a forging must be known and quantitative correlation between the deformation mechanics and metallurgical findings should be established. With this in mind, simulations of pancake forging were performed and the computed results on mechanics were discussed with reference to the metallurgical studies by Chen⁽¹⁵⁾ and by Nadiv, Gegel, and Morgan⁽¹⁶⁾.

Flow stress expressions for Ti6242 $(\alpha + \beta)$ -phase and (β) -phase were derived from experimental data at the Battelle Columbus Laboratories⁽¹⁷⁾ for high strain-rate regime ($0 \sim 10s^{-1}$) and at Wright State University⁽¹⁸⁾ for low strain-rate regime ($0 \sim 0.1s^{-1}$). The effective ranges for the data are $1600^{\circ}F \sim 1850^{\circ}F$ in temperature and $0 \sim 1.0$ in strain.

Thermal properties of Ti6242 alloys for heat transfer were taken from standard handbooks. In Fig. 1, microstructures for starting $(\alpha + \beta)$ -preforms and starting (β) -preforms are shown.

Compression of $(\alpha + \beta)$ -preforms

The preform, which measured 81.25 mm (3.25 inch) in diameter and 81.25 mm (3.25 inch) thick, was heated to $1227^{\circ}K$ ($1775^{\circ}F$), and the dies to $624^{\circ}K$ ($700^{\circ}F$). A computer-controlled hydraulic press compressed the preform with an average strain rate of 3.0/min. Although a glass-type material was used as a lubricant, the temperature difference between the dies and the workpiece prevents effective lubrication. In simulation, therefore, sticking friction was imposed as the interface boundary condition. Using 121 nodes and 100 elements in the workpiece and 114 nodes and 90 elements in the die, calculations were performed up to 60 percent reduction in height with 1 percent height reduction for each step. The computation efficiency was good and an average of seven iterations were needed for convergence in obtaining the velocity field for each step and three more iterations for temperature calculations.

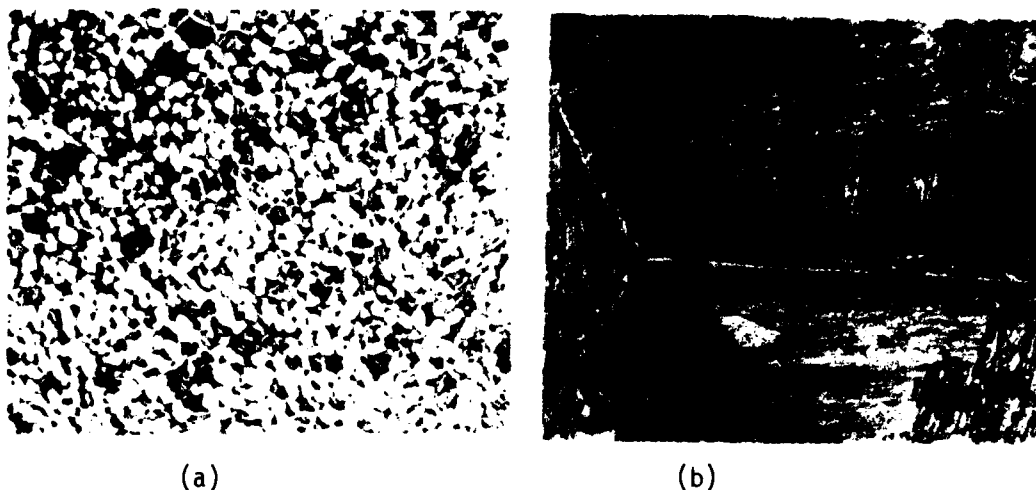
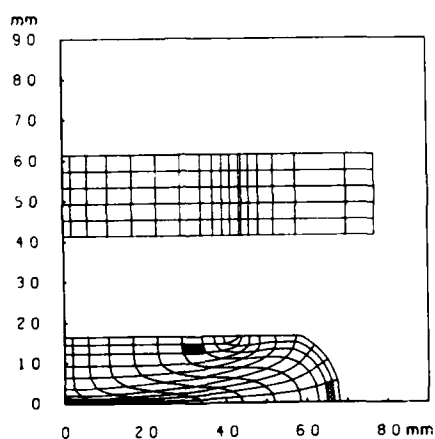


Figure 1: Transverse microstructures for (a) starting $(\alpha + \beta)$ -preforms, and (b) starting (β) -preforms. (Courtesy of Dr. H. Gegel, USAF, Materials Laboratory)



P3: 1775F/700F
3.0 min.⁻¹/1+E

Figure 2: Grid distortion in hot-die forging of $(\alpha + \beta)$ -preform and comparison with experimental macrostructure. (Macrostructure, courtesy of C. C. Chen, Chen-Tech Industries)

Figure 2 shows the grid distortion at the 60 percent reduction in height. A rigid zone beneath the die due to die chilling is evident and, consequently, the shear band formation is distinctively traceable. Because of this nonuniform deformation, the amount of barreling and folding is pronounced. The flow lines obtained by Chen⁽¹⁵⁾ under the same forging conditions in Fig. 2 demonstrate striking similarity with the computed results. It is seen in the experiments that at the upper die face, die chilling was so pronounced that folding left a circular groove around the original circular contact area. The computed result, although it is not noticeable in the figure, indicated also that the first node in the original free cylindrical surface was not touching the die, producing a shallow groove as seen in the experiment.

Figure 3 shows the effective strain distributions after 60 percent deformation. Their main features are the nonuniformity, ranging from almost zero deformation under the dies, to a large compression in the center, and the shear bands that obliquely cross the specimen.

Corresponding temperature distributions are presented in Fig. 4. Clearly, heat flowing from the workpiece to the die balances the heat generated by deformation in the upper half temperature distribution; in the lower half heating occurs above the original temperature, following the same pattern of strain distributions. In the die, temperature rises as expected around the contact areas, and the difference of temperature between the workpiece and the die decreases substantially during the course of deformation.

An attempt was made to correlate the microstructures obtained by Chen, reproduced in Fig. 5, with the information obtained through the calculations. The element 17 (point B) is located in the "rigid" zone below the die. Its temperature decreases all the time, with the tendency to stabilize the $(\alpha + \beta)$ -structure. A total amount of deformation of 13 percent does not liberate energy enough to produce structural changes. It is fair to say that the microstructure that is shown is about the same as the original one.

The studies made by Chen⁽¹⁹⁾ and by Nadiv, Gegel, and Morgan⁽¹⁶⁾ on material properties of Ti6242 indicate that the yield stress softening with

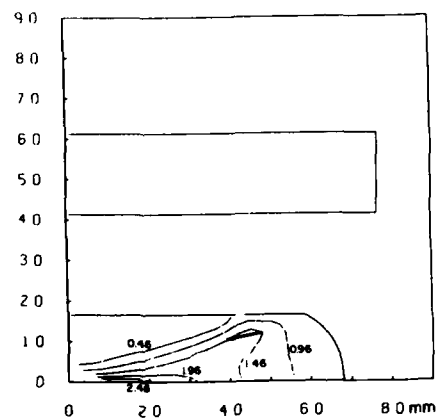


Figure 3: Effective strain distribution at 60 percent reduction in height in $(\alpha + \beta)$ -compression.

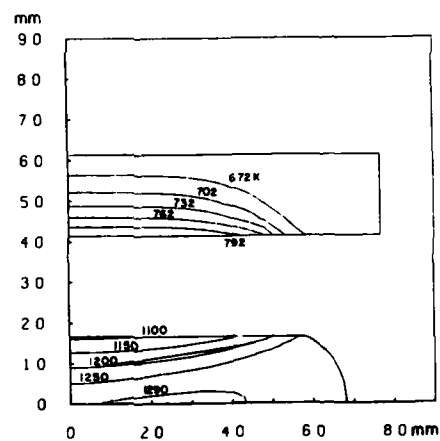


Figure 4: Temperature distribution at 60 percent reduction in height in $(\alpha + \beta)$ -compression.

temperature is governed by a dynamic recrystallization and transformation-induced plasticity, and that such phenomena are particularly noticeable above the transus temperature ($T = 1266^{\circ}\text{K}$).

Around the element 82 (point C), the transus temperature is soon passed during the deformation, and a large amount of deformation also is present. On the other hand, high compressive stresses exist, lowering the transus temperature. Following Nadiv et al.⁽¹⁶⁾ these ingredients produce an extensive transformation of the $(\alpha + \beta)$ -phase into the (β) -phase, mainly from the platelets of the β grains. The amount of (β) -phase is enough to completely surround the α grains, and being the softer phase, will carry most of the deformation. After deformation is completed, and cooling takes place, the equilibrium amounts of α grains and β (platelets of (α) - and (β) -phases) grains is regained, perhaps with a better distribution and a deformation-dependent concentration of grains.

Around the element 99 (point A), temperature increases, but barely pass the nominal transus temperature. The average stress being positive at that point, the transus temperature increases. The amount of deformation, nearly 80 percent, is considerable. Below 1260°K the $(\alpha + \beta)$ -phase, being softer than the microstructure, it is reasonable to assume that deformation happens in both phases, and that due to the high temperatures, dynamic recrystallization is present, which would be responsible for the decrease in grain size observed.

All of the above considerations are qualitative, nevertheless, local process histories on mechanics seem to enlighten metallurgical interpretations based on observations made in similar cases.

Compression of (β) -preforms

Simulation of hot compression of (β) -preform was performed under the same conditions as those for compression of $(\alpha + \beta)$ -preforms in specimen dimensions, initial die and workpiece temperatures, and the strain-rate. The same mesh system was also used for the finite-element computation. The grid distortion at the 62 percent reduction in height, along with the experimental flow lines, is shown in Fig. 6. Comparing the results in Fig. 6 with

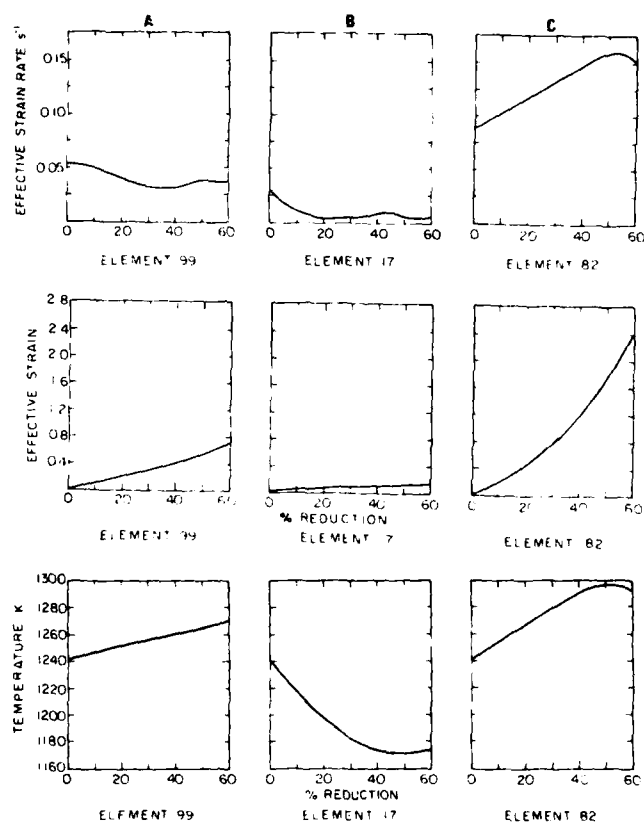
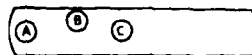
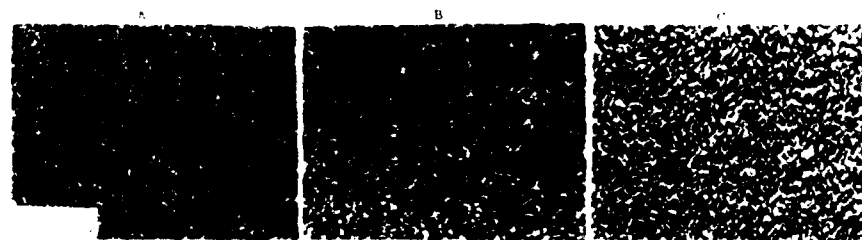


Figure 5: Local strain, strain-rate, and temperature variations during ($\alpha + \beta$)-preform forging and corresponding microstructures after forging. (Microstructures, courtesy of C. C. Chen, Chen-Tech Industries)

the results for $(\alpha + \beta)$ -preform compression given in Fig. 2, the experimental flow lines clearly indicate that strain concentration is more pronounced for the (β) -phase alloy, while the computed grid distortions show little difference between the two materials. The tendency for more strain concentration in the (β) -phase alloy is seen in the computed results, however, when the effective strain distributions for the (β) -phase alloy (Fig. 7) is compared with the results for the $(\alpha + \beta)$ -phase alloy (Fig. 3). The temperature distributions are the same as shown in Fig. 4.

Stresses and their variations during deformation are important for void formation and changes of microstructure. In Fig. 8 the distributions of stress components along the equatorial plane are shown at several deformation stages. Almost from the beginning of compression, the circumferential stress component becomes tensile near the free surface, other stress components being compressive. As deformation continues, the axial stress component becomes tensile near the free surface. At the end of deformation at 62 percent reduction in height, even the average stress becomes tensile near the free surface. The distribution forms are large compressive stresses at the center and the magnitude decreases toward the free surface for all stress components and remain the same during the deformation.

The die pressure distributions are shown in Fig. 9. Up to 30 percent reduction in height the interface area remains the same (friction is sticking). The pressure is least at the center and increases toward the periphery of the contact surface. Then, a part of the originally cylindrical free surface begins contact with the die (folding) and the pressure distribution changes to a friction hill type as seen at 60 percent deformation. It is of interest to note that the first nodal point on the cylindrical surface from the die did not come into contact with the die, while the second, third, ... nodal points come into contact with the die. This results in a groove with the diameter of the original workpiece at the die-workpiece interface. This is consistent with the observation shown in Fig. 6.

Figure 10 shows the microstructures at three locations and computed local strain, strain-rate, and temperature variations during deformation at these locations. Around point B (element 17) the microstructures should not be very different from the original ones, because a very small amount

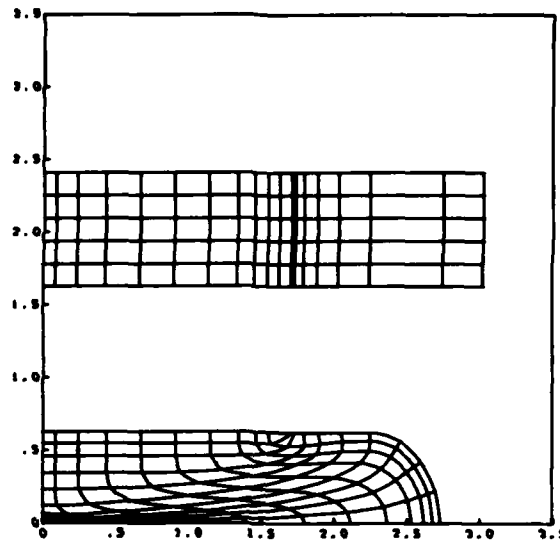


Figure 6: Theoretical grid distortion and comparison with macrostructures in hot-die forging of (β)-preform. (Microstructures, courtesy of C. C. Chen, Chen-Tech Industries).

EFFECTIVE STRAIN CONTOURS WHEN DEFORMED 0.62

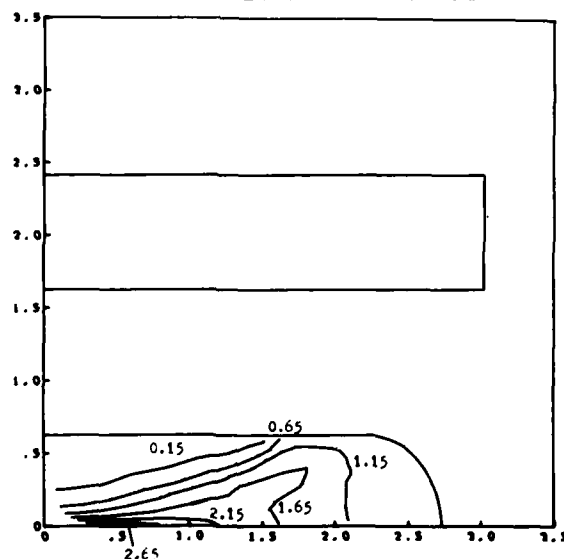


Figure 7: Effective strain distribution at 62 percent reduction in height in (β)-phase alloy compression.

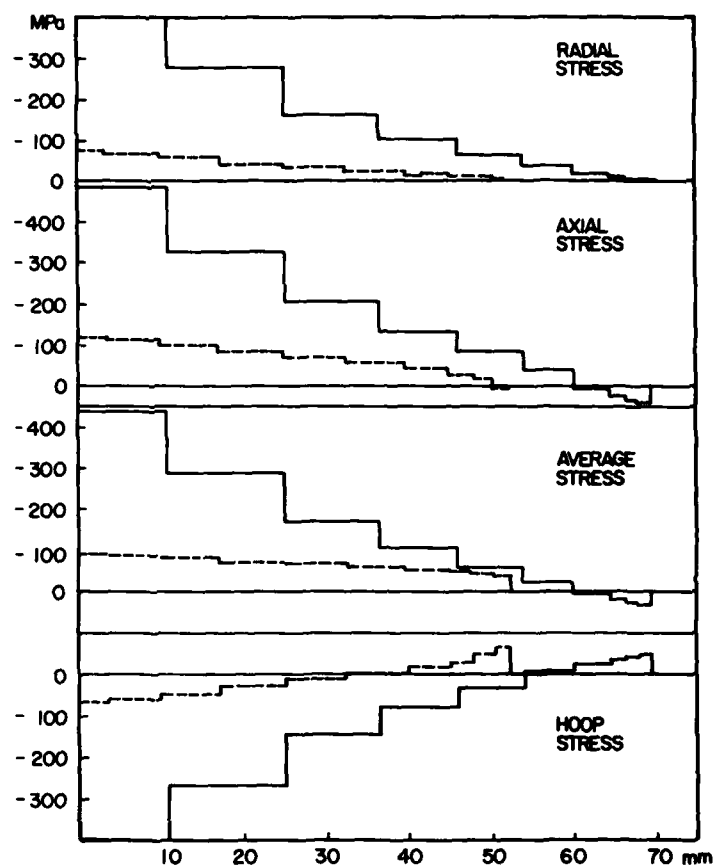


Figure 8: Stress distributions along the equatorial plane at 62 percent reduction in height.

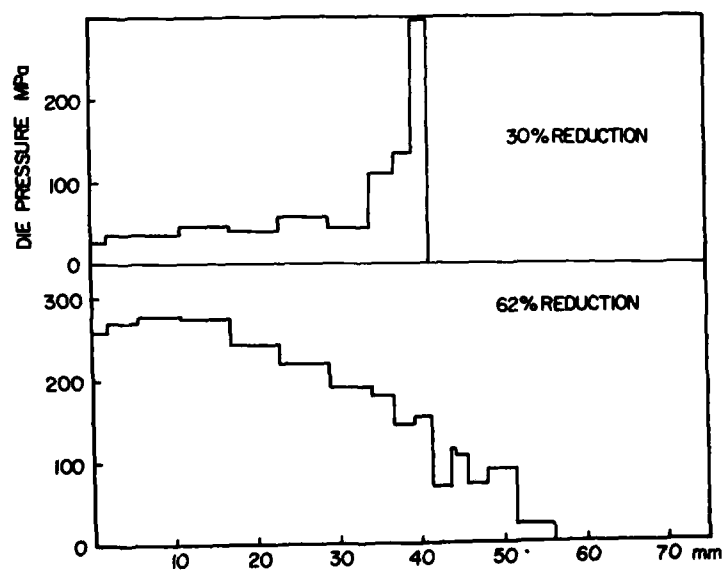


Figure 9: Die pressure distributions at two stages of deformation.

of deformation has occurred. However, it appears that transformation into the $(\alpha + \beta)$ -phase has begun at certain spots. This is probably caused by the workpiece being heated for some time to a temperature just below the transus temperature. Around point A (element 99) the transformation into $(\alpha + \beta)$ -phase is in a more advanced stage. This can be due to a tensile hydrostatic stress and considerable amount of deformation. In the central region C (element 82), the deformation is very large and the reduction in grain size is drastic. A combination of high pressure and temperature in this region makes feasible a full transformation into the (β) -phase, and upon cooling, a new refined grain structure of the (β) -transformed phase is obtained.

Isothermal forging at $(\alpha + \beta)/\beta$ composite

A preform is a cylindrical composite material consisting of a central core of $(\alpha + \beta)$ -phase and an outer ring of (β) -transformed phase, both diffusion-bonded together.

The diameter of the preform, shown in Fig. 11(a), is 140.63 mm (5.625 inch) and its height is 50 mm (2.00 inch). The diameter of the $(\alpha + \beta)$ -phase at the center is 3.00 in. and the taper angle is 20° . Isothermal forging (dies and workpiece at the same initial temperature) at 1750°F at constant ram speed of 0.2 in./min was applied. Total reduction in height was 60 percent. At these high temperatures, the glass-type lubricant is very effective and a friction factor of 0.2 was used along the boundary in computer simulations.

In isothermal forging, very slow speeds are usually used in order to allow generated heat during deformation to spread uniformly throughout the workpiece, and to obtain uniform deformation. If higher speeds can be used without adverse effects, the increase in productivity is obvious. To investigate this aspect, the whole process was simulated again at ten times the original speed.

Grid distortions at 30 percent and 60 percent reduction in height with 0.2 in/min ram speed are shown in Figs. 11(b) and (c), respectively. It took 28 percent reduction for the taper to be absorbed and for deformation to proceed as in a cylinder compression. It is evident from Fig. 11 that the

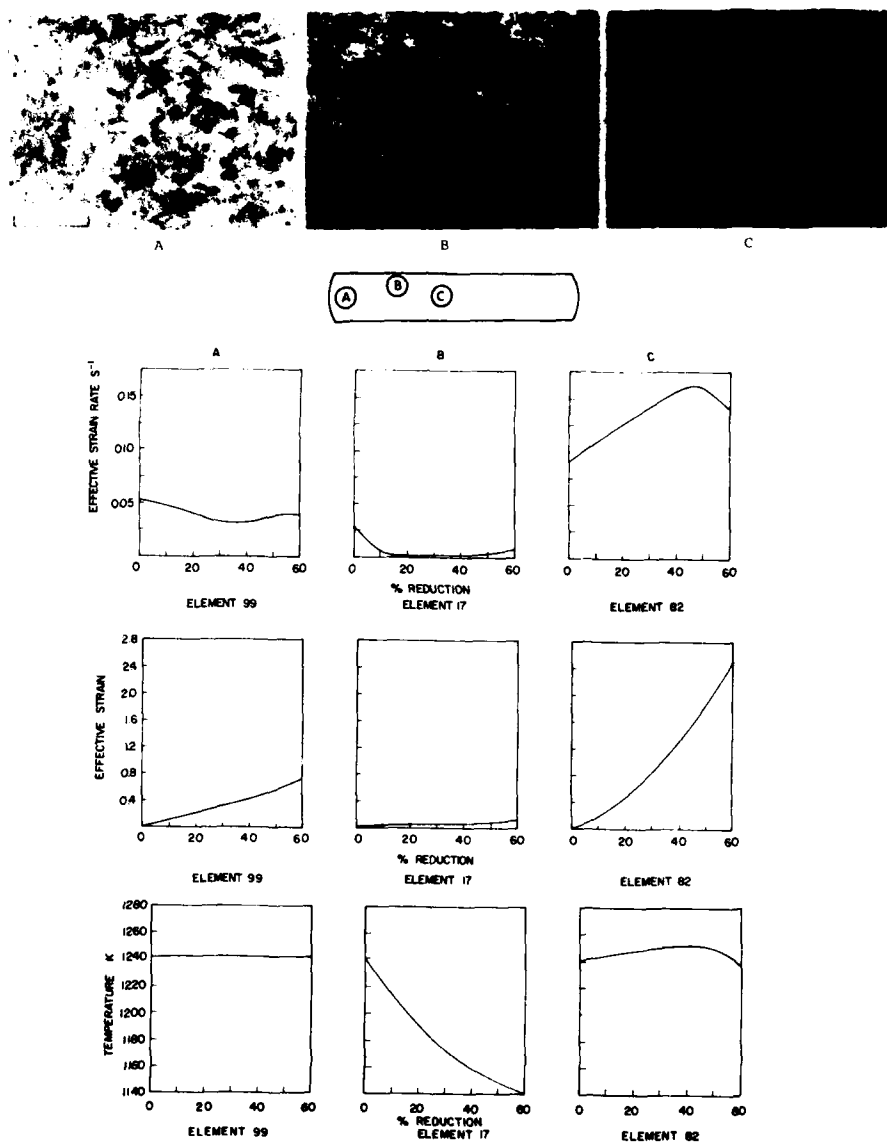


Figure 10: Local strain, strain-rate, and temperature variations during (β)-phase hot-die compression and corresponding microstructures after compression. (Microstructures, courtesy of C. C. Chen, Chen-Tech Industries)

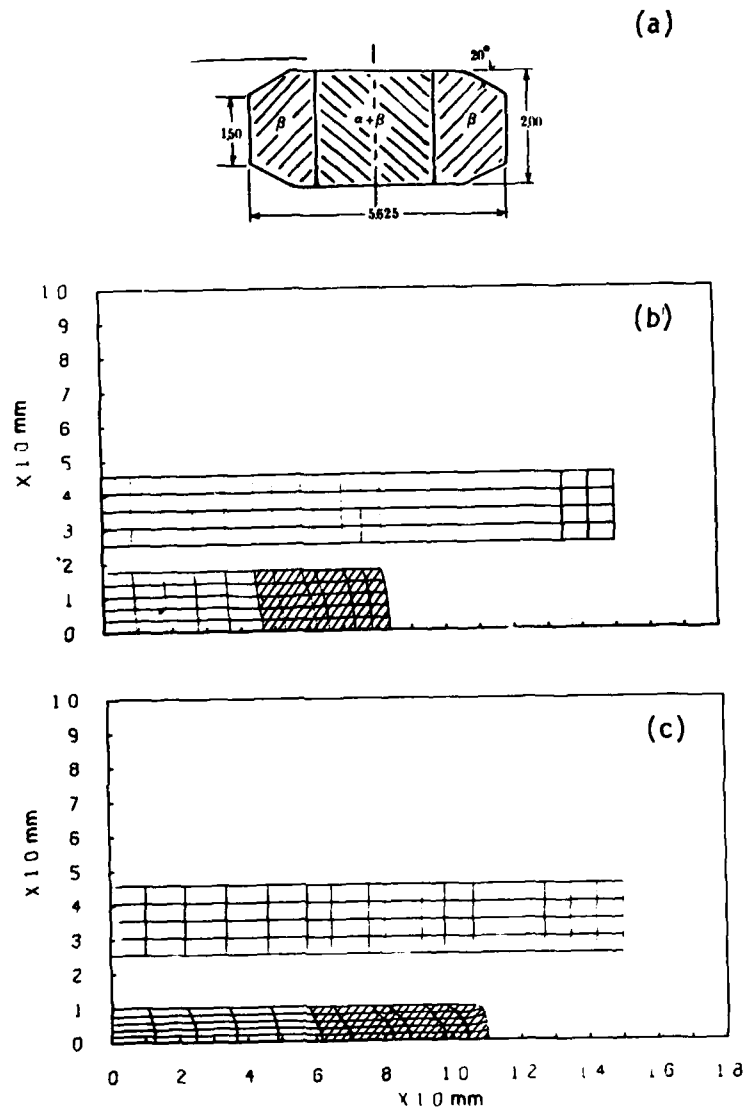


Figure 11: (a) Preform geometry and grid distortions in $(\alpha + \beta)/\beta$ composite forging at (b) 30 percent and (c) 60 percent reduction in height.

deformation is more or less uniform. Homogeneous deformation is further quantitatively shown in the strain distributions given in Fig. 12.

The difference in speed of deformation did not produce any noticeable differences in the over-all deformation process, or even in the local deformation histories. The only differences observed were in the temperature fields obtained (Fig. 13). An average temperature increase of 6.5°K observed in the slow speed deformation jumped to 12.5°K for the faster deformation. However, the temperature gradients are such that the greatest difference between two points in the workpiece is roughly 5°K at the end of deformation. This indicates that the speeds of deformation can be increased (at least to 2.0 in./min) without loss of uniformity of properties, provided the average temperatures reached are not critical.

An example of stress distributions is shown for the mean stress in Fig. 14. Compared with Fig. 8, the magnitude is smaller and the distribution is more uniform. This is due to lower strain-rate (about one-tenth), lower friction at the interface and more uniform temperature distribution.

The resulting microstructures at various locations after forging are shown in Fig. 15. The strain, strain-rate, and temperature variations during forging were found to be almost the same at all locations, and typical variations for 0.2 in./min ram speed are also shown.

The temperature histories indicate that no appreciable changes took place. Therefore, any microstructural modifications must be due to maintaining the workpiece at an elevated temperature for some time (total deformation time is six minutes) under pressure and to the amount of deformation imposed.

On the $\alpha + \beta$ side (points D and E), although the average stresses are negative, the microstructure should be stable. No outstanding amounts of deformation (final strain ≈ 1.0) or temperature rises are locally imposed. Deformation occurs in both phases, and being so slow, the dislocations created by deformation have time to annihilate without needing to recrystallize. Moreover, grain growth would be dampened by the alternating type of structure from grain to grain. Therefore, an unchanged microstructure during deformation should be expected. On the (β)-transformed side (points

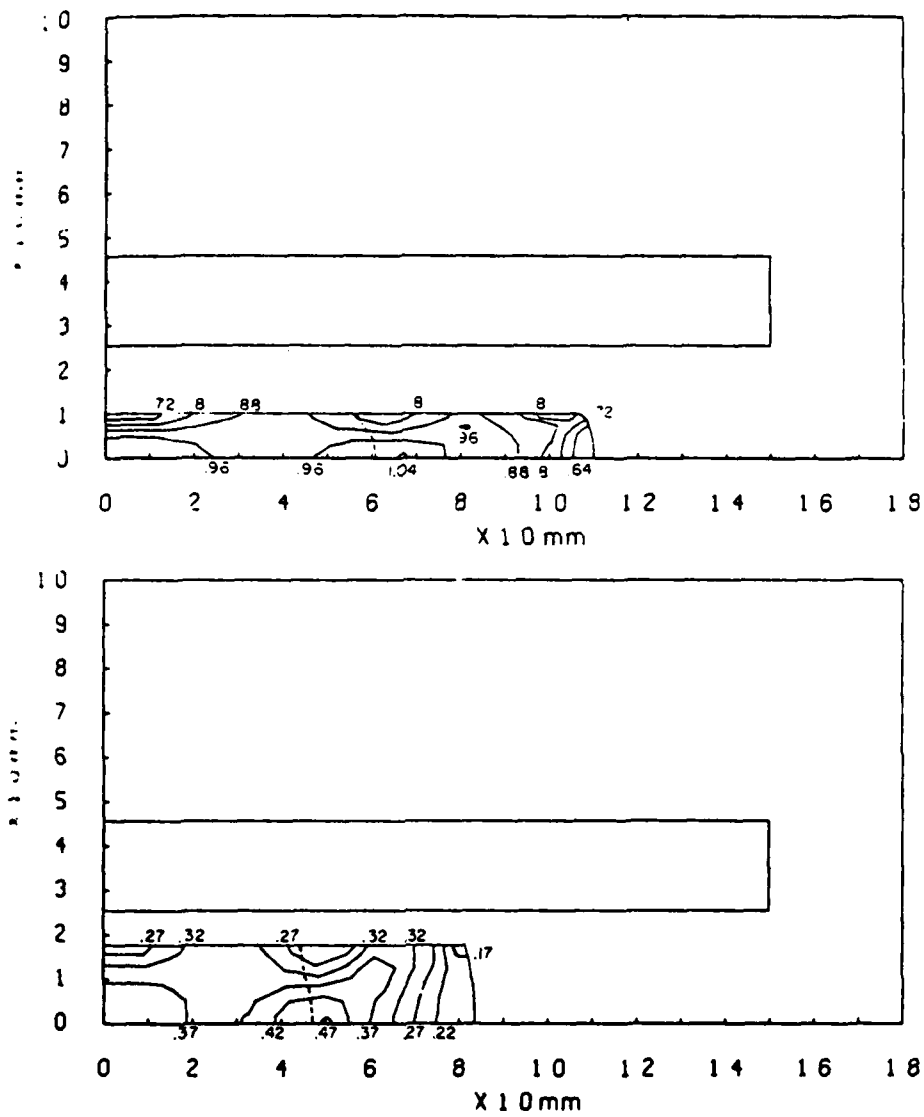


Figure 12: Strain distributions in $(\alpha + \beta)/\beta$ composite forging at 30 percent and 60 percent reduction in height.

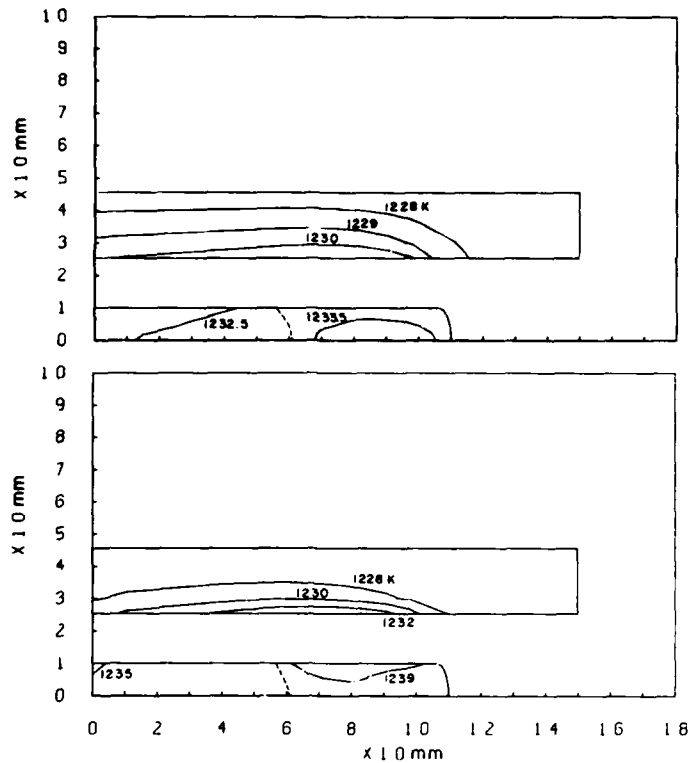


Figure 13: Temperature distributions in $(\alpha + \beta)/\beta$ composite forging at 60 percent reduction at ram speeds of 0.2 in./min and 2.0 in./min.

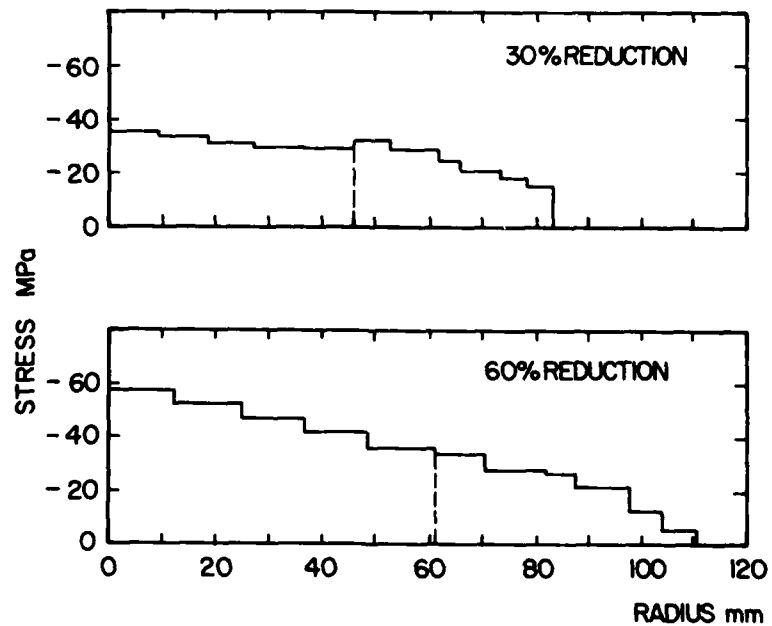


Figure 14: Mean stress distributions along the equatorial plane.

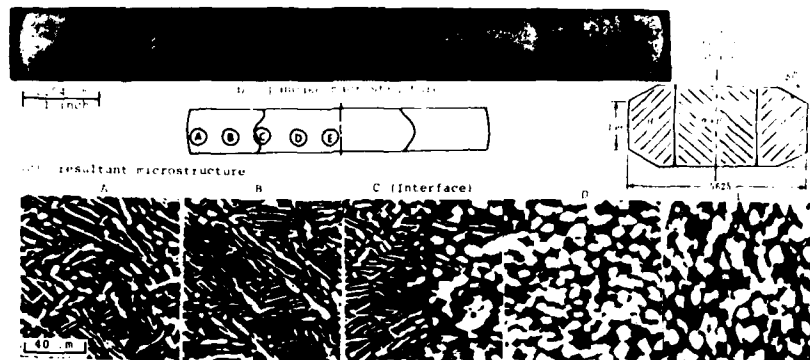


Figure 15: Local strain, strain-rate, and temperature variations during $(\alpha + \beta)/\beta$ composite forging and corresponding microstructures after forging. (Microstructures, courtesy of C. C. Chen, Chen-Tech Industries)

A and B), there is a drive for change into the more stable $\alpha + \beta$ structure, as none of the temperature increases is relevant. Such a drive is originated by high temperatures, time, and deformation that provides energy to nucleate new grain surfaces for diffusion, etc. However, the micrograph of point A when compared to the one of point B show that at A the transformation occurs more rapidly, even with small strains. This can be attributed to stress distributions: in the periphery the stresses are much less compressive than inside, even starting with positive average stress; accordingly, the relative transus temperature is higher, increasing the potential for transformation.

Point C, at the interface, shows both microstructures combined. This indicates the good quality of the bonding and of the nonexistence of secondary effects along the interface due to differences in stiffness of the materials.

Conclusions

The capabilities of a coupled thermoviscoplastic analysis of non-steady-state metalworking processes have been demonstrated. The finite-element analysis was performed for the problems of titanium alloy forging. Simulations of hot-die forging of $(\alpha + \beta)$ -phase and (β) -phase titanium alloys and isothermal forging of $(\alpha + \beta)/\beta$ -composite preform provided the deformation details in terms of stress, strain, strain-rate, and temperature distributions and their variations during forging. The computed local strain, strain-rate, and temperature histories during deformation were plotted at several sites where the resulting microstructures had been obtained and were reported in the literature. An attempt was made to correlate the metallurgical changes with the information obtained through simulation.

Phase transformation is a complex phenomenon and the factors influencing the sequence of events are many. The interpretation presented here is only qualitative and perhaps too simple. However, this development will encourage possible advancements in the interdisciplinary approach to deformation processing for microstructure control. Indeed, a study along this line is currently being carried out by Gegel et al.⁽²⁰⁾.

Acknowledgements

The authors wish to thank Dr. H. L. Gegel, Air Force Wright Aeronautical Laboratories, for initiating the Processing Science Program and the Battelle Columbus Laboratory for its contract for the program under which the present investigation was possible. They are particularly grateful to Dr. C. C. Chen of Chen-Tech Industries for providing the original photographs of micro- and macrostructures of titanium alloys, without which our prime objective of the present work could not have been achieved. They further wish to thank Mr. J. J. Park for carrying out part of the computation and summarizing the results. Typing of the final typescript by Ikuko Workman is also acknowledged.

References

1. Johnson, W. and Kudo, H., "The use of upper-bound solutions for the determination of temperature distributions in fast hot rolling and axisymmetric extrusion processes," Journal of Mechanical Sciences, vol. 1, 1960, p. 175.
2. Tay, A. O., Stevenson, M. G., and Davis, G. V., "Using the finite-element method to determine temperature distributions in orthogonal machining," Proceedings of the Institution of Mechanical Engineers, vol. 188, 55/74, 1974, p. 627.
3. Bishop, J. F. W., "An approximate method for determining the temperatures reached in steady-state motion problems of plane plastic strain," Quarterly Journal of Mechanics and Applied Mathematics, vol. 9, 1956, p. 236.
4. Altan, T. and Kobayashi, S., "A numerical method for estimating the temperature distributions in extrusion through conical dies," Journal of Engineering for Industry, Trans. ASME, vol. 90, 1968, p. 107.
5. Lahoti, G. and Altan, T., "Prediction of temperature distributions in axisymmetric compression and torsion," Journal of Engineering Materials and Technology, Trans. ASME, vol. 97, 1975, p. 113.
6. Nagpal, V., Lahoti, G. D., and Altan, T., "A numerical method for simultaneous prediction of metal flow and temperatures in upset forging of rings," ASME Paper No. 77-WA/PROD-35.
7. Oden, J. T., Bhandari, D. R., Yagawa, O., and Chang, T. J., "A new approach to the finite element formulation and solution of a class of problems in coupled thermoelastoviscoplasticity of crystalline solids," Nuclear Engineering and Design, vol. 24, 1973, p. 420.
8. Zienkiewicz, O. C., Onate, E., and Heinrich, J. C., "Plastic flow in metal forming. I. Coupled thermal behavior in extrusion. II. Thin sheet forming," Application of Numerical Methods to Forming Processes, ASME AMD, vol. 28.

9. Rebelo, N., and Kobayashi, S., "A coupled analysis of viscoplastic deformation and heat transfer--I. Theoretical considerations," to be published in International Journal of Mechanical Sciences, 1981.
10. Rebelo, N., and Kobayashi, S., "A coupled analysis of viscoplastic deformation and heat transfer--II. Applications," to be published in International Journal of Mechanical Sciences, 1981.
11. Oh, S. I., Rebelo, N., and Kobayashi, S., "Finite-element formulation for the analysis of plastic deformation of rate-sensitive materials in metal forming," IUTAM Symposium on Metal Forming Plasticity, Tutzing 1978, p. 273.
12. Zienkiewicz, O. C., The Finite Element Method, 3d ed., McGraw-Hill, New York, 1977.
13. Dahlquist, G., and Bjorck, A., Numerical Methods, Prentice-Hall, New York, 1974.
14. Ralston, A., A First Course in Numerical Analysis, McGraw-Hill, New York, 1965.
15. Chen, C. C., "Processing, structure, and properties of Ti-6Al-2Sn-4Zr-2Mn-0.1 Si alloy forgings," Appendix E, AFML-TR-79-4156, December 1979, p. 254.
16. Nadiv, S., Gegel, H. L., and Morgan, L., "Research on the hot workability of Ti-6242," Appendix B, AFML-TR-79-4156, December 1979, p. 105.
17. Semiatin, S. L., Lahoti, G. D., and Altan, T., "Determination of high-strain-rate-flow-stress data for Ti-6242 using a mechanical press," Appendix C, AFML-TR-79-4156, December 1979, p. 214.
18. Thomas, J. F. Jr., and Dadras, P., "Low strain-rate tests and development of constitutive equations," Appendix A, AFML-TR-79-4156, December 1979, p. 73.
19. Chen, C. C., "Metallurgical fundamentals of Ti-6242 (0.1) alloy forging," Report RD-77-110, Wyman Gordon Co., 1977.
20. Gegel, H. L., Nadiv, S., Malas, J. C., and Morgan, J. T., "Application of process modeling to analysis of microstructural changes during the hot working of a two-phase titanium alloy," Appendix K, AFML-TR-80-4162, October 1980, p. 403.

APPENDIX G

PROCESS MODELING WITH THE
FINITE-ELEMENT METHOD OF ANALYSIS
(PROGRAM ALPID)

S. I. Oh and G. D. Lahoti
Battelle's Columbus Laboratories
Columbus, Ohio 43201

APPENDIX G

PROCESS MODELING WITH THE FINITE ELEMENT METHOD OF ANALYSIS (PROGRAM ALPID)

Introduction

A major objective of mathematical modeling of metal forming processes is to provide necessary information for proper design and control of these processes. Therefore, the method of analysis must be capable of determining the effects of various parameters on metal flow characteristics. Furthermore, the computation efficiency, as well as solution accuracy, is an important consideration for the method to be useful in analyzing metalworking problems. With this viewpoint, the rigid plastic (and rigid viscoplastic) finite element method has been most successful in analyzing a wide class of metal forming problems.

The rigid plastic finite element method (FEM) which was developed by Lee and Kobayashi^[1] has been applied to the analysis of various problems such as solid cylinder upsetting, ring compression, extrusion, and sheet bending [1-7]. The method has been also successfully applied to the prediction of defect formation in upsetting^[8] and extrusion^[9], and the measurement of die-workpiece friction^[10]. It has been extended to rigid viscoplastic material by Oh, Rebelo, and Kobayashi^[11] and applied to upsetting and ring compression in the hot working range.

The major advantage of the finite element method is its ability to generalize. That is, the method can be applied to a wide class of boundary value problems without restrictions of workpiece geometry. This is achieved by the proper discretization procedure used in the finite element method. Metal forming processes, in general, are characterized by loading with dies of various shapes. It seems that a method of discretizing the die boundary conditions, which is comparable to that used in the finite element method, is necessary in order to fully utilize the advantage of the finite element method in metal forming analysis.

In the present report a method is proposed to establish the theoretical foundations of the rigid viscoplastic finite element analysis of metal-forming processes with arbitrarily shaped dies. Then the solutions of the spike forging and the compressor disk forging processes are obtained by using the proposed method.

Rigid Viscoplastic Finite Element Formulation

The rigid viscoplastic material is an idealization of an actual one, by neglecting the elastic response. The material shows the dependence of flow stress on strain rate in addition to the total strain and temperature. Also it can sustain a finite load without deformation. The rigid viscoplastic material which was introduced for the analytical convenience simplifies the solution process with less demanding computational procedure. Moreover it seems that the idealization offers excellent solution accuracies due to the negligible effects of elastic response at large strain in the actual material. For this reason, the rigid viscoplastic material is especially suitable for metal forming analysis at elevated temperature. In this section a finite element formulation of rigid viscoplastic material is described. The discussions are limited to the two-dimensional isothermal deformations.

Consider a body of volume V at a generic moment with the traction \underline{F} prescribed on a portion of the surface, S_F , and the velocity \underline{U} on S_U . Let S_C be the remainder of the surface where the frictional stress \underline{f} acts. The deformation of the body V is characterized by the following field equations.

- (1) Equilibrium conditions, neglecting the body force;

$$\sigma_{ij,j} = 0 \quad (1)$$

where σ_{ij} is a stress component and " , " denotes the differentiation.

- (2) Strain rate-velocity relation;

$$\dot{\epsilon}_{ij} = \frac{1}{2} (v_{i,j} + v_{j,i}) \quad (2)$$

where $\dot{\epsilon}_{ij}$ and v_i are a strain rate component and a velocity component respectively.

(3) Constitutive relation;

$$\sigma_{ij}' = \frac{2}{3} \frac{\bar{\sigma}}{\dot{\bar{\epsilon}}} \dot{\epsilon}_{ij} \quad (3)$$

where σ_{ij}' is the deviatoric stress component, $\bar{\sigma}$ and $\dot{\bar{\epsilon}}$ are defined by $\sqrt{3/2} \sigma_{ij}' \sigma_{ij}'$ and $\sqrt{2/3} \dot{\epsilon}_{ij} \dot{\epsilon}_{ij}$ respectively. The flow stress $\bar{\sigma}$, in general, is a function of total strain, strain rate and temperature.

(4) Boundary condition;

$$\begin{aligned} \sigma_{ij} n_i &= F_j \text{ on } S_F \\ v_i &= U_i \text{ on } S_U \\ |f_s| &= \text{given, } \text{sign}(f_s) = -\text{sign}(\Delta v_s) \text{ on } S_C \end{aligned} \quad (4)$$

where n_i is a component of unit normal to the surface, and Δv_s is slipping velocity.

The field equations (1)-(4) can be put into variational principle as

$$\begin{aligned} \delta \Phi &= \delta \left[\int_V E(\dot{\underline{\epsilon}}^*) dV + \int_V \frac{1}{2} K \dot{\underline{\epsilon}}_{kk}^{*2} dV - \int_{S_C} \left\{ \int_{v_s}^{\dot{v}_s^*} f_s dv_s \right\} dS \right. \\ &\quad \left. - \int_{S_F} F_j v_j^* dS \right] = 0 \end{aligned} \quad (5)$$

where the workfunction $E(\dot{\underline{\epsilon}})$ can be expressed as [12]

$$E(\dot{\underline{\epsilon}}) = \int_0^{\dot{\bar{\epsilon}}} \frac{\bar{\sigma}}{\dot{\bar{\epsilon}}} d\dot{\bar{\epsilon}} \quad (6)$$

Here K is a large positive constant which penalizes the dilatational strain and "*" denotes the restriction of the velocity fields to the trial space.

The discretization of this functional follows the standard procedure and can be found elsewhere.^[13] The distribution function H_i , which is assigned to each node, is introduced such that

$$\begin{aligned} U(\underline{x}) &= \sum_i H_i(\underline{x}) U_i \\ V(\underline{x}) &= \sum_i H_i(\underline{x}) V_i \end{aligned} \quad (7)$$

where $U(\underline{x})$ and $V(\underline{x})$ are the velocity components in x_1 and x_2 direction respectively, U_i and V_i are those at nodal points, and the summations are done over nodal points. In the present investigation 4-node and 9-node isoparametric elements are used.

Substituting equations (6) and (7) into equation (5), the variational functional Φ becomes nonlinear algebraic equations with unknown u_i 's which are velocity components of the nodal points. The stationary point of the functional can be obtained by solving the simultaneous equations

$$\frac{\partial \Phi}{\partial u_i}(u_1, \dots, u_{2M}) = 0, \quad i = 1, \dots, 2M \quad (8)$$

where $\underline{u} = (u_1, u_2, \dots, u_{2M-1}, u_{2M}) = (U_1, V_1, \dots, U_M, V_M)$ and M is the number of nodal points. The solution of the highly nonlinear algebraic simultaneous equations are obtained iteratively by the Newton-Raphson method. The linearized form of equation (8) near the assumed velocity field \underline{u}_0 becomes

$$\left[\frac{\partial \Phi}{\partial u_i} \right]_{\underline{u}=\underline{u}_0} + \left[\frac{\partial^2 \Phi}{\partial u_j \partial u_i} \right]_{\underline{u}=\underline{u}_0} \cdot \Delta u_j = 0 \quad (9)$$

Solving Equation (9) with respect to Δu_j , the assumed velocity field is updated by $u_i + \alpha \Delta u_i$, where $\alpha < 1$. The iterative process continues until the fraction of the correction term, $||\Delta \underline{u}||/||\underline{u}||$ and the calculated nodal point force error norm reach a preassigned value.

In certain cases of rigid viscoplastic deformation, a portion of the workpiece remains rigid. It can be proved that the rigid zone is determined uniquely by the field equations if the work function $E(\dot{\underline{\epsilon}})$ is convex. The

variational function ϕ in equation (5) becomes non-analytic at the solution when the rigid zones are involved and the Newton-Raphson method cannot be used for the solution procedure. The difficulty has been overcome by assuming the material to be linear if $\bar{\epsilon}$ becomes smaller than a small positive number ϵ_0 .^[11] The rigid viscoplastic material in this approach is considered as a limiting case when ϵ_0 becomes infinitely small.

In the finite element method, it is well known that the velocity field given by equation (7) is not flexible enough to provide adequate solutions for incompressible or nearly incompressible deformation. Various suggestions have been made in order to overcome this difficulty in analyzing incompressible linear elastic material^[14,15] and the elastic-plastic material in fully plastic range^[16]. Numerical tests show that the reduced integration for volume strain component gives best results for the present investigation. That is, a 3×3 integration formula is used for distortional energy rate while a 2×2 integration is used for volumetric strain rate with quadratic elements. In relation to the incompressibility, the strain rates and stresses were evaluated at the reduced integration points for best results.

Boundary Conditions and Arbitrarily Shaped Dies

The implementation of a regular boundary condition on S_F or S_U is straightforward and can be found elsewhere.^[11] It seems, however, that the frictional boundary condition along the arbitrarily shaped die surface has not been considered in the framework of FEM. In this section a method, which is natural to FEM, is described by which a systematic implementation of frictional boundary conditions is possible in a unified way for an arbitrarily shaped die. In the present investigation the constant shear friction law is employed which is a common assumption in metal forming analysis.

Consider a curved die surface at a generic moment which is in contact with workpiece as shown in Figure G-1(a). The die boundary condition at the interface can be given by

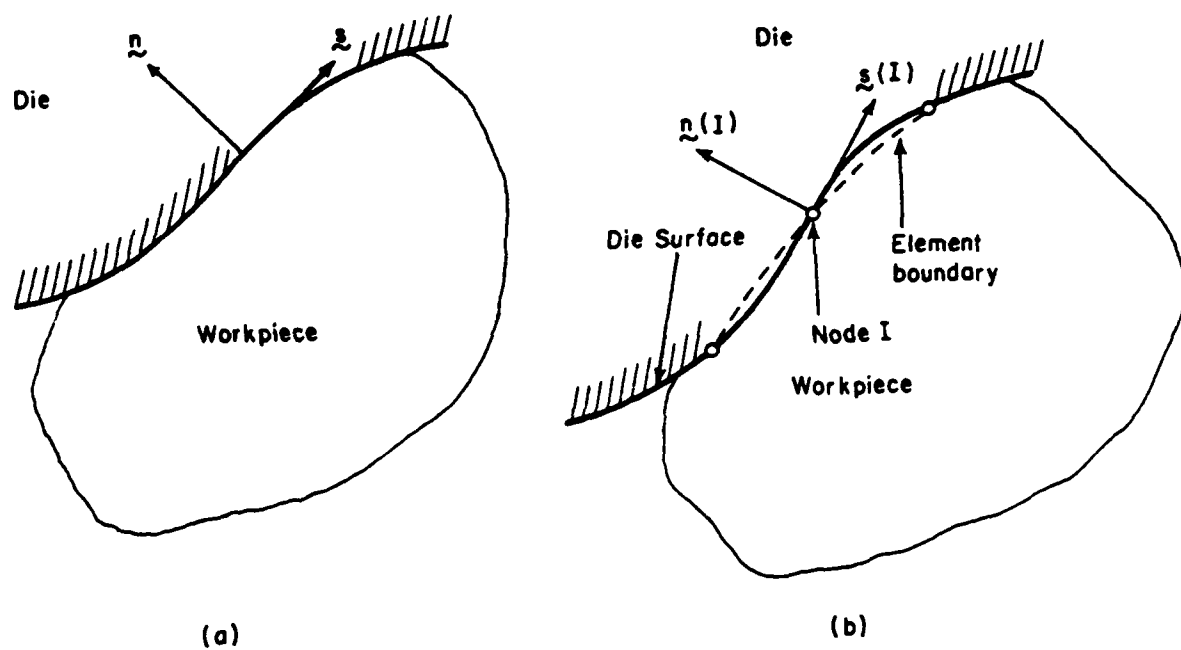


Figure G-1. Schematic Diagram of a Curved Die and a Workpiece.

$$V_n = v_D \cdot \tilde{n}$$

$$f_s = -m k \frac{\Delta v_s}{|\Delta v_s|} \approx -\frac{2}{\pi} m k \tan^{-1} \frac{\Delta v_s}{u_0} \quad (10)$$

where \tilde{n} is unit normal as shown in the figure, and the subscripts n and s denote the normal and tangential direction to the interface, respectively. The expression of f_s in equation (10) has been used for the smooth transition of frictional stress near the neutral point for the flat die surface.^[4] Here Δv_s is slipping velocity, m friction factor, k local flow stress in shear, and u_0 is a very small positive number compared to Δv_s .

The implementation of equation (10) for a curved die is not straightforward since the die surface does not coincide with the workpiece surface defined in FEM approximation. These discrepancies are shown in Figure 1(b). Because of the discrepancy the necessary quantities in equation (10) are not well defined except at the contact node.

In order to overcome the difficulties the boundary condition normal to the surface is enforced at the contacting node and is given by

$$V_n \approx v_D \cdot \tilde{n}_{(1)}$$

where $\tilde{n}_{(1)}$ is the unit normal to the die surface, rather than element surface, at node 1. It is assumed that the slipping velocity Δv_s can be approximated by

$$\begin{aligned} \Delta v_s &= \sum_i H_i \Delta v_{si} \\ &= \sum_i H_i (v_{si} - v_D \cdot \tilde{s}_{(1)}) \end{aligned} \quad (11)$$

Here H_i is the FEM shape function on the surface, v_{si} the tangential velocity of the i-th node, and $\tilde{s}_{(1)}$ the unit tangent to the die surface at the contact node 1.

By substituting equation (11) into f_s expression, the integrand of the die boundary term in equation (5) can be evaluated for a two-dimensional case as

$$\int_{V_s} f_s dv_s = \int_{V_s} - \sum_{ij} \frac{2}{\pi} mkH_j \tan^{-1} \left[\frac{(v_{si} - \tilde{v}_D \cdot \tilde{s}_{(i)}) H_i}{u_0} \right] dv_{sj} \quad (12)$$

The integration of the die boundary term in equation (5) is carried out by Gaussian quadrature considering the element surface as a one-dimensional isoparametric element. Higher order integration is necessary in order that the term can reflect the accurate behavior of f_s near the neutral point where the integrand has large higher order contributions than that of the shape function. Numerical tests show that a five-point integration formula is sufficient for this purpose with a quadratic element.

In a case when a portion of the element boundary is not in contact with the die, the slipping velocities at the free nodes are not defined by equation (12). This difficulty can be overcome easily. The tangential die velocity $\tilde{v}_D \cdot \tilde{s}_{(i)}$ is set to zero for the free node and the small positive number u_0 is replaced by a very large number for the free boundary position. This procedure ensures the consistency of equation (12) on the contact portion and makes the rest traction free.

The present formulation of die boundary condition becomes same as that of Chen and Kobayashi^[4] in the case of the flat die surface with $\tilde{v}_D \cdot \tilde{s} = 0$, except that the present investigation can employ quadratic elements and that surface integration is done numerically. It can be easily shown that the error introduced by the present approach is of the same order as that introduced in the FEM calculation. Therefore, the present formulation does not affect the accuracies of FEM analysis.

Initial Guess

As it can be seen in equation (9), the solution process of the rigid viscoplastic finite element method requires an adequate initial guess velocity field because of nonlinearity in the constitutive equation. Even though the initial guess velocity field does not affect the solution itself, it should be close enough to the solution to achieve the convergence in the iteration process. The initial guess, in general, can be provided by a simple upper bound

solution. It seems, however, that the systematic means of providing the initial guess is essential for the effective application of rigid viscoplastic FEM for complicated metal forming processes. In the present investigation the initial guess was obtained by treating the workpiece as linear viscous material with the viscosity as a function of the material point.

Consider the constitutive equation of linear viscous material

$$\sigma_{ij}' = 2\mu\dot{\epsilon}_{ij} \quad (13)$$

where μ is viscosity. Comparing this with equation (3) it can be seen that the solution of rigid viscoplastic material becomes identical to that of the fictitious linear viscous material with the viscosity

$$\mu = \mu(\dot{\epsilon}) = \frac{1}{3} \frac{\bar{\sigma}}{\dot{\epsilon}} \quad (14)$$

where $\bar{\sigma}$ is the flow stress of the material.

The rigid viscoplastic solution can be obtained by searching for the fictitious material which satisfies the equation (14). This can be done iteratively by updating $\mu = \mu(\dot{\epsilon})$ using equation (14) until $\mu(\dot{\epsilon})$ does not change. This method of solution replaces the initial guess velocity field by the initial "viscosity" distribution. The iteration scheme converges very fast during the early stage of iteration. Then the convergence becomes very slow, especially "near" the solution. Also the numerical experiments show that the iteration is insensitive to the initial viscosity distribution.

In the present formulation the scheme, described above, was used to generate an initial guess for the first step solution as well as for the continuing solutions where the previous step solution cannot be a good initial guess due to the change in deformation modes or due to the free surface folding.

Spike Forging Analysis

In order to validate the present formulation, solutions of the spike forging process were obtained. In spike forging, a cylindrical billet is forged in an impression die containing a central cavity. The deformation

AD-A112 271

BATTELLE COLUMBUS LABS OH
RESEARCH TO DEVELOP PROCESS MODELS FOR PRODUCING A DUAL PROPERTY--ETC(U)
OCT 81 6 D LAHOTI, T ALTAN

F/S 11/6

F33616-78-C-5025

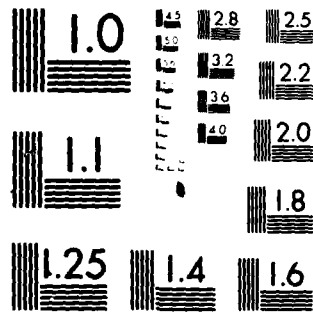
UNCLASSIFIED

AFWAL-TR-81-4130

NL

4-4
AL
2-2-81

END
DATE
FILMED
4-82
DTIC



MICROCOPY RESOLUTION TEST CHART
NATIONAL BUREAU OF STANDARDS-1963-A

characteristics of the spike forging are such that the portion of the material near the outside diameter flows radially while the portion near the center of the top surface is extruded forming a spike. It was observed that the higher spike forms with the higher friction condition if the other process conditions are the same. For this reason the spike forging was suggested to be used for friction test.

Because of the complexity of the deformation pattern, only a few theoretical analyses of the spike forging process can be found. Jain, Bramley, Lee and Kobayashi^[17] analyzed extrusion forging using a flat-top die with a sharp-cornered hole by the upper bound method. By combining a uniform ring-type velocity field with velocity discontinuity, they were able to predict the neutral point location, forging load, and spike height as functions of friction. Altan, et al^[18] solved the spike forging problem by using the modular upper bound method.

Computational Conditions and Procedure

Analysis of spike forging was performed for two different frictions. The frictional factors used in the analyses are $m = 0.3$ and $m = 0.6$. The undeformed circular billet has the dimension of 57.2 mm (2.25 in.) in height and 50.8 mm (2.0 in.) in diameter with chopped corner to secure the stable initial position. The material used in the analysis is $\alpha + \beta$ microstructure Ti-6242-0.1S_i at 954 C (1750 F).^[19] The stress-strain rate relation is shown in Figure G-2. The shape and the dimension of the spike forging dies are shown in Figure G-3. The velocity of the upper die used for the analysis was 25.4 mm/sec (1.0 in/sec.) and the bottom die is stationary. The non-steady state deformation of spike forging was analyzed in a step-by-step manner by treating it quasilinearly during each incremental deformation. The incremental displacement of the upper die for each step is chosen to be 0.02 times of the original workpiece height.

The measure of convergence represented by $||\Delta u||/||u||$ was chosen to be 0.00001.

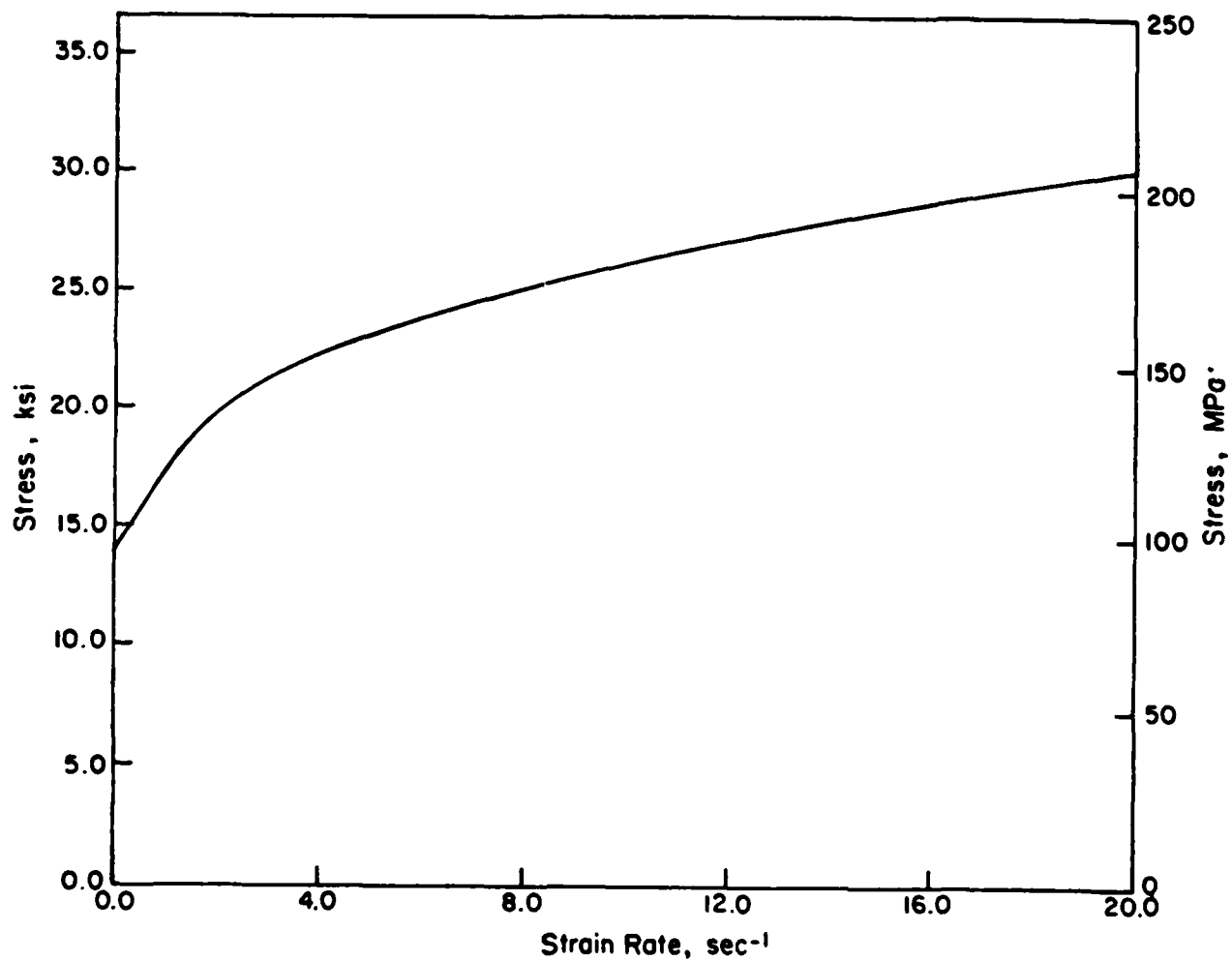


Figure G-2. Stress-Strain Rate Relation of $\alpha+\beta$ Microstructure Ti-6242-0.1Si at 954C (1750F).

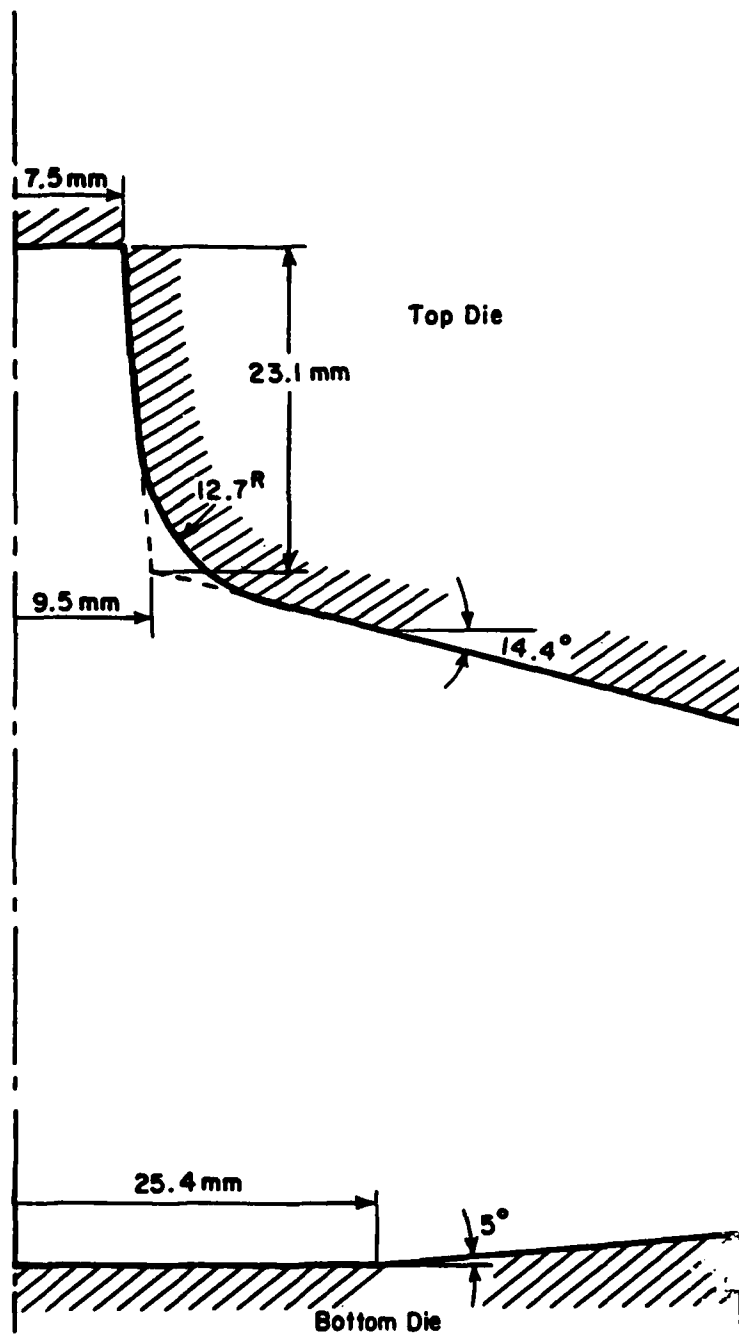


Figure G-3. Schematic Drawing of Spike Forging Dies

Results and Discussions

Figure G-4 shows the undeformed FEM grid used for analysis and the calculated grid distortions at die displacements of $0.2H_0$, $0.4H_0$, and $0.58H_0$. For better comparison the grid distortions of both frictional cases are superimposed on each other. As it can be seen from the figure, the general deformation behavior of spike forging for the two different cases is similar. The solution shows that at an early stage, the deformation is concentrated near the right upper corner of the workpiece where it touches the top die, while the rest of the workpiece undergoes virtually no deformation. Because of this concentration, folding of the top surface starts to take place during the early stage. As the deformation progresses, the deforming zone spreads throughout the workpiece, forming the side surface bulge. Then folding from the side surface to the top and the bottom dies takes place. Throughout the spike forging process the material near the center of the upper surface undergoes virtually no deformation as can be seen from the grid distortions. It can also be seen from the figure that the spike heights are not affected by the friction during the early stages of deformation. The figure shows, however, that higher spike formed with higher friction and that the difference in spike heights with different frictions is large at the die displacement of $0.58H_0$.

The predictions are compared with the experimentally measured spike cross sections. The experimental measurement was carried out with lead specimens at room temperatures by Altan, et al.^[18] The predictions with $m = 0.3$ are compared with lubricated case at the die stroke of $0.58H_0$ in Figure G-5. In Figure G-6, the predicted cross sections are superimposed with those of the dry friction experiments at die displacements of $0.3H_0$, $0.44H_0$ and $0.58H_0$. These figures show that the predictions are in excellent agreement with experiments.

The details of solutions are examined in terms of loads, velocity fields, neutral point locations, changes in spike height and effective strain distributions. The calculated load displacement relations are shown in Figure G-7 for both frictions. It reveals that the load increases slowly during early stages of deformation and then it increases rapidly as the deformation

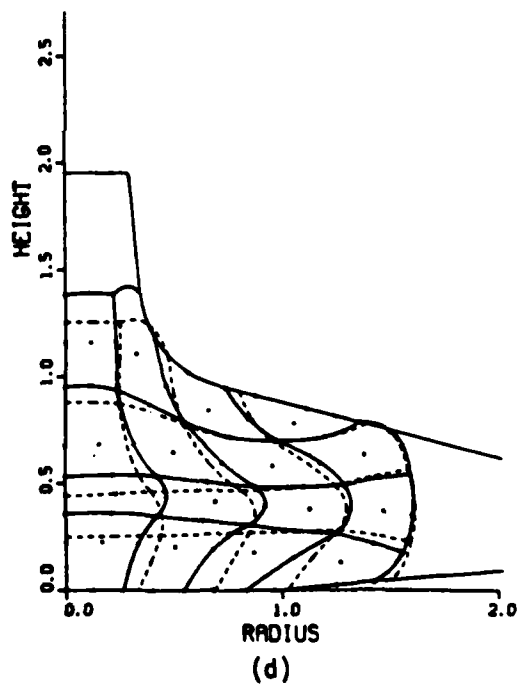
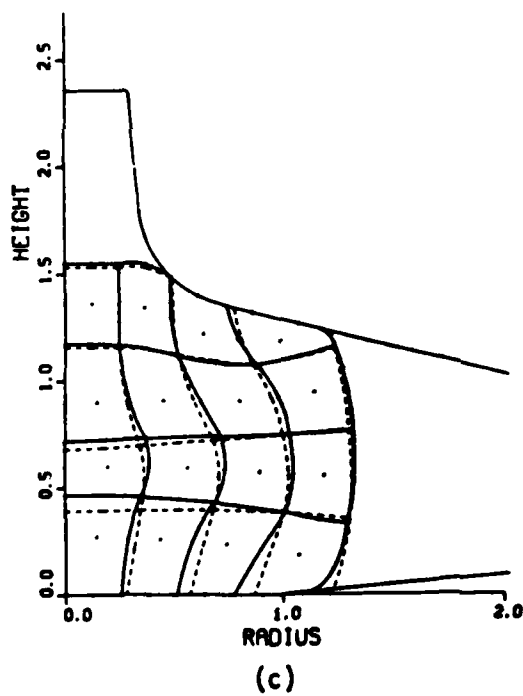
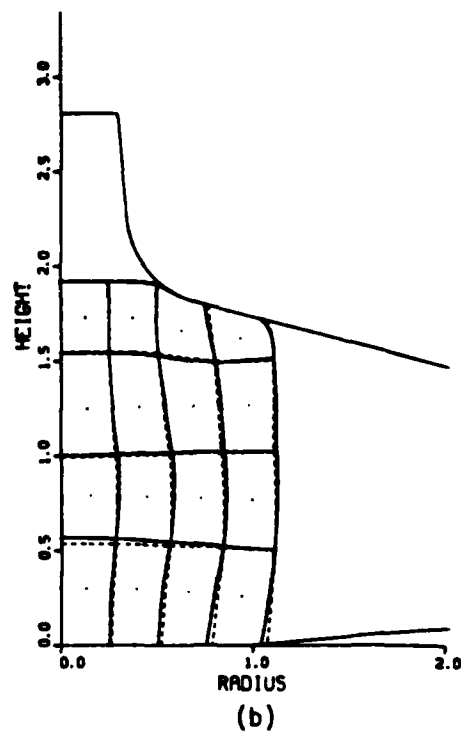
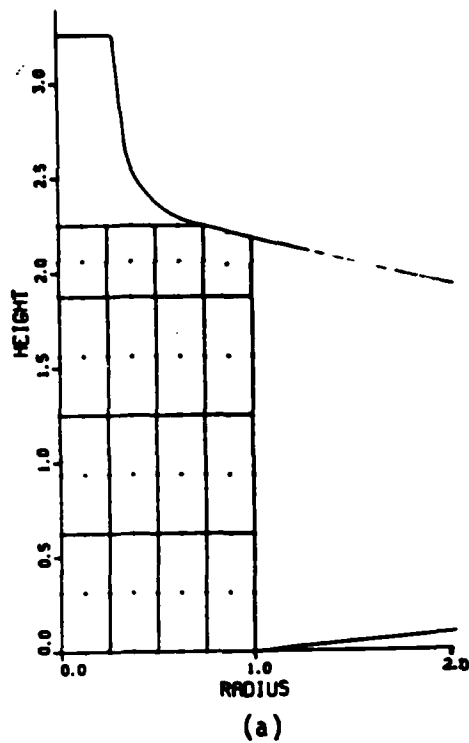


Figure G-4. Calculated FEM Grid Distortions at Die Displacements of (a) $0.0H_o$, (b) $0.2H_o$, (c) $0.4H_o$ and (d) $0.58H_o$, Solid Lines are for $m = 0.6$ and Dotted Lines for $m = 0.3$. Units are Multiples of the Undeformed Radius.

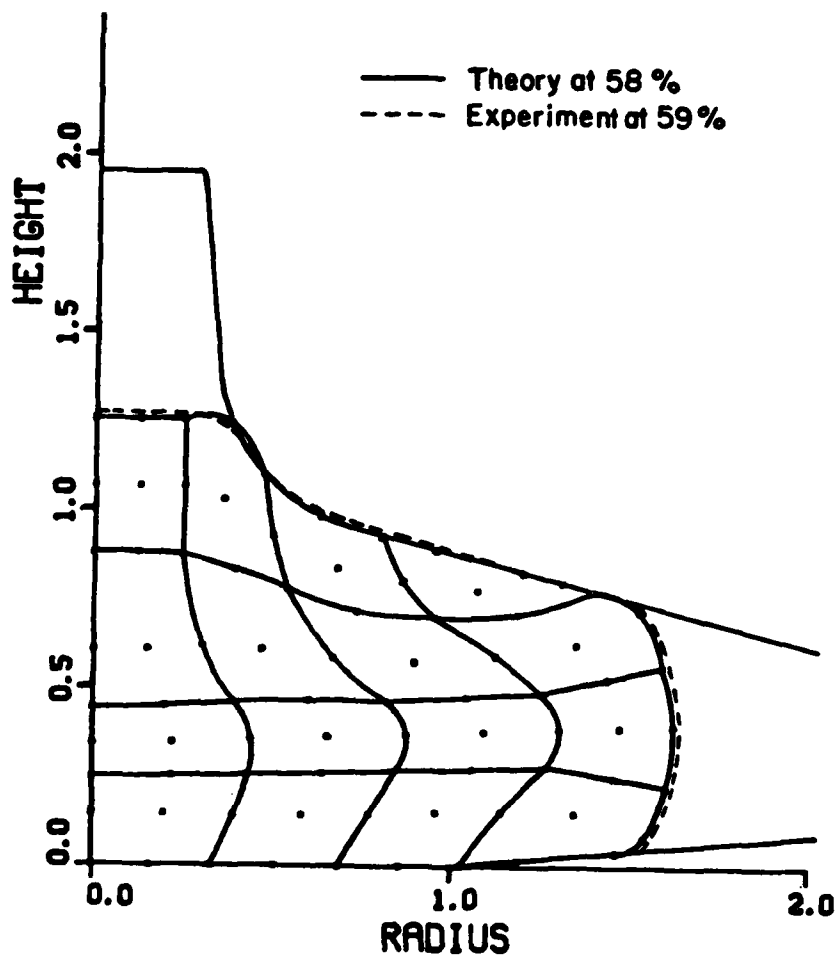


Figure G-5. Predicted Cross Sections Compared with Experiment
at Die Displacement of $0.58H_0$

Prediction: Ti-6242-0.1Si, 854C (1750F), $m = 0.3$

Experiment: Lead, Room Temperature, Lubricated

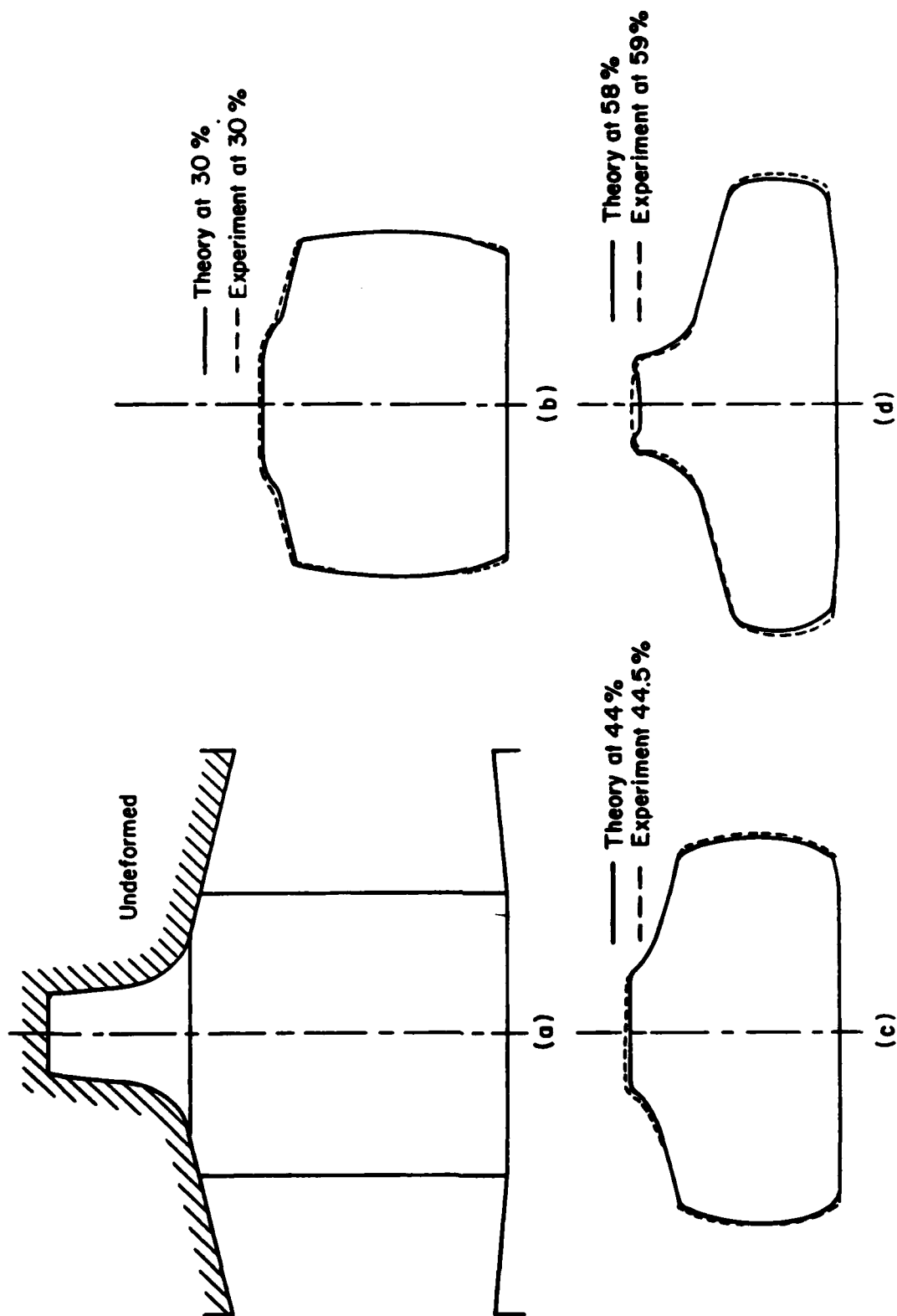


Figure G-6. Predicted Cross Sections Compared with Experiments at Die Displacements of (a) 0.0Ho, (b) 0.3Ho, (c) 0.44Ho and (d) 0.58Ho

Prediction: Ti-6242-0.1Si, 954C (1750F), $m = 0.6$
Experiment: Lead, Room Temperature, Dry Friction

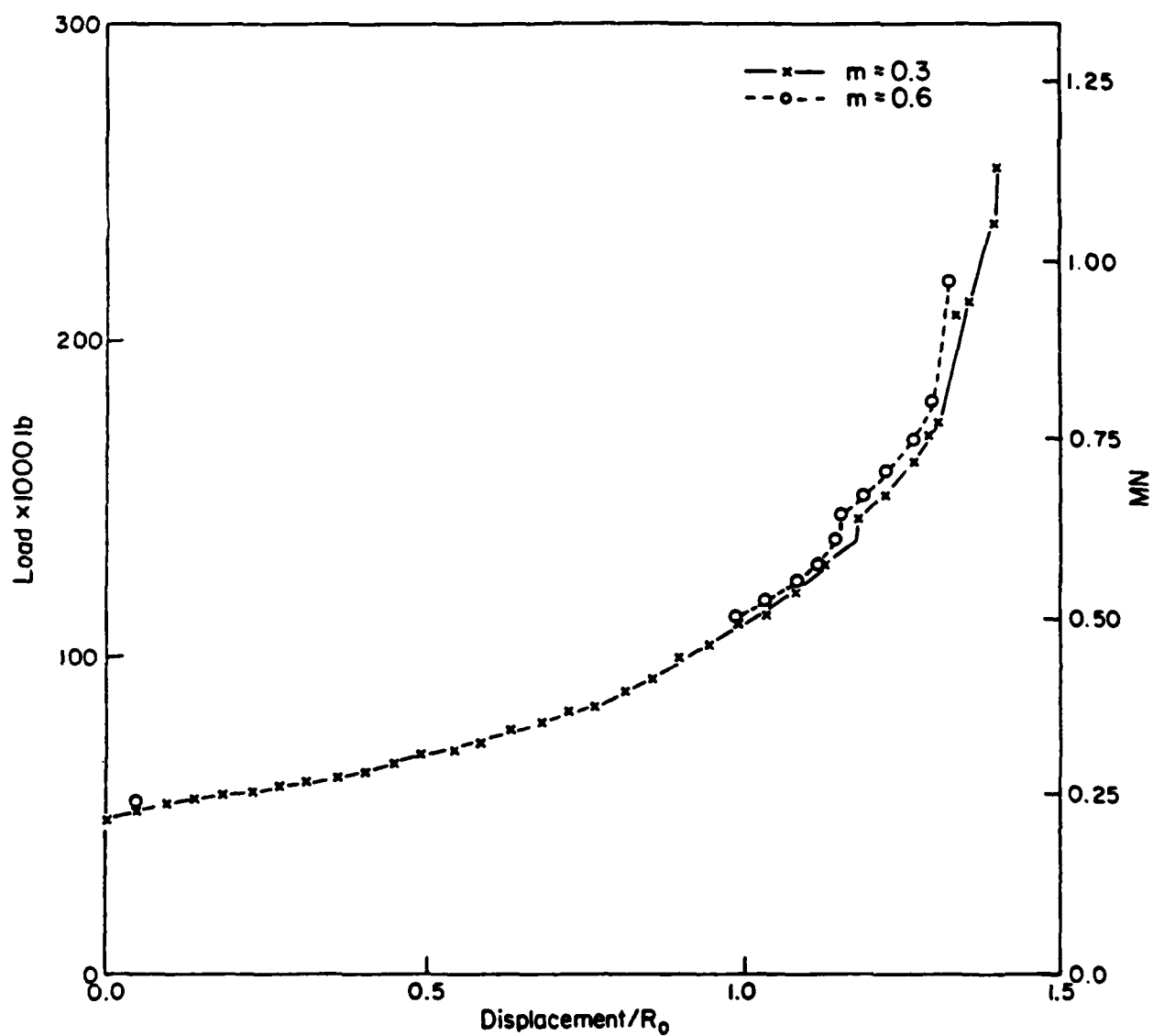


Figure G-7. Calculated Load-Displacement Relations
When $m = 0.3$ and $m = 0.6$.

progresses. Similar trends were found in spike forging experiments with lead and aluminum.^[18] The load values for both frictions are almost identical at the early stages and the load is higher for the higher friction.

The Figures G-8 and G-9 show the local velocity distributions at the die displacements of $0.02H_0$, $0.2H_0$, $0.4H_0$ and $0.58H_0$ for $m = 0.3$ and $m = 0.6$, respectively. The velocities shown in the figures are relative quantities with respect to the upper die. It can be seen from the figures that the deformations at the initial stages of both frictional cases are concentrated near the right upper corner of the workpiece while the rest of the portion is rigid. The relative velocities of spike tip are $0.188 V_D$ and $0.204 V_D$ at the die displacements of $0.2H_0$ and $0.4H_0$, respectively, when $m = 0.3$, and they are $0.193 V_D$ and $0.238 V_D$ when $m = 0.6$. Here V_D is the downward velocity of the upper die. These show that the differences in spike tip velocities with different frictions are relatively small at early stages. The figures show, however, that the flow pattern changes significantly at the die displacement of $0.58H_0$. At this stage the relative velocity of spike tip is about $1.25 V_D$ when $m = 0.6$ while it is $0.465 V_D$ when $m = 0.3$.

As can be seen from the relative velocity patterns, a part of the workpiece flows into the central cavity while the rest of the material flows radially. Because of these two different flow directions, a neutral point forms on the upper die workpiece interface where the relative movement between die and material becomes zero. Figures G-8 and G-9 show the locations of neutral points. In the case of low friction the neutral point does not form at die displacements of $0.02H_0$ and $0.2H_0$, suggesting that the material flows outward at early stages of deformation. As the deformation progresses the neutral point appears near the fillet of the upper die.

Locations of neutral points are shown at die displacements of $0.2H_0$, $0.4H_0$ and $0.58H_0$ when $m = 0.6$ in Figure G-9. Comparing Figure G-8 and Figure G-9 it can be seen that the neutral point forms earlier for higher friction and that its location is farther away from the center axis. In spite of the differences in the locations of the neutral points with different frictions, the relative movements are small along the workpiece-upper die interface for both frictions up to $0.4H_0$ die displacement.

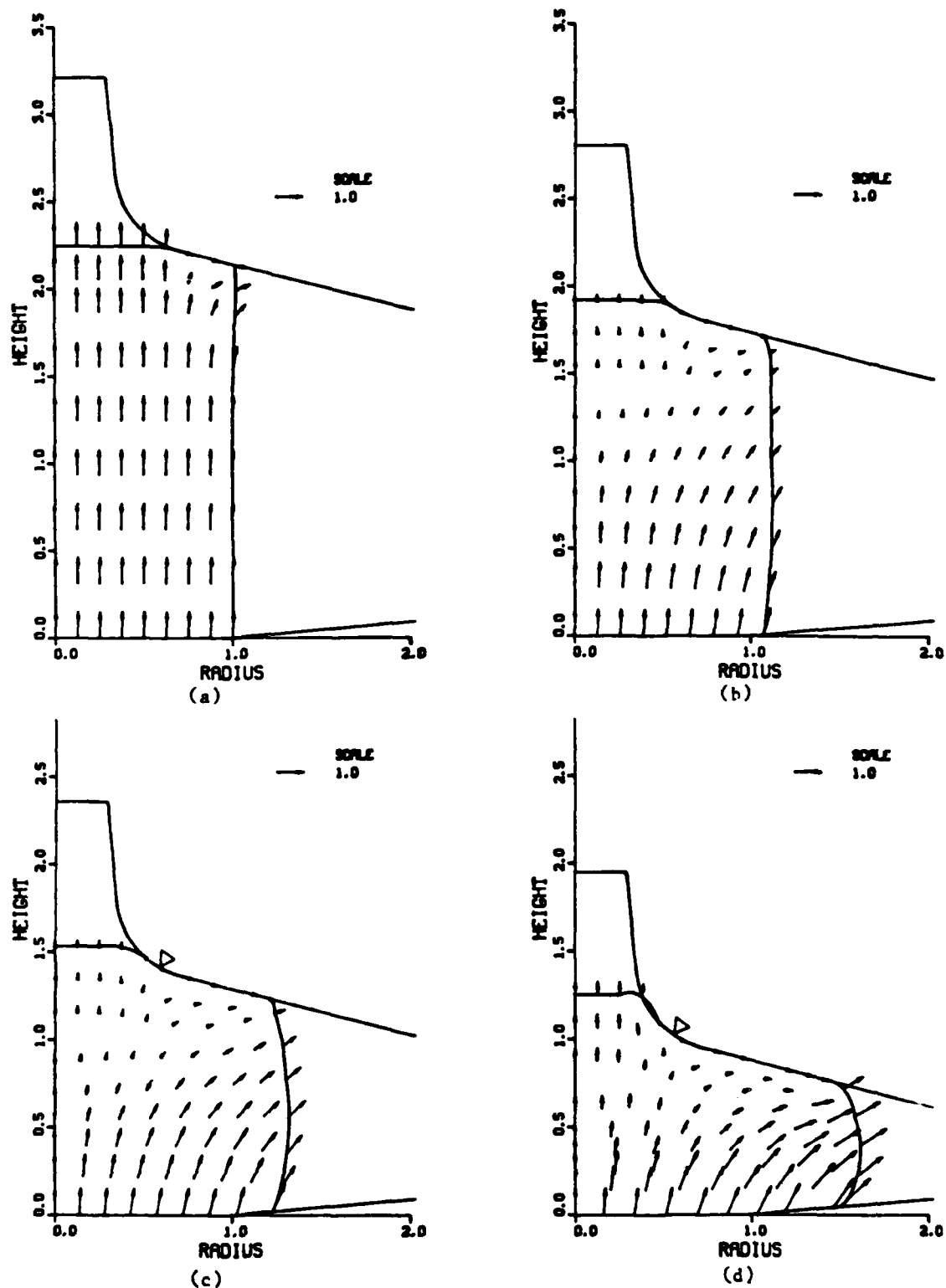


Figure G-8. Relative Velocity Distributions at Die Displacements of (a) $0.02H_0$, (b) $0.2H_0$, (c) $0.4H_0$ and (d) $0.58H_0$ when $m = 0.3$. Δ Denotes the Location of Neutral Point.

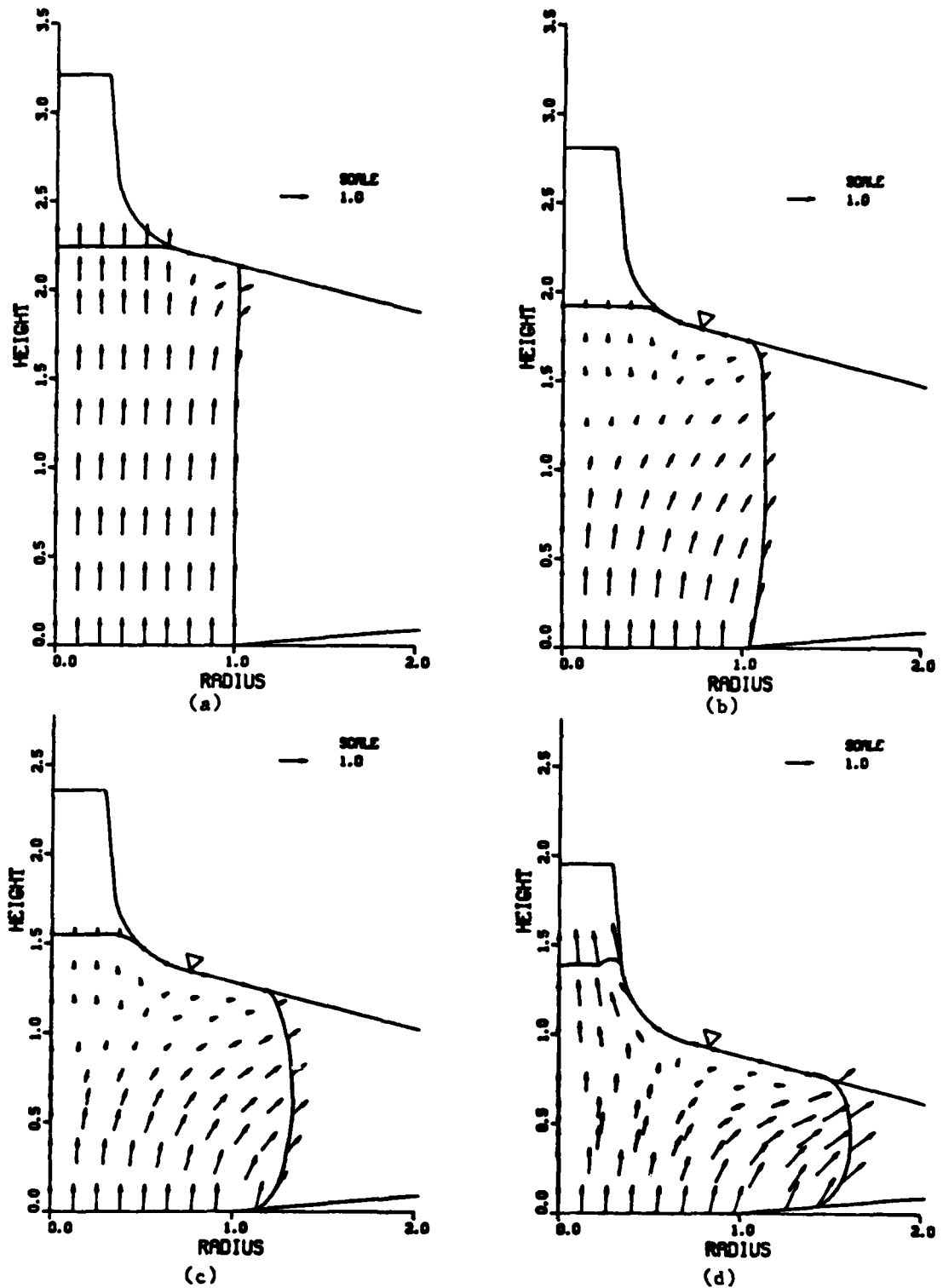


Figure G-9. Relative Velocity Distributions at Die Displacements of (a) $0.02H_o$, (b) $0.2H_o$, (c) $0.4H_o$ and (d) $0.58H_o$ when $m = 0.6$. Δ Denotes the Location of Neutral Point.

Figure G-10 shows the change of spike height as a function of die displacements. It can be seen from the figure that the top surface of the spike moves downward for both friction cases during early stages of deformation. The downward speed slows down and then the spike top surface moves up near the end of the process for both cases. The spike tip reaches its minimum earlier for the higher friction case. The figure shows that the minimum height of 34.8 mm (1.37 in.) is reached at die displacement of 31.5 mm (1.24 in.) in the case of $m = 0.6$ while that of 31.0 mm (1.22 in.) is reached at die displacement of 35.6 mm (1.40 in.) when $m = 0.3$. The figure also reveals that the effect of friction on the spike height is minimal during the early stage of deformation. In the figure the calculated spike height is compared with experimental data^[18] with lead and aluminum specimens. It shows that the friction coefficient is approximately 0.6 in case of dry friction and that it is about 0.3 in the lubricated case.

In the finite element method the local information such as strains, strain rates, and stresses can be easily obtained. The information is used not only to calculate the effect of flow stress on the overall deformation but also to predict defect formation in metal forming processes. In the present paper the total effective strain concentrations are shown in Figure G-11 for both friction cases at die displacements of $0.2H_0$, $0.4H_0$ and $0.58H_0$. As it can be expected from the previous discussions, the general patterns of strain distributions are similar to each other, showing almost no deformation near the spike tip and the highest strain concentration along the band joining the right upper corner of the specimen and middle of the height near the center. It is, however, interesting to note that the strain gradient is higher for the higher friction case, and that the deformation is more uniform in the case of lower friction. The difference in the strain gradient is more evident near the bottom surface of the workpiece.

From the present discussion it can be seen that the effect of friction on the overall deformation of spike forging process is not appreciable until die displacement reaches over, say, $0.4H_0$. This is attributed to the fact that the initial die contact surface area is small compared to overall workpiece volume. Therefore, it is suggested that a larger initial diameter-to-height ratio is recommended for the spike forging to be an effective means of friction test.

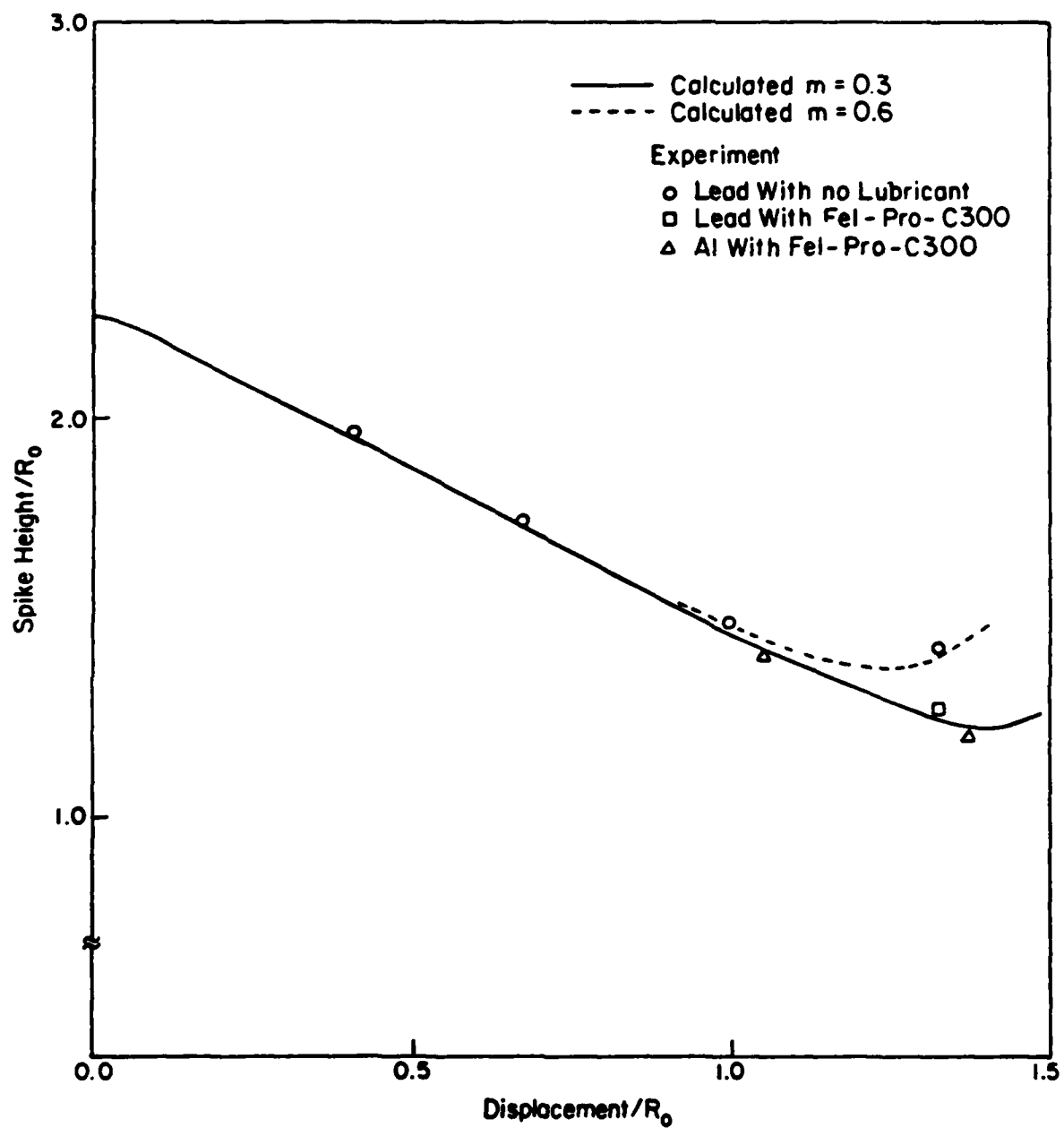


Figure G-10. Variation of Spike Heights When $m = 0.3$ and $m = 0.6$

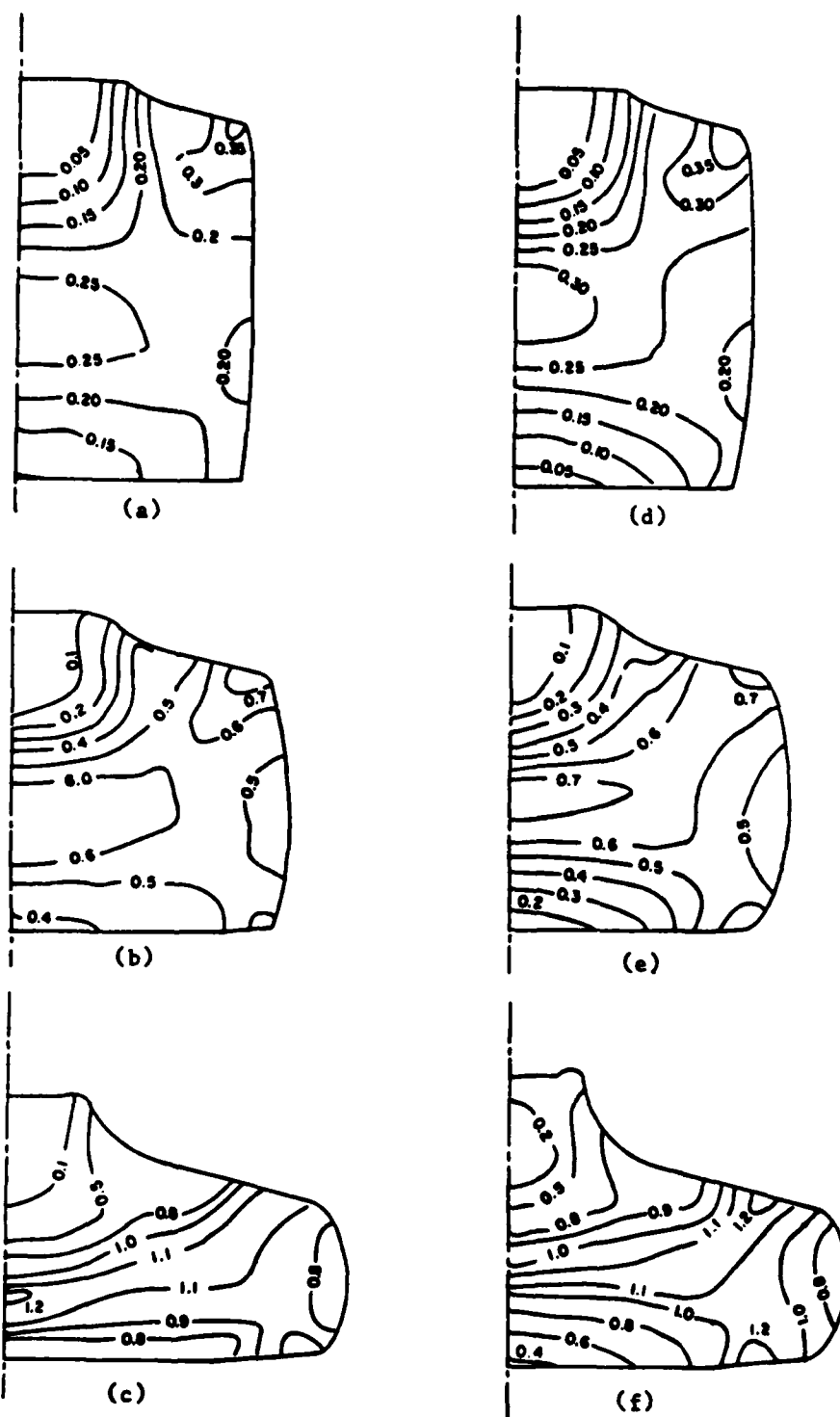


Figure G-11. Effective Strain Distributions at Die Displacements of (a) $0.2H_o$, (b) $0.4H_o$ and (c) $0.58H_o$ when $m = 0.3$ and (d) $0.2H_o$, (e) $0.4H_o$ and (f) $0.58H_o$ when $m = 0.6$.

Compressor Disk Forging Analysis

An isothermal forging process for compressor disks has been analyzed by the present formulation. The desired optimal properties of a compressor disk vary from the bore to the rim, that is, high creep and high fracture toughness in the rim region and high fatigue strength in the bore region. The desired properties in the compressor disk require to have β -microstructure at the rim and $(\alpha + \beta)$ -microstructure at the bore. Several different processes⁽²⁰⁾ were investigated to produce a dual microstructure/property disk. Among these, a direct forging process with β -microstructure preform has been successful in producing a dual property disk. This process is especially attractive because of its simplicity and it can provide an economical and practical method for manufacturing. The basic concept of the process is to control the strain concentration for recrystallization to take place in the central region. The process conditions were chosen from the successful forging conditions reported by Chen⁽²⁰⁾.

Computational Conditions and Procedure

The cylindrical preform shape used in the analysis has the dimension of 158.8 mm (6.5 in.) in diameter and 63.5 mm (2.5 in.) in height. The shape and the dimensions of the disk forging dies are given in Figure G-12. As it can be seen from the figure the bottom and top dies have the identical cavity definitions. The velocity of the upper die used in the simulation is 5.1 mm/min (0.2 in/min) and the bottom die is stationary. The forging is done isothermally at 900 C (1650 F) with the average nominal strain rate of about 0.175 min^{-1} . The slow strain rate in isothermal condition is necessary to prevent the temperature rise due to deformation heating and also to prevent the unstable localization.

Even though the β -microstructure preforms were used for the actual forging, analysis was done for both $(\alpha + \beta)$ and β microstructures preforms to examine the influence of microstructure on the deformation pattern. The flow stress as a function of strain, strain rate, and temperature was obtained from the experiments conducted by Dadras and Thomas,⁽²¹⁾ who, based on their simple

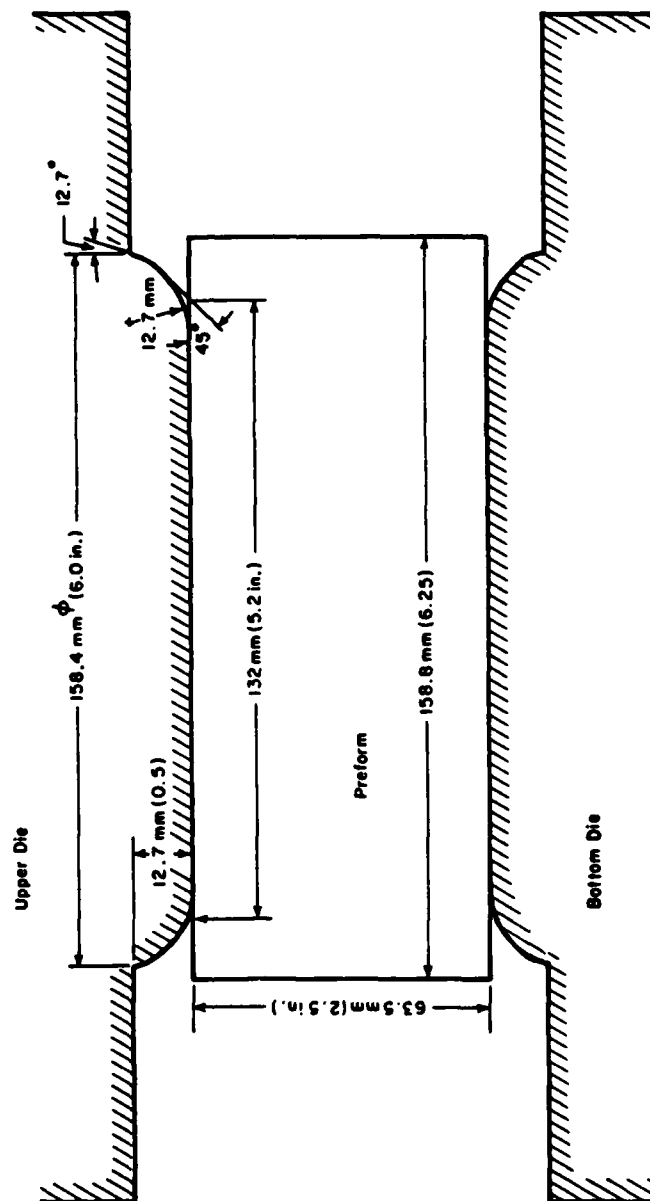


Figure G-12. Schematic Drawing of Disk Forging Die and Preform

compression tests, suggested closed form relations for ($\alpha + \beta$) and β microstructure Ti-6242-0.1Si alloy. Their test range covers from 10^{-3} sec^{-1} to 10^{-1} sec^{-1} for strain rates, from 816 C (1500 F) to 1010 C (1850 F) for temperature, and from 0 to 0.7 for strain. Figure G-13 shows the three-dimensional display of flow stress of ($\alpha + \beta$) microstructure as a function of temperature and strain rate. It has been reported that the flow stress of the ($\alpha + \beta$) microstructure Ti-6242-0.1Si is independent of total accumulated strain at the temperature range shown. Since the simulation is done under isothermal conditions, only the curve marked by the bold line in Figure G-13 was used. The flow stress of β microstructure alloy is a function of strain, strain rate, and temperature. The flow stress of β microstructure at 900 C is plotted in Figure G-14. As can be seen from the figure, the β microstructure exhibits the strain softening behavior. Further, in order to study the effect of friction on the deformation behavior of disk forging process, two different friction shear factors, $m = 0.3$ and $m = 0.65$, were used in the analysis. The summary of the computed conditions is given in Table G-1.

TABLE G-1. PROCESS CONDITIONS USED FOR SIMULATION

Case No.	Microstructure	Temperature ($^{\circ}\text{C}$)	Friction Factor	Die
1	$\alpha + \beta$	900	0.3	open
2	β	900	0.3	open
3	β	900	0.65	open
4	β	900	0.3	trapped

The non-steady state deformation of the disk forging process was analyzed in a step-by-step manner by treating it quasilinearly during each incremental deformation. The incremental displacement of upper die for each

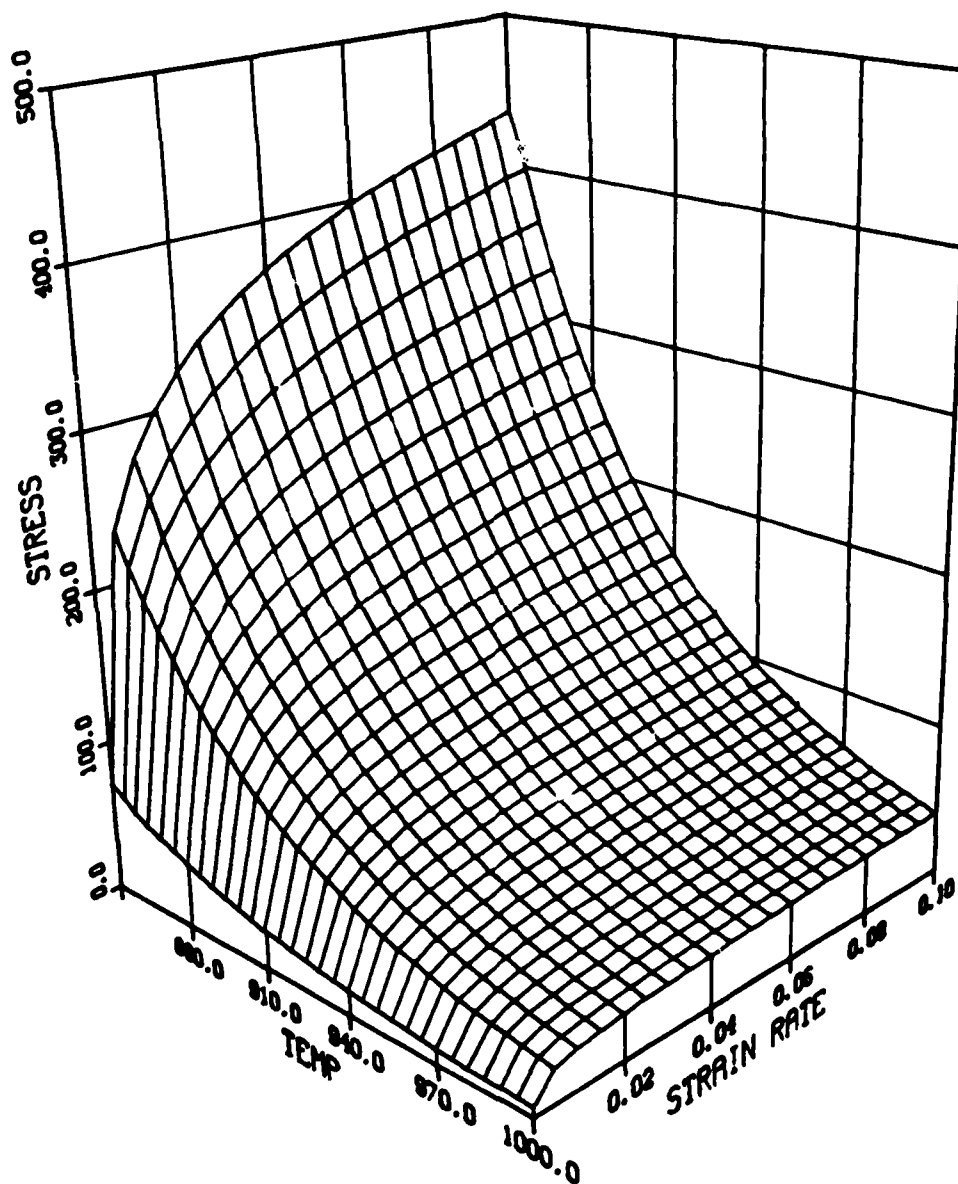


Figure G-13. Flow Stress of (α+β) Ti-6242 at Various Strain Rates and Temperatures
Unit: Stress in MPa, Temperature in °C, and Strain Rate in sec⁻¹.

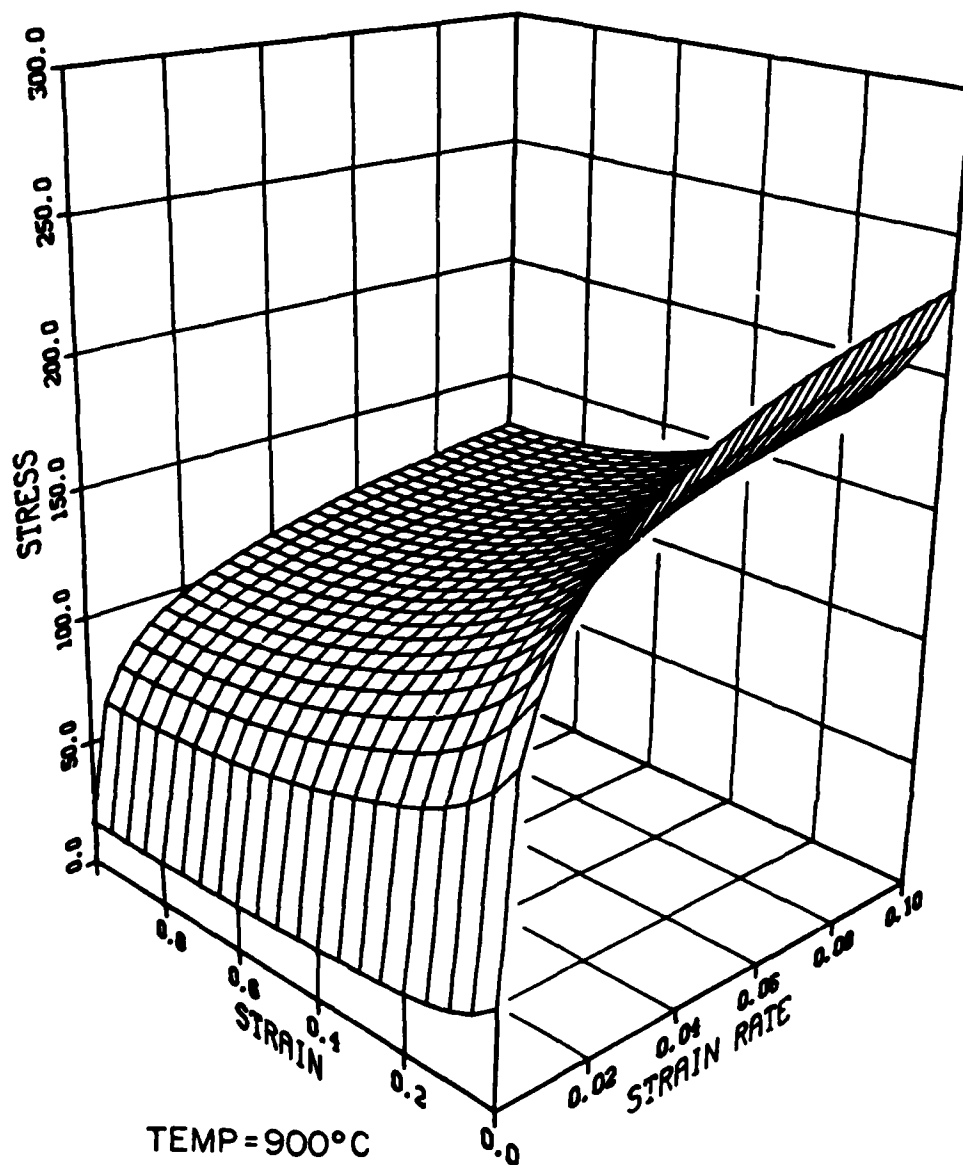


Figure G-14. Flow Stress of β Ti-6242 at 900C and Various Strains and Strain Rates
Unit: Stress in MPa, Strain Rate in sec^{-1} .

step is chosen to be 0.02 times the original preform height. The measure of convergence represented by $||\Delta u||/||u||$ was chosen to be 10^{-4} .

Results and Discussions

Figure G-15 shows the initial FEM grid used in the analysis together with the upper die. Because of the symmetry of the deformation it was sufficient to analyze the quarter section of the forging process. The predicted grid distortions for Case 2 (β -microstructure with $m = 0.3$) are shown in Figure G-16 at various stages of deformation up to 70 percent reduction in height at the center. In the early stage of deformation, the material at the bore is compressed according to the die movement. However, the height of the workpiece near the side surface is reduced very little but the overall diameter increases to accommodate the material which was squeezed out of the bore region. In order to accommodate the difference in height and the increase of diameter, the side surface bulges, and the top and bottom surfaces at the free end form a characteristic shape similar to the one reported earlier⁽²²⁾. As the deformation proceeds, more and more material at the bore is squeezed out and is freed to the rim. The prediction shows that the separation of nodes takes place at the point on the corner circle at approximately 20 ~ 30 degrees from the bore plane. It should be noted, however, that the predicted point of separation is a function of friction and element size near the point of separation.

The barreling of the side surface becomes larger as the reduction increases. The top and bottom surfaces touch the die surfaces at the rim when the reduction in height reaches 45.8 percent. The vertical distance between the die surface at the rim is 59.80 mm (2.35 in.) at this stage. Comparing this with the original preform height of 63.5 mm (2.5 in.), the height of the workpiece at the rim is reduced only 6 percent before it reaches the die surface. At this stage closed cavity rings are formed between the die and the workpiece near the bore-rim transition. As the deformation proceeds, more material is squeezed out of the bore, at the same time more free surface folding takes place at the rim. The surface folding is limited to the top and the bottom surfaces of the workpiece. The folding from the side surface was

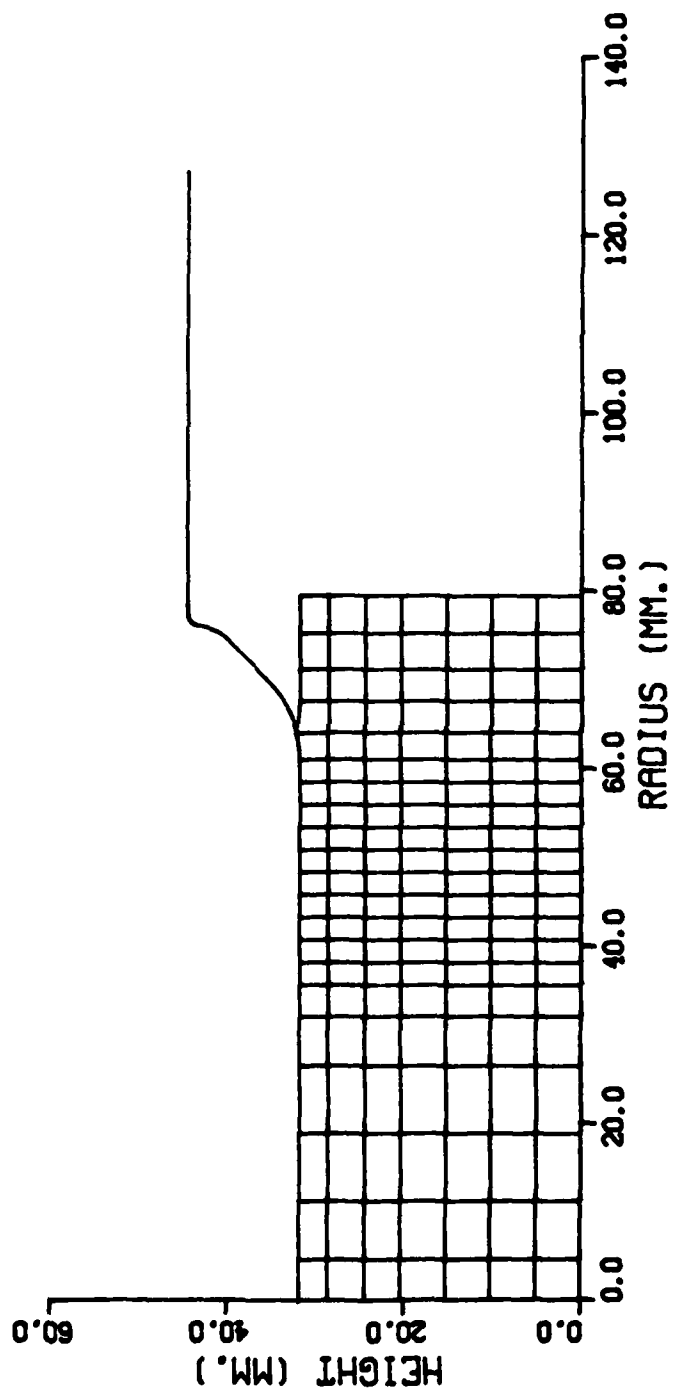


Figure G-15. FEM Grid Used in Analysis of Disk Forging.

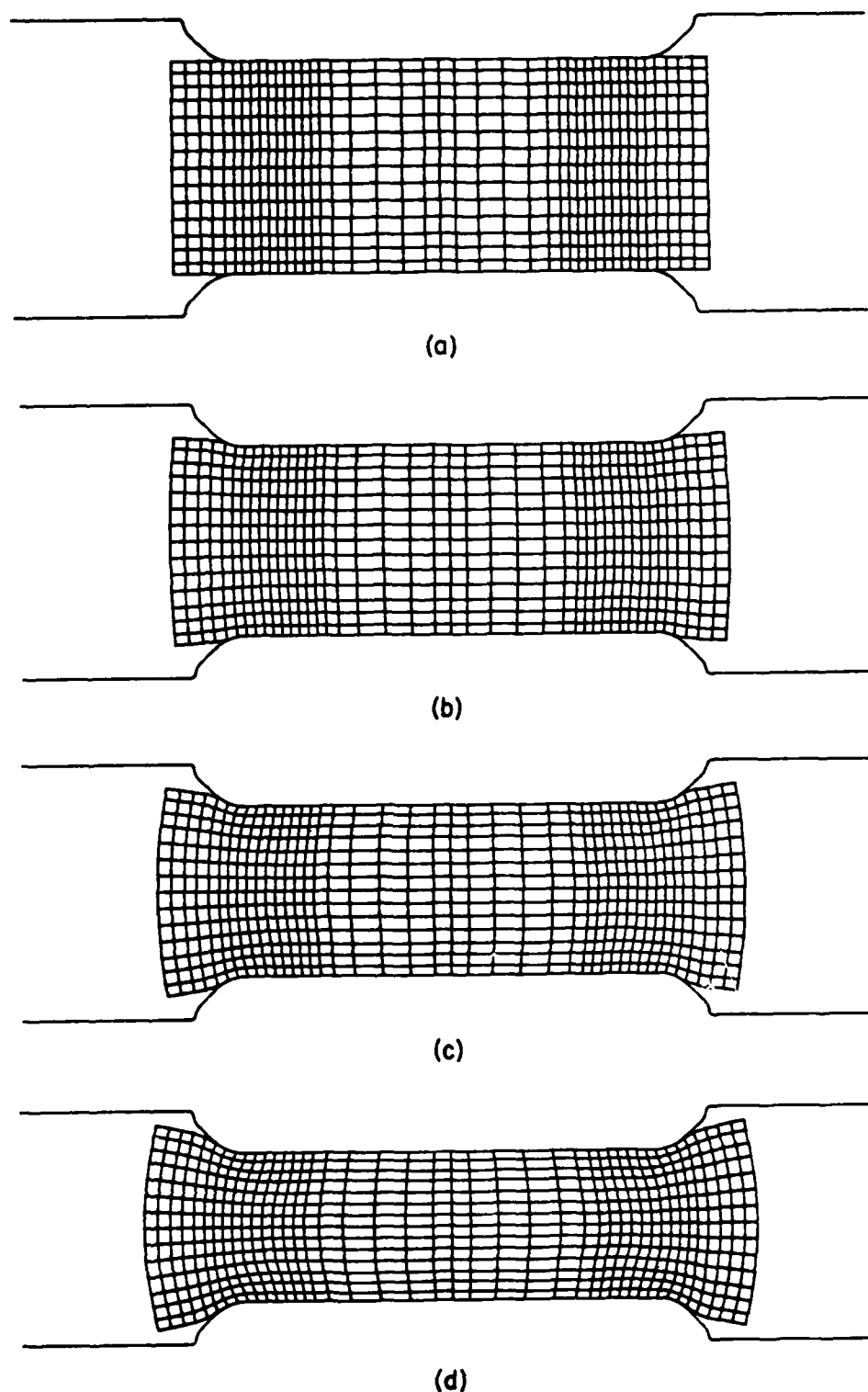
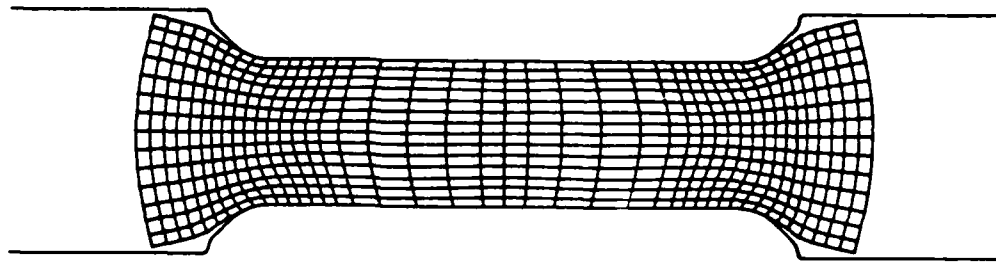
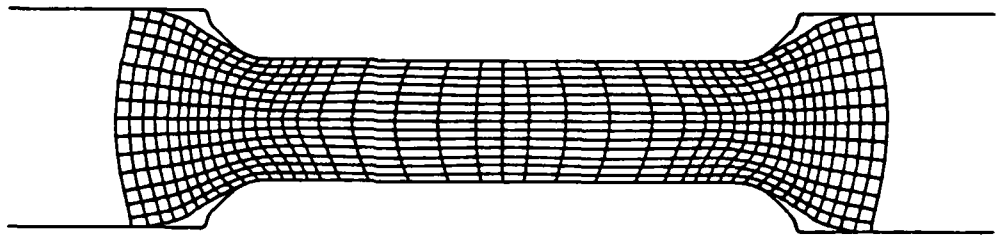


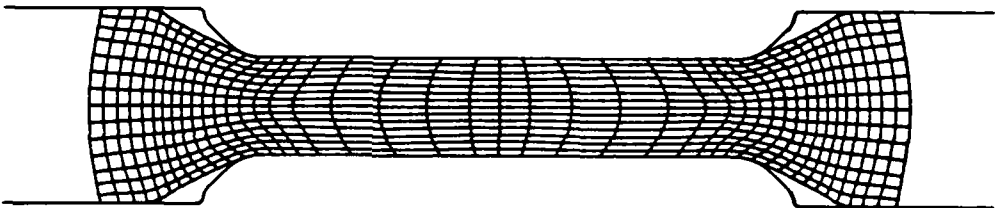
Figure G-16. Predicted Grid Distortions for Disk Forging Ti-6242-0.1Si, β -Microstructure, $m = 0.30$, $T = 900^\circ\text{C}$. (a) Undeformed, (b) 10% Reduction in Height, (c) 20%, (d) 30%, (e) 40%, (f) 50%, (g) 60%, (h) 70%.



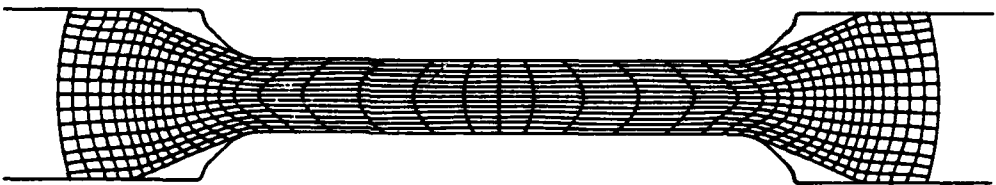
(e)



(f)



(g)



(h)

Figure G-16. Predicted Grid Distortions for Disk Forging (Continued)

not observed. It is interesting to note that the volume of the gap near the bore-rim transition increases with deformation. The shape of the free surface of the workpiece which forms the gap is initially convex upward. This surface becomes flatter with increasing deformation. Moreover, the inner edge of the die contact surface at the rim moves outward. This also contributes to the increase in the gap volume.

Figure G-17, G-18, and G-19 show the quarter sections of predicted grid distortions at 10 percent, 30 percent, 50 percent, and 70 percent reduction in height for Case 1 ($\alpha + \beta$ microstructure, $m = 0.3$), Case 2 (β microstructure, $m = 0.3$), and Case 3 (β microstructure, $m = 0.65$), respectively. Comparing Figures G-17 and G-18, it is interesting to note that the deformation patterns are not affected by the different flow stress behaviors of ($\alpha + \beta$) and β microstructures. In fact the grid distortions are almost identical for Case 1 and Case 2, even though the two microstructures exhibit quite different flow stress behaviors. The predicted behavior may not, however, be considered as a general case, but should be treated as a restricted response under the process conditions.

The grid distortions of Case 2 and Case 3 show the effect of friction on the deformation. One of the major differences that can be seen from the figures is that the element distortion is greater with higher friction in the bore and the neck section. Also the vertical grid lines at the bore, which were originally straight, bulge more with higher friction. It can be seen, however, that the overall workpiece shapes are not affected by friction during the early stages of deformation. In fact, the outside contours of workpieces are not distinguishable until the workpiece surface touches the die at the rim. From this observation it may be said that the bulging of the side surface is mainly due to the material adjustment according to the geometrical constraints. After the free surface of the workpiece at the rim touches the die, the effect of friction on the side surface can be seen from the figure which shows more bulging with higher friction.

Figure G-20 shows the load-displacement relations predicted for the three different cases. The figure shows that the load for Case 1 ($\alpha + \beta$ microstructure, $m = 0.3$) is a monotonically increasing function of die displacement. The increase is rather slow during the early stage, then it

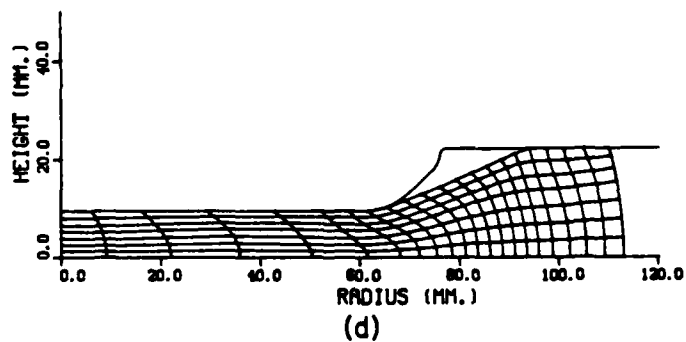
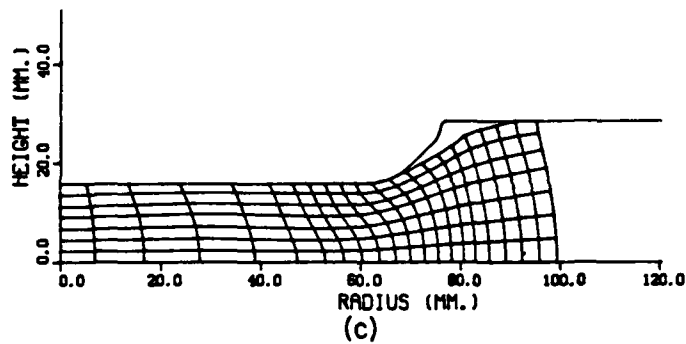
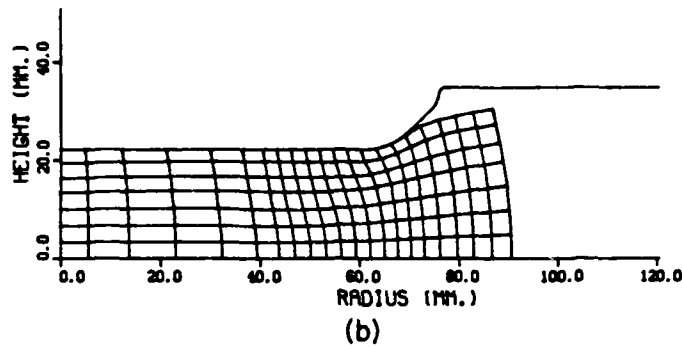
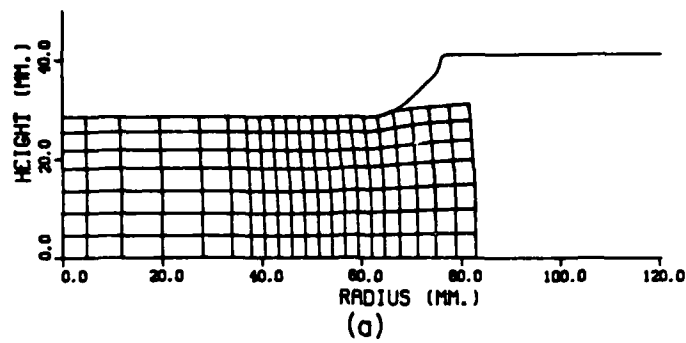


Figure G-17. Predicted Grid Distortion for Disk Forging Ti-6242-0.1Si, ($\alpha+\beta$)-Microstructure, $m = 0.3$, $T = 900C$, (a) 10% Reduction in Height, (b) 30%, (c) 50%, (d) 70%.

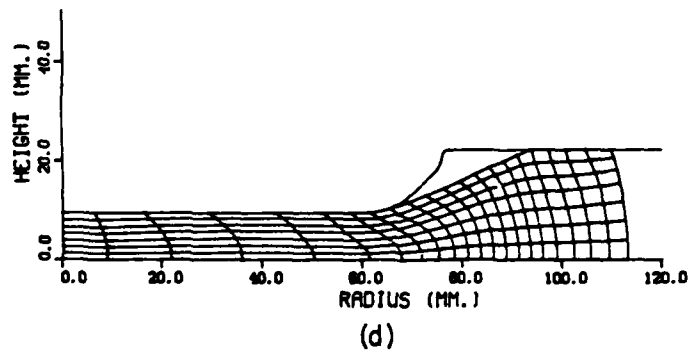
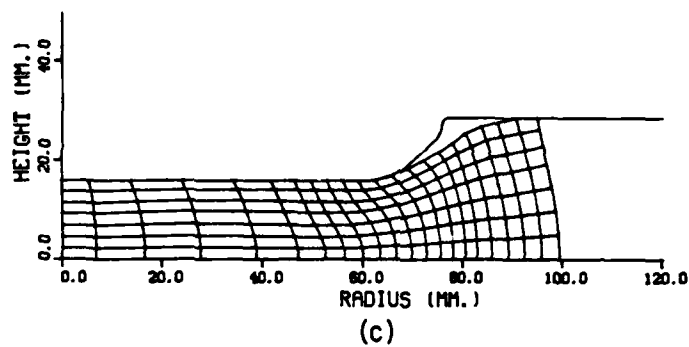
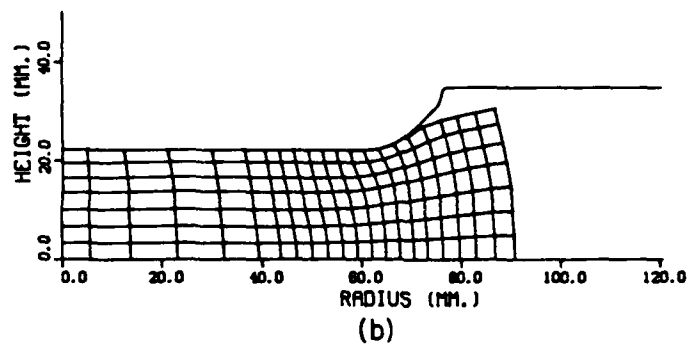
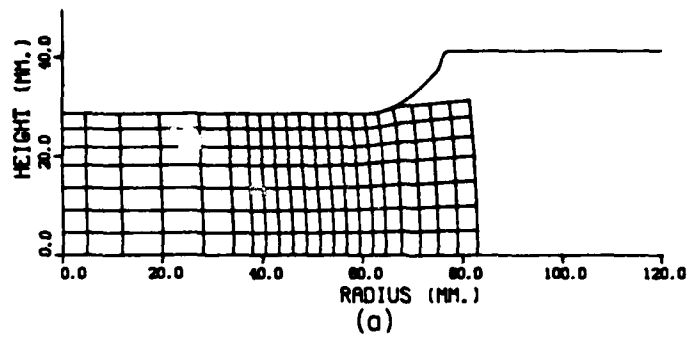
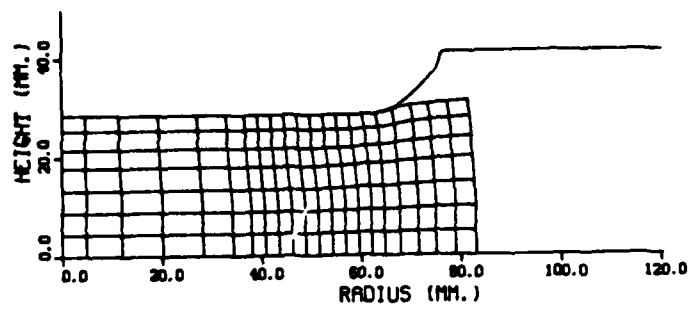
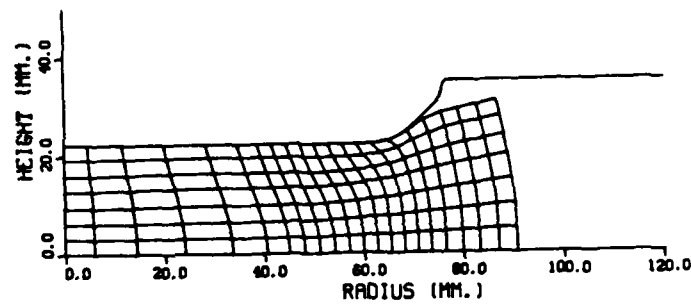


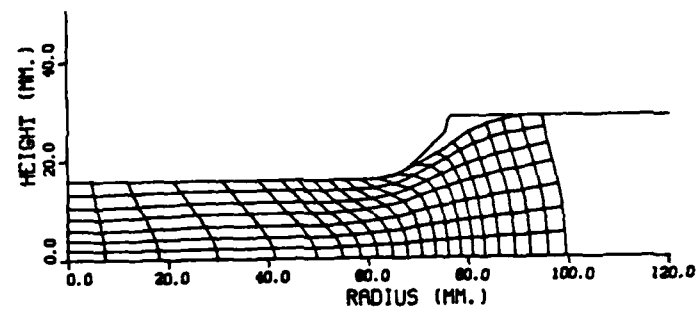
Figure G-18. Predicted Grid Distortion for Disk Forging Ti-6242-0.1Si, β -Microstructure, $m = 0.3$, $T = 900^\circ\text{C}$ (a) 10% Reduction in Height, (b) 30% (c) 50% (d) 70%.



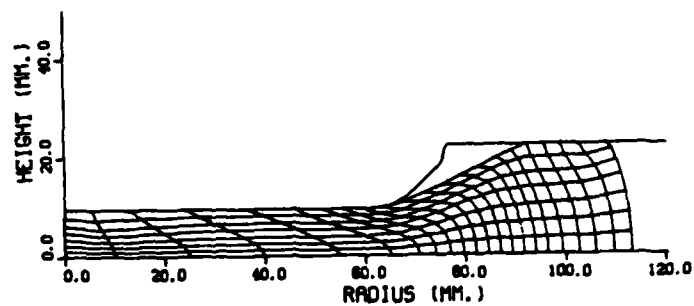
(a)



(b)



(c)



(d)

Figure G-19. Predicted Grid Distortion for Disk Forging Ti-6242-0.1Si, β -Microstructure, $m = 0.65$, $T = 900^\circ\text{C}$ (a) 10% Reduction in Height, (b) 30%, (c) 50% (d) 70%.

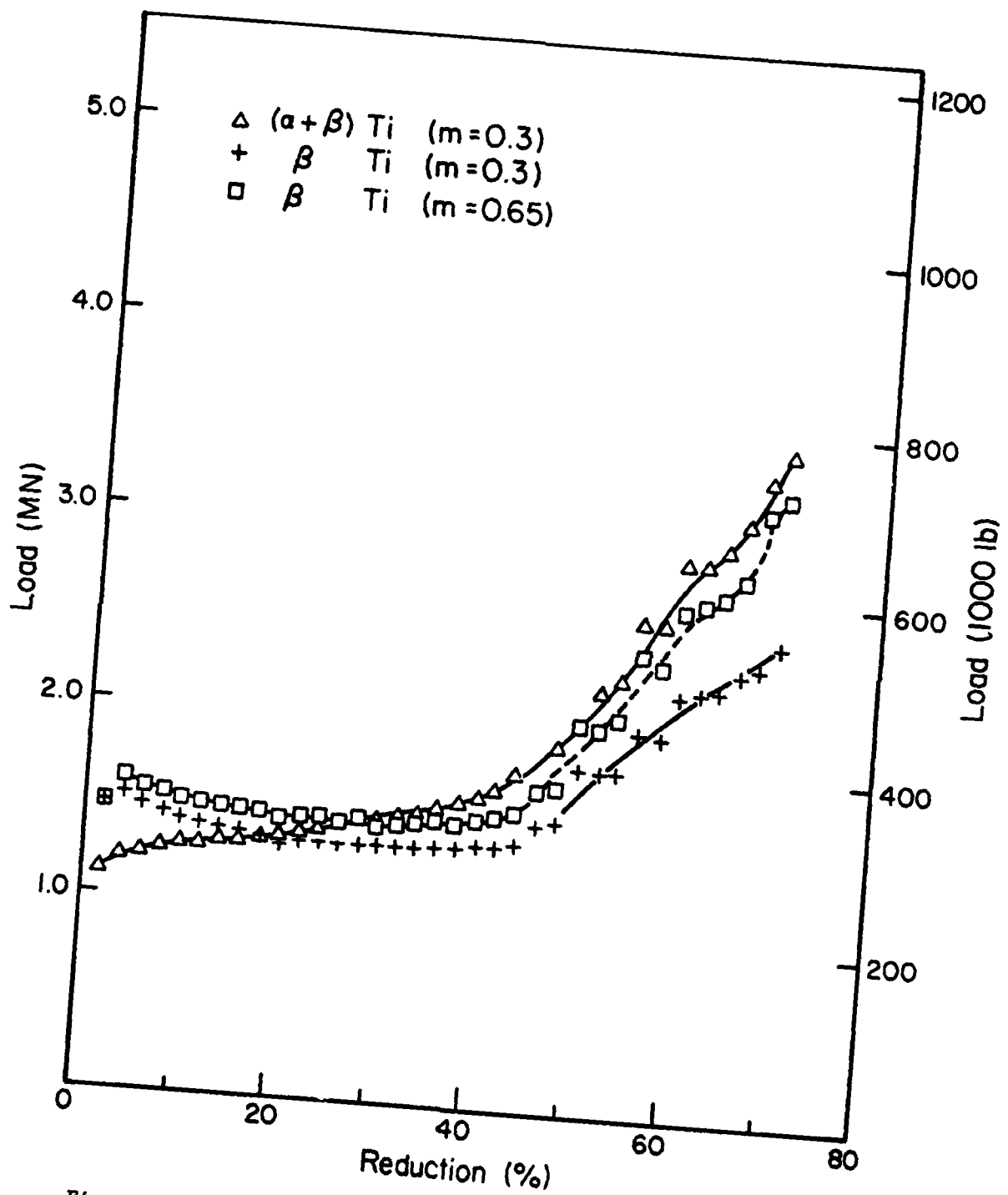
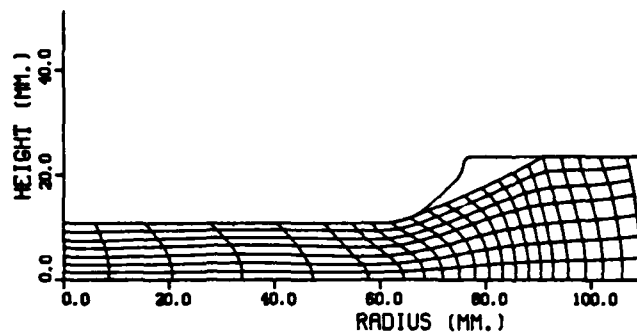


Figure G-20. Computed Forging Load vs. Reduction in Height.

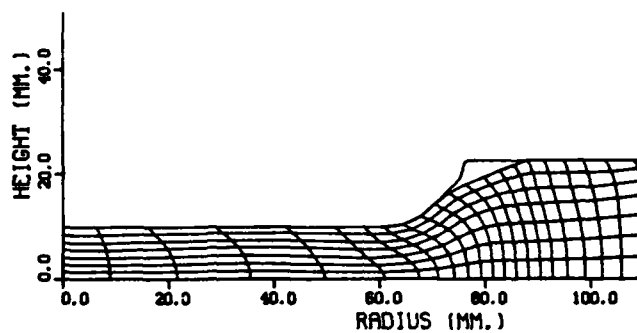
becomes rapid after the free surface at the rim touches the die. The load-displacement relation of Case 2 (β microstructure with $m = 0.3$) shows an interesting contrast to that of $(\alpha + \beta)$ microstructure with same friction. In this case, initially the load is higher than that for Case 1. This is due to the higher flow stress of β microstructure at zero strain. As the deformation progresses, the load decreases and stays constant until the free surface at the rim touches the die. Then the load starts to increase rapidly. The β microstructure with higher friction ($m = 0.65$) exhibits load-displacement characteristics similar to that of β microstructure with lower friction ($m = 0.3$), except that the load is higher for higher friction. The difference in load is relatively small and stays relatively constant during the early stages of deformation. The difference becomes increasingly larger after the workpiece touches the die surface at the rim. The differences in load at various stages of deformation reflect the die-contact surface area which stays relatively constant at the early stage and increases rapidly in the later stages.

From the practical die design viewpoint, it is often required to fill the gap which cannot be filled by the open die forging. Therefore, the deformation and the cavity filling behavior were studied using a trapped die as shown in Figure G-21. The top and the bottom die dimensions are the same as the one for open die forging, except that the radius is limited by the circular block placed outside. The radius of the circular block is 109.5 mm and it was determined in such a way that the die cavity volume is approximately 0.8 percent larger than that of preform volume at 70 percent reduction. In trapped die forging simulation, the process parameters chosen are identical to those of Case 2 except for the die shape.

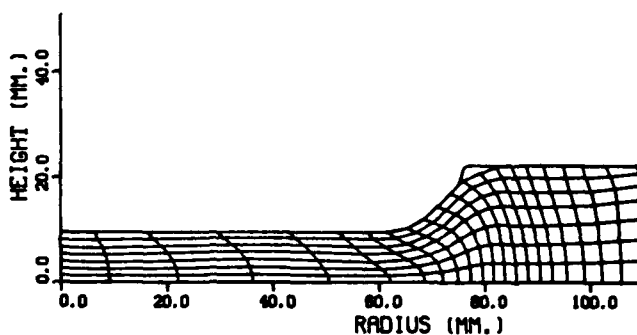
The deformation pattern of a disk forging with the trapped die is identical until the side surface of the workpiece touches the container die wall. The prediction shows that the node at the equator of the side surface touches the container wall at 65.7 percent deformation. Figure G-21 shows the predicted grid distortions at (a) 66 percent, (b) 69 percent, (c) 70 percent, and (d) 70.25 percent deformation. It can be seen from the figure that the gaps formed at both sides of the rim are filled gradually, and that the gap at the outside radius is filled before the one at the inside of the rim. The figure also reveals that the material has not completely filled the cavity at



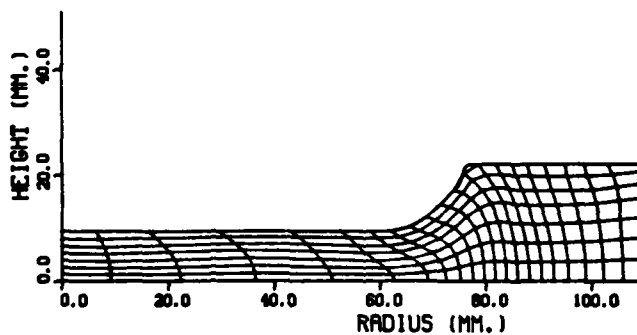
(a)



(b)



(c)



(d)

Figure G-21. Grid Distortion Predicted for Trapped Die Forging Ti-2642-0.1Si, β -Microstructure, $m = 0.3$, 900C. Reduction: (a) 66%, (b) 69%, (c) 70%, (d) 70.25%.

the outside of the rim when the deformation reaches 70.25 percent reduction. The simulation was stopped at this stage where no free nodes are left to reflect the actual corner filling behavior of the material.

In the trapped die forging, the material flow during the final stage is limited by the contour of the dies. That is, the material will fill the die cavity completely if sufficient pressure is applied. Therefore it may be more useful to calculate the required minimum die load to fill the gaps. The predicted load vs. die displacement relation is shown in Figure G-22 for trapped die forging and it is compared with that of open die forging (Case 2). Since the deformation of the two cases are identical to each other until the side surface touches the container die, the early portion of the load for the open die forging also represents that of trapped die forging. It can be seen from the figure that the load required for trapped die forging increases very rapidly after 65.7 percent deformation at which the initial contact between the side surface of the workpiece and container wall was predicted. The prediction shows that the load required for trapped die forging is about 4.5 times that required for open die forging at the final stage, 70 percent reduction in height. It appears that the value is within the reasonable range even though the actual experimental loads are not available. It should be also noted that the present grid system may not allow a sufficient degree of freedom to describe contour filling accurately during the final stage of deformation.

The predicted velocity distribution for Case 1 is shown in Figure G-23. The figure shows that the material flow at the rim in the early stage is mainly horizontal, which was expected from the grid distortion. Comparing the velocity fields near free surface which forms the cavity at 50 percent and 70 percent reductions, it can be seen that the surface moves outward faster at 70 percent reduction suggesting the increase of the gap volume.

The strain distributions at various stages of deformation are the most important information in predicting the microstructure of the workpiece since it has been found that the recrystallization at the bore is directly related to the amount of the strain localization. Figures G-24, G-25, and G-26 show the predicted effective strain concentrations at 30 percent, 50 percent, and 70 percent for Cases 1, 2, and 3, respectively. The figures show

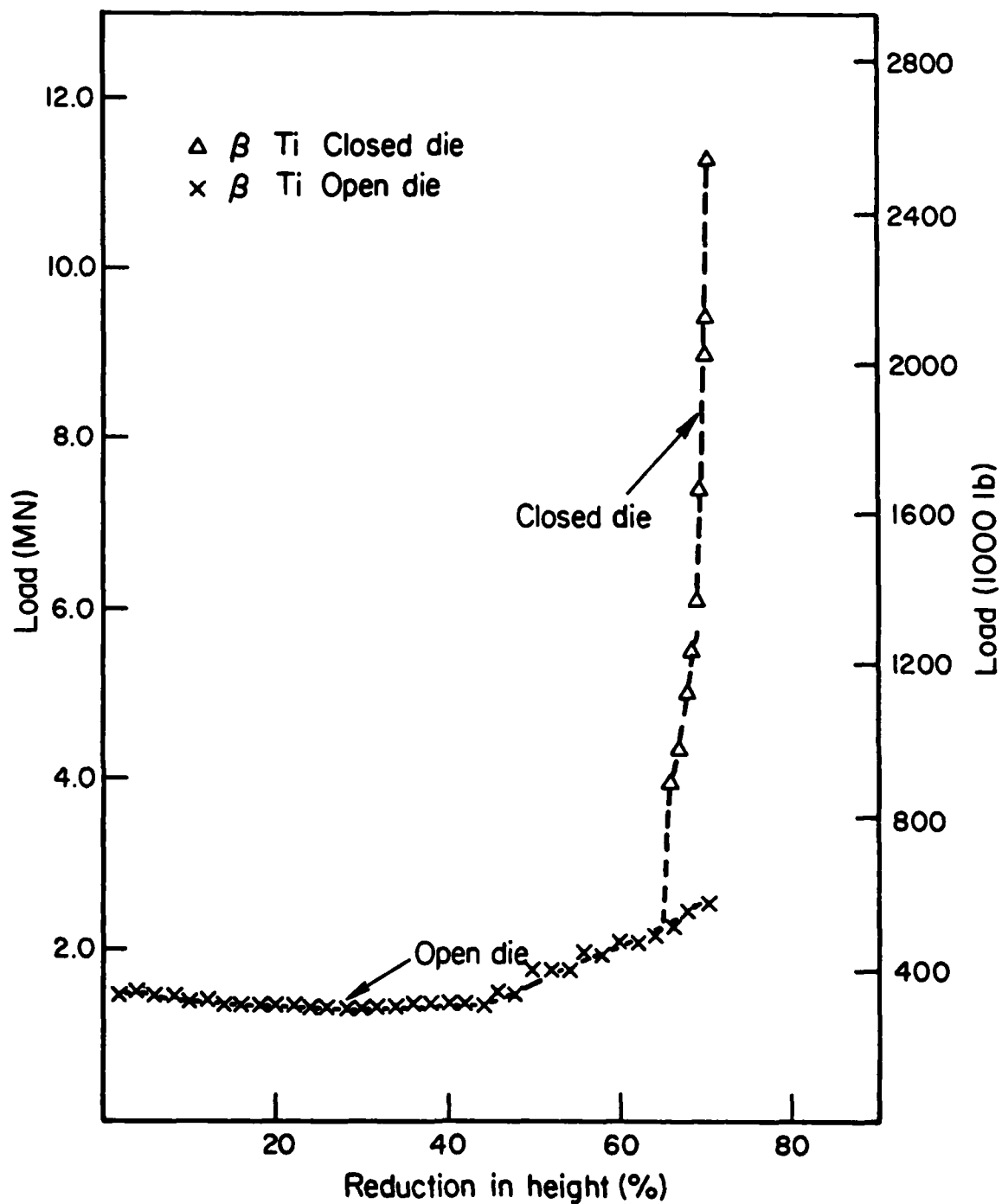
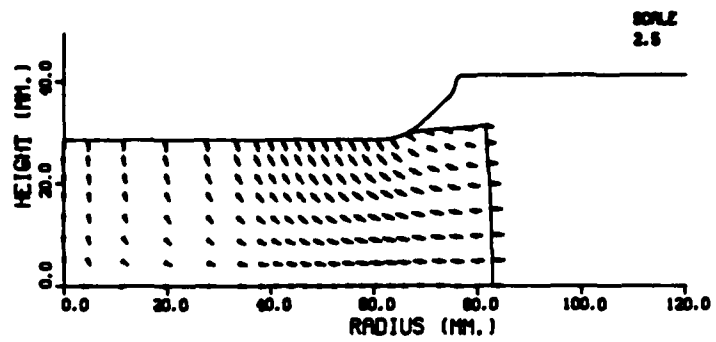
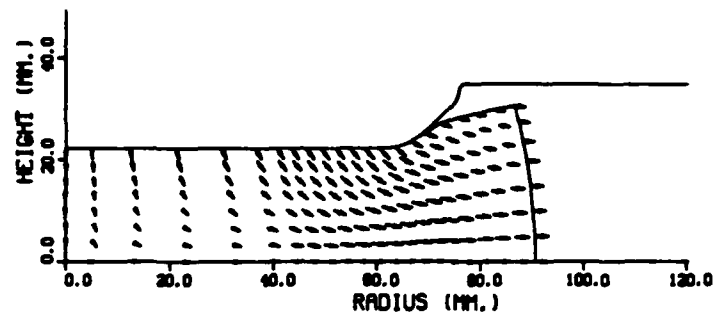


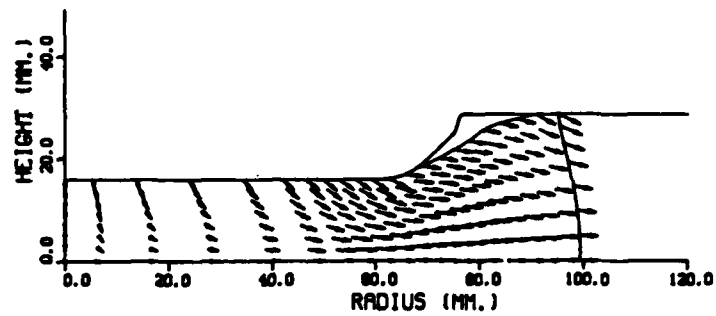
Figure G-22. Computed Forging Load for Trapped Die
Ti-6242-0.1Si, $m = 0.3$, $T = 900^\circ\text{C}$.



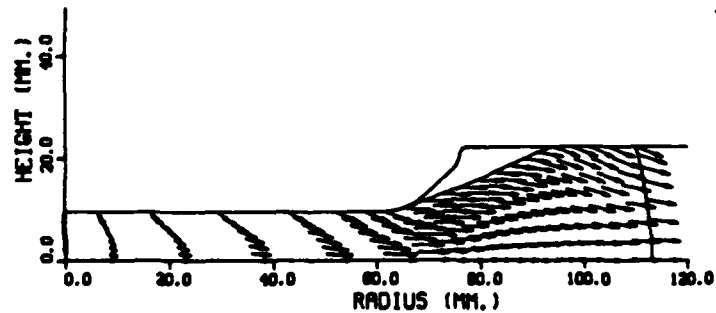
(a)



(b)



(c)



(d)

Figure G-23. Predicted Velocity Distributions Ti-6242-0.1Si, ($\alpha+\beta$)-Microstructure, $m = 0.3$, $T = 900^\circ\text{C}$ (a) 10% Reduction in Height, (b) 30%, (c) 50%, (d) 70%.

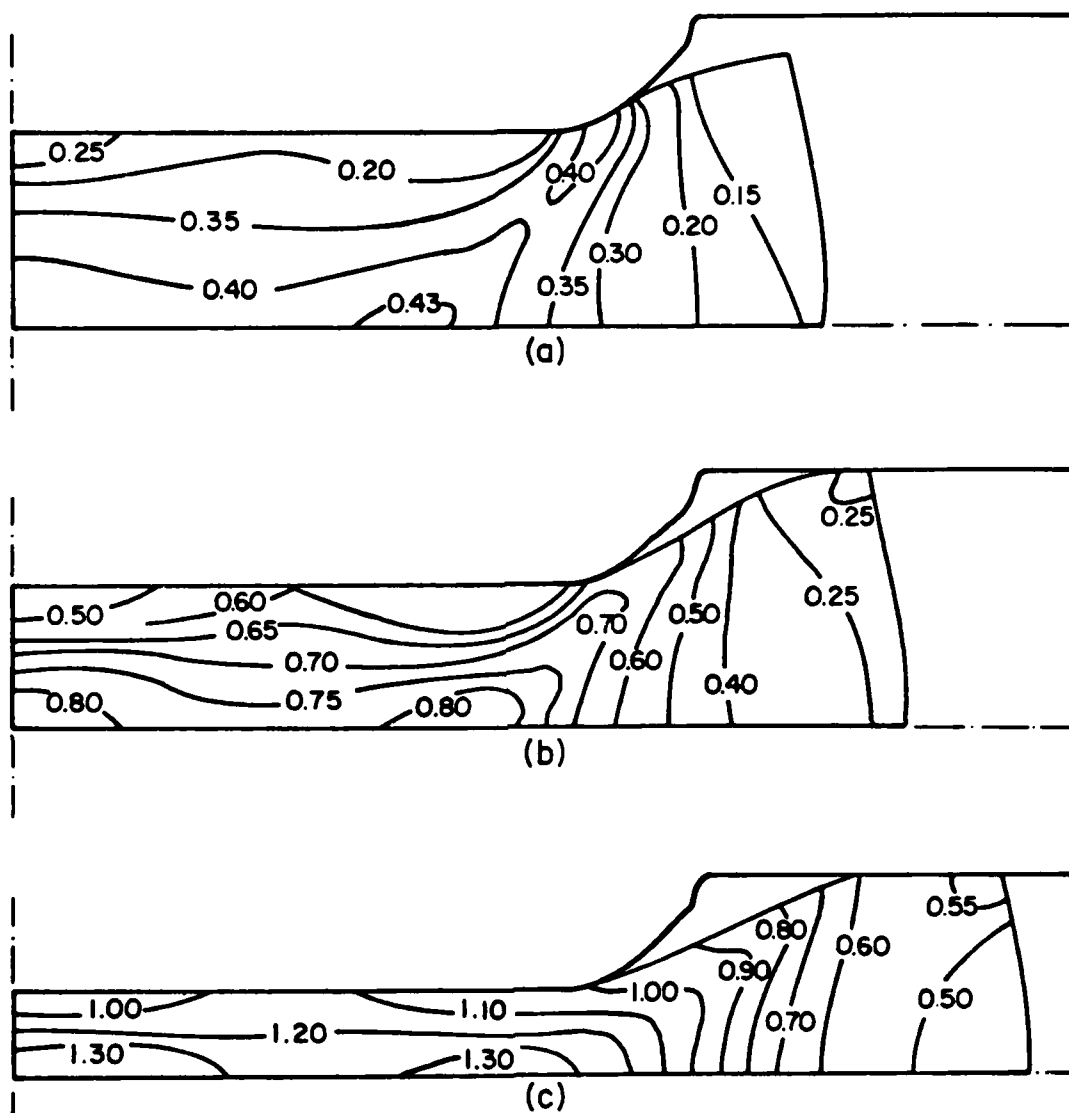


Figure G-24. Effective Strain Distribution Ti-6242-0.1Si, ($\alpha+\beta$) Microstructure, 900C, $m = 0.30$, (a) 30% Reduction in Height at Center, (b) 50%, (c) 70%.

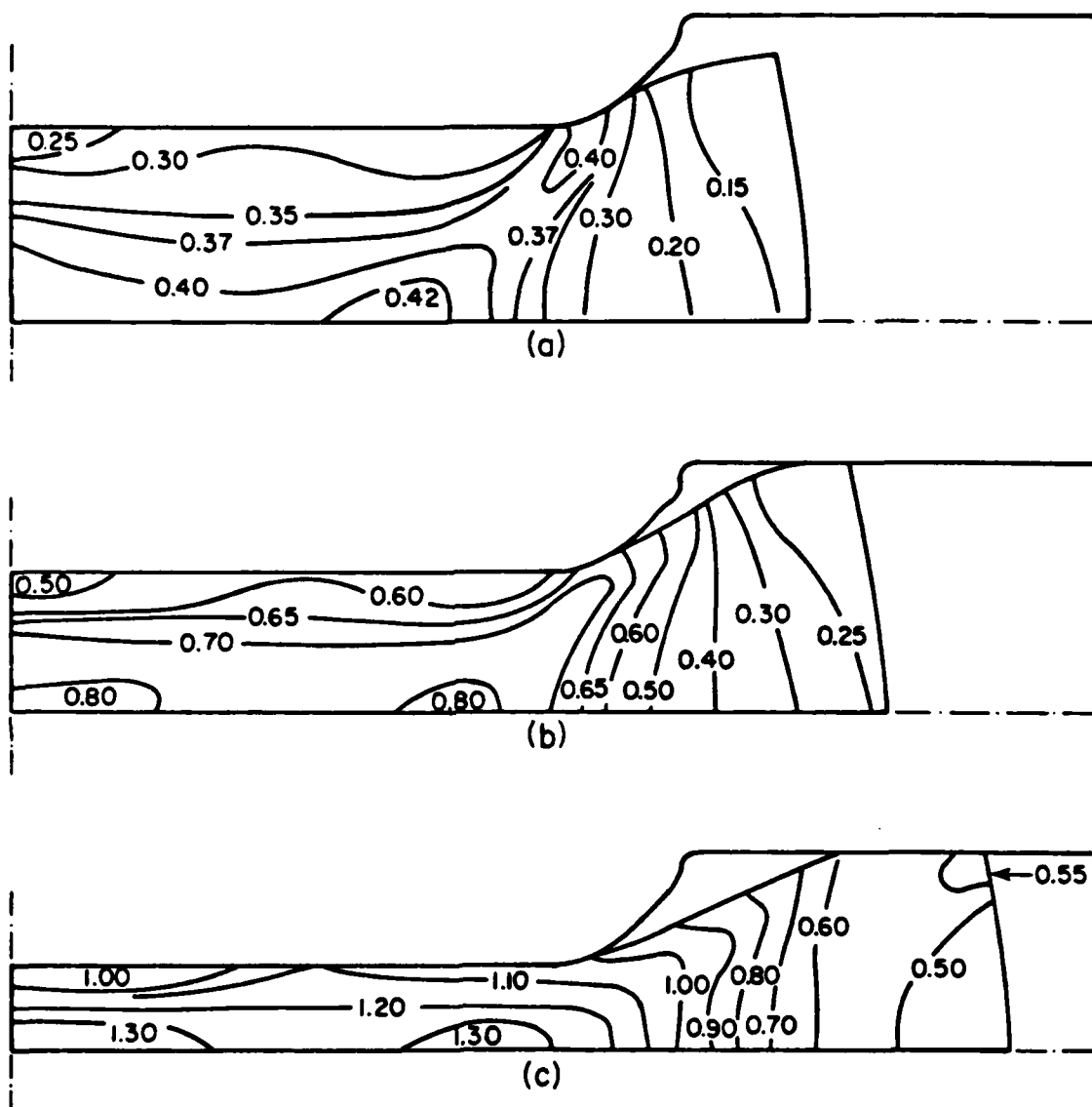


Figure G-25. Effective Strain Distribution Ti-6242-0.1Si, β -Microstructure, 900C, $m = 0.30$ (a) 30% Reduction in Height at Center, (b) 50%, (c) 70%.

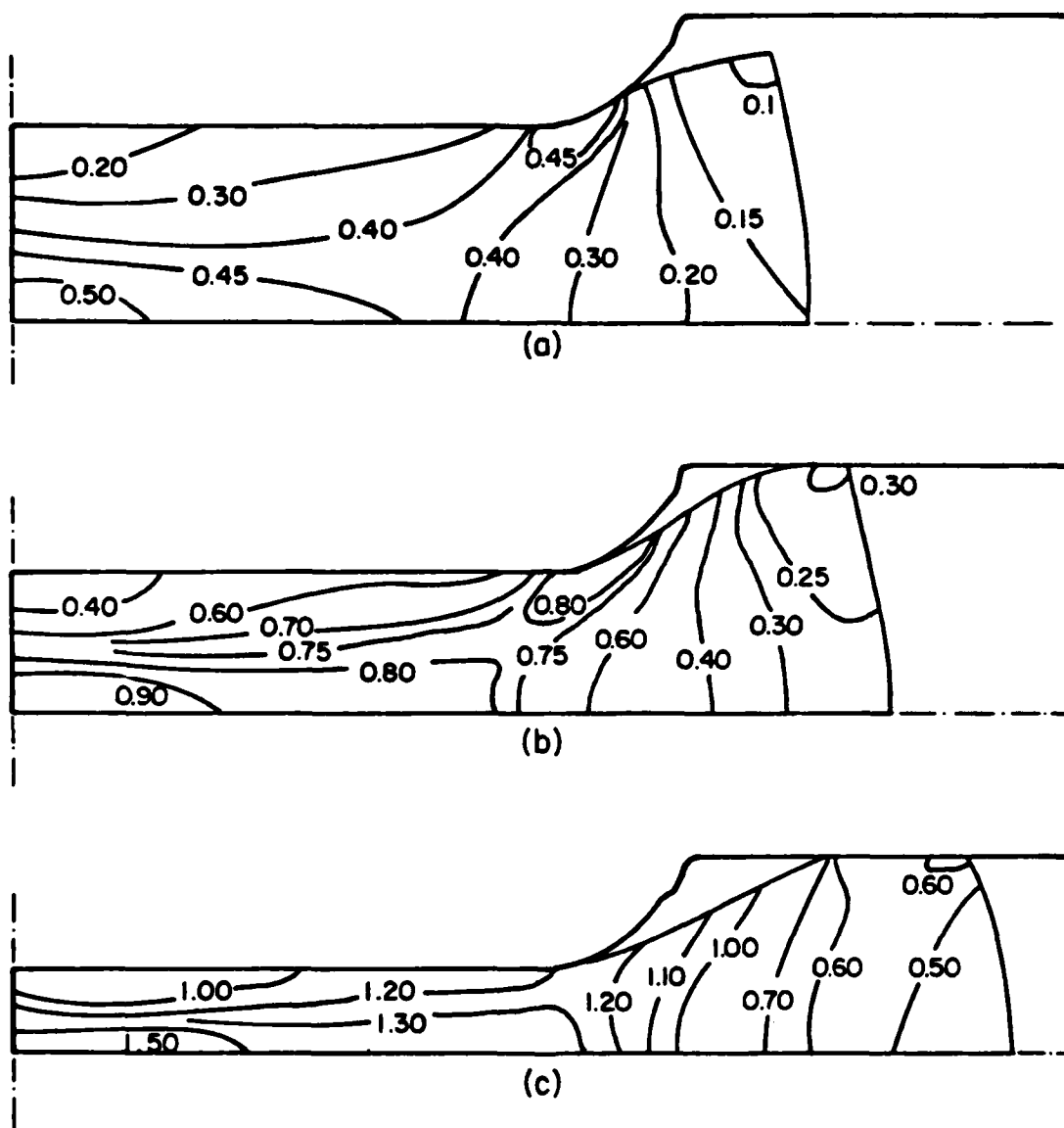


Figure G-26. Effective Strain Distribution Ti-6242-0.1Si, β -Microstructure, 900C, $m = 0.65$ (a) 30% Reduction in Height at Center, (b) 50%, (c) 70%.

that the strain is higher at the bore than it is at the rim, and that the highest strain concentrations are observed along the conical surface extending with the 45-degree angle from the periphery of the bore to the interior of the workpiece. This concentration is more evident during the early stage of deformation. In the bore, the strain is lowest at the top surface near the axis. In the neck and rim region the strain decreases with increasing radius. The strain concentrations shown in the figures confirm the experimentally observed microstructure where the severe recrystallizations were observed at the bore and they were gradual at the neck and rim. As it was expected from the grid distortions, the strain concentrations of two different microstructures, $(\alpha + \beta)$ (Figure G-24) and β (Figure G-25) are identical. However, the prediction shows the influence of the friction on the strain concentration. Comparing Figure G-25 and Figure G-26, it can be seen that the strain concentration is more uniform with lower friction. The effect of friction on the strain concentration is more pronounced at the region between the rim and bore. The strain at the region especially near the free surface is about 20 percent higher for the case of higher friction than that for the lower friction at the 70 percent reduction in height. This difference represents the additional redundant deformation induced by higher friction.

Figures G-27 and G-28 show the instantaneous strain rate distributions at 30 percent, 50 percent, and 70 percent reductions in height for Case 2 and Case 3, respectively. The figures show that the general trends of instantaneous strain distribution are similar to those of strain concentration; that is, higher strain rate at the bore and the gradual decrease in strain rate from the bore to the rim. It can also be seen that the strain rate distribution is more uniform in the case of lower friction. It is also interesting to note that the strain rates are more or less uniform at the bore during the final stage of deformation. The strain rate at the bore at this stage is higher for higher friction.

The hydrostatic stress has a profound influence on the formation of voids and their growth⁽²³⁾. Therefore the region of high hydrostatic stress, especially of tensile hydrostatic stress is considered as a potential site for failure. The predicted hydrostatic stress distributions for Case 2 and Case 3 are shown at 30 percent, 50 percent, and 70 percent reductions in height in

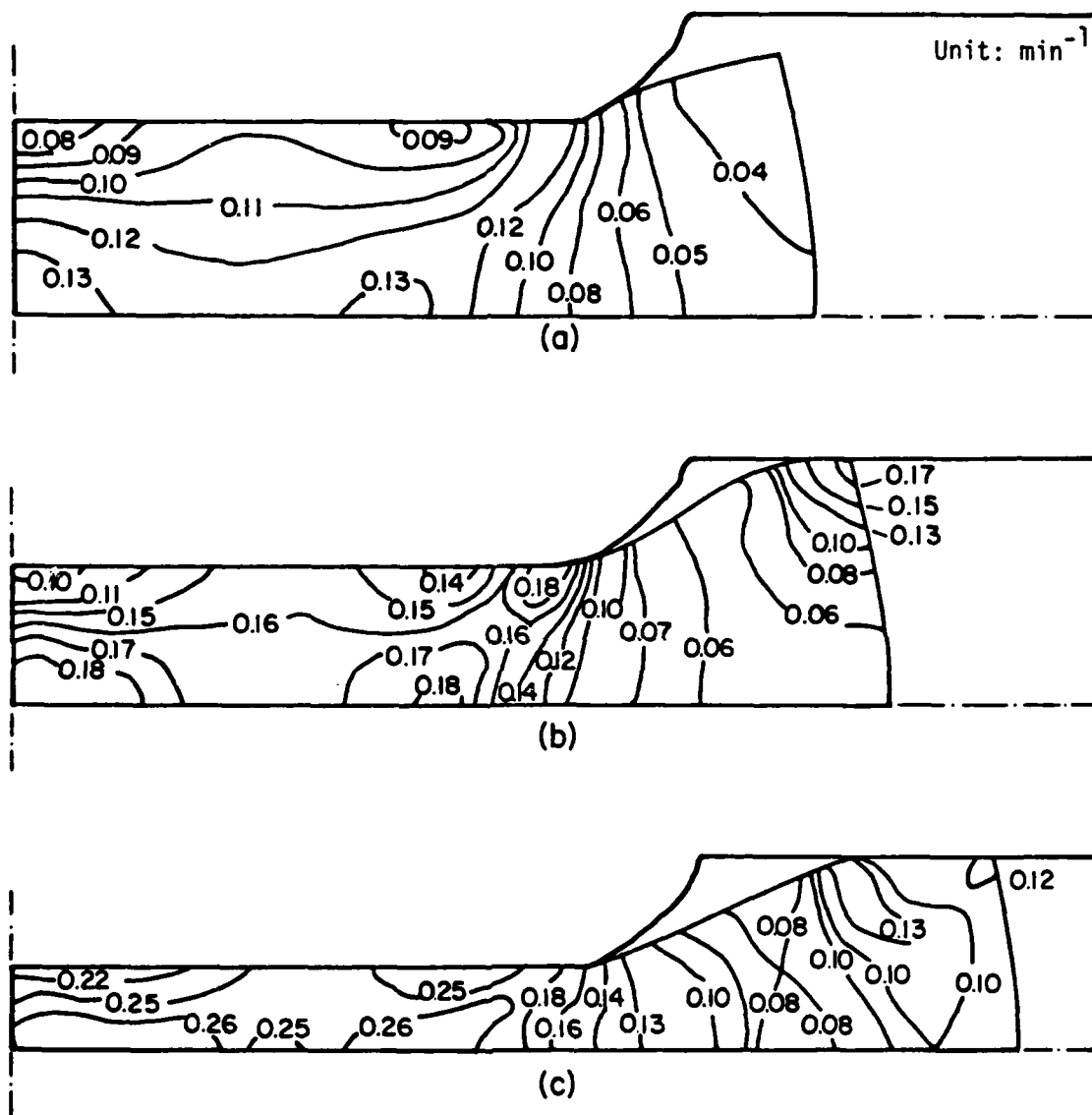


Figure G-27. Effective Strain Rate Distribution Ti-6242-0.1Si, β -Microstructure, 900C, $m = 0.30$ (a) 30% Reduction in Height at Center, (b) 50%, (c) 70%.

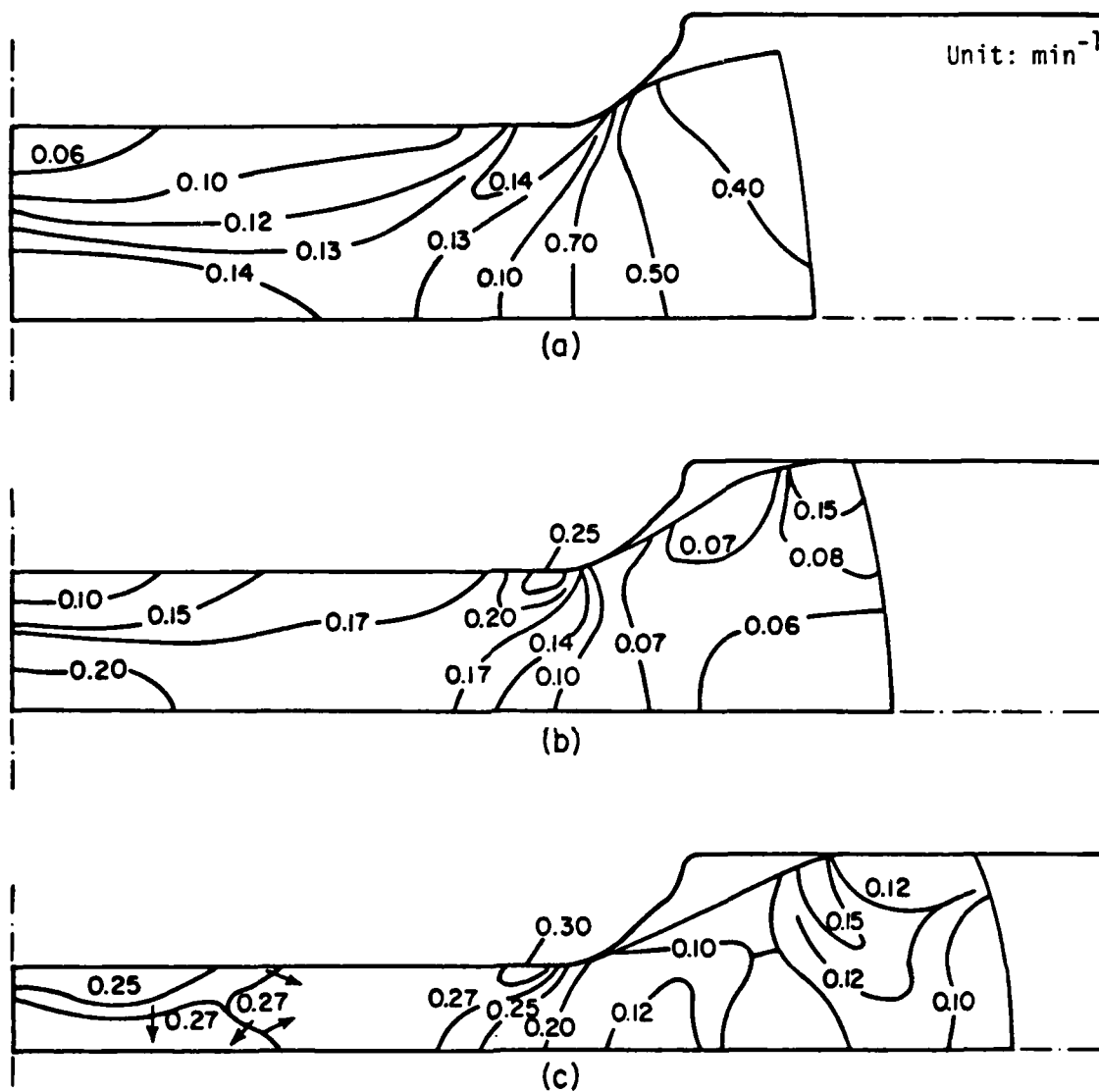


Figure G-28. Effective Strain Rate Distribution Ti-6242-0.1Si, β -Microstructure, 900C, $m = 0.65$, (a) 30% Reduction in Height at Center, (b) 50%, (c) 70%.

Figures G-29 and G-30, respectively. It can be seen from Figure G-29 that the hydrostatic stresses at the bore region are compressive throughout the deformation and that the compressive stresses are highest at the axis. The compressive stresses decrease toward the periphery of the bore. It can also be seen from the figure that the hydrostatic stress on the region outside of the bore is positive during the early stage of the deformation. The maximum hydrostatic stress occurs along the equator of the side surface and also along the free surface near the periphery of the bore. At 50 percent deformation where the workpiece surface is in contact with the die at the rim, the hydrostatic stress at the rim becomes mostly negative and the tensile region is reduced to a small portion near the free surface connecting the bore and the rim. With further deformation the tensile region becomes smaller. It is interesting to note that the pressure gradient becomes steeper as the bore becomes thinner.

The effect of friction on the distribution of hydrostatic stress can be seen by comparing Figures G-29 and G-30. As can be seen from Figure G-30, the general trends of hydrostatic stress distributions with higher friction are similar to those with lower friction. Comparing the hydrostatic stress distributions for both friction cases, the compressive stresses at the bore region are higher for higher friction. During an early stage of deformation, the stress on the region outside of the bore is positive and the magnitude is the same for both frictions. The figure reveals, however, that the positive hydrostatic stress regions near the free surface connecting the bore and the rim are smaller for the higher friction at 50 percent and 70 percent reductions. The smaller tensile hydrostatic stress regions are due to the higher frictional stress on the die-workpiece interface at the rim. Figures G-29 and G-30 indicate that the free surface near the outside of the bore are the potential sites for fracturing in the sense that the site undergoes relatively high hydrostatic stress and high strain⁽²³⁾.

Figure G-31 shows the strain and the strain rate contours of trapped die forging simulation at 70 percent reduction in height. Comparing Figure G-31(a) with Figure G-25, the strain at the bore for the trapped die forging is almost the same as that for open die forging. The figures show, however, that the strain of the trapped die forging is higher than that of open die

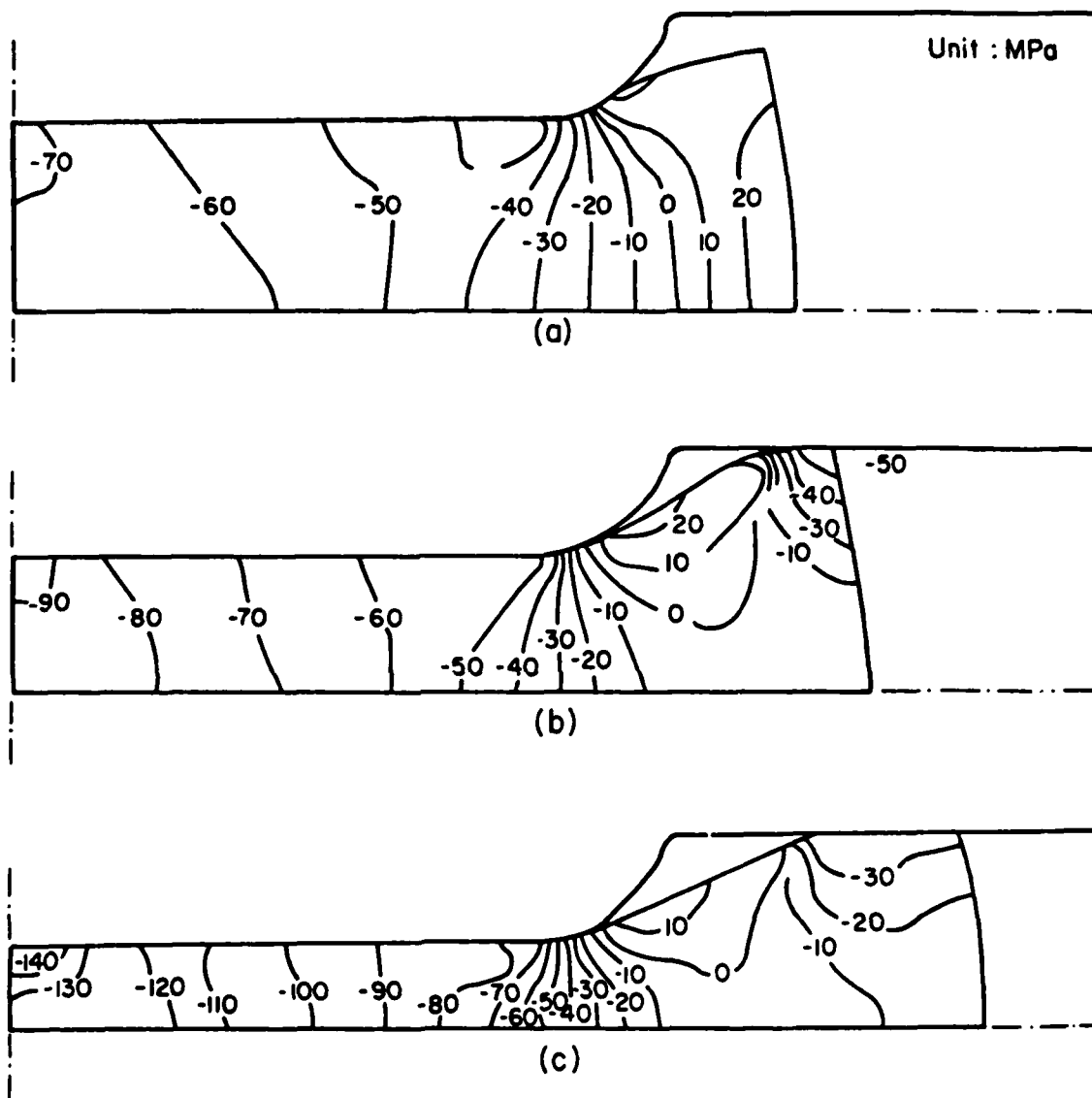


Figure G-29. Mean Stress (Hydrostatic Component) Distribution
 Ti-6242-0.1Si, β -Microstructure, 900C, $m = 0.30$
 (a) 30% Reduction in Height at Center, (b) 50%, (c) 70%.

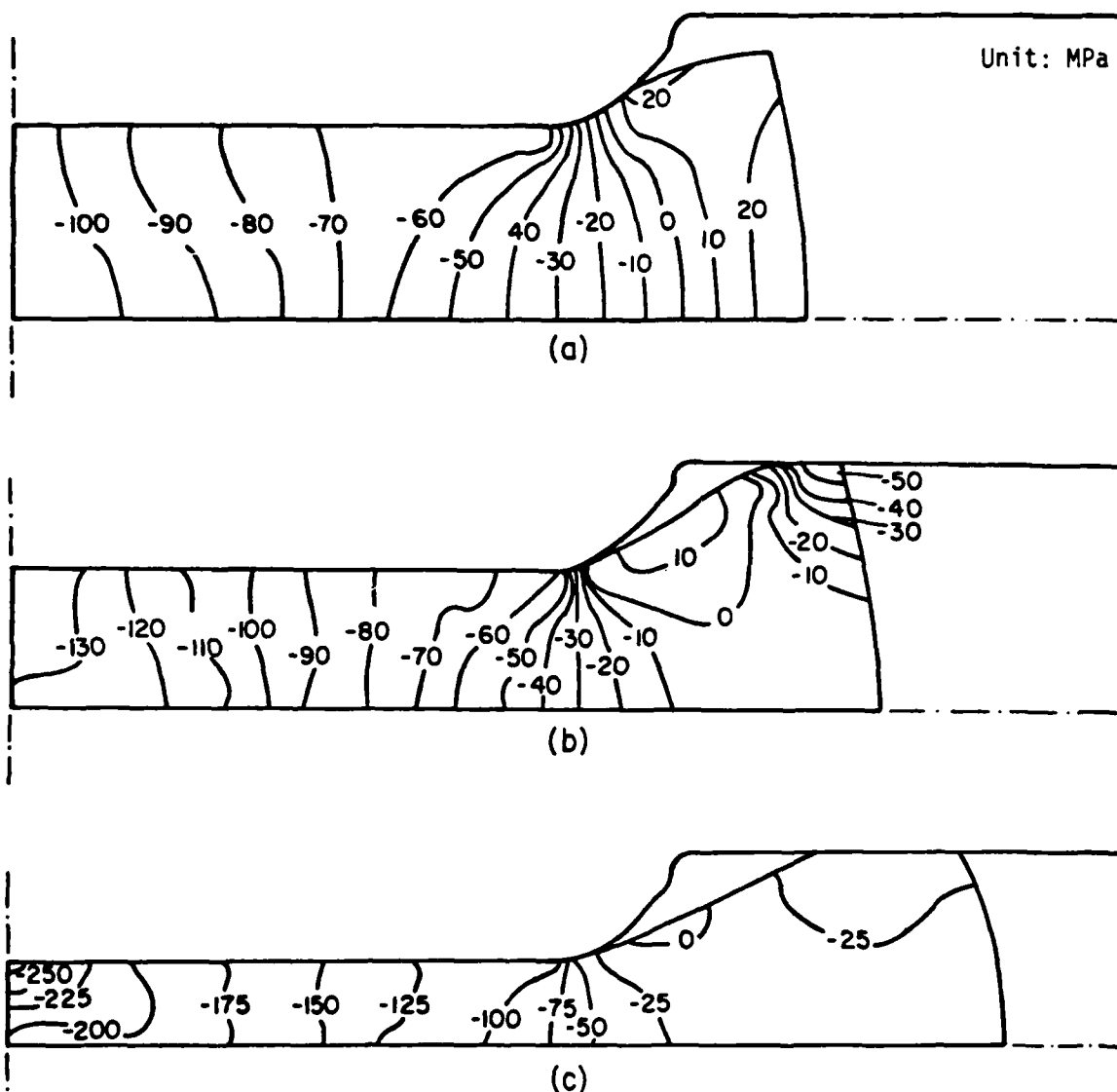


Figure G-30. Mean Stress (Hydrostatic Component) Distribution
 Ti-6242-0.1Si, β -Microstructure, 900C, $m = 0.65$
 (a) 30% Reduction in Height at Center, (b) 50%,
 (c) 70%.

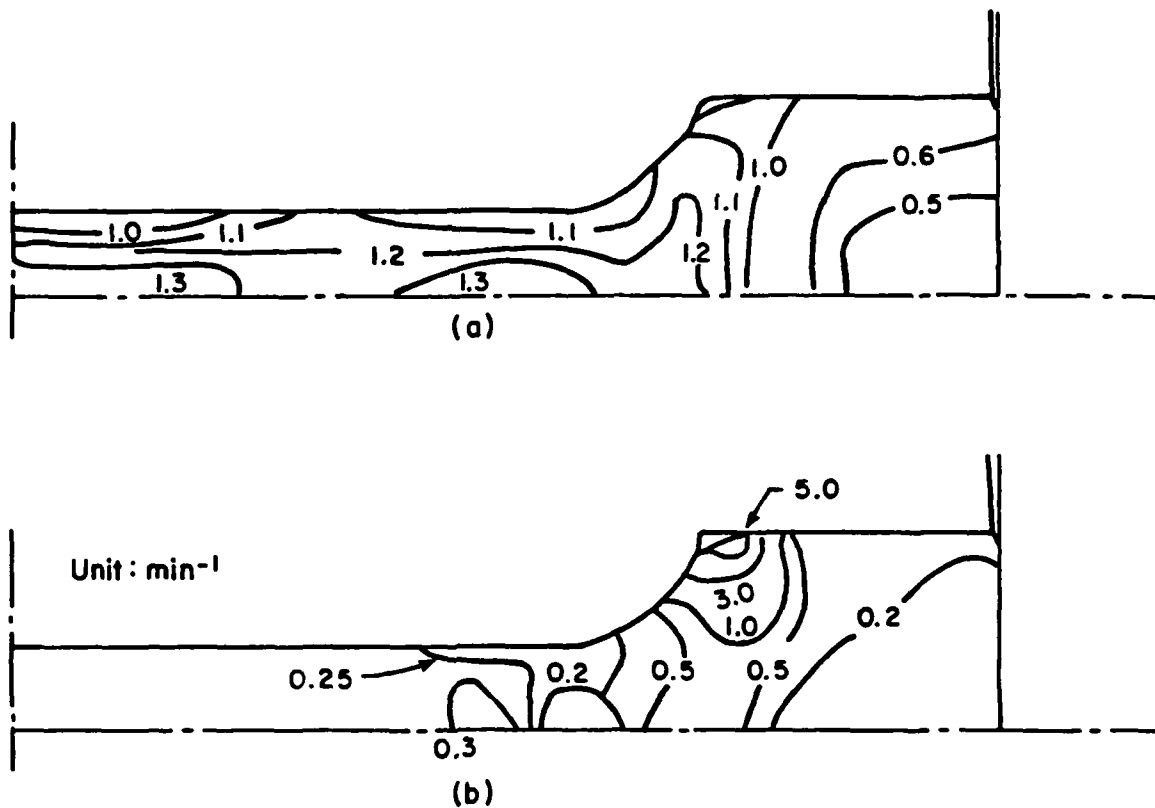


Figure G-31. Strain and Strain Rate Contour of Trapped Die Forging Simulation at 70% Reduction in Height (a) Strain, (b) Strain Rate.

forging at the rim and the neck. Figure G-31(a) also reveals that the strain differences are highest at the neck between the bore and the rim. Figure G-31(b) shows the instantaneous strain rate distribution during the final stage of cavity filling. It can be seen from the figure that the strain rates at the bore and at most of the rim are relatively uniform and the same as the nominal rates. However, there is a band extending vertically at the neck where the strain rates are very high. The strain rates are higher toward the free surface which forms the cavity. The prediction shows that the strain rate near the cavity is more than 20 times the nominal strain rate.

Conclusions

A method is established to discretize the die boundary conditions in the framework of rigid viscoplastic finite element method. The method is natural to FEM and general enough to treat the arbitrarily shaped dies in a unified manner. Improvements are made on the computational efficiencies of rigid viscoplastic FEM by introducing an automated initial guess generation scheme. It seems that the discretization of die boundary conditions, together with the initial guess generation scheme, is an essential step towards the development of a general purpose FEM code for metal forming analysis.

Based on the formulation given in this Appendix a finite element method program, ALPID, was written in FORTRAN language. The program ALPID offers various choices of elements, and it does not require the initial guesses as input. Furthermore, the program can handle the axisymmetric and plane strain processes with arbitrarily shaped dies.

Solutions of the spike forging process with two different frictional conditions are obtained by the program ALPID method. The solutions are discussed and compared with experiments. The comparisons show that they are in excellent agreement with experiments. A new billet geometry is proposed, based on the analysis, for the spike forging to be a more effective means of measuring friction stresses.

Isothermal forgings of the dual microstructure/property compressor disk with two different preform microstructures and two different frictions were obtained by ALPID. The deformation mechanics of the process was analyzed

in terms of the loads, the material flows, strain accumulations and the strain rate concentrations. The effect of process parameters, such as flow stress and friction, on the deformation mechanics of disk forgings were also studied. The preliminary study on the predicted strain distribution confirms the microstructure distributions observed experimentally. Further detailed study should be done to correlate the microstructure distribution and strain accumulation. Such a study eventually will establish a means of predicting the microstructure/property distributions in forged components.

REFERENCES

1. Lee, C. H. and Kobayashi, S., "New Solutions to Rigid-Plastic Deformation Problems Using a Matrix Method", Trans. ASME, J. of Engr. for Ind., Vol. 95, 1973, p 865.
2. Shah, S. N., Lee, C. H., and Kobayashi, S., "Compression of Tall, Circular, Solid Cylinders Between Parallel Flat Dies", Proc. Int. Conf. Prod. Engr., Tokyo, 1974, p 295.
3. Matsumoto, H., Oh, S. I., and Kobayashi, S., "A Note on the Matrix Method for Rigid-Plastic Analysis of Ring Compression", Proc. of the 18th MTDR Conference, London, Sept. 1977, p 3.
4. Chen, C. C. and Kobayashi, S., "Rigid-Plastic Finite-Element Analysis of Ring Compression", Applications of Numerical Method of Forming Processes, ASME-AMD, Vol. 28, 1978, p 163.
5. Chen, C. C., Oh, S. I., and Kobayashi, S., "Ductile Fracture in Axisymmetric Extrusion and Drawing--Part 1 Deformation Mechanics of Extrusion and Drawing", Trans. ASME, J. Engr. for Ind., Vol. 101, 1979, p 23.
6. Chen, C. C. and Kobayashi, S., "Rigid-Plastic Finite Element Analysis of Plane-Strain Closed-Die Forging", Process Modeling - Fundamentals and Applications to Metals, ASM, 1980, p 167.
7. Oh, S. I. and Kobayashi, S., "Finite Element Analysis of Plane-Strain Sheet Bending", Int. J. of Mech. Sci., Vol. 22, 1980, p 538.
8. Oh, S. I. and Kobayashi, S., "Workability of Aluminum Alloy 7075-T6 in Upsetting and Rolling", Trans. ASME, J. Engr. Ind., 1976, p 800.
9. Oh, S. I., Chen, C. C., and Kobayashi, S., "Ductile Fracture in Axisymmetric Extrusion and Drawing--Part 2 Workability in Extrusion and Drawing", Trans. ASME, J. Engr. for Ind., Vol. 101, 1979, p 36.
10. Oh, S. I., Kobayashi, S., and Thomsen, E. G., "Calculation of Frictional Stress Distribution at the Die-Workpiece Interface for Simple Upsetting", Proceedings of the North American Metalworking Research Conference, May 1975.
11. Oh, S. I., Rebelo, N., and Kobayashi, S., "Finite Element Formulation for the Analysis of Plastic Deformation of Rate-Sensitive Materials for Metal Forming", Metal Forming Plasticity, IUTAM Symposium, Tutzing, Germany, 1978, p 273.
12. Hill, R., "New Horizons in the Mechanics of Solids", J. Mech. Phys. Solids, Vol. 5, 1956, p 66.

13. Zienkiewicz, O. C., The Finite Element Method, 3rd ed., McGraw-Hill, 1977.
14. Fried, I., "Finite Element Analysis of Incompressible Material by Residual Energy Balancing", Int. J. of Solids and Structures, Vol. 10, p 993.
15. Malkus, D. S., "A Finite Element Displacement Model Valid for Any Value of the Compressibility", Int. J. Solids Structures, Vol. 12, 1976, p 231.
16. Nagtegaal, J. C., Parks, D. M., and Rice, J. R., "On Numerically Accurate Finite Element Solutions in the Fully Plastic Range", Computer Methods in Applied Mechanics and Engineering, Vol. 4, 1974, p 153.
17. Jain, S. C., Bramley, A. N., Lee, C. H., and Kobayashi, S., "Theory and Experiment in Extrusion Forging", Proc. 11th Int. Conf. of MTDR, 1971, p 1097.
18. Altan, T., Clauer, A. H., Lahoti, G. D., Rosenfield, A. R., and Subramanian, T. L., "Effect of Hot Forging Variables Upon Microstructure and Properties of Metals and Alloys", Final Report, AFOSR-76-2971.
19. Semiatin, S. L., Lahoti, G. D., and Altan, T., "Determination and Analysis of Flow Stress Data for Ti-6242 at Hot Working Temperatures", Process Modeling - Fundamentals and Applications to Metals, ASM, 1980, p 387.
20. Chen, C. C., "Processing, Structure, and Property of Ti-6Al-2Sn-4Zr-2Mo-0.1Si Alloy Forgings", APPENDIX E Research to Develop Process Models for Producing a Dual Property Titanium Alloy Compressor Disk, Technical Report AFWAL-TR-80-4162.
21. Dadres, P., and Thomas, J. F., Jr., "Characterization and Modelling for Forging Deformation of Ti-6Al-2Sn-4Zr-0.1Si", APPENDIX A1, Research to Develop Process Models for Producing a Dual Property Titanium Alloy Compressor Disk, Technical Report AFWAL-TR-80-4162.
22. Charmouard, A., Closed Die Forging (in French), Part I, Dunod, Paris, 1964.
23. Malas, J. C., Gegel, H. L., Oh, S. I., and Lahoti, G. D., "Metallurgical Validation of a Finite-Element Program for the Modeling of Isothermal Forging Process", to be published.

APPENDIX H

ECONOMIC MODELS FOR PORCESSING ALTERNATIVES

Vijay Tipnis and Uday Wative
Tipnis Associates, Inc.
Cincinnati, Ohio 45242

APPENDIX I

ECONOMIC MODELS FOR PROCESSING ALTERNATIVES

Introduction

How to reduce processing and life cycle costs while improving material utilization and properties of critical aerospace components is one of the key challenges of the 1980's. Such a challenge requires an integrated application of material science, mechanics and computer aided design and manufacturing, to develop processing technologies that are significantly more productive and less costly than the best methods available today.

Traditionally, most process development projects have concentrated on the establishment of conceptual and technological feasibility before considering the economic feasibility. While this appears to be a logical approach, it is not uncommon to find that after substantial research and development expenditures to establish conceptual and technological feasibility, the process was found not to be economically feasible.

Recently, a novel approach was introduced for the evaluation of economic feasibility early during the conceptual and technological feasibility stages^(1,2,3). This approach allows identification of 'opportunity windows' and 'targets' where the technological development should be directed for the process to be economically feasible. This approach is being applied successfully to the investigation of laser-assisted and high speed machining.

In this investigation, the above approach is extended for non-machining operations, especially for the integration of process and microeconomic models and for the introduction of life cycle economic models for process development. The scope of this investigation is focused on the Process Models for producing dual property Titanium Alloy Compressor disk.

1.1 Objectives: To develop economic models for various alternative

process plans which can be potentially used for manufacturing of compressor disk forgings from Ti6242 alloy.

1.2 Statement of the Problem: At various stages during the conceptual and technological process research and development there is a need to know in which direction the process should be developed for it to be competitive and cost effective as compared to the alternatives. The dual property Ti6242 alloy disk forging research and development is the specific application addressed here.

1.3 Technical Approach: The technical approach pursued involved the development of a comprehensive economic model for the dual property turbine disks and alternatives. The economic models involved three levels: (1) microeconomic models at individual process level, (2) macroeconomic models at sequence of processes, and (3) life cycle cost model level. These three levels allow investigation of economic trade-offs either individually or in an integrated manner (the trade-offs, desirable and undesirable, between performance, acquisition costs, and life cycle costs are shown in Table I). Thus, the processing and life cycle trade-offs can be investigated in terms of the targets and opportunity windows for specific processes.

The comprehensive economic models include the following:

(a) Time elements starting from input material to the finished forging and continuing through the machining and manufacturing sequence required to obtain machined compressor disks. Lead times, especially for die design and die making will be included.

(b) Cost elements including material, operating, recurring tooling, die design and die making, vacuum or atmosphere maintenance, lubrication, and energy and capital investment costs.

(c) Life cycle costs including fuel, maintenance and replacement, and operation and support costs.

TABLE I: Trade-Offs Between Performance, Acquisition
and Life Cycle Costs

P = Performance; AC = Acquisition Cost; LC = Life Cycle Cost;
↑ Indicates up; ↓ Indicates down; ↔ Indicates same as.

	Case	P	AC	LC	($\Delta AC + \Delta LC$)
Most Desirable	1	↑	↓	↓	>0
	2	↑	↑	↓	>0
	3	↑	↓	↑	>0
Desirable	4	↔	↓	↓	>0
	5	↔	↑	↓	>0
	6	↔	↓	↑	>0
Acceptable	7	↑	↑	↑	<0
	8	↔	↑	↑	<0
Unacceptable	9	↓	↓	↓	>0
	10	↓	↑	↓	>0
	11	↓	↓	↑	>0
	12	↓	↑	↑	<0

The following processing alternatives to produce compressor disk forgings were investigated:

- 1). Conventional press forge + machining.
- 2). Isothermal and hot die forging + machining.
- 3). Hot Isostatic Pressing (HIP) + Hot Forging + machining.
- 4). Dual property disk forging + machining.

Since for Ti6242 alloy (or any other Ti alloy) HIP is not yet a viable alternative, little information was available on time and cost elements for the alternative. Nonetheless, other alternatives were investigated with the available data.

This report contains a systematic economic model structure for the investigation of alternatives involved in forging + machining operations, at individual process level, process sequence level, and life cycle cost level. Specifically included are the following:

1. Systematic step-by-step processing sequences for the above alternatives.
2. Assumptions and equations for economic models.
3. Conclusions and recommendations.

The economic models presented in this report lay a foundation for future extension of the economic models to include the waiting, transportation, tooling, and support functions within a computer integrated and automated forge shop of the future.

Structure of Economic Models for Processing Alternatives

Economic models of discrete parts manufacturing processes and manufacturing systems are constructed to evaluate the economic impact of processing and manufacturing alternatives. These models essentially involve the determination of time and cost savings from a new process. These savings are weighed against the added investment required to adopt the new manufacturing process.

Two levels of economic models have been introduced for the evaluation of new process development: (1) Macroeconomic models - these deal with the aggregate times and costs, and (2) Microeconomic models - these deal with the individual time and cost elements associated with each processing step (see Figure 1)⁽¹⁾. If all the detailed time and cost information about every stroke/cut involved within every processing sequence were appropriately summed, then the cumulative sum of all times and costs in the microeconomic model will be identical to that of the macroeconomic model. In practice, often only the aggregate information (such as route sheets and process plans) on a processing sequence is readily available, and hence, the macroeconomic models must be constructed directly from this available data. The application of microeconomic models is restricted to a few selected individual strokes/cuts where important economic trade-offs between the process rate, consumable costs, and process constraints are to be investigated. The microeconomic models embody operating process models, and hence, are useful to establish guidelines for process development.

2.1 Macroeconomic Models for Near Net Shape Processes: For evaluating the impact of NNS processes such as dual property disk, a hierarchy of cost models as shown in Figure 2 is needed. At the root level, the cost model is composed of the raw material cost plus the

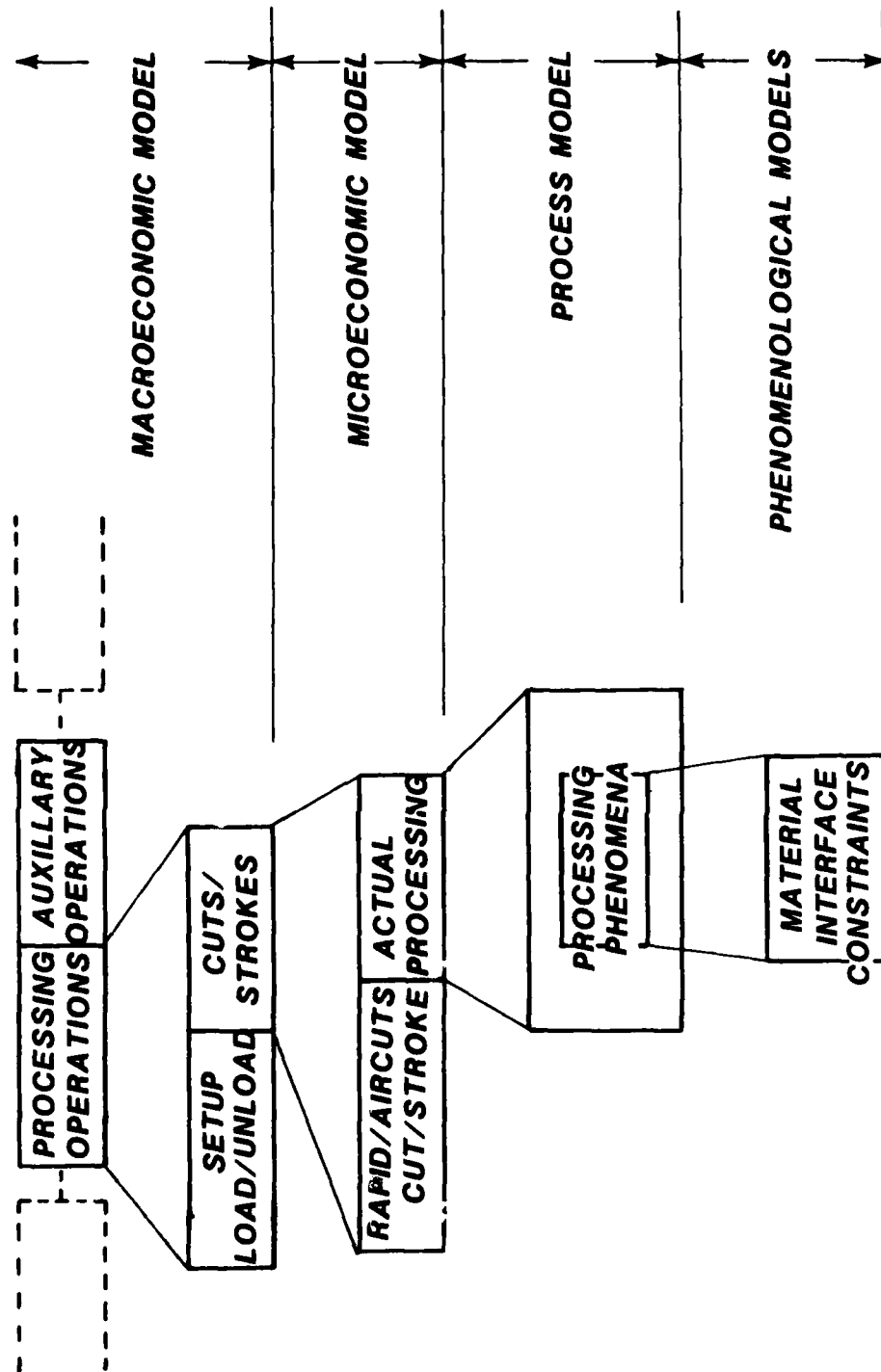


FIGURE 1: RELATIONSHIP BETWEEN MACROECONOMIC, MICROECONOMIC, PROCESS, AND PHENOMENOLOGICAL MODELS

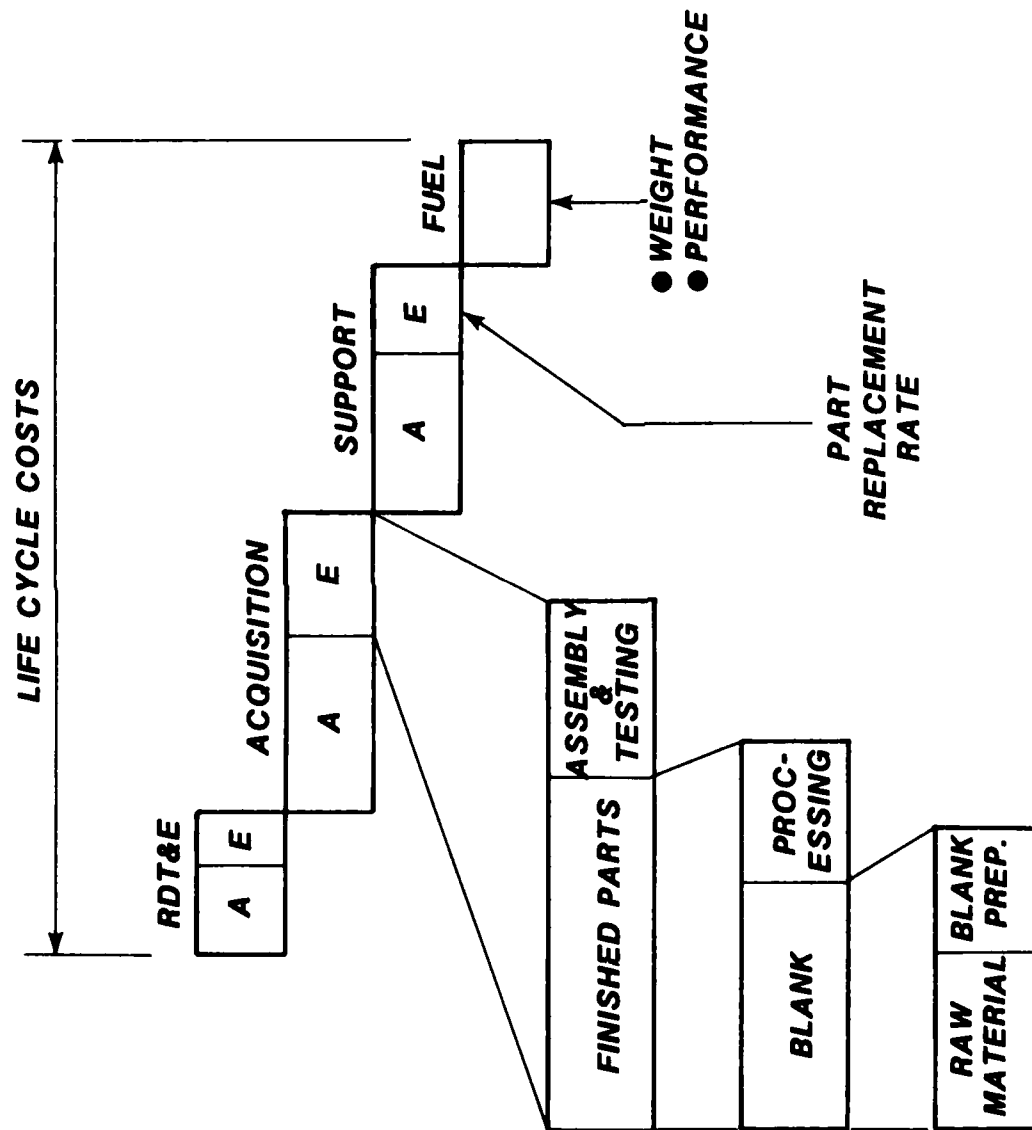


FIGURE 2: HIERARCHY OF COSTS FOR NNS PROCESSING ALTERNATIVES

blank preparation cost such as NNS forging. This becomes the blank cost at the parts manufacturing level to the aerospace engine manufacturer. The blank (e.g., NNS forging) cost plus the manufacturing cost becomes the finished part cost. The finished part cost of all finished parts, plus the assembly and testing cost becomes the system acquisition cost of the aerospace system. The total cost is the acquisition cost plus the life cycle cost involved in operating and maintaining the aerospace system.

The NNS macroeconomic models applicable to the hierarchy of cost models shown in Figure 2, should be able to determine the potential impact of a Near Net Shape process (for example, dual property disk forging process) at each acquisition cost level as well as on the life cycle costs related to part replacement and fuel costs related to weight and performance.

2.2 Relationship to Process Model

To illustrate the relationship between the microeconomic models and the process models, refer to Figure 3 schematic block diagrams. The process model shown at the top right-hand corner of this figure refers to the processing inputs, constraints, and outputs of a processing unit such as a machine tool, forging press, etc. Each processing unit has a specific range of input parameters called operating variables such as speed, feed, depths, etc. for a machine tool. The processing unit is designed to operate within these input parameter ranges. The processing unit also has constraints placed on it due to the design of the unit such as maximum and minimum velocities, pressure, temperature, and performance limits such as vibration, chatter, and power. The optimization at a given processing unit involves maximizing the outputs for a given material/geometry configuration within the limits of the processing unit. The optimization leads to the desired input settings for given output levels for the specific operating unit, provided the work material meets the desired quality level (dimensions, accuracies, finish, integrity, etc.) and provided it does not violate the constraints of plastic and thermal instabilities, fracture, friction, and wear.

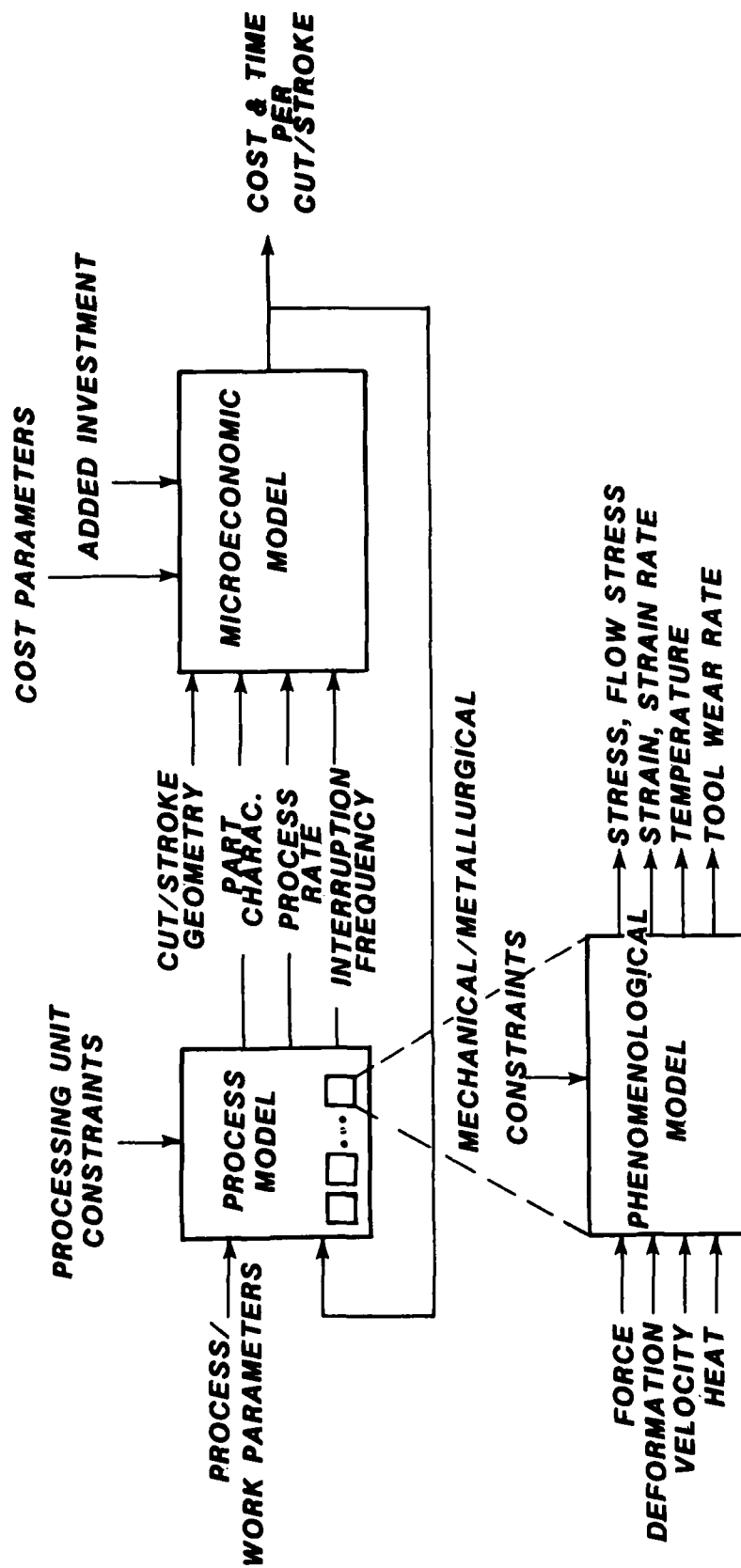


FIGURE 3: RELATIONSHIP BETWEEN PROCESS AND MICROECONOMIC MODELS

The outputs from the process model, namely process rate and process interruption frequency are inputs to the microeconomic model (block diagram shown in the upper left hand corner of Figure 3). Also, specific cut/stroke geometry is input to the microeconomic model. The economic constraints are the specific processing unit operating cost rate including energy costs, labor rate, consumable cost, material cost, and added investment. The outputs of the microeconomic model are cost/cut or stroke and time/cut or stroke. In order to minimize either cost or time per cut or stroke, the microeconomic model generates a feedback to the inputs of the process model. For optimization of the economics of the cut or stroke, trade-off functions between process rate and process interruption frequency have been established⁽⁴⁾.

2.3 Relationship to Life Cycle Cost Models

Life Cycle Cost (LCC) models are being used to access the overall impact on Life Cycle Cost of an airframe/engine system due to changes in life-limiting component material or shape as well as mission requirements^(5,6). These LCC models primarily focus on the preliminary detailed design phase for examination of the impact of specific engine cost drivers in RDT&E, production and operation/support. Application of LCC models to perform trade-off studies on life-limiting engine parts such as HIP high pressure spool, turbine aft shaft, turbine rotor and compressor rotor has demonstrated that the LCC models are sensitive to small design changes⁽⁵⁾. Also, the LCC models have been applied by the engine developer and the procuring agency to determine cost/performance trade-offs during the advanced development stages of an engine⁽⁶⁾. No doubt, similar LCC models have been applied to airframe components. However, during the advanced design/technology development stage, due to the lack of exact definition of the mission, engine/airframe interface, or new materials/processes/design concepts, meaningful production costs and performance trade-offs are not often feasible through LCC models⁽⁶⁾.

The time frame for the application of the various economic models is shown in Figure 4.

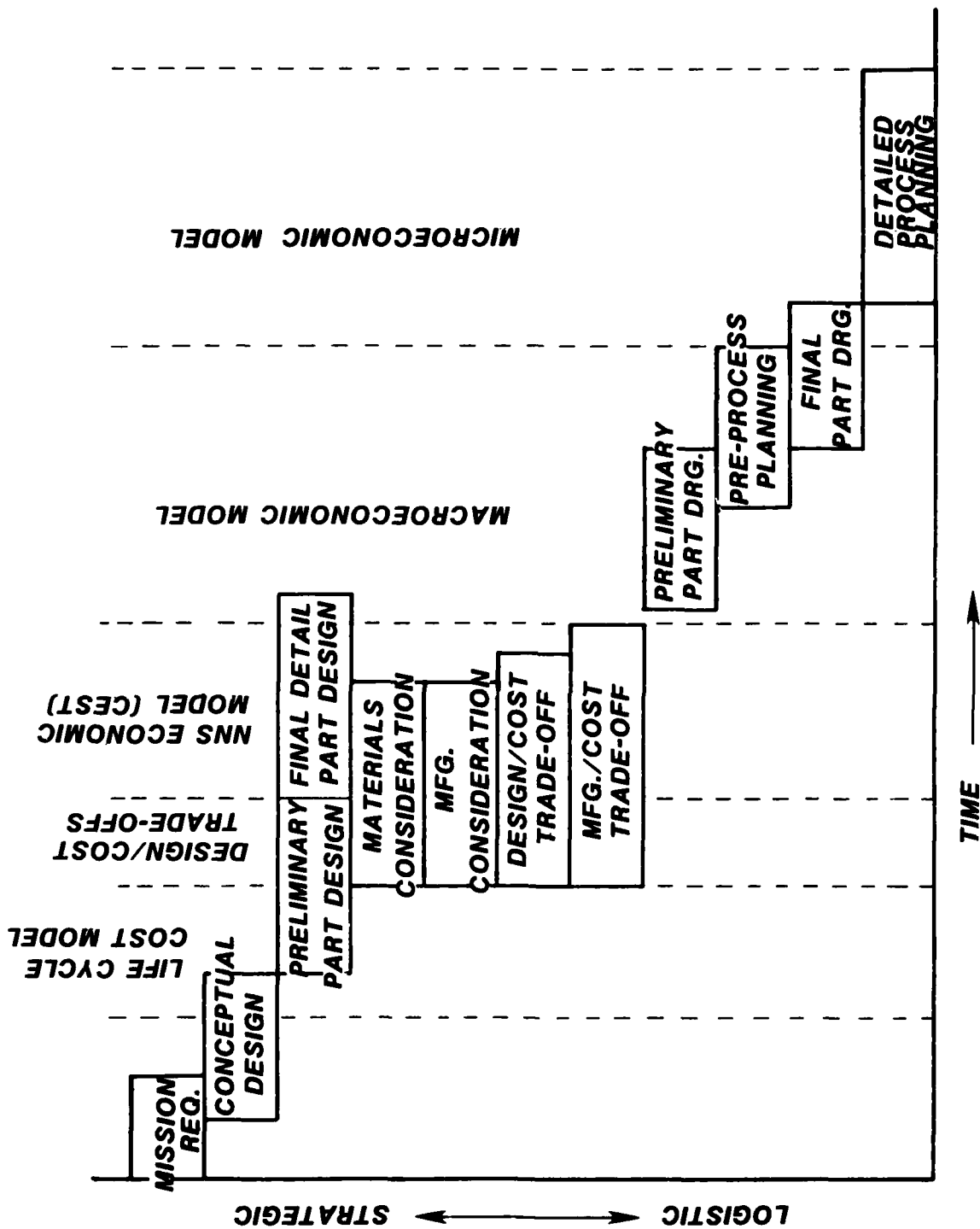


FIGURE 4: TIME FRAME AND ACTIVITIES FOR APPLICATION OF ECONOMIC MODELS DURING DESIGN / MANUFACTURING

The decisions for adopting a specific type of Near Net Shape technology for production parts arise when engine/airframe qualification tests have been successfully completed and production orders are forthcoming. At this stage, economic models detailed enough to establish Cost Effective Shape Technology for each production part are needed. As a step towards establishing such NNS economic models, the integration of the macroeconomic model with the pertinent aspects of the Life Cycle Cost (LCC) model such as acquisition and fuel cost has been accomplished. The resultant NNS economic model structure is suitable for the investigation of sensitivities and trade-offs between competing NNS processing technologies.

Table I is a representation of the interaction between component performance, acquisition cost, and the total life cycle cost. The first three cases can be considered to be highly desirable; the next three desirable; cases 7 and 8 may or may not be acceptable; the last four cases are clearly undesirable. In order to make decisions in the 'desirable' and 'acceptable' regions, an investigation of life cycle cost is imperative. In the other two regions - 'highly desirable' and 'unacceptable' - calculation of life cycle costs would be useful, since an exact figure can be obtained to show just how good (or bad) a particular option really is.

Del Formulation: The change in overall life cycle cost produced by modifying either the production process or the physical characteristics of a particular part can be expressed as:

$$\Delta LCC = \Delta(RDT\&E) + \Delta(ACQ) + \Delta(O\&S) + \Delta(FUEL) \quad (1)$$

where:

$\Delta(RDT\&E)$ = Cost of research, design, testing and evaluation

$\Delta(ACQ)$ = Acquisition cost

$\Delta(O\&S)$ = Cost of operation and support

$\Delta(FUEL)$ = Fuel costs

For simplicity, $\Delta(\text{RTD\&E})$ is ignored; however, the analysis can be extended to include $\Delta(\text{RTD\&E})$, if necessary. The remaining terms in equation (1) can be expanded as follows:

$$\begin{aligned}\Delta\text{ACQ} &= \Delta(\text{Raw Material}) + \Delta(\text{Blank Fabrication}) + \Delta(\text{Manufacturing}) \\ &\quad + \Delta(\text{Assembly})^* \\ &= \Delta C_{\text{rm}} + \Delta \left[\sum_{n_p} \{ (t_p + 1/N t_s) (LMS_p) \} + C_{\text{tc}} + C_c \right]_{\text{Blank Fab.}} (P) \\ &\quad + \Delta \left[\sum_{n_p} \{ (t_p + 1/N t_s) (LMS_p) \} + C_{\text{tc}} + C_c \right]_{\text{Mfg.}} (P) \quad (2)\end{aligned}$$

It is necessary to separate blank fabrication costs and manufacturing operations on the completed blank, because each phase is normally handled by a separate manufacturer.

Changing the physical characteristics (i.e., low cycle fatigue life, creep resistance, etc.) of a component influences the cost of operation and support through two primary mechanisms:

(a) Part replacement costs due to failure could be reduced if the life of the part is increased (i.e., the replacement frequency is decreased). In addition, for critical components, there would be a reduced probability of engine replacement.

(b) Inventory carrying costs could be reduced if fewer parts have to be maintained in inventory.

$$\therefore \Delta(\text{O\&S}) = \Delta(\text{Part/Engine Replacement}) + \Delta(\text{Inventory})$$

Expanding these terms we get:

$$\Delta(\text{O\&S}) = [\Delta(\text{epf} \times \text{PC})] (1 - \text{pe}) + [(\Delta \text{epf}) \times \text{pe} \times \text{EC}] + [(\Delta \text{nv}) \times \text{PC}] i \quad (3)$$

Finally, the change in fuel cost can be expressed as:

$$\Delta(\text{FUEL})/\text{yr.} = \sum_M [H \times \text{FC} \times \{ \Delta(\text{cf}) \times \text{ne} \}] \quad (4)$$

*Changes in costs at the assembly level have not been considered in the present model. They should be included for such applications as BLISK. Nomenclature is included at the end of this appendix.

The term $\Delta(cf)$ represents the change in fuel consumption rate per engine, and is determined by two factors:

(a) An improvement in physical characteristics (such as high temperature strength) of a critical component may permit more efficient engine operating conditions (i.e., higher temperature, pressure). This would lead to a lower fuel consumption for developing a given thrust.

(b) A decrease in component weight would reduce the aircraft weight and thus decrease the overall thrust which needs to be developed for a given mission. This would decrease the fuel consumption rate.

A factor which has not been accounted for is that an improvement in fuel consumption would enable a decrease in the weight of fuel which has to be carried, and thus decrease the aircraft weight. This reduced weight would improve fuel efficiency.

The various interactions between material properties, engine performance, and aircraft weight are depicted in Figure 5.

Thus, the equation for the overall change in life cycle cost can be obtained by substituting Equations (2), (3), and (4) in Equation (1).

2.4 Model Structure for Processing Alternatives

The model for evaluating costs at the process level (refer to Figure 1) has been formulated within the framework established in Section 2.2. The hierarchy of costs associated with system acquisition is depicted in Figure 2. It should be noted that in practice, each stage of manufacture (blank fabrication, blank processing, and assembly) is normally accomplished by a separate manufacturer.

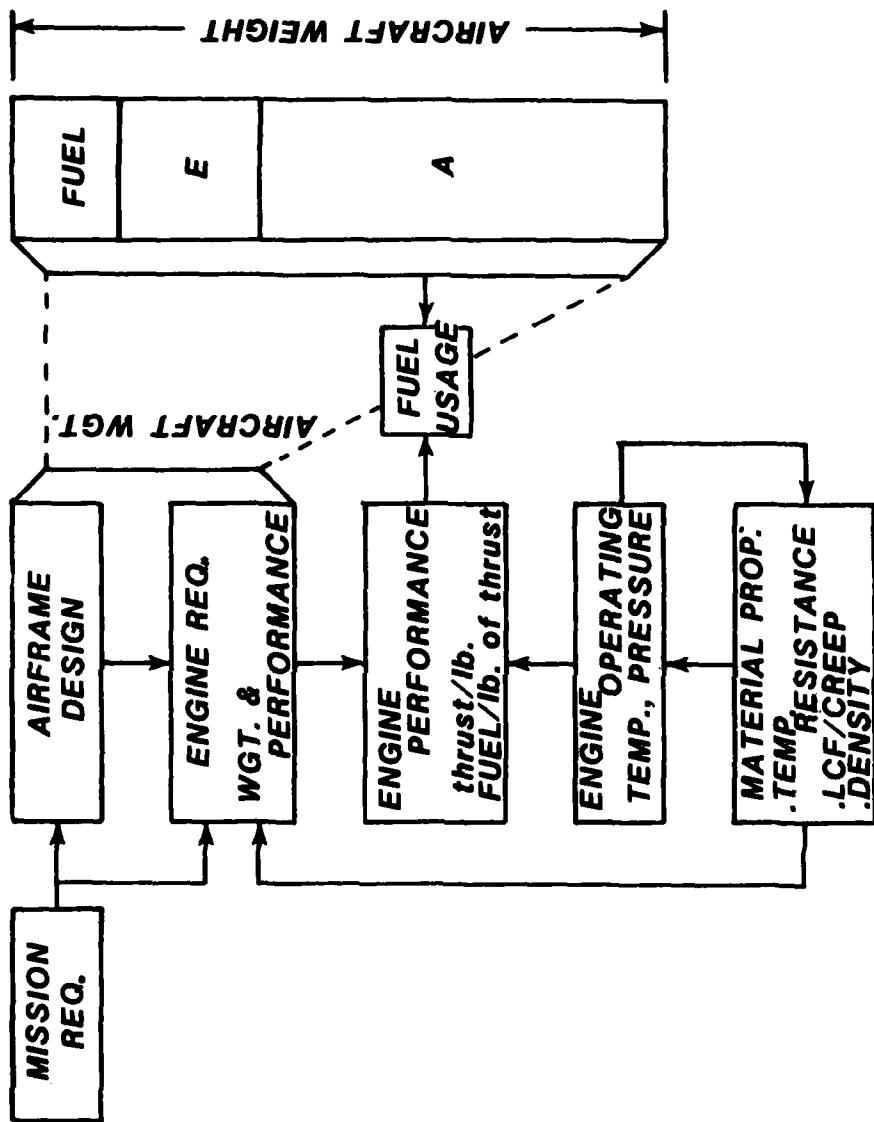


FIGURE 5: INFLUENCE OF ENGINE PERFORMANCE AND WEIGHT ON FUEL USAGE COSTS

Assuming that each competing process produces a finished part with identical geometric and surface finish characteristics (though not necessarily the same mechanical and metallurgical properties), the costs at the level of engine assembly will not be affected. Therefore, costs at that stage of manufacture are ignored.

Within these constraints, the total processing time is given by:

$$T = \sum_p \left[\sum_{np} \{t_p + 1/N t_s + t_w + t_t\} \right] \quad (5)$$

The total cost for a process is given by:

$$C = \sum_p C_{rm} + \sum_p \left[\sum_{np} \{ (t_p + 1/N t_s) (LMS_p) + (t_w + t_t) (oc) + ctc + cn \} \right] \begin{matrix} \text{Blank} \\ \text{Fab.} \end{matrix} \\ + \sum_p \left[\sum_{np} \{ (t_p + 1/N t_s) (LMS_p) + (t_w + t_t) (oc) + ctc + cn \} \right]_{Mfg.} \quad (6)$$

It is assumed that a separate value can be specified for the LMS (Labor + Machine + Support) rate at each work station, which is frequently not possible. In that case, an estimated average (or weighted average) value can be used, resulting in a simplification of Equation 6.

2.5 Sensitivity Analysis of Macro Model

Following the previously established framework^(1,2,3) sensitivity analysis for blank preparation and part manufacturing is established below:

Total time savings/part:

$$\Delta T = \{T_p + (1/N) T_s\} - \{\alpha T_p + (1/N) \beta T_s\} \quad (7)$$

Total cost savings/part:

$$\Delta C = C_{rm} (1-\epsilon) + \{ (T_p + 1/N T_s) LMS - (\alpha T_p + 1/N \beta T_s) (\sigma LMS) \} \\ + C_{tc} (1-\delta) + C_c (1-\gamma) \quad (8)$$

The necessary condition for economic feasibility of a new process is:

$$\Delta C + \Delta T(oc) > 0 \quad (9)$$

Substituting for ΔC and ΔT from Equations (7) and (8) into condition (9), we get the necessary condition:

$$C_{rm} (1-\epsilon) + [(T_p + 1/N T_s) (LMS + oc) - (\alpha T_p + 1/N \beta T_s) (\sigma LMS + oc)] \\ + C_{tc} (1-\delta) + C_c (1-\gamma) > 0 \quad (10)$$

By solving inequality (10) for one of the sensitivity parameters, we can obtain the necessary limiting values for each parameter. For example, solving for ϵ , we get:

$$\epsilon < 1 + 1/C_{rm} \{ (T_p + 1/N T_s) (LMS + oc) - (\alpha T_p + 1/N \beta T_s) (\sigma LMS + oc) \\ + C_{tc} (1-\delta) + C_c (1-\gamma) \} \quad (11)$$

The sufficiency condition^(1,2,3) is obtained by utilizing discounted cash flow, and applying a minimum Return on Investment (ROI). This can be expressed as:

$$\phi \{ \Delta C + \Delta T(oc) \} P > (\Delta I_0) \quad (12)$$

$$\text{where } \phi = \text{discount factor} = \sum_{t=1}^n \frac{1}{(1+k)^t}$$

Substituting for ΔC and ΔT , from equations (7) and (8) into condition (12), we get the following sufficiency condition:

$$P \phi \{ C_{rm} (1-\epsilon) + (T_p + 1/N T_s) (LMS + oc) - (\alpha T_p + 1/N \beta T_s) (\sigma LMS + oc) \\ + C_{tc} (1-\delta) + C_c (1-\gamma) \} \geq (\Delta I_0) \quad (13)$$

Once again, this equation can be solved for the parameters of interest. For example, solving for α and ϵ respectively, we get:

$$\alpha < -1/N \beta T_s + \frac{1}{(\sigma LMS + oc)} C_{rm} (1 - \epsilon) + (T_p + 1/N T_s) (LMS + oc) + (C_{tc} (1 - \delta) + C_c (1 - \gamma) - \Delta I_0 / P\phi) \quad (14)$$

$$\epsilon < 1 + 1/C_{rm} \{ (T_p + 1/N T_s) (LMS + oc) - (\alpha T_p + 1/N \beta T_s) (\sigma LMS + oc) + C_{tc} (1 - \gamma) + C_c (1 - \delta) - \Delta I_0 / P\phi \} \quad (15)$$

2.6 Microeconomic Sensitivity of Material Cost

As discussed in the previous section, macroeconomic sensitivity analysis can be used to define regions of economic feasibility for such parameters as ϵ (material cost parameter), α (processing time parameter), etc.

Each of these parameters is, however, determined by various contributory factors. For example, the raw material cost for an NNS process is affected by the NNS envelope thickness, material losses during blank fabrication, the form of the raw material (i.e., billet or powder), the percentage of rare or strategic materials in the alloy (whose price could fluctuate widely) etc. Various combinations of these factors could give rise to the same value of ϵ .

Since material cost is an important constituent of the finished part cost, a more detailed analysis for this factor is justified. In general, the cost of raw material, C_{rm} , is given by:

$$C_{rm} = (\text{Weight})(\text{Form factor})(\text{Cost/pound of alloy}) \quad (16)$$

where the form of the raw material could be either powder or billet.

The weight of raw material needed depends on the finished part weight, the envelope weight, and the weight of material lost in blank fabrication. The cost per pound of the alloy is determined by the cost per pound of each constituent material, and the alloying percentage of each constituent. For simplicity, the alloy constituents are grouped in two classes: strategic materials, which are rare or difficult to obtain (whose price is likely to increase enormously in the future), and widely available, or ordinary materials (whose prices are likely to be fairly stable).

Quantifying these factors, raw material cost can be expressed as:

$$C_{rm} = (1 \times e \times W_f)(f) \left[\sum_{\text{Strategic}} p_i \times crm_i + \sum_{\text{Ordinary}} p_j \times crm_j \right] \quad (17)$$

$$\text{Then, } \epsilon = \frac{C'_{rm}}{C_{rm}}$$

$$\epsilon = \frac{(1' \times e' \times W_f)}{(1 \times e \times W_f)} \left(\frac{f'}{f} \right) \left(\frac{\sum_{\text{Strategic}} p_i \times crm_i + \sum_{\text{Ordinary}} p_j \times crm_j}{\sum_{\text{Strategic}} p_i \times crm_i + \sum_{\text{Ordinary}} p_j \times crm_j} \right)$$

$$\epsilon = \frac{\epsilon_1 \times \epsilon_2 \times \epsilon_3}{crm} \left(\sum_{\text{Strategic}} p_i \times crm_i + \sum_{\text{Ordinary}} p_j \times crm_j \right) \quad (18)$$

where: $\epsilon_1 = 1'/1$ $\epsilon_3 = f'/f$ $crm = \text{cost/pound of raw material in the original process}$
 $\epsilon_2 = e'/e$

By varying the parameters in Equation (12), we can evaluate the region of feasibility for ϵ . The intersection of this region with the region of economic feasibility (obtained through the macroeconomic sensitivity analysis) then provides feasible ranges for each of the parameters.

Application to Ti6242 Alloy Compressor Disk

Introduction

The selection of particular processing sequence for manufacturing a given component should be based on a thorough evaluation of the technological and economic feasibility of competing processes. In this section, the application of macroeconomic analysis to the evaluation of the latter criterion is demonstrated. The component selected for analysis is a dual property Ti6242 compressor disk. Four alternative processing sequences could be utilized to manufacture this product:

- a) Conventional press forge + machining
- b) Isothermal and hot die forging + machining
- c) Hot Isostatic Pressing (HIP) + hot forging + machining
- d) Dual property disk forging + machining

As depicted in Figure 2, each of these processing sequences can be broken down into a hierarchy of manufacturing stages, each of which makes a contribution to the cost of the finished part. At the lowest level the incoming raw material (whether in the form of raw melt or billets) is processed into the form of a blank. At the next level this blank undergoes a series of manufacturing operations in order to produce the desired finished product.

In order to form a basis for comparison, it is necessary that each of the processes should produce a finished component which either equals or exceeds a pre-selected set of baseline properties (eg., dimensional tolerances, finish, low cycle fatigue strength, and creep resistance). If these baseline properties are exceeded, then

it is conceivable that the overall life cycle cost will be decreased. In the case of the Ti6242 compressor disk, this irreducible set of properties is established by the existing manufacturing process - conventional press forging.

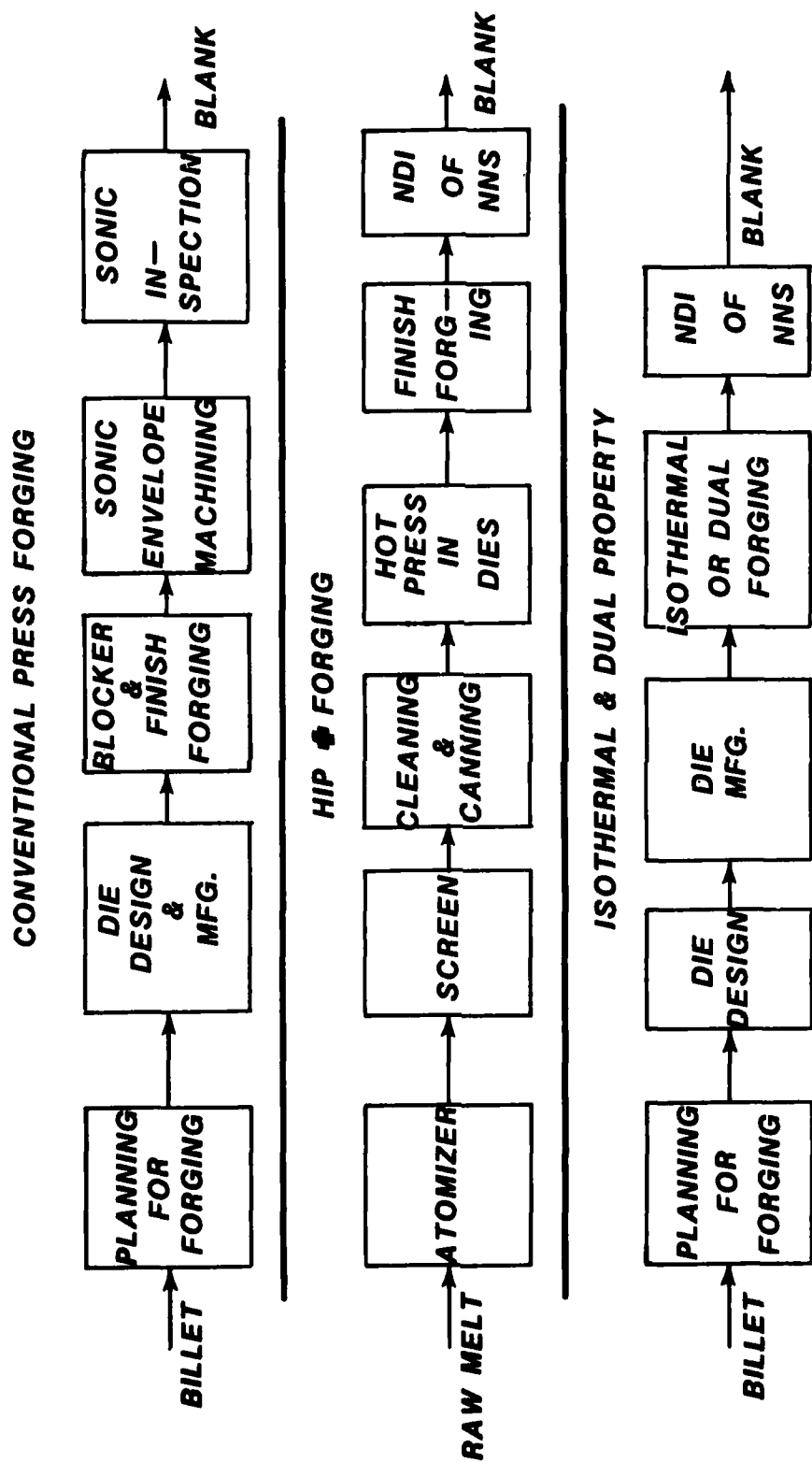
3.1 Processing Sequences

Figure 6 illustrates the manufacturing sequences for the four processes during the blank fabrication phase. Detailed operation sheets are included in the Appendix. It should be noted that HIP'ing of Titanium alloys is not yet a viable technique, due to difficulties at the stage of powder formation. However, the sequence of operations necessary has been established, and cost estimates can be made based on the present level of technology.

At the second level of manufacture, the processing operations for the four processes differ in the rough machining and targeting requirements. Only conventional press forging requires rough machining; the other three processes produce near net shape parts which can directly be finish machined. However, due to the minimal envelope thickness of these NNS processes, they require extensive targeting and positioning operations. Detailed processing steps are at the end of the appendix (after Nomenclature).

3.2 Time and Cost Parameters

The major time parameters necessary for this analysis are the manufacturing lead times for each process, setup times for each operation (based on a fixed lot size of 50 parts), and the processing times for each operation. The processing time is the largest of the machine time, planned labor time, and actual processing time obtained after applying allowances to the planned labor time. Figure 7 illustrates the definitions of these terms.



**FIGURE 6: ALTERNATIVE BLANK FABRICATION SEQUENCES
FOR Ti6242 COMPRESSOR DISK**

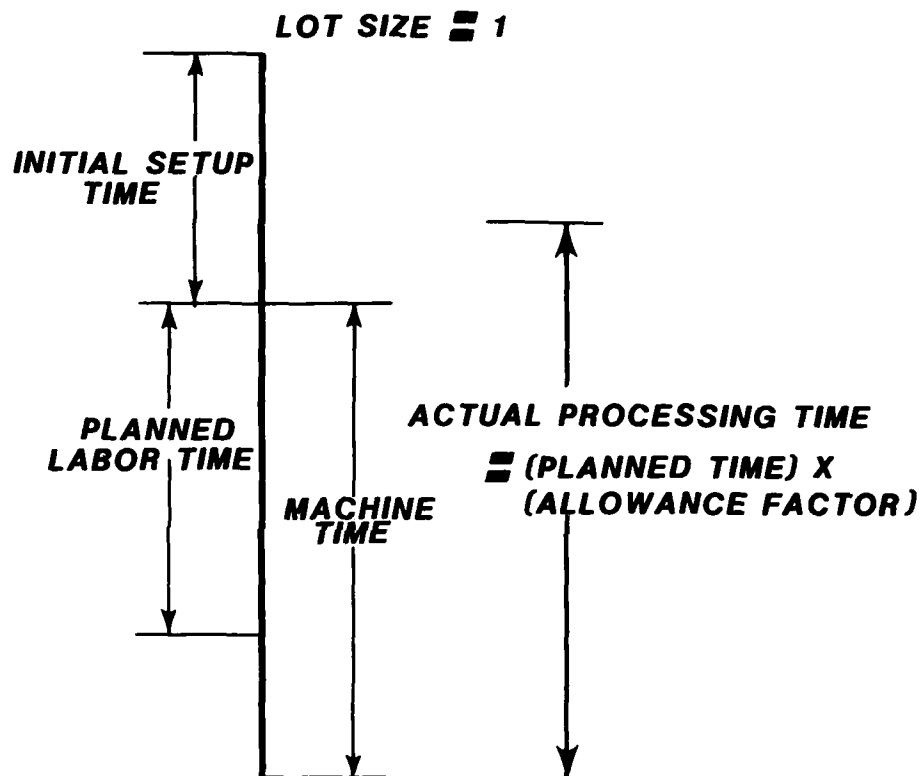


FIGURE 7: DEFINITIONS OF ROUTE SHEET TIME DATA

The cost parameters necessary for macroeconomic analysis are those identified in Section 2.4. Briefly, they are: the raw material cost (C_{rm}), the consumable cost (C_c), the cost of tooling, die design and die fabrication (C_{tc}), and the cost rate (LMS_p) for each operation.

3.3 Sensitivity Analysis Parameters

In order to conduct a cost-sensitivity analysis for manufacturing the compressor disk, the equations developed in Section 2.5 were used. To establish compatibility of the available data with the model requirements, a few parameters need to be defined in detail.

The total processing time (T) includes the processing and setup time at the blank preparation as well as manufacturing levels. Similarly, T_p and T_s are the total processing time and total setup time respectively, for both stages of manufacture.

Initial values for the sensitivity parameters ($\alpha, \beta, \gamma, \delta, \epsilon, \sigma$) were obtained by reference to the results of the detailed macroeconomic analysis presented in the next section.

Although the value of the LMS (Labor + Machine + Support) cost rate varies widely from operation to operation, a weighted average rate can be used to describe the overall cost rate for a process.

3.4 Comparison of Alternatives

Blank Fabrication Level: The input at this level of manufacture is the raw material. The output is the completed blank. The detailed process sheets are included in the Appendix.

Table II lists the percentage distributions of processing costs for each of the alternatives. Tables III and IV list the cost and time element for each process.

It will be seen from these tables that the raw material cost is a major factor consisting of 60 to 75% of the total cost at this level of manufacture. A decrease in this cost item, particularly in the case of HIP, will drastically affect the total cost.

Manufacturing Level: The input during this phase is the completed blank, and the output is the finished part. Detailed process sheets are listed in the Appendix.

Table V lists the percentage distributions of processing costs. Tables VI and VII list the cost and time elements.

It will be noted that the requirement for rough machining is eliminated for the three NNS processes, but an additional operation, targeting, is required. The homogenous microstructure produced by HIP allows a 25% increase in the machining rate for that process.

Figure 8 is an illustration of cumulative cost expenditures at each point in the processing cycle.

3.5 Sensitivity Analysis for Compressor Disk

In order to demonstrate the application of sensitivity analysis, it will be used to compare conventional press forging with HIP + forging. The parameters used are those defined in Sections 2.4 and 3.3.

The most important sensitivity parameters for this component are: α , influencing the total processing time, and ϵ , affecting the cost of raw material. The other parameters are less important, either because the cost elements they influence are negligible, or because they will not be substantially influenced by future process development.

BLANK FABRICATION LEVEL

TABLE II: Percentage Distribution of Processing Costs
During Blank Fabrication

	PROCESS			
	Conv. Press	HIP+ Forge	Iso- Thermal	Dual Property
Container & Powder Preparation		18.6		
HIP		5.5		
Pre-Machining	1.8	2.0	2.3	2.5
Pre-Forming	3.6	4.1	3.9	4.0
Cleaning/Preparation	0.5			
Blocking	6.5			
Cleaning/Trimming/Preparation	4.2	4.8	3.0	3.1
Finish Forging	5.8	4.9	20.7	18.5
Cleaning/Trimming/Preparation	2.1	2.4	2.6	2.6
Heat-Treatment	12.9	14.6	17.2	17.7
Machining	50.6	25.9	34.4	35.4
Inspection	11.5	13.1	15.3	15.8
Testing/Shipping	0.5	0.6	0.7	0.7
Total:	100%	100%	100%	100%
Total Cost/Part:	<u>\$775.80</u>	<u>\$683.30</u>	<u>\$581.85</u>	<u>\$565.60</u>

BLANK FABRICATION LEVEL

TABLE III: Cost Elements (Lot Size = 50 Parts)

	C	H	I	D
Raw Material Cost (\$/part)	950	1900	712.5	712.5
Tooling Cost (\$/lot)	550	5000	5000	5000
Processing Cost (\$/part)	775.8	683.3	581.85	565.6
Consumable Cost (\$/lot)	400	350	350	350
Total Cost (\$/part)	1744.8	2690.3	1401.35	1385.1

TABLE IV: Time Elements

	C	H	I	D
Lead Time (months)	3	9	6	6
Total Process Time (hrs./part)	19.14	18.04	12.83	12.73

C = Conventional; H = HIP + forge; I = Isothermal; D = Dual Property

MANUFACTURING LEVEL

TABLE V: Percentage Distribution of Processing Costs
During Manufacture

	C	H	I	D
Rough Turning	31.3			
Targeting		23.2	20.5	20.5
Finish Turning	23.3	24.9	27.0	27.0
Machining	16.9	16.8	19.5	19.5
Preparation/Inspection	12.9	16.8	14.9	14.9
Finish Machining	6.5	6.4	7.6	7.6
Cleaning/Inspection	9.1	11.9	10.5	10.5
Total:	100%	100%	100%	100%
	<u>\$2031.12</u>	<u>\$1554.22</u>	<u>\$1756.02</u>	<u>\$1756.02</u>

TABLE VI: Cost Elements (Lot Size = 50 Parts)

	C	H	I	D
Blank Cost (\$/part)	1744.8	2690.3	1401.35	1385.1
Processing Cost (\$/part)	2031.12	1554.22	1756.02	1756.02
Consumable Costs (\$/part)	300	200	200	200
Total Cost (\$/part)	4075.92	4444.52	3357.37	3341.12

TABLE VII: Time Elements

	C	H	I	D
Setup Time (hrs./lot)	34	213	213	213
Manufacturing Time (hrs./part)	75.62	56.04	62.87	62.87
Total Processing Time (hrs./part)	76.3	60.3	67.13	67.13

C = Conventional; H = HIP + forge; I = Isothermal; D = Dual Property

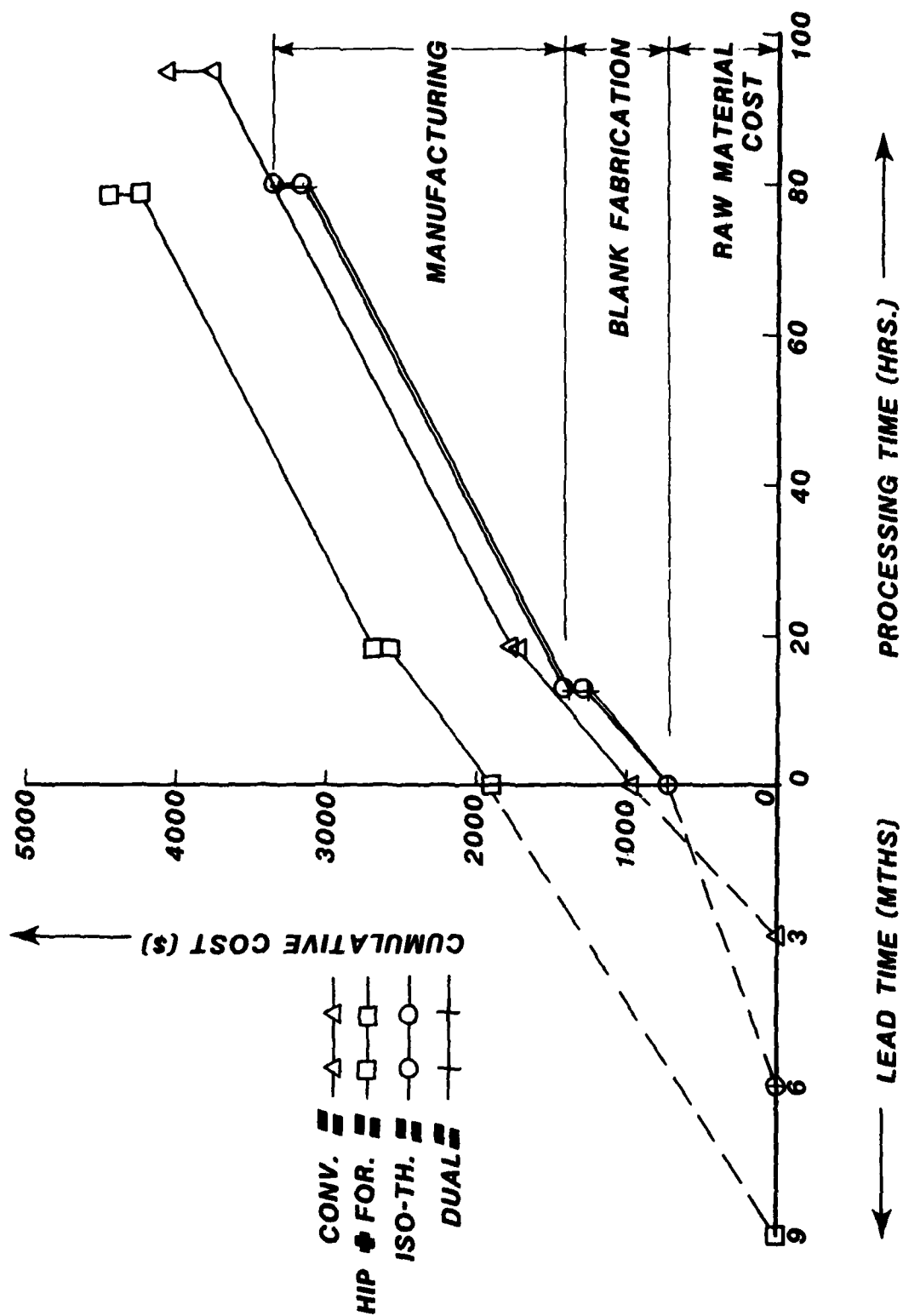


FIGURE 8: CUMULATIVE COST AND TIME EXPENDITURES DURING MANUFACTURING

Further, it is not likely that the total processing time, T_p can be improved very significantly in the future for the HIP process. On the other hand, the material cost is very high compared to the other processes, mainly because the technology for producing Titanium alloy powder is still in the developmental phase. Therefore, raw material cost is going to play a major role in the eventual acceptance or rejection of this process.

The parameter values used in the subsequent analysis were obtained from the results presented in Section 3.4. These values are:

Baseline data for conventional forging:

C_{rm} = Cost of raw material/part = \$950

C_{tc} = Cost of tooling/part = \$11

C_c = Consumable costs/part = \$308

T_p = Total processing time = 75.62 hrs./part

T_s = Total setup time = 34 hrs./lot

LMS = Weighted average of cost rates = \$28.83/hr.

N = Lot size = 50

Sensitivity parameters:

$\alpha = T_p' / T_p = 0.74$

$\beta = T_s' / T_s = 6.3$

$\gamma = C_{tc}' / C_{tc} = 9.1$

$\delta = C_c' / C_c = 0.67$

$\epsilon = C_{rm}' / C_{rm} = 2.0$

$\sigma = LMS' / LMS = .977$

Assumptions:

P = Number of parts produced/year = 400

ΔI_0 = Additional investment = \$400k

k = (Interest + Inflation) rate = 20%

DROI = Desired return on investment = 20%

In Figure 9, the additional investment, ΔI_0 , is assumed to vary between zero and one million dollars. The payback period, t , is the reciprocal of the desired return on investment. Thus, in Figure 2, the DROI varies from 33% to 10%. The individual plots represent the maximum value that ϵ , the raw material cost factor, can take if the investment is to be justified under the given conditions. Thus, only the area below each curve is within the feasible region for HIP.

Alternatively, if it is decided that a certain value for the payback period must be obtained before the investment will be committed, then the plot will enable the determination of the maximum investment level which is feasible. The area to the right of the individual curves is within the feasible region.

The economically feasible regions in Figure 9 are those marked. The process is only feasible for a payback period greater than 5 years, and an added investment of less than 200 thousand dollars.

Figure 10 illustrates how the number of parts which will be produced per year affects the limiting values for raw material cost. As may be imagined, the larger the yearly production, the higher is the maximum raw material cost which is permissible.

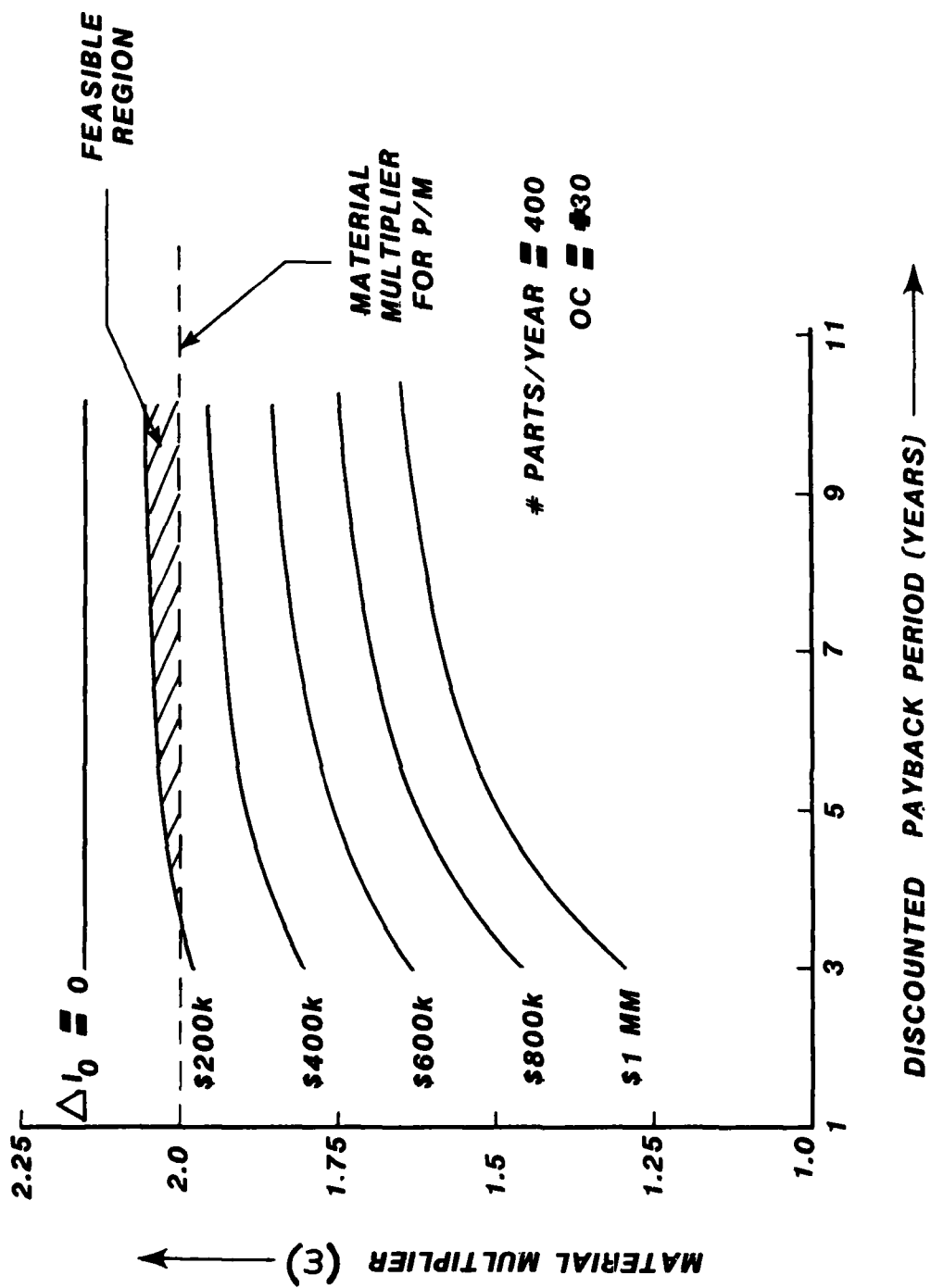


**FIGURE 9: SENSITIVITY ANALYSIS FOR HIP \clubsuit FORGING,
MATERIAL MULTIPLIER vs. PAYBACK PERIOD
DISCOUNTED**

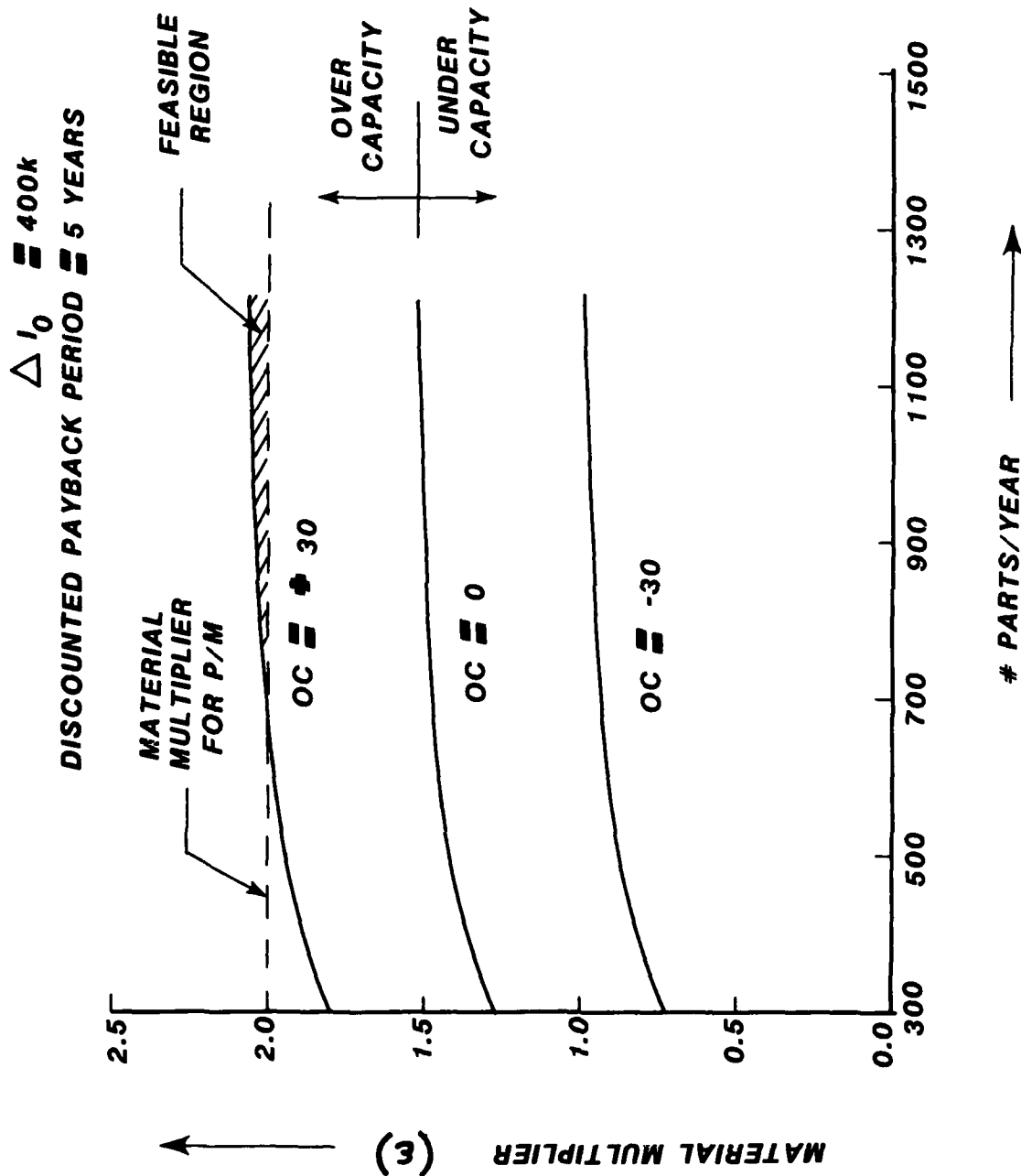


FIGURE 10: SENSITIVITY ANALYSIS FOR HIP + FORGING.
MATERIAL MULTIPLIER vs. NUMBER OF PARTS PRODUCED/YEAR

Three scenarios are depicted in Figure 10, based on the value of the opportunity cost, oc . A positive value for oc implies that the job shop is working at a high utilization rate, and therefore that the decrease in processing time that HIP represents would be very valuable. A negative opportunity cost, on the other hand, implies that the job shop is under-utilized, and so a decrease in processing time would not help the overall operation of the job shop very greatly.

The economically feasible region in Figure 10 is the shaded area. Note that the process is feasible only with a positive opportunity cost (i.e., when the shop is operating under capacity).

In addition to the variables examined here, sensitivity analysis could also be used to evaluate a number of other trade-offs and economic decisions, such as:

High ΔI_0 (low LMS) vs. Low ΔI_0 (high LMS) to examine a capital intensive vs. a labor intensive process.

High setup time (low processing time) vs. Low setup time (high processing time).

The affect that inflation rate and interest rate will have on a contemplated investment.

The influence of non-uniform cash flows (in this example the initial investment is lump sum, and savings are assumed to accrue uniformly), etc.

Conclusions

Previously developed macro- and microeconomic models of machining and life cycle cost models formed the basis for the establishment of the following economic models for NNS alternatives:

- 1) A Life Cycle Cost model to analyze the interaction between system acquisition costs and overall costs over the life cycle of the system.
- 2) A macroeconomic model to examine acquisition costs at the processing sequence level.
- 3) A macroeconomic sensitivity analysis to examine the trade-offs between the major cost parameters at the sequence level.
- 4) A microeconomic sensitivity analysis of the factors influencing raw material costs.

To illustrate the application of the NNS macroeconomic model, four alternatives for the Ti6242 compressor disk were investigated: conventional press forging, HIP + forging, isothermal forging, and dual property hot die forging. The data for the illustration was obtained from the experiments on dual property disk. The following specific conclusions can be drawn:

- A) The HIP + forge process is presently uneconomical. Although blank preparation costs for the process are comparable with conventional forging, and further processing costs are actually lower, the high cost of Titanium powder causes the overall acquisition cost to be much higher. Further research on powder preparation techniques is therefore indicated.
- B) The isothermal process is cost-effective compared to conventional

forging. Raw material, blank fabrication, and further processing costs are all lower for this process. Tooling costs are somewhat higher, but not enough to influence the decision.

C) Dual property hot die forging has a cost structure very similar to that of isothermal forging. The conclusions for this process are identical to those discussed for isothermal forging.

Recommendations

In the future, work should be directed toward validation and extension of the existing models. The following specific activities need to be undertaken:

- 1) The existing models should be thoroughly validated by applying them to several existing components.
- 2) In order to have available a complete methodology for the selection of a processing sequence, two additional models should be developed.

The first is a microeconomic model for forging processes, which would allow cost trade-offs to be made at a processing unit. The model should examine the interactions between process rate and interruption frequency, tool cost, machine down time, etc.

The second model required is for the macroeconomic analysis of auxiliary costs (coolant/lubrication, rework, maintenance, in-process inspection, etc.). At present, these costs are incorporated in the existing model in the form of overall estimates. In view of the importance of these costs, a method for optimizing these parameters is needed.

Finally, a model should be developed for the representation of the part throughput time through the forge shop. This would include part waiting and transportation times, rework, operator controlled times, etc.

References

- (1) V. A. Tipnis, S. J. Mantel, Jr., and G. L. Ravignani, "Economic Models for Process Development," Process Modeling Activity Proceedings, October 1980, ASM.
- (2) V. A. Tipnis, G. L. Ravignani, and S. J. Mantel, Jr., "Economic Feasibility of Laser Assisted Machining (LAM). Presented at the NAMRC IX Conference.
- (3) V. A. Tipnis, S. J. Mantel, Jr., and G. L. Ravignani, "Sensitivity Analysis for Macroeconomic and Microeconomic Models of New Manufacturing Processes." To be presented at the CIRP Toronto Conference, September 1981. Annals of the CIRP, Volume 30/1.
- (4) G. L. Ravignani, M. Y. Friedman, and V. A. Tipnis, "Cutting Rate - Tool Life Functions (R-T-F), General Theory and Applications", Annals of the CIRP, Volume 25/1/1977, pp. 295-301.
- (5) W. W. Shoemaker, "Life Cycle Cost as a Tool in the Detail Design of Advanced Propulsion Systems," AIAA/SAE/ASME, Sixteenth Joint Propulsion Conference, Hartford, Connecticut, June 30 - July 2, 1980.
- (6) F. W. Tegarden and W. W. Shoemaker, "Life Cycle Cost in Advanced Technology Engine Development," SAE Aerospace Meeting, San Diego, California, November 27-30, 1978.

Nomenclature

- LMS = (Labor + Machine + Support) cost rate (money/hr.)
- C_{tc} = Tooling cost for entire process per part (money/part)
- C_c = Consumable cost for entire process per part (money/part)
- oc = Opportunity cost rate (farmout rate - inhouse rate)
- C_{rm} = Cost of raw material per part (money/part)
- crm_i = Cost per pound of individual materials in an alloy
- LMS_p = (Labor + Machine + Support) cost rate for a processing unit (money/hr.)
- ctc = Tooling cost per part at a processing unit (money/part)
- cn = Consumable cost per part at a processing unit (money/part)
- γC_{tc} = Total tooling cost per part for the new process (money/part)
- δC_c = Total consumable cost per part for the new process (money/part)
- ϵC_{rm} = Cost of raw material per part for the new process (money/part)
- σLMS = (Labor + Machine + Support) cost rate for the new process (money/hr.)
- T_p = Total processing time for a process (hrs./part)
- T_s = Total setup time for a process (hrs.)
- t_p = Processing time per part at a processing unit (hrs./part)
- t_s = Setup time at a processing unit (hrs.)
- tw = Waiting time per part at a processing unit (hrs./part)
- tt = Transportation time per part to a processing unit (hrs./part)
- αT_p = Total processing time per part for the new process (hrs./part)
- βT_s = Total setup time for the new process (hrs.)

N = Lot size
 np = Number of processing units in sequence
 P = Number of parts produced per year
 epf = Expectation of number of part failures per year
 pe = Probability that part failure will lead to engine replacement
 nv = Average number of parts maintained in inventory
 PC = Part replacement cost (money)
 EC = Engine replacement cost (money)
 H = Average number of flight hours per year (hrs./year)
 FC = Cost per gallon of fuel (money/gallon)
 cf = Specific fuel consumption (gallons/hour/engine)
 ne = Number of engines in a plane
 l = (Raw material weight)/(Blank weight)
 e = (Blank weight)/(Finished part weight)
 W_f = Finished part weight
 f = Form factor for raw material as compared to standard billet
 p_i = Fraction (by weight) of individual elements in an alloy
 ΔI₀ = Added investment necessary for the new process (money)
 ROI = Return on investment

$$\phi = \text{Discount factor} = \sum_{t=1}^n \frac{1}{(1+k)^t}$$
 k = Discount rate = (interest rate + inflation rate)
 t = Payback period (= 1/ROI)

PROCESSING SEQUENCES

ESTIMATED COST RATE AND MAN HOURS FOR FULL SCALE Ti6242 COMPRESSOR DISK BLANK FABRICATION PHASE

Sequence Code	Operation	Cost Rate (\$/hr.)	Manhours per piece			
			C	H	I	D
I	Container Fabrication	30	-	0.6	-	-
CONTAINER & POWDER PREPARATION	Powder Blending & Screening	30	-	2.5	-	-
	Powder Filling	25	-	0.5	-	-
	Degassing	35	-	0.3	-	-
	Container Sealing	30	-	0.2	-	-
	Leak Checking	25	-	0.2	-	-
II HIP, TAP DENSITY CHECK, CONTAINER REMOVAL	HIP'ing	80	-	0.4	-	-
	Tap Density Check	25	-	0.2	-	-
	Container Removal	10	-	0.1	-	-
III PRE-MACHINING & PREPARATION	Cut to Weight & S/N	25	.25	.25	.25	.25
	Chamfer Ends	25	.15	.15	.15	.15
	Blast and Coat	25	.15	.15	.15	.15

C = Conventional; H = HIP + forge; I = Isothermal; D = Dual Property

ESTIMATED COST RATE AND MAN HOURS FOR FULL SCALE Ti6242 COMPRESSOR DISK
BLANK FABRICATION PHASE (cont'd)

Sequence Code	Operation	Cost Rate (\$/hr.)	Manhours per piece			
			C	H	I	D
IV PRE-FORMING	Setup Die, Heat and Press	50	.12	.12	.12	.12
	Heat, Flatten/Upset/Pre-forming	100	.20	.20	.15	.15
	Dis-assemble Dies	100	.02	.02	.02	.02
V CLEANING/ PREPARATION	Blast and Coat	25	.15	-	-	-
VI BLOCKING	Setup Die Heat & Blocker Dies	225	.20	-	-	-
	Heat and Block	225	.20	-	-	-
VII CLEANING/ TRIMMING/ PREPARATION	Trim F'ash	25	.50	.50	-	-
	Blast, Salt Descale, Etch Clean	25	.25	.25	.25	.25
	Grind & Inspect	25	.40	.40	.30	.30
	Blast & Coat	25	.15	.15	.15	.15

C = Conventional; H = HIP + forge; I = Isothermal; D = Dual Property

ESTIMATED COST RATE AND MAN HOURS FOR FULL SCALE Ti6242 COMPRESSOR DISK
BLANK FABRICATION PHASE (cont'd)

Sequence Code	Operation	Cost Rate (\$/hr.)	Manhours per piece			
			C	H	I	D
VIII FINISH FORGE	Setup Finish Dies	35	.08	.08	.16	.16
	Setup Heat	100	.04	.04	-	-
	Heat Dies	100	-	-	.25	.20
	Heat & Finish Forge	225	.15	.10	.35	.30
	Remove Dies from Press	225	.02	.02	.05	.05
IX CLEANING/ TRIMMING	Blast, Salt Descale, Chem. Etch	25	.08	.08	.05	.05
	Grind and Inspect	25	.40	.40	.30	.30
X HEAT TREAT	Heat Treatment	100	1.0	1.0	1.0	1.0
XI MACHINING	Blast	25	.08	.08	.05	.05
	Chem. Mill .010 to .020 inch per surface	25	.10	.10	.10	.10
	Setup VTL	35	.02	.02	.02	.02
	Remove Test Ring	35	.56	.56	.56	.56
	Setup VTL	35	.02	.02	.02	.02

C = Conventional; H = HIP + forge; I = Isothermal; D = Dual Property

ESTIMATED COST RATE AND MAN HOURS FOR FULL SCALE Ti6242 COMPRESSOR DISK
BLANK FABRICATION PHASE (cont'd)

Sequence Code	Operation	Cost Rate (\$/hr.)	Manhours per piece			
			C	H	I	D
XI (cont'd) MACHINING	Machine OD & Remove Flash	35	1.5	.5	.5	.5
	Finish Machine Side One	35	6.0	3.0	3.0	3.0
	Finish Machine Side Two	35	3.0	1.5	1.5	1.5
XII INSPECTION	Sonic & Sonic Review	35	1.4	1.4	1.4	1.4
	Dye Penetrant	25	.08	.08	.08	.08
	Dimensional Check	25	.40	.40	.40	.40
	Zyglow Inspect	25	.80	.80	.80	.80
	Grind and Inspect	25	.33	.33	.33	.33
	Brinell, Mark/ Identification	25	.10	.10	.10	.10
XIII PACKING	Pack for Shipping	25	.07	.07	.07	.07

C = Conventional; H = HIP + forge; I = Isothermal; D = Dual Property

ESTIMATED COST RATE AND MAN HOURS FOR FULL SCALE Ti6242 COMPRESSOR DISK
BLANK PROCESSING

Operation Code	Operation Description	Cost Rate (\$/hr.)	Setup Time (hrs./lot)	Processing Time (hrs./ piece)			
				C	H	I	D
I ROUGH TURN	Face Turn	30	3.0	1.78	-	-	-
	Rough Contour	30	5.0	5.73	-	-	-
	Semi-Finish	30	5.0	5.80	-	-	-
	Turn Fwd. Rim	30	4.0	3.16	-	-	-
	Turn Aft. Rim	30	4.0	4.28	-	-	-
II TARGET	Target	30	4.0/ Piece	-	8.0	8.0	8.0
III FINISH TURN	Finish Fwd. Web	30	4.0	6.03	4.5	6.03	6.03
	Finish Aft. Web	30	4.0	5.59	4.2	5.59	5.59
	Bench Inspect	25	0.0	0.7	0.7	0.7	0.7
	Inspect Coupon	28	0.0	1.0	1.0	1.0	1.0
	Inspect Slots	25	0.0	3.0	3.0	3.0	3.0

C = Conventional; H = HIP + forge; I = Isothermal; D = Dual Property

ESTIMATED COST RATE AND MAN HOURS FOR FULL SCALE Ti6242 COMPRESSOR DISK
BLANK PROCESSING (cont'd)

Operation Code	Operation Description	Cost Rate (\$/hr.)	Setup Time (hrs./lot)	Processing Time (hrs./ piece)			
				C	H	I	D
IV MACHINING	Pre-Break Slots	25	0.0	2.82	2.2	2.82	2.82
	Radius Slots	30	0.2	0.8	0.6	0.8	0.8
	Mill Slots	30	4.0	8.19	6.2	8.19	8.19
V PREPARATION INSPECTION	Deburr	20	0.0	7.65	7.65	7.65	7.65
	Dimension Inspect	20	0.0	2.0	2.0	2.0	2.0
	Degrease	20	0.0	0.19	0.19	0.19	0.19
	Process FPI	20	0.0	0.4	0.4	0.4	0.4
	FPI	20	0.0	0.31	0.31	0.31	0.31
	Shot Peen	20	0.0	2.53	2.53	2.53	2.53
VI FINISH MACHINING	Size Fwd. Rabbets	30	0.0	2.4	1.8	2.4	2.4
	Size Aft. Rabbets	30	1.0	2.0	1.5	2.0	2.0

C = Conventional; H = HIP + forge; I = Isothermal; D = Dual Property

ESTIMATED COST RATE AND MAN HOURS FOR FULL SCALE Ti6242 COMPRESSOR DISK
BLANK PROCESSING (cont'd)

Operation Code	Operation Description	Cost Rate(\$/hr.)	Setup Time (hrs./lot)	Processing Time (hrs./ piece)			
				C	H	I	D
VII	Inspect Rabbets	20	0.0	0.93	0.93	0.93	0.93
CLEANING/ INSPECTION	Deburr	20	0.0	3.9	3.9	3.9	3.9
	Degrease	20	0.0	0.19	0.19	0.19	0.19
	Process FPI	20	0.0	0.4	0.4	0.4	0.4
	FPI Rabbets	20	0.0	0.24	0.24	0.24	0.24
	Shot Peen Rabbets	20	0.0	1.6	1.6	1.6	1.6
	Grit Blast	20	0.0	0.0	0.0	0.0	0.0
	Final Inspect	20	0.0	2.0	2.0	2.0	2.0

C = Conventional; H = HIP + forge; I = Isothermal; D = Dual Property

DATE
FILMED
→ 8